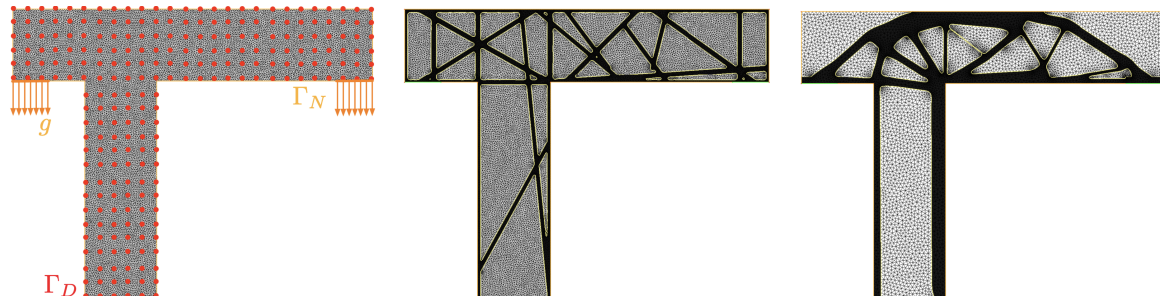
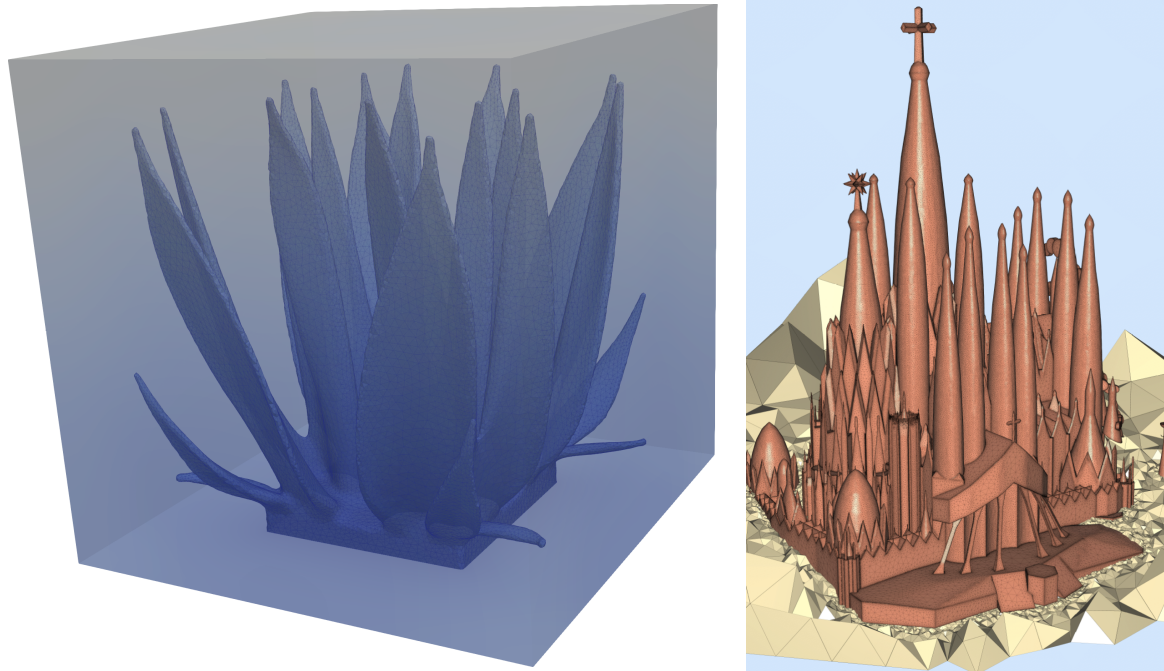


Habilitation à diriger des recherches  
A few contributions in shape and topology optimization

Charles Dapogny



Rapporteurs :

- Bertrand Maury (*Laboratoire de Mathématiques d'Orsay*)
- Robert V. Kohn (*Courant Institute of Mathematical Sciences, New York University*)
- James A. Sethian (*Department of Mathematics, University of California, Berkeley*)

Soutenue publiquement à Grenoble le 15 Avril 2024, devant un jury composé de :

Fioralba Cakoni  
Antonin Chambolle  
Robert V. Kohn  
Bertrand Maury  
Bruno Levy  
Nicolas Moës  
Édouard Oudet

*Department of mathematics, Rutgers University*  
*Centre de Mathématiques de la Décision, Université Paris-Dauphine*  
*Courant Institute of Mathematical Sciences, New York University*  
*Laboratoire de Mathématiques d'Orsay, Université Paris-Saclay*  
*Inria Paris-Saclay*  
*École Centrale de Nantes*  
*Laboratoire Jean Kuntzmann, Université Grenoble Alpes*



# Remerciements

Les travaux rapportés dans ce mémoire et les aventures humaines en filigrane sont avant tout les fruits de rencontres et d'échanges exceptionnels.

Je suis tout d'abord redevable aux trois rapporteurs de ce manuscrit : c'est une chance extraordinaire que des personnalités scientifiques telles que Robert Kohn, Bertrand Maury et James Sethian aient consacré tant de temps à une lecture aussi minutieuse de ce document. Leur patience, leur intérêt et leur bienveillance m'honorent. Je ne suis pas moins flatté que des experts tels que Fioralba Cakoni, Nicolas Moës, Antonin Chambolle et Bruno Levy prennent part au jury de soutenance. Le fait qu'Édouard préside ce dernier occupe bien sûr une place particulière, tant son soutien et ses conseils avisés ont été cruciaux : nos très nombreuses discussions et collaborations ont guidé le contenu et la rédaction de ce manuscrit, pour le meilleur et pour le pire !

Il faut dire que, dès mes premiers pas dans le monde de la recherche, j'ai eu la chance de bénéficier d'un entourage exceptionnel. Je pense bien sûr à Grégoire, qui m'a tant appris, m'a toujours encouragé et soutenu. Quelques années plus tard, je suis émerveillé comme au premier jour de constater à quel point ses connaissances encyclopédiques, son engagement et sa générosité ont été le ciment d'une famille mathématique aussi solide et agréable. Je pense également à Pascal ; bien que nous ayons moins d'occasions naturelles d'interagir depuis son envol vers les cimes de la Tour Zamansky, je suis ravi, mais pas surpris, qu'il trouve toujours le temps de bavarder autour d'un café (ou deux). Et comment oublier Marc et Georgios ? De nombreuses années et quelques changements professionnels plus tard, c'est une richesse exceptionnelle que nous continuons, pour encore longtemps j'espère, à échanger des idées (pas toujours lumineuses !) concernant l'optimisation de formes... entre autres. En grandissant (un peu), j'ai eu la chance immense de découvrir l'univers américain auprès de Michael, qui a eu la générosité de me recruter sur un thème à propos duquel je ne connaissais rien et la patience de me le faire découvrir. Je suis sincèrement heureux que nous puissions continuer à travailler ensemble, maintenant avec Éric et Yves.

Après avoir réalisé le hold-up du siècle et peu étudié le choix d'un laboratoire d'affectation, Grenoble s'est très rapidement imposé comme une évidence. Édouard (encore lui !) et Éric m'ont immédiatement inclus dans tous leurs projets – autant d'opportunités de découvrir de bien belles choses : des mathématiques passionnantes, de superbes montagnes, du bon vin. Malheureusement, je reste un piètre skieur ; quant à grimper... Mon épanouissement à Grenoble leur doit beaucoup. J'ai toujours pris beaucoup de plaisir à discuter avec Raf, de mécanique un peu, beaucoup de voyages et de plein d'autres choses passionnantes ! Avec Franck, j'ai adoré courir, prendre des bières pour parler de bouquins, de séries, et aussi de maths – ce sont finalement nos discussions de comptoir qui se sont concrétisées en véritable collaboration scientifique... Je suis persuadé que l'on saura réitérer l'expérience ! Le plaisir quotidien du LJK doit évidemment beaucoup à Sylvain, pour toutes ces discussions (que d'aucuns qualifieront de commérages), pour ce tandem d'enseignants de choc en AFCD, et pour cette belle compétition quant à savoir qui laisserait traîner le plus d'affaires de sport dans le bureau... qu'il remporte haut-la-main. Un grand merci également à Boris, Clément, Manu, Jérôme, Stéphane, à G aëlle, Cathy, et à quelques petits jeunes maintenant partis : Matthias, Eloi, Anatole, Nils.

De nombreux autres collaborateurs, un peu plus distants, ont également beaucoup compté pour moi. J'ai beaucoup aimé travailler avec Cécile – qui nous a malheureusement quittés trop tôt – Samuel, Yannick, François, Alex, Marc, et plus récemment avec Peter et Alessio. Même si nous ne collaborons pas (encore !) à proprement parler, j'ai toujours beaucoup de plaisir à discuter avec François Murat, Antoine Henrot, Dorin Bucur. Je dois des remerciements particuliers à Algiane, qui s'est tant investie dans le projet **mmg** ; celui-ci n'aurait jamais pu trouver une telle maturité sans ses efforts constants.

Autant que les maîtres, les étudiants avec qui j'ai eu la chance de partager m'ont énormément appris. Je suis vraiment ravi que Nicolas et Florian aient choisi de s'orienter vers une carrière académique, dans laquelle ils excellent déjà, et qui nous donnera – je l'espère – l'occasion de collaborer à nouveau. La relève est assurée par une nouvelle génération non moins méritante : nos discussions avec Carlos, puis Julien, me comblient de bonheur.

J'ai la chance de compter de nombreux autres amis dans la recherche. Un grand merci à Lise-Marie et Tonatiuh, pour leur accueil à Tucson, et toutes ces discussions épineuses. Merci aussi à Swann, Thibault, Vincent, et bien sûr Pierre et Mamadou, amis de longue date et acteurs d'un superbe séjour au Sénégal (sauf le retour...).

Je ne peux pas terminer ces remerciements sans quelques mots peut-être encore plus personnels. J'aimerais dire à mes amis de toujours, Alex, Maro, Matthieu, combien ils comptent pour moi, combien le fait que l'on se voie maintenant trop peu ne veut en rien dire qu'ils sont moins importants.

J'ai la chance d'avoir été adopté par une chouette belle-famille, où l'on mange bien, boit beaucoup d'adjuvants (pour l'inspiration), joue bien, et où l'on fait de belles balades en montagne... Que demander de plus ?

Au terme de cette page, de loin la plus longue et difficile à écrire de ce mémoire, à ma famille : Môman, Pôpa, Nonow, Marion, Tata – je n'oublie pas la Petite dernière. Je ne trouve pas les mots pour décrire ce que vous m'apportez, combien vous comptez. À Blanche, qui me fait tant découvrir, qui me soutient depuis tout ce temps, dans les moments les plus difficiles... pour encore longtemps, je l'espère. Sans vous, rien de tout cela n'aurait de sens.

# Contents

Chapter 1. Preliminaries: Shape and topology optimization algorithms and their implementation	23
1.1. A FEW SELECTED HISTORICAL MILESTONES . . . . .	23
1.1.1. The isoperimetric inequality	23
1.1.2. Optimal design in architecture	24
1.1.3. Optimal design and the calculus of variations	24
1.1.4. Toward modern shape and topology optimization in structural and aeronautical engineering	25
1.2. MATHEMATICAL MODELS FOR CONDUCTIVE MEDIA AND LINEARLY ELASTIC STRUCTURES . . . . .	26
1.2.1. The conductivity equation	26
1.2.2. Linear elastic structures	29
1.2.3. Shape optimization of elastic structures	37
1.3. MATHEMATICAL REPRESENTATION OF SHAPES AND THEIR VARIATIONS . . . . .	38
1.3.1. The thorny question of the representation of shapes	38
1.3.2. Non existence of optimal shapes: the homogenization phenomenon	39
1.3.3. Shape derivatives	41
1.3.4. Topological derivatives	53
1.3.5. A focus on the Hilbertian method for handling shape derivatives	54
1.4. NUMERICAL IMPLEMENTATION OF SHAPE OPTIMIZATION ALGORITHMS . . . . .	56
1.4.1. General outline of a shape and topology optimization algorithm	56
1.4.2. Preliminaries about meshes	57
1.4.3. Basic stakes about remeshing	58
1.4.4. The historical Lagrangian methods for shape optimization	59
1.4.5. Density-based formulations	60
1.4.6. The level set method for shape optimization	63
1.4.7. The level set based mesh evolution method	67
1.4.8. Bringing topological derivatives into play	71
Appendices	75
1.A. TECHNICAL FACTS . . . . .	75
1.A.1. A short reminder of the differential geometry of hypersurfaces	76
1.A.2. Change of variables formulas	77
1.A.3. The Green's formula	78
1.A.4. The implicit function theorem	79
1.A.5. Linear interpolation on the unit sphere of a Hilbert space	79
1.A.6. A glimpse of elliptic regularity	79
Chapter 2. Shape and topology optimization under uncertainties	85
2.1. OPTIMAL DESIGN IN THE WORST-CASE SCENARIO . . . . .	87

2.1.1. A formal, general linearization method for worst-case design	87
2.1.2. A couple of numerical results	89
2.2. SHAPE OPTIMIZATION UNDER POROSITY CONSTRAINTS.....	91
2.2.1. Formal presentation of the mathematical model	92
2.2.2. Two numerical examples of robust optimization of shapes taking into account the emergence of porosities	94
2.3. OPTIMAL DESIGN UNDER RANDOM UNCERTAINTIES .....	96
2.3.1. Formal presentation of the main ideas in an abstract setting	97
2.3.2. A few numerical results	101
2.4. A PERSPECTIVE: DISTRIBUTIONALLY ROBUST SHAPE OPTIMIZATION .....	103
2.4.1. Formal presentation of the main ideas	104
2.4.2. Two numerical examples	106
2.4.3. Perspectives	108
<b>Appendices</b>	110
2.A. A FEW WORDS ABOUT MEASURE THEORY .....	110
2.B. THE KARHUNEN-LOÈVE DECOMPOSITION .....	112
2.B.1. Preliminaries about tensor products of Hilbert spaces	113
2.B.2. An abstract decomposition theorem for elements in tensor product spaces	114
2.B.3. The Karhunen-Loève decomposition of square-integrable random fields	116
<b>Chapter 3. Geometric and manufacturing constraints in shape and topology optimization</b>	119
3.1. PRELIMINARIES: THE SIGNED DISTANCE FUNCTION TO A DOMAIN AND ITS APPLICATIONS IN SHAPE OPTIMIZATION .....	119
3.1.1. About the signed distance function	120
3.1.2. Differentiability of the signed distance function with respect to the domain	122
3.1.3. Modeling geometric constraints using the signed distance function	123
3.2. AN EFFICIENT, GENERAL PURPOSE OPTIMIZATION ALGORITHM .....	126
3.2.1. Abstract presentation of the algorithm	126
3.2.2. Application in shape and topology optimization and a numerical example	128
3.3. A VARIATIONAL METHOD FOR THE EVALUATION OF THE SHAPE DERIVATIVES OF GEOMETRIC FUNCTIONS.....	129
3.3.1. A formal insight about the main idea	131
3.3.2. Numerical illustrations	133
3.4. MODELING OF CONSTRAINTS ON SHAPES FOR ARCHITECTURAL DESIGN .....	135
3.4.1. Presentation of the mechanical setting and of a guiding example	136
3.4.2. Instilling diversity in the optimized shape by changing the specifications of the test-case	137
3.4.3. Constraints about the resemblance with a target design	138
3.4.4. Promoting the emergence of bars and walls by using constraints based on the anisotropic signed distance function	138
3.5. IMPOSING CONSTRAINTS ON THE OVERHANG REGIONS OF SHAPES .....	141
3.5.1. A few facts about additive manufacturing	141
3.5.2. An intuitive, geometric description, and its limitations	143
3.5.3. A layer-by-layer mechanical functional for overhang constraints	144
3.5.4. Two numerical applications of layer-by-layer mechanical constraints for overhang features	147
3.6. TAKING INTO ACCOUNT THE ANISOTROPIC MATERIAL PROPERTIES INDUCED BY ADDITIVE MANUFACTURING INTO THE OPTIMAL DESIGN PROCESS .....	149
3.6.1. Two different models for the construction of shapes	150

3.6.2. Numerical examples	153
3.7. PERSPECTIVE: SIMILARITY CONSTRAINTS USING OPTIMAL TRANSPORT	155
Appendices	157
3.A. THE COAREA FORMULA	157
Chapter 4. Asymptotic analysis of partial differential equations and applications in shape and topology optimization	159
4.1. PRELIMINARIES: SMALL INCLUSIONS AS A REPRESENTATIVE STARTER	159
4.1.1. Fundamental solutions and Green's functions	160
4.1.2. Fractional and exterior Sobolev spaces	162
4.1.3. Layer potentials	165
4.1.4. Asymptotic expansions in the presence of “small” inhomogeneities	166
4.1.5. A model calculation of a low-volume asymptotic expansion, and return to topological derivatives	172
4.2. A PARADIGM TO UNDERSTAND SHAPE, TOPOLOGICAL AND DENSITY DERIVATIVES IN A UNIFIED FASHION	175
4.2.1. A consistent, density-based relaxation of a shape optimization problem	175
4.2.2. A shape and topology optimization algorithm and numerical example	178
4.2.3. A density-based counterpart to the perimeter functional	178
4.3. OPTIMIZATION OF THE SHAPE OF REGIONS SUPPORTING BOUNDARY CONDITIONS	182
4.3.1. A model problem in the conductivity setting	183
4.3.2. A brief account of the regularity of $u_\Omega$	185
4.3.3. Calculation of the shape derivative of $J(\Omega)$ when $\Sigma_N$ is optimized	185
4.3.4. Calculation of the shape derivative of $J(\Omega)$ when $\Sigma_D$ is optimized	187
4.3.5. An approximate shape derivative in the Dirichlet-Neumann case	188
4.3.6. Two numerical examples	189
4.4. SENSITIVITY WITH RESPECT TO SINGULAR CHANGES IN THE SUPPORT OF BOUNDARY CONDITIONS	191
4.4.1. A general representation formula for the perturbed potential by the alteration of boundary conditions on a “small” subset of $\partial\Omega$	194
4.4.2. Replacement of boundary conditions on a vanishing surface ball	196
4.5. UNIFORM ESTIMATES IN THE PRESENCE OF THIN INHOMOGENEITIES	198
4.6. THE TOPOLOGICAL LIGAMENT	202
4.6.1. Approximate ligament derivatives based on thin tubular inhomogeneities	204
4.6.2. Three applications of topological ligaments in structural mechanics	206
4.7. A FEW PERSPECTIVES ABOUT ASYMPTOTIC ANALYSIS	211
4.7.1. Uniform replacements of solutions to parameter dependent boundary value problems	211
4.7.2. Shape and topology optimization of the regions bearing boundary conditions	213
4.7.3. Sensitivity of the voltage potential within a domain with respect to the onset of a crack on its boundary	214
Appendices	215
4.A. FUNCTIONS WITH BOUNDED VARIATIONS	215
4.B. A BRIEF REMINDER OF $\Gamma$ -CONVERGENCE	216
Chapter 5. Shape and topology optimization in challenging physical contexts	219
5.1. SHAPE AND TOPOLOGY OPTIMIZATION OF THERMAL-FLUID-STRUCTURE INTERACTING SYSTEMS	219
5.1.1. Presentation of the general framework	220

5.1.2. Numerical examples of optimal design of three-physics systems	222
5.2. OPTIMIZATION OF MAXIMUM PROBABILITY DOMAINS IN QUANTUM CHEMISTRY .....	229
5.2.1. Presentation of the physical context	229
5.2.2. Shape optimization for maximum probability domains	234
5.2.3. Two numerical examples	237
5.3. OPTIMIZATION OF THE SHAPE OF NANOPHOTONIC DEVICES .....	240
5.3.1. Nanophotonic devices and the transport of light	241
5.3.2. Optimization of nanophotonic devices	244
5.3.3. Numerical examples	246
5.4. PERSPECTIVES: OPTIMAL DESIGN OF AN ELECTRIC MOTOR .....	250
Chapter 6. A few more general and long-term perspectives	253
6.1. FURTHER DEVELOPMENTS ABOUT REMESHING .....	253
6.1.1. Insertion of lines into a simplicial mesh	253
6.1.2. Evolution of open curves and surfaces	255
6.1.3. Parallel remeshing	257
6.2. A SHAPE AND TOPOLOGY OPTIMIZATION FRAMEWORK FEATURING A REPRESENTATION OF SHAPES WITH LAGUERRE DIAGRAMS .....	258





# Notations

The following notations are used throughout the manuscript.

*Calculus in the Euclidean spaces  $\mathbb{R}^d$ :*

- The real and imaginary parts of a complex number  $z \in \mathbb{C}$  are respectively denoted by  $\operatorname{Re}(z)$  and  $\operatorname{Im}(z)$ .
- The Euclidean norm of a vector  $x = (x_1, \dots, x_d) \in \mathbb{R}^d$  is denoted by  $|x| = (x_1^2 + \dots + x_d^2)^{1/2}$ .
- The Euclidean distance  $d(x, A)$  between a point  $x \in \mathbb{R}^d$  and a set  $A \subset \mathbb{R}^d$  is:

$$d(x, A) = \inf_{y \in A} |x - y|.$$

- The Hausdorff distance  $d^H(K_1, K_2)$  between two compact subsets  $K_1, K_2 \subset \mathbb{R}^d$  is:

$$d^H(K_1, K_2) = \max(\rho(K_1, K_2), \rho(K_2, K_1)), \text{ where } \rho(K_1, K_2) = \sup_{x \in K_1} d(x, K_2).$$

- The vector product  $u \times v \in \mathbb{R}^3$  between two vectors  $u = (u_1, u_2, u_3)$  and  $v = (v_1, v_2, v_3)$  in  $\mathbb{R}^3$  is defined by:

$$u \times v = (u_2 v_3 - u_3 v_2, u_3 v_1 - u_1 v_3, u_1 v_2 - u_2 v_1).$$

- When  $x = (x_1, \dots, x_d)$  is a vector in  $\mathbb{R}^d$  and  $\alpha = (\alpha_1, \dots, \alpha_d) \in \mathbb{N}^d$  is a multi-index, we denote:

$$x^\alpha = x_1^{\alpha_1} \dots x_d^{\alpha_d}.$$

- The unit sphere in  $\mathbb{R}^d$  is denoted by  $\mathbb{S}^{d-1} := \{x \in \mathbb{R}^d, |x| = 1\}$ .
- We denote by  $\mathbb{R}_{\text{sym}}^{d \times d}$  the vector space of symmetric,  $d \times d$  matrices with real-valued entries.
- The Frobenius inner product between two square matrices  $M, N \in \mathbb{R}^{d \times d}$  is denoted by

$$M : N := \sum_{i,j=1,\dots,d} m_{ij} n_{ij},$$

and we denote by  $\|M\| := (M : M)^{1/2}$  the associated norm.

- The Kronecker symbol  $\delta_{ij}$  of size  $d$  is:

$$\forall i, j = 1, \dots, d, \quad \delta_{ij} = \begin{cases} 1 & \text{if } i = j, \\ 0 & \text{otherwise.} \end{cases}$$

*Functional spaces:*

- When  $A$  is a subset of an arbitrary set  $X$ , we denote by  $\mathbb{1}_A : X \rightarrow \mathbb{R}$  the characteristic function of  $A$ :

$$\forall x \in X, \quad \mathbb{1}_A(x) = \begin{cases} 1 & \text{if } x \in A, \\ 0 & \text{otherwise.} \end{cases}$$

- When  $(X, \mathcal{E})$  is an abstract measure space equipped with a positive measure  $\mu$  (see [Section 2.A](#)) and  $p \in [1, \infty)$ , we denote by  $L^p(X, \mu)$  the space of  $\mu$  measurable functions  $f : X \rightarrow \mathbb{R}$  with integrable  $p^{\text{th}}$  power:

$$L^p(X, \mu) = \left\{ f : X \rightarrow \mathbb{R} \text{ measurable, } \int_X |f(x)|^p d\mu(x) < \infty \right\}.$$

It is a Banach space when equipped with the norm

$$\|f\|_{L^p(X, \mu)} := \left( \int_X |f(x)|^p d\mu(x) \right)^{\frac{1}{p}}.$$

- When  $(X, \mathcal{E})$  is an abstract measure space equipped with a positive measure  $\mu$ ,  $L^\infty(X, \mu)$  stands for the vector space of  $\mu$  measurable functions on  $\Omega$  whose essential supremum

$$\|f\|_{L^\infty(X, \mu)} := \inf_{m \geq 0} \{ |f(x)| \leq m \text{ for } \mu \text{ a.e. } x \in X \}$$

is finite. It is a Banach space when equipped with the norm  $\|\cdot\|_{L^\infty(\Omega)}$ .

- When  $X = \Omega$  is an open or closed subset of the Euclidean space  $\mathbb{R}^d$  and  $\mu$  is the Lebesgue measure, we simply denote these spaces by  $L^p(\Omega)$ ,  $p \in [1, \infty]$ .
- When  $\Xi$  is a measure space, we denote by  $\mathcal{P}(\Xi)$  the space of probability measures on  $\Xi$ , see [Definition 2.A.2](#).
- When  $\Xi$  is a locally compact and separable metric space, we denote by  $\mathcal{M}_{\text{loc}}(\Xi)$  the space of Radon measures on  $\Xi$ , and by  $\mathcal{M}(\Xi)$  the space of finite Radon measures on  $\Xi$ , see [Definition 2.A.7](#).
- When  $(E, \|\cdot\|_E)$  and  $(F, \|\cdot\|_F)$  are normed vector spaces, we denote by  $\mathcal{L}(E, F)$  the space of continuous and linear mappings from  $E$  into  $F$ .
- When  $(E, \|\cdot\|)$  is a Banach space, we denote by  $B(x, r)$  the open ball centered at a point  $x \in E$ , with radius  $r > 0$ .
- When  $\Omega$  is a Lipschitz domain of  $\mathbb{R}^d$ , we denote by  $n_\Omega$  – or simply  $n$  when no confusion is possible – the unit normal vector to  $\partial\Omega$ , pointing outward  $\Omega$ .
- When  $\Omega$  is an open subset of  $\mathbb{R}^d$ , we equivalently denote by  $\mathcal{D}(\Omega)$  or  $\mathcal{C}_c^\infty(\Omega)$  the space of smooth functions with compact support inside  $\Omega$ , and by  $\mathcal{D}'(\Omega)$  the space of distributions on  $\Omega$ . The duality between these spaces is expressed by the bracket:

$$\langle T, \varphi \rangle, \quad T \in \mathcal{D}'(\Omega), \quad \varphi \in \mathcal{D}(\Omega).$$

We also denote by  $\mathcal{E}'(\Omega)$  is the space of distributions with compact support in  $\Omega$ .

- When  $\Omega$  is a Lipschitz domain of  $\mathbb{R}^d$  and  $k \geq 0$ , we denote by  $\mathcal{C}^k(\overline{\Omega})$  the space of the restrictions to  $\overline{\Omega}$  of functions of class  $\mathcal{C}^k$  on  $\mathbb{R}^d$ .
- When  $\Omega$  is an open subset of  $\mathbb{R}^d$ , for all  $m \in \mathbb{N}$  and  $p \in [1, \infty]$ ,  $W^{m,p}(\Omega)$  is the Sobolev space of functions in  $L^p(\Omega)$  whose distributional derivatives up to order  $m$  belong to  $L^p(\Omega)$ :

$$W^{m,p}(\Omega) = \left\{ u \in L^p(\Omega), \quad \forall \alpha \in \mathbb{N}^d, \quad |\alpha| \leq m, \quad \frac{\partial u}{\partial x^\alpha} \in L^p(\Omega), \right\}.$$

When  $p = 2$ , the space  $W^{m,p}(\Omega)$  is denoted by  $H^m(\Omega)$ .

- When  $\Omega$  is a smooth bounded domain, for an arbitrary integer  $m \geq 0$ ,  $H^m(\partial\Omega)$  stands for the Sobolev space of functions  $u \in L^2(\partial\Omega)$  whose tangential derivatives up to order  $m$  also belong to  $L^2(\partial\Omega)$ ; the space  $H^{-m}(\partial\Omega)$  is the topological dual of  $H^m(\partial\Omega)$ .
- For the definition of fractional Sobolev spaces  $H^s(\Gamma)$  defined on a region  $\Gamma$  of the boundary of a domain  $\Omega$ , see [Section 4.1.2](#).
- When  $\Omega$  is a bounded, Lipschitz domain of  $\mathbb{R}^d$  and  $\Gamma_D$  is a region of the boundary  $\partial\Omega$ , we denote by

$$H_{\Gamma_D}^1(\Omega) := \{ u \in H^1(\Omega), \quad u = 0 \text{ on } \Gamma_D \}$$

the subspace of  $H^1(\Omega)$  composed of functions with vanishing trace on  $\Gamma_D$ .

- For the definition of exterior Sobolev spaces  $W^{1,-1}(\Omega_e)$ , defined on the complement  $\Omega_e = \mathbb{R}^d \setminus \overline{\Omega}$  of a bounded domain  $\Omega \subset \mathbb{R}^d$ , see [Section 4.1.2](#).

# Introduction

This document summarizes the research work that I have been conducting since my recruitment as a CNRS junior researcher and affectation to the Laboratoire Jean Kuntzmann, in January 2015.

A great deal of this work revolves around the subject of shape and topology optimization, which, as the name suggests, is about optimizing the design of an object with respect to a performance criterion. This age-old idea has aroused a surge of enthusiasm in the recent decades: the development of efficient optimal design methods, enabled by the tremendous advances made in hardware capabilities and mathematical programming methods, is ever more relevant in the current context where the prices of raw materials are skyrocketing, see [Fig. 0.0.1](#) for a few illustrations of concrete applications.

From the mathematical point of view, a basic shape optimization problem can be formulated as follows:

$$\min_{\Omega} J(\Omega),$$

where a domain  $\Omega$  in  $\mathbb{R}^d$  ( $d = 2, 3$  in practice) is optimized with respect to a cost function  $J(\Omega)$ . This slightly unconventional problem is rendered even more disconcerting by the potentially intricate definition of  $J(\Omega)$ : in concrete applications, the latter often depends on  $\Omega$  via the solution to a boundary value problem characterizing its physical behavior.

This difficult setting raises fascinating questions from the theoretical viewpoint, as well as challenging modeling and computational issues, such as the device of a convenient means to represent the shape and its large deformations during the optimization process, the formulation of geometric and manufacturing constraints, the treatment of realistic physical situations, to name just a few.

A few of these topics are considered in the present manuscript, whose general organization is outlined below. Briefly, it is composed of six chapters; the first [Chapter 1](#) gathers some background material about shape and topology optimization which is useful in most of the developments presented in the document. The next [Chapters 2](#) to [5](#) focus on four different research axes; they generally start with some more specific preliminary material, including tentative overviews of the work related to the reported investigations, and they end with a few perspectives. The final [Chapter 6](#) broaches some more general directions for future work. The manuscript is written in an expository, self-contained way insofar as possible. Formal descriptions and insights about the main ideas of the described works, sometimes expressed in particular, simple cases, are often preferred to strictly rigorous discussions, with the hope that these choices facilitate easy reading; the reader is generally referred to the published versions of the corresponding works for complete details.

## **Chapter 1: Preliminaries: shape and topology optimization algorithms and their implementation**

This first chapter collects some background material around the subject of shape and topology optimization, mainly. It contains no original result per se, but it is rather intended as a fairly detailed presentation of a few theoretical and technical ingredients that are perhaps not so easily found as is in the literature. The expert reader may skip this chapter shamelessly, but we hope that its contents can be useful to the newcomer.

After a few historical notes about the development and practice of the idea of shape and topology optimization, we describe the two mathematical and physical settings in which most of our discussions take place, namely the conductivity equation and the linear elasticity system. We give a special emphasis on

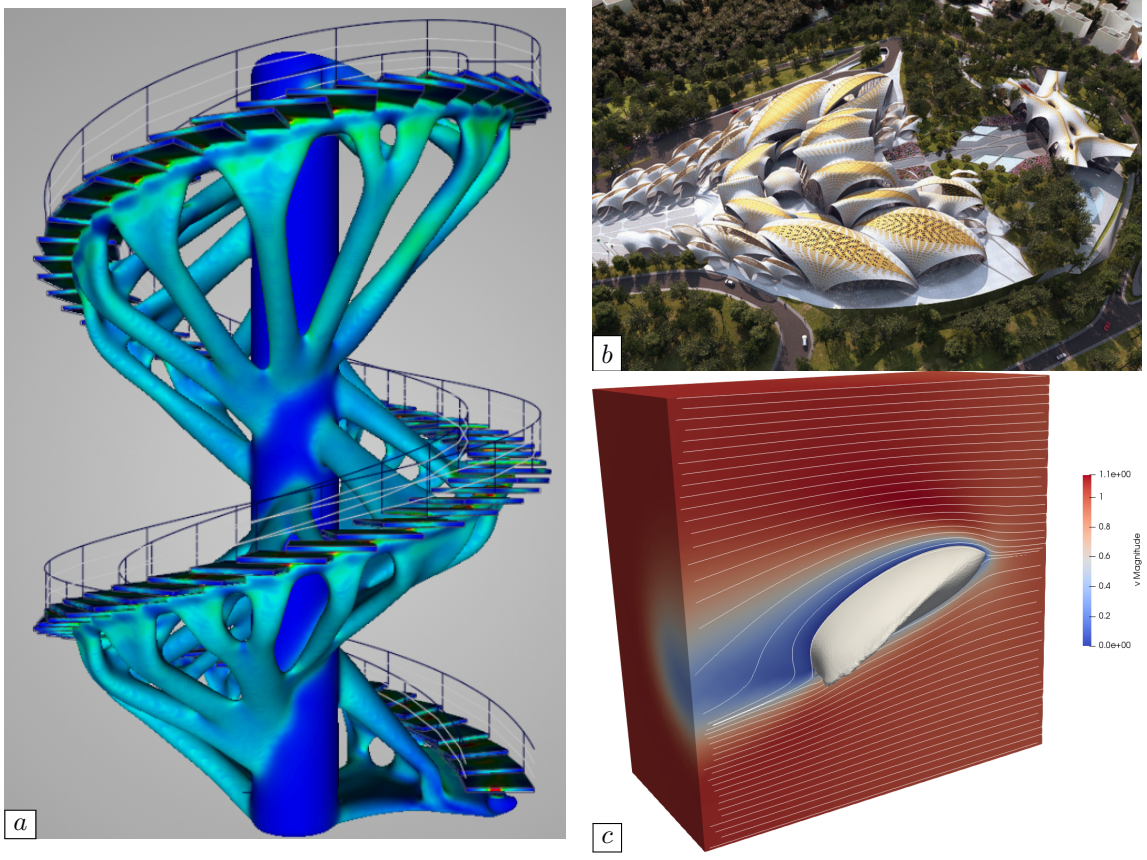


FIGURE 0.0.1. (a) Optimization of the shape of a staircase by the commercial software *ansys*; (b) Optimized design of the roof of a convention center under the form of a shell (Picture from [8]); (c) Optimized profile of a wing for the maximization of its lift.

the latter, recalling essential concepts about the modeling of elastic structures, such as the descriptions of deformations and stresses, the role of constitutive laws, and we formulate optimal design problems in this context.

The main mathematical framework used to deal with shape optimization problems is introduced next, namely, the boundary variation method of Hadamard, leading to the notion of shape derivative. We outline the calculation of the shape derivatives of basic functionals such as the volume or the perimeter, and the general trail to calculate the shape derivatives of “complex” functionals of the domain, depending on the latter via the solution to a boundary value problem is explained in detail. We seize this opportunity to present the key argument, namely, the celebrated adjoint method from optimal control, in an abstract and general context. A few other topics are broached, such as the flexible Hilbertian method to identify shape gradients from shape derivatives, and the concurrent type of sensitivity with respect to the domain encoded in topological derivatives.

The second part of this chapter is more directly concerned with numerical implementation. We present the historical algorithms, based on the deformation of a computational mesh of the structure, insisting on its limitations to motivate the more modern methods presented subsequently. After a digression about meshing, we present the level set method in a general fashion, and its application in the field of shape optimization. We also detail a recent strategy, combining the latter with remeshing techniques to allow for an accurate, meshed representation of the shape throughout the optimization process. For completeness, we also outline two different usages of topological derivatives in the context of optimal design algorithms.

This chapter ends with a few appendices gathering technical tools used throughout the manuscript, and notably, a primer in the differential geometry of surfaces, and a glimpse of the regularity theory for elliptic boundary value problems.

## Chapter 2: Shape and topology optimization under uncertainties

This second chapter summarizes a series of investigations dealing with the optimization of a design, generically denoted by  $h$ , with respect to a cost function  $\mathcal{C}(h, \xi)$  which also depends on physical data  $\xi \in \Xi$ . The nominal optimization problem, when the parameter  $\xi$  is assumed to be known exactly, reads:

$$\min_h \mathcal{C}(h, \xi).$$

Unfortunately, the performance of the design resulting from this optimization program is usually very sensitive to “small” perturbations of  $\xi$ . Depending on the available information about these uncertain data, different strategies may be undertaken to make the optimal design process “robust” with respect to uncertainties about  $\xi$ .

At first, we place ourselves in the situation where no information is available about  $\xi$ , except for a maximum bound  $m$  on its amplitude  $\|\xi\|$ . The perhaps most reasonable means to enforce robustness with respect to such uncertainties is then to minimize the worst value of the cost when  $\xi$  has maximum amplitude  $m$ , i.e.

$$\min_h J_{\text{wc}}(h), \text{ where } J_{\text{wc}}(h) := \sup_{\substack{\xi \in \Xi \\ \|\xi\| \leq m}} \mathcal{C}(h, \xi).$$

We present a general, formal approach for approximating the worst-case functional  $J_{\text{wc}}(h)$  when  $m$  is “small”, which is based on a Taylor expansion of the cost functional  $\mathcal{C}(h, \cdot)$ .

Following a similar line of thinking, we next deal with a concrete application of this type of methodology in the context of mechanical structures plagued by an uncontrolled level of porosity.

The main drawback of these pessimistic approaches is that they lead to designs  $h$  with poor nominal performance for the sake of anticipating a worst-case scenario which is unlikely to occur.

When the law  $\mathbb{P} \in \mathcal{P}(\Xi)$  of the uncertain parameter  $\xi$  is available, a probabilistic quantity of the cost can be considered, such as its expectation:

$$\min_h J_{\text{mean}}(h), \text{ where } J_{\text{mean}}(h) := \int_{\Xi} \mathcal{C}(h, \xi) d\mathbb{P}(\xi).$$

Again, a method based on the linearization of the cost  $\mathcal{C}(h, \cdot)$  allows to derive a tractable approximation of the functional  $J_{\text{mean}}(h)$ .

In turn, this paradigm is flawed as it rests on the knowledge of the law  $\mathbb{P}$  of  $\xi$ , which is often known imperfectly, through a set of few observations. A recent paradigm to cope with this conceptual drawback is that of distributional robustness, whereby the worst value of the expected cost is minimized when the law  $\mathbb{Q}$  of  $\xi$  is “close” to a nominal, measured law  $\mathbb{P}$  within a maximum “distance”  $m$ :

$$\min_h J_{\text{dr}}(h), \text{ where } J_{\text{dr}}(h) := \sup_{\substack{\mathbb{Q} \in \mathcal{P}(\Xi), \\ W(\mathbb{Q}, \mathbb{P}) \leq m}} \int_{\Xi} \mathcal{C}(h, \xi) d\mathbb{Q}(\xi),$$

where  $W(\cdot, \cdot)$  is a distance over probability measures on  $\Xi$ . Leveraging recent results from convex duality theory, we reformulate this problem as a tractable optimal design problem when  $W(\cdot, \cdot)$  is the Wasserstein distance.

This chapter ends with two appendices, devoted to general notions about measure theory and to the more specific subject of the Karhunen-Loève decomposition of an infinite-dimensional uncertain parameter on a countable basis – a tool which underlies many assumptions about the structure of the uncertain data made in this chapter.

## Chapter 3: Geometric and manufacturing constraints in shape and topology optimization

This chapter is devoted to the modeling and treatment of constraints in shape and topology optimization, with a particular emphasis on those related to the manufacturing of shapes. It starts with some background

material about the signed distance function  $d_\Omega$  to a shape  $\Omega \subset \mathbb{R}^d$ , which is a key ingredient in the mathematical formalization of geometric constraints about the thickness of  $\Omega$ , the distance between its members, etc.

Two useful mathematical tools are then discussed:

- A general-purpose constrained optimization algorithm is introduced, which lends itself to a very convenient use in the context of shape and topology optimization.
- A variational method is proposed to simplify dramatically the numerical evaluation of the shape derivatives of functions depending on the domain  $\Omega$  via the signed distance function  $d_\Omega$ , which usually involve awkward quantities such as the principal curvatures and the normal rays to  $\partial\Omega$ .

We then motivate and devise a few geometric constraints which are specific to the field of architecture. In particular, constraints about the resemblance of the optimized shape with a target design are considered, as well as constraints about an anisotropic version of its thickness.

The next part of this chapter is devoted to the burning field of additive manufacturing, also referred to as 3d printing. In spite of the unprecedented freedom offered in terms of the complexity of the constructed design, these modern construction processes impose new constraints on the design process. They notably experience difficulties with overhang features – large regions hanging over void without sufficient support from the lower structure. We explain why the “naive” geometric modeling of overhang constraints fails to penalize the onset of such regions, and we propose a more sophisticated, layer-by-layer mechanical functional based on a simplified model of the construction process. Still in the context of shapes produced by additive manufacturing, we also try and appraise the anisotropic behavior of the elastic material induced by the particular trajectory of the printing machine.

This chapter ends with a new perspective about the aforementioned modeling of constraints imposing the resemblance of the optimized design  $\Omega$  with a general target object, thanks to the notion of Wasserstein distance from optimal transport theory.

#### **Chapter 4: Asymptotic analysis of partial differential equations and applications in shape and topology optimization**

This chapter deals with several questions pertaining to the field of asymptotic analysis, some of which find original applications in shape and topology optimization.

A quite lengthy preliminary exposition sets the common scene of our developments. At first, several classical notions from functional analysis and potential theory are recalled, including the notion of Green’s function and the definition of fractional Sobolev spaces on a region of the boundary of a domain. We then present the more specific question of how “small” perturbations of the material properties in a physical boundary value problem influence its solution. We collect a few key related results, that we try to present under an intuitive and formal perspective.

The first original work reported in this chapter deals with a unifying paradigm for the concepts of shape derivative, topological derivative, and density-based derivative in optimal design. We introduce a general strategy to convert a shape optimization problem into a density-based topology optimization problem, relying on the classical idea of “filtering”, and we prove that the derivatives of the functionals involved in the latter converge to the shape or the topological derivatives involved in the former, as the filtering parameter tends to 0. This result suggests a new numerical strategy for solving optimal design problems which naturally combines shape and topological derivatives. We also outline how to extend these ideas to the important case of perimeter functionals, which is not covered by the general theory.

The next topic considered in this chapter is the effect on the solution to a physical problem of modifications of the regions of the boundary of the defining domain bearing its boundary conditions. Our investigations take two different paths. On the one hand, we consider “regular” perturbations of such regions, by smooth diffeomorphisms, in the spirit of the classical method of Hadamard. The “shape derivative” of a generic performance criterion with respect to modifications of these regions is difficult to calculate and evaluate, as it involves the knowledge of the singular behavior of the physical solution near there. To alleviate this difficulty, we introduce a consistent approximation of the boundary value problem at stake, and of the attached shape optimization problem, where the sharp transition between regions bearing different boundary conditions is smoothed. On the other hand, we analyze the complementary question of “singular”

perturbations of these regions supporting boundary conditions, such as the replacement of a homogeneous Neumann boundary condition with a homogeneous Dirichlet boundary condition on a “small” boundary region  $\omega_\varepsilon$ . We then provide a general representation formula for the solution to the perturbed problem, under minimal assumptions on the vanishing subset  $\omega_\varepsilon$ , and we make this formula explicit in the case where  $\omega_\varepsilon$  is a surface ball with vanishing radius  $\varepsilon$ .

The study presented next is of rather theoretical interest, although it is motivated by natural considerations. It deals with the uniform behavior of the solution to a model boundary value problem in the setting of the conductivity equation when the material coefficients undergo perturbations of arbitrarily large magnitude inside a “thin” inclusion subset of the defining domain.

We then explore a related problem of “small” inhomogeneities from a computational perspective, by revisiting the idea of “topological ligament”. This rather exotic concept measures the sensitivity of the solution to a boundary value problem (and of a related quantity of interest) with respect to the graft of a thin ligament to the domain. To the best of our knowledge, no implementation of this difficult concept was available before this study. By looking at thin tubular inclusion asymptotics, we provide a general calculation method of approximate topological ligament expansions. These are used to address various issues in shape optimization, and notably to insert bars to a structure with a “too poor” topology in the course of a classical shape optimization process, to optimize the auxiliary scaffolds of a shape constructed by additive manufacturing which presents overhang features, and to provide a “clever” initialization in the optimization of truss structures.

We conclude this chapter with a few perspectives for future research, related to the implementation of the aforementioned results about regular and singular perturbations of the boundary conditions within a boundary value problem, and to uniform asymptotic expansions of the solutions to various perturbations of boundary value problems.

### **Chapter 5: Shape and topology optimization in challenging physical contexts**

This chapter broaches several investigations of shape and topology optimization problems arising in less classical and perhaps more challenging physical situations than that of mechanical structures.

At first, we consider a generic three-physics setting, taking into account fluid, structure and thermal effects, which encompasses in particular fluid-structure interaction problems as well as heat exchanger models.

The next study deals with an original foray of shape and topology optimization in quantum chemistry. The identification of classical chemical structures (such as the electron pairs in the Lewis theory) from quantum mechanics quantities (the wave function of the system) is expressed as a rather peculiar shape optimization problem – a paradigm referred to as the theory of maximum probability domains. We analyze this problem from the theoretical viewpoint, showing existence of global solutions under mild assumptions, and we present a numerical algorithm tailored to its specificities.

We then consider the optimization of the shape of nanophotonic devices, which are components used to manipulate light at the microscopic level, whose physical behavior is described by the time-harmonic Maxwell’s equations.

We conclude this chapter with the description of an ongoing work devoted to the optimization of the structure of an electric motor.

### **Chapter 6: A few more general and long-term perspectives**

In this final chapter, we outline a few research directions which are perhaps less directly related to the main topics discussed in the manuscript.

At first, we present three natural but non trivial extensions of the remeshing algorithms used repeatedly in the work summarized in this report. These concern the explicit discretization of curves and open surfaces in an ambient mesh – an operation which finds applications in the numerical simulation of fault lines, cracked domains, or shells – and the parallel implementation of remeshing algorithms, which would ease their use in the context of large scale numerical simulations.

Secondly, we outline an original and promising framework for shape and topology optimization, featuring a very robust numerical representation of shapes which completely differs from those used in this manuscript. It leverages tools from computational geometry (such as Laguerre diagrams – a weighted variant of Voronoi

diagrams), optimal transport theory, and the recent “virtual element method” for solving boundary value problems on general polygonal meshes.

The material presented in this manuscript is based on the following journal articles, teaching supports and open-source implementations.

### List of published works.

- [A1] C. DAPOGNY, F. IUTZELER, A. MEDA, and B. THIBERT, *Entropy-regularized Wasserstein distributionally robust shape and topology optimization*, arXiv preprint arXiv:2209.01500 (2022).
- [A2] C. DAPOGNY, *Optimisation de formes*, To appear in La Gazette des Mathématiciens (2022).
- [A3] C. DAPOGNY and F. FEPPON, *Shape optimization using a level set based mesh evolution method: an overview and tutorial*, in preparation (2022).
- [A4] G. BALARAC, F. BASILE, P. BÉNARD, F. BORDEU, J.-B. CHAPELIER, L. CIRROTTOLA, G. CAUMON, C. DAPOGNY, P. FREY, A. FROEHLY, et al., *Tetrahedral remeshing in the context of large-scale numerical simulation and high performance computing*, Maths in Action 11 (2022), pp. 129–164.
- [A5] E. BONNETIER, C. DAPOGNY, and M. S. VOGELIUS, *Small perturbations in the type of boundary conditions for an elliptic operator*, Journal de Mathématiques Pures et Appliquées 167 (2022), pp. 101–174.
- [A6] S. AMSTUTZ, C. DAPOGNY, and A. FERRER, *A consistent approximation of the total perimeter functional for topology optimization algorithms*, ESAIM: Control, Optimisation and Calculus of Variations 28 (2022), p. 18.
- [A7] B. BRAIDA, J. DALPHIN, C. DAPOGNY, P. FREY, and Y. PRIVAT, *Shape and topology optimization for maximum probability domains in quantum chemistry*, Numerische Mathematik (2022), pp. 1–48.
- [A8] F. FEPPON, G. ALLAIRE, C. DAPOGNY, and P. JOLIVET, *Body-fitted topology optimization of 2D and 3D fluid-to-fluid heat exchangers*, Computer Methods in Applied Mechanics and Engineering 376 (2021), p. 113638.
- [A9] C. DAPOGNY, *The topological ligament in shape optimization: an approach based on thin tubular inhomogeneities asymptotics*, SMAI Journal of Computational Mathematics (2021), pp. 185–266.
- [A10] C. DAPOGNY, *A connection between topological ligaments in shape optimization and thin tubular inhomogeneities*, Comptes Rendus Mathématique 358.2 (2020), pp. 119–127.
- [A11] F. FEPPON, G. ALLAIRE, C. DAPOGNY, and P. JOLIVET, *Topology optimization of thermal fluid-structure systems using body-fitted meshes and parallel computing*, Journal of Computational Physics (2020), p. 109574.
- [A12] G. ALLAIRE, C. DAPOGNY, and F. JOUVE, *Shape and topology optimization*, in Geometric partial differential equations, part II, A. Bonito and R. Nochetto eds., Handbook of Numerical Analysis, vol. 22 (2021), pp. 1–132.
- [A13] C. DAPOGNY, N. LEBBE, and E. OUDET, *Optimization of the shape of regions supporting boundary conditions*, Numerische Mathematik 146.1 (2020), pp. 51–104.
- [A14] F. FEPPON, G. ALLAIRE, and C. DAPOGNY, *Null space gradient flows for constrained optimization with applications to shape optimization*, ESAIM: Control, Optimisation and Calculus of Variations 26 (2020), p. 90.
- [A15] F. FEPPON, G. ALLAIRE, and C. DAPOGNY, *A variational formulation for computing shape derivatives of geometric constraints along rays*, ESAIM: Mathematical Modelling and Numerical Analysis 54.1 (2020), pp. 181–228.

- [A16] N. LEBBE, A. GLIÈRE, K. HASSAN, C. DAPOGNY, and E. OUDET, *Shape optimization for the design of passive mid-infrared photonic components*, Optical and Quantum Electronics 51.5 (2019), pp. 1–14.
- [A17] N. LEBBE, C. DAPOGNY, E. OUDET, K. HASSAN, and A. GLIERE, *Robust shape and topology optimization of nanophotonic devices using the level set method*, Journal of Computational Physics 395 (2019), pp. 710–746.
- [A18] J. MARTINEZ-FRUTOS, G. ALLAIRE, C. DAPOGNY, and F. PERIAGO, *Structural optimization under internal porosity constraints using topological derivatives*, Computer Methods in Applied Mechanics and Engineering 345 (2019), pp. 1–25.
- [A19] E. BONNETIER, C. DAPOGNY, F. TRIKI, and H. ZHANG, *The plasmonic resonances of a bowtie antenna*, Anal. Theory Appl. 35 (2019), pp. 85–116.
- [A20] F. FEPPON, G. ALLAIRE, F. BORDEU, J. CORTIAL, and C. DAPOGNY, *Shape optimization of a coupled thermal fluid–structure problem in a level set mesh evolution framework*, SeMA Journal (2019), pp. 1–46.
- [A21] C. DAPOGNY, R. ESTEVEZ, A. FAURE, and G. MICHAELIDIS, *Shape and topology optimization considering anisotropic features induced by additive manufacturing processes*, Computer Methods in Applied Mechanics and Engineering 344 (2019), pp. 626–665.
- [A22] G. ALLAIRE, C. DAPOGNY, R. ESTEVEZ, A. FAURE, and G. MICHAELIDIS, *Structural optimization under overhang constraints imposed by additive manufacturing technologies*, Journal of Computational Physics 351 (2017), pp. 295–328.
- [A23] C. DAPOGNY, P. FREY, F. OMNÈS, and Y. PRIVAT, *Geometrical shape optimization in fluid mechanics using FreeFem++*, Structural and Multidisciplinary Optimization (2017), pp. 1–28.
- [A24] É. BONNETIER, C. DAPOGNY, and F. TRIKI, *Homogenization of the eigenvalues of the Neumann–Poincaré operator*, Archive for Rational Mechanics and Analysis 234.2 (2019), pp. 777–855.
- [A25] S. AMSTUTZ, C. DAPOGNY, and À. FERRER, *A consistent relaxation of optimal design problems for coupling shape and topological derivatives*, Numerische Mathematik (2016), pp. 1–60.
- [A26] G. ALLAIRE, C. DAPOGNY, A. FAURE, and G. MICHAELIDIS, *Shape optimization of a layer by layer mechanical constraint for additive manufacturing*, Comptes Rendus Mathématique 355.6 (2017), pp. 699–717.
- [A27] C. DAPOGNY, A. FAURE, G. MICHAELIDIS, G. ALLAIRE, A. COUVELAS, and R. ESTEVEZ, *Geometric constraints for shape and topology optimization in architectural design*, Computational Mechanics 59.6 (2017), pp. 933–965.
- [A28] M. DE BUHAN, C. DAPOGNY, P. FREY, and C. NARDONI, *An optimization method for elastic shape matching*, Comptes Rendus Mathématique 354.8 (2016), pp. 783–787.
- [A29] C. DAPOGNY and M. S. VOGELIUS, *Uniform asymptotic expansion of the voltage potential in the presence of thin inhomogeneities with arbitrary conductivity*, Chinese Annals of Mathematics, Series B 38.1 (2017), pp. 293–344.
- [A30] G. ALLAIRE and C. DAPOGNY, *A deterministic approximation method in shape optimization under random uncertainties*, SMAI Journal of computational mathematics 1 (2015), pp. 83–143.
- [A31] M. DAMBRINE, C. DAPOGNY, and H. HARBRECHT, *Shape optimization for quadratic functionals and states with random right-hand sides*, SIAM journal on control and optimization 53.5 (2015), pp. 3081–3103.
- [A32] G. ALLAIRE, C. DAPOGNY, and P. FREY, *Shape optimization with a level set based mesh evolution method*, Computer Methods in Applied Mechanics and Engineering 282 (2014), pp. 22–53.

- [A33] G. ALLAIRE and C. DAPOGNY, *A linearized approach to worst-case design in parametric and geometric shape optimization*, Mathematical Models and Methods in Applied Sciences 24.11 (2014), pp. 2199–2257.
- [A34] G. ALLAIRE, C. DAPOGNY, G. DELGADO, and G. MICHAILIDIS, *Multi-phase structural optimization via a level set method*, ESAIM: Control, Optimisation and Calculus of Variations 20.2 (2014), pp. 576–611.
- [A35] C. DAPOGNY, C. DOBRZYNISKI, and P. FREY, *Three-dimensional adaptive domain remeshing, implicit domain meshing, and applications to free and moving boundary problems*, Journal of computational physics 262 (2014), pp. 358–378.
- [A36] G. ALLAIRE, C. DAPOGNY, and P. FREY, *A mesh evolution algorithm based on the level set method for geometry and topology optimization*, Structural and Multidisciplinary Optimization 48.4 (2013), pp. 711–715.
- [A37] G. ALLAIRE, C. DAPOGNY, and P. FREY, *Topology and geometry optimization of elastic structures by exact deformation of simplicial mesh*, Comptes Rendus Mathematique 349.17-18 (2011), pp. 999–1003.
- [A38] C. BUI, C. DAPOGNY, and P. FREY, *An accurate anisotropic adaptation method for solving the level set advection equation*, International Journal for Numerical Methods in Fluids 70.7 (2012), pp. 899–922.
- [A39] C. DAPOGNY and P. FREY, *Computation of the signed distance function to a discrete contour on adapted triangulation*, Calcolo 49.3 (2012), pp. 193–219.

Note that, out of coherency, the works [A24, A19] are not described in this document.

#### List of teaching material.

- [C1] E. BONNETIER and C. DAPOGNY, *An introduction to shape and topology optimization*. Online course (slides, codes) available at: <https://membres-ljk.imag.fr/Charles.Dapogny/coursoptim.html>. 2020.
- [C2] C. DAPOGNY, *An introduction to the level set method*. Online course (slides, lecture notes) available at: <https://membres-ljk.imag.fr/Charles.Dapogny/teaching.html>. 2015.
- [C3] C. DAPOGNY, *Refresher: differential calculus and applications*. Online course (lecture notes) available at: <https://membres-ljk.imag.fr/Charles.Dapogny/teaching.html>. 2022.
- [C4] C. DAPOGNY, *Localized plasmonic resonances and the Neumann-Poincaré operator: homogenization and bowties*. Mini-course (slides) available at: <https://membres-ljk.imag.fr/Charles.Dapogny/teaching.html>. 2019.
- [C5] C. DAPOGNY, *An introduction to the level set method and its applications to meshing*. Mini-course (slides) available at: <https://membres-ljk.imag.fr/Charles.Dapogny/teaching.html>. 2023.

#### List of open-source softwares.

- [S1] C. DAPOGNY and F. FEPPON, *S0tuto*, a pedagogic and open-source implementation of the level set based mesh evolution method. 2023. URL: <https://github.com/dapogny/sotuto> (visited on 01/01/2023).
- [S2] C. DAPOGNY, C. DOBRZYNISKI, P. FREY, and A. FROELHY, *mmg*, a platform for 2d, 3d and surface remeshing. 2023. URL: <https://www.mmgtools.org> (visited on 01/01/2023).

- [S3] C. BUI, C. DAPOGNY, and P. FREY, *advection, a solver for linear advection equation on a simplicial computational mesh*. 2023. URL: <https://github.com/ISCDtoolbox/Advection> (visited on 01/01/2023).
- [S4] C. DAPOGNY and P. FREY, *mshdist, an algorithm for calculating the signed distance function on a simplicial computational mesh*. 2023. URL: <https://github.com/ISCDtoolbox/Mshdist> (visited on 01/01/2023).



# Chapter 1

## Preliminaries: Shape and topology optimization algorithms and their implementation

Elaborating upon the review articles [A2, A4, A12] and the contents of the course [C1], this chapter collects preliminary material about shape and topology optimization which is used repeatedly throughout the manuscript. It is admittedly rather long, but we hope that it can serve as a self-contained introduction to the main aspects of the discipline, while positioning the research contributions presented in the subsequent chapters with respect to the past and ongoing developments in the field. The reader who is already familiar with these concepts may shamelessly skip most of its contents. Some more specific background material is provided later, in the relevant chapters.

### 1.1 A FEW SELECTED HISTORICAL MILESTONES

The general idea of optimizing the shape of an object has long been an obsession for scientists, and also artists, ... Before delving into the modern developments of shape optimization in the next sections, we present here a few of its noteworthy historical forays.

#### 1.1.1. The isoperimetric inequality

If we except the fact that life itself tends to favor optimal patterns via the selection process – see e.g. [114, 157] about the optimal character of the structure of beehives and the shape of eggs, respectively –, the perhaps first occurrence of shape optimization in history dates back to the myth of the foundation of Carthage, in 814 B.C. Virgil's Aeneid (Book I, 16) reports that<sup>1</sup>, after her brother Pygmalion had murdered her husband, Dido fled with her servants to reach the coasts of the current Tunisia. At her arrival, she requested a piece of land from the local landlord Jarbas, who would sarcastically grant her “what could be encompassed by a bull's hide”. The ingenious queen cut the hide into very thin slices to enclose as large an area as possible, shaped as a half-disk against the shore, see Fig. 1.1.1 (a).

Without knowing, Dido had the intuition that the disk is the solution to the isoperimetric problem

$$\max_{\Omega \subset \mathbb{R}^2} \text{Vol}(\Omega) \text{ s.t. } \text{Per}(\Omega) = P_T,$$

aiming at maximizing the volume  $\text{Vol}(\Omega) = \int_{\Omega} dx$  of a two-dimensional domain under a constraint  $P_T$  on its perimeter  $\text{Per}(\Omega) = \int_{\partial\Omega} ds$ .

---

1

*“They sailed to the place where today you'll see  
Stone walls going higher and the citadel  
Of Carthage, the new town. They bought the land,  
Called Drumskin from the bargain made, a tract  
They could enclose with one bull's hide.”*

A similar rationale underlies the circular shape of ancient fortified towns, which is driven by the motivation to enclose the largest area, for a given length of fortifications, see Fig. 1.1.1 (b).



FIGURE 1.1.1. (a) *Aerial view of antique Carthage (Credits: J.-C. Golvin)*; (b) *Map of the fortifications of ancient Paris*.

The isoperimetric problem has inspired numerous scientists and philosophers from the Antiquity: Euclid, Archimedes, Zenodora, Pappus, to name a few. The optimal character of the disk has been the focus of much attention; elegant analyses were conducted (notably by J. Steiner) in this direction, all incomplete because they would take for granted the existence of an optimal shape for the isoperimetric problem. This non trivial fact could only be proved thanks to the new concepts in the calculus of variations introduced by K. Weierstrass in the middle of the XVIII<sup>th</sup> century, turning the previous attempts into complete proofs.

### 1.1.2. Optimal design in architecture

Since their early construction works, humans have strived to optimize the shape of buildings to make them more robust or lighter. For instance, the structure of the ancient Egyptian pyramids reveals a high level of concern with optimization [63].

A pioneering step toward the systematic optimization of buildings was achieved by the British engineer Robert Hooke, who was concerned with the design of a self-supporting arch. He postulated in 1675 that

*“As hangs a flexible cable so, inverted, stand the touching pieces of an arch.”*

According to this principle, by inverting the shape of a catenary, in equilibrium under its own weight and the tension efforts, one obtains the design of an arch in equilibrium under its weight and compression efforts.

Since then, architects have drawn inspiration from such principles to design constructions, from their general outlook to their fine structure. Modern optimization methods now allow to take into account more precisely and more systematically constraints on the geometry of a building, such as the width of its columns, but also its mechanical performance (in terms of vibrations, wear, etc.).

### 1.1.3. Optimal design and the calculus of variations

The great headway made in differential calculus, calculus of variations and their applications to the modeling of physical phenomena (notably, in acoustics, electrostatics) have steadily paved the way to more complex problems of optimal design, that involve a taste of the physical behavior of shapes via ordinary or partial differential equations. In this direction, relying on a simplified model based on the Laplace equation, Newton investigated the shape of a projectile that would encounter minimal resistance from air friction. In a similar spirit, Lagrange sought the most robust shape of a column; President Thomas Jefferson himself tried to optimize the shape of a ploughshare.

One representative question of these studies, which achieved posterity, was formulated by Lord Rayleigh in 1896, in his book [312]. He conjectured that among all homogeneous membranes fixed at their boundary, that with lowest fundamental frequency is the disk: mathematically, the disk is the unique minimizer of the problem

$$\min_{\Omega \subset \mathbb{R}^2} \lambda_{\Omega}, \text{ s.t. } \text{Vol}(\Omega) = V_T,$$

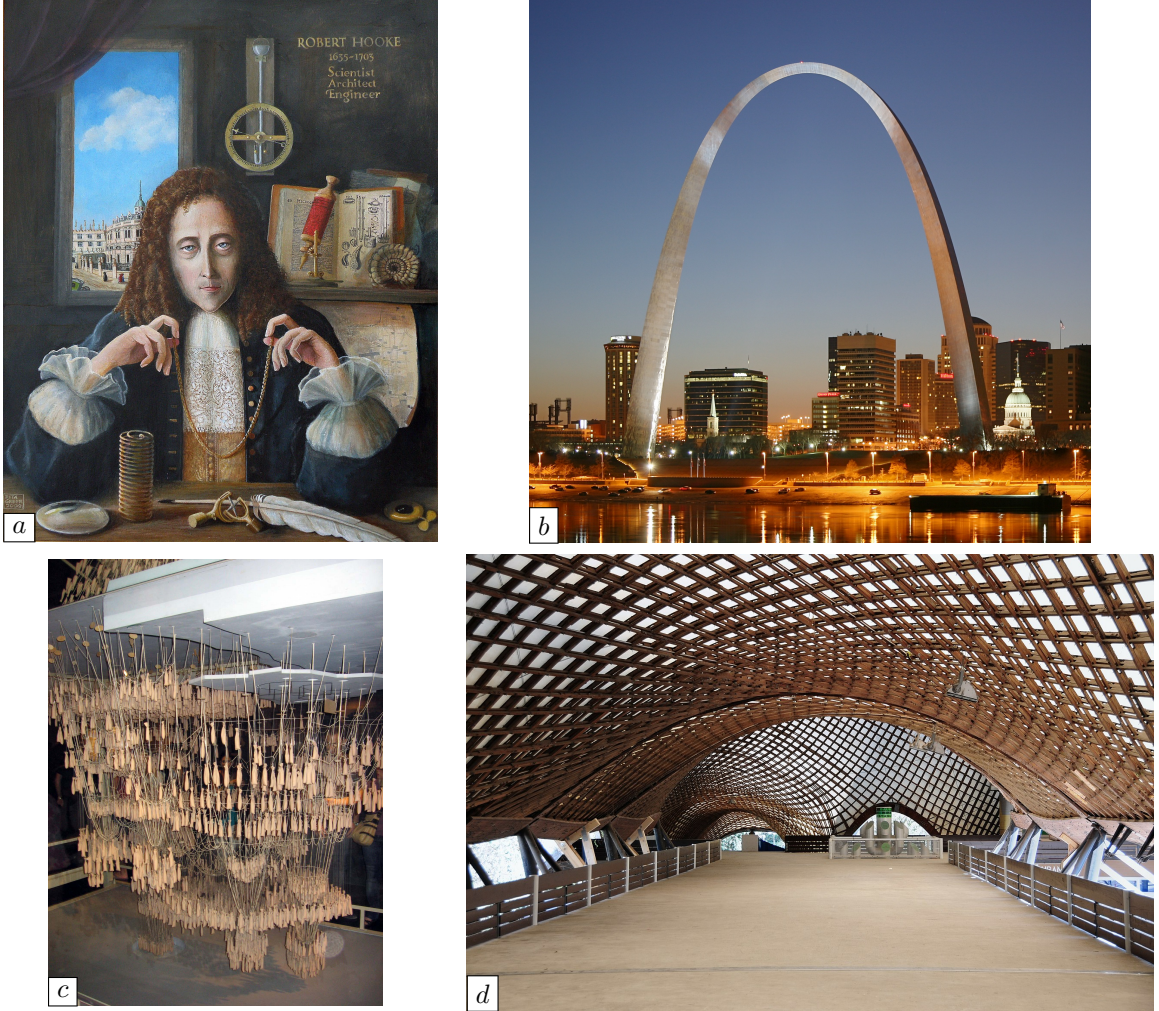


FIGURE 1.1.2. *Shape optimization in architecture: (a) Robert Hooke with the catenary; (b) The St Louis vault (Missouri) is a ‘weighted catenary’; (c) Funicular model (assembly of catenaries) underlying the construction of the Sagrada Familia by Gaudi; (d) Optimization of the roof of the Olympic centre of Munchen (H. Berberich).*

where  $V_T$  is a volume target. Here,  $\lambda_\Omega$  is the first eigenvalue of the Laplace operator with homogeneous Dirichlet boundary conditions, i.e. the smallest (positive) value  $\lambda$  such that the boundary value problem

$$\begin{cases} -\Delta u = \lambda u & \text{in } \Omega, \\ u = 0 & \text{on } \partial\Omega, \end{cases}$$

has a non trivial solution  $u$ . This conjecture fostered the rise of spectral optimization; it was demonstrated about 30 years later by Faber and Krahn, see also [305] for a reference book summarizing many related mathematical concepts.

#### 1.1.4. Toward modern shape and topology optimization in structural and aeronautical engineering

The first optimal design studies in mechanical engineering date back to 1869, when Maxwell started to inquire about the optimization of truss structures, i.e. structures made of bars, see Fig. 1.1.3 (a). His work was considerably extended by Michell in 1904.

These investigations have been limited to theoretical aspects until the 1960's. The concurrent advent of efficient optimization algorithms and numerical methods for the simulation of physical phenomena (notably, the finite element method) and of powerful computational resources has then fostered the device and implementation of automatic optimal design techniques. In particular, these developments have enabled major headway in aeronautical engineering, such as the optimization of wing profiles, see Fig. 1.1.3 (b).

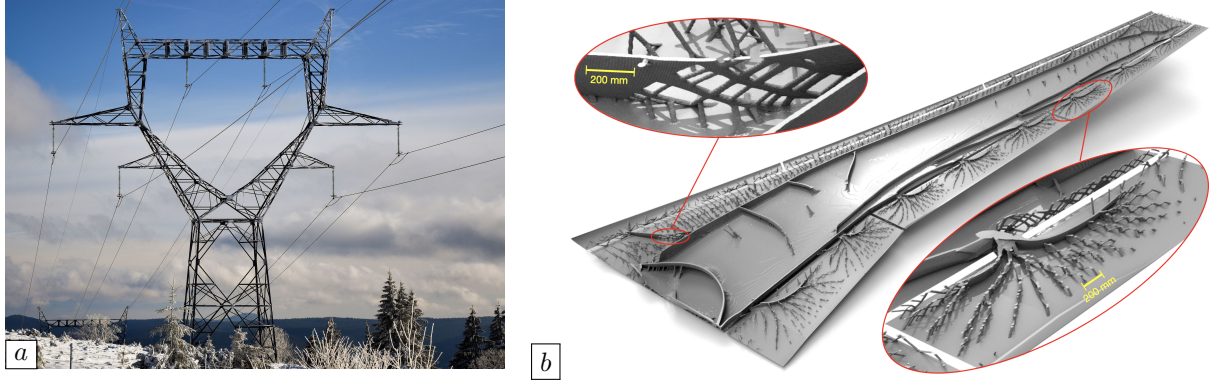


FIGURE 1.1.3. *Optimal design in engineering: (a) An electric pylon is one example of a truss structure; (b) Optimization of the internal structure of the wing of a plane (image excerpted from [1]).*

Nowadays, the dramatic increase in the cost of raw materials makes it necessary to optimize all kinds of mechanical components from the early stages of design. Several engineering softwares (such as **Altair OptiStruct**, or **Ansys Discovery**, to name a few) have emerged from these concerns, but numerous issues have yet to be addressed.

## 1.2 MATHEMATICAL MODELS FOR CONDUCTIVE MEDIA AND LINEARLY ELASTIC STRUCTURES

Most of the discussions of this manuscript take place in the physical context of conductive media or in that of linearly elastic structures, which we briefly present in Section 1.2.1 and Section 1.2.2, respectively. We then set the scene of shape and topology optimization in Section 1.2.3.

### 1.2.1. The conductivity equation

This section is devoted to the conductivity equation, whose mathematical simplicity will often allow to expose our arguments with a minimum amount of technicality.

#### 1.2.1.1. The one-phase conductivity equation

In the present setting, a shape is a bounded, Lipschitz domain  $\Omega \subset \mathbb{R}^d$  ( $d = 2$  or  $3$  in practice), representing a device made of a material with (a priori inhomogeneous) conductivity  $\gamma(x)$ . The voltage potential inside the medium is denoted by  $u$ , or  $u_\Omega$  when its dependence on  $\Omega$  needs to be emphasized. The induced electric current  $j : \Omega \rightarrow \mathbb{R}^d$  describes the stream of charges within  $\Omega$ ; it is given by the following constitutive law:

$$(1.2.1) \quad j(x) = -\gamma(x)\nabla u(x), \quad x \in \Omega,$$

i.e. the electric charges flow from large to low values of the potential. Usually,  $u$  is grounded (i.e. it is set to 0) on a subset  $\Gamma_D$  of the boundary  $\partial\Omega$ ; an external field  $g : \Gamma_N \rightarrow \mathbb{R}$  is applied on a disjoint subset  $\Gamma_N \subset \partial\Omega$ , and the remaining boundary  $\Gamma = \partial\Omega \setminus (\overline{\Gamma_D} \cup \overline{\Gamma_N})$  is free. Eventually,  $\Omega$  contains electric charges whose density evolves at the steady rate  $f$ , see Fig. 1.2.1 (a) for an illustration.

The behavior of the potential  $u$  inside  $\Omega$  is governed by a boundary value problem, which stems from the charge conservation principle. The latter imposes that, for any subdomain  $\omega$  of  $\Omega$ , the electric current passing through the surface  $\partial\omega$  should coincide with the change in the total charge inside  $\omega$ , that is:

$$\int_{\partial\omega} j \cdot n \, ds = \int_{\omega} f \, dx,$$

where  $n \equiv n_{\omega}$  stands for the unit normal vector to  $\partial\omega$ , pointing outward  $\omega$ . An application of Green's formula from [Proposition 1.A.10](#) then yields:

$$\int_{\omega} (\operatorname{div}(j) - f) \, dx = 0,$$

and since this relation holds for any subdomain  $\omega \Subset \Omega$ , we arrive at

$$-\operatorname{div}(\gamma \nabla u) = f \text{ in } \Omega.$$

Summarizing the previous considerations, the steady state  $u$  of the voltage potential inside  $\Omega$  is the solution to the following conductivity equation:

$$(Cond) \quad \begin{cases} -\operatorname{div}(\gamma \nabla u) = f & \text{in } \Omega, \\ u = 0 & \text{on } \Gamma_D, \\ \gamma \frac{\partial u}{\partial n} = 0 & \text{on } \Gamma, \\ \gamma \frac{\partial u}{\partial n} = g & \text{on } \Gamma_N. \end{cases}$$

From the mathematical viewpoint, the coefficient  $\gamma$  is assumed to be smooth, say  $\gamma \in \mathcal{C}^{\infty}(\overline{\Omega})$ , and it is elliptic, i.e. uniformly bounded away from 0 and  $\infty$ :

(Ell-Cond) There exist constants  $0 < \alpha \leq \beta < \infty$  s.t.  $\forall x \in \Omega, \alpha \leq \gamma(x) \leq \beta$ .

The data  $f$  and  $g$  belong to  $L^2(\Omega)$  and  $L^2(\Gamma_N)$ , respectively. The function  $u$  is sought within the functional space

$$H_{\Gamma_D}^1(\Omega) := \{u \in H^1(\Omega), u = 0 \text{ on } \Gamma_D\},$$

and it is the unique solution in the latter to the following variational problem:

$$(1.2.2) \quad \text{Search for } u \in H_{\Gamma_D}^1(\Omega) \text{ s.t. for all } v \in H_{\Gamma_D}^1(\Omega), \quad \int_{\Omega} \gamma \nabla u \cdot \nabla v \, dx = \int_{\Omega} f v \, dx + \int_{\Gamma_N} g v \, ds.$$

The classical Lax-Milgram theory ensures the well-posedness of this problem, see e.g. [\[14\]](#).

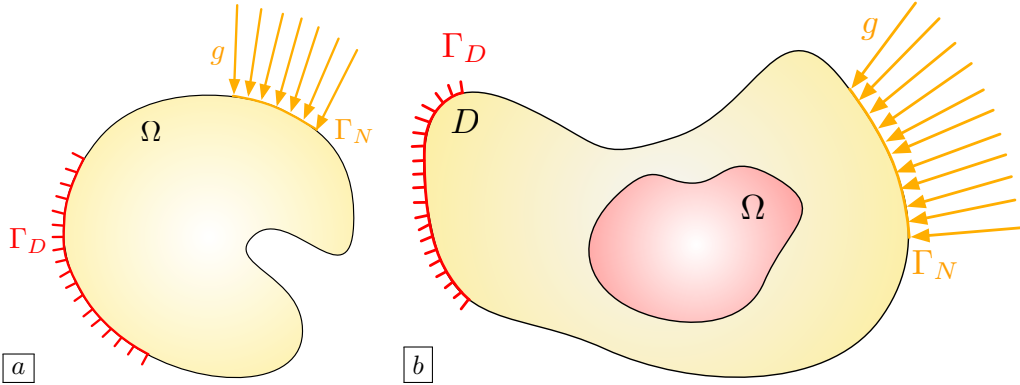


FIGURE 1.2.1. (a) Setting of the one-phase conductivity equation of [Section 1.2.1.1](#); (b) Setting of the two-phase conductivity equation of [Section 1.2.1.2](#).

**Remark 1.2.1** Depending on the assumptions on the domain  $\Omega$ , the conductivity  $\gamma$  and the data  $f$  and  $g$ , the solution  $u_{\Omega}$  to (Cond) may be more regular than what is predicted by the application of the Lax-Milgram framework to (1.2.2). Loosely speaking, the following facts hold true:

- If  $\gamma$ ,  $f$  and  $g$  are smooth, then  $u_{\Omega}$  is smooth inside any subdomain  $\omega \Subset \Omega$ .

- Moreover, if the boundary  $\partial\Omega$  is smooth, then for any point  $x_0 \in \partial\Omega \setminus (\partial\Gamma_D \cup \partial\Gamma \cup \partial\Gamma_N)$ , there exists an open neighborhood  $\omega$  of  $x_0$  in  $\mathbb{R}^d$  such that  $u_\Omega$  is smooth in  $\omega \cap \bar{\Omega}$ .
- Even if  $\partial\Omega$ ,  $\gamma$ ,  $f$  and  $g$  are smooth,  $u_\Omega$  is not “very regular” near the points  $x_0 \in \partial\Gamma_D \cup \partial\Gamma \cup \partial\Gamma_N$  where the boundary conditions of the problem (Cond) change types. This fact has a deep physical meaning that we shall study in more details in [Section 4.3](#).

We refer to [Section 1.A.6](#) for a glimpse about the elliptic regularity theory leading to these conclusions, and to §9.6 in [95] for a more detailed presentation.

### 1.2.1.2. The two-phase conductivity equation

We now turn to a variation of the previous setting, which is illustrated on [Fig. 1.2.1](#) (b): we consider the voltage potential  $u$  inside a physical device  $D \subset \mathbb{R}^d$  composed of two distinct materials, one with high conductivity  $\gamma_1 \in \mathcal{C}^\infty(\bar{\Omega})$ , occupying the Lipschitz subdomain  $\Omega \subset D$ , also denoted by  $\Omega_1$ , and the other with low conductivity  $\gamma_0 \in \mathcal{C}^\infty(\bar{\Omega_0})$ , which occupies the complement  $\Omega_0 := D \setminus \bar{\Omega}$ ; both functions  $\gamma_0$  and  $\gamma_1$  satisfy (Ell-Cond). We still assume that the boundary  $\partial D$  is divided into three disjoint subregions  $\Gamma_D, \Gamma_N, \Gamma$ , with a similar meaning as in the previous [Section 1.2.1.1](#):  $u$  is grounded on  $\Gamma_D$ , an electric current  $g : \Gamma_N \rightarrow \mathbb{R}$  is imposed on  $\Gamma_N$ , and the region  $\Gamma$  is free. Denoting by  $f : D \rightarrow \mathbb{R}$  the density of charges inside  $D$ , the potential  $u$  – also denoted by  $u_\Omega$  when it comes to stress its dependence on the phase  $\Omega$  – satisfies the following two-phase conductivity equation:

$$(1.2.3) \quad \begin{cases} -\operatorname{div}(\gamma \nabla u) = f & \text{in } D, \\ u = 0 & \text{on } \Gamma_D, \\ \gamma \frac{\partial u}{\partial n} = g & \text{on } \Gamma_N, \\ \gamma \frac{\partial u}{\partial n} = 0 & \text{on } \partial D \setminus (\bar{\Gamma_D} \cup \bar{\Gamma_N}), \end{cases} \quad \text{where } \gamma(x) := \begin{cases} \gamma_0(x) & \text{if } x \in \Omega_0, \\ \gamma_1(x) & \text{otherwise.} \end{cases}$$

The variational formulation for this problem reads: search for  $u \in H_{\Gamma_D}^1(D)$  such that,

$$\forall v \in H_{\Gamma_D}^1(D), \quad \int_D \gamma \nabla u \cdot \nabla v \, dx = \int_D f v \, dx + \int_{\Gamma_N} g v \, ds.$$

In this model, the conductivity  $\gamma$  has a particular structure: it is piecewise smooth, with jumps at the interface  $\partial\Omega$  between the phases  $\Omega_0$  and  $\Omega_1$ . A simple calculation reveals that the restrictions  $u_0 = u|_{\Omega_0}$  and  $u_1 = u|_{\Omega_1}$  of  $u$  to  $\Omega_0$  and  $\Omega_1$  satisfy the following coupled problems:

Search for  $(u_0, u_1) \in H^1(\Omega_0) \times H^1(\Omega_1)$  s.t.

$$\begin{cases} -\operatorname{div}(\gamma_0 \nabla u_0) = f & \text{in } \Omega_0, \\ u_0 = 0 & \text{on } \Gamma_D \cap \bar{\Omega_0}, \\ \gamma_0 \frac{\partial u_0}{\partial n} = g & \text{on } \Gamma_N \cap \bar{\Omega_0}, \\ \gamma_0 \frac{\partial u_0}{\partial n} = 0 & \text{on } (\partial D \cap \partial\Omega_0) \setminus (\bar{\Gamma_D} \cup \bar{\Gamma_N}), \end{cases} \quad \text{and} \quad \begin{cases} -\operatorname{div}(\gamma_1 \nabla u_1) = f & \text{in } \Omega_1, \\ u_1 = 0 & \text{on } \Gamma_D \cap \bar{\Omega_1}, \\ \gamma_1 \frac{\partial u_1}{\partial n} = g & \text{on } \Gamma_N \cap \bar{\Omega_1}, \\ \gamma_1 \frac{\partial u_1}{\partial n} = 0 & \text{on } (\partial D \cap \partial\Omega_1) \setminus (\bar{\Gamma_D} \cup \bar{\Gamma_N}), \end{cases}$$

complemented with the transmission conditions

$$u_0 = u_1 \text{ and } \gamma_0 \frac{\partial u_0}{\partial n} = \gamma_1 \frac{\partial u_1}{\partial n} \text{ on } \partial\Omega \cap D.$$

These conditions express the continuity of the potential  $u$  and of the electric current  $j = -\gamma \nabla u$  at the interface between  $\Omega_0$  and  $\Omega_1$ .

**Remark 1.2.2** The boundary-value problem (Cond) and its two-phase counterpart (1.2.3) admit various physical interpretations beyond the realm of conductive media. For instance, they are used in the study of dielectric devices, where they account for the potential  $u$  inside a medium with permittivity  $\gamma$ . They are also ubiquitous in the field of thermics, where  $u$  stands for the temperature inside the medium,  $\gamma$  is the thermal conductivity, and the constitutive law (1.2.1) is the familiar Fourier’s law, whereby the heat flux  $j$  is oriented from hot to cold regions.

### 1.2.1.3. The ersatz material approximation

For various purposes, it is useful to approximate the conductivity equation (Cond) attached to a domain  $\Omega \subset \mathbb{R}^d$  by a counterpart posed on a larger domain  $D$ . One possibility to achieve this goal – usually referred

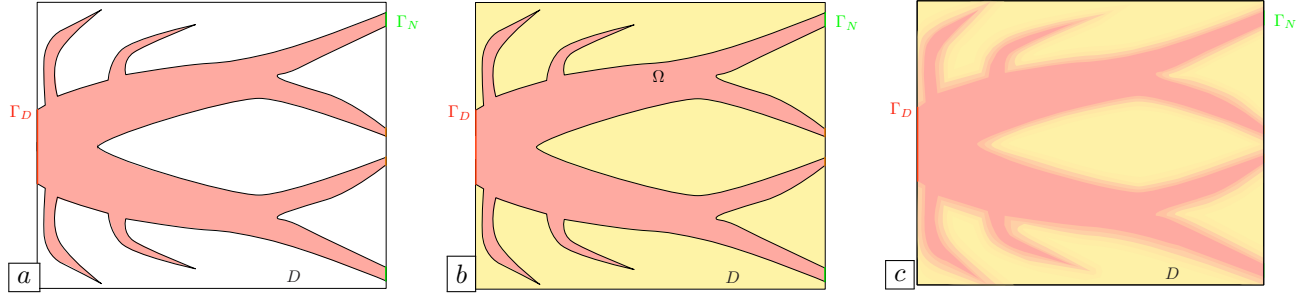


FIGURE 1.2.2. *Ersatz material approximations of the “ideal” situation of a dielectric medium  $\Omega$  inside a large box  $D$  (in (a)); the latter can be approximated by the situation where the “void” region  $D \setminus \bar{\Omega}$  is filled with a very soft material (b), and, going further, by the situation where the resulting discontinuous material properties are smoothed (in (c)).*

to as the “ersatz material approximation” in the literature – hinges on a two-phase conductivity equation of the form (1.2.3).

Let  $\Omega \subset \mathbb{R}^d$  be a shape as in Section 1.2.1, and let  $u$  be the voltage potential, solution to (Cond). Let  $D \subset \mathbb{R}^d$  be a larger, “hold-all” domain. For simplicity, we assume that the regions  $\Gamma_D$  and  $\Gamma_N$  bearing respectively homogeneous Dirichlet and inhomogeneous Neumann boundary conditions are comprised in the boundary  $\partial D$ , so that only the part  $\Gamma$  of  $\partial\Omega$  where  $\Omega$  is surrounded by void lies strictly inside  $D$ , see Fig. 1.2.2.

We approximate the system (Cond) by the following one, where the void in  $D \setminus \bar{\Omega}$  is mimicked by the presence of a very soft material, with conductivity  $\eta\gamma$ , for a “small” parameter  $\eta \ll 1$  (typically,  $\eta = 1e^{-3}$  or  $1e^{-4}$ ):

$$(1.2.4) \quad \begin{cases} -\operatorname{div}(\gamma_\eta \nabla u_\eta) = (\eta + (1 - \eta)\mathbf{1}_\Omega)f & \text{in } D, \\ u_\eta = 0 & \text{on } \Gamma_D, \\ \gamma_\eta \frac{\partial u_\eta}{\partial n} = g & \text{on } \Gamma_N, \\ \gamma_\eta \frac{\partial u_\eta}{\partial n} = 0 & \text{on } \partial D \setminus (\bar{\Gamma}_D \cup \bar{\Gamma}_N), \end{cases} \quad \text{where } \gamma_\eta(x) := \begin{cases} \gamma(x) & \text{if } x \in \Omega, \\ \eta\gamma(x) & \text{otherwise.} \end{cases}$$

Note that here,  $\gamma(x)$  stands for any smooth extension of the conductivity  $\gamma \in \mathcal{C}(\bar{\Omega})$  when  $x \notin \bar{\Omega}$ .

It is sometimes preferable to use a smoothed version  $\widetilde{\gamma_\eta}$  of the above discontinuous conductivity  $\gamma_\eta$ , as exemplified on Fig. 1.2.2. This notably allows the solution  $\widetilde{u}_\eta$  to the resulting boundary value problem to be smooth, see Remark 1.2.1 and Section 1.A.6.

Let us insist that this ersatz material approximation is possible because the transition between the full and ersatz materials in (1.2.4) replaces that between material and void in the reference problem (Cond), i.e. the soft material  $\eta\gamma$  mimicks the presence of void near  $\Gamma$ , which is encoded in the homogeneous Neumann boundary condition on  $\Gamma$  in the reference problem (Cond). This ersatz material approximation has been proved rigorous in [140]: under mild technical assumptions that we omit for brevity, the following convergence holds:

$$\|u_\eta - u\|_{H^1(\Omega)} \xrightarrow{\eta \rightarrow 0} 0.$$

It can be generalized to several contexts, including that of linear elasticity. A counterpart in the case where other boundary conditions are imposed on  $\Gamma$  (e.g. homogeneous Dirichlet boundary conditions) is possible and relevant in some contexts (notably in fluid mechanics), but demands alternative approximate systems, see for instance Chap. VII in [92] about this point.

## 1.2.2. Linear elastic structures

In this section, we slip into the physical setting of linearly elastic structures, which is relatively simple from the mathematical viewpoint and lends itself to rich applications.

From the physical viewpoint, elasticity refers to the ability of an object to undergo deformations when it is subjected to external stresses, and to revert exactly to its original configuration when these stresses are released. The theory of linearized elasticity, which is specialized to the description of “small” deformations, is essentially composed of three ingredients, that are discussed next: [Section 1.2.2.1](#) is devoted to the kinematic description of an elastic shape, i.e. to the representation of its motion, regardless of the efforts that have caused it; [Section 1.2.2.2](#) presents the modeling of the internal and external efforts applied on an elastic shape; [Section 1.2.2.3](#) introduces the concept of constitutive relation, relating the deformation of a shape to the stresses that are responsible for it. In [Section 1.2.2.4](#), we summarize these developments and we provide the mathematical framework for the study of the linear elasticity equations. Finally, in [Section 1.2.2.5](#), we discuss energy considerations related to elastic structures. We refer to classical textbooks such as [194, 321, 352] for further details about the modeling of elastic structures.

**Remark 1.2.3** *Although the natural applications of structural mechanics take place in the three-dimensional setting  $d = 3$ , the mathematical theory of linear elasticity can be formulated in a unified way for any  $d \geq 2$ . The 2d linear elasticity equations can be interpreted as a reduction of the 3d theory in the case of structures which are invariant in one dimension, say  $e_3$ . Two cases occur, which are illustrated on [Fig. 1.2.3](#):*

- *Plane stress 2d elasticity is used to describe a structure  $\Omega$  which is very thin in the direction  $e_3$ : the internal and external efforts applied to  $\Omega$  are assumed to be purely two-dimensional.*
- *Plane strain 2d elasticity corresponds to the case of a very thick structure  $\Omega$  in the direction  $e_3$ : the deformations undergone by  $\Omega$  are assumed to be contained in the plane spanned by  $e_1$  and  $e_2$ .*

Formally, both situations differ solely in how the material properties of the 3d structure are turned into 2d equivalent ones, see [Section 1.2.2.3](#).

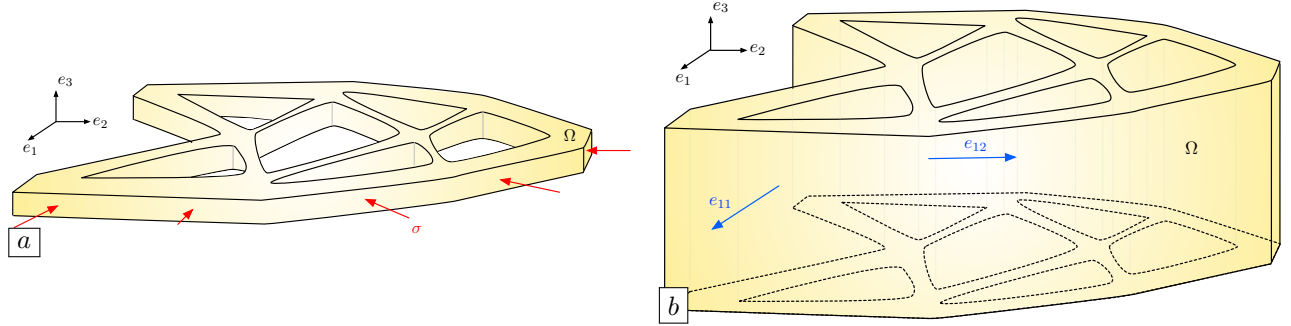


FIGURE 1.2.3. (a) The stresses experienced by a structure in plane stress situation are purely two-dimensional; (b) The strain of a structure in plane strain situation is purely two-dimensional.

### 1.2.2.1. Kinematic description of linearly elastic structures

The usual description of an elastic structure is Lagrangian. It is based on the configuration at rest of the structure, which is a domain  $\Omega \subset \mathbb{R}^d$ , and on the displacement vector field  $u : \Omega \rightarrow \mathbb{R}^d$ , which encodes the location  $x + u(x)$  of any point  $x \in \Omega$  after deformation: the deformed configuration of the structure is  $(\text{Id} + u)(\Omega)$ , as depicted on [Fig. 1.2.4](#).

In the present manuscript, we only consider the setting of linear elasticity, where the displacement  $u$  and all its derivatives are assumed to be “small”, which allows for major simplifications in the mathematical equations.

The relative motion of the points of a structure  $\Omega$  undergoing a displacement  $u$  is measured in terms of the linearized strain tensor  $e(u) : \Omega \rightarrow \mathbb{R}_{\text{sym}}^{d \times d}$ , defined by:

$$e(u) = \frac{1}{2}(\nabla u + \nabla u^T).$$

For a point  $x \in \Omega$ , the physical interpretation of the matrix  $e(u)(x)$  is as follows, see [Fig. 1.2.5](#):

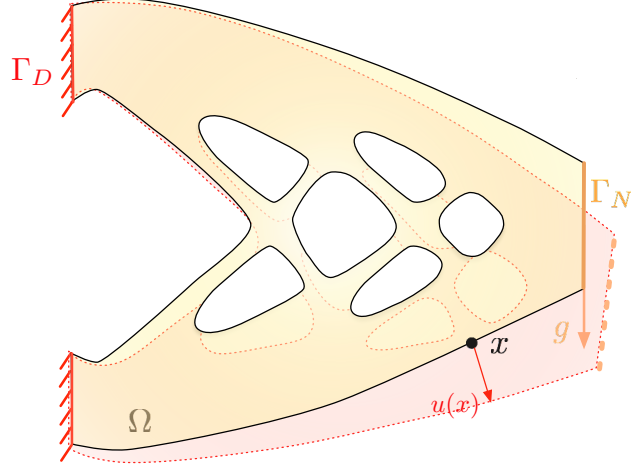


FIGURE 1.2.4. The elastic structure  $\Omega$  realizes the displacement  $u$  under the effect of body forces  $f : \Omega \rightarrow \mathbb{R}^d$  and surface loads  $g : \Gamma_N \rightarrow \mathbb{R}^d$ .

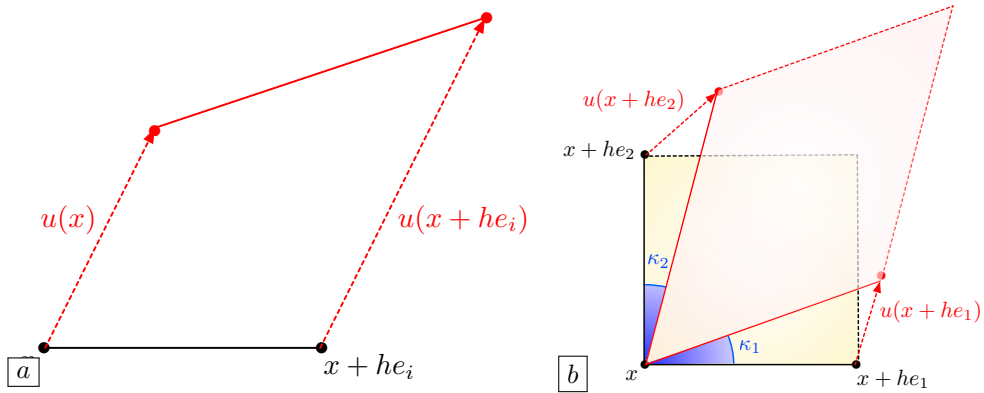


FIGURE 1.2.5. Physical interpretation of the entries of the strain tensor  $e(u)(x)$ ; (a) The diagonal entry  $e(u)(x)_{ii}$  appraises the variation of the segment  $[x, x + he_i]$  after deformation; (b) The off-diagonal entry  $e(u)(x)_{12}$  measures the variation of the angle between  $[x, x + he_1]$  and  $[x, x + he_2]$  after deformation.

- For  $i = 1, \dots, d$ , the diagonal entry  $e(u)(x)_{ii}$  encodes the stretching or the compression effect induced by  $u$  in the direction  $e_i$ ; the length  $h \ll 1$  of the small line segment with endpoints  $x$  and  $x + he_i$  becomes, after deformation:

$$|x + he_i + u(x + he_i) - (x + u(x))| \approx h + he(u)(x)_{ii}.$$

- For  $i, j = 1, \dots, d$ ,  $i \neq j$ ,  $e(u)(x)_{ij}$  measures the distortion of angles between the directions  $e_i$  and  $e_j$ ; more precisely,

$$e(u)(x)_{ij} = \frac{1}{2}(\kappa_1 + \kappa_2), \text{ where } \kappa_1 \approx \tan \kappa_1 \approx \frac{\partial u_2}{\partial x_1}, \text{ and } \kappa_2 \approx \tan \kappa_2 \approx \frac{\partial u_1}{\partial x_2}.$$

Another means to appraise how  $e(u)$  accounts for the deformation of lengths and angles induced by  $u$  is the following. Let  $[0, 1] \ni t \mapsto \gamma(t)$  be a curve drawn within  $\Omega$ , with length:

$$\ell(\gamma) = \int_0^1 |\gamma'(t)| dt.$$

The deformed version of  $\gamma$  is the curve  $[0, 1] \ni t \mapsto (\text{Id} + u)(\gamma(t))$ , whose length equals:

$$\begin{aligned}\ell((\text{Id} + u) \circ \gamma) &= \int_0^1 \sqrt{C(u)(\gamma(t))\gamma'(t) \cdot \gamma'(t)} dt, \\ &\approx \ell(\gamma) + \int_0^1 e(u)(\gamma(t)) \frac{\gamma'(t)}{|\gamma'(t)|} \cdot \frac{\gamma'(t)}{|\gamma'(t)|} |\gamma'(t)| dt,\end{aligned}$$

where  $C(u)$  is the right Cauchy-Green strain tensor defined by

$$C(u) = (\mathbf{I} + \nabla u)^T (\mathbf{I} + \nabla u).$$

The latter depends in a nonlinear way on  $u$ , and it measures exactly the deformation of lengths incurred by the displacement  $u$ . The linearized strain tensor  $e(u)$  is the linear part of the tensor  $\frac{1}{2}(C(u) - \mathbf{I})$ . Considering  $e(u)$  in place of  $C(u)$  is the first source of linearity in the classical linear elasticity model; this simplification is called the “geometric linearity assumption”.

### 1.2.2.2. Description of efforts

The second ingredient in the description of an elastic structure  $\Omega$  is the representation of internal and external efforts, also called stresses. This task involves Cauchy’s stress tensor  $\sigma : \Omega \rightarrow \mathbb{R}^{d \times d}$ : for any point  $x \in \Omega$  and any unit vector  $n \in \mathbb{S}^{d-1}$ ,  $\sigma(x)n$  is the force applied by the outer medium on the face of an infinitesimally small cube of material around  $x$ , see [Fig. 1.2.6](#). The entries of the tensor  $\sigma(x)$  can be separated between traction-compression entries and shear components, as depicted on [Fig. 1.2.6](#) (b), (c):

- For  $i = 1, \dots, d$ ,  $\sigma(x)_{ii}$  represents the  $i^{\text{th}}$  component of the force applied on the face oriented by  $e_i$ ; it thus accounts for a compression effect when  $\sigma(x)_{ii} < 0$ , and a stretching (or dilation) effect if  $\sigma(x)_{ii} > 0$ .
- For  $i, j = 1, \dots, d$ ,  $i \neq j$ , the off-diagonal entry  $\sigma(x)_{ij}$  is the  $i^{\text{th}}$  component of the force applied on the face oriented by  $e_j$ ; it accounts for a shearing effect, whereby this face undergoes a tangential deformation.

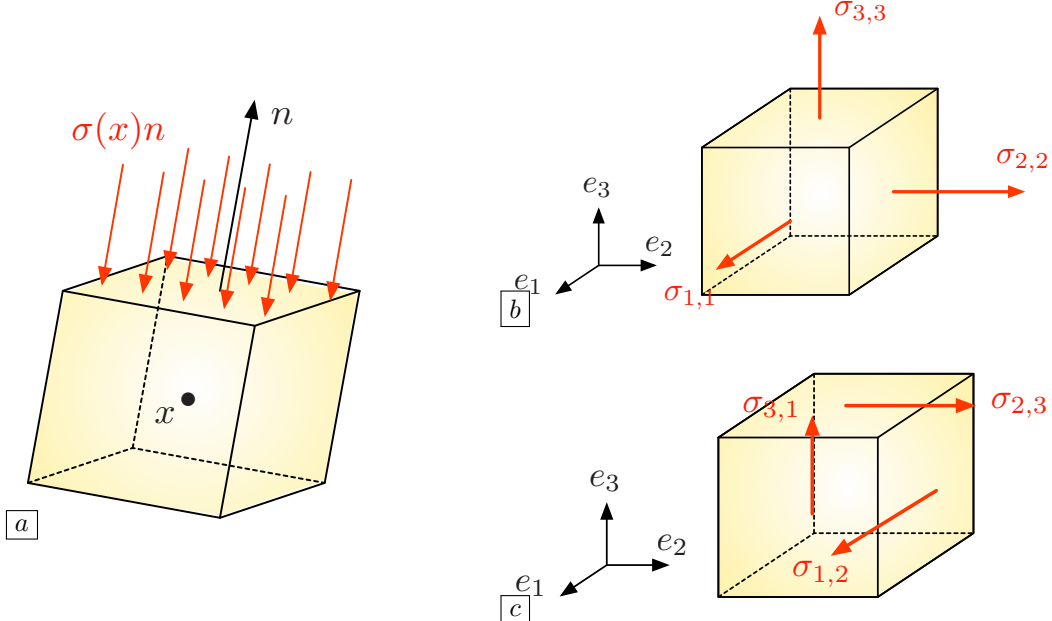


FIGURE 1.2.6. (a) For  $x \in \Omega$  and  $n \in \mathbb{S}^{d-1}$ , the vector  $\sigma(x)n$  is the force imposed by the outer medium onto the face oriented by  $n$  of a small cube around  $x$ ; (b) The diagonal entries of  $\sigma(x)$  account for the compression efforts felt by this cube; (c) The off-diagonal entries encode the shear effects imposed on this cube.

The stress tensor allows to express the conditions of equilibrium of a structure  $\Omega$ . Let  $f : \Omega \rightarrow \mathbb{R}^d$  be the density of body forces (e.g. gravity) at play in  $\Omega$ , and let  $g : \Gamma_N \rightarrow \mathbb{R}^d$  be the density of surface loads, applied on a fixed subset  $\Gamma_N$  of  $\partial\Omega$ . Then:

- The law of balance of linear momentum states that, for each subdomain  $\omega \Subset \Omega$ , the sum of the body forces inside  $\omega$  and the forces applied by the rest of the structure on  $\partial\omega$  must vanish, i.e.

$$\int_{\omega} f \, dx + \int_{\partial\omega} \sigma n \, ds = 0.$$

After application of the Green's formula of [Proposition 1.A.10](#), this rewrites:

$$\int_{\omega} (\operatorname{div}(\sigma) + f) \, dx = 0,$$

and since this relation should hold for any subdomain  $\omega \Subset \Omega$ , it follows:

$$-\operatorname{div}(\sigma) = f \text{ in } \Omega.$$

- Applying the same principle inside a small enough subdomain  $\omega \subset \Omega$  whose boundary contains a portion of  $\Gamma_N$ , we obtain:

$$\int_{\omega} f \, dx + \int_{\partial\omega \cap \Gamma_N} g \, ds + \int_{\partial\omega \setminus \overline{\Gamma_N}} \sigma n \, ds = 0,$$

that is:

$$\int_{\omega} f \, dx + \int_{\partial\omega} \sigma \cdot n \, ds + \int_{\partial\omega \cap \Gamma_N} g \, ds - \int_{\partial\omega \cap \Gamma_N} \sigma n \, ds = 0.$$

Using Green's formula on the second term in the above left-hand side together with the fact that  $-\operatorname{div}(\sigma) = f$  inside  $\omega$ , we obtain that the first two terms of the above equation vanish; since  $\omega$  is arbitrary, this entails:

$$\sigma n = g \text{ on } \Gamma_N.$$

Note that this fact can also be understood as an application of the law of reciprocal actions.

- According to the law of balance of angular momentum, no subdomain  $\omega \Subset \Omega$  should undergo rotational efforts induced by the outer medium; the (non trivial) Cauchy's theorem shows that this requirement is equivalent to the fact that  $\sigma$  should be symmetric:

$$\forall x \in \Omega, \quad \sigma(x) \in \mathbb{R}_{\text{sym}}^{d \times d}.$$

#### 1.2.2.3. A wee bit of rheology: constitutive laws

The above description of an elastic structure is completed by a constitutive relation between the stress  $\sigma$  inside  $\Omega$  and the induced strain  $e(u)$ . In multiple applications, it is supposed to be linear, of the form:

$$\sigma = Ae(u), \text{ or equivalently } e(u) = S\sigma.$$

Here, the a priori inhomogeneous (i.e. space dependent) tensor  $A$  and its inverse  $S$  are the Hooke's tensor and the compliance tensor of the material, respectively. For  $x \in \Omega$ ,  $A(x)$  and  $S(x)$  are linear mappings from  $\mathbb{R}_{\text{sym}}^{d \times d}$  into itself, encoding the local properties of the constituent material of  $\Omega$  around  $x$ , in a way which we now discuss more precisely. To this end, we focus on the three-dimensional context; the 2d case is evoked in [Remark 1.2.4](#). Also, to simplify the discussion, we assume the considered material to be homogeneous.

In general,  $A$  is a fourth-order tensor  $A = \{A_{ijkl}\}_{i,j,k,l=1,\dots,3}$  with the following symmetries:

$$\forall i, j, k, l = 1, \dots, 3, \quad A_{ijkl} = A_{klji}, \text{ and } A_{ijkl} = A_{jikl} = A_{ijlk}.$$

Hence,  $A$  has 21 independent entries. Fortunately, most materials present symmetries, which allows to reduce the number of these independent entries:

- Isotropic materials exhibit the same behavior in all directions of space; their Hooke's tensor  $A$  is completely characterized by two scalar parameters  $\lambda$  and  $\mu$ , called the Lamé parameters of the material:

$$(1.2.5) \quad \forall \xi \in \mathbb{R}_{\text{sym}}^{3 \times 3}, \quad A\xi = 2\mu\xi + \lambda \operatorname{tr}(\xi)I.$$

The parameter  $\mu$  is called the shear modulus; it corresponds to the angular deviation caused by a unit shear stress, see Fig. 1.2.7 (a); the physical interpretation of  $\lambda$  is unfortunately not as clear. Usually, two more physical quantities  $E$  and  $\nu$  are used, from which  $\lambda$  and  $\mu$  can be retrieved as:

$$\mu = \frac{E}{2(1+\nu)}, \text{ and } \lambda = \frac{E\nu}{(1+\nu)(1-2\nu)}.$$

The Young's modulus  $E$  measures the resistance of the material to traction and compression, and the Poisson's ratio  $\nu$  measures its resistance to transverse deformations, see Fig. 1.2.7.

- A more general class of materials is that of orthotropic materials. These possess three orthogonal planes of symmetry, and as a result, they enjoy different properties along the corresponding axes. They are characterized by one Young's modulus  $E_i$  in each direction  $i = 1, 2, 3$ , one Poisson's ratio  $\nu_{ij}$  and one shear modulus  $G_{ij}$  for each pair  $i \neq j$ . One example of an orthotropic material is depicted on Fig. 1.2.8 (a).
- Transversely isotropic materials have a particular form of orthotropy. They have one plane of symmetry, and show an isotropic behavior within any plane parallel to the latter. The physical properties of a material with transverse isotropy, say in direction  $e_3$ , are characterized by five independent parameters: two Young's moduli  $E_3$  and  $E_1 = E_2$  encoding the resistance to stretching in the transverse and longitudinal directions, respectively, two Poisson's ratios  $\nu_{13} = \nu_{23}$  and  $\nu_{12}$  and the shear modulus  $G_{13} = G_{23}$  between the transverse and longitudinal directions. One example of a transversely isotropic material is depicted on Fig. 1.2.8 (a).

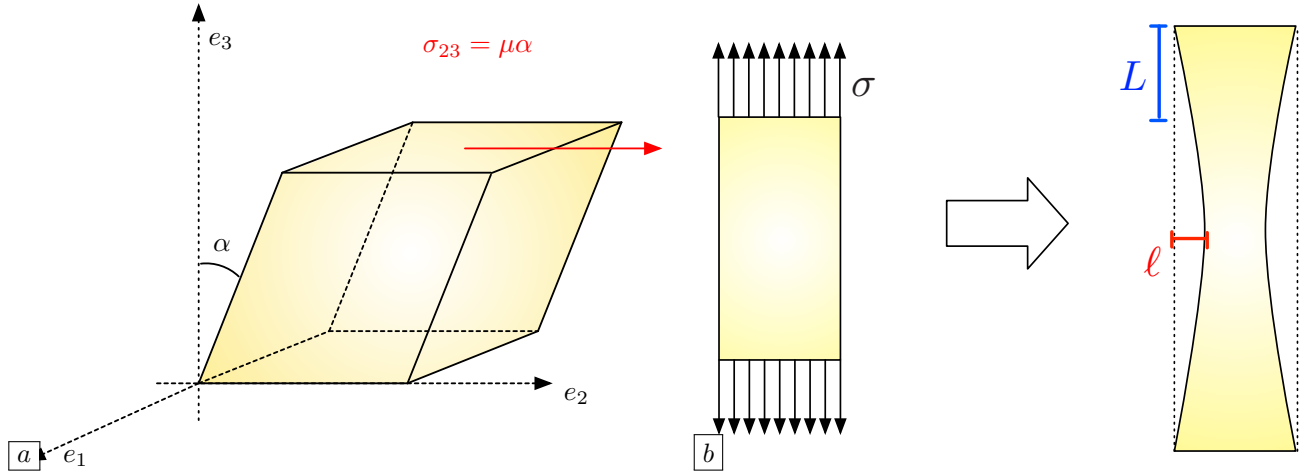


FIGURE 1.2.7. (a) The shear modulus  $\mu$  accounts for the force  $\sigma_{23} = \mu\alpha$  that should be applied on the face oriented by  $e_3$  of a piece of material in the transverse direction  $e_2$  to create an angle  $\alpha$  with the  $e_3$  direction; (b) The Young's modulus  $E = \sigma/L$  accounts for the amplitude of the force  $\sigma$  needed to stretch a piece of material by a length  $L$ ; the Poisson's ratio  $\nu = -l/L$  measures the relative transverse displacement in this process.

**Remark 1.2.4** The above considerations related to the elastic properties of structures take place in the physically prevalent setting of three space dimensions. The definition of the Hooke's tensor  $A$  of a 2d structure depends on how the latter accounts for a 3d one which is invariant in the  $e_3$  direction, see Remark 1.2.3. In plane stress, where the components  $\sigma_{i3} = \sigma_{3i}$  of the stress tensor vanish ( $i = 1, 2, 3$ ), the Lamé parameters  $\lambda$  and  $\mu$  characterizing the 2d tensor  $A$  in (1.2.5) are obtained from the Young's modulus  $E$  and the Poisson's ratio  $\nu$  of the 3d material via the relations:

$$\mu = \frac{E}{2(1+\nu)}, \text{ and } \lambda = \frac{E\nu}{1-\nu^2}.$$



FIGURE 1.2.8. (a) Wood is an orthotropic material with large stiffness in the direction of the grain, low stiffness in the radial direction, and intermediate stiffness in the azimuthal direction; (b) Fiber-reinforced concrete is a transversely isotropic material: it is much stiffer in the direction of the metallic fibers than in the orthogonal directions.

In plane strain, where the components  $e(u)_{i3} = e(u)_{3i}$  of the strain tensor vanish, one has instead:

$$\mu = \frac{E}{2(1+\nu)}, \text{ and } \lambda = \frac{E\nu}{(1+\nu)(1-2\nu)}.$$

**Remark 1.2.5** The strain tensor  $e(u)$  is by essence a Lagrangian quantity, as it is defined on the reference configuration  $\Omega$  of the structure. On the contrary, stresses are naturally expressed in the Eulerian variable, i.e. on the deformed configuration  $(\text{Id} + u)(\Omega)$ . Hence, the constitutive law should relate  $e(u)$  with a transported version of the stress tensor  $\sigma$  onto the reference configuration, called the Piola-Kirchoff stress tensor. In the present setting, this difficulty is ignored since both notions of stress tensors coincide at leading order, as the displacement of the structure is small, see the discussion in Chap. 13 of [352] about this point.

#### 1.2.2.4. The linear elasticity system

Gathering the concepts of the previous sections, we are in position to write down a prototype for boundary-value problems in the physical context of linearly elastic structures.

Let  $\Omega \subset \mathbb{R}^d$  be a structure which is attached on a region  $\Gamma_D$  of its boundary; it is submitted to body forces  $f : \Omega \rightarrow \mathbb{R}^d$  and surface loads  $g : \Gamma_N \rightarrow \mathbb{R}^d$ , applied on a region  $\Gamma_N$  of  $\partial\Omega$  disjoint from  $\Gamma_D$ , see again Fig. 1.2.4. The displacement  $u$  of  $\Omega$  – also denoted by  $u_\Omega$  – is the solution to the following system:

$$(1.2.4) \quad \begin{cases} -\text{div}(Ae(u)) = f & \text{in } \Omega, \\ u = 0 & \text{on } \Gamma_D, \\ Ae(u)n = g & \text{on } \Gamma_N, \\ Ae(u)n = 0 & \text{on } \Gamma. \end{cases}$$

The mathematical framework associated to this system is similar to that presented in Section 1.2.1.1. The Hooke's tensor  $A : \Omega \rightarrow \mathcal{L}(\mathbb{R}_{\text{sym}}^{d \times d}, \mathbb{R}_{\text{sym}}^{d \times d})$  is a smooth enough mapping satisfying the following ellipticity property:

$$(1.2.6) \quad \text{There exist constants } 0 < \alpha \leq \beta < \infty \text{ s.t. } \forall x \in \Omega, \forall \xi \in \mathbb{R}_{\text{sym}}^{d \times d}, \quad \alpha \|\xi\|^2 \leq A(x)\xi : \xi \leq \beta \|\xi\|^2.$$

The body forces and surface loads  $f$  and  $g$  belong to the respective spaces  $L^2(\Omega)^d$  and  $L^2(\Gamma_N)^d$  and the displacement  $u$  is sought as the solution to the variational problem:

$$(1.2.7) \quad \text{Search for } u \in H_{\Gamma_D}^1(\Omega)^d \text{ s.t. } \forall v \in H_{\Gamma_D}^1(\Omega)^d, \quad \int_{\Omega} Ae(u) : e(v) \, dx = \int_{\Omega} f \cdot v \, dx + \int_{\Gamma_N} g \cdot v \, ds,$$

whose well-posedness follows from the Lax-Milgram theory – the ellipticity of the involved bilinear form being a consequence of (1.2.6) and the Korn's inequality, see for instance [129].

**Remark 1.2.6** The elliptic regularity theory, which loosely speaking ensures that, under suitable assumptions on  $\Omega$ ,  $f$  and  $g$ , the solution  $u$  to (Elas) is “smooth”, can be deployed pretty much as in the scalar case of the conductivity equation evoked in Remark 1.2.1. As is exemplified in the sketch provided in Section 1.A.6, the pivotal ingredient of this theory is the ellipticity assumption (1.2.6), ensuring a control of the norm of  $u$  in terms of the operator  $u \mapsto -\operatorname{div}(Ae(u))$ .

**Remark 1.2.7** The ersatz material approximation discussed in Section 1.2.1.3 has a straightforward counterpart in the framework of linear elasticity.

### 1.2.2.5. Energy considerations in linear elasticity

Much intuition about the behavior of an elastic structure can be gleaned from energetic considerations.

Let us assume that the structure  $\Omega$  under scrutiny is in a deformed state characterized by the displacement  $u$ . One may prove that the work done by internal forces when this structure is further displaced by a small increment  $v$  equals:

$$(1.2.8) \quad - \int_{\Omega} \sigma(u) : e(v) \, dx.$$

Equivalently, in order to bring the structure from the configuration defined by  $u$  to that defined by  $u + v$ , one has to supply an amount of energy equal to  $\int_{\Omega} \sigma(u) : e(v) \, dx$ . Note that, when  $v$  is of the form  $v = dh u$  with  $dh \ll 1$ , the work (1.2.8) is negative, indicating that internal forces always work again the motion.

The total strain energy needed to bring  $\Omega$  from rest to  $(\operatorname{Id} + u)(\Omega)$  is obtained by integrating the above increment between both configurations, which reads:

$$\int_0^1 \int_{\Omega} \sigma(hu) : e(u) \, dx \, dh = \frac{1}{2} \int_{\Omega} \sigma(u) : e(u) \, dx.$$

Physically, the elastic energy of a system is the potential energy stored in the latter as the deformation occurs under the effect of work performed on it. This energy can then be converted and released under various forms, such as kinetic or thermal energy.

Likewise, when the structure is further deformed according to a small increment  $v$  from the deformed configuration characterized by  $u$ , the work of external loads is

$$\int_{\Omega} f \cdot v \, dx + \int_{\Gamma_N} g \cdot v \, ds.$$

This quantity is positive when  $v$  is oriented in the direction of the forces  $f$  and  $g$ : intuitively, these then work in favor of the motion by handing energy to the system. The total work of  $f$  and  $g$  when  $\Omega$  passes from rest to the deformed configuration  $(\operatorname{Id} + u)(\Omega)$  is obtained by a similar integration as above:

$$\int_{\Omega} f \cdot u \, dx + \int_{\Gamma_N} g \cdot u \, ds.$$

Finally, the total energy  $E(u)$  stored by  $\Omega$  in the displacement from rest to  $(\operatorname{Id} + u)(\Omega)$  equals:

$$E(u) := \frac{1}{2} \int_{\Omega} \sigma(u) : e(u) \, dx - \int_{\Omega} f \cdot u \, dx - \int_{\Gamma_N} g \cdot u \, ds.$$

The actual displacement  $u_{\Omega}$  of  $\Omega$ , which we have characterized as the solution to (Elas) in the previous section, is obtained by minimizing  $E(u)$  among all the possible displacements of the structure, that is:

$$(1.2.9) \quad u_{\Omega} = \arg \min_{u \in H_{\Gamma_D}^1(\Omega)^d} E(u).$$

The mathematical equivalence between (Elas) and (1.2.9) follows from a classical application of the Lax-Milgram theory. Note that, using the variational problem (1.2.7) satisfied by  $u_{\Omega}$ , the minimum value of the energy  $E(u)$  reads:

$$E(u_{\Omega}) = \min_{u \in H_{\Gamma_D}^1(\Omega)^d} E(u) = -\frac{1}{2} \int_{\Omega} Ae(u_{\Omega}) : e(u_{\Omega}) \, dx.$$

This quantity is always nonpositive, reflecting that the application of external forces  $f$  and  $g$  to the structure  $\Omega$  always triggers a motion of the latter by conveying energy (which is thus subtracted from its potential energy).

### 1.2.3. Shape optimization of elastic structures

Having set the physical background of our investigations, we now enter into the core of the matter discussed in this manuscript and we sketch a typical shape and topology optimization problem, retaining the physical context of elastic structures to set ideas:

$$(\mathcal{P}) \quad \min_{\Omega \in \mathcal{U}_{\text{ad}}} J(\Omega) \text{ s.t. } \begin{cases} G(\Omega) = 0, \\ H(\Omega) \leq 0. \end{cases}$$

In this formulation,

- $\mathcal{U}_{\text{ad}}$  is the set of admissible shapes  $\Omega$ , which often encompasses “hard constraints” on shapes  $\Omega$ , for instance that their boundary should enclose fixed regions of space;
- $J(\Omega)$  is the objective function;
- $G(\Omega)$  and  $H(\Omega)$  are collections of  $p$  and  $q$  real-valued equality and inequality constraint functionals, respectively.

Most physically relevant objective and constraint functions often depend on the structure  $\Omega$  in a complicated way, via the elastic displacement  $u_\Omega$ , solution to the boundary-value problem (Elas) posed on  $\Omega$  – a “state” equation in the jargon of shape and topology optimization. For instance, the objective function  $J(\Omega)$  may stand for one of the following quantities of interest:

- The compliance  $C(\Omega)$ , defined by:

$$(1.2.10) \quad C(\Omega) = \int_{\Omega} f \cdot u_\Omega \, dx + \int_{\Gamma_N} g \cdot u_\Omega \, ds = \int_{\Omega} A e(u_\Omega) : e(u_\Omega) \, dx.$$

According to Section 1.2.2.5, this quantity is a global measure of the inverse of the rigidity of  $\Omega$ : it can be equivalently interpreted as (twice) the total elastic energy stored in  $\Omega$ , or as the work done by the external loads when  $\Omega$  passes from rest to its deformed configuration.

- A least-square discrepancy  $D(\Omega)$  between the displacement  $u_\Omega$  of  $\Omega$  and a target displacement  $u_T \in L^2(\mathbb{R}^d)^d$ :

$$(1.2.11) \quad D(\Omega) = \int_{\Omega} k(x) |u_\Omega - u_T|^2 \, dx,$$

where  $k \in L^\infty(\mathbb{R}^d)$  is a weighting factor. Among other applications, such a criterion is useful in the design of mechanical actuators (also called compliant mechanisms), i.e. devices that realize a prescribed displacement when submitted to given input efforts, see e.g. [337].

- A criterion based on the level of stress inside the structure

$$S(\Omega) = \left( \int_{\Omega} \|\sigma(u_\Omega)\|^p \, dx \right)^{\frac{1}{p}}, \quad \sigma(u) \equiv A e(u),$$

as a differentiable approximation of the supremum  $\sup_{x \in \Omega} \|\sigma(u_\Omega)(x)\|$  as  $p \rightarrow \infty$ . Such functionals are of utmost importance in engineering, as the maximum level of stress inside  $\Omega$  is an indicator of where fracture is likely to occur first.

The constraints featured in the problem  $(\mathcal{P})$  could represent:

- Requirements about maximum bounds  $V_T$  or  $P_T$  on the volume  $\text{Vol}(\Omega)$  or the perimeter  $\text{Per}(\Omega)$  of  $\Omega$ , respectively, where:

$$\text{Vol}(\Omega) = \int_{\Omega} \, dx, \quad \text{and} \quad \text{Per}(\Omega) := \int_{\partial\Omega} \, ds.$$

- Geometric constraints imposed by the manufacturing process, such as thickness constraints, casting constraints – for which we refer to [261] and the references therein – or constraints imposed by additive manufacturing technologies, as we shall study in detail in Chapter 3.

Our discussions will sometimes be eased by considering unconstrained variants of the shape optimization problem  $(\mathcal{P})$ , of the form

$$(\mathcal{P}_{\text{uncons}}) \quad \min_{\Omega \in \mathcal{U}_{\text{ad}}} \mathcal{L}(\Omega),$$

where  $\mathcal{L}(\Omega)$  may be a weighted sum of an objective function  $J(\Omega)$  and a constraint function  $G(\Omega)$  or  $H(\Omega)$  in the above list.

### 1.3 MATHEMATICAL REPRESENTATION OF SHAPES AND THEIR VARIATIONS

One central issue in both theoretical and numerical investigations in shape and topology optimization lies in the selection of an appropriate representation of the “shape” and of a suitable notion of differentiation with respect to the latter in view of its optimization. After general discussions about the description of shapes in [Section 1.3.1](#) and the non existence of an optimal design in [Section 1.3.2](#), we focus on the context where the shape is represented as a bounded domain of  $\mathbb{R}^d$ : we present the notion of shape derivative in [Section 1.3.3.1](#), and that of topological derivative in [Section 1.3.4](#), with a lesser level of detail.

#### 1.3.1. The thorny question of the representation of shapes

Early shape optimization approaches rely on a description of shapes by a collection of parameters  $\mathcal{P}$ , lying in a finite- or infinite-dimensional vector space. The set  $\mathcal{P}$  may have various natures and origins:

- (i) In engineering, shapes are modeled thanks to a Computer-Aided Design (CAD) software, via a parametrization of their boundary by polynomial curves in 2d (e.g. Bézier curves, B-Splines or NURBS), or portions of surfaces in 3d, see [Fig. 1.3.1 \(a\)](#) and [175]. It is then natural to imagine that the set  $\mathcal{P}$  of the coefficients (or control points) of such a representation could serve as design variable for optimization.
- (ii) Discretize-then-optimize shape optimization approaches for a problem such as  $(\mathcal{P})$  start with a discretization of the optimized domain  $\Omega$ , typically by means of a computational mesh; this yields a natural parametrization via the collection  $\mathcal{P}$  of the positions of the vertices of this mesh, as in [Fig. 1.3.1 \(b\)](#). The state variable  $u_\Omega$  is then replaced by the solution  $u_{\mathcal{P}}$  to a discrete finite element system whose coefficients depend on  $\mathcal{P}$ . The objective and constraint criteria in  $(\mathcal{P})$  are in turn converted into functions of  $\mathcal{P}$ , say  $J(\mathcal{P})$ ,  $G(\mathcal{P})$  and  $H(\mathcal{P})$ , and the optimization is conducted in this finite-dimensional context.
- (iii) In particular situations, the optimized object  $\Omega$  is naturally described by a function in a fixed subset of a (possibly infinite-dimensional) vector space. For instance, an elastic plate is characterized by its height  $h \in \{h \in L^\infty(\mathcal{S}), 0 \leq h(x) \leq h_{\max} \text{ for a.e. } x \in \mathcal{S}\}$  over a fixed cross-section  $\mathcal{S} \subset \mathbb{R}^2$ , see [Fig. 1.3.1 \(c\)](#).

These approaches share the feature that the optimization variable belongs to a fixed subset of a vector space, so that at least theoretically speaking, it is simple to define “small variations” of a shape. From the mathematical viewpoint, such shape optimization problems boil down to optimal control problems, where the control variable operates in the coefficients of a partial differential equation. This intuitive practice unfortunately suffers from major difficulties: at first, the choice of an adequate set of parameters  $\mathcal{P}$  is delicate when the shape is a complex object. Besides, in practice, it may be difficult to realize small variations of these parameters: for instance, when  $\mathcal{P}$  accounts for the CAD parameters of the shape, the practical realization of a change in  $\mathcal{P}$  requires to generate a new CAD model. Last but not least, the optimized design can only be described in terms of the a priori selected parameters, which inherently limits the possibility to predict innovative solutions.

One second shape and topology optimization paradigm deals with shapes as domains  $\Omega \subset \mathbb{R}^d$ . This is the intuitive choice that we shall retain in most of this manuscript. As we have seen in [Section 1.2.3](#), it allows for a clear mathematical formulation of the mechanical criteria driving the optimization process, in terms of partial differential equations posed on  $\Omega$ . From the technical vantage, as we shall see in the next [Sections 1.3.3](#) and [1.3.4](#), efficient methods are available to define and numerically realize “small” variations of domains, leaving the room for a great freedom in the considered designs. Such approaches are not free from drawbacks, though. Notably, they are usually very sensitive to the existence of multiple local minimizers, that we shall evoke in the next [Section 1.3.2](#).

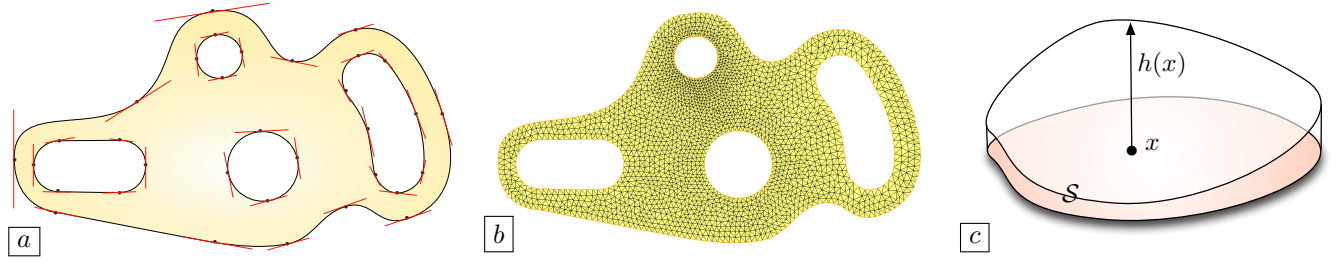


FIGURE 1.3.1. A 2d shape  $\Omega$  can be parametrized by (a) The finite-dimensional collection  $\mathcal{P}$  of the positions of control points and associated tangent vectors of a CAD representation, or (b) The positions of the vertices of a computational mesh. (c) A plate  $\Omega$  can be parametrized by its height  $h \in L^\infty(\mathcal{S})$  over a fixed cross-section  $\mathcal{S} \subset \mathbb{R}^2$ .

Let us eventually mention another popular philosophy in the field of engineering, where it bears the name “topology optimization”. This strategy is rooted in the homogenization theory (see [Section 1.3.2](#) for a glimpse): it downright consists in dropping the conventional representation of a shape as a domain  $\Omega \subset \mathbb{R}^d$ , or equivalently via its characteristic function  $\mathbb{1}_\Omega$ , taking the “black” and “white” values 0 and 1 outside and inside  $\Omega$ , respectively. Instead, a density function  $h : \mathbb{R}^d \rightarrow [0, 1]$  is used, which is allowed to take intermediate “grayscale” values between 0 and 1. This practice requires a consistent reformulation of the physical problem for the state variable  $u_\Omega$  in terms of the density  $h$ , so as to endow the “grayscale” regions with material properties – a task which is delicate in many realistic situations. The resulting optimal design problem boils down to a parametric optimization problem, of the form described at the beginning of this section. Such topology optimization approaches were introduced in the seminal article [69], and were thence considerably developed, see e.g. [70] for an overview, and [Section 1.4.5](#) for a brief presentation of the numerical realization of this idea.

### 1.3.2. Non existence of optimal shapes: the homogenization phenomenon

This section deals with the perhaps first issue that comes to mind in the treatment of shape optimization problems, that of the existence of solutions, or more precisely, the general non existence of an optimal design. The study of this effect is not central in this manuscript, but its manifestations are ubiquitous in material science and in the numerical practice of shape and topology optimization; hence, we solely provide a brief intuition, refer to e.g. [16, 97, 123, 276, 277] for more advanced presentations. To set ideas, this discussion arises in the context of structural optimization problems of the form  $(\mathcal{P})$  introduced in [Section 1.2.3](#), but the main concepts are far more general.

The fact that “most” shape optimization problems do not possess a solution has a physical origin in the homogenization theory. Qualitatively, for a general objective function  $J(\Omega)$  and a given volume  $\text{Vol}(\Omega)$ , better and better designs  $\Omega$  can always be obtained from an initial one by making more and more, smaller and smaller holes, with similar geometric patterns, see [Fig. 1.3.2](#) for an illustration.

A globally optimal design would thus be attained as a “composite design”  $(\rho, A)$ , defined on a large “hold-all” domain  $D$  by a local density of material  $\rho$  and a microstructure tensor  $A$ , encoding a local arrangement of material and void:

$$(1.3.1) \quad (\rho, A) \in \{\theta \in L^\infty(D, [0, 1]), A(x) \in G_{\rho(x)} \text{ for a.e. } x \in D\},$$

where:

- $\rho(x) \in [0, 1]$  is the local proportion of material around  $x \in D$ :  $\rho(x) = 1$  (resp.  $\rho(x) = 0$ ) indicates that  $x$  is surrounded by material (resp. void).
- $A(x) : \mathbb{R}_{\text{sym}}^{d \times d} \rightarrow \mathbb{R}_{\text{sym}}^{d \times d}$  is the microstructure tensor, in the set  $G_{\rho(x)}$  of all the tensors obtained by mixing material  $A$  and void (or an ersatz material  $\eta A$ ,  $\eta \ll 1$ ) in proportions  $\rho(x)$  and  $(1 - \rho(x))$ ;

see [Fig. 1.3.3](#) for an illustration.

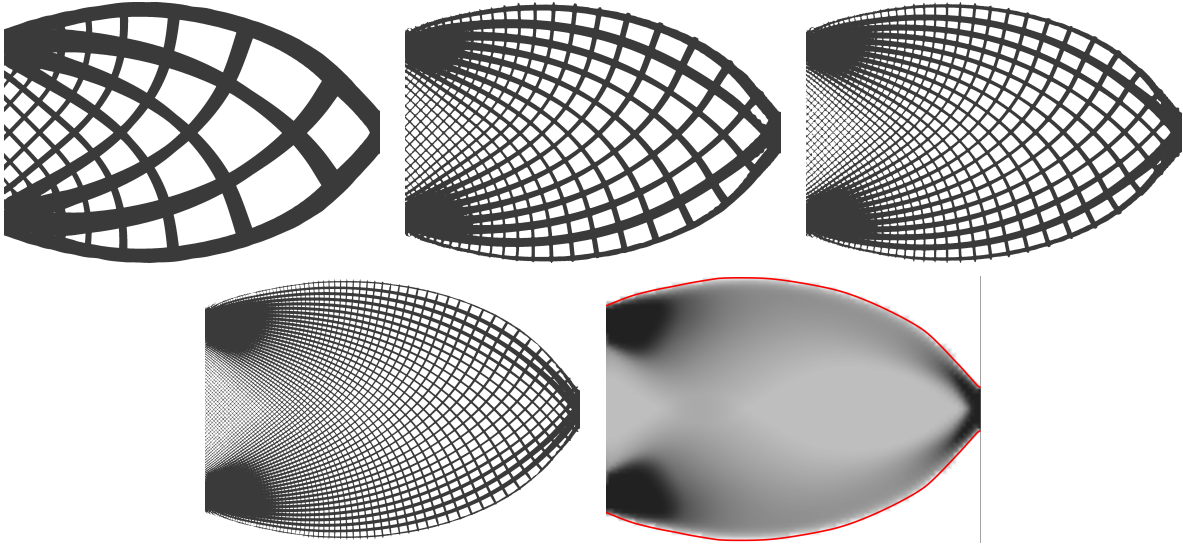


FIGURE 1.3.2. *The homogenization phenomenon is the trend that better designs can be obtained by making more numerous, smaller holes inside designs, until the point that porous designs, outside the range of “true shapes” are reached.*

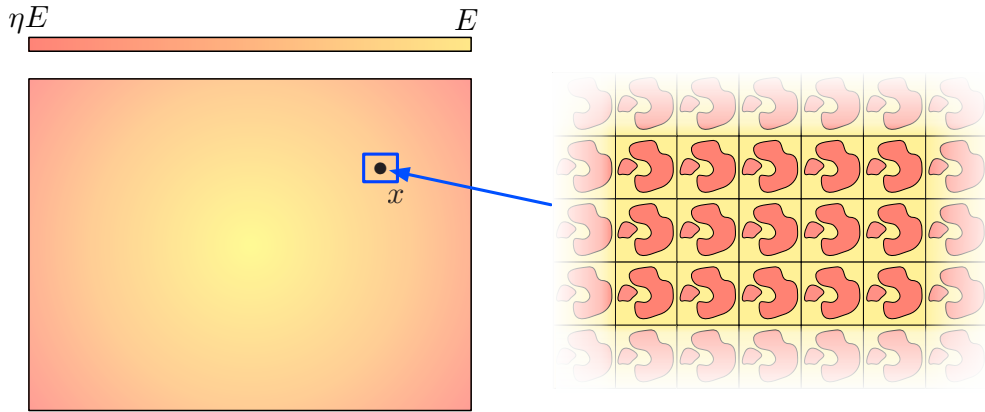


FIGURE 1.3.3. *Composite design obtained by a microscopic repartition of void and material.*

However optimal, such composite designs are often undesirable in practice, as they are difficult to fabricate. Practitioners thus strive to tame the trend for designs to develop smaller and smaller features in the course of the optimization process; this usually takes on two opposite forms.

- *Restriction of the set of admissible designs:* Imposing additional constraints on the optimized design  $\Omega$  in the formulation  $(\mathcal{P})$  of the problem may discourage the presence of too small patterns. For instance, imposing a constraint on the perimeter of shapes [27], on their uniform Lipschitz regularity [120], or on their number of holes in 2d [349] are so many means to prevent the onset of the homogenization phenomenon, see [201] for a more detailed account. From the numerical viewpoint, the minimum length scale imposed by the mesh size acts by itself as such a mechanism. However, this homogenization effect explains why shape and topology optimization problems usually have so many local minima, and why their numerical resolution is so sensitive to the initial design, the mesh, etc.
- *Relaxation:* Instead of preventing the emergence of composite designs, homogenization-based topology optimization accepts them by enlarging the class of admissible designs to composite designs of

the form (1.3.1), and by giving a meaning to the formulation  $(\mathcal{P})$  when the variable  $\Omega$  is changed for such a more general design. The resulting, relaxed problem often possesses an optimal design, see [19, 16] about this method.

The previous discussion emphasizes that the natural formulation of shape optimization problems featuring domains as shapes is bound to suffer from the existence of multiple local minima. Fortunately, in practice, these local minima, which are close to an input initial design over which “small” improvements are expected, are already quite desirable – and sometimes more desirable than a globally optimal design which would be very far from the initial guess and thus raise the need for an altogether different construction process.

**Remark 1.3.1** *With the advent of additive manufacturing technologies, which are allegedly capable of assembling designs with an arbitrary level of complexity, homogenization-based optimal design techniques have recently experienced a rebirth of interest. Notably, the interesting deshomogenization approach makes it possible to extract minimizing sequences of “black-and-white” designs, with a controlled length-scale, from the knowledge of the homogenized solution to a shape optimization problem, see the seminal article [295] and [22, 197] for recent developments about this issue.*

### 1.3.3. Shape derivatives

From this section on, we slip into the context where the optimized design is described by a bounded, Lipschitz domain  $\Omega \subset \mathbb{R}^d$ ; we recall some basic material about shape derivatives, which are central to several works presented in this manuscript.

#### 1.3.3.1. The boundary-variation method of Hadamard and the definition of shape derivatives

The notion of differentiation with respect to the domain that we shall use in most of this manuscript can be traced back to the early work of Hadamard [200]. A complete and rigorous framework was introduced in the article [275], a comprehensive account of which can be found in the more recent book [201].

Let  $\Omega \subset \mathbb{R}^d$  ( $d = 2, 3$ ) be a shape, that is, a bounded and Lipschitz domain. The method of Hadamard hinges on variations of  $\Omega$  of the form:

$$(1.3.2) \quad \Omega_\theta := (\text{Id} + \theta)(\Omega), \text{ where } \theta \in W^{1,\infty}(\mathbb{R}^d, \mathbb{R}^d), \|\theta\|_{W^{1,\infty}(\mathbb{R}^d, \mathbb{R}^d)} < 1.$$

Roughly speaking,  $\Omega_\theta$  is obtained from  $\Omega$  by displacing its points according to the “small” vector field  $\theta$ , see Fig. 1.3.4 for an illustration.

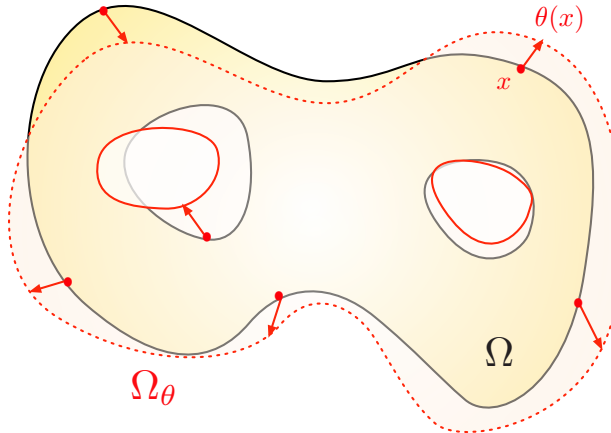


FIGURE 1.3.4. *The variation  $\Omega_\theta$  of  $\Omega$  is obtained by displacing its points according to  $\theta$ .*

In (1.3.2),  $W^{1,\infty}(\mathbb{R}^d, \mathbb{R}^d)$  stands for the Banach space of vector-valued functions in  $L^\infty(\mathbb{R}^d)^d$  whose first-order derivatives in the sense of distributions are also functions in  $L^\infty(\mathbb{R}^d)^d$ . Equivalently,  $W^{1,\infty}(\mathbb{R}^d, \mathbb{R}^d)$  is

the space of Lipschitz vector fields on  $\mathbb{R}^d$  with uniformly bounded Lipschitz modulus, and it holds:

$$\begin{aligned} \|\theta\|_{W^{1,\infty}(\mathbb{R}^d, \mathbb{R}^d)} &= \|\theta\|_{L^\infty(\mathbb{R}^d)^d} + \|\nabla \theta\|_{L^\infty(\mathbb{R}^d)^{d \times d}}, \\ &= \sup_{x \in \mathbb{R}^d} |\theta(x)| + \sup_{\substack{x, y \in \mathbb{R}^d \\ x \neq y}} \frac{|\theta(y) - \theta(x)|}{|x - y|}. \end{aligned}$$

We refer to [174] about the equivalence between these two functional viewpoints.

The variations  $\Omega_\theta$  are “close” to  $\Omega$  insofar as they express “small” perturbations of its boundary; in particular, they all share the same topology, as asserted by the next proposition.

**Proposition 1.3.2** *For all  $\theta \in W^{1,\infty}(\mathbb{R}^d, \mathbb{R}^d)$  with  $\|\theta\|_{W^{1,\infty}(\mathbb{R}^d, \mathbb{R}^d)} < 1$ , the mapping  $(\text{Id} + \theta)$  is a Lipschitz homeomorphism from  $\mathbb{R}^d$  into itself with Lipschitz inverse.*

The previous ingredients lead to the notion of shape derivative.

**Definition 1.3.3** *One function  $J(\Omega)$  of the domain is shape differentiable at a particular shape  $\Omega$  if the mapping  $\theta \mapsto J(\Omega_\theta)$ , defined on a neighborhood of 0 in  $W^{1,\infty}(\mathbb{R}^d, \mathbb{R}^d)$  and taking values in  $\mathbb{R}$ , is Fréchet differentiable at  $\theta = 0$ . The corresponding derivative  $J'(\Omega)(\theta)$  is called the shape derivative of  $J(\Omega)$  at  $\Omega$ , and the following expansion holds:*

$$J(\Omega_\theta) = J(\Omega) + J'(\Omega)(\theta) + o(\theta), \text{ where } \frac{|o(\theta)|}{\|\theta\|_{W^{1,\infty}(\mathbb{R}^d, \mathbb{R}^d)}} \xrightarrow{\theta \rightarrow 0} 0.$$

Intuitively, the shape derivative  $J'(\Omega)(\theta)$  appraises the variations in the objective function when the shape  $\Omega$  is displaced according to the “small” vector field  $\theta$ .

The notion of shape derivative is handful for a variety of purposes. From the theoretical point of view, it allows to express the necessary optimality conditions for a problem of the form  $(\mathcal{P})$ . From the practical point of view, it is a convenient tool to calculate descent directions. For instance, when the unconstrained problem  $(\mathcal{P}_{\text{uncons}})$  is considered, any vector field  $\theta \in W^{1,\infty}(\mathbb{R}^d, \mathbb{R}^d)$  such that  $\mathcal{L}'(\Omega)(\theta) < 0$  yields “better” variations  $\Omega_{t\theta}$  of  $\Omega$  for  $t > 0$  small enough:

$$\mathcal{L}(\Omega_{t\theta}) = \mathcal{L}(\Omega) + t\mathcal{L}'(\Omega)(\theta) + o(t) < \mathcal{L}(\Omega).$$

**Remark 1.3.4** *In the practice of Hadamard’s method, the deformations  $\theta$  are often restricted to a subspace of  $\Theta_{\text{ad}}$  of  $W^{1,\infty}(\mathbb{R}^d, \mathbb{R}^d)$  composed of more regular vector fields, so that the variations  $\Omega_\theta$  be better than just Lipschitz regular (provided  $\Omega$  is too): one often considers the spaces  $C^{k,\infty}(\mathbb{R}^d, \mathbb{R}^d)$  composed of vector fields  $\theta : \mathbb{R}^d \rightarrow \mathbb{R}^d$  of class  $C^k$ , which are bounded on  $\mathbb{R}^d$ , together with all their derivatives up to order  $k$ . A similar restriction can be used to impose various constraints on the variations  $\Omega_\theta$ : for instance, a region  $\Gamma_D \subset \partial\Omega$  belongs to the boundaries of all variations  $\Omega_\theta$  if  $\theta$  is required to vanish on  $\Gamma_D$ . In order to keep the presentation simple, this technicality is ignored in the following.*

**Remark 1.3.5** *An equivalent, alternative formulation of Hadamard’s method, sometimes referred to as the “velocity method” in the literature, relies on variations of the shape  $\Omega$  via the flow of the vector field  $\theta$ , i.e. variations of the form*

$$T_\theta(\Omega), \text{ where } T_\theta(x) = \chi_\theta(1, 0, x) \text{ and } \begin{cases} \frac{d\chi}{dt}(t, 0, x) = \theta(\chi(t, 0, x)) & \text{for } t > 0, \\ \chi(0, 0, x) = x. \end{cases}$$

Both methods give rise to the same notion of differentiation with respect to the domain, see Rem. 5.2.9 in [201]. We refer to [343] for a more exhaustive presentation of this point of view.

### 1.3.3.2. Structure of shape derivatives

The shape derivatives of “most” functionals of the domain have a quite intuitive structure: they only depend on the values of the normal component  $\theta \cdot n$  of the deformation  $\theta$  on the boundary  $\partial\Omega$ , as asserted by the following proposition, see §5.9.2 in [201] for a proof and Fig. 1.3.5 for an illustration.

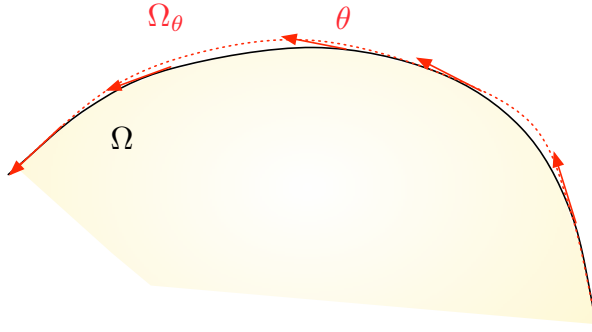


FIGURE 1.3.5. At first order, a tangential deformation  $\theta$  (i.e.  $\theta \cdot n = 0$  on  $\partial\Omega$ ) results in a convection of the shape  $\Omega$ ; at first order,  $J(\Omega_\theta) \approx J(\Omega)$  and it is expected that  $J'(\Omega)(\theta) = 0$ .

**Proposition 1.3.6** Let  $\Omega \subset \mathbb{R}^d$  be a bounded domain of class  $\mathcal{C}^1$ , and let  $J$  be a function of the domain such that the mapping

$$\mathcal{C}^{1,\infty}(\mathbb{R}^d, \mathbb{R}^d) \ni \theta \mapsto J(\Omega_\theta) \in \mathbb{R}$$

is Fréchet differentiable at 0. Then,

$$\forall \theta \in \mathcal{C}^{1,\infty}(\mathbb{R}^d, \mathbb{R}^d) \text{ s. t. } \theta \cdot n = 0 \text{ on } \partial\Omega, \quad J'(\Omega)(\theta) = 0.$$

In fact, the shape derivatives that we shall consider will often have the slightly more precise surface expression

$$(1.3.3) \quad J'(\Omega)(\theta) = \int_{\partial\Omega} v_\Omega \theta \cdot n \, ds,$$

where  $v_\Omega : \partial\Omega \rightarrow \mathbb{R}$  is a scalar function, depending on the considered functional  $J(\Omega)$ , on the solution  $u_\Omega$  to the considered state equation, on a suitable “adjoint state”  $p_\Omega$ , etc.

The structure (1.3.3) is quite desirable in the practical use of shape derivatives. For instance, when the unconstrained optimization problem  $(\mathcal{P}_{\text{uncons}})$  is considered, a descent direction  $\theta$  is immediately obtained by setting

$$(1.3.4) \quad \theta = -v_\Omega n \text{ on } \partial\Omega.$$

We shall return to the issue of extracting descent directions from shape derivatives in [Section 1.3.5](#).

### 1.3.3.3. First examples of shape derivatives

This section deals with the calculation of the derivatives of some functionals which depend on the domain  $\Omega$  in a relatively “simple” way, that is, via the integration of fixed, smooth enough functions on  $\Omega$  or its boundary  $\partial\Omega$  (in particular, no physical state equation is involved).

The first result of interest is stated in the following proposition, which is Th. 5.2.2 in [\[201\]](#). We provide a brief sketch of its proof, as it illustrates one of the key ingredients in the general calculation procedure of shape derivatives.

**Proposition 1.3.7** Let  $f \in W^{1,1}(\mathbb{R}^d)$  be a function, and let the shape functional  $F(\Omega)$  be defined by

$$(1.3.5) \quad F(\Omega) = \int_{\Omega} f \, dx.$$

Then  $F$  is shape differentiable at any bounded, Lipschitz domain  $\Omega$ , and its derivative reads:

$$(1.3.6) \quad \forall \theta \in W^{1,\infty}(\mathbb{R}^d, \mathbb{R}^d), \quad F'(\Omega)(\theta) = \int_{\Omega} \operatorname{div}(f\theta) \, dx = \int_{\partial\Omega} f\theta \cdot n \, ds.$$

*Sketch of proof.* By definition, the quantity  $F(\Omega_\theta)$  equals

$$F(\Omega_\theta) = \int_{\Omega_\theta} f \, dx,$$

and we rely on the change of variables formula of [Proposition 1.A.7](#) to transport this integral back to the reference domain  $\Omega$ :

$$F(\Omega_\theta) = \int_{\Omega} |\det(\mathbf{I} + \nabla\theta)| f \circ (\mathbf{Id} + \theta) \, dx.$$

The variable  $\theta$  appears solely in the integrand of the above expression, whose components have the following expansions:

- The mapping  $\theta \mapsto |\det(\mathbf{I} + \nabla\theta)|$ , from  $W^{1,\infty}(\mathbb{R}^d, \mathbb{R}^d)$  into  $\mathbb{R}$ , is Fréchet differentiable at  $\theta = 0$ , and

$$|\det(\mathbf{I} + \nabla\theta)| = 1 + \operatorname{div}(\theta) + o(\theta).$$

- The mapping  $\theta \mapsto f \circ (\mathbf{Id} + \theta)$ , from a neighborhood of 0 in  $W^{1,\infty}(\mathbb{R}^d, \mathbb{R}^d)$  into  $L^1(\Omega)$ , is Fréchet differentiable at  $\theta = 0$ , and

$$f \circ (\mathbf{Id} + \theta) = f + \nabla f \cdot \theta + o(\theta).$$

Finally, using the product rule and the Lebesgue dominated convergence theorem, it follows that the mapping  $\theta \mapsto F(\Omega_\theta)$  is Fréchet differentiable at  $\theta = 0$ , with derivative

$$\forall \theta \in W^{1,\infty}(\mathbb{R}^d, \mathbb{R}^d), \quad F'(\Omega)(\theta) = \int_{\Omega} (\operatorname{div}(\theta) f + \nabla f \cdot \theta) \, dx.$$

This is the first expression in [\(1.3.6\)](#); the second one follows from the Green's formula of [Proposition 1.A.10](#).  $\square$

This formula plays a central role in continuum mechanics, where it is referred to as Reynolds' theorem. It is used, in particular, in the derivation of the equations of motions from conservation principles, see [Fig. 1.3.6 \(a\)](#) for an illustration.

As an immediate byproduct, by letting  $f \equiv 1$ , we obtain the shape derivative of the volume functional

$$\forall \theta \in W^{1,\infty}(\mathbb{R}^d, \mathbb{R}^d), \quad \operatorname{Vol}'(\Omega)(\theta) = \int_{\Omega} \operatorname{div}(\theta) \, dx = \int_{\partial\Omega} \theta \cdot n \, ds.$$

The next proposition and its proof are conceptually similar, see Prop. 5.4.4 in [\[201\]](#).

**Proposition 1.3.8** *Let  $\Omega \subset \mathbb{R}^d$  be a bounded domain of class  $\mathcal{C}^3$ , and let  $g \in W^{2,1}(\mathbb{R}^d)$ . Consider the functional:*

$$G(\Omega) = \int_{\partial\Omega} g \, ds;$$

*then  $G(\Omega)$  is shape differentiable at  $\Omega$  when deformations  $\theta$  are chosen in the space  $\mathcal{C}^{1,\infty}(\mathbb{R}^d, \mathbb{R}^d)$  (see [Remark 1.3.4](#)) and its shape derivative is:*

$$G'(\Omega)(\theta) = \int_{\partial\Omega} \left( \frac{\partial g}{\partial n} + \kappa g \right) (\theta \cdot n) \, ds,$$

*where  $\kappa : \partial\Omega \rightarrow \mathbb{R}$  is the mean curvature of  $\partial\Omega$ , oriented so that  $\kappa(x) > 0$  when  $\Omega$  is locally convex around  $x \in \partial\Omega$ .*

By letting  $g \equiv 1$ , we obtain the shape derivative of the perimeter functional

$$\forall \theta \in \mathcal{C}^{1,\infty}(\mathbb{R}^d, \mathbb{R}^d), \quad \operatorname{Per}'(\Omega)(\theta) = \int_{\partial\Omega} \kappa \theta \cdot n \, ds,$$

see [Fig. 1.3.6 \(b\)](#) for an illustration.

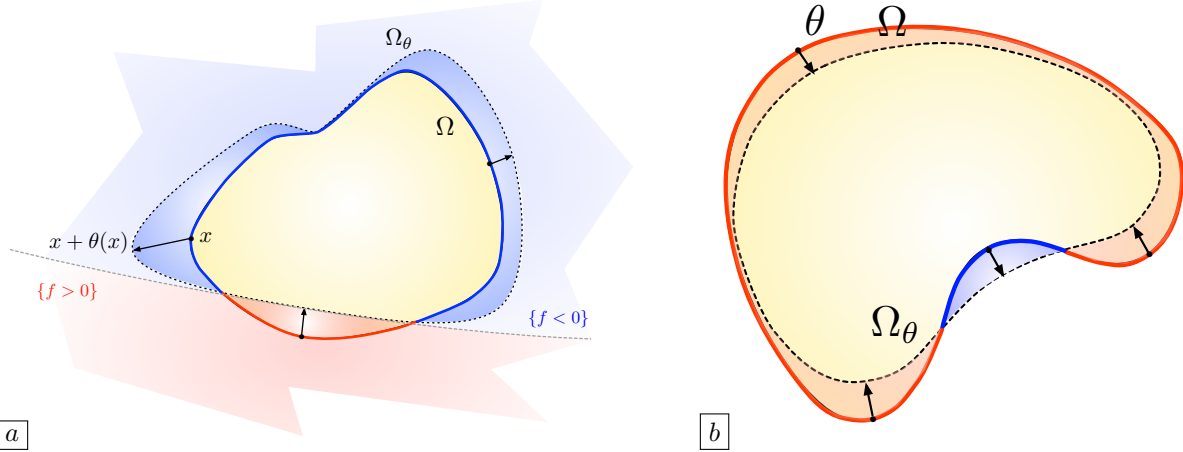


FIGURE 1.3.6. *Intuitive meanings of the shape derivatives in Propositions 1.3.7 and 1.3.8.*  
(a) The quantity  $F(\Omega_\theta)$  in (1.3.5) is decreased when  $\theta$  imposes that  $\Omega$  expand in the regions where  $f < 0$  and retract where  $f > 0$ . (b) The perimeter  $\theta \mapsto \text{Per}(\Omega_\theta)$  is decreased when  $\theta \cdot n > 0$  where  $\kappa < 0$  (i.e. the “holes” of  $\Omega$  are filled), and when  $\theta \cdot n < 0$  where  $\kappa > 0$  (the “bumps” of  $\Omega$  are resorbed).

#### 1.3.3.4. Lagrangian and Eulerian derivatives of a function defined on the shape

The previous section has considered functions featuring a “simple” dependence with respect to the domain  $\Omega$ . We presently discuss how to differentiate a functional  $J(\Omega)$  involving a physical quantity  $u_\Omega$  characterized as the solution to boundary value problem posed on  $\Omega$ .

The crucial point is to give a precise meaning to the differentiability of the mapping  $\Omega \mapsto u_\Omega$ . This is not a straightforward task since  $u_\Omega$  lies in a space of functions defined on  $\Omega$ , say  $H_0^1(\Omega)$  to set ideas. One could think about two ways of defining such a notion of differentiability, which are illustrated on Fig. 1.3.7:

- *Eulerian point of view:* For a fixed point  $x \in \Omega$ , and for  $\theta \in W^{1,\infty}(\mathbb{R}^d, \mathbb{R}^d)$  small enough,  $x$  belongs to the perturbed shape  $\Omega_\theta$ . Hence, the mapping

$$(1.3.7) \quad W^{1,\infty}(\mathbb{R}^d, \mathbb{R}^d) \ni \theta \mapsto u_{\Omega_\theta}(x) \in \mathbb{R}$$

is well-defined for small enough  $\theta$ , and it makes sense to inquire about its derivative at  $\theta = 0$ . When it exists, we shall denote this “Eulerian” derivative by  $u'_\Omega(\theta)(x)$ .

- *Lagrangian point of view:* The transported mapping

$$(1.3.8) \quad \bar{u}_\Omega(\theta) := u_{\Omega_\theta} \circ (\text{Id} + \theta)$$

is well-defined from the unit open ball in  $W^{1,\infty}(\mathbb{R}^d, \mathbb{R}^d)$  into  $H_0^1(\Omega)$ , and one could consider its differentiation at  $\theta = 0$ . When it exists, we denote this “Lagrangian” derivative of  $\Omega \mapsto u_\Omega$  by  $\dot{u}_\Omega(\theta) \in H_0^1(\Omega)$ .

Going further, if both notions of derivatives were to make sense, we would expect that the following relation hold:

$$\dot{u}_\Omega(\theta) = u'_\Omega(\theta) + \nabla u_\Omega \cdot \theta,$$

which is obtained by a formal application of the chain rule to the mapping  $\theta \mapsto u_{\Omega_\theta} \circ (\text{Id} + \theta)$ .

However natural the Eulerian viewpoint could seem at first glance, it proves more difficult to make rigorous. Intuitively, how “small”  $\theta$  has to be for the mapping (1.3.7) to be well-defined actually depends on  $x$ . Notably, this mapping is ill-defined when  $x \in \partial\Omega$ , and taking into account the boundary conditions satisfied by  $u_\Omega$  is expected to be difficult in the calculation of its derivative. On the contrary, the Lagrangian viewpoint is much more adequate to carry out analyses on  $u_\Omega$ , since the transported function  $\bar{u}_\Omega(\theta)$  is not just defined pointwise, but as a mapping taking values in a fixed functional space.

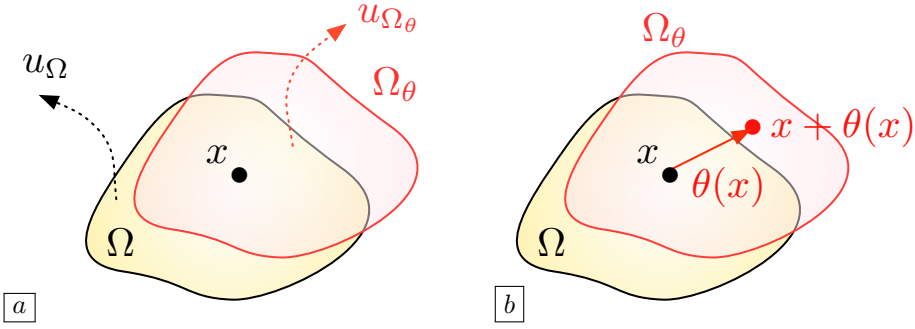


FIGURE 1.3.7. Two different notions for the differentiation of a function defined on the variable domain  $\Omega$ : (a) The calculation of the Eulerian derivative  $u'_\Omega(\theta)(x)$  requires to “freeze” the point  $x$  and differentiate the mapping  $\theta \mapsto u_{\Omega_\theta}(x)$ ; (b) The Lagrangian derivative  $\dot{u}_\Omega(\theta)(x)$  transports the point  $x$  into  $x + \theta(x)$  and the domain  $\Omega$  into  $\Omega_\theta$  at the same time.

The rigorous formalization of these intuitions is provided in the following definition, which takes place in the case of functions  $u_\Omega$  in  $H_0^1(\Omega)$ , but can be readily generalized to different contexts.

**Definition 1.3.9** Let  $\Omega \mapsto u_\Omega$  be a mapping which to a bounded Lipschitz domain  $\Omega \subset \mathbb{R}^d$  associates a function  $u_\Omega \in H_0^1(\Omega)$ .

- This mapping has a Lagrangian derivative  $\dot{u}_\Omega(\theta)$  at a shape  $\Omega$  if the transported mapping  $\bar{u}_\Omega(\theta)$  in (1.3.8), defined from a neighborhood of 0 in  $W^{1,\infty}(\mathbb{R}^d, \mathbb{R}^d)$  into  $H_0^1(\Omega)$ , is Fréchet differentiable at  $\theta = 0$ .
- This mapping has a Eulerian derivative  $u'_\Omega(\theta)$  at  $\Omega$  if it has a Lagrangian derivative  $\dot{u}_\Omega(\theta)$  and if  $u_\Omega \in H^2(\Omega)$ . The quantity  $u'_\Omega(\theta)$  is then defined by

$$u'_\Omega(\theta) = \dot{u}_\Omega(\theta) - \nabla u_\Omega \cdot \theta \in H^1(\Omega).$$

When the existence of a Lagrangian (and Eulerian) derivative of  $u_\Omega$  is known, the shape derivative of a quantity of interest depending on this function is easily inferred.

**Proposition 1.3.10** Let  $j : \mathbb{R} \rightarrow \mathbb{R}$  be a smooth function satisfying the following growth conditions

$$(Growth-j) \quad |j(u)| \leq C(1 + |u|^2), \quad |j'(u)| \leq C(1 + |u|), \quad \text{and} \quad |j''(u)| \leq C,$$

for a certain constant  $C > 0$ . Let  $\Omega \mapsto u_\Omega \in H^1(\Omega)$  be a mapping with a Lagrangian derivative  $\dot{u}_\Omega(\theta)$  at a shape  $\Omega$ . Then  $J(\Omega)$  is shape differentiable at  $\Omega$ , and its derivative reads

$$(1.3.9) \quad J'(\Omega)(\theta) = \int_\Omega \left( \operatorname{div}(\theta) j(u_\Omega) + j'(u_\Omega) \dot{u}_\Omega(\theta) \right) dx.$$

If in addition  $\Omega \mapsto u_\Omega$  has a Eulerian derivative  $u'_\Omega(\theta)$  at  $\Omega$ , this formula rewrites:

$$(1.3.10) \quad J'(\Omega)(\theta) = \int_{\partial\Omega} j(u_\Omega) \theta \cdot n ds + \int_\Omega j'(u_\Omega) u'_\Omega(\theta) dx.$$

*Sketch of proof.* The growth conditions (Growth-j) ensure that all the integrals featured in the above formulas are well-defined. Again, we use the change of variables formula of Proposition 1.A.7 to reformulate  $J(\Omega_\theta)$  as an integral posed on the reference domain  $\Omega$ . This yields:

$$J(\Omega_\theta) = \int_\Omega |\det(I + \nabla \theta)| j(\bar{u}_\Omega(\theta)) dx,$$

where the transported mapping  $\bar{u}_\Omega(\theta) = u_{\Omega_\theta} \circ (\operatorname{Id} + \theta)$  is naturally brought into play. Here,

- We have already seen in the proof of [Proposition 1.3.7](#) that the mapping  $\theta \mapsto |\det(I + \nabla\theta)|$  is Fréchet differentiable at  $\theta = 0$ , with derivative

$$|\det(I + \nabla\theta)| = 1 + \operatorname{div}(\theta) + o(\theta).$$

- The Lagrangian differentiability of  $u_\Omega$  and the chain rule entail that

$$j(\bar{u}_\Omega(\theta)) = j(u_\Omega) + j'(u_\Omega)\dot{u}_\Omega(\theta) + o(\theta).$$

By the product rule, we immediately obtain the first formula [\(1.3.9\)](#).

The formula [\(1.3.10\)](#) follows directly from the definition of Eulerian derivative.  $\square$

**Remark 1.3.11** *The formula [\(1.3.10\)](#) for  $J'(\Omega)(\theta)$  has an intuitive structure which expresses a formal application of the chain rule. The first term in the right-hand side of [\(1.3.10\)](#) corresponds to the shape derivative of the mapping  $\Omega \mapsto \int_\Omega f \, dx$  where the fixed function  $f$  is chosen to be  $j(u_\Omega)$ , according to [Proposition 1.3.7](#). The second term is, formally, the shape derivative of the mapping  $\Omega \mapsto \int j(u_\Omega) \, dx$ , where the domain of integration is kept fixed (equal to  $\Omega$ ).*

### 1.3.3.5. Shape derivatives of mechanical functionals of the domain

In this section, we exemplify how the previous concepts can be implemented to calculate the shape derivative of a functional depending on the domain  $\Omega$  via a physical state  $u_\Omega$  which is the solution to a boundary value problem posed on  $\Omega$ . The trail of the proof illustrates the general and rigorous procedure to achieve such a purpose.

In order to keep the presentation at the lowest level of technicality while still exposing the salient ideas of the methodology, we consider the following model situation. For any shape  $\Omega$ , we denote by  $u_\Omega$  the unique solution in  $H_0^1(\Omega)$  to the Laplace equation

$$(1.3.11) \quad \begin{cases} -\Delta u_\Omega = f & \text{in } \Omega, \\ u_\Omega = 0 & \text{on } \partial\Omega, \end{cases}$$

where the source term  $f$  belongs to  $L^2(\mathbb{R}^d)$ .

We then aim to calculate the shape derivative of the functional

$$(1.3.12) \quad J(\Omega) = \int_\Omega j(u_\Omega) \, dx,$$

where  $j : \mathbb{R} \rightarrow \mathbb{R}$  is a smooth function satisfying the growth conditions [\(Growth- \$j\$ \)](#).

**Theorem 1.3.12** *The functional  $J(\Omega)$  in [\(1.3.12\)](#) is differentiable at any bounded Lipschitz domain  $\Omega$ , and its derivative has the following volume expression:*

$$(1.3.13) \quad J'(\Omega)(\theta) = \int_\Omega \operatorname{div}(\theta) j(u_\Omega) \, dx + \int_\Omega (\operatorname{div}(\theta) I - \nabla\theta - \nabla\theta^T) \nabla u_\Omega \cdot \nabla p_\Omega \, dx - \int_\Omega (f \operatorname{div}(\theta) + \nabla f \cdot \theta) p_\Omega \, dx,$$

where  $p_\Omega$  is an adjoint state, defined as the unique solution in  $H_0^1(\Omega)$  to the boundary value problem:

$$(1.3.14) \quad \begin{cases} -\Delta p_\Omega = -j'(u_\Omega) & \text{in } \Omega, \\ p_\Omega = 0 & \text{on } \partial\Omega. \end{cases}$$

If the domain  $\Omega$  is of class  $C^2$ , this formula can be rewritten under the following surface form:

$$(1.3.15) \quad J'(\Omega)(\theta) = \int_{\partial\Omega} \left( j(u_\Omega) - \frac{\partial u_\Omega}{\partial n} \frac{\partial p_\Omega}{\partial n} \right) (\theta \cdot n) \, ds.$$

*Sketch of proof.* We proceed in four steps.

*Step 1.* We prove that the mapping  $\Omega \mapsto u_\Omega$  has a Lagrangian derivative  $\dot{u}_\Omega(\theta)$  and we characterize this quantity.

This task relies on the application of the implicit function [Theorem 1.A.11](#), after expressing the transported function  $\bar{u}_\Omega(\theta) = u_{\Omega_\theta} \circ (\operatorname{Id} + \theta) \in H_0^1(\Omega)$  as the solution to an equation with coefficients depending on  $\theta$ .

Let us start from the variational formulation for  $u_{\Omega_\theta} \in H_0^1(\Omega_\theta)$ :

$$\forall v \in H_0^1(\Omega_\theta), \quad \int_{\Omega_\theta} \nabla u_{\Omega_\theta} \cdot \nabla v \, dx = \int_{\Omega_\theta} f v \, dx.$$

Like in the proof of [Proposition 1.3.7](#), we use the change of variables formula from [Proposition 1.A.7](#) to transport the integrals on  $\Omega_\theta$  back to the reference domain  $\Omega$ ; this yields:

$$\begin{aligned} \forall v \in H_0^1(\Omega_\theta), \quad \int_{\Omega} |\det(I + \nabla\theta)| \left( \nabla u_{\Omega_\theta} \circ (\text{Id} + \theta) \right) \cdot \left( \nabla v \circ (\text{Id} + \theta) \right) \, dx = \\ \int_{\Omega} |\det(I + \nabla\theta)| (f \circ (\text{Id} + \theta))(v \circ (\text{Id} + \theta)) \, dx. \end{aligned}$$

Now, using the change of test functions  $w = v \circ (\text{Id} + \theta) \in H_0^1(\Omega)$ , an elementary calculation based on the identity

$$\forall v \in H_0^1(\Omega_\theta), \quad (\nabla v) \circ (\text{Id} + \theta) = (I + \nabla\theta)^{-T} \nabla(v \circ (\text{Id} + \theta))$$

reveals that  $\overline{u_\Omega}(\theta)$  is the unique function in  $H_0^1(\Omega)$  satisfying:

$$(1.3.16) \quad \forall w \in H_0^1(\Omega), \quad \int_{\Omega} A(\theta) \nabla \overline{u_\Omega}(\theta) \cdot \nabla w \, dx = \int_{\Omega} |\det(I + \nabla\theta)| f \circ (\text{Id} + \theta) w \, dx,$$

where  $A(\theta) : \mathbb{R}^d \rightarrow \mathbb{R}^{d \times d}$  is the matrix-valued function

$$A(\theta) = |\det(I + \nabla\theta)| (I + \nabla\theta)^{-1} (I + \nabla\theta)^{-T}.$$

The variational problem [\(1.3.16\)](#) can be rewritten under the form of an equation posed between functional spaces, with parameters depending on  $\theta$ : denoting by  $B(0, 1)$  the unit open ball in  $W^{1,\infty}(\mathbb{R}^d, \mathbb{R}^d)$ ,  $\overline{u_\Omega}(\theta)$  is the unique solution  $u \in H_0^1(\Omega)$  to the equation

$$(1.3.17) \quad \mathcal{F}(\theta, u) = 0,$$

where  $\mathcal{F} : B(0, 1) \times H_0^1(\Omega) \rightarrow H^{-1}(\Omega)$  is defined by

$$\forall w \in H_0^1(\Omega), \quad \mathcal{F}(\theta, u)(w) = \int_{\Omega} A(\theta) \nabla u \cdot \nabla w \, dx - \int_{\Omega} |\det(I + \nabla\theta)| f \circ (\text{Id} + \theta) w \, dx.$$

We now verify that:

- The mapping  $\mathcal{F} : B(0, 1) \times H_0^1(\Omega) \rightarrow H^{-1}(\Omega)$  is Fréchet differentiable.
- The partial derivative  $\frac{\partial \mathcal{F}}{\partial u}(0, u_\Omega) : H_0^1(\Omega) \rightarrow H^{-1}(\Omega)$ , given by:

$$\forall w \in H_0^1(\Omega), \quad \frac{\partial \mathcal{F}}{\partial u}(0, u_\Omega)(w) = \int_{\Omega} \nabla u_\Omega \cdot \nabla w \, dx$$

is an isomorphism, owing to the Lax-Milgram theorem.

The implicit function [Theorem 1.A.11](#) then ensures that the solution mapping  $\theta \mapsto \overline{u_\Omega}(\theta)$  to the equation [\(1.3.17\)](#) is Fréchet differentiable at  $\theta = 0$ , i.e.  $u_\Omega$  has a Lagrangian derivative  $\dot{u}_\Omega(\theta)$  at  $\Omega$ . We may now take derivatives in the variational formulation [\(1.3.16\)](#), to obtain the following characterization of  $\dot{u}_\Omega(\theta)$ :

$$(1.3.18) \quad \forall w \in H_0^1(\Omega), \quad \int_{\Omega} \nabla \dot{u}_\Omega(\theta) \cdot \nabla w \, dx = - \int_{\Omega} (\text{div}(\theta) I - \nabla\theta - \nabla\theta^T) \nabla u_\Omega \cdot \nabla w \, dx + \int_{\Omega} (f \text{div}(\theta) + \nabla f \cdot \theta) w \, dx.$$

*Step 2. We infer that  $J(\Omega)$  is shape differentiable and we calculate its derivative.*

From the existence of the Lagrangian derivative for  $u_\Omega$ , [Proposition 1.3.10](#) allows to conclude that  $J(\Omega)$  is shape differentiable at  $\Omega$ , with derivative

$$(1.3.19) \quad J'(\Omega)(\theta) = \int_{\Omega} \left( \text{div}(\theta) j(u_\Omega) + j'(u_\Omega) \dot{u}_\Omega(\theta) \right) \, dx.$$

The resulting expression, although perfectly rigorous, is a little unsatisfactory in the perspective of applications: the calculation of  $J'(\Omega)(\theta)$  passes through that of  $u_\Omega$  – which can be realized by solving [\(1.3.11\)](#) once and for all, independently of the deformation  $\theta$  – and of  $\dot{u}_\Omega(\theta)$ , which requires the resolution of the  $\theta$ -dependent problem [\(1.3.18\)](#). In particular, formula [\(1.3.19\)](#) does not easily lend itself to the identification of a descent direction  $\theta$  such that  $J'(\Omega)(\theta) < 0$ , see the discussion in the end of [Section 1.3.3.1](#).

*Step 3.* We reformulate  $J'(\Omega)(\theta)$  by introducing the adjoint state  $p_\Omega$ .

This task relies on the adjoint method, pertaining to the general framework of optimal control, that we describe in a more systematic fashion in the next [Section 1.3.3.6](#). We also refer to [240] and [304] for a comprehensive introduction to the latter.

Let us consider the function  $p_\Omega \in H_0^1(\Omega)$  defined in [\(1.3.14\)](#), whose variational formulation reads:

$$(1.3.20) \quad \forall v \in H_0^1(\Omega), \quad \int_{\Omega} \nabla p_\Omega \cdot \nabla v \, dx = - \int_{\Omega} j'(u_\Omega) v \, dx.$$

Then, [\(1.3.19\)](#) rewrites:

$$(1.3.21) \quad \begin{aligned} J'(\Omega)(\theta) &= \int_{\Omega} \left( \operatorname{div}(\theta) j(u_\Omega) + j'(u_\Omega) \dot{u}_\Omega(\theta) \right) dx \\ &= \int_{\Omega} \operatorname{div}(\theta) j(u_\Omega) dx - \int_{\Omega} \nabla p_\Omega \cdot \nabla \dot{u}_\Omega(\theta) dx \\ &= \int_{\Omega} \operatorname{div}(\theta) j(u_\Omega) dx + \int_{\Omega} (\operatorname{div}(\theta) I - \nabla \theta - \nabla \theta^T) \nabla u_\Omega \cdot \nabla p_\Omega dx - \int_{\Omega} (f \operatorname{div}(\theta) + \nabla f \cdot \theta) p_\Omega dx, \end{aligned}$$

where we have used the variational formulation [\(1.3.20\)](#) of the adjoint state  $p_\Omega$  with the test function  $v = \dot{u}_\Omega(\theta) \in H_0^1(\Omega)$  to pass from the first line to the second one, and the variational formulation [\(1.3.18\)](#) of the Lagrangian derivative  $\dot{u}_\Omega(\theta)$  with test function  $w = p_\Omega \in H_0^1(\Omega)$  to pass from the second line to the third one. The resulting expression is the desired volume form [\(1.3.13\)](#) for  $J'(\Omega)(\theta)$  which is thus completely explicit with respect to  $\theta$ : once the calculations of  $u_\Omega$  and  $p_\Omega$  are achieved,  $J'(\Omega)(\theta)$  can be calculated for any deformation  $\theta \in W^{1,\infty}(\mathbb{R}^d, \mathbb{R}^d)$  without any additional resolution of a boundary value problem.

A close inspection of the above series of equalities sheds light on how the adjoint problem [\(1.3.14\)](#) and its variational formulation [\(1.3.20\)](#) were coined. The introduction of  $p_\Omega$  is meant to transform the expression  $\int_{\Omega} j'(u_\Omega) \dot{u}_\Omega dx$ , where the quantity  $\dot{u}_\Omega(\theta)$  depends implicitly on  $\theta$ , via [\(1.3.18\)](#), into an expression featuring an explicit dependence on  $\theta$ . The right-hand side of the variational formulation [\(1.3.20\)](#) is exactly what is needed for the passage between the first and the second lines of [\(1.3.21\)](#), i.e. to lift the quantity  $\int_{\Omega} j'(u_\Omega) \dot{u}_\Omega dx$  into a quantity of the form  $\int_{\Omega} \nabla \dot{u}_\Omega \cdot \nabla w dx$  for an adequate choice of the test function  $w$ . Since this quantity has exactly the structure of the operator in [\(1.3.18\)](#) through which we have access to  $\dot{u}_\Omega(\theta)$ , the passage from the second to the third line in [\(1.3.21\)](#) is allowed.

*Step 4.* We perform integration by parts to obtain the surface form.

The obtained result is not yet completely satisfactory, since we would like to obtain an expression for  $J'(\Omega)(\theta)$  showing the surface structure [\(1.3.3\)](#).

The passage from the volume expression [\(1.3.13\)](#) to the surface formula [\(1.3.15\)](#) relies on the following strategy. We perform integration by parts in all the terms [\(1.3.13\)](#) featuring derivatives of  $\theta$ , which is possible provided  $u_\Omega$  and  $p_\Omega$  are more regular than mere  $H^1(\Omega)$  functions. This fact in turn relies on the classical elliptic regularity theory, which ensures that, provided  $\Omega$  is of class  $C^2$ , these functions belong to  $H^2(\Omega)$ , see [Section 1.A.6](#) and the references therein about this point.

The aforementioned integration by parts yield an expression for  $J'(\Omega)(\theta)$  of the form

$$(1.3.22) \quad J'(\Omega)(\theta) = \int_{\Omega} S_\Omega \cdot \theta \, dx + \int_{\partial\Omega} v_\Omega \theta \cdot n \, ds + \int_{\partial\Omega} t_\Omega \cdot \theta_{\partial\Omega} \, ds,$$

where  $S_\Omega : \Omega \rightarrow \mathbb{R}^d$ ,  $v_\Omega : \partial\Omega \rightarrow \mathbb{R}$  and  $t_\Omega : \partial\Omega \rightarrow \mathbb{R}^d$  are functions depending on  $J(\Omega)$ ,  $u_\Omega$ ,  $p_\Omega$ . We now remark that an expression of this form for  $J'(\Omega)(\theta)$  must be unique, i.e. if  $\widetilde{S}_\Omega$ ,  $\widetilde{v}_\Omega$  and  $\widetilde{t}_\Omega$  are other functions such that

$$J'(\Omega)(\theta) = \int_{\Omega} \widetilde{S}_\Omega \cdot \theta \, dx + \int_{\partial\Omega} \widetilde{v}_\Omega \theta \cdot n \, ds + \int_{\partial\Omega} \widetilde{t}_\Omega \cdot \theta_{\partial\Omega} \, ds,$$

then necessarily  $\widetilde{S}_\Omega = S_\Omega$ ,  $\widetilde{v}_\Omega = v_\Omega$  and  $\widetilde{t}_\Omega = t_\Omega$ . Hence, if we believe that  $J'(\Omega)(\theta)$  has a surface structure of the form [\(1.3.3\)](#), it must hold that  $S_\Omega = 0$  and  $t_\Omega = 0$  in [\(1.3.22\)](#).

Let us carry out this strategy; integrating by parts all the terms featuring derivatives of  $\theta$  in (1.3.13), and using the elementary identities (1.A.1) and (1.A.2), we obtain:

$$\begin{aligned} J'(\Omega)(\theta) &= \int_{\partial\Omega} j(u_\Omega)(\theta \cdot n) \, ds + \int_{\partial\Omega} \nabla u_\Omega \cdot \nabla p_\Omega(\theta \cdot n) \, ds - \int_{\partial\Omega} \left( \nabla u_\Omega \cdot \theta \frac{\partial p_\Omega}{\partial n} + \nabla p_\Omega \cdot \theta \frac{\partial u_\Omega}{\partial n} \right) \, ds \\ &\quad - \int_{\partial\Omega} f p_\Omega(\theta \cdot n) \, ds + \int_{\Omega} S_\Omega \cdot \theta \, dx, \end{aligned}$$

for some vector field  $S_\Omega : \Omega \rightarrow \mathbb{R}^d$  depending on  $u_\Omega$  and  $p_\Omega$ , whose explicit expression is not reported for brevity. Since  $u_\Omega = 0$  and  $p_\Omega = 0$  on  $\partial\Omega$ , all the tangential derivatives of  $u_\Omega$  and  $p_\Omega$  vanish on  $\partial\Omega$ , so that:

$$J'(\Omega)(\theta) = \int_{\partial\Omega} j(u_\Omega)(\theta \cdot n) \, ds - \int_{\partial\Omega} \frac{\partial u_\Omega}{\partial n} \frac{\partial p_\Omega}{\partial n} (\theta \cdot n) \, ds + \int_{\Omega} S_\Omega \cdot \theta \, dx.$$

It must now hold that  $S_\Omega = 0$  according to the above principle, which can be verified by elementary, albeit tedious calculations. The desired surface expression (1.3.15) of the shape derivative  $J'(\Omega)(\theta)$  is then obtained.  $\square$

**Remark 1.3.13** *The above methodology can be adapted to a wide variety of physical situations and objective functions. For instance, in the structural optimization context of Section 1.2.3 where the displacement  $u_\Omega$  of the optimized structure  $\Omega$  is the solution to the linear elasticity system (Elas), it allows to prove that, if  $\Omega$  is sufficiently regular and deformations  $\theta$  vanish on  $\overline{\Gamma_D} \cup \overline{\Gamma_N}$ ,*

- The compliance functional  $C(\Omega)$  defined by (1.2.10) is shape differentiable, with derivative:

$$C'(\Omega)(\theta) = \int_{\Gamma} \left( 2f \cdot u_\Omega - Ae(u_\Omega) : e(u_\Omega) \right) \theta \cdot n \, ds.$$

- The least-square functional  $D(\Omega)$  in (1.2.11) is shape differentiable, with derivative:

$$D'(\Omega)(\theta) = \int_{\Gamma} \left( k(x) |u_\Omega - u_T|^2 + Ae(u_\Omega) : e(p_\Omega) - f \cdot p_\Omega \right) \theta \cdot n \, ds,$$

where the adjoint state  $p_\Omega$  is the unique solution in  $H_{\Gamma_D}^1(\Omega)^d$  to the system:

$$\begin{cases} -\operatorname{div}(Ae(p_\Omega)) = -2k(x)(u_\Omega - u_T) & \text{in } \Omega, \\ p_\Omega = 0 & \text{on } \Gamma_D, \\ Ae(p_\Omega)n = 0 & \text{on } \Gamma_N \cup \Gamma. \end{cases}$$

### 1.3.3.6. A more general perspective on the adjoint method

The adjoint method is the cornerstone of the proof of Theorem 1.3.12. Loosely speaking, it is a very general calculation technique of the derivatives of functions depending on the considered variable in an implicit way, via the solution to an equation.

To better appraise this feature, let us place ourselves in the following abstract setting: let  $(H, \langle \cdot, \cdot \rangle_H)$  be a Hilbert space of designs. Each element  $h \in H$  is characterized by a state  $u(h)$ , lying in another Hilbert space  $(V, \langle \cdot, \cdot \rangle_V)$ . The latter is characterized as the solution to a “physical” equation, of the form:

$$(1.3.23) \quad \mathcal{F}(h, u(h)) = 0,$$

where  $\mathcal{F} : H \times V \rightarrow V$  is a smooth function.

We aim to differentiate a function of the form

$$J(h) = j(u(h)), \text{ where } j : V \rightarrow \mathbb{R} \text{ is a smooth function.}$$

The first step towards this goal is to verify that  $H \ni h \mapsto u(h) \in V$  is differentiable. This usually follows from the application of the implicit function Theorem 1.A.11 to the equation (1.3.23), as in the first step of the proof of Theorem 1.3.12. Once this property is proved, by taking derivatives in (1.3.23), we obtain an equation for the derivative  $u'(h)(\hat{h})$ :

$$(1.3.24) \quad \forall \hat{h} \in H, \quad \left[ \frac{\partial \mathcal{F}}{\partial h}(h, u(h)) \right] \hat{h} + \left[ \frac{\partial \mathcal{F}}{\partial y}(h, u(h)) \right] u'(h)(\hat{h}) = 0.$$

On the other hand, we may also calculate the derivative of  $J(h)$ ; a simple use of the chain rule produces:

$$J'(h)(\hat{h}) = \left\langle j'(u(h)), u'(h)(\hat{h}) \right\rangle_V,$$

where we have introduced the gradient  $j'(u(h)) \in V$  of  $j$  at  $u(h)$ . We now wish to eliminate the “tedious” derivative  $u'(h)(\hat{h})$  from the previous equation, since the latter depends in a “difficult”, implicit way on the direction  $\hat{h}$ , via (1.3.24). To achieve this, we introduce the adjoint state  $p(h) \in V$  as the solution to the equation:

$$(1.3.25) \quad \left[ \frac{\partial \mathcal{F}}{\partial u}(h, u(h)) \right]^* p(h) = -j'(u(h)),$$

where the notation  $^*$  refers to the adjoint of an operator between Hilbert spaces. A calculation then yields:

$$\begin{aligned} J'(h)(\hat{h}) &= \left\langle j'(u(h)), u'(h)(\hat{h}) \right\rangle_V \\ &= -\left\langle \left[ \frac{\partial \mathcal{F}}{\partial u}(h, u(h)) \right]^* p(h), u'(h)(\hat{h}) \right\rangle_V \\ &= -\left\langle \left[ \frac{\partial \mathcal{F}}{\partial u}(h, u(h)) \right] u'(h)(\hat{h}), p(h) \right\rangle_V \\ &= \left\langle \left[ \frac{\partial \mathcal{F}}{\partial h}(h, u(h)) \right] \hat{h}, p(h) \right\rangle_V \\ &= \left\langle \left[ \frac{\partial \mathcal{F}}{\partial h}(h, u(h)) \right]^* p(h), \hat{h} \right\rangle_H. \end{aligned}$$

The resulting expression is explicit in terms of the direction  $\hat{h}$ , and it can be evaluated in no time once  $u(h)$ , then  $p(h)$  have been calculated.

In this seemingly harmless sequence of equalities, we have used:

- The definition (1.3.25) of the adjoint state  $p(h)$  to pass from the first line to the second one;
- The definition of the adjoint mapping  $\left[ \frac{\partial \mathcal{F}}{\partial u}(h, u(h)) \right]^*$  to pass from the second line to the third one;
- The “variational formulation” (1.3.24) for the derivative  $u'(h)(\hat{h})$  to pass from the third line to the penultimate one;
- The definition of the adjoint mapping  $\left[ \frac{\partial \mathcal{F}}{\partial h}(h, u(h)) \right]^*$  to terminate the calculation.

This sheds some light on the construction of the adjoint problem (1.3.25): its right-hand side is exactly what is needed to express the element  $j'(u(h)) \in V$  (second line) under a form which allows, by transposition of the left-hand side of (1.3.25), to use the only available information about the derivative  $u'(h)(\hat{h})$ .

### 1.3.3.7. The formal method of Céa

In the previous Section 1.3.3.5, we have presented the general, rigorous strategy for calculating the derivative of a functional of the domain. We now briefly exemplify an alternative, formal method to achieve this goal, which is due to Céa, see [111] and also [26] for a detailed presentation. The setting is exactly that of the previous section: we consider the shape functional  $J(\Omega)$  in (1.3.12), depending on the domain  $\Omega$  via the solution  $u_\Omega$  to the Laplace equation (1.3.11).

Céa’s method is inspired from optimization theory: it consists in “twisting” the values of the function  $J(\Omega)$  so that it rewrites as the value of a Lagrangian functional at a critical point. More precisely, it holds:

$$(1.3.26) \quad \forall p \in H^1(\mathbb{R}^d), \quad \lambda \in H^1(\mathbb{R}^d), \quad J(\Omega) = \mathcal{L}(\Omega, u_\Omega, p, \lambda),$$

where for each shape  $\Omega$ , the mapping  $\mathcal{L}(\Omega, \cdot, \cdot, \cdot) : H^1(\mathbb{R}^d) \times H^1(\mathbb{R}^d) \times H^1(\mathbb{R}^d) \rightarrow \mathbb{R}$  is defined by:

$$\begin{aligned} \mathcal{L}(\Omega, u, p, \lambda) &= \int_{\Omega} j(u) \, dx + \int_{\Omega} (-\Delta u - f)p \, dx + \int_{\partial\Omega} \lambda u \, ds \\ &= \int_{\Omega} j(u) \, dx + \int_{\Omega} \nabla u \cdot \nabla p \, dx - \int_{\Omega} f p \, dx + \int_{\partial\Omega} \left( \lambda u - \frac{\partial u}{\partial n} p \right) \, ds. \end{aligned}$$

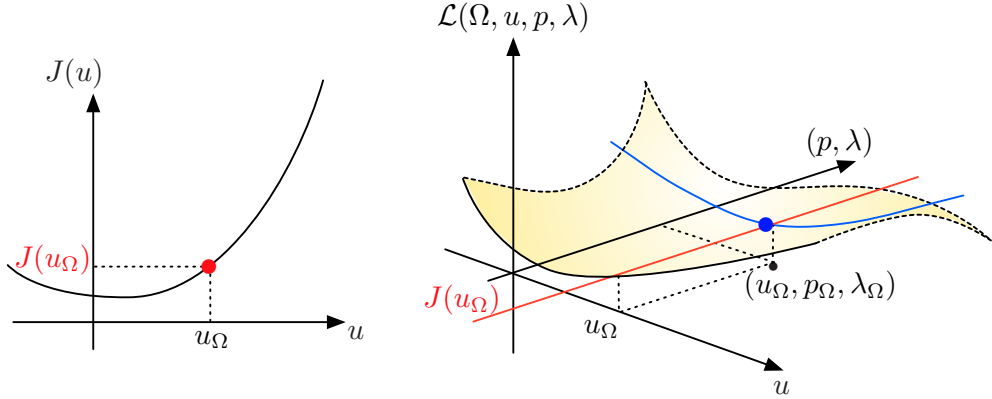


FIGURE 1.3.8. Céa’s method turns the quantity  $J(\Omega) = \int_{\Omega} j(u_{\Omega}) \, dx$  into a critical value of the Lagrangian  $\mathcal{L}(\Omega, \cdot, \cdot, \cdot)$ . Indeed, the Lagrange multiplier  $(p_{\Omega}, \lambda_{\Omega})$  is sought in such a way that the Lagrangian has a critical point at  $(u_{\Omega}, p_{\Omega}, \lambda_{\Omega})$  with the same value  $\mathcal{L}(\Omega, u_{\Omega}, p_{\Omega}, \lambda_{\Omega}) = J(\Omega)$  (red line). This rewriting is particularly convenient since, by the so-called “envelope theorem”, the derivative of the parametrized critical point  $\Omega \mapsto \mathcal{L}(\Omega, u_{\Omega}, p_{\Omega}, \lambda_{\Omega})$  boils down to the explicit derivative of  $\mathcal{L}$  with respect to  $\Omega$ , which is simple to calculate, see (1.3.29).

Intuitively, the dummy variable  $u \in H^1(\mathbb{R}^d)$  represents the state  $u_{\Omega}$ ; it is constrained to satisfy the equation  $-\Delta u = f$  in  $\Omega$  by the Lagrange multiplier  $p \in H^1(\mathbb{R}^d)$  and the boundary condition  $u = 0$  on  $\partial\Omega$  is imposed thanks to  $\lambda \in H^1(\mathbb{R}^d)$ , see Fig. 1.3.8. Crucially, the three variables  $u$ ,  $p$  and  $\lambda$  are independent of  $\Omega$ , as they belong to spaces of functions defined on the whole space  $\mathbb{R}^d$ . Note also that the relation (1.3.26) obviously implies that

$$(1.3.27) \quad J(\Omega) = \inf_{u \in H^1(\mathbb{R}^d)} \sup_{p, \lambda \in H^1(\mathbb{R}^d)} \mathcal{L}(\Omega, u, p, \lambda),$$

but unless the integrand  $j$  is a convex function of  $u$ , the above inf-sup has no reason to be a “true” saddle point.

Let us now search for the critical points of the Lagrangian  $\mathcal{L}(\Omega, \cdot, \cdot, \cdot)$ , which are the triples  $(u, p, \lambda) \in H^1(\mathbb{R}^d) \times H^1(\mathbb{R}^d) \times H^1(\mathbb{R}^d)$  where its partial derivatives vanish. Elementary calculations, which are for instance detailed in [A12], reveal that

$$\begin{cases} \forall \hat{p} \in H^1(\mathbb{R}^d), \frac{\partial \mathcal{L}}{\partial p}(\Omega, u, p, \lambda)(\hat{p}) = 0, \\ \forall \hat{\lambda} \in H^1(\mathbb{R}^d), \frac{\partial \mathcal{L}}{\partial \lambda}(\Omega, u, p, \lambda)(\hat{\lambda}) = 0 \end{cases} \Rightarrow u = u_{\Omega}, \text{ the solution to (1.3.11),}$$

and

$$\forall \hat{p} \in H^1(\mathbb{R}^d), \frac{\partial \mathcal{L}}{\partial p}(\Omega, u_{\Omega}, p, \lambda)(\hat{p}) = 0 \Rightarrow \begin{cases} p = p_{\Omega}, \text{ the solution to (1.3.14),} \\ \lambda = \lambda_{\Omega} := -\frac{\partial p_{\Omega}}{\partial n} \text{ on } \partial\Omega. \end{cases}$$

With this information in hand, we return to the expression (1.3.26). We admit that the state mapping  $\Omega \mapsto u_{\Omega}$  has a Eulerian derivative, which is where the method becomes purely formal; we have seen in Section 1.3.3.4 that this property typically requires stronger regularity for  $u_{\Omega}$  than that guaranteed by the Lax-Milgram framework for the boundary value problem (1.3.11). A formal differentiation with respect to the domain in (1.3.26) yields the following identity, which is valid for all  $p, \lambda \in H^1(\mathbb{R}^d)$ :

$$(1.3.28) \quad J'(\Omega)(\theta) = \frac{\partial \mathcal{L}}{\partial \Omega}(\Omega, u_{\Omega}, p, \lambda)(\theta) + \frac{\partial \mathcal{L}}{\partial u}(\Omega, u_{\Omega}, p, \lambda)(u'_{\Omega}(\theta)).$$

The first term in the above right-hand side is fairly simple, as it is the derivative of the explicit dependence of the expression  $\mathcal{L}(\Omega, u, p, \lambda)$  with respect to  $\Omega$ , the result being then evaluated at  $u = u_{\Omega}$ ,  $p$  and  $\lambda$ . The second

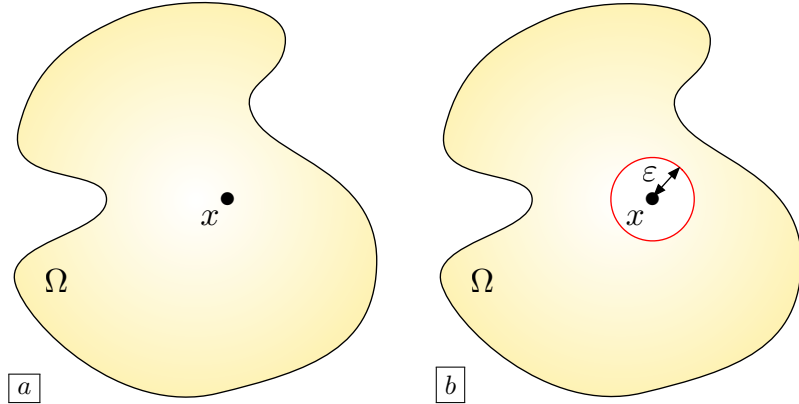


FIGURE 1.3.9. Variation  $\Omega_{x,\varepsilon}$  (in (b)) of a shape  $\Omega$  (depicted in (a)) used in the definition of topological derivative.

term is more difficult to handle, since it features the awkward Eulerian derivative  $u'_\Omega(\theta)$  of  $u_\Omega$ . To overcome this issue, we take advantage of the fact that the expression (1.3.28) holds for any choice of  $p \in H^1(\mathbb{R}^d)$ ,  $\lambda \in H^1(\mathbb{R}^d)$  to select suitable particular instances of these parameters: we have just seen that  $\frac{\partial \mathcal{L}}{\partial u}$  vanishes when  $p = p_\Omega$  and  $\lambda = -\frac{\partial p_\Omega}{\partial n}$ . With these particular choices, (1.3.28) becomes:

$$(1.3.29) \quad J'(\Omega)(\theta) = \frac{\partial \mathcal{L}}{\partial \Omega}(\Omega, u_\Omega, p_\Omega, \lambda_\Omega)(\theta),$$

which is readily calculated by using [Propositions 1.3.7](#) and [1.3.8](#). This finally yields

$$J'(\Omega)(\theta) = \int_{\partial\Omega} \left( j(u_\Omega) - \frac{\partial u_\Omega}{\partial n} \frac{\partial p_\Omega}{\partial n} \right) (\theta \cdot n) \, ds,$$

which is the desired surface form (1.3.15) of the shape derivative  $J'(\Omega)(\theta)$ .

This method can be justified under particular assumptions, involving notably the convexity of  $j$ , under which (1.3.27) really accounts for a saddle point; this task hinges on a theorem for differentiating the value of a Lagrangian functional at a saddle point with respect to a parameter, see Chap. 10 in [\[156\]](#) and [\[356\]](#) in the more general context of optimal control of partial differential equations.

Let us conclude this presentation of Céa's method with a word of caution: in several important cases where the state mapping  $\Omega \mapsto u_\Omega$  does not admit a Eulerian derivative (which is the case when  $u_\Omega$  fails to be "regular enough"), this method leads to erroneous results. This phenomenon arises for instance in the context of two-phase optimization [\[A34, 294\]](#), and when the transition region between boundary conditions is optimized, as we shall study in the next [Section 4.3](#).

### 1.3.4. Topological derivatives

The boundary variation method of Hadamard accounts for the sensitivity of a function of the domain with respect to "small" perturbations of the boundary of the latter. In particular, [Proposition 1.3.2](#) ensures that all variations  $\Omega_\theta$ ,  $\|\theta\|_{W^{1,\infty}(\mathbb{R}^d, \mathbb{R}^d)} < 1$  of a shape  $\Omega$  are homeomorphic to  $\Omega$ , and thus share the same topology – in particular, they have the same number of holes in 2d. Hence, in principle, this type of variation of shapes does not allow for topological changes. In numerical practice, this is not exactly true, and we shall see that a small abuse of the above framework (and the use of a suitable numerical method) allows for certain topological changes, see [Remark 1.4.4](#). However, in any event, this framework does not allow to appraise how  $J(\Omega)$  can be improved by nucleating holes inside  $\Omega$ : this is the purpose of introducing topological derivatives.

The concept of topological derivative relies on variations  $\Omega_{x,\varepsilon}$  of a domain  $\Omega \subset \mathbb{R}^d$  of the form:

$$\Omega_{x,\varepsilon} = \Omega \setminus \overline{B(x, \varepsilon)}, \text{ for } x \in \Omega, \varepsilon \ll 1,$$

i.e.  $\Omega_{x,\varepsilon}$  is a version of  $\Omega$  where a tiny hole with radius  $\varepsilon$  has been nucleated around  $x$ , see [Fig. 1.3.9](#).

**Definition 1.3.14** A function of the domain  $J(\Omega)$  has a topological derivative at  $x \in \Omega$  if there exists a function  $\rho(\varepsilon)$  such that  $\rho(\varepsilon) \rightarrow 0$  as  $\varepsilon \rightarrow 0$  and  $g(x) \in \mathbb{R}$  such that the following expansion holds:

$$J(\Omega_{x,\varepsilon}) = J(\Omega) + \rho(\varepsilon)g(x) + o(\rho(\varepsilon)), \text{ where } \frac{|o(\rho(\varepsilon))|}{\rho(\varepsilon)} \xrightarrow{\varepsilon \rightarrow 0} 0.$$

The number  $g(x)$  is called the topological derivative of  $J(\Omega)$  at  $x$  and is denoted by  $dJ_T(\Omega)(x)$ .

The calculation of topological derivatives fits in the framework of asymptotic analysis, which generally analyzes “small”, often singular perturbations in partial differential equations. A model calculation of a topological derivative is presented in [Section 4.1.5](#). For the moment, let us solely mention that this task can be realized by various techniques: layer potentials, or adjoint method, see for instance [\[42, 187, 289, 342\]](#).

We shall see in [Section 1.4.8](#) how the information contained in topological derivatives can be exploited in numerical algorithms.

### 1.3.5. A focus on the Hilbertian method for handling shape derivatives

As we have seen in the previous sections, the perturbations  $\theta$  of shapes featured by the method of Hadamard belong to the Banach space  $W^{1,\infty}(\mathbb{R}^d, \mathbb{R}^d)$ , or a subspace of the latter. However, as we shall see, it is useful for a wide variety of purposes to endow the space of deformations with a Hilbertian structure. The so-called Hilbertian method, introduced in [\[53, 100, 152, 307\]](#) (see also [\[271\]](#)), aimed to achieve this goal, is the cornerstone of many useful operations in shape optimization.

Let  $(V, \langle \cdot, \cdot \rangle_V)$  be a Hilbert space which is continuously embedded in  $W^{1,\infty}(\mathbb{R}^d, \mathbb{R}^d)$ , and let  $J(\Omega)$  be a function with shape derivative  $J'(\Omega)(\theta)$  at some shape  $\Omega \subset \mathbb{R}^d$ . The latter is a continuous linear form on  $W^{1,\infty}(\mathbb{R}^d, \mathbb{R}^d)$ , and so it is also a continuous and linear form on  $V$ . Hence, according to the Riesz representation theorem, there exists an element  $\theta_J \in V$  such that:

$$(1.3.30) \quad \forall v \in V, \quad J'(\Omega)(v) = \langle \theta_J, v \rangle_V.$$

Mathematically,  $\theta_J \in V$  is the gradient associated to the continuous and linear form  $V \ni v \mapsto J'(\Omega)(v) \in \mathbb{R}$ . Regardless of the choice of  $V$  (as long as it fulfills the above requirements), the vector field  $-\theta_J$  realizes a descent direction for  $J(\Omega)$  since, for  $t > 0$  small enough:

$$(1.3.31) \quad \begin{aligned} J(\Omega_{-t\theta_J}) &= J(\Omega) - tJ'(\Omega)(\theta_J) + o(t) \\ &= J(\Omega) - t\langle \theta_J, \theta_J \rangle_V + o(t) \\ &< 0. \end{aligned}$$

Besides,  $-\theta_J$  inherits from additional properties with respect to vector fields lying merely in  $W^{1,\infty}(\mathbb{R}^d, \mathbb{R}^d)$ , which are encoded in the space  $V$  (higher regularity, etc.).

Another avatar of this strategy consists in selecting a Hilbert space  $(V, \langle \cdot, \cdot \rangle_V)$  which contains  $W^{1,\infty}(\mathbb{R}^d, \mathbb{R}^d)$ . This is possible provided the shape derivative  $\theta \mapsto J'(\Omega)(\theta)$  admit an extension into a continuous and linear form on  $V$ . In this situation, it is still possible to calculate a Riesz representative  $\theta_J \in V$  for the derivative  $V \ni v \mapsto J'(\Omega)(v) \in \mathbb{R}$ , i.e. a vector field satisfying [\(1.3.30\)](#). This assumption actually corresponds to a kind of “regularity” assumption about the ingredients of the shape derivative  $J'(\Omega)(\theta)$ . For instance, the surface expression [\(1.3.15\)](#) of the shape derivative calculated in [Section 1.3.3.5](#) can be extended into a continuous and linear form on  $H^1(\mathbb{R}^d)^d$  as soon as the state and adjoint functions  $u_\Omega$  and  $p_\Omega$  belong to  $W^{1,\infty}(\Omega)$ . Note however that this second practice is mostly formal: although the produced “descent direction”  $-\theta_J$  does satisfy  $J'(\Omega)(-\theta_J) < 0$ , it is not clear how to account for a variation of  $\Omega$  according to the perturbation  $-\theta_J$  since the latter does not belong to  $W^{1,\infty}(\mathbb{R}^d, \mathbb{R}^d)$ .

Let us provide a few concrete application examples:

- The perhaps most natural implementation of this idea is to set

$$V = H^m(\mathbb{R}^d)^d, \text{ with the inner product } \langle u, v \rangle_V := \sum_{|\alpha| \leq m} \int_{\mathbb{R}^d} \frac{\partial^{|\alpha|} u}{\partial x^\alpha} \cdot \frac{\partial^{|\alpha|} v}{\partial x^\alpha} dx,$$

where the exponent  $m$  is chosen sufficiently large so that  $V$  is continuously embedded in  $W^{1,\infty}(\mathbb{R}^d, \mathbb{R}^d)$  owing to the Sobolev embedding theorem, see e.g. [\[7\]](#) about this point.

- A common practice consists in the choice:

$$V = H^1(\mathbb{R}^d)^d, \text{ with the inner product } \langle u, v \rangle_V := \alpha^2 \int_D \nabla u : \nabla v \, dx + \int_D u \cdot v \, dx,$$

involving a parameter  $\alpha$  which can be interpreted as a smoothing length scale. Note that, as we have discussed above, this choice is not rigorous, since  $H^1(\mathbb{R}^d)^d$  is not a subset of  $W^{1,\infty}(\mathbb{R}^d, \mathbb{R}^d)$ .

- As we have seen in [Section 1.3.3.2](#), when the shape derivative  $J'(\Omega)(\theta)$  has the nice structure

$$\forall \theta \in W^{1,\infty}(\mathbb{R}^d, \mathbb{R}^d), \quad J'(\Omega)(\theta) = \int_{\partial\Omega} v_{\Omega} \theta \cdot n \, ds,$$

for some scalar field  $v_{\Omega} : \partial\Omega \rightarrow \mathbb{R}$ , it is tempting to consider a descent direction  $\theta$  such that:

$$(1.3.32) \quad \theta = -v_{\Omega} n \text{ on } \partial\Omega.$$

In the language introduced in this section, this amounts to selecting  $\theta$  as the  $L^2(\partial\Omega)^d$  gradient of  $J'(\Omega)(\theta)$ . However straightforward, this choice is often ill-suited. Indeed, the field  $v_{\Omega}$  is often not very regular, and its practical calculation may be riddled with numerical artifacts, as it involves the derivatives of  $H^1$  solutions to boundary value problems posed on  $\Omega$ , see for instance the expression [\(1.3.15\)](#). Besides, the choice [\(1.3.32\)](#) only sets the values of  $\theta$  on  $\partial\Omega$ . As we shall see, most numerical methods actually rely on descent directions defined on the whole space  $\mathbb{R}^d$ , or at least a large computational domain  $D$  in practice.

- Yet another choice is  $V = H^1(D)^d$ , where  $D$  is a large computational domain, containing all the shapes of interest. It is endowed with the following inner product, induced by the linearized elasticity operator:

$$\forall u, v \in H^1(D)^d, \quad \langle u, v \rangle_V = \int_D (Ae(u) : e(v) + u \cdot v) \, dx.$$

Intuitively, this choice tends to produce gradients which induce little compression inside the domain  $D$  (as they mimick elastic displacements). In this definition, the Hooke's tensor  $A$  can be chosen to be inhomogeneous, with a stronger Young's modulus in the regions of space where compression effects should be avoided. This practice is especially useful when a mesh deformation method is used in the numerical framework, as we shall see in [Section 1.4.4](#).

**Remark 1.3.15** *From the practical point of view, the resolution of the identification problem [\(1.3.30\)](#) amounts to the resolution of a “simple” boundary value problem (at least, with respect to those defining the state and adjoint mappings) which can be conveniently solved by the finite element method on a fixed mesh of a computational domain  $D$ .*

Let us summarize some of the manifold applications of the “Hilbertian trick” described in this section.

- It makes it possible to extract descent directions from the volume expressions of shape derivatives (see e.g. [\(1.3.13\)](#)), which is not as straightforward a task as it is from their surface expression, see [Section 1.3.3.2](#). This use of the volume expression of shape derivatives turns out to guarantee a better consistence between the theoretical formulation of the shape optimization problem and its numerical discretization, see [\[190, 203\]](#) for more details.
- Many optimization algorithms take advantage of a Hilbertian structure for the optimization variable, see notably the next [Section 3.2](#).
- It allows to calculate descent directions with user-defined properties. For instance, using  $V = H^m(\mathbb{R}^d, \mathbb{R}^d)$  with a large exponent  $m$  yields gradients with better regularity than that of the natural space  $W^{1,\infty}(\mathbb{R}^d, \mathbb{R}^d)$ . Also, using a space such as that  $H_{\Gamma_D}^m(\mathbb{R}^d, \mathbb{R}^d)$  of vector fields vanishing on a fixed common region  $\Gamma_D$  to all optimized shapes imposes that the produced descent direction vanish on this subset.

**Remark 1.3.16** *One may wonder about the “best” choice of a Hilbert space  $V$  (and the corresponding inner product  $\langle \cdot, \cdot \rangle_V$ ) to extract a gradient from the shape derivative of a functional  $J(\Omega)$ . This feature mainly depends on the targeted application, which guides the particular “effects” that are desirable for descent directions (in terms of smoothness, rigidity, etc.). Let us emphasize again that any choice fitting with the*

above strategy yields a descent direction for  $J(\Omega)$ , see again (1.3.31). To the best of our knowledge, there is no simple means to appraise which choice would entail the “best” decrease in the value of the objective function, unless the second order expansion of  $\theta \mapsto J(\Omega_\theta)$  is considered.

## 1.4 NUMERICAL IMPLEMENTATION OF SHAPE OPTIMIZATION ALGORITHMS

This section deals with the application of the theoretical material of the previous sections to the device of numerical shape and topology optimization algorithms. After providing the general template of such an algorithm in Section 1.4.1, we recall a few basic but central notions related to meshing and remeshing in Sections 1.4.2 and 1.4.3. We then propose in Section 1.4.4 a first, intuitive and historical algorithm, which illustrates the difficulties related to meshing faced by most implementations of shape and topology optimization algorithms. For comparison purpose and further reference, we briefly present in the next Section 1.4.5 the general sketch of density-based topology optimization methods. We then turn in Section 1.4.6 to the level set method for shape and topology optimization, before describing in Section 1.4.7 a variant of the latter which additionally makes it possible to account for the evolution of a mesh of the optimized shape, however dramatic it may be. We finally present two implementations of the notion of topological derivative in Section 1.4.8.

### 1.4.1. General outline of a shape and topology optimization algorithm

To set ideas, let us go back to a model structural optimization problem such as that introduced in Section 1.2.3:

$$(\mathcal{P}) \quad \min_{\Omega} J(\Omega) \text{ s.t. } \begin{cases} G(\Omega) = 0, \\ H(\Omega) \leq 0, \end{cases}$$

where the objective and constraint functions  $J(\Omega)$ ,  $G(\Omega)$  and  $H(\Omega)$  depend on the optimized shape  $\Omega$  via the displacement  $u_\Omega$ , solution to the linear elasticity system (Elas). A generic algorithm based on the concept of shape derivative for this problem is summarized in Algorithm 1.

---

**Algorithm 1** Generic shape gradient algorithm.

---

**Initialization:** Initial shape  $\Omega^0$ .  
**for**  $n = 0, \dots$ , until convergence **do**

- (1) Calculate the solution  $u_{\Omega^n}$  (resp.  $p_{\Omega^n}$ ) to the state (resp. adjoint) equation posed in  $\Omega^n$ .
- (2) From the theoretical formulas for the derivatives  $J'(\Omega)(\theta)$ ,  $G'(\Omega)(\theta)$  and  $H'(\Omega)(\theta)$ , infer a descent direction  $\theta^n$  from  $\Omega^n$  for the problem  $(\mathcal{P})$ .
- (3) Deform  $\Omega^n$  according to  $\theta^n$  for a small descent step  $\tau^n > 0$ , so that the new shape

(1.4.1) 
$$\Omega^{n+1} := (\text{Id} + \tau^n \theta^n)(\Omega^n)$$
 is “better” than the previous one in view of  $(\mathcal{P})$ .

**end for**  
**return**  $\Omega^n$

---

Briefly, at each iteration  $n$  of the process, indexed by the superscript  $n$ , the state equation (Elas) for  $u_{\Omega^n}$  (as well as the adjoint equation for  $p_{\Omega^n}$ ) is solved on the current shape  $\Omega^n$  (Step 1); this task can be realized via the finite element method, provided a mesh of  $\Omega^n$  is available. Then, (Step 2) a descent direction for  $(\mathcal{P})$  is extracted from the shape derivatives  $J'(\Omega)(\theta)$ ,  $G'(\Omega)(\theta)$  and  $H'(\Omega)(\theta)$ . In the particular case where  $(\mathcal{P})$  does not feature constraints and where the surface form (1.3.3) of  $J'(\Omega)(\theta)$  is available, this task can for instance rely on the simple rule (1.3.4), as proposed in Section 1.3.3.2. In the general situation, it requires a constrained optimization algorithm, which often leverages the Hilbertian method presented in Section 1.3.5. We shall return to this issue in Section 3.2, where a novel optimization algorithm is proposed, which is especially suited for shape optimization. The main issue raised by the implementation of any strategy of the form of Algorithm 1 lies in the update of the optimized shape (Step 3), and more accurately in the inadequacy of this operation with the requirements of Step 1: in a nutshell, it is difficult to find a means to represent shapes which is equally suitable for conducting mechanical computations on them and for tracking

their evolution. This concern has been acknowledged since the early implementations of shape optimization algorithms; it is by no means specific to the discipline, being rather a general bottleneck in the numerical tracking of evolving physical interfaces. We shall see a few attempts to address this issue in the subsequent sections.

### 1.4.2. Preliminaries about meshes

In this section, we introduce some basic material about simplicial meshes; we refer to e.g. [87, 121, 182, 244, 353] for further details about these issues.

Let  $\Omega \subset \mathbb{R}^d$  be a bounded domain; a *mesh* of  $\Omega$  is a collection  $\mathcal{T} = \{T_i\}_{i=1, \dots, N_T}$  of open simplices (i.e. triangles in 2d, tetrahedra in 3d), accounting for a covering of  $\Omega$ , in the sense that

$$\overline{\Omega} = \bigcup_{i=1}^{N_T} \overline{T_i}.$$

In addition, we assume that

- $\mathcal{T}$  is *valid*: the simplices  $T_i$  are mutually disjoint:  $T_i \cap T_j = \emptyset$ ,  $i \neq j$ ,
- $\mathcal{T}$  is *conforming*: each intersection  $\overline{T_i} \cap \overline{T_j}$ ,  $i \neq j$ , is reduced to either a vertex, an edge, or (in 3d) a face of  $\mathcal{T}$ .

Additionnally, a mesh  $\mathcal{T}$  usually contains information about a surface mesh  $\mathcal{S}$ , that is, a set  $\{S_j\}_{j=1, \dots, N_S}$  gathering edges (in 2d) or triangles (in 3d)  $S_j \subset \mathbb{R}^d$ . In the most simple situations,  $\mathcal{S}$  is made of the external faces of the simplices  $T \in \mathcal{T}$ , as a (approximate) representation of the boundary of  $\Omega$ . However, in some applications,  $\Omega$  is composed of several subdomains, whose simplices are identified with different labels. Then,  $\mathcal{S}$  also contains the elements of the inner boundaries of these subregions, see Fig. 1.4.10 (right) below for an example.

Usually, the creation of a mesh  $\mathcal{T}$  of  $\Omega$  starts from the datum of a surface mesh  $\mathcal{S}$  of the boundary  $\partial\Omega$ , which is often supplied by a CAD software in 3d. Thence, several strategies are available to fill the volume of  $\Omega$  with simplices conforming to the elements in  $\mathcal{S}$ , the perhaps most efficient ones being based on the constrained Delaunay algorithm, see for instance [121, 182] for detailed presentations of the latter. Without entering into details, let us mention that, in spite of having been extensively addressed for decades, mesh generation is still a delicate issue when complicated shapes  $\Omega$  are considered.

Beyond the aforementioned mild requirements, it is often desirable to evaluate “how well” a mesh  $\mathcal{T}$  lends itself to accurate numerical simulations. This feature can be appraised in at least two independent ways, which are illustrated on Fig. 1.4.1.

- Most numerical methods experience trouble when  $\mathcal{T}$  contains very flat, nearly degenerate elements. For instance, such configurations are well-known to increase dramatically the condition number of finite element systems based on this mesh, thus slowing down iterative matrix solvers, see e.g. the books [130, 173] about this classical issue. Several quantities are used in the literature to discriminate “well-shaped elements”  $T_i$  (i.e. that are close from being regular), from “ill-shaped” ones (i.e. that are nearly degenerate); for instance, the following measure of the quality of a tetrahedron  $T \subset \mathbb{R}^3$  is quite popular in the literature:

$$\mathcal{Q}(T) = \alpha \frac{\text{Vol}(T)}{\left( \sum_{i=1}^6 |e_i|^2 \right)^{\frac{3}{2}}}.$$

Here, the  $e_i$ ,  $i = 1, \dots, 6$  are the edges of  $T$ ,  $\text{Vol}(T)$  is its volume, and  $\alpha$  is a normalization factor, such that  $\mathcal{Q}(T)$  equals 1 when  $T$  is regular, and it is close to 0 when  $T$  is nearly degenerate.

- Another crucial feature in the evaluation of the quality of  $\mathcal{T}$  is related to an issue that we have overlooked so far. Often, the domain  $\Omega$  of interest is smooth, with a curved boundary  $\partial\Omega$ , while the faces of the surface triangulation  $\mathcal{S}$ , intended as a discrete approximation of the latter, are planar. Hence, it should be required that  $\mathcal{S}$  be a close approximation of the smooth surface  $\partial\Omega$  up to a

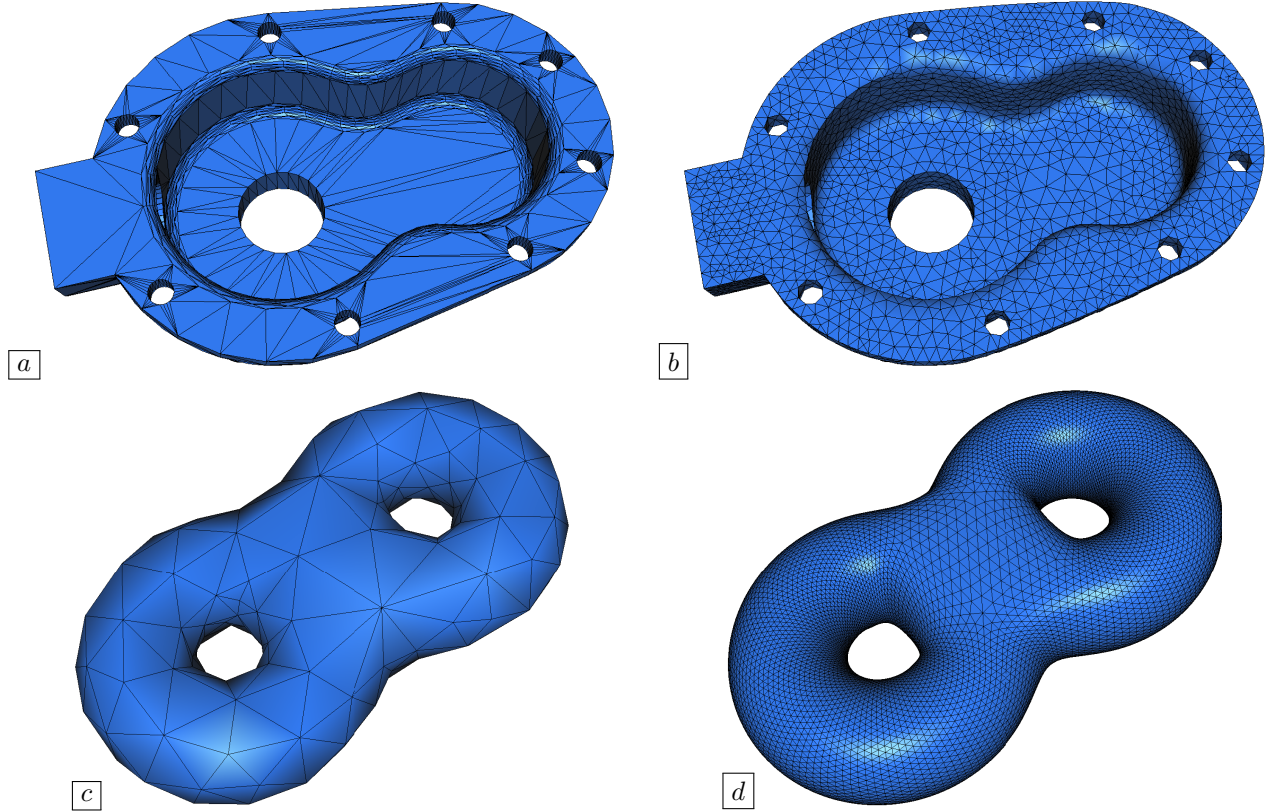


FIGURE 1.4.1. (a) Fine geometric approximation of a domain  $\Omega_1$ , with a mesh containing bad quality elements; (b) Good quality mesh of  $\Omega_1$ ; (c) Good quality mesh, yet poor geometric approximation of a domain  $\Omega_2$ ; (d) Mesh of  $\Omega_2$  accounting for a fine geometric approximation of the latter.

certain tolerance, for instance that

$$(1.4.2) \quad d^H(\mathcal{S}, \partial\Omega) \leq \varepsilon,$$

where  $d^H(\cdot, \cdot)$  is the Hausdorff distance between compact subsets of  $\mathbb{R}^d$  and  $\varepsilon$  is a user-defined tolerance threshold.

Grossly speaking, this requirement is fulfilled when the density of the mesh is such that  $\mathcal{S}$  features smaller and more numerous elements in the regions of  $\partial\Omega$  with large curvature.

Summarizing, we shall require from a mesh  $\mathcal{T}$  of  $\Omega$  that each simplex  $T_i$  have quality  $Q(T_i)$  close to 1, and that the surface mesh  $\mathcal{S}$  be a “close” approximation of the continuous surface  $\partial\Omega$ .

### 1.4.3. Basic stakes about remeshing

As suggested by the name, remeshing assumes the datum of a tetrahedral mesh  $\mathcal{T}$  of  $\Omega$  which is valid and conforming, but may still be unsuitable for computation: it may suffer from poor element quality, or its surface part  $\mathcal{S}$  may account for a poor geometric approximation of the curved boundary  $\partial\Omega$  (or other, internal surfaces), in the sense that the property (1.4.2) is not satisfied. Remeshing aims to modify  $\mathcal{T}$  into a high-quality mesh  $\tilde{\mathcal{T}}$  of  $\Omega$ , whose element density is well-tailored to its geometric features.

This objective is usually achieved thanks to a series of local operations, which are applied iteratively; these are briefly described below, and illustrated on Fig. 1.4.2 in the two-dimensional context.

- *Edge split:* When an edge  $pq$  is “too long”, a new vertex  $m$  is inserted in the mesh  $\mathcal{T}$ ;  $pq$  is replaced by the two edges  $pm$  and  $mq$  and the connectivity of  $\mathcal{T}$  is updated accordingly.

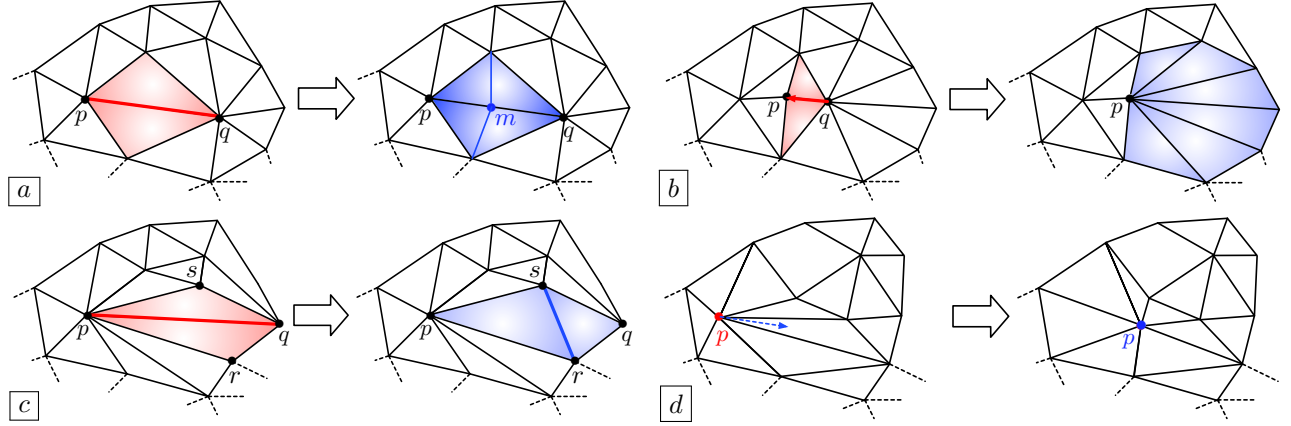


FIGURE 1.4.2. (a) Split of the “long” edge  $pq$ : a new point  $m$  is inserted in  $\mathcal{T}$  and the triangles sharing this edge are subdivided accordingly; (b) Collapse of point  $q$  onto  $p$ : the two red triangles are erased, and  $q$  is replaced by  $p$  in all the other triangles connected to  $q$  (in blue); (c) Swap of the edge  $pq$  (in red): the connection  $pq$  is replaced with the alternative configuration, featuring the edge  $rs$  (in blue); (d) Relocation of the vertex  $p$  while maintaining all the connections in the mesh.

- *Edge collapse*: When an edge  $pq$  is “too short”, its endpoints  $p$  and  $q$  are merged and the connections of the mesh  $\mathcal{T}$  are updated accordingly.
- *Edge swap*: An edge  $pq$  is removed from the mesh  $\mathcal{T}$  and the “shell” of  $pq$ , consisting of all the tetrahedra sharing this edge, is adequately reconnected.
- *Vertex relocation*: A vertex  $p$  is moved slightly, while all its connections remain unaltered.

Each of these operators exists under two different versions, depending on whether it is applied to a surface configuration, involving tetrahedra bearing surface triangles  $S_j \in \mathcal{S}$ , or to an internal one. For instance, when an internal edge  $pq$  of  $\mathcal{T}$  is split, the inserted point  $m$  is usually chosen as the midpoint of  $p$  and  $q$ ; on the contrary, when  $pq \in \mathcal{S}$  is a boundary edge,  $m$  is rather placed on the continuous surface  $\partial\Omega$ . In practice, since this “ideal” surface is unknown, the position of  $m$  is inferred from those of  $p$  and  $q$ , and other associated geometric quantities (such as the normal vectors at  $p$  and  $q$ ).

In the above description, the criterion whereby an edge  $pq$  is deemed to be “too long” (or “too short”) may depend on the situation. For instance,  $pq$  may be “too long” with respect to a user’s prescription for the size of the elements of the mesh or, when  $pq \in \mathcal{S}$  is a surface edge, it may be considered to be “too long” with respect to the curvature of  $\partial\Omega$ , as its size entails a too coarse geometric approximation of  $\partial\Omega$ .

Last but not least, let us emphasize that the use of the above remeshing operators should be carefully monitored: several checks are in order so as to prevent the emergence of invalid configurations.

These methods have been implemented in the open-source library `mmg` [S2], based on the work in [A35].

#### 1.4.4. The historical Lagrangian methods for shape optimization

The historical “Lagrangian” realizations of shape optimization algorithms such as [Algorithm 1](#) hinge on a representation of the shape by means of a computational mesh, see for instance [26, 271, 303].

In a nutshell, at each iteration  $n$  of the optimization process, the shape  $\Omega^n$  is discretized by means of a simplicial mesh  $\mathcal{T}^n$ . Thus, the mechanical computations on  $\Omega^n$  involved in the evaluation of the state  $u_{\Omega^n}$  and the adjoint  $p_{\Omega^n}$  (Step 1 in [Algorithm 1](#)) can be conducted in an accurate way, for instance by means of the finite element method. Thence, a descent direction  $\theta^n$  for the problem  $(\mathcal{P})$  can be calculated (Step 2). The update  $\Omega^{n+1} = (\text{Id} + \tau^n \theta^n)(\Omega^n)$  of the shape (Step 3) and that of the mesh  $\mathcal{T}^n$  into a mesh  $\mathcal{T}^{n+1}$  of  $\Omega^{n+1}$  are the tedious operations in this framework, as it is notoriously difficult to realize the evolution of a mesh in a robust way, especially when the imposed displacement of the latter is “large”, not even mentioning the case where it induces changes in the topology of the shape. For instance, the “naive” use of the update

rule

$$(1.4.3) \quad \text{For each vertex } x \in \mathcal{T}^n, \quad x \mapsto x + \tau^n \theta^n(x),$$

inevitably creates very stretched, bad quality, and even overlapping elements.

Admittedly, a number of heuristics allow to make this strategy more robust. For instance, in [56], an elastic displacement is assigned to the interior nodes of the mesh  $\mathcal{T}^n$ , with the hope that this should help decrease the compression and degeneration of elements occurring during the motion. The deformation induced by the corresponding vector field is applied as long as the mesh stays valid and remeshing is periodically applied to improve the quality of the elements that end up badly distorted during the process, see also [60, 160]. Nevertheless, such mesh deformation methods are usually reserved to deal with “small” evolutions of the shape.

An illustration of this procedure is given in Fig. 1.4.3. The educational article [A23] proposes a pedagogical implementation of these ideas in **FreeFem** accompanied with an open-source code, in the context of the optimization of the shape of fluid domains.

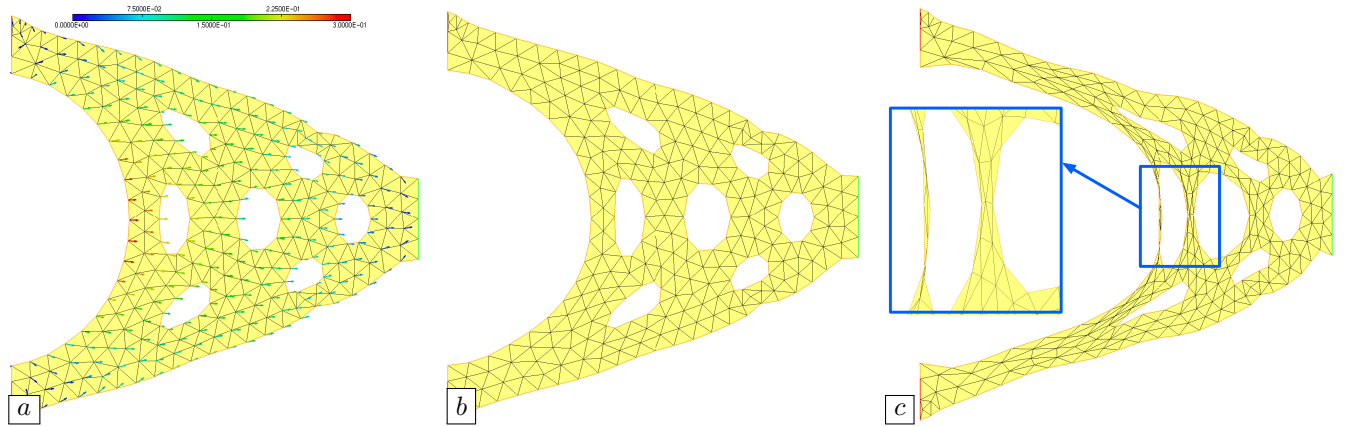


FIGURE 1.4.3. (a) Mesh  $\mathcal{T}^n$  of the shape  $\Omega^n$  with the descent direction  $\theta^n$  discretized at its vertices; (b) Updated mesh  $\mathcal{T}^{n+1}$  of  $\Omega^{n+1} := (\text{Id} + \tau^n \theta^n)(\Omega^n)$  obtained by using the rule (1.4.3) with a “small enough” time step  $\tau^n$ ; (c) Invalid mesh  $\mathcal{T}^{n+1}$  when the chosen time step  $\tau^n$  is “too large” (code available on the webpage of the course [C1]).

**Remark 1.4.1** Recently, two interesting series of work (at least) based on such mesh deformation strategies have proved able to account for impressively large evolutions of domains.

- The so-called *Deformable Simplicial Complex* method proposed in [266] couples the update rule (1.4.3) with a heuristic strategy to handle topological changes, based on the detection of stretched simplices near the boundary of the evolving mesh, see [128] in the context of shape and topology optimization.
- The *X-mesh* method proposed in [269] proceeds by moving the vertices of the mesh according to (1.4.3) up the point where the measure of some of its elements equals 0. The motion is then relayed from one node to its neighbour while leaving unchanged the connectivity of the mesh before the evolution is resumed. This strategy relies on the assumption that the numerical resolution of boundary value problems can be achieved on meshes with degenerate elements.

#### 1.4.5. Density-based formulations

The idea of using density functions in place of (the characteristic functions  $\mathbb{1}_\Omega$  of) shapes  $\Omega$  in the formulation of optimal design problems was introduced in [69] as a simplified, heuristic version of the homogenization method. It has given rise to the most prevalent techniques in this field, which are often referred to as “topology optimization methods”. While originally developed in the context of structural mechanics, they have

since then been adapted to a wide range of physical situations, including fluid mechanics [88], electromagnetism [2], etc. As they are widespread in the engineering literature, and since we shall at times leverage such formulations in this manuscript, we briefly present these approaches in this section, referring to [70, 338] for further details.

Essentially, the design variable, accounting for a mechanical structure, is a density function  $h$  defined on a large, fixed computational box  $D \subset \mathbb{R}^d$  and taking values in the interval  $[0, 1]$ , with the meaning that

- $h(x) = 1$  at “black” points  $x \in D$  surrounded by material;
- $h(x) = 0$  in “white” regions of  $D$  which are completely empty of material;
- $h(x) \in (0, 1)$  when  $x$  accounts for a “grayscale” arrangement of material and void in respective proportions  $h(x)$  and  $(1 - h(x))$ .

As usual, the considered structure is assumed to be clamped on a region  $\Gamma_D \subset \partial D$ , submitted to forces  $f : D \rightarrow \mathbb{R}^d$  and surface loads  $g : \Gamma_N \rightarrow \mathbb{R}^d$ , applied on a region  $\Gamma_N \subset \partial D$  disjoint from  $\Gamma_D$ ; its elastic displacement  $u_h \in H_{\Gamma_D}^1(D)^d$  is characterized by the following counterpart of the linear elasticity system (Elas):

$$(1.4.4) \quad \begin{cases} -\operatorname{div}(A(h)e(u_h)) = f & \text{in } D, \\ u_h = 0 & \text{on } \Gamma_D, \\ A(h)e(u_h)n = g & \text{on } \Gamma_N, \\ A(h)e(u_h)n = 0 & \text{on } \partial D \setminus (\overline{\Gamma_D} \cup \overline{\Gamma_N}). \end{cases}$$

Here, the material law  $A(h)$  is meant to endow the “grayscale” region where  $h(x) \in (0, 1)$  with physical properties; it satisfies:

$$A(t) = \eta A \text{ if } t \leq 0 \text{ and } A(t) = A \text{ if } t \geq 1,$$

where  $A$  is the Hooke’s law of the reference material and  $\eta \ll 1$  is a “small” ersatz parameter, so that the soft material  $\eta A$  mimicks void, see Section 1.2.1.3. In the seminal contribution [69], this function  $A(h)$  was inspired by the homogenization theory (see e.g. [16]): it was constructed by selecting one microstructure pattern parametrized by the local density  $h$ , calculating the homogenized tensor  $A(h_i)$  for a few values  $h_i$ ,  $i = 1, \dots, N$ , and interpolating the mapping  $h \mapsto A(h)$  from these data, see Fig. 1.4.4.

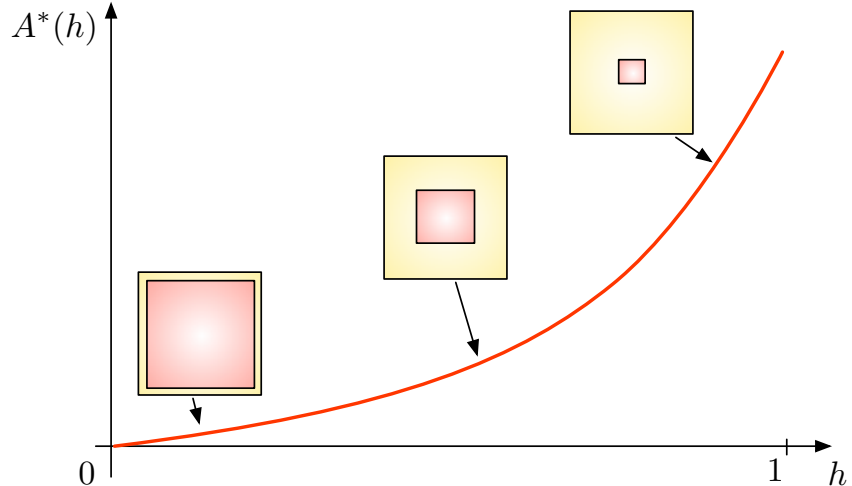


FIGURE 1.4.4. *Material law  $h \mapsto A(h)$  obtained by parametrizing a microstructure with the local volume fraction, and reconstructing a continuous function from a few samples  $A(h_i)$ .*

Soon after, the common practice evolved into using an interpolation profile  $\zeta \in \mathcal{C}^\infty(\mathbb{R})$  satisfying the properties

$$\zeta(t) \in [0, 1], \quad \zeta(t) = \eta \text{ if } t \leq 0, \text{ and } \zeta(t) = 1 \text{ if } t \geq 1,$$

to define the material law

$$(1.4.5) \quad A(h) = \zeta(h)A.$$

A common choice about  $\zeta$  is the so-called SIMP law (Solid Isotropic Material with Penalization), defined by:

$$\zeta(t) = \eta + t^3(1 - \eta), \quad t \in [0, 1],$$

but multiple possibilities are available beyond this one.

With this replacement, it is simple to devise density-based counterparts for the objective and constraint functions of the design presented in [Section 1.2.3](#), as well as for the optimal design problems in there. The resulting, density-based topology optimization problems fall into the framework of parametric optimization, or optimal control problems, as the design variable  $h \in L^\infty(D, [0, 1])$  belongs to a fixed functional space. It can be treated by a standard use of the adjoint method presented in [Section 1.3.3.6](#).

Without entering into details, let us eventually mention the important technical feature of filtering in density-based topology optimization [90, 96]. Often, the design variable  $h \in L^\infty(D, [0, 1])$  is involved in the material law via a filtered version: [\(1.4.5\)](#) is replaced with

$$A(h) = \zeta(L_\varepsilon h)A,$$

where  $L_\varepsilon$  is an operator acting on density functions which is meant to impose a desired effect on  $h$ . The most common filter is of the form

$$L_\varepsilon h = \chi_\varepsilon * h, \text{ where } \chi_\varepsilon \text{ is a smooth convolution kernel.}$$

This practice imposes a length-scale on the spatial variations of the density  $h$ ; it helps to remedy the non existence of optimal designs and to deal with numerical artifacts, such as checkerboards. Other examples of filters include so-called morphology filters, imposing minimum and maximum thickness constraints, see [360].

Open-source implementations of such topology optimization methods are proposed in the articles [47, 336], see also [Figs. 1.4.5](#) and [1.4.6](#) for a numerical example treated with this method.

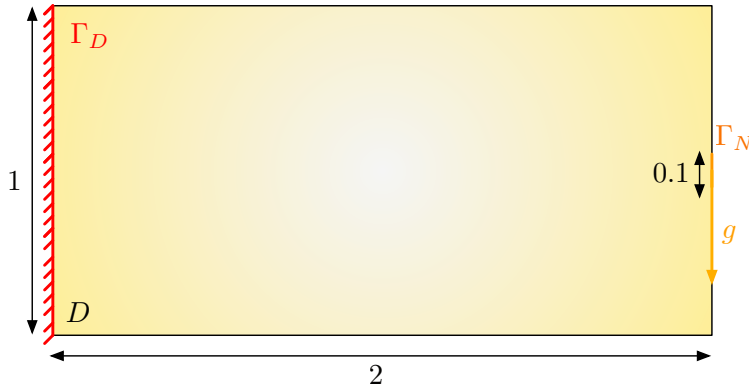


FIGURE 1.4.5. *Setting of the 2d cantilever example, as considered in [Section 1.4.5](#): the structure is clamped on the left-hand side  $\Gamma_D$  of  $\partial D$ , and a unit vertical load  $g = (0, -1)$  is applied on a region  $\Gamma_N$  in the middle of the right-hand side of  $\partial D$ . The density-based version of the compliance  $C(h) = \int_D A(h)e(u_h) : e(u_h) \, dx$  is minimized under a constraint on the volume  $\text{Vol}(h) = \int_D h \, dx$ .*

This framework is appealing for multiple reasons:

- It is relatively simple to implement, as the optimal design problem boils down to the parametric optimization of a function defined on a fixed mesh of the computational domain  $D$ .
- It is less prone to fall into local minima when compared to geometric optimization methods.

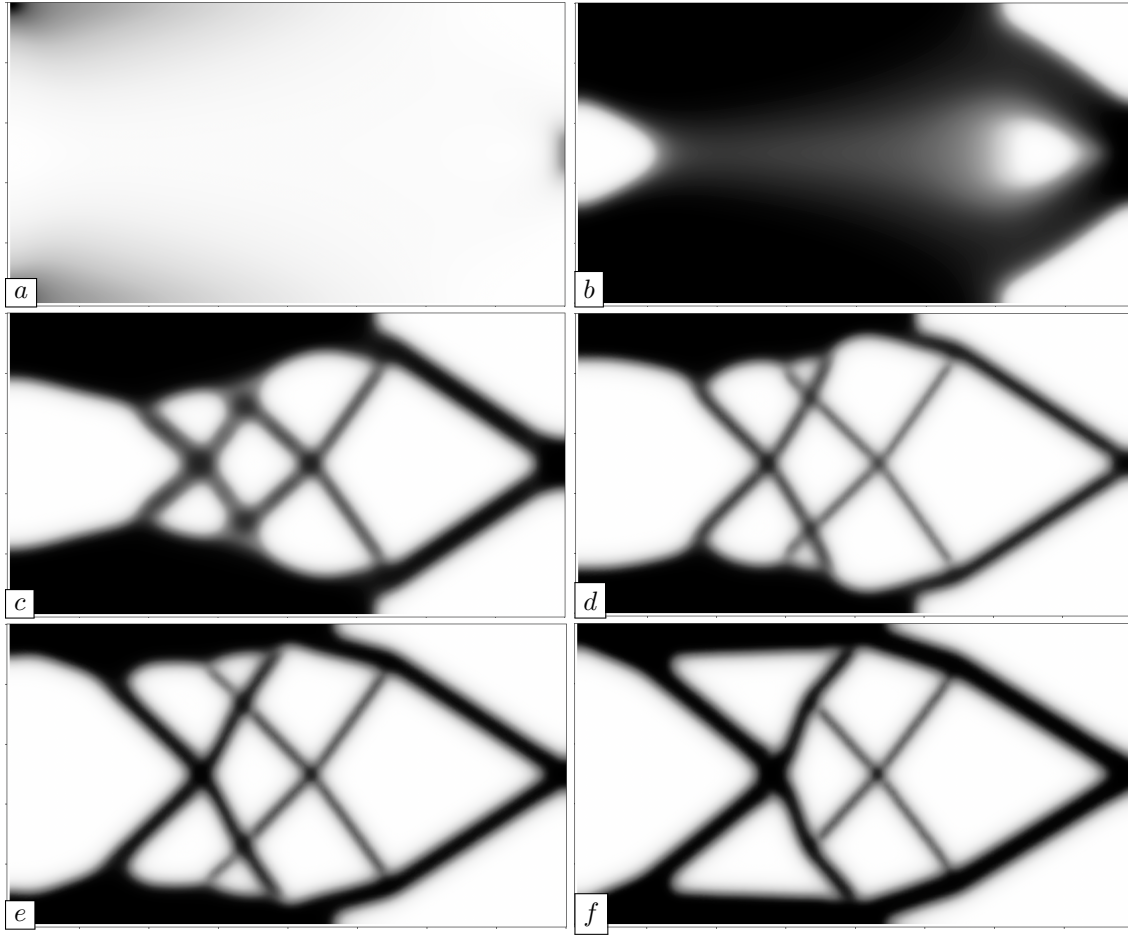


FIGURE 1.4.6. Iterations (a) 0, (b) 25, (c) 50, (d) 75, (e) 100 and (f) 200 in the cantilever test case tackled with the SIMP method of [Section 1.4.5](#) (code available on the webpage of the course [[C1](#)]).

It unfortunately suffers from a significant drawback: as the notion of shape is lost, it may prove difficult to devise density-based counterparts of some objective or constraint functionals, for instance those involving the geometry of shapes, such as their curvature, thickness, etc. Besides, the adoption of density functions as designs raises the need to approximate the physical equations of the problem. In the context of mechanical structures, the ersatz material method described in [Section 1.2.1.3](#) combined with heuristic material laws of the form [\(1.4.5\)](#) provide relevant results (although some problems may show up in the calculation of eigenmodes, with the appearance of so-called parasitic “ghost modes”, localized in the ersatz material), but similar approximations may prove more difficult to construct in challenging physical contexts, such as that of fluid-structure interaction.

#### 1.4.6. The level set method for shape optimization

This section deals with shape and topology optimization frameworks leveraging the level set method – a general paradigm in numerical simulation which allows for a robust “black-and-white” description of the shape and of its evolution, leveraging an implicit representation. We first give a general presentation of this method in [Section 1.4.6.1](#), before specializing to the shape optimization context in [Section 1.4.6.2](#).

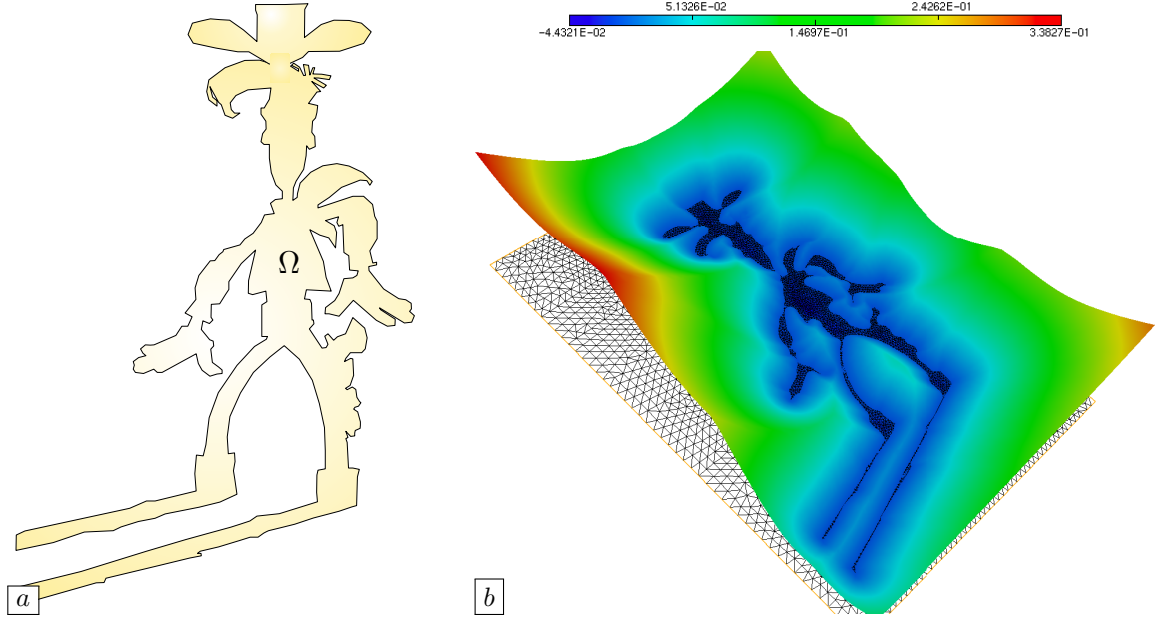


FIGURE 1.4.7. (a) One 2d domain; (b) Graph of an associated level set function  $\phi$ .

#### 1.4.6.1. The level set method for tracking the evolution of a domain

The level set method was introduced in the seminal article [292] as a means to track the motion of a domain evolving according to its mean curvature. It rapidly became a key numerical method for the robust description of the evolution of a front, in a wide variety of contexts. We refer for instance to [333, 291] about the main theoretical and numerical aspects of the method, and to the recent review chapter [326] for some of its recent extensions.

The level set method hinges on an implicit representation of a shape  $\Omega$  contained in a fixed computational domain  $D$ , as the negative subdomain of a scalar, “level set” function  $\phi : D \rightarrow \mathbb{R}$  satisfying the following properties:

$$(LS) \quad \forall x \in D, \quad \begin{cases} \phi(x) < 0 & \text{if } x \in \Omega, \\ \phi(x) = 0 & \text{if } x \in \partial\Omega, \\ \phi(x) > 0 & \text{if } x \in D \setminus \overline{\Omega}, \end{cases}$$

see Fig. 1.4.7.

Formally, the motion of a (smooth) shape  $\Omega(t) \subset D$  over a time period  $(0, T)$ , according to a velocity field  $V(t, \cdot) : D \rightarrow \mathbb{R}^d$ , translates in terms of an associated level set function  $\phi(t, \cdot)$  (i.e. (LS) holds at each  $t \in [0, T]$ ) as the following advection-like equation:

$$(LS\text{-adv}) \quad \frac{\partial \phi}{\partial t}(t, x) + V(t, x) \cdot \nabla \phi(t, x) = 0, \quad \text{for } (t, x) \in (0, T) \times D.$$

In the particular case where the velocity field is consistently oriented along the normal vector to  $\Omega(t)$ , that is

$$V(t, x) = v(t, x)n_t(x),$$

where  $v(t, x)$  is a (smooth) scalar field and

$$(1.4.6) \quad n_t(x) = \frac{\nabla \phi(t, x)}{|\nabla \phi(t, x)|}$$

is the unit normal vector to  $\partial\Omega(t)$  pointing outward  $\Omega(t)$ , the above equation rewrites as a Hamilton-Jacobi-like equation:

$$(LS-HJ) \quad \frac{\partial\phi}{\partial t}(t, x) + v(t, x)|\nabla\phi(t, x)| = 0, \quad \text{for } (t, x) \in (0, T) \times D.$$

We refer to [28, 192] for the rigorous derivation of these equations, and notably as regards their mathematical setting and physical meaning in the inevitable situation where  $\phi$  or  $V$  are not “smooth enough”.

Note that, strictly speaking, (LS-adv) is not a true advection equation as the vector field  $V(t, x)$  generally depends on  $\Omega(t)$ , thus on  $\phi(t, x)$  itself, in a very complex manner. For instance,  $V(t, x)$  may involve physical quantities attached to  $\Omega(t)$ , which are solutions to boundary value problems posed on the latter. The numerical treatment of (LS-adv) is then achieved by discretizing the time period  $(0, T)$  into a collection of “small” subintervals of the form  $(t^n, t^{n+1})$ , over which  $V(t, x)$  can be frozen in time as

$$\forall t \in (t^n, t^{n+1}), \quad V(t, x) \approx V(t^n, x),$$

so that (LS-adv) is approximated by a series of “true” advection equations, with known, stationary vector fields  $V(t^n, x)$ .

**Remark 1.4.2** *Since the evolving domain  $\Omega(t)$  is never discretized explicitly (i.e. with a mesh) in the framework of the level set method, a number of operations where it is involved are a priori difficult to realize, such as the calculation of integrals on  $\Omega(t)$ ,  $\partial\Omega(t)$ , etc. Fortunately, several numerical recipes are available to conduct these tasks with a reasonable accuracy, see [333, 291].*

**Remark 1.4.3** *The theory of the level set method is independent of the choice of a level set function for the initial domain  $\Omega = \Omega(0)$ . In practice the considered level set function  $\phi$  for  $\Omega$  is often chosen to be the signed distance function  $d_\Omega$  to  $\Omega$ , defined by*

$$(SDF) \quad d_\Omega(x) = \begin{cases} -d(x, \partial\Omega) & \text{if } x \in \Omega, \\ 0 & \text{if } x \in \partial\Omega, \\ d(x, \partial\Omega) & \text{otherwise,} \end{cases}$$

where  $d(x, \partial\Omega) = \min_{p \in \partial\Omega} |x - p|$  is the Euclidean distance function to  $\partial\Omega$ .

This choice bestows stability on the numerical practice of the level set method, as it satisfies the so-called Eikonal property:

$$(1.4.7) \quad |\nabla d_\Omega(x)| = 1 \text{ for a.e. } x \in \mathbb{R}^d.$$

Grossly speaking,  $d_\Omega$  is a good trade-off between a “too steep” level set function which causes artifacts in the detection of the boundary  $\partial\Omega$ , and a “too flat” one, making the evaluation of formulas such as (1.4.6) unstable. Unfortunately, even though the initial datum  $\phi(0, \cdot)$  is chosen as the signed distance function to  $\Omega(0)$ ,  $\phi(t, \cdot)$  rapidly loses the desirable properties of such functions – in particular, (1.4.7) ceases to hold. A common practice in the implementation of the level set method consists in redistancing: the iterative resolution process of (LS-adv) is periodically interrupted, and the level set function is restored to be a signed distance function, see [127] about these details.

In a nutshell, the level set method conveniently allows to encode the difficult evolution problem of  $\Omega$  into a partial differential equation posed in a fixed computational domain  $D$ . The numerical practice of the level set method thus relies on two fundamental operations: the calculation of the signed distance function to a shape  $\Omega \subset D$  and the resolution of the level set evolution equation (LS-adv) or (LS-HJ). Various algorithms are available to these ends, depending on the nature of the computational support of  $D$ . We shall present in Sections 1.4.7.1 and 1.4.7.2 below some numerical methods adapted to the case of a simplicial mesh.

#### 1.4.6.2. The level set method for shape and topology optimization

The use of the level set method in optimal design was proposed in [332, 293] as a robust means to capture the evolution of the shape; it was later made more systematic in the seminal references [24, 25, 362].

To set ideas, let us once again use the structural optimization setting of Section 1.2.3. A large computational domain  $D \subset \mathbb{R}^d$  is introduced, which contains all the shapes  $\Omega$  of interest. Usually, for practical

convenience, the non optimizable regions  $\Gamma_D$  and  $\Gamma_N$  of  $\partial\Omega$  bearing homogeneous Dirichlet and inhomogeneous Neumann boundary conditions are chosen as subsets of  $\partial D$ .

The domain  $D$  is equipped with a fixed mesh  $\mathcal{T}$ , for instance a Cartesian grid or a simplicial mesh. Each shape  $\Omega \subset D$  is represented by means of an associated level set function  $\phi : D \rightarrow \mathbb{R}$  (i.e. (LS) holds), which is in practice discretized at the vertices of  $D$  and interpolated from these data (i.e. in a piecewise linear fashion) when its values are needed at other points  $x \in D$ .

The difficult task in this framework lies in the solution of boundary value problems such as that (Elas) for the elastic displacement  $u_\Omega$  (Step 1 in [Algorithm 1](#)), since the shape  $\Omega$  is not equipped with a mesh. To circumvent this drawback, one typically uses the ersatz material method, presented in [Section 1.2.1.3](#): since the only region  $\Gamma$  of  $\partial\Omega$  which is subject to optimization bears homogeneous Neumann boundary conditions,  $u_\Omega$  can be approximated by the solution  $u_{\Omega,\eta}$  to the following problem, posed on  $D$  as a whole:

$$(1.4.8) \quad \begin{cases} -\operatorname{div}(A_{\Omega,\eta}e(u_{\Omega,\eta})) = f & \text{in } D, \\ u_{\Omega,\eta} = 0 & \text{on } \Gamma_D, \\ A_{\Omega,\eta}e(u_{\Omega,\eta})n = g & \text{on } \Gamma_N, \\ A_{\Omega,\eta}e(u_{\Omega,\eta})n = 0 & \text{on } \partial D \setminus (\overline{\Gamma_D} \cup \overline{\Gamma_N}), \end{cases} \quad \text{where } A_{\Omega,\eta}(x) = \begin{cases} A & \text{if } x \in \Omega, \\ \eta A & \text{otherwise,} \end{cases}$$

where the void  $D \setminus \overline{\Omega}$  is filled by a “very soft” material, with Hooke’s law  $\eta A$ ,  $\eta \ll 1$ . This problem can be solved on the fixed mesh  $\mathcal{T}$  of  $D$  by approximating the tensor  $A_{\Omega,\eta}$  from the values of  $\phi$ , see [Remark 1.4.2](#).

After this first step of [Algorithm 1](#), the calculation of a descent direction  $\theta^n$  for the optimization problem at hand (Step 2) and the evolution of  $\Omega^n$  according to  $\theta^n$  (Step 3) can be conducted efficiently in the framework of the level set method, see [Section 1.4.6.1](#) and the numerical algorithms presented in [Section 1.4.7](#).

This procedure is summarized in [Algorithm 2](#) and a numerical example is presented in [Fig. 1.4.8](#), dealing with the same physical situation as that in [Section 1.4.5](#).

---

**Algorithm 2** The level set method for shape and topology optimization.

---

**Initialization:**

- Mesh  $\mathcal{T}$  of the computational domain  $D$ ;
- Level set function  $\phi^0 : D \rightarrow \mathbb{R}$  representing the initial shape  $\Omega^0$ .

**for**  $n = 0, \dots$ , until convergence **do**

- (1) Calculate an approximate version of the elastic displacement  $u_{\Omega^n}$  and of the adjoint state  $p_{\Omega^n}$  on  $\mathcal{T}$  by solving the ersatz material problem (1.4.8).
- (2) From the theoretical formulas for the shape derivatives  $J'(\Omega)(\theta)$ ,  $G'(\Omega)(\theta)$  and  $H'(\Omega)(\theta)$ , infer a descent direction  $\theta^n : D \rightarrow \mathbb{R}^d$  for  $(\mathcal{P})$  according to the selected constrained optimization algorithm.
- (3) Solve the level set advection equation (LS-adv) on  $\mathcal{T}$  with (time-independent) velocity  $V(t, x) = \theta^n(x)$ , initial datum  $\phi_0 = \phi^n$  and final time  $T = \tau^n$ ; a level set function  $\phi^{n+1}$  for the new shape  $\Omega^{n+1}$  is obtained.

**end for**

**return** Level set function  $\phi^n$  for the optimized design  $\Omega^n$ .

---

**Remark 1.4.4** It may seem surprising that the shape change topology in the course of the optimization process depicted on [Fig. 1.4.8](#). Indeed, as we have seen in [Section 1.3.3.1](#), the updated versions  $\Omega^{n+1} = (\operatorname{Id} + \tau^n \theta^n)(\Omega^n)$  of  $\Omega^n$  with  $\tau^n \|\theta^n\|_{W^{1,\infty}(\mathbb{R}^d, \mathbb{R}^d)} < 1$  are homeomorphic to  $\Omega^n$ , and in particular, share the same topology. As a matter of fact, when the step  $\tau^n$  is “too large”,  $\tau^n \theta^n$  may have norm larger than 1, thus violating the rigorous setting of Hadamard’s method.

In practice, this abuse does not pose much problem, as it is systematically verified that  $\Omega^{n+1}$  is “better” than  $\Omega^n$  in view of  $(\mathcal{P})$ ; the time step  $\tau^n$  is then reduced when this fails to be the case. The fact that, often, such updates involving topological changes lead to improvements of the shape suggests that shape derivatives do contain information of a “topological nature”, see [Section 4.2](#) for investigations in this direction.

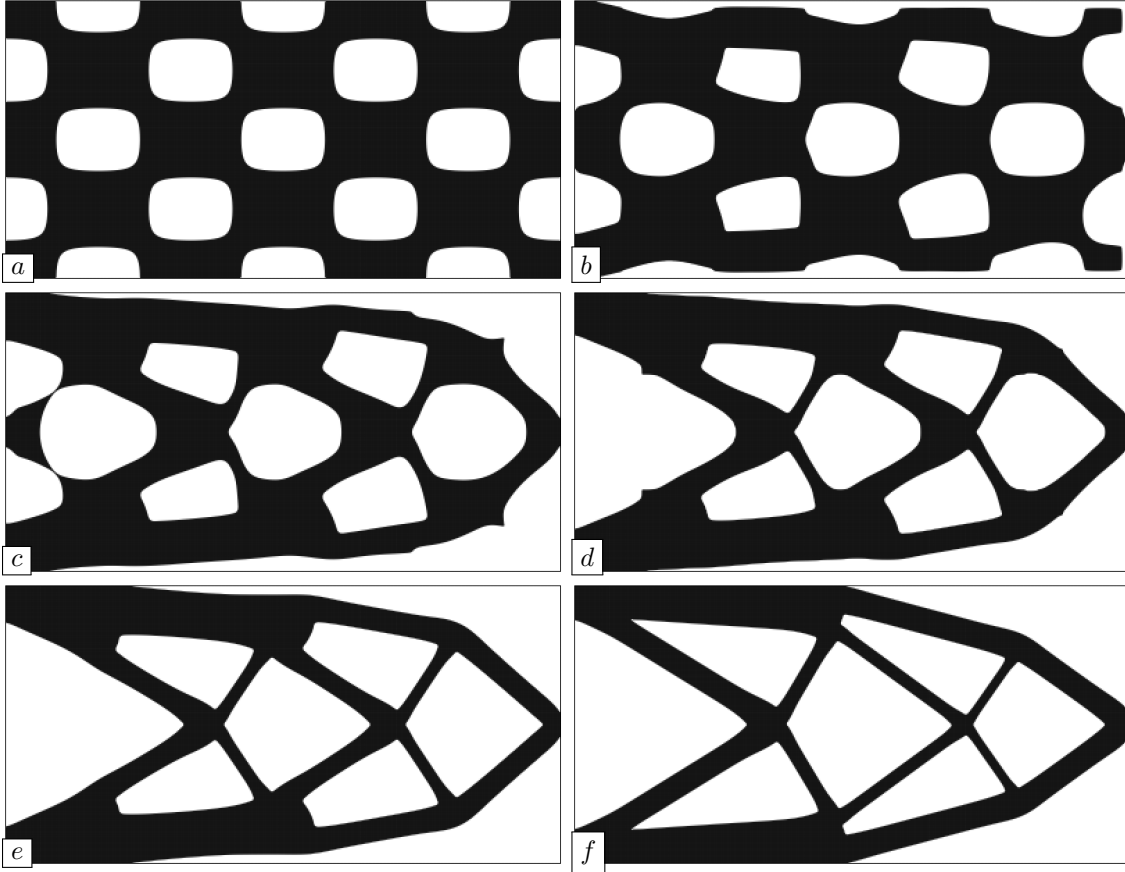


FIGURE 1.4.8. Iterations (a) 0, (b) 5, (c) 10, (d) 15, (e) 25 and (f) 200 in the cantilever shape optimization test case tackled with the level set method in [Section 1.4.6.2](#).

Summarizing, the level set method is a robust strategy for shape and topology optimization, which allows to account for arbitrarily large deformations of the shape. One drawback is that it does not feature an explicit discretization of the optimized shape, so that approximations of the state and adjoint equations for  $u_\Omega$  and  $p_\Omega$  are needed. In the next section, we present a variant of this method which remedies this difficulty.

#### 1.4.7. The level set based mesh evolution method

In this section, we present a variant of the level set method for shape and topology optimization which still benefits from its robust description of the motion of the shape, but also enjoys accurate mechanical computations, performed on a meshed representation of the latter. This method was first implemented in the physical context of elastic structures [A37, A36, A32]; its range was then extended to various physical contexts in the articles [A20, A11, A8], which will be presented in the later [Chapter 5](#). We also refer to [A3] for a review of the subject, which is accompanied with a tutorial and an open-source educative code [S1]. Let us finally mention that similar strategies, based on some of the numerical tools described in the next [Sections 1.4.7.1](#) to [1.4.7.3](#) have been used in [159, 235, 236, 278] in the contexts of fracture mechanics, reaction-diffusion phenomena, etc.

The salient feature of this level set based mesh evolution method is that, at each stage  $n$  of the optimization process, the computational domain  $D$  is equipped with a (valid, conforming) simplicial mesh  $\mathcal{T}^n$  in which the shape  $\Omega^n$  and its complement  $D \setminus \overline{\Omega^n}$  are explicitly discretized, as submeshes  $\mathcal{T}_{\text{int}}^n$ ,  $\mathcal{T}_{\text{ext}}^n$ , see [Fig. 1.4.9](#) (a). Hence, two complementary representations of  $\Omega^n$  are available:

- On the one hand,  $\Omega^n$  is meshed exactly, by the submesh  $\mathcal{T}_{\text{int}}^n$  of  $\mathcal{T}^n$ , which allows to carry out accurate mechanical calculations.
- On the other hand,  $\Omega^n$  is known as the negative subdomain of a level set function  $\phi^n : D \rightarrow \mathbb{R}$ , discretized at the vertices of the total mesh  $\mathcal{T}^n$  of  $D$ . This allows for a robust description of the motion of  $\Omega^n$  by means of the level set method.

The cornerstone of this method is a set of numerical algorithms allowing to pass from one representation to the other whenever needed.

This level set based mesh evolution method is sketched in [Algorithm 3](#) and its main stages are illustrated on [Fig. 1.4.9](#). The next sections provide a little more details about the main operations of this framework: in [Section 1.4.7.1](#), we discuss the calculation of the signed distance function to the shape. Then, in [Section 1.4.7.2](#), we outline the resolution of the level set evolution equation [\(LS-adv\)](#) in the context where the mesh of the computational domain is simplicial. Finally, in [Section 1.4.7.3](#), we overview the meshing operations involved in the passage from a level set to a meshed representation of shapes.

---

**Algorithm 3** The level set based mesh evolution method.

---

**Initialization:** Mesh  $\mathcal{T}^0$  of the computational domain  $D$ , enclosing a mesh  $\mathcal{T}_{\text{int}}^0$  of  $\Omega^0$  as a submesh.  
**for**  $n = 0, \dots$ , until convergence **do**

- (1) Calculate the signed distance function  $\phi^n = d_{\Omega^n}$  to  $\Omega^n$  at the vertices of  $\mathcal{T}^n$ .
- (2) Calculate the displacement  $u_{\Omega^n}$  (and the adjoint state  $p_{\Omega^n}$ ) by solving the corresponding boundary value problem [\(Elas\)](#) on the interior part  $\mathcal{T}_{\text{int}}^n$  of  $\mathcal{T}^n$ .
- (3) Infer a descent direction  $\theta^n$  on  $\mathcal{T}^n$  for [\(P\)](#) thanks to a constrained optimization algorithm.
- (4) Choose a small enough time step  $\tau^n$  and calculate a level set function  $\tilde{\phi}^{n+1}$  for the new shape  $\Omega^{n+1} := (\text{Id} + \tau^n \theta^n)(\Omega^n)$  on the mesh  $\mathcal{T}^n$  by solving the level set evolution equation [\(LS-adv\)](#) over  $(0, \tau^n)$  with velocity field  $V(t, x) = \theta^n(x)$  and initial condition  $\phi_0 = \phi^n$ .
- (5) Create a new mesh  $\mathcal{T}^{n+1}$  of  $D$  where  $\Omega^{n+1}$  is explicitly discretized, from the datum of the level set function  $\tilde{\phi}^{n+1}$  on  $\mathcal{T}^n$ .

**end for**  
**return** Mesh  $\mathcal{T}^n$  of  $D$  where  $\Omega^n$  is discretized as a submesh  $\mathcal{T}_{\text{int}}^n$ .

---

#### 1.4.7.1. Calculating the signed distance function to a discrete contour

This section deals with the first step of each iteration  $n$  of [Algorithm 3](#), the reference to which is omitted for notational simplicity: one aims to construct one particular level set function  $\phi$  for a shape  $\Omega \subset D$ , namely the signed distance function  $d_{\Omega}$  in [\(SDF\)](#), out of a meshed representation of the latter (Step (1) in [Algorithm 3](#)), see the discussion in [Remark 1.4.3](#).

Let the computational domain  $D$  be endowed with a simplicial mesh  $\mathcal{T}$  and let  $\Omega \subset D$  be a shape; we wish to calculate the quantity  $\phi(x) = d_{\Omega}(x)$  at all vertices  $x \in \mathcal{T}$ . Note that in the workflow of [Algorithm 3](#),  $\Omega$  is supplied as an explicit submesh  $\mathcal{T}_{\text{int}}$  of  $\mathcal{T}$ , but for the purpose of this section, it could actually be given under a different format, for instance via a mesh  $\mathcal{T}_{\Omega}$  of its own right which is not a submesh of  $\mathcal{T}$ .

The numerical calculation of  $d_{\Omega}$  can be conducted in a variety of manners. “Geometric” algorithms involve an exhaustive calculation of the distance  $d(x, \partial\Omega)$  from  $x$  to  $\partial\Omega$  at every vertex  $x$  of  $\mathcal{T}$ . Although this operation can be made efficient owing to a number of heuristics – see e.g. [\[255, 357\]](#) and the references therein – we rather rely on a method in the class of “propagation algorithms”, which comprise two steps:

- (1) The function  $\phi$  is initialized with (an approximation of) the exact value of  $d_{\Omega}$  at the vertices of  $\mathcal{T}$  which are “close” to  $\partial\Omega$  (for instance, at the vertices of the simplices  $T \in \mathcal{T}$  intersecting  $\partial\Omega$ ), and with large, positive or negative values elsewhere. This stage is elementary; however, depending on the input format and of the complexity of the geometry of  $\Omega$ , it may prove tedious from the implementation viewpoint, and time-consuming in practice, see e.g. [\[148\]](#).
- (2) The calculation of the signed distance  $\phi(x) = d_{\Omega}(x)$  is realized from the vertices  $x \in \mathcal{T}$  closest to  $\partial\Omega$  to farther ones, by relying on a discretization of the Eikonal equation [\(1.4.7\)](#). This purpose

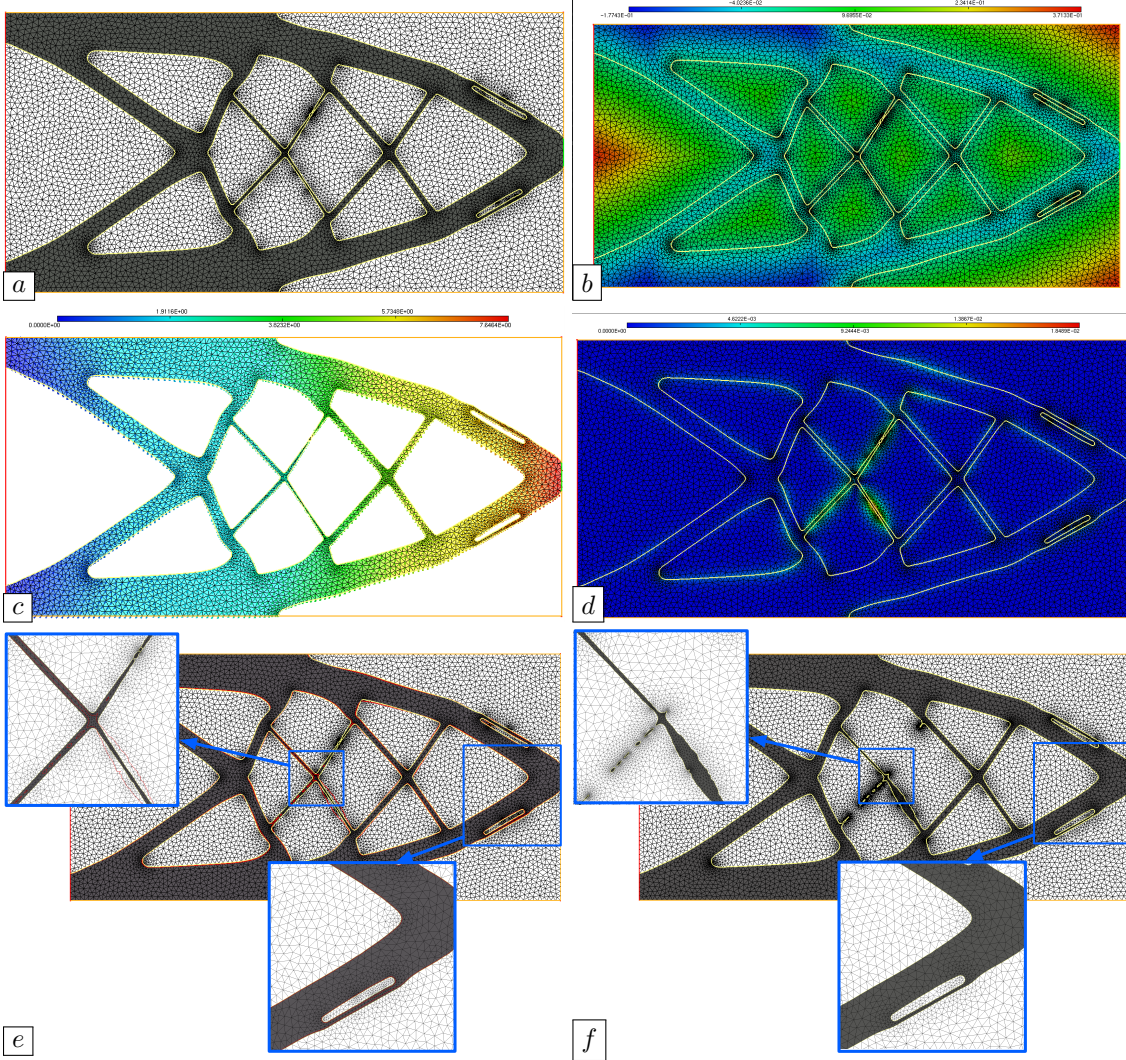


FIGURE 1.4.9. Illustration of the main stages of the mesh evolution method sketched in Section 1.4.7. (a) Mesh  $\mathcal{T}^n$  of the computational domain  $D$ ; the submesh  $\mathcal{T}_{\text{int}}^n$  of  $\Omega^n$  consists of the black elements, and that  $\mathcal{T}_{\text{ext}}^n$  of  $D \setminus \overline{\Omega^n}$  is made of the white elements; (b) isovales of the signed distance function  $\phi^n$  to  $\Omega^n$ , calculated on  $\mathcal{T}^n$ ; (c) solution  $u_{\Omega^n}$  to the elasticity system on the mesh  $\mathcal{T}_{\text{int}}^n$  of  $\Omega^n$ ; (d) descent direction  $\theta^n$  on the whole mesh  $\mathcal{T}^n$ ; (e) level set function  $\tilde{\phi}^{n+1}$  on the mesh  $\mathcal{T}^n$ ; the 0 level set of  $\tilde{\phi}^{n+1}$  is depicted in red; (f) new mesh  $\mathcal{T}^{n+1}$  with the new shape  $\Omega^{n+1}$  enclosed as the submesh  $\mathcal{T}_{\text{int}}^{n+1}$  (made of the black elements).

is greatly simplified when the computational mesh  $\mathcal{T}$  is a Cartesian grid, since high-order finite difference schemes are available.

The most popular algorithm in this second category is certainly the fast marching method, see [331] for an overview and [215] for an adaptation to the case where the computational mesh is simplicial; let us also mention the fast sweeping method [381]. In the previous work [A39], we have proposed an algorithm based on the properties of the so-called redistancing equation, an open-source implementation of which is available in the library `mshdist` [S4].

#### 1.4.7.2. Solving the advection equation

In this section, we turn to the numerical resolution of the equation (LS-adv) accounting for the evolution of the shape.

Let us consider the generic situation, occurring at each iteration  $n$  of the process described in [Algorithm 3](#): a level set function  $\phi = \phi^n : D \rightarrow \mathbb{R}$  accounting for the current shape  $\Omega = \Omega^n$  is supplied via its values at the vertices of a simplicial mesh  $\mathcal{T} = \mathcal{T}^n$  of the computational domain  $D$ . Analogously, the velocity field  $V : D \rightarrow \mathbb{R}^d$  driving the evolution of the shape, which is the descent direction  $\theta^n$  at the current iteration, is supplied at the vertices of  $\mathcal{T}$ . We aim to compute the solution  $\psi(t, x)$  to the following advection equation:

$$(1.4.9) \quad \begin{cases} \frac{\partial \psi}{\partial t}(t, x) + V(x) \cdot \nabla \psi(t, x) = 0 & \text{for } t \in (0, T), \quad x \in D, \\ \psi(0, x) = \phi(x) & \text{for } x \in D, \end{cases}$$

and notably its values  $\psi(T, x)$  at the final time  $t = T$ , which stands for the time step  $\tau^n$ .

Numerical methods for the resolution of (1.4.9) are numerous when the computational support is a Cartesian grid of  $D$ , which allows for the use of high-order finite difference methods. In our context where it is a simplicial mesh, this issue is a little less classical and deserves a few comments.

We rely on the method of characteristics proposed in [302], which is close in spirit to the semi-Lagrangian scheme developed in [346]; see alternatively [172] about the use of discontinuous Galerkin methods, and [4, 61] for the construction of numerical schemes for more general Hamilton-Jacobi equations on simplicial meshes.

The method of characteristics is based on the analytical formula for the solution to (1.4.9). The latter is expressed in terms of the characteristic curves  $t \mapsto X(t, t_0, x)$  of the velocity field  $V(x)$ , emerging from an arbitrary point  $x \in D$  at a time  $t_0$ . Such a function is defined as the solution to the ordinary differential equation:

$$(1.4.10) \quad \begin{cases} \frac{d}{dt} X(t, t_0, x) = V(X(t, t_0, x)) & \text{for } t \in \mathbb{R}, \\ X(t_0, t_0, x) = x. \end{cases}$$

Intuitively,  $t \mapsto X(t, t_0, x)$  is the trajectory of a particle located in  $x$  at time  $t = t_0$ , which is transported according to the velocity field  $V(x)$ . The exact solution to (1.4.9) is then given by:

$$(1.4.11) \quad \forall t \in (0, T), \quad x \in D, \quad \psi(t, x) = \phi(X(0, t, x)),$$

which expresses the natural fact that the value of  $\psi$  at time  $t$  and point  $x$  is the value of the initial datum  $\phi$  at the initial position  $X(0, t, x)$  of the particle lying in  $x$  at time  $t$ .

One simple means to exploit the closed-form formula (1.4.11) is to directly discretize it: for each vertex  $x \in \mathcal{T}$ , the ordinary differential equation (1.4.10) is solved for the “backward” characteristic curve  $t \mapsto X(t, T, x)$ , for instance by a Runge-Kutta 4 scheme;  $\phi$  is then evaluated at the “foot”  $X(0, T, x)$  of this characteristic line. This task requires adequate data structures to efficiently identify the simplices of the mesh  $\mathcal{T}$  containing the discretization points involved in the integration of these characteristic lines.

**Remark 1.4.5** *The origin  $X(0, T, x)$  of the characteristic curve passing through  $x$  at  $t = T$  may lie outside  $D$ . This notably happens when the velocity field  $V(x)$  is pointing inward  $D$  on at least one portion of the boundary  $\partial D$ . In such a case, the information supplied in (1.4.9) is not sufficient to guarantee the well-posedness of this equation (as one would have to add a boundary condition on the “entrant” part of  $\partial D$ ); in numerical practice, it is customary to endow  $\psi(T, x)$  with a consistent value by extrapolating the value of  $\phi$  (and the characteristic curve  $t \mapsto X(t, T, x)$ ) outside  $D$ .*

An open-source implementation of this algorithm is proposed in the `advection` code [S3], based on the article [A38].

#### 1.4.7.3. Explicit discretization of the negative subdomain of a level set function

The last key operation in the realization of [Algorithm 3](#) assumes the data of a simplicial mesh  $\mathcal{T}$  of the computational domain  $D$ , and of the values at its vertices of a level set function  $\phi : D \rightarrow \mathbb{R}$  for a shape  $\Omega \subset D$ . We aim to create a new mesh  $\tilde{\mathcal{T}}$  which is valid, conforming, with high quality, and contains two submeshes  $\tilde{\mathcal{T}}_{\text{int}}$  and  $\tilde{\mathcal{T}}_{\text{ext}}$  of  $\Omega$  and  $D \setminus \overline{\Omega}$ , respectively.

This task can be conducted within two steps, which are illustrated on [Fig. 1.4.10](#).

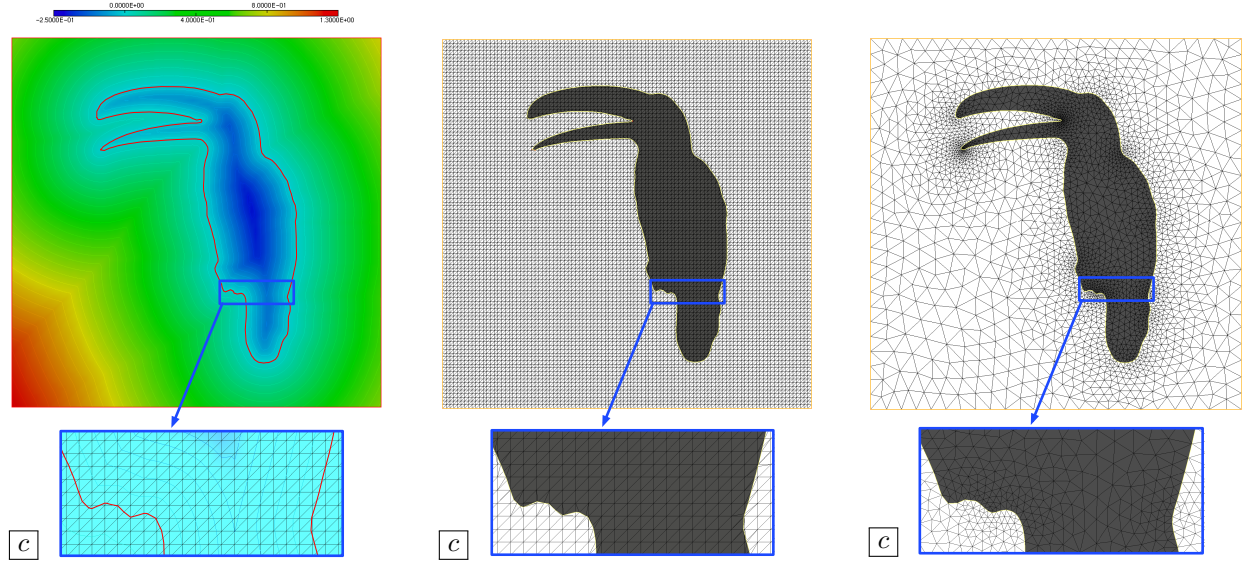


FIGURE 1.4.10. (a) One level set function  $\phi$  is defined at the vertices of the mesh  $\mathcal{T}$  of the square-shaped computational domain  $D$ ; its 0 level set (which is not explicitly discretized in  $\mathcal{T}$ ) is depicted in red; (b) Explicit discretization of the 0 level set of  $\phi$  into the mesh  $\mathcal{T}$ ; the intermediate, low-quality mesh  $\mathcal{T}_{\text{temp}}$  is obtained; (c) High-quality mesh  $\tilde{\mathcal{T}}$  obtained after remeshing  $\mathcal{T}_{\text{temp}}$ .

- (1) The 0 level set  $\partial\Omega = \{x \in D, \phi(x) = 0\}$  of  $\phi$  is identified from the values of  $\phi$  at the vertices of  $\mathcal{T}$ , and it is discretized explicitly into  $\mathcal{T}$ . This stage is simple and relies on the marching tetrahedra algorithm [161], as a variant of the well-known marching cubes algorithm [247]: each simplex  $T \in \mathcal{T}$  crossed by  $\partial\Omega$  is subdivided according to a pattern. This ends up with a valid, conforming mesh  $\mathcal{T}_{\text{temp}}$  of  $D$ , where  $\Omega$  is explicitly discretized, but which generally has very bad quality.
- (2) The valid, conforming, albeit ill-shaped mesh  $\mathcal{T}_{\text{temp}}$  is remeshed into a fine quality mesh  $\tilde{\mathcal{T}}$  of  $D$ , where  $\Omega$  and  $D \setminus \bar{\Omega}$  are explicitly discretized. This task leverages the remeshing methods presented in [Section 1.4.3](#).

This operation is implemented in the open-source `mmg` library [S2].

#### 1.4.7.4. A 3d numerical example: shape optimization of a cantilever

We conclude this presentation of the level set based mesh evolution method with the treatment of the classical 3d cantilever optimization test-case, whose details are depicted on [Fig. 1.4.11](#). The results are reported on [Fig. 1.4.12](#).

The shape visibly undergoes dramatic deformations, including changes of its topology, while it is meshed exactly at each iteration of the process, thus ensuring an accurate solution of relate boundary value problems, such as the state and adjoint equations, which can be accomplished thanks to a finite element solver used in a black-box fashion.

We shall see various illustrations of this level set based mesh evolution strategy in more challenging physical contexts in [Chapter 5](#).

#### 1.4.8. Bringing topological derivatives into play

The method of Hadamard recalled in [Section 1.3.3.1](#) makes it possible to optimize a shape by iterative deformations of its boundary. This practice allows for certain topological changes, up to a slight abuse of the theoretical framework: different parts of  $\partial\Omega$  may collide and merge, see [Remark 1.4.4](#). However, not all topological changes can occur, though. With this description of shapes and their deformations, holes cannot

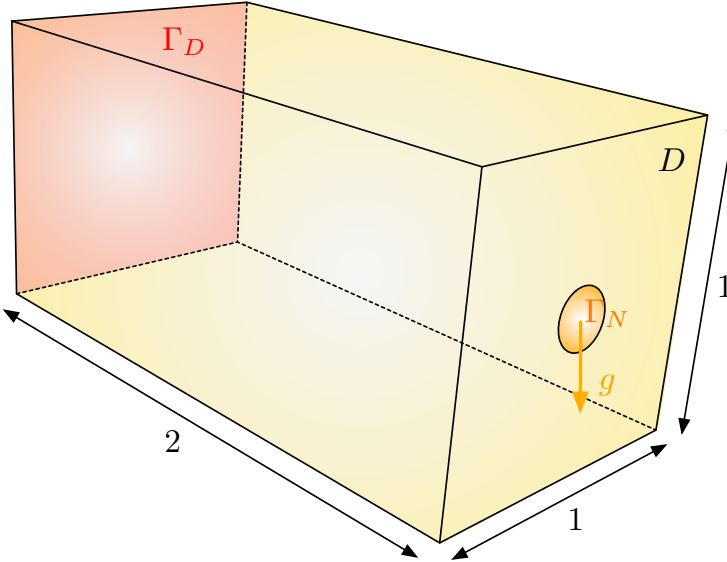


FIGURE 1.4.11. *Setting of the 3d cantilever example, considered in Section 1.4.7.4: the structure is clamped on one face  $\Gamma_D$  of  $\partial D$ , and a unit vertical load  $g = (0, 0, -1)$  is applied on a region  $\Gamma_N$  in the middle of the opposite face. The compliance  $C(\Omega) = \int_{\Omega} Ae(u_{\Omega}) : e(u_{\Omega}) \, dx$  of the shape  $\Omega$  is minimized under a constraint on the volume  $\text{Vol}(\Omega)$ .*

emerge in the bulk of shapes. To allow for such operations, the use of the sensitivity with respect to the emergence of small holes, which is contained in topological derivatives, is pivotal. In this section, we present two different strategies to leverage this information.

#### 1.4.8.1. *A coupling between the Hadamard's method and topological derivatives*

At first, it is natural to combine the independent sensitivities of a functional of the domain encoded in shape and topological derivatives. A simple strategy based on this principle was proposed in [21], which is easily integrated into any shape optimization algorithm based on the level set method, such as [Algorithms 2](#) and [3](#). Briefly, the process featured in there is interrupted (say, every 5 or 10 iterations), and the topological derivative of  $J(\Omega)$  is calculated. A small hole (e.g. of the size of a mesh element) is inserted where it is most negative, or a small percentage of material is removed where the topological derivative is most negative. Then the boundary variation process is resumed.

A numerical example illustrating this strategy is provided in [Fig. 1.4.13](#), in the context of the benchmark 2d bridge test-case, whose specifications are reported on [Fig. 1.4.13](#) (a). Interestingly, although the initial structure  $\Omega^0$  has a very simple topology, multiple holes are created with the help of the information contained in topological derivatives, which then freely evolve, and sometimes disappear, under the effect of the boundary variation method.

**Remark 1.4.6** *In principle, this idea could also be integrated in a classical, mesh-based optimization algorithm, such as that described in Section 1.4.4, but it is typical in this strategy that newly created holes (which are multiple) will tend to merge. This would precipitate the failure of the algorithm, see nevertheless [128].*

#### 1.4.8.2. *A standalone, fixed point algorithm*

The information contained in topological derivatives can be exploited in an alternative, standalone fashion. In this spirit, a topology optimization algorithm leveraging only this type of sensitivity with respect to the domain was proposed in [43] and analyzed in [41].

The rationale of this method is better explained in the two-phase version of the structural optimization setting of [Section 1.2.3](#): a hold-all domain  $D$  is given, and it is made of two phases  $\Omega_1 = \Omega$  and  $\Omega_0 = D \setminus \overline{\Omega}$ ,

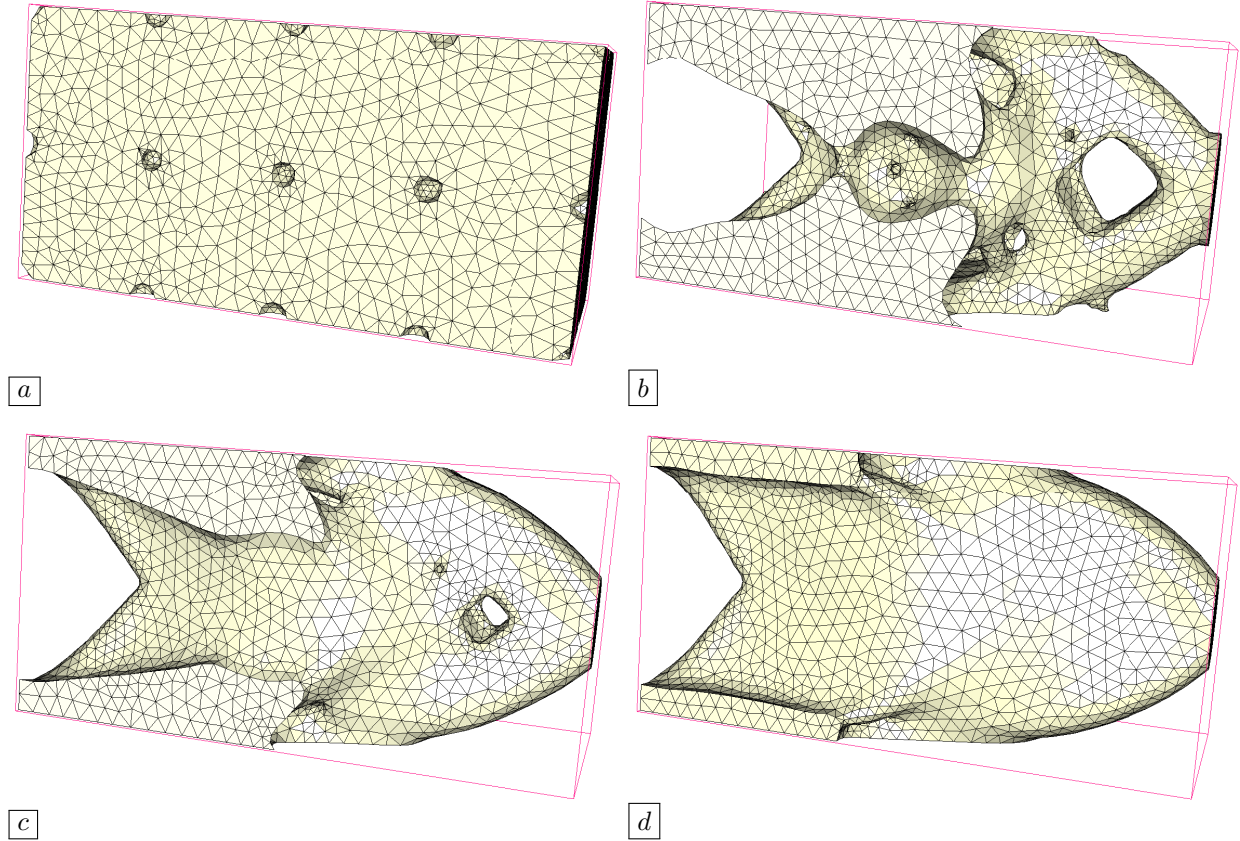


FIGURE 1.4.12. Iterations (a) 0, (b) 50, (c) 120 and (d) 200 (final) of the three-dimensional cantilever example presented in [Section 1.4.7.4](#).

built from a shape  $\Omega \Subset D$ . Each phase  $\Omega_i$  is made of a material with Hooke's tensor  $A_i$ , Young's modulus  $E_i$  and Poisson's ratio  $\nu_i$ . The structure  $D$  is clamped on a region  $\Gamma_D \subset \partial D$ ; body forces  $f \in L^2(D)^d$  are at play and surface loads  $g \in L^2(\Gamma_N)^d$  are applied on a subset  $\Gamma_N$  of  $\partial D$  disjoint from  $\Gamma_D$ .

In this context, the elastic displacement  $u_\Omega \in H_{\Gamma_D}^1(D)^d$  of the total structure  $D$  is the unique solution to the boundary value problem:

$$\begin{cases} -\operatorname{div}(A_\Omega e(u_\Omega)) = f & \text{in } D, \\ u_\Omega = 0 & \text{on } \Gamma_D, \\ A_\Omega e(u_\Omega)n = g & \text{on } \Gamma_N, \\ A_\Omega e(u_\Omega)n = 0 & \text{on } \partial D \setminus (\overline{\Gamma_D} \cup \overline{\Gamma_N}), \end{cases} \quad \text{where } A_\Omega(x) = \begin{cases} A_1 & \text{if } x \in \Omega_1, \\ A_0 & \text{otherwise.} \end{cases}$$

We aim to minimize a weighted sum of the compliance of the structure and the volume of the phase  $\Omega$ , say:

$$(1.4.12) \quad \min_{\Omega} \mathcal{L}(\Omega), \text{ where } \mathcal{L}(\Omega) = C(\Omega) + \ell \operatorname{Vol}(\Omega),$$

and

$$C(\Omega) = \int_D A_\Omega e(u_\Omega) : e(u_\Omega) \, dx = \int_D f \cdot u_\Omega \, dx + \int_{\Gamma_N} g \cdot u_\Omega \, ds.$$

In this two-phase setting, we denote by  $\Omega_{x,r}$  the variation of  $\Omega$  inducing a change of the material properties of  $D$  inside a ball centered at  $x \in D$ , with radius  $r$ , that is:

$$\Omega_{x,r} = \begin{cases} \Omega \setminus \overline{B(x,r)} & \text{if } x \in \Omega_1, \\ \Omega \cup B(x,r) & \text{if } x \in \Omega_0. \end{cases}$$

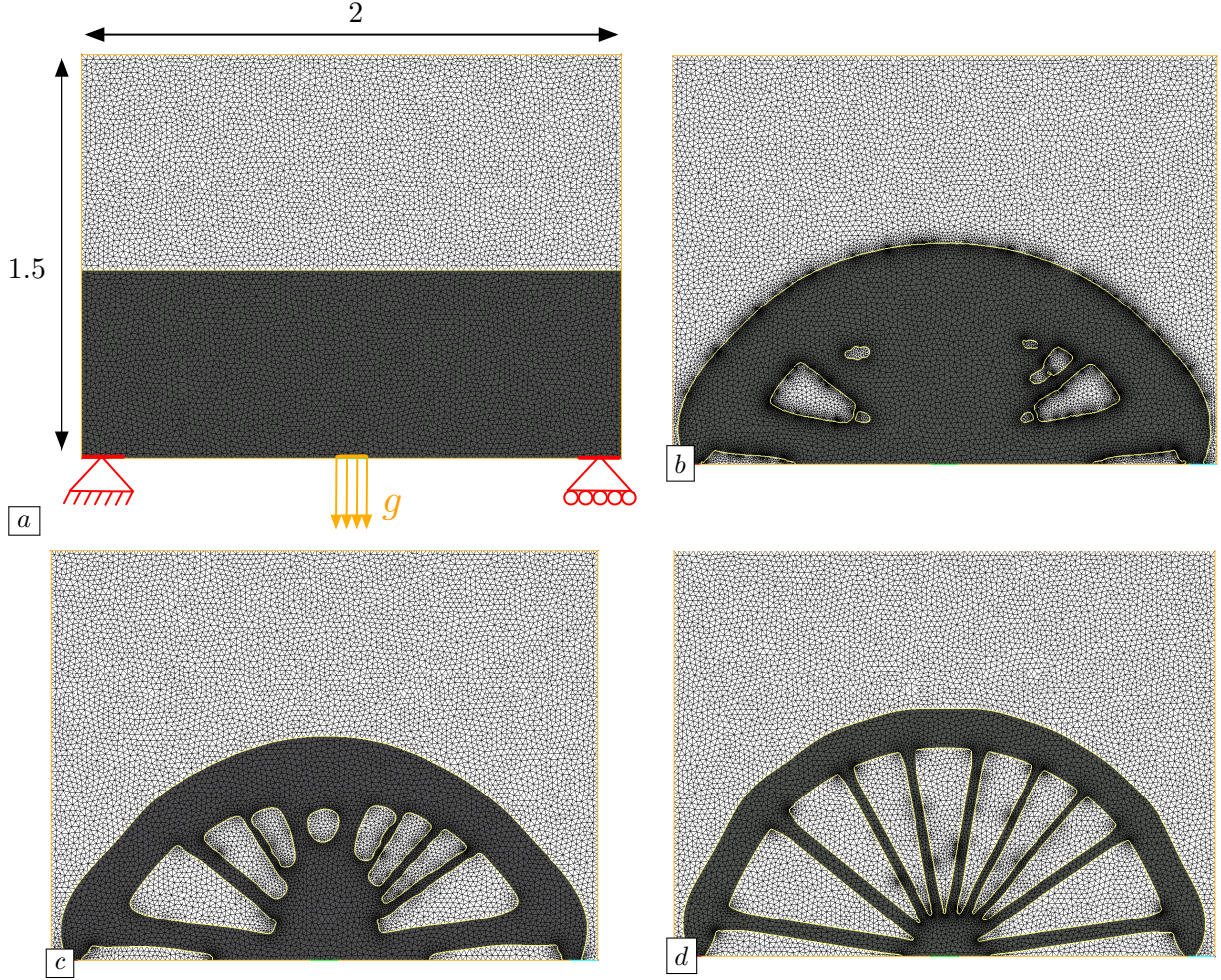


FIGURE 1.4.13. Iterations (a) 0, (b) 26, (c) 40 and (d) 150 of the optimization of the shape of a 2d bridge with the combined use of shape and topological derivatives proposed in Section 1.4.8.1.

We also assume that the topological derivative of the shape functional  $\mathcal{L}(\Omega)$  is available under the following format:

$$(1.4.13) \quad \mathcal{L}(\Omega_{x,r}) = \mathcal{L}(\Omega) + s_\Omega(x)g_\Omega(x)r^d + o(r^d), \text{ where } s_\Omega(x) = \begin{cases} -1 & \text{if } x \in \Omega, \\ 1 & \text{otherwise.} \end{cases}$$

The following two-dimensional result is excerpted from [83, 193]:

**Theorem 1.4.7** *Let the space dimension  $d$  equal 2 and let  $\Omega \Subset D$  be any shape inducing the two phases  $\Omega_1 = \Omega$  and  $\Omega_0 = D \setminus \bar{\Omega}$ . The function  $\mathcal{L}(\Omega)$  in (1.4.12) has then a topological derivative  $g_\Omega^T(x)$  at any point  $x \in \Omega_0 \cup \Omega_1$ , whose expression reads:*

$$g_\Omega^T(x) = s_\Omega(x) \mathbb{P}\sigma(u_\Omega(x)) : e(u_\Omega(x)) + \ell.$$

*In this formula,  $\mathbb{P}$  is the fourth-order Pólya-Szegö polarization tensor, given by:*

$$(1.4.14) \quad \forall e \in \mathbb{R}_{\text{sym}}^{d \times d}, \quad \mathbb{P}e = \frac{1}{\rho_2\rho_3 + \tau_1} \left( (1 + \rho_2)(\tau_1 - \rho_3)e + \frac{1}{2}(\rho_1 - \rho_2) \frac{\rho_3(\rho_3 - 2\tau_3) + \tau_1\tau_2}{\rho_1\rho_3 + \tau_2} \text{tr}(e)I \right),$$

where

$$(1.4.15) \quad \rho_1 = \frac{1+\nu}{1-\nu}, \rho_2 = \frac{3-\nu}{1+\nu}, \rho_3 = \frac{E^*}{E}, \tau_1 = \frac{1+\nu^*}{1+\nu}, \tau_2 = \frac{1-\nu^*}{1-\nu} \quad \text{and} \quad \tau_3 = \frac{\nu^*(3\nu-4)+1}{\nu(3\nu-4)+1},$$

and we have posed:

- If  $x \in \Omega_1$ ,  $E = E_1$ ,  $E^* = E_0$ ,  $\nu = \nu_1$ , and  $\nu^* = \nu_0$ ,
- If  $x \in \Omega_0$ ,  $E = E_0$ ,  $E^* = E_1$ ,  $\nu = \nu_0$ , and  $\nu^* = \nu_1$ .

This expansion allows to express the necessary conditions for a shape  $\Omega$  to be optimal in view of the information supplied by topological derivatives. If such is the case, it must hold that:

- For all  $x \in \Omega_1$ ,  $g_\Omega(x) < 0$ ;
- For all  $x \in \Omega_0$ ,  $g_\Omega(x) > 0$ ,

i.e. the value of  $\mathcal{L}(\Omega)$  is increased (at leading order in the expansion (1.4.13)) if  $\Omega$  is replaced by the perturbation  $\Omega_{x,r}$ .

In order to exploit this information in practice, let us introduce a level set function  $\phi : D \rightarrow \mathbb{R}$  for  $\Omega$ , i.e. (LS) holds. We express the above optimality conditions in terms of  $\phi$ : if  $\Omega$  is a local minimizer of  $\mathcal{L}(\Omega)$ , it holds:

$$\forall x \in \Omega_0 \cup \Omega_1, \quad \begin{cases} \phi(x) < 0 & \Rightarrow g_\Omega(x) < 0, \\ \phi(x) > 0 & \Rightarrow g_\Omega(x) > 0; \end{cases}$$

in other terms,  $g_\Omega$  is one level set function for  $\Omega$ . Since any positive multiple of  $\phi$  is still a level set function for  $\Omega$ , we may without loss of generality impose that  $\|\phi\|_{L^2(D)} = 1$ , and so the necessary optimality conditions for  $\Omega$  can be enforced by requiring that:

$$\Omega = \left\{ x \in D, \phi(x) < 0 \right\}, \quad \text{where } \phi = \frac{1}{\|g_\Omega\|_{L^2(D)}} g_\Omega.$$

We search for a shape  $\Omega \subset D$  satisfying these conditions thanks to a fixed point method with relaxation, adapted to the case where the handled functions have unit norm. Indexing iterations by  $n = 0, \dots$ , we denote with a superscript  $n$  the values of the various quantities at stake at iteration  $n$ , namely  $\phi^n$ ,  $g^n := g_{\Omega^n}$ , etc.; we also let  $\tilde{g}^n := \frac{1}{\|g^n\|_{L^2(D)}} g^n$ . The closed-form expressions of Section 1.A.5 for the linear interpolation between vectors on the unit sphere of a Hilbert space lead to the following formula for the update of  $\phi$ :

$$\phi^{n+1} = \frac{1}{\sin a^n} \left( \sin((1 - \tau^n)a^n) \phi^n + \sin(\tau^n a^n) \tilde{g}^n \right),$$

where  $a^n \in [0, \pi]$  is the angle  $a^n = \arccos((\phi^n, \tilde{g}^n)_{L^2(D)})$  and  $\tau^n \in (0, 1)$  is a time step.

An example of the use of this strategy is provided in Fig. 1.4.14, in the context of the benchmark optimal mast test case, whose details are reported on Fig. 1.4.14 (a). The corresponding code can be downloaded from the webpage of the course [C1].

**Remark 1.4.8** Let us mention yet another use of topological derivatives in optimal design: in the article [101] dealing with inverse problems, the topological derivative is incorporated as a source term in the Hamilton-Jacobi evolution equation. In a similar spirit, a reaction-diffusion equation is used in [373] to update a level set function for the shape, where the diffusion term comes from a perimeter penalization, and the reaction term corresponds to the topological derivative of the objective function. To the best of our knowledge, these two methods are essentially heuristic and it would be interesting to explore their theoretical fundations.

## 1.A TECHNICAL FACTS

In this appendix, we gather a few technical facts which are useful for various purposes in this introduction, and throughout the manuscript.

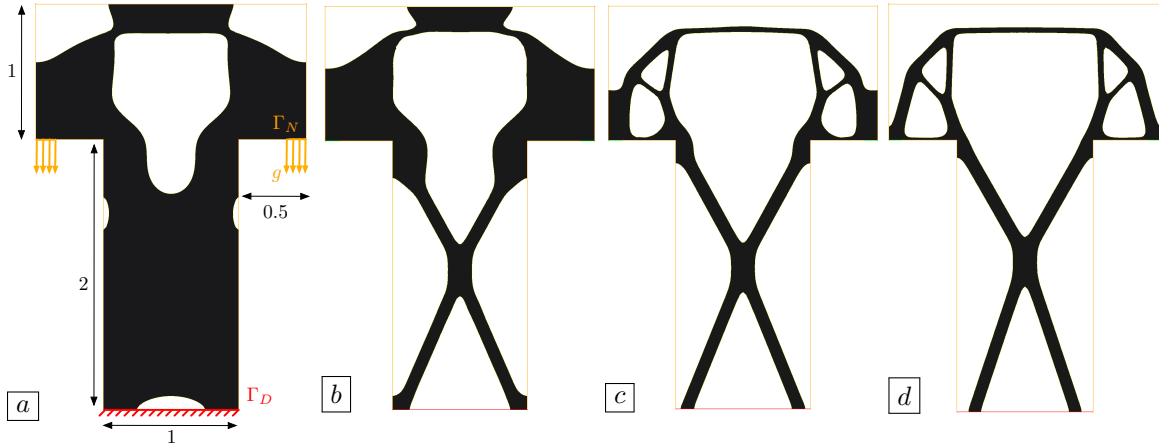


FIGURE 1.4.14. Iterations (a) 1, (b) 10, (c) 50 and (d) 100 of the optimization of the shape of a 2d mast with the fixed point algorithm based on topological derivatives of [Section 1.4.8.2](#).

### 1.A.1. A short reminder of the differential geometry of hypersurfaces

This appendix gathers basic material about the differential geometry of hypersurfaces in  $\mathbb{R}^d$ , and sets some notation used throughout the manuscript; we refer to classical treaties such as e.g. [\[306\]](#) for exhaustive presentations of these concepts.

For simplicity, throughout this section, we restrict ourselves to the case of a closed hypersurface  $\Gamma = \partial\Omega$  which is the boundary of a smooth bounded domain  $\Omega \subset \mathbb{R}^d$ , although most of this material can be extended to the case of a general smooth, oriented hypersurface in  $\mathbb{R}^d$ . We denote by  $n : \Gamma \rightarrow \mathbb{R}^d$  the unit normal vector field to  $\Gamma$ , pointing outward  $\Omega$ .

**Definition 1.A.1** For all  $x \in \Gamma$ , the tangent plane  $T_x\Gamma$  to  $\Gamma$  at  $x$  is the  $(d-1)$  hyperplane with normal vector  $n(x)$ . It is equipped with the inner product induced by that of the ambient space  $\mathbb{R}^d$ , and its elements are called tangent vectors to  $\Gamma$  at  $x$ .

The restriction to tangent planes of the inner product of  $\mathbb{R}^d$  naturally induces a notion of intrinsic distance on the surface  $\Gamma$ .

**Definition 1.A.2** The geodesic distance  $d^\Gamma(p, q)$  between any two points  $p, q \in \Gamma$  is the length of the shortest curve between  $p$  and  $q$  traced on  $\Gamma$ :

$$d^\Gamma(p, q) = \inf \int_0^1 |\gamma'(t)| dt,$$

where the infimum is taken over all curves  $\gamma : [0, 1] \rightarrow \Gamma$  of class  $\mathcal{C}^1$  such that  $\gamma(0) = p$  and  $\gamma(1) = q$ .

The following statement is concerned with the presentation of the main differential operators acting on functions or vector fields on the surface  $\Gamma$ .

**Proposition-Definition 1.A.3** In the above context,

- Let  $f : \Gamma \rightarrow \mathbb{R}$  be a function of class  $\mathcal{C}^1$ ; then there exists an extension  $\tilde{f} : U \rightarrow \mathbb{R}$  of  $f$  which is of class  $\mathcal{C}^1$  on an open neighborhood  $U$  of  $\Gamma$  in  $\mathbb{R}^d$ . The tangential gradient  $\nabla_\Gamma f(x)$  of  $f$  at some point  $x \in \Gamma$  is then defined by:

$$\nabla_\Gamma f(x) = \nabla \tilde{f}(x) - (\nabla \tilde{f}(x) \cdot n(x)) n(x),$$

where  $\tilde{f}$  is any such extension of  $f$ .

Equivalently, for any  $x \in \Gamma$ ,  $\nabla_\Gamma f$  is the unique vector in  $T_x\Gamma$  such that:

$$\forall h \in T_x\Gamma, \quad df_x(h) = \nabla_\Gamma f(x) \cdot h,$$

where  $df_x : T_x\Gamma \rightarrow \mathbb{R}$  is the differential of the real-valued mapping  $f : \Gamma \rightarrow \mathbb{R}$  at  $x$ .

- Let  $V : \Gamma \rightarrow \mathbb{R}^d$  be a vector field of class  $C^1$  on  $\Gamma$ ; then there exists an extension  $\tilde{V} : U \rightarrow \mathbb{R}^d$  of  $V$  which is of class  $C^1$  on an open neighborhood  $U$  of  $\Gamma$  in  $\mathbb{R}^d$ . The tangential divergence  $\operatorname{div}_\Gamma V(x)$  of  $V$  at  $x$  is then defined by

$$\operatorname{div}_\Gamma \tilde{V}(x) = \operatorname{div} \tilde{V}(x) - \nabla \tilde{V}(x) n(x) \cdot n(x),$$

where  $\tilde{V}$  is any such extension of  $V$ .

- Let  $f : \Gamma \rightarrow \mathbb{R}$  be a function of class  $C^2$ . The action of the Laplace-Beltrami operator  $\Delta_\Gamma$  on  $f$  is given by:

$$\Delta_\Gamma f = \operatorname{div}_\Gamma(\nabla_\Gamma f).$$

We next turn to the second-order structure of the hypersurface  $\Gamma$ , and notably to the notion of curvature, see Fig. 1.A.1 for an illustration.

#### Definition 1.A.4

- Let  $x \in \Gamma$ , and let  $\tau \in T_x\Gamma$  be a unit tangent vector, that is  $|\tau| = 1$ . The curvature of  $\Gamma$  at  $x \in \Gamma$  in the direction  $\tau$  is the quantity

$$\kappa_{x,\tau} := \left. \frac{d}{ds} \left( n(\gamma(s)) \right) \right|_{s=0} \cdot \gamma'(0),$$

where  $\gamma : (-\varepsilon, \varepsilon) \rightarrow \mathbb{R}^d$  is any curve traced on  $\Gamma$ , defined on some neighborhood of 0 in  $\mathbb{R}$  and such that  $\gamma(0) = 0$  and  $\gamma'(0) = \tau$ .

- The second fundamental form of  $\Gamma$  at  $x \in \Gamma$  is the bilinear form  $\Pi_\Gamma(x) : T_x\Gamma \times T_x\Gamma \rightarrow \mathbb{R}$  defined by:

$$\forall \tau, \zeta \in T_x\Gamma, \quad \Pi_\Gamma(x)(\tau, \zeta) = \nabla_\Gamma n(x) \tau \cdot \zeta.$$

In particular, the curvature  $\kappa_{x,\tau}$  of  $\Gamma$  at  $x$  in some unit direction  $\tau \in T_x\Gamma$  equals  $\Pi_\Gamma(x)\tau \cdot \tau$ .

Intuitively, the curvature  $\kappa_{x,\tau}$  of  $\Gamma$  at  $x$  in a tangent direction  $\tau \in T_x\Gamma$  appraises how the surface bends near  $x$  in the direction  $\tau$ .

**Definition 1.A.5** Let  $x \in \Gamma$ ; the principal curvatures of  $\Gamma$  at  $x$  are the eigenvalues of the second fundamental form  $\Pi_\Gamma(x)$ ; its eigenvectors  $(\tau_1(x), \dots, \tau_{d-1}(x))$  are the principal directions of  $\Gamma$  at  $x$ ; they form an orthonormal basis of  $T_x\Gamma$ , which can be completed into an orthonormal basis  $(\tau_1(x), \dots, \tau_{d-1}(x), n(x))$  of the space  $\mathbb{R}^d$ .

The mean curvature  $\kappa(x)$  of  $\Gamma$  at a point  $x \in \Gamma$  is defined by

$$\kappa(x) = \kappa_1(x) + \dots + \kappa_{d-1}(x).$$

**Remark 1.A.6** With these definitions, the mean curvature  $\kappa(x)$  of  $\Gamma$  at  $x \in \Gamma$  is positive when the domain  $\Omega$  is locally convex near  $x$ .

#### 1.A.2. Change of variables formulas

The following change of variables formula via a Lipschitz diffeomorphism is found in Chap. 3 of [174].

**Proposition 1.A.7** Let  $\Omega \subset \mathbb{R}^d$  be a bounded, Lipschitz domain and let  $T : \Omega \rightarrow T(\Omega)$  be a bijective Lipschitz mapping, with Lipschitz inverse. Then, for any function  $f \in L^1(T(\Omega))$ , the function  $f \circ T$  belongs to  $L^1(\Omega)$  and:

$$\int_{T(\Omega)} f \, dx = \int_\Omega |\det \nabla T| f \circ T \, dx.$$

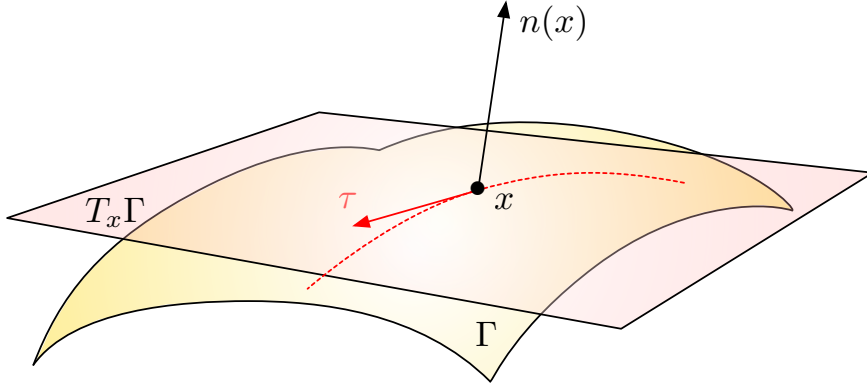


FIGURE 1.A.1. Illustration of the main concepts about the differential geometry of an hypersurface  $\Gamma \subset \mathbb{R}^d$  introduced in Section 1.A.1; the curvature  $\kappa_{x,\tau}$  of is by definition the curvature of the red dotted curve.

Note that the above statement implicitly hinges on Rademacher's theorem, whereby  $\nabla T$  exists almost everywhere on  $\mathbb{R}^d$ .

The above formula has a counterpart when it comes to changing variables in surface integrals, see Prop. 5.4.3 in [201].

**Proposition 1.A.8** *Let  $\Omega \subset \mathbb{R}^d$  be a bounded domain of class  $C^1$ , and let  $n : \partial\Omega \rightarrow \mathbb{R}^d$  be the unit normal vector to  $\partial\Omega$ , pointing outward  $\Omega$ . Let  $T : \Omega \rightarrow T(\Omega)$  be a diffeomorphism of class  $C^1$ . Then, for any function  $g \in L^1(T(\partial\Omega))$ ,  $g \circ T$  belongs to  $L^1(\partial\Omega)$ , and*

$$\int_{T(\partial\Omega)} g \, ds = \int_{\partial\Omega} |\text{com}(\nabla T)n| g \circ T \, ds.$$

**Remark 1.A.9** *The quantity  $|\text{com}(\nabla T)n|$  is sometimes called the tangential Jacobian attached to  $T$ . It is a quantity involving in the transformation rule for the normal vector  $n$ , as the unit normal vector to  $T(\partial\Omega)$  equals*

$$n_{T(\partial\Omega)}(T(x)) = \frac{\text{com}(\nabla T)(x)n(x)}{|\text{com}(\nabla T)(x)n(x)|}, \quad x \in \partial\Omega.$$

### 1.A.3. The Green's formula

The Green's formula is the counterpart in multiple space dimensions of the basic integration by parts formula for functions on the real line. Among its numerous avatars, let us state the following one.

**Proposition 1.A.10 (Green's formula).** *Let  $\Omega \subset \mathbb{R}^d$  be a bounded Lipschitz domain, and let  $n = (n_1, \dots, n_d)$  be the unit normal vector to  $\partial\Omega$ , pointing outward  $\Omega$ . Then, for any function  $f \in W^{1,1}(\Omega)$ , it holds for all  $i = 1, \dots, d$ :*

$$\int_{\Omega} \frac{\partial f}{\partial x_i} \, dx = \int_{\partial\Omega} f n_i \, ds.$$

For convenience, we provide below two identities which are easily derived from Green's formula: for  $\theta \in W^{1,\infty}(\mathbb{R}^d, \mathbb{R}^d)$  and  $u \in W^{1,1}(\Omega)$ ,

$$(1.A.1) \quad \int_{\Omega} \text{div}(\theta)u \, dx = \int_{\partial\Omega} u(\theta \cdot n) \, ds - \int_{\Omega} \theta \cdot \nabla u \, dx,$$

and for  $\theta \in W^{1,\infty}(\mathbb{R}^d, \mathbb{R}^d)$  and  $v, z \in W^{1,1}(\Omega)^d$ ,

$$(1.A.2) \quad \int_{\Omega} \nabla \theta v \cdot z \, dx = \int_{\partial\Omega} (\theta \cdot z)(v \cdot n) \, ds - \int_{\Omega} \text{div}(v)\theta \cdot z \, dx - \int_{\Omega} \nabla z v \cdot \theta \, dx.$$

#### 1.A.4. The implicit function theorem

For the convenience of the reader, we recall the statement of the implicit function theorem, which is used repeatedly across this document. We refer to e.g. Th. 5.9 in Chap. 1 of [224] about the present version.

**Theorem 1.A.11** (*Implicit function theorem*). *Let  $\Theta, E, F$  be Banach spaces,  $\mathcal{V} \subset \Theta$ ,  $U \subset E$  be open sets, and  $\mathcal{F} : \mathcal{V} \times U \rightarrow F$  be a function of class  $\mathcal{C}^p$  for  $p \geq 1$ . Let  $(\theta_0, u_0) \in \mathcal{V} \times U$  be such that  $\mathcal{F}(\theta_0, u_0) = 0$  and assume that:*

*The differential  $d_u \mathcal{F}(\theta_0, u_0) : E \rightarrow F$  is a linear isomorphism.*

*Then there exist open neighborhoods  $\mathcal{V}' \subset \mathcal{V}$  of  $\theta_0$  in  $\Theta$  and  $U' \subset U$  of  $u_0$  in  $E$ , and a mapping  $g : \mathcal{V}' \rightarrow U'$  of class  $\mathcal{C}^p$  satisfying the properties:*

- $g(\theta_0) = u_0$ ,
- For all  $\theta \in \mathcal{V}'$ , the equation  $\mathcal{F}(\theta, u) = 0$  has a unique solution  $u$  in the set  $U'$ , which is given by  $u = g(\theta)$ .

#### 1.A.5. Linear interpolation on the unit sphere of a Hilbert space

Let  $(H, \langle \cdot, \cdot \rangle_H)$  be a Hilbert space, and let  $u, v \in H$  be two vectors with unit norm. The spherical linear interpolation formula was introduced in [335] as an elegant, closed-form expression for a function  $\varphi(t) : [0, 1] \rightarrow H$  satisfying the following properties:

- $\varphi$  realizes an interpolation between  $u$  and  $v$ , i.e.  $\varphi(0) = u$  and  $\varphi(1) = v$ ;
- For all  $t \in [0, 1]$ , the vector  $\varphi(t)$  has unit norm;
- The function  $\varphi$  has constant angular velocity.

in order to derive an expression for  $\varphi$ , let us first restrict ourselves to the two-dimensional subspace  $F$  of  $H$  generated by  $u$  and  $v$ . We consider the orthonormal basis of  $F$  composed by the vector  $u$  and a second vector  $w$ , obtained from  $v$  by the Gram-Schmidt orthonormalization process:

$$w = \frac{v - \langle u, v \rangle_H u}{\|v - \langle u, v \rangle_H u\|_H}.$$

Introducing the angle  $\theta = \arccos(\langle u, v \rangle_H) \in [0, \pi]$  between  $u$  and  $v$ , it follows that

$$\|v - \langle u, v \rangle_H u\|_H^2 = 1 + \cos^2 \theta - 2\langle u, v \rangle_H \cos \theta = 1 - \cos^2 \theta = \sin^2 \theta,$$

whence we obtain the following expressions:

$$w = \frac{1}{\sin \theta} (v - (\cos \theta)u), \text{ and } v = (\cos \theta)u + (\sin \theta)w.$$

We then define the spherical linear interpolation  $\varphi(t)$  between  $u$  and  $v$  by:

$$\forall t \in [0, 1], \quad \varphi(t) = \cos(t\theta)u + \sin(t\theta)w,$$

which obviously satisfies the above requirements. Eventually, a simple calculation allows to express  $\varphi(t)$  in terms of  $u$  and  $v$  only:

$$\begin{aligned} \varphi(t) &= \left( \cos(t\theta) - \frac{\sin(t\theta) \cos(\theta)}{\sin(\theta)} \right) u + \frac{\sin(t\theta)}{\sin(\theta)} v \\ &= \frac{\sin((1-t)\theta)}{\sin(\theta)} u + \frac{\sin(t\theta)}{\sin(\theta)} v. \end{aligned}$$

#### 1.A.6. A glimpse of elliptic regularity

On several occasions in this chapter, we have encountered the fact that the solution to a second-order elliptic boundary value problem posed on a domain  $\Omega$  enjoys higher regularity than that predicted by the Lax-Milgram theory invoked to justify its existence and uniqueness. It is actually a very general fact that such solutions are “as smooth as permitted by the regularity of the domain and the data”.

This regularizing effect of elliptic equations is a central topic in the thriving literature about partial differential equations. Instead of abstract generalities, we limit ourselves with providing a typical statement from this theory; as the method of proof is very general and can be adapted to multiple contexts, we outline a short sketch of the latter, relying on §9.6 of [95] for a rigorous treatment.

**Theorem 1.A.12** Let  $\Omega \subset \mathbb{R}^d$  be a bounded domain of class  $C^{k+2}$ , and let  $f \in H^k(\Omega)$ . Then, the unique solution  $u \in H_0^1(\Omega)$  to the equation

$$(1.A.3) \quad \begin{cases} -\Delta u = f & \text{in } \Omega, \\ u = 0 & \text{on } \partial\Omega, \end{cases}$$

belongs to  $H^{k+2}(\Omega)$ , and the following estimate holds:

$$\|u\|_{H^{k+2}(\Omega)} \leq C\|f\|_{H^k(\Omega)},$$

for a constant  $C > 0$  which only depends on  $k$  and  $\Omega$ .

*Sketch of proof.* We focus on the case where  $k = 0$ , that is, we prove that if  $f \in L^2(\Omega)$ , then the solution  $u$  to (1.A.3) belongs to  $H^2(\Omega)$ ; the complete statement of the theorem follows by induction.

The proof follows the method of translations introduced in [9]. For a function  $u : \overline{\Omega} \rightarrow \mathbb{R}$ , a point  $x \in \overline{\Omega}$ , and a vector  $h \in \mathbb{R}^d$  such that  $x + h \in \overline{\Omega}$ , the difference quotient  $D_h u$  is defined by

$$D_h u(x) = \frac{u(x + h) - u(x)}{|h|}.$$

The following characterization of functions in  $H^1(\Omega)$  is the cornerstone of the argument.

**Lemma 1.A.13** The following statements are equivalent:

- (i)  $u \in H^1(\Omega)$  and there exists  $C > 0$  such that  $\left\| \frac{\partial u}{\partial x_i} \right\|_{L^2(\Omega)} \leq C$  for  $i = 1, \dots, d$ ;
- (ii) There exists  $C > 0$  such that:

$$\forall i = 1, \dots, d, \quad \forall \varphi \in \mathcal{C}_c^\infty(\Omega), \quad \left| \int_{\Omega} u \frac{\partial \varphi}{\partial x_i} \, dx \right| \leq C \|\varphi\|_{L^2(\Omega)}.$$

- (iii) There exists  $C > 0$  such that for any open subset  $\omega \Subset \Omega$ , and any vector  $h \in \mathbb{R}^d$  with  $|h| < \text{dist}(\omega, \partial\Omega)$ ,

$$\|D_h u\|_{L^2(\omega)} \leq C.$$

In addition, one may take  $C = \|\nabla u\|_{L^2(\Omega)}$  in each of the above statements.

We then proceed in three steps.

*Step 1: Interior regularity.* We prove that for every cut-off function  $\chi \in \mathcal{C}_c^\infty(\Omega)$ , one has:

$$(1.A.4) \quad \chi u \in H^2(\Omega), \quad \text{and} \quad \|\chi u\|_{H^2(\Omega)} \leq C\|f\|_{L^2(\Omega)},$$

for a constant  $C > 0$  depending only on  $\chi$  and  $\Omega$ .

At first, a simple calculation yields the following equation for the function  $\chi u$ :

$$(1.A.5) \quad -\Delta(\chi u) = g, \quad \text{where} \quad g := -(\Delta\chi)u - 2\nabla\chi \cdot \nabla u - \chi f \in L^2(\mathbb{R}^d).$$

Under variational form,  $\chi u$  is the unique solution in  $H_0^1(\Omega)$  to the variational problem:

$$(1.A.6) \quad \forall v \in H_0^1(\Omega), \quad \int_{\Omega} \nabla(\chi u) \cdot \nabla v \, dx = \int_{\Omega} gv \, dx.$$

As  $g$  is in  $L^2(\Omega)$  and  $\text{supp}(g)$  is a compact subset of  $\Omega$ , for every  $i = 1, \dots, d$ , the distributional derivative  $\frac{\partial g}{\partial x_i}$  is an element of  $H^{-1}(\Omega)$ .

Intuitively, we know from the standard Lax-Milgram theory that the variational problem

$$\text{Search for } w_i \in H_0^1(\Omega) \text{ s.t. } \forall v \in H_0^1(\Omega), \quad \int_{\Omega} \nabla w_i \cdot \nabla v \, dx = \left\langle \frac{\partial g}{\partial x_i}, v \right\rangle_{H^{-1}(\Omega), H_0^1(\Omega)},$$

obtained from (1.A.6) by formally taking derivatives, has a unique solution  $w_i \in H_0^1(\Omega)$ . Comparing with (1.A.6), we expect that  $w_i$  should coincide with  $\frac{\partial}{\partial x_i}(\chi u)$ , in which case  $\chi u$  would belong to  $H^2(\Omega)$ , as expected.

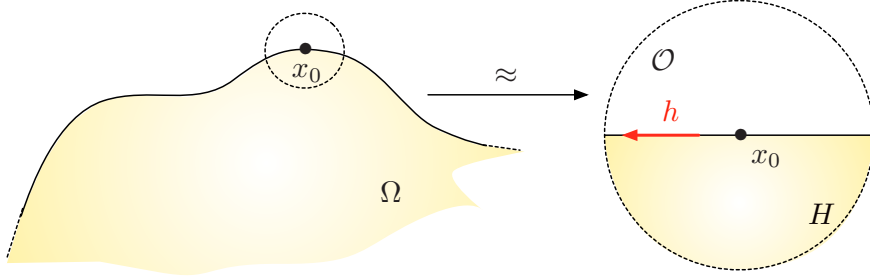


FIGURE 1.A.2. *Localization around a boundary point  $x_0 \in \partial\Omega$  in the sketch of proof of Theorem 1.A.12.*

The formalization of this idea relies on [Lemma 1.A.13](#): for an arbitrary, “small enough” vector  $h \in \mathbb{R}^d$ , let us take  $v = D_{-h}D_h(\chi u)$  as test function in the variational formulation [\(1.A.6\)](#) for  $\chi u$ , which is possible because  $\text{supp}(\chi u)$  is a compact subset of  $\Omega$ ; this yields:

$$\int_{\Omega} \nabla(\chi u) \cdot \nabla(D_{-h}D_h(\chi u)) \, dx = \int_{\Omega} g D_{-h}D_h(\chi u) \, dx.$$

A “discrete integration by parts” (i.e. a change of variables) in this identity yields:

$$\int_{\Omega} \nabla(D_h(\chi u)) \cdot \nabla(D_h(\chi u)) \, dx = \int_{\Omega} g D_{-h}D_h(\chi u) \, dx.$$

Now using the Cauchy-Schwarz inequality with [Lemma 1.A.13](#) ((i)  $\Rightarrow$  (iii)), we arrive at:

$$\|\nabla(D_h(\chi u))\|_{L^2(\Omega)^d}^2 \leq \|g\|_{L^2(\Omega)} \|\nabla(D_h(\chi u))\|_{L^2(\Omega)^d},$$

and so:

$$\|D_h(\nabla(\chi u))\|_{L^2(\Omega)^d} \leq \|g\|_{L^2(\Omega)}.$$

It then follows from [Lemma 1.A.13](#) ((iii)  $\Rightarrow$  (i)) that  $\nabla(\chi u)$  belongs to  $H^1(\Omega)^d$  and satisfies the desired estimate [\(1.A.4\)](#).

*Step 2: Regularity near the boundary.* Let  $x_0$  be any point on  $\partial\Omega$ ; we prove that there exists a bounded open set  $\mathcal{O}$  containing  $x_0$  such that for any cut-off function  $\chi \in \mathcal{C}_c^\infty(\mathbb{R}^d)$  with compact support inside  $\overline{\mathcal{O}}$ ,

$$(1.A.7) \quad \chi u \in H^2(\Omega), \text{ and } \|\chi u\|_{H^2(\Omega)} \leq C\|f\|_{L^2(\Omega)},$$

for a constant  $C > 0$  depending on  $\Omega$  and  $\chi$ .

Since  $\partial\Omega$  is “smooth”, we may take  $\mathcal{O}$  so small that  $\partial\Omega$  is “nearly flat” around  $x_0$  (say,  $\Omega$  coincide with the lower half-space  $H := \{x = (x_1, \dots, x_d), x_d < 0\}$  near  $x_0$ ), see [Fig. 1.A.2](#). Also, because  $x_0$  belongs to  $\partial\Omega$ , the method of translations can only be implemented with horizontal vectors  $h \in \mathbb{R}^d$ , i.e. with  $h_d = 0$ , so that  $x + h$  belongs to  $\overline{\Omega}$  when  $h$  is “small enough”. Doing so, it is possible to prove the existence of a constant  $C > 0$  such that:

$$\forall i = 1, \dots, d-1, \quad \frac{\partial}{\partial x_i}(\chi u) \in H^1(\Omega), \text{ and } \left\| \frac{\partial}{\partial x_i}(\chi u) \right\|_{H^1(\Omega)} \leq C\|f\|_{L^2(\Omega)}.$$

This shows that all the partial derivatives  $\frac{\partial^2 u}{\partial x_i \partial x_j}$  belong to  $L^2(\Omega)$  and satisfy the estimate in [\(1.A.7\)](#) for  $i = 1, \dots, d$  and  $j = 1, \dots, d-1$ . It thus remains to prove that the last second order derivative  $\frac{\partial^2}{\partial x_d^2}(\chi u)$  also belongs to  $L^2(\Omega)$ . To achieve this, we return to the strong form of the equation [\(1.A.5\)](#), which guarantees that:

$$\frac{\partial^2}{\partial x_d^2}(\chi u) = g - \sum_{i=1}^{d-1} \frac{\partial^2}{\partial x_i^2}(\chi u),$$

which then obviously belongs to  $L^2(\Omega)$  and satisfies the desired estimate [\(1.A.7\)](#).

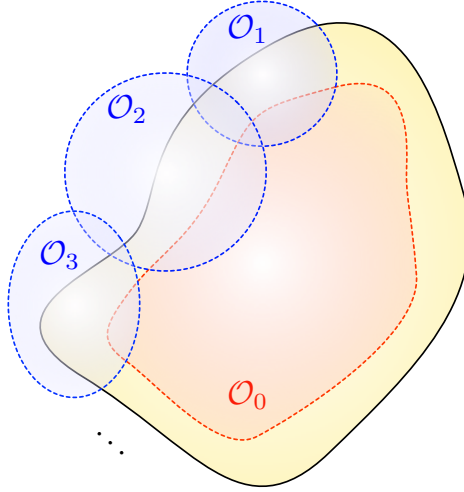


FIGURE 1.A.3. *Covering of  $\bar{\Omega}$  used in the final step of the proof of Theorem 1.A.12.*

Note that the rigorous justification of this second step hinges on a change of variables in the equation (1.A.5) via a diffeomorphism  $T$  of  $\mathbb{R}^d$  such that:

$$T(B(0, r)) \subset \mathcal{O} \text{ for } r > 0 \text{ small enough, and } T(H \cap B(0, r)) = \Omega \cap T(B(0, r)).$$

*Step 3: Global regularity.* By using a partition of unity argument, we “glue” the local results from the two previous steps.

By compactness of  $\bar{\Omega}$ , there exist open subsets  $\mathcal{O}_0 \Subset \Omega$ , and  $\mathcal{O}_1, \dots, \mathcal{O}_N \subset \mathbb{R}^d$  as in the statement of Step 2 such that:

$$\bar{\Omega} \subset \bigcup_{i=0}^N \mathcal{O}_i,$$

see Fig. 1.A.3. Let then  $\{\theta_i\}_{i=0, \dots, N}$  be a partition of unity associated to the covering  $\{\mathcal{O}_i\}_{i=0, \dots, N}$ , i.e.

$$\forall i \in \{0, \dots, N\}, \quad \theta_i \in \mathcal{C}_c^\infty(\mathcal{O}_i), \quad \theta_i \geq 0, \quad \text{and} \quad \sum_{i=0}^N \theta_i = 1 \text{ on } \bar{\Omega}.$$

The solution  $u$  to (1.A.3) can now be decomposed as:

$$u = \theta_0 u + \sum_{i=1}^N \theta_i u,$$

where the first term  $\theta_0 u$  belongs to  $H^2(\Omega)$ , with  $\|\theta_0 u\|_{H^2(\Omega)} \leq C\|f\|_{L^2(\Omega)}$  on account of Step 1, and each term  $\theta_i u$  fulfills the same properties on account of Step 2.

This last step terminates the proof. □

#### Remark 1.A.14

- *Elliptic regularity is a very general phenomenon: similar statements hold for other types of boundary conditions (for instance when the Dirichlet condition in (1.A.3) is replaced with a Neumann, or Robin boundary condition), and other partial differential operators such as those featured in the linearized elasticity system (Elas), or the Stokes equations.*
- *There are however important cases where elliptic regularity fails, with clear physical obstructions. Let us mention two of them:*

- *Two-phase problems.* We have seen in [Section 1.2.1.2](#) that the solution  $u \in H^1(D)$  to the two-phase conductivity equation [\(1.2.3\)](#) involving two phases  $\Omega_1 := \Omega \Subset D$  and  $\Omega_0 := D \setminus \overline{\Omega}$  inside a given (smooth) domain  $D \subset \mathbb{R}^d$ , made of material with different, say constant conductivities  $\gamma_1, \gamma_0 > 0$  satisfies the following jump relations:

$$\forall x \in \partial\Omega, \quad u_0(x) = u_1(x) \text{ and } \left( \gamma_0 \frac{\partial u_0}{\partial n} \right)(x) = \left( \gamma_1 \frac{\partial u_1}{\partial n} \right)(x),$$

where  $u_0, u_1$  are the restrictions of  $u$  to  $\Omega_0, \Omega_1$ , respectively. The second condition, corresponding to the continuity of the flux through the interface  $\partial\Omega$  implies that the gradient  $\nabla u$  cannot have a continuous normal component across  $\partial\Omega$ , so that  $u$  cannot belong to  $H^2(\Omega)$ .

Note however that an adaptation of the proof of [Theorem 1.A.12](#) allows to show that the restrictions  $u_0, u_1$  of  $u$  to  $\Omega_0$  and  $\Omega_1$  belong to  $H^2(\Omega_0)$  and  $H^2(\Omega_1)$ , respectively.

- *Change in boundary conditions.* The solution  $u$  to a boundary value problem equipped with mixed boundary conditions is typically not smooth near the points  $x_0 \in \partial\Omega$  where the boundary conditions change types. More precisely, let for instance  $u$  be the unique solution in  $H^1(\Omega)$  to the problem:

$$\begin{cases} -\Delta u = f & \text{in } \Omega, \\ u = 0 & \text{on } \Gamma_D, \\ \frac{\partial u}{\partial n} = 0 & \text{on } \Gamma_N, \end{cases}$$

posed inside a smooth bounded domain  $\Omega \subset \mathbb{R}^d$ , involving a smooth source  $f \in \mathcal{C}^\infty(\overline{\Omega})$ , and featuring homogeneous Dirichlet boundary conditions on a subset  $\Gamma_D \subset \partial\Omega$  and homogeneous Neumann boundary conditions on the complement  $\Gamma_N := \partial\Omega \setminus \overline{\Gamma_D}$ .

One may prove that  $u$  enjoys  $H^2$  regularity in the neighborhood of any point  $x_0$  inside  $\Omega$ , or of any point  $x_0 \in \partial\Omega \setminus \Sigma$ , where  $\Sigma := \overline{\Gamma_D} \cap \overline{\Gamma_N}$  is the region where boundary conditions change types. On the other hand,  $u$  shows a “weakly singular behavior” at such points  $x_0 \in \Sigma$  (i.e. it is no more regular than  $H^{3/2-\eta}$  for some  $\eta > 0$ ). We shall return to this issue in [Section 4.3](#).



# Chapter 2

## Shape and topology optimization under uncertainties

The objective and constraint functions involved in realistic optimal design problems depend on the physical behavior of the shape, which is usually appraised mathematically via the solution to a boundary-value problem. The specifications of the configuration at hand are incorporated into the latter via parameters, whose values are rarely known with sufficient accuracy. In the context of structural mechanics, this situation incarnates as follows:

- Loads are typical of physical data marred by large uncertainties. They are often measured indirectly by devices such as load cells, which are inherently prone to errors. They may also be changing in an unpredictable way due to alterations in the external medium, see [Fig. 2.0.1 \(a\)](#).
- The physical properties of the constituent material of shapes (encoded in the Young's modulus and the Poisson's ratio) are also source of uncertainties. They may be difficult to estimate because of the presence of heterogeneities or impurities, and they may be altered under uncontrolled variations of the temperature or of the humidity of the ambient medium.
- Often, the geometry of shapes itself is known imperfectly. The actual design of a shape may differ significantly from its blueprint counterpart because of unexpected manufacturing errors, or it may end up deteriorated in time under the effect of wear, see [Fig. 2.0.1 \(b\)](#).

Unfortunately, even very small uncertainties may greatly jeopardize the optimal character of a design, as illustrated by the following example, excerpted from [\[124\]](#).

**Example 2.0.1** *Let us consider the optimization of the constituent material of a fixed square-shaped domain  $D \subset \mathbb{R}^d$  whose upper and lower sides are subjected to a vertical traction load  $g$ , see [Fig. 2.0.2](#). The setting is that of the homogenization method, broached in [Section 1.3.2](#): given a weak and a strong elastic materials with respective Hooke's tensors  $A_0, A_1$ , we optimize the composite structure  $(\theta, A^*)$  within  $D$ , made of*

- *A density function  $\theta : D \rightarrow [0, 1]$  encoding the local volume fraction of the strong material  $A_1$ ;*
- *A microstructure tensor  $A^*$  whose value  $A^*(x)$  at each point  $x \in D$  is the effective tensor of a mixture of  $A_0$  and  $A_1$  in proportions  $(1 - \theta(x))$  and  $\theta(x)$ , respectively.*

*We aim to minimize a weighted sum of the compliance of  $D$  and the volume of strong material:*

$$\min_{(\theta, A^*)} J(\theta, A^*), \text{ where } J(\theta, A^*) := C(\theta, A^*) + \ell \int_D \theta \, dx.$$

*It can be proved rigorously, at least when neither of the two phases  $A_0, A_1$  is degenerate, that an optimal composite structure for this problem is a rank 1 laminate material with lamination direction  $e_1$ , that is, an arrangement of  $A_0$  and  $A_1$  into vertical stripes at the microscopic level, optimized to sustain a perfectly vertical load, see the proof of Th. 4.1.2.1 in [\[16\]](#) and [Fig. 2.0.2](#).*

*The inspection of the explicit expression for the homogenized tensor  $A^*$  reveals that it is degenerate: the entries  $A_{1212}^*, A_{1211}^*$  and  $A_{1222}^*$  vanish, see Chap. 7 in [\[26\]](#) for precise expressions. The structure  $D$  filled with the material is therefore incapable of sustaining the slightest shear strain: the compliance is infinite as soon as a small perturbation is added to the horizontal component of  $g$ .*

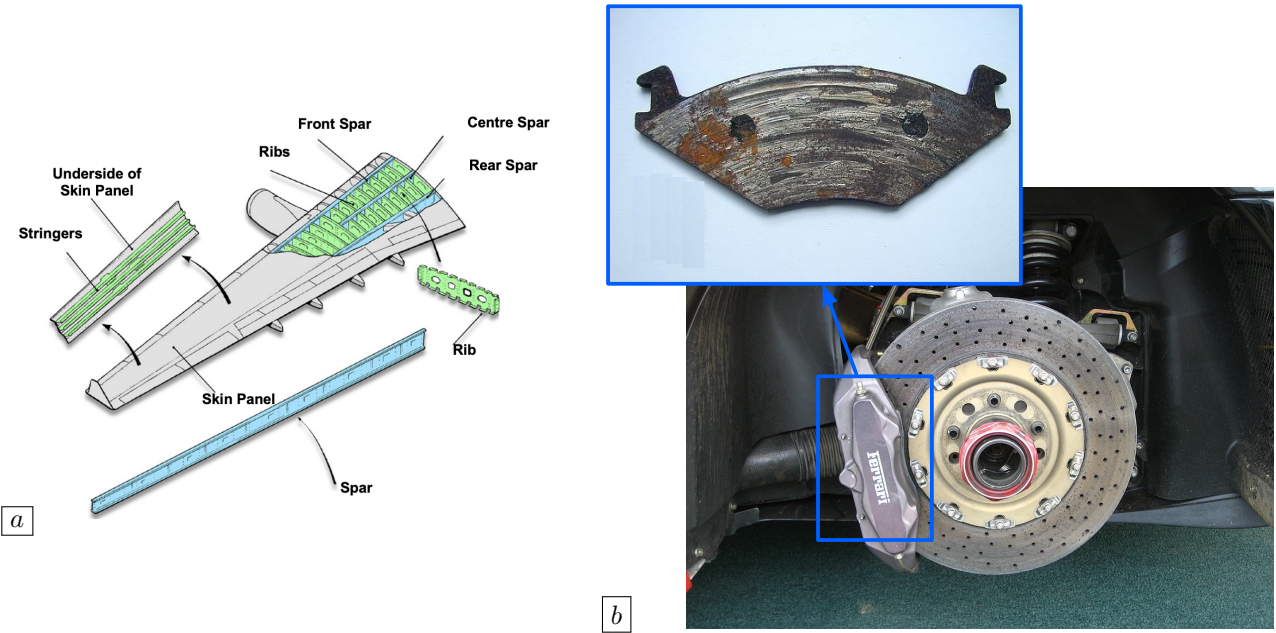


FIGURE 2.0.1. (a) The rib structure of the wing of a plane has to cope with unpredictable and multiple diffuse loads during flight [220]; (b) scratched geometry of a brake pad under the effect of wear.

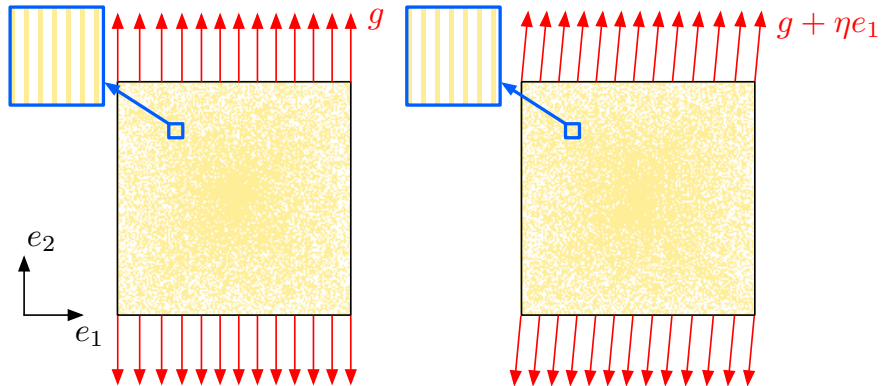


FIGURE 2.0.2. An optimal microstructure for the vertical load  $g$  is the worst possible design as soon as a (however small) horizontal component is added to  $g$ .

This chapter summarizes the investigations conducted in the articles [A33, A31, A30, A18, A1], which generally aim to develop robust expressions of optimal design problems with respect to certain sources of uncertainties. This challenging issue has recently received much attention from both academic and industrial communities, see e.g. [339, 257] for overviews.

Most of the developments presented in this chapter lend themselves to a formulation which is independent of the particular shape and topology optimization framework. For this reason, we adopt insofar as possible a formal abstract setting, which shall be specialized when needed: we consider the optimization of a design variable  $h$  with respect to a cost  $\mathcal{C}(h, f)$  which also depends on the physical data  $f$  of the situation:

$$(2.0.1) \quad \min_h \mathcal{C}(h, f).$$

The strategies to make optimal design problems aware of uncertainties usually fall into one of the following two categories, depending on the available knowledge about the data  $f$ :

- Worst-case formulations are grounded on the fact that nothing is known about  $f$ , except for a maximum bound  $m$  on their deviation to a known reference value  $f_0$ . The robust version of (2.0.1) then reads:

$$(2.0.2) \quad \min_h \sup_{\|f-f_0\| \leq m} \mathcal{C}(h, f).$$

- In probabilistic formulations, the data  $f$  are modeled by a random variable, defined over an abstract probability space  $(\mathcal{O}, \mathcal{F}, \mathbb{P})$ , with known law. The aim is then to minimize a statistical quantity of the cost, such as its expectation

$$\min_h \int_{\mathcal{O}} \mathcal{C}(h, f(\omega)) d\mathbb{P}(\omega),$$

or the probability

$$\mathbb{P}\left\{\omega \in \mathcal{O}, \mathcal{C}(h, f(\omega)) > \alpha\right\}.$$

that its value exceed a safety threshold  $\alpha$ .

This chapter is organized as follows. The first [Section 2.1](#) summarizes investigations related to worst-case optimal design; a general strategy is presented to address such problems. The next [Section 2.2](#) deals with an issue which is fairly close in essence to this worst-case optimization paradigm, in the context of a source of uncertainties quite specific to the shape optimization context: the presence of “small” porosities inside the structure. Based on the articles [\[A30, A31\]](#), the next [Section 2.3](#) deals with probabilistic approaches for shape and topology optimization. As we shall see in multiple occasions in this chapter, both worst-case and probabilistic viewpoints suffer from severe drawbacks. In particular, the latter assumes the perfect knowledge of the law of the uncertain data (or at least of some of its moments), which is unrealistic. Summarizing the work of the preliminary note [\[A1\]](#), we present in [Section 2.4](#) a more realistic perspective: introducing the recent idea of distributional robustness in the context of shape and topology optimization, we optimize the worst-case value of a risk measure (typically the expectation) of the cost function when the actual (unknown) law of uncertainties is “close” to a nominal, estimated law. This chapter ends with two appendices: in [Section 2.A](#), we recall a few basic notions from measure theory. Then, [Section 2.B](#) is about the so-called Karhunen-Loève expansion of a random field, giving a rigorous ground to the finite-dimensional structure of the random uncertainties considered in this chapter.

## 2.1 OPTIMAL DESIGN IN THE WORST-CASE SCENARIO

This first section deals with worst-case versions of optimal design problems, of the form (2.0.2). It is based on the work [\[A33\]](#), written at the end of my Ph. D. thesis. After presenting the proposed approximation method for such problems in a formal and general setting in [Section 2.1.1](#), two concrete examples are discussed in [Section 2.1.2](#).

### 2.1.1. A formal, general linearization method for worst-case design

Let us first introduce a formal and abstract optimal design framework which will be considered on several occurrences in this chapter. The design variable  $h$  is sought within a set  $\mathcal{H}$  of admissible designs, and the physical data  $f$  belong to a Banach space  $(\Xi, \|\cdot\|_{\Xi})$  (or a subset of the latter). The performance of a design  $h$  when the data  $f$  are at play is measured in terms of a cost function  $\mathcal{C}(h, f)$ . The optimal design of interest, when the data of the problem equal  $f$  reads:

$$(2.1.1) \quad \min_{h \in \mathcal{H}} \sup_{\|f-f_0\|_{\Xi} \leq m} \mathcal{C}(h, f),$$

where constraints are omitted for simplicity. Often,  $\mathcal{C}(h, f)$  has the structure:

$$(2.1.2) \quad \mathcal{C}(h, f) = S(f, u_{h,f}), \text{ for some smooth function } S : \mathcal{H} \times V \rightarrow \mathbb{R},$$

as it depends on the physical situation via a state  $u_{h,f}$ , characterized as the unique solution in a Hilbert space  $(V, \langle \cdot, \cdot \rangle_V)$  to a design-dependent linear system of the form:

$$(2.1.3) \quad \mathcal{A}(h)u_{h,f} = b(f).$$

For simplicity of the exposition, the design  $h$  and the data  $f$  only appear in the operator  $\mathcal{A}(h)$  and in the right-hand side  $b(f)$  of this equation.

For instance, this setting comprises that of elastic structures introduced in [Section 1.2.3](#): the design variable  $h$  then stands for the shape  $\Omega$ , the data  $f$  are (for instance) the applied external loads, and the cost  $\mathcal{C}(h, f)$  may represent the compliance of the structure, depending on its elastic displacement  $u_{h,f}$ .

As the starting assessment of worst-case approaches, the only available information about the data  $f$  is that they differ from a reference, unperturbed value  $f_0$  by a perturbation  $\hat{f}$  with maximum amplitude  $m > 0$ . The worst-case counterpart of [\(2.1.1\)](#) then reads:

$$\min_{h \in \mathcal{H}} J_{\text{wc}}(h), \text{ where } J_{\text{wc}}(h) := \sup_{\|f - f_0\|_{\Xi} \leq m} \mathcal{C}(h, f).$$

Unfortunately, this bi-level program is untractable, except in very specific situations; we seek to construct an approximate worst-case functional  $\tilde{J}_{\text{wc}}(h)$  which lends itself to an easier analysis. To achieve this, we leverage the ‘‘closeness’’ of  $f = f_0 + \hat{f}$  (that is, the ‘‘smallness’’ of  $\hat{f}$ ) with the unperturbed value  $f_0$  to linearize the cost  $f \mapsto \mathcal{C}(h, f)$  around  $f_0$ :

$$(2.1.4) \quad \mathcal{C}(h, f) \approx \mathcal{C}(h, f_0) + \frac{\partial \mathcal{C}}{\partial f}(h, f_0)(\hat{f}).$$

We then define our formal approximation  $\tilde{J}_{\text{wc}}(h)$  of  $J_{\text{wc}}(h)$  to be the largest value of the first-order approximation of  $f \mapsto \mathcal{C}(h, f)$  when  $\|\hat{f}\|_{\Xi} \leq m$ :

$$\tilde{J}_{\text{wc}}(h) = \sup_{\|\hat{f}\|_{\Xi} \leq m} \left( \mathcal{C}(h, f_0) + \frac{\partial \mathcal{C}}{\partial f}(h, f_0)(\hat{f}) \right).$$

Recognizing the supremum of an affine mapping over a ball in a Banach space, this quantity rewrites:

$$(2.1.5) \quad \tilde{J}_{\text{wc}}(h) = \mathcal{C}(h, f_0) + m \left\| \frac{\partial \mathcal{C}}{\partial f}(h, f_0) \right\|_{\Xi^*},$$

where  $\Xi^*$  is the dual of the Banach space  $\Xi$ . This expression is not yet fully satisfactory: it brings into play the partial derivative  $\frac{\partial \mathcal{C}}{\partial f}$  of the cost  $\mathcal{C}$  with respect to the data  $f$  which is uneasy to handle, as  $\mathcal{C}$  depends on  $f$  via the solution  $u_{h,f}$  to [\(2.1.3\)](#), see [\(2.1.2\)](#). To make the quantity  $\frac{\partial \mathcal{C}}{\partial f}$  more explicit, we rely on the first-order expansion of the mapping  $f \mapsto \mathcal{C}(h, f)$  around  $f_0$ , which reads:

$$(2.1.6) \quad \begin{aligned} \text{For } f = f_0 + \hat{f}, \text{ } \hat{f} \text{ ‘‘small’’, } \mathcal{C}(h, f) &= S(f, u_{h,f}) \\ &\approx S(f_0, u_{h,f_0}) + \frac{\partial S}{\partial f}(f_0, u_{h,f_0})(\hat{f}) + \frac{\partial S}{\partial u}(f_0, u_{h,f_0})(u_{h,f_0}^1(\hat{f})). \end{aligned}$$

Here, we have introduced the derivative  $u_{h,f_0}^1(\hat{f}) := \frac{\partial u_{h,f}}{\partial f} \Big|_{f=f_0}(\hat{f})$  of the state function at  $f = f_0$ . The latter is characterized by the following equation obtained by differentiation of [\(2.1.3\)](#):

$$\mathcal{A}(h)u_{h,f_0}^1(\hat{f}) = \frac{\partial b}{\partial f}(f_0)(\hat{f}).$$

We now give another expression to the last term in the right-hand side of [\(2.1.6\)](#) thanks to the adjoint method, which is summarized in [Section 1.3.3.6](#). Let the adjoint state  $p_{h,f_0} \in V$  be defined as the solution to the equation

$$(2.1.7) \quad \mathcal{A}(h)^T p_{h,f_0} = -\frac{\partial S}{\partial u}(f_0, u_{h,f_0}),$$

where we have identified the derivative  $\frac{\partial S}{\partial u}(f_0, u_{h,f_0})$  of  $S$  at  $(f_0, u_{h,f_0})$  with its gradient in the Hilbert space  $V$ , up to a small abuse of notation. The familiar series of transformations involved in adjoint-based computations reads in the present context:

$$\begin{aligned}\frac{\partial S}{\partial u}(f_0, u_{h,f_0})(u_{h,f_0}^1(\hat{f})) &= -\left\langle \mathcal{A}(h)^T p_{h,f_0}, u_{h,f_0}^1(\hat{f}) \right\rangle_V \\ &= -\left\langle \mathcal{A}(h)u_{h,f_0}^1(\hat{f}), p_{h,f_0} \right\rangle_V \\ &= -\left\langle \frac{\partial b}{\partial f}(f_0)(\hat{f}), p_{h,f_0} \right\rangle_V \\ &= -\left\langle \frac{\partial b}{\partial f}(f_0)^T p_{h,f_0}, \hat{f} \right\rangle_{\Xi^*, \Xi},\end{aligned}$$

where  $\frac{\partial b}{\partial f}(f_0)^T : V \rightarrow \Xi^*$  is the adjoint of the mapping  $\frac{\partial b}{\partial f}(f_0) : \Xi \rightarrow V$ . Eventually, (2.1.6) becomes:

$$\mathcal{C}(h, f) \approx \mathcal{C}(h, f_0) + \frac{\partial S}{\partial f}(f_0, u_{h,f_0})(\hat{f}) - \left\langle \frac{\partial b}{\partial f}(f_0)^T p_{h,f_0}, \hat{f} \right\rangle_{\Xi^*, \Xi}.$$

Inserting this identity in (2.1.5), our approximate worst-case functional  $\tilde{J}_{\text{wc}}(h)$  rewrites:

$$\tilde{J}_{\text{wc}}(h) = \mathcal{C}(h, f_0) + m \left\| \frac{\partial S}{\partial f}(f_0, u_{h,f_0}) - \frac{\partial b}{\partial f}(f_0)^T p_{h,f_0} \right\|_{\Xi^*}.$$

Note that in practice, the quantity  $\left( \frac{\partial S}{\partial f}(f_0, u_{h,f_0}) - \frac{\partial b}{\partial f}(f_0)^T p_{h,f_0} \right)$  is more “regular” than a mere element of  $\Xi^*$ : it actually belongs to the Banach pre-dual space  $\Upsilon$  of  $\Xi$ , i.e.  $\Xi = \Upsilon^*$ . In this case, the dual norm above equals that of  $\Upsilon$ .

The approximate worst-case functional  $\tilde{J}_{\text{wc}}(h)$  can be incorporated into a classical optimal design problem, either as an objective, or as a constraint function. The calculation of its derivative with respect to the design  $h$ , which is required in the implementation of typical constrained optimization algorithms can be realized thanks to the adjoint method, see again Section 1.3.3.6. Let us emphasize that this calculation is a little tedious, as  $\tilde{J}_{\text{wc}}(h)$  depends on  $h$  via the solution  $u_{h,f_0}$  to the state equation (2.1.3) and that  $p_{h,f_0}$  to the adjoint equation (2.1.7).

**Remark 2.1.1** *The above approximation procedure is formal: it is usually not verified that first-order expansion of the supremum of a function coincides with the supremum of its first-order expansion, see nevertheless [198] for a very particular situation where such is the case. In general, the approximate worst-case functional  $\tilde{J}_{\text{wc}}(h)$  can only be expected to be a rough account of the exact one  $J_{\text{wc}}(h)$ , whose minimization instills in the optimized design  $h$  “good trends” towards robustness with respect to perturbations on the data  $f$ .*

## 2.1.2. A couple of numerical results

As we have mentioned, the above procedure for constructing approximate worst-case functionals encompasses a whole gamut of optimal design situations. In this section, we discuss two such instances of shape optimization problems.

### 2.1.2.1. Robust shape optimization of a 2d bridge under load uncertainties

This first example deals with the problem of robust design of structures with respect to the compliance when perturbations are expected over the applied loads. This problem has been extensively considered in the literature; its very particular structure allows for a quite explicit treatment, see [44, 124, 153].

We consider the optimization of the design of a 2d bridge: as depicted on Fig. 2.1.1 (a), the shapes  $\Omega$  are contained in a box  $D$  with size  $2 \times 1.5$ ; they are clamped near their bottom-left corner, and the vertical displacement is prevented around their bottom-right corner. In the unperturbed situation, a body force  $f_0 = (0, -10)$  is applied on a region in the middle of the bottom side of  $D$ , and the perturbed versions of the force  $f$  read:

$$f = f_0 + \hat{f}, \text{ where } \hat{f} \text{ has maximum amplitude } m \text{ and is concentrated on the blue rectangles.}$$

The cost  $\mathcal{C}(\Omega, f)$  of a shape  $\Omega$  when body forces  $f$  are at play is the compliance:

$$\mathcal{C}(\Omega, f) = \int_{\Omega} f \cdot u_{\Omega, f} \, dx,$$

where  $u_{\Omega, f}$  is the solution to the linear elasticity system (Elas). We solve the constrained optimization problem

$$(2.1.8) \quad \min_{\Omega} \tilde{\mathcal{J}}_{\text{wc}}(\Omega) \text{ s.t. } \text{Vol}(\Omega) = V_T,$$

involving the approximate worst-case compliance functional  $\tilde{\mathcal{J}}_{\text{wc}}(\Omega)$  constructed in the previous section, with the volume target  $V_T = 0.75$ .

As far as the numerical resolution is concerned, the classical level set method for shape optimization is used on a fixed mesh of  $D$ , see Section 1.4.6.2. Several examples are presented on Fig. 2.1.1, associated to different values of the magnitude  $m$  of expected perturbations over the nominal force  $f_0$ .

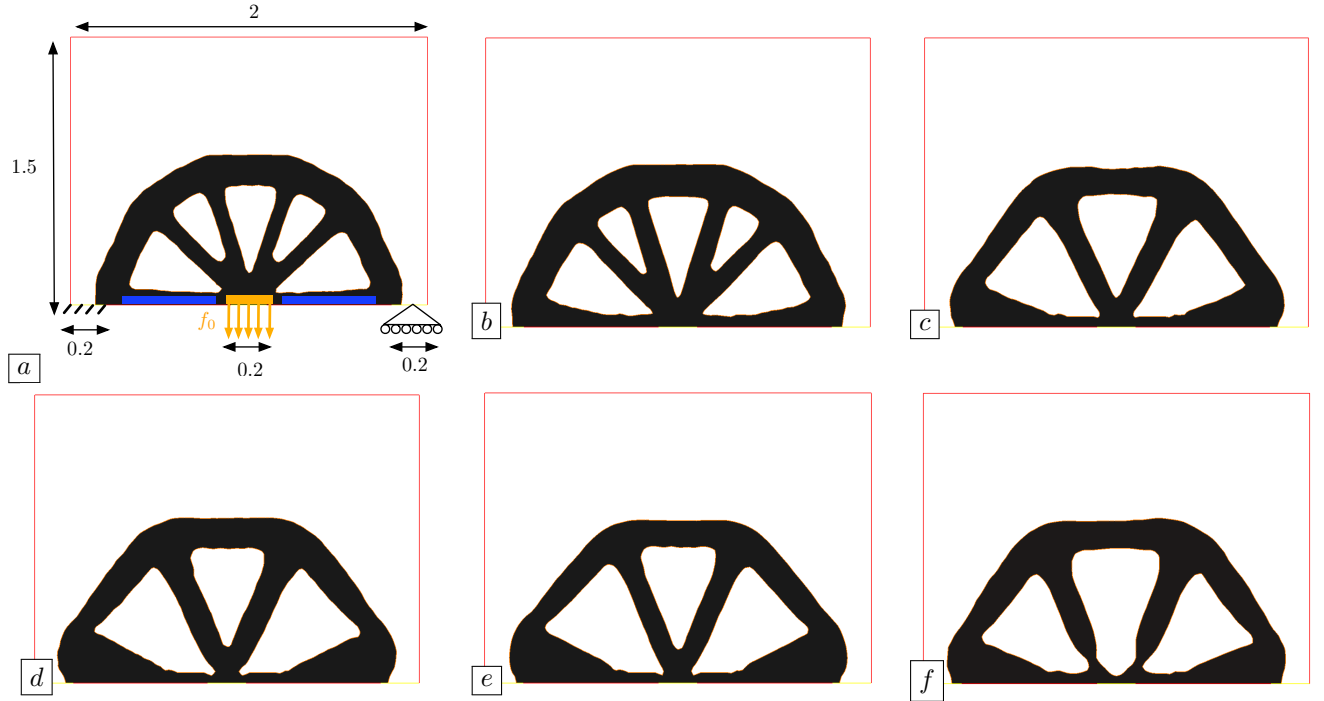


FIGURE 2.1.1. Optimized design of the 2d bridge considered in Section 2.1.2.1 with respect to the approximate worst-case compliance minimization problem (2.1.8) with an amplitude  $m$  over perturbations  $\hat{f}$  equal to (a) 0 (unperturbed case), with details of the test-case (b) 0.2, (c) 0.5, (d) 1, (e) 1.5 and (f) 2.

The mechanical analysis of these results complies with the general trends of worst-case formulations of optimal design problems. The robust designs show an improved (i.e. lower) value of the compliance than the design optimized for the unperturbed load  $f_0$  when the actual force  $f$  is a (significant) perturbation of  $f_0$ ; on the other hand, the nominal performance of the robust designs (i.e. the value of the compliance when the unperturbed force  $f_0$  is applied) gets dramatically deteriorated as  $m$  increases. In other terms, anticipating the worst-case scenario leads to designs with poor nominal performance.

### 2.1.2.2. Worst-case optimization of a gripping mechanism in the presence of geometric uncertainties

This section illustrates how the above framework allows to handle uncertainties on the geometry of the shape  $\Omega$  itself – an issue which is considered with other techniques in e.g. [118, 139, 198, 379].

Perturbations of the geometry of a shape  $\Omega$  are considered as variations of  $\Omega$  in the sense of the Hadamard method (see [Section 1.3.3](#)) with maximum amplitude  $m$  in the supremum norm:

$$\Omega_\theta = (\text{Id} + \theta)(\Omega), \quad \theta \in W^{1,\infty}(\mathbb{R}^d, \mathbb{R}^d), \quad \|\theta\|_{W^{1,\infty}(\mathbb{R}^d, \mathbb{R}^d)} < 1 \text{ and } \|\theta\|_{L^\infty(\mathbb{R}^d)^d} < m.$$

To set ideas, let us consider the following constraint-free minimization problem of a cost function  $\mathcal{C}(\Omega)$ :

$$(2.1.9) \quad \min_{\Omega} \mathcal{C}(\Omega).$$

Its worst-case version when geometric perturbations of maximum amplitude  $m$  are expected reads:

$$\min_{\Omega} J_{\text{wc}}(\Omega), \quad \text{where } J_{\text{wc}}(\Omega) := \sup_{\|\theta\|_{L^\infty(\mathbb{R}^d)^d} \leq m} \mathcal{C}(\Omega_\theta).$$

Let us assume that the shape derivative of  $\mathcal{C}(\Omega)$  enjoys the desirable surface structure discussed in [Section 1.3.3.2](#), say

$$\mathcal{C}'(\Omega)(\theta) = \int_{\partial\Omega} v_\Omega \theta \cdot n \, ds,$$

for some scalar field  $v_\Omega : \partial\Omega \rightarrow \mathbb{R}$  which encodes all the first-order information about the shape sensitivity of  $\mathcal{C}(\Omega)$ . Our formal method yields the following approximate problem:

$$(2.1.10) \quad \begin{aligned} \min_{\Omega} \tilde{J}_{\text{wc}}(\Omega), \quad \text{where } \tilde{J}_{\text{wc}}(\Omega) &:= \sup_{\|\theta\|_{L^\infty(\mathbb{R}^d)^d} \leq m} \left( \mathcal{C}(\Omega) + \int_{\partial\Omega} v_\Omega \theta \cdot n \, ds \right), \\ &= \mathcal{C}(\Omega) + m \int_{\partial\Omega} |v_\Omega| \, ds. \end{aligned}$$

This problem can be addressed with the methods presented in [Chapter 1](#). Note that, roughly speaking, the shape derivative of  $\tilde{J}_{\text{wc}}(\Omega)$  involves the second-order sensitivity of  $\mathcal{C}(\Omega)$  with respect to the domain.

To illustrate this idea, let us consider the 2d optimization example of the shape of a gripping mechanism. As depicted on [Fig. 2.1.2](#) (a), shapes are contained in a box  $D$  with size  $1 \times 1$ ; they are clamped near their upper- and lower-left corner, and a force  $g = (-0.1, 0)$  is applied at the middle of their left-hand side. We aim that the displacement  $u_\Omega$  of the shape  $\Omega$  comply with a target displacement  $u_T : D \rightarrow \mathbb{R}^2$  so that the jaws (the blue regions on [Fig. 2.1.2](#) (a)) close. To achieve this, we solve the optimization problem (2.1.9) with the cost function

$$\mathcal{C}(\Omega) = \int_{\Omega} k(x) |u_\Omega - u_T|^2 \, dx,$$

where  $k \in L^\infty(\mathbb{R}^d)$  is an indicator function for the fixed region near the jaws of  $\Omega$ .

We solve the approximate robust problem (2.1.10) for several values of the expected amplitude  $m$  of the geometric perturbations; the results are displayed on [Fig. 2.1.2](#).

Inspection of the results yields similar conclusions to those of the previous [Section 2.1.2.1](#): the nominal performance of the shape gets degraded as  $m$  increases. This phenomenon is highlighted by [Fig. 2.1.3](#) where the displaced configurations of the optimized designs of [Fig. 2.1.2](#) are represented (without application of geometric perturbations). For large values of  $m$ , the jaws of the mechanism barely move closer from one another.

## 2.2 SHAPE OPTIMIZATION UNDER POROSITY CONSTRAINTS

Relying on the general idea developed in the previous [Section 2.1.1](#) about worst-case optimal design, this section deals with a source of uncertainties which is naturally expressed in the more specific context of shape optimization: the presence of porosities inside the optimized shape. Such defects are indeed ubiquitous in engineering; for instance,

- Porosity often shows up in the course of the casting process, where the shape is constructed upon solidification of a liquid material poured into a mold. Bubbles of air are trapped during the solidification stage, jeopardizing the material strength, see [273] and [Fig. 2.2.1](#) (a).
- Porosity is a fairly common effect in welding [384] – an operation during which two parts are fused together to form a joint upon cooling. It is entailed by small gas holes distributed randomly all over the weld bead, thus weakening the weld, see [Fig. 2.2.1](#) (b).

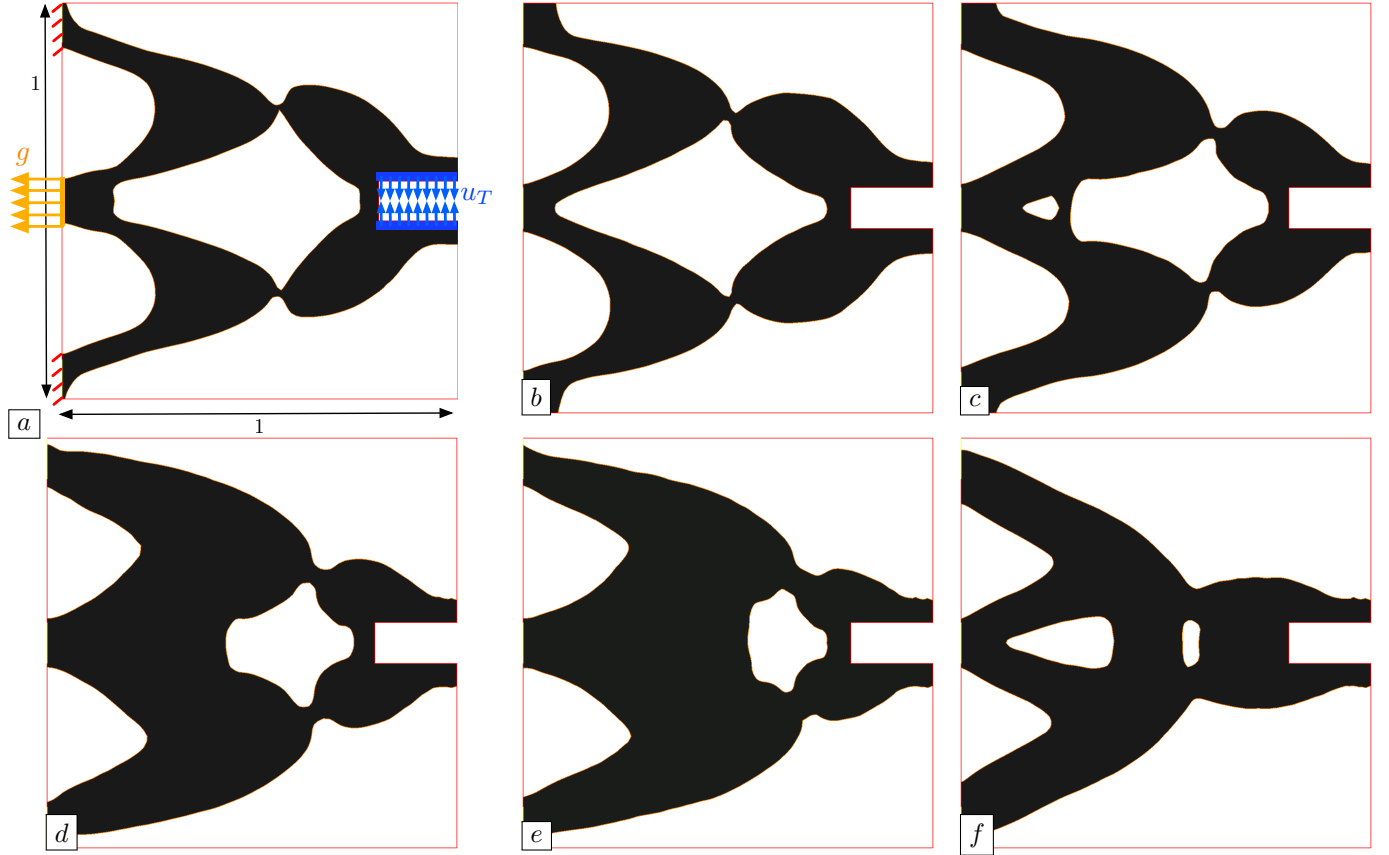


FIGURE 2.1.2. Optimized design of the 2d gripping mechanism considered in [Section 2.1.2.2](#) under geometric uncertainties with magnitude  $m$  equal to (a) 0 (unperturbed case), with details of the test-case (b) 0.002, (c) 0.007, (d) 0.009, (e) 0.01 and (f) 0.02.

- Porosity also affects most additive manufacturing techniques (see [Section 3.5.1](#) for a short presentation), and notably the popular Electron Beam Melting technology [351], and [Fig. 2.2.1](#) (c).

Uncontrolled porosity defects are very harmful to mechanical structures in practice: they degrade the reliability and quality of materials, and they make structures more prone to crack initiation and fatigue. This raises the need to enforce robustness of structures with respect to the presence of porosities. In spite of its importance, this topic seems to have received very little attention from the optimal design literature, see nevertheless [107]. This section is based on the work [A18].

### 2.2.1. Formal presentation of the mathematical model

Let us slip into the context of structural optimization introduced in [Section 1.2.3](#): let  $\mathcal{C}(\Omega)$  be a cost function of the optimized elastic structure  $\Omega \subset \mathbb{R}^d$ . As usual in this manuscript,  $\mathcal{C}(\Omega)$  depends on  $\Omega$  via the elastic displacement  $u_\Omega : \Omega \rightarrow \mathbb{R}^d$ , solution to the linear elasticity system [\(Elas\)](#).

In the perspective of devising a version of  $\mathcal{C}(\Omega)$  which is robust with respect to the presence of “small” porosities inside  $\Omega$ , we consider topological perturbations of a shape  $\Omega \subset \mathbb{R}^d$  of the form

$$\Omega_{x,r} = \Omega \setminus \overline{B(x,r)}, \quad x \in \Omega, \quad r \ll 1,$$

i.e.  $\Omega_{x,r}$  is a version of  $\Omega$  where a small hole with radius  $r$  has been nucleated around  $x$ .

We impose that the cost  $\mathcal{C}(\Omega)$  of  $\Omega$  be “not too much degraded” when a hole with “small” size  $r$  emerges in its bulk, that is:

$$(2.2.1) \quad \forall x \in \Omega, \quad \mathcal{C}(\Omega_{x,r}) \leq (1 + \eta) \mathcal{C}(\Omega),$$

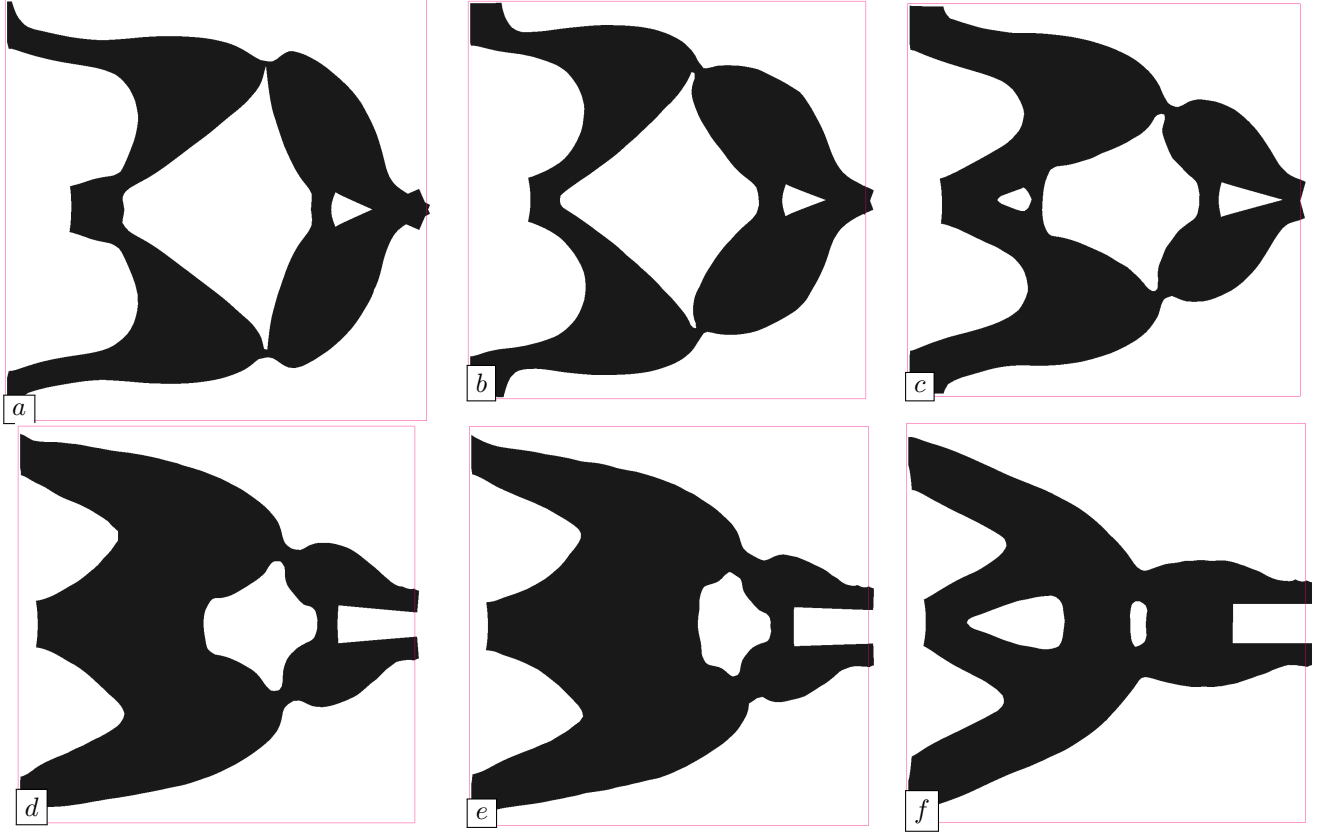


FIGURE 2.1.3. *Displaced configurations of the optimized gripping mechanisms in Section 2.1.2.2 when anticipating geometric uncertainties with magnitude  $m$  equal to (a) 0, (b) 0.002, (c) 0.007, (d) 0.009, (e) 0.01 and (f) 0.02.*

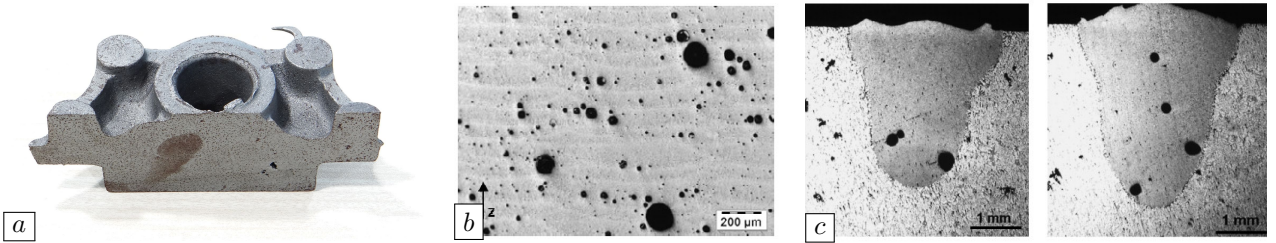


FIGURE 2.2.1. *Examples of porosity defects in mechanical engineering: (a) Shrinkage porosity in casting (source: <http://efoundry.iitb.ac.in/Defects/shrinkage.html>); (b) weld metal porosity [199]; (c) Hydrogen pores in a 3D-printed aluminum alloy [366].*

where  $\eta > 0$  is a given tolerance threshold (depending on  $r$ ).

In order to make this requirement amenable to numerical computations, we leverage the smallness of the hole  $r$ : the cost  $\mathcal{C}(\Omega_{x,r})$  of the perturbed structure  $\Omega_{x,r}$  can be related to  $\mathcal{C}(\Omega)$  thanks to the topological derivative  $d\mathcal{C}_T(\Omega)$  of  $\mathcal{C}(\Omega)$  – a notion introduced in Section 1.3.4. This yields the following expansion:

$$(2.2.2) \quad \mathcal{C}(\Omega_{x,r}) = \mathcal{C}(\Omega) + r^d d\mathcal{C}_T(\Omega)(x) + o(r^d).$$

Hence, retaining only the leading order in terms of  $r$  in (2.2.1), we consider the following approximate requirement for  $\Omega$  to be robust with respect to the emergence of porosities with size  $r$ :

$$(2.2.3) \quad \forall x \in \Omega, \quad r^d d\mathcal{C}_T(\Omega)(x) \leq \eta \mathcal{C}(\Omega).$$

Eventually, we are led to replace  $\mathcal{C}(\Omega)$  with the functional

$$(2.2.4) \quad J_{\text{por}}(\Omega) := \int_{\Omega} j_{\text{por},\Omega}(x) \, dx, \text{ where } j_{\text{por},\Omega}(x) = \frac{1}{2} \left[ d\mathcal{C}_T(\Omega)(x) - \frac{\eta}{r^d} \mathcal{C}(\Omega) \right]_+,$$

and  $[t]_+ = \max(t, 0)$  is the positive part of a real number  $t$ .

The latter can be used in a standard shape and topology optimization algorithm like those presented in [Chapter 1](#), either as the objective, or as a constraint function, whose values should be kept under a “small” positive threshold. Loosely speaking, the calculation of the shape derivative of  $J_{\text{por}}(\Omega)$  amounts to “differentiating the topological derivative of  $\mathcal{C}(\Omega)$  with respect to the domain”, a task which can be conducted thanks to the techniques exemplified in [Section 1.3.3](#), however technically tedious.

**Remark 2.2.1** *The above mathematical description of porosity patterns could legitimately be criticized. Beyond the formal replacement of the requirement (2.2.1) by the leading-order approximation (2.2.3), the topological expansion (2.2.2) only accounts for the nucleation of one “small” hole inside  $\Omega$ , or at best of a collection of finitely many isolated holes. Hence, the description of small porosities spread out at random inside the shape  $\Omega$  would rather rely on the homogenization theory.*

## 2.2.2. Two numerical examples of robust optimization of shapes taking into account the emergence of porosities

### 2.2.2.1. Robust minimization of the stress within an L-shaped beam

Our first example deals with the optimization of an L-shaped beam: inside a domain  $D$  with size  $100 \times 100$ , the optimized shape  $\Omega$  is clamped on its upper side, and a vertical load  $g = (0, -3)$  is applied at the middle of its right-hand side.

In a first step, we minimize the compliance of  $\Omega$  under a volume constraint, without taking into account the effect of porosity; using the standard level set method for shape and topology optimization (see [Section 1.4.6.2](#)), we solve the problem

$$(2.2.5) \quad \min_{\Omega} C(\Omega) \text{ s.t. } \text{Vol}(\Omega) = V_T, \text{ where } C(\Omega) = \int_{\Omega} A e(u_{\Omega}) : e(u_{\Omega}) \, dx,$$

and the volume target is set to  $V_T = 0.35 \text{Vol}(D)$ . The resulting shape  $\Omega^*$  is represented on the left column of [Fig. 2.2.2](#).

We now bring into play the porosity constraint functional  $J_{\text{por}}(\Omega)$  constructed by (2.2.4) from the following cost function  $\mathcal{C}(\Omega)$  evaluating the stress within  $\Omega$ :

$$\mathcal{C}(\Omega) = \int_{\Omega} \|\sigma(u_{\Omega})\|^2 \, dx,$$

and where the parameters  $r$  and  $\eta$  are set to 0.625 and 0.01, respectively. Starting from  $\Omega^*$ , we solve the new problem:

$$(2.2.6) \quad \min_{\Omega} C(\Omega) \text{ s.t. } \begin{cases} J_{\text{por}}(\Omega) = 0, \\ \text{Vol}(\Omega) = V_T. \end{cases}$$

The optimized design is depicted on the right column of [Fig. 2.2.2](#); the main difference between the latter and  $\Omega^*$  is that the reentrant corner has been significantly rounded.

### 2.2.2.2. Robust minimization of the compliance within a double hook

In this second, 3d example, the design of a double hook structure is investigated, see [Fig. 2.2.3](#) (a). The T-shaped working domain is clamped at the top of the T-leg and two vertical loads  $g = (0, 0, -5)$  are applied in the middle of the faces at the end of the T-shafts. The initial shape is represented in [Fig. 2.2.3](#) (b).

Since we are interested in studying the impact of porosity on shapes, and because the latter is expected to weaken especially thin regions of the structure, a low volume constraint  $V_T = 0.04 \text{ Vol}(D)$  is imposed. This raises the need for a high-resolution discretization of the domain. Taking advantage of symmetry, only one quarter of  $D$  is considered, which is meshed with  $192 \times 48 \times 272$  hexahedral eight-node linear Finite Elements, so that the Finite Element model is composed of 2.506.752 elements and 7.745.283 degrees of

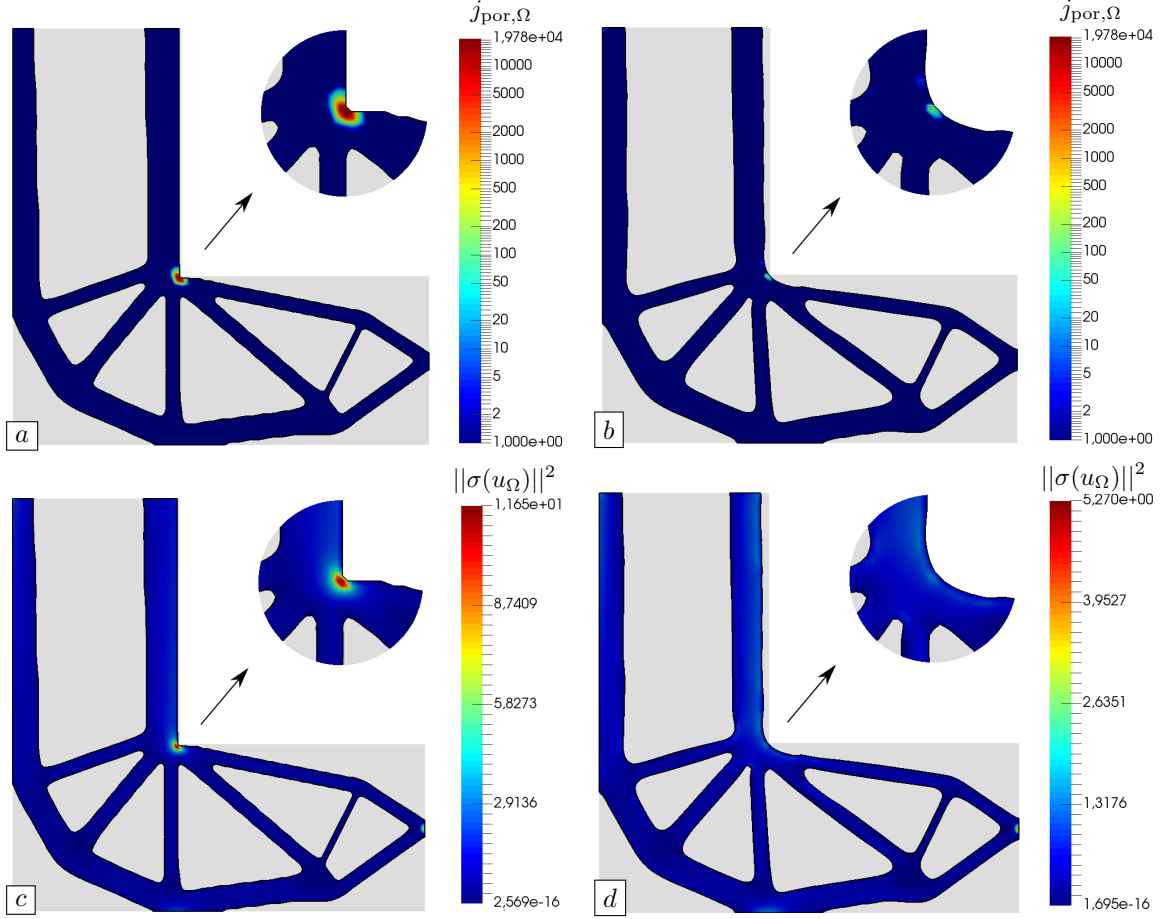


FIGURE 2.2.2. Optimized designs in the L-shaped beam test case of Section 2.2.2.1; (left column) shape  $\Omega^*$  without porosity constraint: (a) distribution of the integrand  $j_{por,\Omega}$  and (c) distribution of the stress intensity  $\|\sigma(u_\Omega)\|^2$ ; (right column) using the porosity constraint: (b) distribution of the integrand  $j_{por,\Omega}$  and (d) distribution of the stress intensity  $\|\sigma(u_\Omega)\|^2$ .

freedom. The latter is solved thanks to the GPU implementation of a matrix-free geometrical multigrid PCG described in [251].

We first minimize the compliance  $C(\Omega)$  of  $\Omega$  under the volume constraint  $\text{Vol}(\Omega) = V_T$  without porosity constraint- i.e. (2.2.5) is solved; the resulting optimized shape  $\Omega^*$  is displayed on Fig. 2.2.5 (a).

We then incorporate the porosity constraint  $J_{por}(\Omega)$  constructed from the compliance for a tolerance parameter  $\eta = 0.0003$  and  $\rho = 0.5$  – i.e.  $J_{por}(\Omega)$  is defined by (2.2.4) with  $\mathcal{C}(\Omega) = C(\Omega)$ . Starting from  $\Omega^*$ , we solve the problem (2.2.6); the evolutions of the compliance, the porosity constraint and the volume in the course of the optimization process are depicted in Fig. 2.2.4. From the value  $J_{por}(\Omega^*) = 66$ , the porosity constraint functional smoothly converges to the value 0.062 within 20 iterations. Meanwhile, the compliance  $C(\Omega)$  of the structure is increased by only 1.8%.

The isolines of the integrand  $j_{por,\Omega}$  of  $J_{por}(\Omega)$  are shown in Fig. 2.2.5. As expected, a significant reduction in the peak value of  $c_{\Omega,1}$  is achieved. This reduction is obtained by removing thin bars and smoothing sharp regions. Note that the surface in the out-of-plane direction is inflated near the reentrant corner of the hook from the initial to the final design, see Fig. 2.2.6.

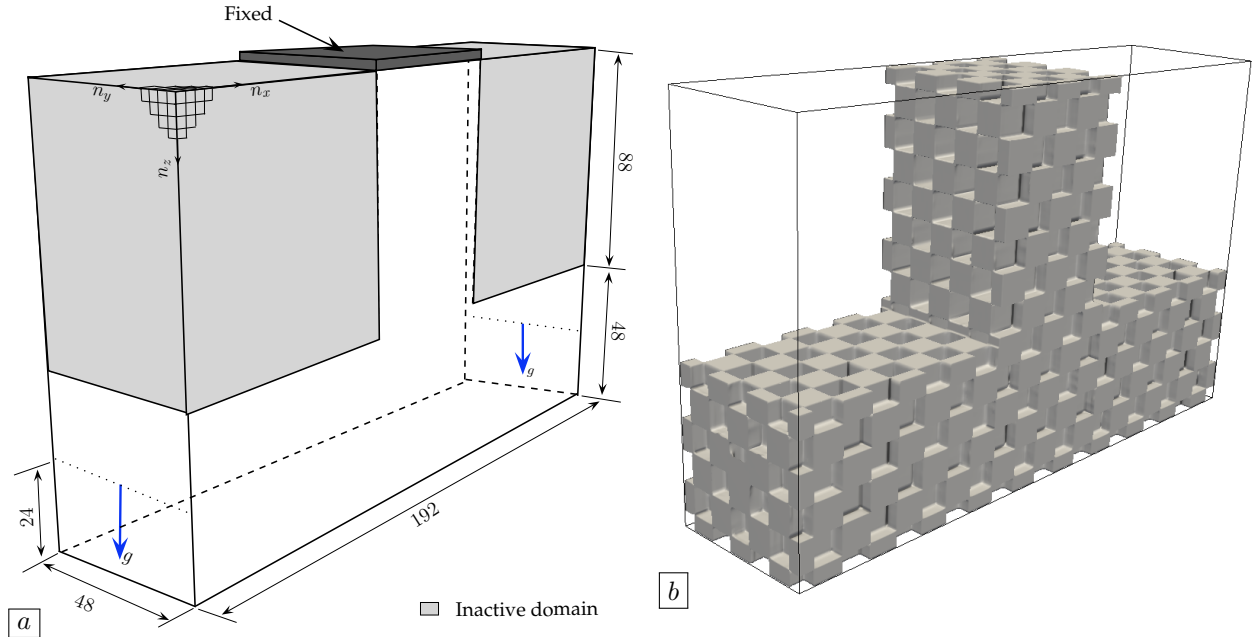


FIGURE 2.2.3. Setting of the 3d double hook test case of [Section 2.2.2.2](#): (a) computational domain  $D$  with boundary conditions; (b) initial shape.

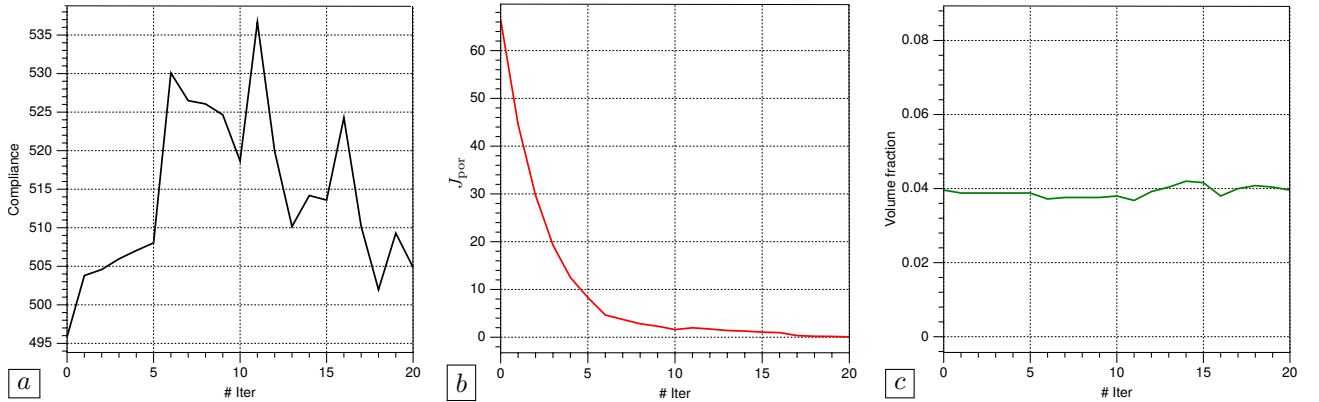


FIGURE 2.2.4. Convergence histories for (a) the compliance, (b) the porosity constraint functional and (c) the volume in the 3d double hook test case of [Section 2.2.2.2](#).

### 2.3 OPTIMAL DESIGN UNDER RANDOM UNCERTAINTIES

The investigations of this section arise in a conceptual setting which is similar to that introduced in [Section 2.1.1](#). A design variable  $h$  is optimized with respect to a cost function  $\mathcal{C}(h, f)$  which depends on the data  $f$  of the physical configuration at stake; these data still read as the sum of an unperturbed, reference value  $f_0$ , and an unknown perturbation  $\hat{f}$ , but a little more information is available about  $\hat{f}$  than a mere maximum bound on its amplitude: it is a random variable whose law is known – or at least some of its moments. This setting is fairly common in robust optimal design, see e.g. [\[139, 167, 252, 253\]](#). Leveraging this information, we construct robust optimal design criteria approximating the mean value of the cost, its variance, or a failure probability.

This section is based on the works [\[A30, A31\]](#); after presenting the key ingredients of our constructions in [Section 2.3.1](#), we discuss two numerical examples in [Section 2.3.2](#).

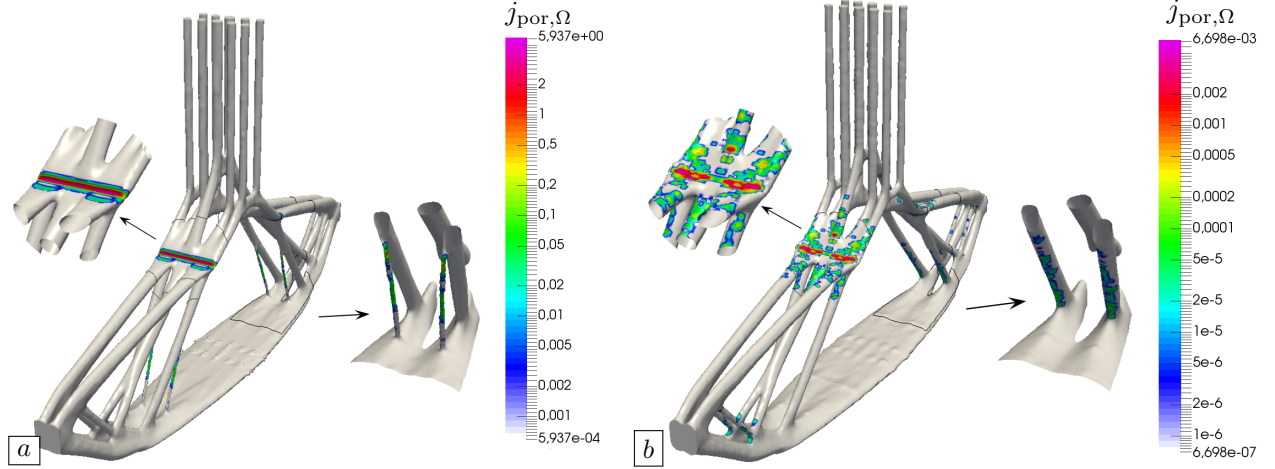


FIGURE 2.2.5. *Distribution of the integrand  $j_{por,\Omega}$  in the optimized 3d double hook of Section 2.2.2.2 for (a) the optimized shape  $\Omega^*$  (without porosity constraint), and (b) the optimized shape taking into account porosity constraint.*

### 2.3.1. Formal presentation of the main ideas in an abstract setting

Let us bring the abstract and formal setting of Section 2.1.1 back into use: we aim to optimize a design variable  $h \in \mathcal{H}$  with respect to a cost function  $\mathcal{C}(h, f) = S(f, u_{h,f})$ . The latter depends on the physical data  $f \in \Xi$  via a state  $u_{h,f}$ , which is the solution in the Hilbert space  $(V, \|\cdot\|_V)$  to the equation

$$\mathcal{A}(h)u_{h,f} = b(f),$$

see (2.1.2) and (2.1.3).

The actual data  $f = f_0 + \hat{f}$  deviate from a known reference value  $f_0$  by a ‘‘small’’ perturbation  $\hat{f}$  which is uncertain, say  $f \equiv \hat{f}(\omega)$  where the event variable  $\omega$  belongs to a probability space  $(\mathcal{O}, \mathcal{F}, \mathbb{P})$ . In practice, it is often unnecessary to refer to this event space, as it contains too much unnecessary – and unavailable – information. Instead, the probability law of  $\hat{f}$  is given, which is the push-forward  $\hat{f}_\#\mathbb{P}$  of the measure  $\mathbb{P}$  to the data space  $\Xi$ , that is:

$$(2.3.1) \quad \forall A \subset \Xi, \quad \hat{f}_\#\mathbb{P}(A) = \mathbb{P} \left\{ \omega \in \mathcal{O}, \hat{f}(\omega) \in A \right\}.$$

Loosely speaking, only the information about the probability for  $\hat{f}$  to take particular values is retained, and not the individual events for which this occurs. For the purpose of this section, however, it is clearer to keep the mention to this event space.

We rely on the following assumptions about  $\hat{f}$ :

- $\hat{f}$  is ‘‘small’’; depending on the situation, this may mean that  $\hat{f}(\omega)$  is ‘‘small’’ for all event  $\omega$  – i.e.  $\hat{f}$  is small as an element in  $L^\infty(\mathcal{O}, \Xi)$  – or that it is ‘‘small’’ for ‘‘most’’ events  $\omega \in \mathcal{O}$ , but that it may occasionally take ‘‘large’’ values – i.e.  $\hat{f}$  is ‘‘small’’ as an element in  $L^p(\mathcal{O}, \Xi)$  for some  $1 \leq p < \infty$ .
- $\hat{f}$  has a finite-dimensional structure: it arises as a finite sum

$$(2.3.2) \quad \hat{f}(\omega) = \sum_{i=1}^N f_i \xi_i(\omega),$$

where the  $f_i \in \Xi$  are deterministic data and the  $\xi_i(\omega)$  are real-valued random variables with mean value 0 and identity covariance matrix:

$$(2.3.3) \quad \int_{\mathcal{O}} \xi_i(\omega) d\mathbb{P}(\omega) = 0, \text{ and } \int_{\mathcal{O}} \xi_i(\omega) \xi_j(\omega) d\mathbb{P}(\omega) = \delta_{ij}, \quad i, j = 1, \dots, N.$$

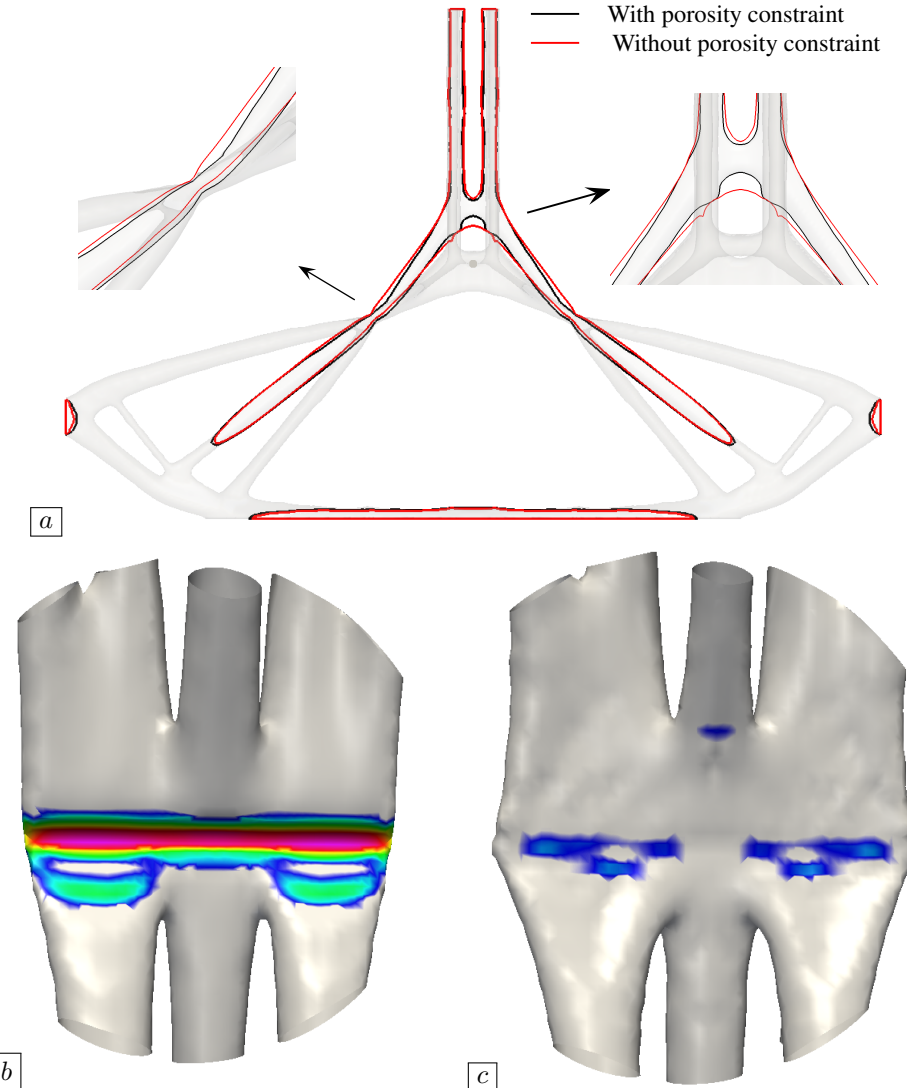


FIGURE 2.2.6. Comparison between the optimized designs for the 3d double hook problem of Section 2.2.2.2 obtained with and without porosity constraint; (a) cut in the plane  $y = 0$ ; (bottom row) zoom near the corner of (b) the optimized shape  $\Omega^*$  without porosity constraint, and (c) the optimized shape considering the porosity constraint  $J_{\text{por}}(\Omega)$ .

Such a structure is typical of random variables in  $L^2(\mathcal{O}, \Xi)$  when  $\Xi$  is a Hilbert space: it results in this case from the truncation of a Karhunen-Loeve expansion for  $\hat{f}(\omega)$ , see Section 2.B.

In this setting, we wish to address optimal design problems featuring two types of statistical quantities:

- Some moments of the uncertain cost  $\mathcal{C}(h, f_0 + \hat{f}(\omega))$ , such as its mean value  $J_{\text{mean}}(h)$ , defined by:

$$(2.3.4) \quad J_{\text{mean}}(h) = \int_{\mathcal{O}} \mathcal{C}(h, f_0 + \hat{f}(\omega)) \, d\mathbb{P}(\omega),$$

or its variance  $J_{\text{var}}(h)$ , given by:

$$(2.3.5) \quad J_{\text{var}}(h) = \int_{\mathcal{O}} \left( \mathcal{C}(h, f_0 + \hat{f}(\omega)) - J_{\text{mean}}(h) \right)^2 \, d\mathbb{P}(\omega).$$

- A failure probability  $J_{\text{fail}}(h)$  of the design  $h$ :

$$(2.3.6) \quad J_{\text{fail}}(h) = \mathbb{P}\left\{\omega \in \mathcal{O}, \quad \mathcal{C}(h, f_0 + \hat{f}(\omega)) > \alpha\right\},$$

where  $\alpha$  is a threshold encoding the maximum value of the cost guaranteeing a safe use of  $h$ .

Unfortunately, these quantities and their derivatives with respect to the design are difficult to calculate in practice, as their expressions feature integrals over the event space  $\mathcal{O}$ , whose evaluation requires advanced and very costly numerical methods, such as Monte-Carlo algorithms, (isotropic or anisotropic) sparse grid collocation methods [252, 285], etc, see e.g. [230] for an overview.

To alleviate this issue, we leverage the “smallness” and “finite-dimensionality” of  $\hat{f}$  to construct approximate versions of the functionals  $J_{\text{mean}}(h)$ ,  $J_{\text{var}}(h)$  and  $J_{\text{fail}}(h)$ . Our developments hinge on the second-order expansions of the mappings  $f \mapsto \mathcal{C}(h, f)$  and  $f \mapsto u_{h,f}$ . Let us write:

$$u_{h,f} \approx u_{h,f_0} + u_{h,f_0}^1(\hat{f}) + \frac{1}{2}u_{h,f_0}^2(\hat{f}, \hat{f}), \text{ where}$$

$$u_{h,f_0}^1(\hat{f}) := \left. \frac{\partial u_{h,f}}{\partial f} \right|_{f=f_0}(\hat{f}) \text{ and } u_{h,f_0}^2(\hat{f}, \hat{f}) := \left. \frac{\partial u_{h,f}^1(\hat{f})}{\partial f} \right|_{f=f_0}(\hat{f})$$

are the first- and second-order derivatives of the state mapping  $f \mapsto u_{h,f}$ , which are the solutions in  $V$  to the respective equations:

$$\mathcal{A}(h)u_{h,f_0}^1(\hat{f}) = \frac{\partial b}{\partial f}(f_0)(\hat{f}), \text{ and } \mathcal{A}(h)u_{h,f_0}^2(\hat{f}, \hat{f}) = \frac{\partial^2 b}{\partial f^2}(f_0)(\hat{f}, \hat{f}).$$

The cost function  $\mathcal{C}(h, f)$  can be expanded in a similar fashion thanks to the chain rule:

$$(2.3.7) \quad \begin{aligned} \mathcal{C}(h, f_0 + \hat{f}) &= S(f_0 + \hat{f}, u_{h,f_0+\hat{f}}) \\ &\approx S(f_0, u_{h,f_0}) + \frac{\partial S}{\partial f}(f_0, u_{h,f_0})(\hat{f}) + \frac{\partial S}{\partial u}(f_0, u_{h,f_0})(u_{h,f_0}^1(\hat{f})) \\ &\quad + \frac{1}{2} \left( \frac{\partial^2 S}{\partial f^2}(f_0, u_{h,f_0})(\hat{f}, \hat{f}) + 2 \frac{\partial^2 S}{\partial f \partial u}(f_0, u_{h,f_0})(\hat{f}, u_{h,f_0}^1(\hat{f})) + \right. \\ &\quad \left. \frac{\partial^2 S}{\partial u^2}(f_0, u_{h,f_0})(u_{h,f_0}^1(\hat{f}), u_{h,f_0}^1(\hat{f})) + \frac{\partial S}{\partial u}(f_0, u_{h,f_0})(u_{h,f_0}^2(\hat{f}, \hat{f})) \right). \end{aligned}$$

### 2.3.1.1. Approximation of moments of the cost function

We first construct an approximate version  $\tilde{J}_{\text{mean}}(h)$  of the mean value  $J_{\text{mean}}(h)$  of the uncertain cost  $\mathcal{C}(h, f_0 + \hat{f}(\omega))$ , see (2.3.4). To this end, we first insert the finite-dimensional structure (2.3.2) into the truncated expansion (2.3.7) to second-order, which yields:

$$(2.3.8) \quad \begin{aligned} \mathcal{C}(h, f_0 + \hat{f}(\omega)) &\approx S(f_0, u_{h,f_0}) + \sum_{i=1}^N c_{1,i} \xi_i(\omega) + \sum_{i=1}^N \sum_{j \neq i} c_{2,ij} \xi_i(\omega) \xi_j(\omega) \\ &\quad + \frac{1}{2} \sum_{i=1}^N \left( \frac{\partial^2 S}{\partial f^2}(f_0, u_{h,f_0})(f_i, f_i) + 2 \frac{\partial^2 S}{\partial f \partial u}(f_0, u_{h,f_0})(f_i, u_{h,f_0}^1(f_i)) + \frac{\partial^2 S}{\partial u^2}(f_0, u_{h,f_0})(u_{h,f_0}^1(f_i), u_{h,f_0}^1(f_i)) \right. \\ &\quad \left. + \frac{\partial S}{\partial u}(f_0, u_{h,f_0})(u_{h,f_0}^2(f_i, f_i)) \right) \xi_i(\omega)^2. \end{aligned}$$

where the terms  $c_{1,i}$  and  $c_{2,ij}$ ,  $i \neq j$  belong to  $V$  and do not depend on the event variable  $\omega$ ; these terms do not need to be made explicit for our purpose.

Our approximate functional  $\tilde{J}_{\text{mean}}(h)$  is then defined to be the mean value of the above expression:

$$(2.3.9) \quad \begin{aligned} \tilde{J}_{\text{mean}}(h) &= S(f_0, u_{h,f_0}) + \frac{1}{2} \sum_{i=1}^N \frac{\partial^2 S}{\partial f^2}(f_0, u_{h,f_0})(f_i, f_i) + \sum_{i=1}^N \frac{\partial^2 S}{\partial f \partial u}(f_0, u_{h,f_0})(f_i, u_{h,i}^1) \\ &\quad + \frac{1}{2} \sum_{i=1}^N \frac{\partial^2 S}{\partial u^2}(f_0, u_{h,f_0})(u_{h,f_0,i}^1, u_{h,f_0,i}^1) + \frac{1}{2} \frac{\partial S}{\partial u}(f_0, u_{h,f_0})(u_{h,f_0}^2), \end{aligned}$$

where we have defined the reduced sensitivities:

$$(2.3.10) \quad u_{h,f_0,i}^1 = u_{h,f_0}^1(f_i) \text{ and } u_{h,f_0}^2 = \sum_{i=1}^N u_{h,f_0}^2(f_i, f_i),$$

as the solutions to the following equations:

$$(2.3.11) \quad \mathcal{A}(h)u_{h,f_0,i}^1 = \frac{\partial b}{\partial f}(f_0)(f_i), \text{ and } \mathcal{A}(h)u_{h,f_0}^2 = \sum_{i=1}^N \frac{\partial^2 b}{\partial f^2}(f_0)(f_i, f_i).$$

Note that the terms involving the quantities  $c_{1,i}$  and  $c_{2,ij}$  vanish when passing from (2.3.8) to (2.3.9) owing to the assumptions (2.3.3) on the random variables

An approximation  $\tilde{J}_{\text{var}}(h)$  of the variance functional in (2.3.5) can be constructed by following a similar trail:

$$\tilde{J}_{\text{var}}(h) = \sum_{i=1}^N \left( \frac{\partial S}{\partial f}(f_0, u_{h,f_0})(f_i) + \frac{\partial S}{\partial u}(f_0, u_{h,f_0})(u_{h,f_0,i}^1) \right)^2.$$

Both functions  $\tilde{J}_{\text{mean}}(h)$  and  $\tilde{J}_{\text{var}}(h)$  can be integrated into classical optimal design problems. Their derivatives are obtained by a tedious calculation thanks to the adjoint method, exactly along the lines of Section 1.3.3.6.

**Remark 2.3.1** *The computational cost entailed by the calculation of the approximate functions  $\tilde{J}_{\text{mean}}(h)$  and  $\tilde{J}_{\text{var}}(h)$  may be large, depending on the number  $N$  of elements in the sum (2.3.2):  $(N+2)$  linear systems have to be solved for the evaluation of  $J_{\text{mean}}(h)$ , associated to the functions  $u_{h,f_0}$ ,  $u_{h,f_0,i}^1$  and  $u_{h,f_0}^2$  and  $(N+2)$  adjoint systems are involved in the calculation of its derivative. In practice,  $N$  corresponds to the number of retained modes after truncation of a Karhunen-Loëve expansion for  $f$ . For instance, when the correlation kernel of  $\hat{f}$  is analytic, one may prove that its eigenvalues decay exponentially fast, and so do the norms of the data  $f_i$ . Then, only a few modes are needed for the decomposition (2.3.2) to be an accurate approximation of  $\hat{f}$ , see again Section 2.B about these questions.*

**Remark 2.3.2** *The approximate function  $\tilde{J}_{\text{mean}}(h)$  in (2.3.9) has a remarkably simple expression in the particular case where the cost  $S(f, u)$  is quadratic in terms of  $u$  and the state mapping  $f \mapsto u_{h,f}$  is quadratic, say:*

$$S(f, u) = \langle \mathcal{B}u, u \rangle_V, \text{ where } \mathcal{B} : V \rightarrow V \text{ is a linear and continuous mapping.}$$

*This situation arises for instance in the context of structural optimization of Section 1.2.3 when the cost function  $C(h, f)$  is the compliance and the data  $f$  stand for loads. It then turns out that  $\tilde{J}_{\text{mean}}(h)$  coincides with the exact mean-value function  $J_{\text{mean}}(h)$  and:*

$$\tilde{J}_{\text{mean}}(h) = S(f_0, u_{h,f_0}) + \sum_{i=1}^N \langle \mathcal{B}u_{h,f_0,i}^1, u_{h,f_0,i}^1 \rangle_V.$$

### 2.3.1.2. Approximation of probability of failure

We now turn to the device of a suitable approximation  $\tilde{J}_{\text{fail}}(h)$  of the failure probability  $J_{\text{fail}}(h)$  defined in (2.3.6). The main idea echoes to the so-called First-Order Reliability Method (FORM) in the context of reliability-based optimization, see [126]: we rely on an additional assumption about the uncertainty  $\hat{f}$ : the

random variables  $\xi_i$  are Gaussian and independent. In particular, the cumulative distribution function of any of the  $\xi_i$  reads:

$$\mathbb{P}\left\{\omega \in \mathcal{O}, \xi_i(\omega) < t\right\} = \Phi(t) := \frac{1}{\sqrt{2\pi}} \int_{-\infty}^t e^{-u^2/2} du.$$

This assumption is satisfied, for instance, in the case when  $\hat{f}$  is a Gaussian random field, see [Section 2.B.3](#).

Let us rewrite the truncated expansion of the cost in [\(2.3.8\)](#) at first-order under the following form:

$$\mathcal{C}(h, f_0 + \hat{f}(\omega)) \approx b(h) + a(h) \cdot \xi(\omega),$$

with

$$b(h) = S(f_0, u_{h,f_0}), \text{ and } a_i(h) = \frac{\partial S}{\partial f}(f_0, u_{h,f_0})(f_i) + \frac{\partial S}{\partial u}(f_0, u_{h,f_0})(u_{h,f_0,i}^1), \quad i = 1, \dots, N,$$

where the functions  $u_{h,f_0,i}$  satisfy [\(2.3.10\)](#) and [\(2.3.11\)](#). We define our approximate functional  $\tilde{J}_{\text{fail}}(h)$  to be the probability that this truncated expansion exceed  $\alpha$ , that is:

$$\tilde{J}_{\text{fail}}(h) = \mathbb{P}\left\{\omega \in \mathcal{O}, b(h) + a(h) \cdot \xi(\omega) > \alpha\right\}.$$

Since the random vector  $\xi = (\xi_1, \dots, \xi_N)$  is Gaussian, this quantity can be calculated explicitly. Indeed,

$$\tilde{J}_{\text{fail}}(h) = \frac{1}{(2\pi)^{N/2}} \int_{\{\xi \in \mathbb{R}^N, b(h) + a(h) \cdot \xi > \alpha\}} e^{-\frac{|\xi|^2}{2}} d\xi.$$

This expression is the integral of a multi-variate Gaussian function on a half-space of  $\mathbb{R}^N$ ; introducing any orthogonal transformation  $A : \mathbb{R}^N \rightarrow \mathbb{R}^N$  such that  $Ae_N = \frac{a(h)}{|a(h)|}$ , we obtain by the successive use of a change of variables and the Fubini theorem:

$$\begin{aligned} \tilde{J}_{\text{fail}}(h) &= \frac{1}{(2\pi)^{N/2}} \int_{\{\xi \in \mathbb{R}^N, e_d \cdot A^T \xi > \frac{\alpha - b(h)}{|a(h)|}\}} e^{-\frac{|\xi|^2}{2}} d\xi \\ &= \frac{1}{(2\pi)^{N/2}} \int_{\{\xi \in \mathbb{R}^N, e_d \cdot \zeta > \frac{\alpha - b(h)}{|a(h)|}\}} e^{-\frac{|\zeta|^2}{2}} d\zeta \\ &= \frac{1}{(2\pi)^{1/2}} \int_{\{\zeta_1 \in \mathbb{R}, \zeta_1 > \frac{\alpha - b(h)}{|a(h)|}\}} e^{-\frac{\zeta_1^2}{2}} d\zeta_1 \\ &= \Phi\left(-\frac{\alpha - b(h)}{|a(h)|}\right). \end{aligned}$$

Again,  $\tilde{J}_{\text{fail}}(h)$  may be integrated as the objective or a constraint into a classical optimal design algorithm; its derivative may be calculated thanks to the classical adjoint method.

**Remark 2.3.3** *The approximation procedures discussed in this section can be rigorously justified under some assumptions which depend on the particular situation. Loosely speaking,  $\tilde{J}_{\text{mean}}(h)$  can be proved to be a second-order approximation of  $J_{\text{mean}}(h)$  in terms of the “smallness” of the deviation  $\hat{f}$  between  $f$  and  $f_0$ ;  $\tilde{J}_{\text{var}}(h)$  and  $\tilde{J}_{\text{fail}}(h)$  can likewise be proved to be first-order approximations of  $J_{\text{var}}(h)$  and  $J_{\text{fail}}(h)$ , respectively.*

### 2.3.2. A few numerical results

#### 2.3.2.1. Optimization of the shape of a 2d bridge under random load uncertainties

This first numerical example arises in the exact same physical context as the 2d bridge test case considered in [Section 2.1.2.1](#), see [Fig. 2.3.1](#) (top, left): shapes are contained in a working domain  $D$  with size  $2 \times 1.5$ ; they are clamped near their lower-left corner, their vertical displacement is prevented near their lower-right corner, and a reference body force  $f_0 = (0, -10)$  is applied on a region around the center of their lower side. The perturbations  $\hat{f}(\omega)$  on these forces are expected to be of the form:

$$\forall x \in D, \quad \hat{f}(x, \omega) = \sum_{i=1}^2 f_i(x) \xi_i(\omega),$$

where the loads  $f_1, f_2$  equal  $(0, -m)$  and are supported on either of the blue regions of [Fig. 2.3.1](#) (top, left).

The cost  $\mathcal{C}(\Omega, f)$  of a shape  $\Omega$  when the actual loads equal  $f$  is the compliance:

$$\mathcal{C}(\Omega, f) = \int_{\Omega} f \cdot u_{\Omega, f} \, dx,$$

and we aim to minimize a weighted sum of the (approximate) mean value and standard deviation of this cost, under a volume constraint, that is, we solve:

$$\min_{\Omega} \tilde{J}_{\text{mean}}(\Omega) + \delta \sqrt{\tilde{J}_{\text{var}}(\Omega)}, \text{ s.t. } \text{Vol}(\Omega) = V_T,$$

where the volume target is set to  $V_T = 0.75$ .

The level set method for shape and topology optimization is used on a fixed mesh of  $D$  to this end, see [Section 1.4.6.2](#) for a presentation of the latter. The results obtained for different values of the parameters  $m$  and  $\delta$  are represented on the first 3 rows of [Fig. 2.3.1](#).

It is instructive to compare them with those produced by the worst-case approach described in [Section 2.1](#), which are displayed on the last row of [Fig. 2.3.1](#). As expected, the nominal performance of shapes is worse when using the worst-case approach. This confirms the previous observation that worst-case optimal design formulations generally produce very pessimistic designs, so that a probabilistic approach should be preferred when some statistical information is available about the uncertainties.

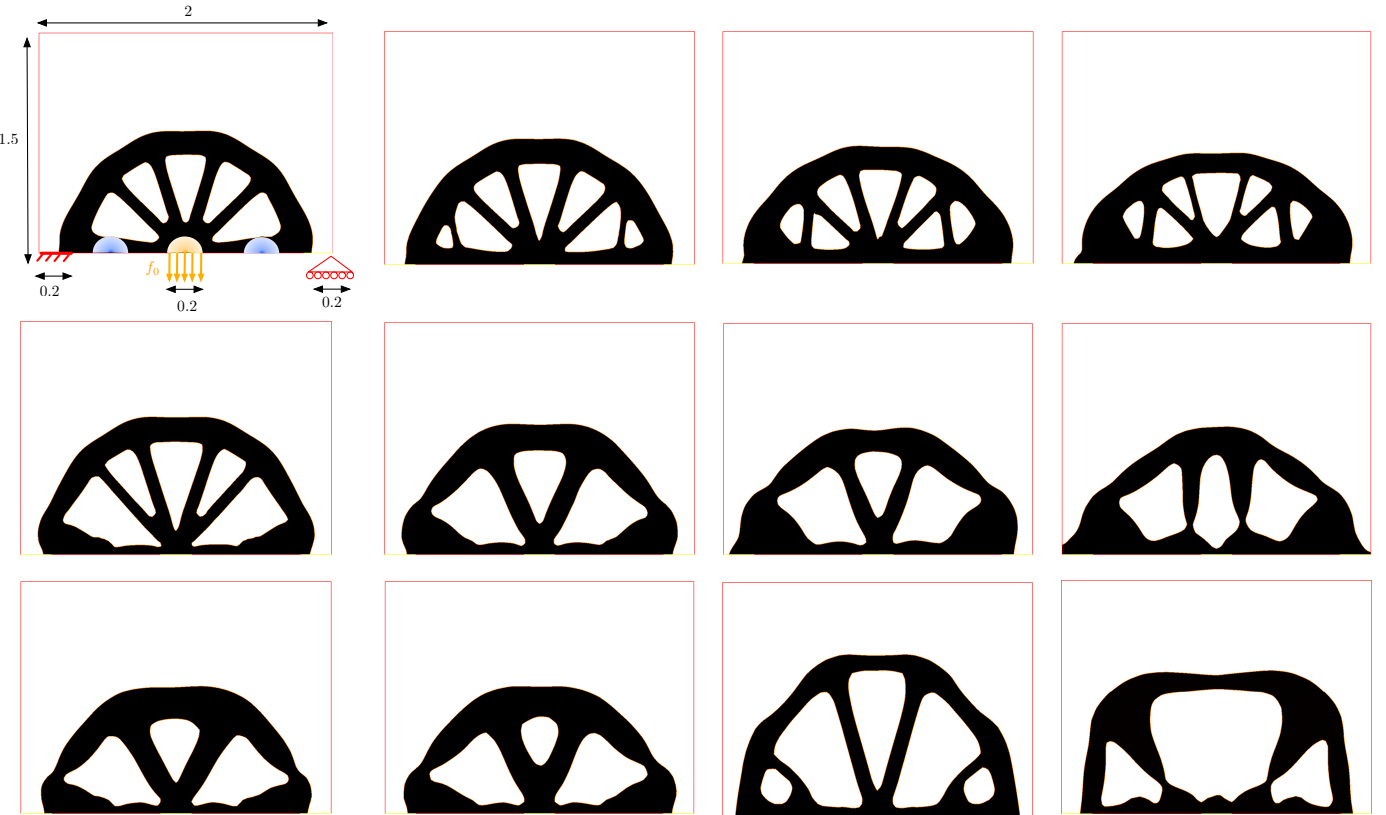


FIGURE 2.3.1. Optimized shapes in the bridge optimization example under random load uncertainties of [Section 2.3.2.1](#); the parameter values are (Upper row)  $\delta = 0$  and  $m = 1$  (with details of the test-case),  $2, 5, 10$ ; (middle row)  $\delta = 3$  and  $m = 1, 2, 5, 10$ ; (bottom row) Optimized shapes for the linearized worst-case design approach with  $m = 1, 2, 5, 10$ .

### 2.3.2.2. Optimization of a 2d gripping mechanism under random material uncertainties

This second example deals with the treatment of uncertainties over the elastic properties of the constituent material of shapes, and more precisely over the Young's modulus  $E$  of the material, see [Section 1.2.2.3](#) for an explanation.

The shape optimization setting of interest is that of the classical gripping mechanism test-case, as depicted in [Fig. 2.3.2](#) (top, left). The considered shape  $\Omega$  is enclosed in a  $1 \times 1$  working domain  $D$  in 2d. It is clamped on its upper- and lower-left corners, and a horizontal load  $g = (0.1, 0)$  is applied on a region around the center of its left-hand side. In the reference configuration,  $\Omega$  is made of an elastic material with homogeneous Young's modulus  $E(x) = E_0 = 1$  and Poisson's ratio  $\nu = 0.3$ .

We aim to optimize the design of  $\Omega$  so that its jaws (the blue parts in [Fig. 2.3.2](#) (top, left)) close in the deformed configuration, which is characterized by the solution  $u_{\Omega, E}$  to [\(Elas\)](#). To this end, we consider the cost function  $\mathcal{C}(\Omega, E)$  defined by:

$$\mathcal{C}(\Omega, E) = \int_{\Omega} k(x) |u_{\Omega, E} - u_T|^2 \, dx,$$

where  $k(x)$  is a weighting factor supported near the jaws and the target displacement  $u_T$  is tuned so that the jaws of the mechanism close.

The considered uncertainties  $\widehat{E}$  over the Young's modulus  $E(x)$  of the material are described by a random field  $\widehat{E} \equiv \widehat{E}(x, \omega)$ , see [Section 2.B](#). The covariance kernel of the latter is defined by:

$$\forall x, y \in D, \quad \text{Cov}(\widehat{E})(x, y) = m^2 e^{-\frac{|x-y|}{\delta}},$$

where  $m$  is the amplitude of perturbations and the characteristic length  $\delta$  is set to 0.1. A Karhunen-Loëve decomposition of this random field is performed (see again [Section 2.B](#)), then truncated after its first three terms, so that  $\widehat{E}$  has the form

$$\widehat{E}(x, \omega) = \sum_{i=1}^3 E_i(x) \xi_i(\omega),$$

where  $E_i(x)$  are deterministic functions on  $D$  and the  $\xi_i$  are centered, normalized and uncorrelated random variables.

In this context, we solve the robust optimization problem

$$\min_{\Omega} \widetilde{J}_{\text{mean}}(\Omega)$$

for different values of the parameters  $m$ ; the results are depicted on [Fig. 2.3.2](#). Understandably, as the magnitude of uncertainties grows, the hinges of the device get thicker in order to accommodate more pessimistic situations, to the expense of the nominal performance of the shape.

## 2.4 A PERSPECTIVE: DISTRIBUTIONALLY ROBUST SHAPE OPTIMIZATION

This section is a natural continuation of the investigations of the previous [Section 2.3](#) about random uncertainties. It addresses a conceptual flaw in the modeling of the uncertain data  $f(\omega)$ , whose law is assumed to be known exactly. This assumption is unrealistic as most often in practice, it can at best be estimated.

Recently, the paradigm of distributionally robust optimization has emerged as an elegant means to overcome this conceptual shortcoming, see [\[239, 309, 367, 383\]](#). In this framework, one minimizes the worst (i.e. largest) value  $\sup_{\mathbb{Q}} \int_{\Xi} \mathcal{C}(h, f) \, d\mathbb{Q}(f)$  of the expectation of the cost  $\mathcal{C}(h, f)$  of a design  $h$  (or of another of risk measure depending on the latter) when the actual law  $\mathbb{Q}$  of  $f$  is “close” to a known nominal law  $\mathbb{P}$ , obtained e.g. by empirical sampling. To the best of our knowledge, distributional robustness has hitherto been restricted to quite academic situations; the present work aims to introduce this idea in the realm of optimal design.

After a general presentation of the incorporation of distributional robustness in optimal design in [Section 2.4.1](#), we sketch two numerical illustrations in [Section 2.4.2](#). This section is based on the short note [\[A1\]](#), which heralds longer-term investigations, a few perspectives of which are outlined in [Section 2.4.3](#).

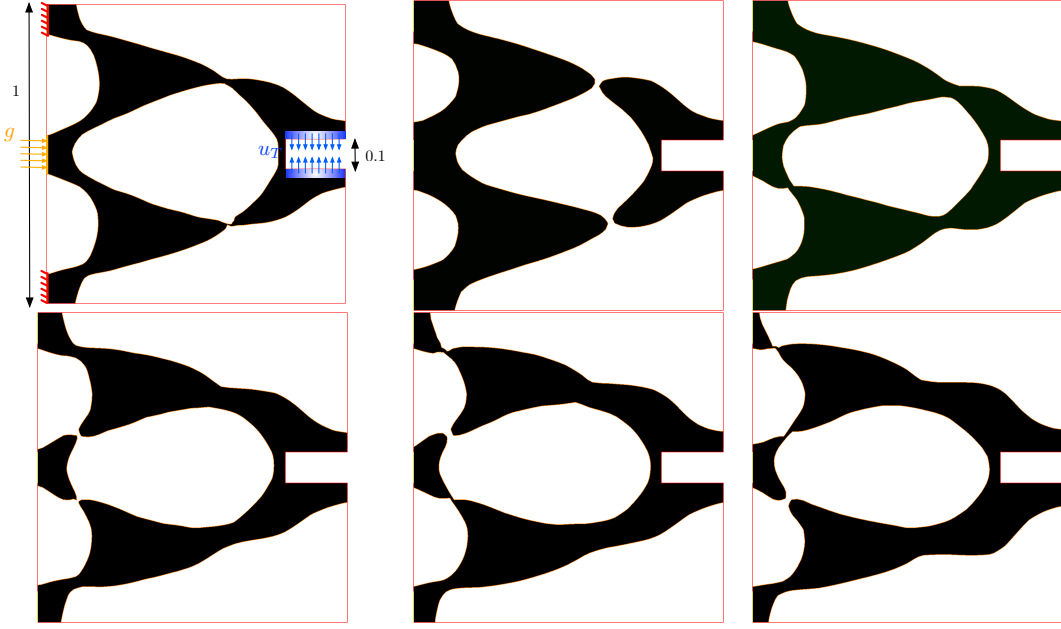


FIGURE 2.3.2. (From left to right, top to bottom) Optimized gripping mechanisms obtained in Section 2.3.2.2 when perturbations of order  $m = 0$  (with details of the test-case),  $0.5, 1, 1.5, 2, 2.5$  are expected over the Young's modulus of the material.

#### 2.4.1. Formal presentation of the main ideas

Let us slip again into the abstract optimal design setting introduced in Section 2.1.1: we aim to optimize a design variable  $h \in \mathcal{H}$  with respect to a cost function  $\mathcal{C}(h, f)$  which depends on the uncertain data  $f \in \Xi$  of the physical situation. Unlike that of the previous Section 2.3, the present discussion does not need to refer to the event space  $\mathcal{O}$ , but only to the laws (2.3.1) of the considered random variables as elements in the set  $\mathcal{P}(\Xi)$  of probability measures on the data set  $\Xi$ . The notation  $\mathbb{P}$  used in the previous section for the probability measure on  $\mathcal{O}$  now stands for such a probability law. Additionally, we suppose that the set  $\Xi$  containing all possible data is a compact subset of  $\mathbb{R}^d$ . Again, in practice, this reduction can be obtained by retaining only the dominant data functions in a Karhunen-Loëve decomposition of  $f$ , see Section 2.B.

The considered data  $f$  are governed by a probability law  $\mathbb{Q} \in \mathcal{P}(\Xi)$  which is unknown. Fortunately,  $\mathbb{Q}$  can be estimated by a nominal law  $\mathbb{P}$ , which is typically the empirical sum of a series of observations  $f_i \in \Xi$ ,  $i = 1, \dots, N$ :

$$\mathbb{P} = \frac{1}{N} \sum_{i=1}^N \delta_{f_i}.$$

We then assume that  $\mathbb{Q}$  is “close” to  $\mathbb{P}$  within a maximum distance  $m$ .

This notion of distance between probability measures in  $\mathcal{P}(\Xi)$  can be appraised in a variety of manners. The most prevalent quantity used to this end in the literature is certainly the so-called Kullback-Leibler divergence, which suffers from the undesirable feature to be infinite as soon as the two considered measures do not have the same support, see [178, 322].

Following the contributions [185, 270], to circumvent this drawback, we rely on the Wasserstein distance from optimal transport theory [260, 322]. The latter is defined by the following formula:

$$(2.4.1) \quad \forall \mathbb{P}, \mathbb{Q} \in \mathcal{P}(\Xi), \quad W(\mathbb{P}, \mathbb{Q}) = \inf \int_{\Xi \times \Xi} c(f, \zeta) d\pi(f, \zeta),$$

where the infimum is taken over transport plans  $\pi \in \mathcal{P}(\Xi \times \Xi)$  between  $\mathbb{P}$  and  $\mathbb{Q}$ . These are probability measures on the product space  $\Xi \times \Xi$  whose first and second marginals  $\pi_1$  and  $\pi_2$  coincide with  $\mathbb{P}$  and  $\mathbb{Q}$ ,

respectively, that is:

$$\forall \varphi \in \mathcal{C}(\Xi), \quad \int_{\Xi \times \Xi} \varphi(f) d\pi(f, \zeta) = \int_{\Xi} \varphi(f) d\mathbb{P}(f), \text{ and } \int_{\Xi \times \Xi} \varphi(\zeta) d\pi(f, \zeta) = \int_{\Xi} \varphi(\zeta) d\mathbb{Q}(\zeta).$$

Intuitively, the ground cost  $c(f, \zeta)$  on the set  $\Xi$  of loads measures the cost of “moving a unit of mass” from  $f$  to  $\zeta$ , and  $\pi(f, \zeta)$  encodes the “quantity of mass” transported from  $f$  to  $\zeta$ . In the following, the function  $c(\cdot, \cdot)$  is assumed to be quadratic:  $c(f, \zeta) := |f - \zeta|^2$ . We refer e.g. to [322] about the properties of the Wasserstein distance, and to [299] for an overview of its use in applications.

With these definitions at hand, the distributionally robust version of the cost function  $\mathcal{C}(h, f)$  is the worst (maximum) value of the expected cost when the law  $\mathbb{Q} \in \mathcal{P}(\Xi)$  of the uncertain parameter  $f$  is at distance less than a given threshold  $m$  from the nominal law  $\mathbb{P}$ :

$$(2.4.2) \quad J_{\text{dr}}(h) = \sup_{\substack{\mathbb{Q} \in \mathcal{P}(\Xi) \\ W(\mathbb{P}, \mathbb{Q}) \leq m}} \int_{\Xi} \mathcal{C}(h, f) d\mathbb{Q}(f).$$

**Remark 2.4.1** In the distributionally robust optimization literature, the subset of  $\mathcal{P}(\Xi)$  gathering the possible probability laws of the uncertain data (over which the supremum is taken in (2.4.2)) is often called the ambiguity set. In the present study, this set is made of the probability laws which are “close” to the nominal law  $\mathbb{P}$  within a certain distance, but other types of ambiguity sets would be worth considering, see Section 2.4.3.

This functional is unfortunately difficult to incorporate into a minimization problem for the design  $h$ , as it would turn the latter into a worst-case problem. To alleviate this issue, we consider the entropy-regularized version of the Wasserstein distance proposed in [138]:

$$(2.4.3) \quad W_{\varepsilon}(\mathbb{P}, \mathbb{Q}) = \inf_{\substack{\pi \in \mathcal{P}(\Xi \times \Xi) \\ \pi_1 = \mathbb{P}, \pi_2 = \mathbb{Q}}} \left\{ \int_{\Xi \times \Xi} c(f, \zeta) d\pi(f, \zeta) + \varepsilon H(\pi) \right\},$$

where  $\varepsilon > 0$  is a “small” smoothing parameter, the entropy  $H(\pi)$  of an element  $\pi \in \mathcal{P}(\Xi \times \Xi)$  is defined by

$$H(\pi) = \begin{cases} \int_{\Xi \times \Xi} \log \frac{d\pi}{d\pi_0} d\pi & \text{if } \pi \text{ is absolutely continuous w.r.t. } \pi_0, \\ \infty & \text{otherwise,} \end{cases}$$

and  $\pi_0 \in \mathcal{P}(\Xi \times \Xi)$  is a reference coupling. According to [54], a judicious choice about  $\pi_0$ , offering nice theoretical guarantees, is provided by the following formula:

$$(2.4.4) \quad \pi_0(f, \zeta) = \mathbb{P}(f) d\nu_f(\zeta), \quad \text{with } d\nu_f(\zeta) := \alpha_f e^{-\frac{c(f, \zeta)}{2\sigma}} \mathbb{1}_{\Xi}(\zeta) d\zeta$$

for some  $\sigma > 0$  and a normalization factor  $\alpha_f$  ensuring that  $d\nu_f$  is a probability distribution on  $\Xi$ . Precisely, the above definition means that

$$\text{For all continuous functions } \varphi : \Xi \times \Xi \rightarrow \mathbb{R}, \quad \int_{\Xi \times \Xi} \varphi(f, \zeta) d\pi_0(f, \zeta) = \int_{\Xi} \left( \int_{\Xi} \varphi(f, \zeta) d\nu_f(\zeta) \right) d\mathbb{P}(f).$$

We are now in position to introduce the entropy-regularized version of the distributionally robust functional  $J_{\text{dr}}(h)$ :

$$(2.4.5) \quad J_{\text{dr}, \varepsilon}(h) = \sup_{\substack{\mathbb{Q} \in \mathcal{P}(\Xi) \\ W_{\varepsilon}(\mathbb{P}, \mathbb{Q}) \leq m}} \int_{\Xi} \mathcal{C}(h, f) d\mathbb{Q}(f).$$

At first glance, the functional  $J_{\text{dr}, \varepsilon}(h)$  does not seem more tractable than  $J_{\text{dr}}(h)$ ; the key observation is that it admits a convenient dual reformulation as a minimum value. This fact is expressed by the following result from convex analysis, whose mild assumptions are omitted, and which is proved in a more general context in [54], see also [361].

**Proposition 2.4.2** Let  $\Xi$  be a convex and compact subset of  $\mathbb{R}^d$ ,  $\varphi : \Xi \rightarrow \mathbb{R}$  be a continuous function and let  $\mathbb{P} \in \mathcal{P}(\Xi)$  be a probability measure. For a sufficiently small value of  $\sigma$ , the following equality holds:

$$\sup_{W_\varepsilon(\mathbb{P}, \mathbb{Q}) \leq m} \int_{\Xi} \varphi(f) d\mathbb{Q}(f) = \inf_{\lambda \geq 0} \left\{ \lambda m + \lambda \varepsilon \int_{\Xi} \log \left( \int_{\Xi} e^{\frac{\varphi(\zeta) - \lambda c(f, \zeta)}{\lambda \varepsilon}} d\nu_f(\zeta) \right) d\mathbb{P}(f) \right\}.$$

This formula yields the following alternative expression of  $J_{\text{dr}, \varepsilon}(h)$  as a minimum value:

$$(2.4.6) \quad J_{\text{dr}, \varepsilon}(h) = \inf_{\lambda \geq 0} \left\{ \lambda m + \lambda \varepsilon \int_{\Xi} \log \left( \int_{\Xi} e^{\frac{\mathcal{C}(h, f) - \lambda c(f, \zeta)}{\lambda \varepsilon}} d\nu_f(\zeta) \right) d\mathbb{P}(f) \right\}.$$

The latter can be readily incorporated into a standard optimal design problem. To illustrate this fact, let us consider an optimal design program of the form

$$(2.4.7) \quad \min_h J_{\text{dr}, \varepsilon}(h) \text{ s.t. } C(h) = 0,$$

where  $C(h)$  is an equality constraint functional which does not depend on the data for simplicity. This problem is equivalent to the following one

$$(2.4.8) \quad \min_{\substack{h, \\ \lambda \geq 0}} \mathcal{D}(h, \lambda) \text{ s.t. } C(h) = 0, \text{ where } \mathcal{D}(h, \lambda) := \lambda m + \lambda \varepsilon \int_{\Xi} \log \left( \int_{\Xi} e^{\frac{\mathcal{C}(h, f) - \lambda c(f, \zeta)}{\lambda \varepsilon}} d\nu_f(\zeta) \right) d\mathbb{P}(f),$$

and the optimized variable is now the pair  $(h, \lambda)$ .

Such a problem can be solved by a standard constrained optimization algorithm, once the derivatives of  $\mathcal{D}(h, \lambda)$  have been calculated with respect to both variables  $h$  and  $\lambda$ , which follows from a standard (albeit a little tedious) adjoint-based calculation, see [Section 1.3.3.6](#).

**Remark 2.4.3** A similar duality result to that of [Proposition 2.4.2](#) actually holds when the regularized quantity  $W_\varepsilon(\mathbb{P}, \mathbb{Q})$  is replaced by the true Wasserstein distance  $W(\mathbb{P}, \mathbb{Q})$ , leading to a reformulation of the distributionally robust function  $J_{\text{dr}}(h)$  in [\(2.4.2\)](#) of the form [\(2.4.6\)](#). The latter is however more difficult to handle from the numerical viewpoint since it involves the supremum  $\sup_{\zeta \in \Xi} (\mathcal{C}(h, \zeta) - \lambda c(f, \zeta))$  in place of the “smooth” log-sum-exp approximation  $\varepsilon \log \left( \int_{\Xi} e^{\frac{\mathcal{C}(h, \zeta) - \lambda c(f, \zeta)}{\lambda \varepsilon}} d\nu_f(\zeta) \right)$  featured in [\(2.4.6\)](#), see [\[185\]](#).

## 2.4.2. Two numerical examples

### 2.4.2.1. Distributionally robust density-based optimization of a 2d bridge under load uncertainties

Let us first consider a numerical example in the context of density-based topology optimization, which is briefly described in [Section 1.4.5](#). The designs are density functions  $h : D \rightarrow [0, 1]$  defined on a fixed computational domain  $D$  with size  $1 \times 1$ . They represent 2d bridges insofar as

- $h(x) = 0$  in regions of  $D$  surrounded by void,
- $h(x) = 1$  in regions of  $D$  surrounded by the elastic material,
- $h(x) \in (0, 1)$  represents a mixture of material and void in respective proportions  $h(x)$  and  $(1 - h(x))$ .

The considered designs  $h$  are clamped on the bottom side  $\Gamma_D$  of  $\partial D$  and subjected to a constant load  $f$  distributed on the upper side  $\Gamma_N$ , see [Fig. 2.4.1](#) (top, left) for details. The nominal probability law  $\mathbb{P}$  for  $f$  is constructed from one single observation  $f_1$ , corresponding to a unit vertical load:

$$\mathbb{P} = \delta_{f_1}, \quad f_1 = (0, -1).$$

The entropic regularization coefficient  $\varepsilon$  is  $1e^{-2}$  and the parameter  $\sigma$  appearing in the reference coupling  $\pi_0$  in [\(2.4.4\)](#) equals  $1e^{-3}$ .

In this context, we solve the following distributionally robust topology optimization problem

$$(2.4.9) \quad \min_{h \in \mathcal{U}_{\text{ad}}} J_{\text{dr}, \varepsilon}(h) \text{ s.t. } \text{Vol}(h) = V_T,$$

for several values of the tolerance parameter  $m$  and the target volume  $V_T = 0.2$ . The optimized designs are represented on [Fig. 2.4.1](#). Understandably enough, the optimized designs develop thin branches to cope with larger loads, with horizontal components, and their nominal performance  $\mathcal{C}(h, f_1)$  gets increasingly bad as  $m$  increases.

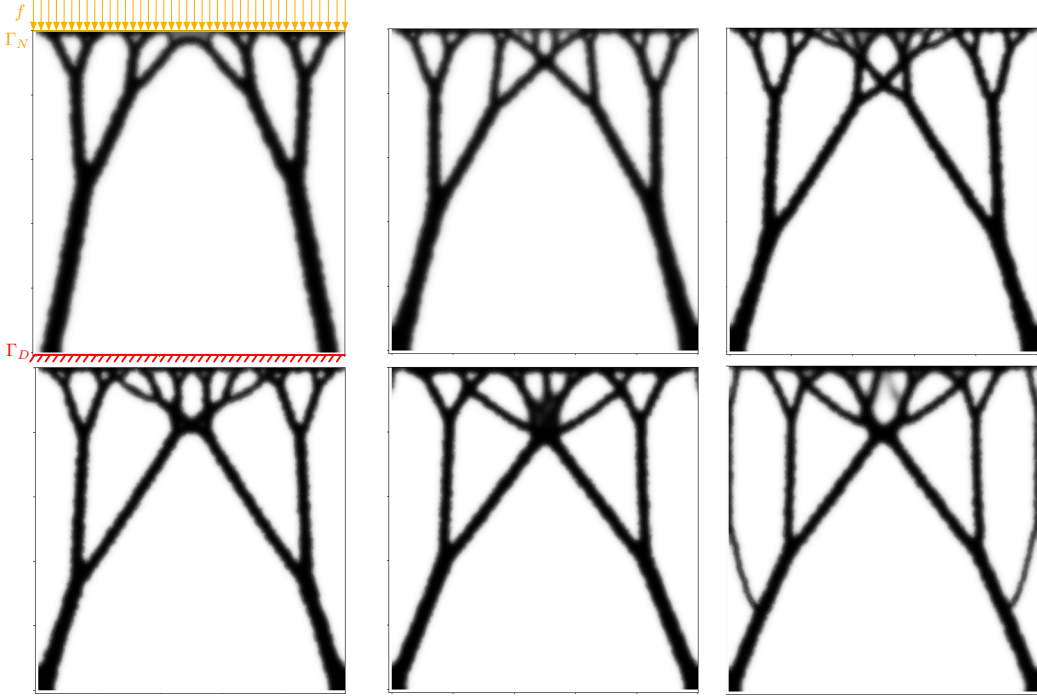


FIGURE 2.4.1. (From left to right, top to bottom) Optimized density in the distributionally robust bridge topology optimization example of Section 2.4.2.1 for  $m = 0$  (with details of the test-case) and  $m = 0.25, 0.52, 0.6, 0.9, 1$ .

#### 2.4.2.2. Distributionally robust optimization of the shape of a 2d cantilever under load uncertainties

One second example is about the optimization of a 2d cantilever beam, and it is treated from the geometric shape optimization viewpoint of Section 1.2.3: the considered designs are shapes  $\Omega$ , contained in the fixed computational domain  $D = [0, 2] \times [0, 1]$ . They are clamped on their left-hand side  $\Gamma_D \subset \partial D$  and a constant load  $f \in \Xi$  is applied on a small region  $\Gamma_N$  at the middle of their right-hand side, see Fig. 2.4.2 for the details. We rely on the mesh evolution method of Section 1.4.7 to track the evolution of the mesh of the optimized shape.

Again, the nominal law  $\mathbb{P}$  for the load is constructed from only one sample  $f_1$ :

$$\mathbb{P} = \delta_{f_1}, \quad f_1 = (-1, 0).$$

The parameters  $\varepsilon$  and  $\sigma$  equal respectively  $1e^{-2}$  and  $1e^{-3}$ .

We solve several instances of the distributionally robust problem

$$(2.4.10) \quad \min_{\Omega} J_{\text{dr}, \varepsilon}(\Omega) \quad \text{s.t.} \quad \text{Vol}(\Omega) = V_T$$

for various values of  $m$  and the volume target  $V_T = 0.6$ . The results are reported on Fig. 2.4.2; one verifies that the nominal performance of the designs tends to deteriorate when the size of the parameter  $m$  increases.

**Remark 2.4.4** *In both experiments, the resulting designs with  $m = 0$  do not correspond exactly with those that we would obtain by minimizing the compliance in the situation where only the nominal load is applied. For example, in the instance of the cantilever test case of Section 2.4.2.2 with  $m = 0$ , we would intuitively expect to obtain a straight horizontal bar joining the regions  $\Gamma_N$  and  $\Gamma_D$ . This apparent inconsistency is due to the fact that, for fixed  $\varepsilon > 0$ , the regularized Wasserstein distance  $W_\varepsilon(\mathbb{P}, \mathbb{Q})$  in (2.4.3) is only an approximation of the true Wasserstein distance  $W(\mathbb{P}, \mathbb{Q})$  in (2.4.1). In particular, it is well-known in the literature (see e.g. [178]) that  $W_\varepsilon(\mathbb{P}, \mathbb{Q})$  is not a distance, so that the supremum in the right-hand side of (2.4.5) may not be attained when the probability law  $\mathbb{Q}$  is the nominal law  $\mathbb{P}$ .*

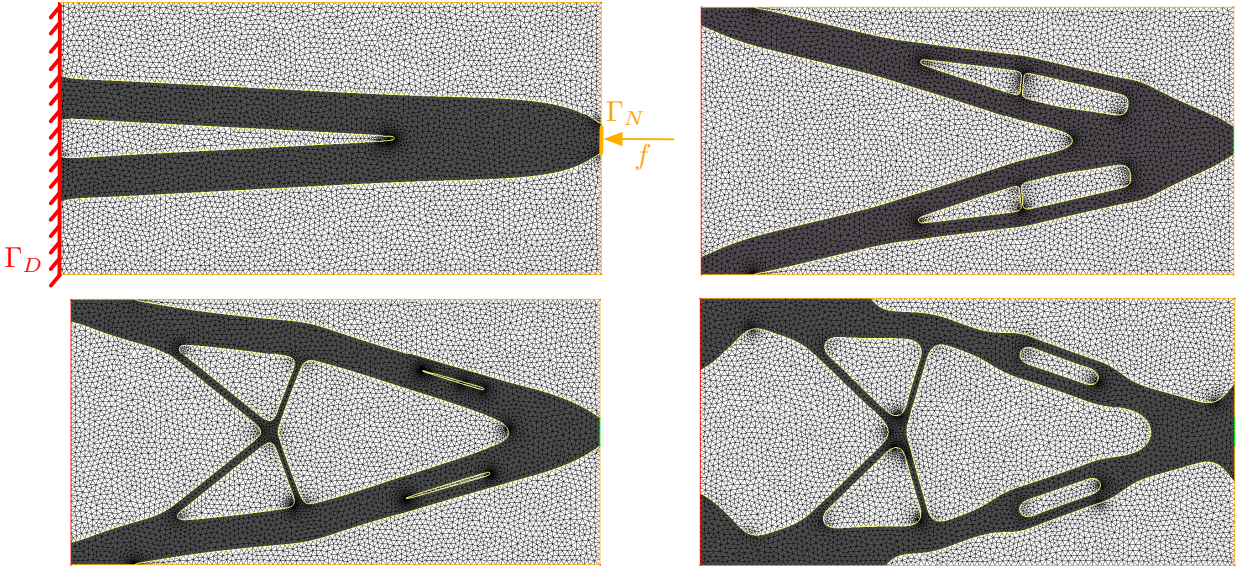


FIGURE 2.4.2. (From left to right, top to bottom) Optimized, distributionally robust shapes of the cantilever of [Section 2.4.2.2](#) for  $m = 0$  (with details of the test-case), optimized shapes for  $m = 1, 1.5, 2$ .

### 2.4.3. Perspectives

As illustrated by the investigations reported in [Sections 2.4.1](#) and [2.4.2](#), distributional robustness is a promising viewpoint for the treatment of uncertain data. Its recent developments, collected in the survey [\[309\]](#), open the way to various applications, notably in optimal design. These will be the focus of further investigation, in the context of the Ph.D. thesis of J. Prando (co-supervised by B. Thibert and myself), initiated in October, 2022.

One immediate extension of this work concerns the treatment of more realistic and complex physical situations, involving nominal probability distributions  $\mathbb{P}$  built from more than one single sample  $f_1$ . This should increase significantly the computational burden of evaluating the probabilistic integrals featured in [\(2.4.8\)](#), calling for the use of advanced numerical strategies based on e.g. parallel computing, efficient isotropic or anisotropic grid collocation methods (see again [\[230\]](#)), or dimensionality reduction techniques (such as the reduced basis method) to calculate multiple solutions of the defining partial differential equations associated to different parameters, see e.g. [\[202\]](#).

Another natural continuation of the work presented in this section is to consider using other ambiguity sets than the Wasserstein ball with center  $\mathbb{P}$  and radius  $m$  in the construction of the distributionally robust functional  $J_{\text{dr}}(h)$  in [\(2.4.2\)](#) or its approximation [\(2.4.5\)](#):

- As we have mentioned in [Remark 2.4.4](#), the entropy-regularized Wasserstein distance  $W_\varepsilon(\mathbb{P}, \mathbb{Q})$  in [\(2.4.3\)](#) is not a distance. This has the undesirable consequence that the ambiguity set featured in the construction [\(2.4.5\)](#) is not reduced to the nominal law  $\mathbb{P}$  when the radius  $m$  is set to 0. To remedy this concern, one could consider replacing  $W_\varepsilon(\mathbb{P}, \mathbb{Q})$  with another entropy-regularized version of the Wasserstein distance  $W(\mathbb{P}, \mathbb{Q})$  called the Sinkhorn distance, see [\[178, 328\]](#). It would then be interesting to investigate whether a convenient dual reformulation of the function  $J_{\text{dr},\varepsilon}(h)$  as a minimum value holds in this seemingly more complex case.
- One could consider ambiguity sets defined by constraints on the moments of its elements  $\mathbb{Q} \in \mathcal{P}(\Xi)$ ; for instance, ambiguity sets made of the laws  $\mathbb{Q}$  whose expectation and covariance matrix equal given reference values, exactly or up to a tolerance, have been considered in [\[80, 154\]](#).

- A surrogate (i.e. a larger set) of the ambiguity set considered in the previous study is the so-called Gelbrich hull, which is composed of probability laws  $\mathbb{Q}$  satisfying certain inequalities on their expectation and covariance matrix. This surrogate is sharp, in the sense that both ambiguity sets coincide in several particular cases, for instance when the nominal law  $\mathbb{P}$  is elliptic. In any event, when the cost function  $f \mapsto \mathcal{C}(h, f)$  is quadratic with respect to the data, which is the case in several important problems in practice (for instance, when  $\mathcal{C}(h, f)$  stands for the compliance of an elastic structure  $h$ , and the data  $f$  represent the loads), the distributionally robust function (2.4.2) devised from the Gelbrich ambiguity set can be expressed as the minimum value of a semi-definite program, see for instance [222] and the references therein. One could then give a tractable reformulation of a constrained minimization problem involving  $J_{\text{dr}}(h)$ , by an argument similar to that used in the construction of (2.4.8).

One third perspective for future work is to replace the expectation of the uncertain cost  $f \mapsto \mathcal{C}(h, f)$  in the definition (2.4.2) of the distributionally robust functional  $J_{\text{dr}}(h)$  by another probabilistic quantity, or measure of risk, see for instance [334]. For instance, one could consider building a distributionally robust version of the variance of the cost. Another very interesting measure of risk is the conditional value at risk [318, 317] – also referred to as expected shortfall or superquantile depending on the field – that we now briefly discuss.

The cumulative distribution function of the cost  $\mathcal{C}(h, \cdot)$ , when it is seen as a random variable on  $\Xi$ , is defined by:

$$\forall t \in \mathbb{R}, \quad \Psi(h, t) = \mathbb{P}\{\mathcal{C}(h, f) \leq t\}.$$

This function is non decreasing, and its admits limits 0 and 1 when  $t \rightarrow -\infty$  and  $+\infty$ , respectively. It is continuous from the right, but it might fail to be continuous from the left because of the existence of subsets in  $\Xi$  with non-empty measure where  $\mathcal{C}(h, \cdot)$  takes the value  $t$ .

For a given threshold  $\beta$ , the  $\beta$  value at risk  $\alpha_\beta(h)$  of  $\mathcal{C}(h, f)$  is the inverse of the cumulative distribution function, in the sense that:

$$\alpha_\beta(h) := \inf \left\{ t \in \mathbb{R}, \quad \Psi(h, t) \geq \beta \right\}.$$

Intuitively, the cost  $\mathcal{C}(h, f)$  takes values lower than  $\alpha_\beta(h)$  with probability  $\beta$ , see Fig. 2.4.3; hence, it is worthwhile to try and minimize  $\alpha_\beta(h)$  with respect to the design  $h$  for a fixed threshold  $\beta$ . Unfortunately, this quantity suffers from several shortcomings, one of them being that it does not provide any information about the magnitude reached by the cost in the events where the bound  $\alpha_\beta(h)$  is not verified.

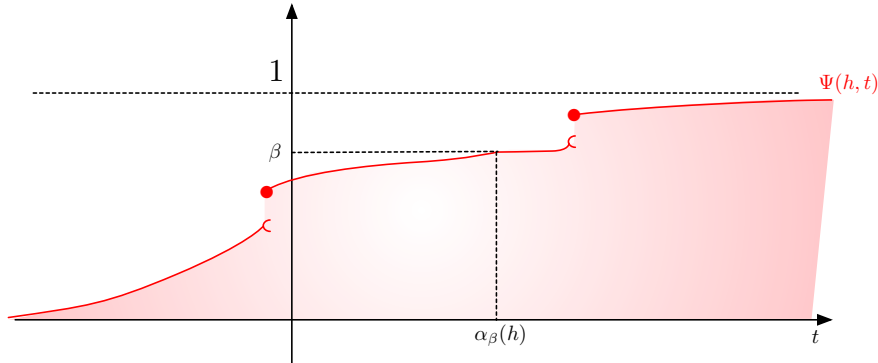


FIGURE 2.4.3. The  $\beta$  value at risk  $\alpha_\beta(h)$  of a cost function  $\mathcal{C}(h, f)$  is the inverse of the cumulative distribution function  $\Phi(h, \cdot)$ .

For this reason, the  $\beta$  conditional value at risk  $\phi_\beta(h)$  is often preferred as a more “robust” quantity of interest. The latter is defined as the expectation of the cost when the latter exceeds the threshold  $\alpha_\beta(h)$

guaranteed by the  $\beta$  value at risk:

$$\phi_\beta(h) = \frac{1}{1-\beta} \int_{\{f \in \Xi, \mathcal{C}(h, f) \geq \alpha_\beta(h)\}} \mathcal{C}(h, f) d\mathbb{P}(f).$$

Among its multiple interests, the conditional value at risk conveniently allows to give tractable formulations to failure probability constraints, see [315].

From the computational vantage, one interesting feature of  $\phi_\beta(h)$  is the following reformulation as the minimum value of an expectation:

$$(2.4.11) \quad \phi_\beta(h) = \inf_{\alpha \in \mathbb{R}} \left\{ \alpha + \frac{1}{1-\beta} \int_{\Xi} [\mathcal{C}(h, f) - \alpha]_+ d\mathbb{P}(f) \right\},$$

see [318, 317] about this property. This formula lends itself to an incorporation of the conditional value at risk of a cost function in optimal design problems, in the spirit of the reformulation (2.4.8) of (2.4.7). This idea was recently exploited in the context of density-based topology optimization in the article [169]; to go further, it would be interesting to use (2.4.11) to construct a tractable, distributionally robust version of the  $\beta$  conditional value at risk of a cost function of the design. This task seems reasonable as (2.4.11) features the minimum value of an expectation, which is typically a structure where distributional robustness can be imposed in a tractable way, as we have seen in Section 2.4.1.

Let us also mention other interesting measures of risk which could be given worthwhile distributionally robust counterparts, such as the shortfall [79], the entropic value at risk [11] – which is a convenient surrogate for the conditional value at risk –, or again the buffered probability of failure [316].

Eventually, yet another question of interest in the continuation of the work conducted in Sections 2.4.1 and 2.4.2 is the calculation of the derivative of the worst-case expectation

$$m \mapsto \sup_{W_\varepsilon(\mathbb{P}, \mathbb{Q}) \leq m} \int_{\Xi} \mathcal{C}(h, f) d\mathbb{Q}(f)$$

at  $m = 0$ , see [62] for a related study. A closed form formula for this derivative would pave the way to the device of an approximate (and hopefully easier to calculate) distributionally robust version of  $J_{\text{dr}, \varepsilon}(h)$  by retaining only the leading-order terms of the minimized function in terms of  $m$ , as we have done in Section 2.1.

## 2.A A FEW WORDS ABOUT MEASURE THEORY

This appendix gathers a few basic concepts about measure theory which are useful on several occurrences in this manuscript. We refer to classical textbooks such as [29, 48] for more details about this subject.

Let  $X$  be a non empty set, and let  $\mathcal{E}$  be a  $\sigma$ -algebra composed of subsets of  $X$ , so that  $(X, \mathcal{E})$  is a measure space.

**Definition 2.A.1** *A positive measure on the measure space  $(X, \mathcal{E})$  is a mapping  $\mu : \mathcal{E} \rightarrow [0, \infty]$  such that*

- $\mu(\emptyset) = 0$ ;
- *( $\sigma$ -additivity) For any sequence  $(E_n)_{n \geq 0}$  of mutually disjoint elements of  $\mathcal{E}$ , it holds:*

$$\mu \left( \bigcup_{n=0}^{\infty} E_n \right) = \sum_{n=0}^{\infty} \mu(E_n).$$

*The positive measure  $\mu$  is said to be finite when  $\mu(X) < \infty$ .*

Among positive measures, we distinguish the particularly interesting class of probability measures.

**Definition 2.A.2** *A probability measure  $\mu$  on the space  $(X, \mathcal{E})$  is a positive measure with total mass  $\mu(X) = 1$ . The triple  $(X, \mathcal{E}, \mu)$  is then called probability space.*

We now introduce the notion of  $\mathbb{R}^m$ -valued measure.

**Definition 2.A.3** *Let  $m \geq 1$ ; an  $\mathbb{R}^m$ -valued measure on  $(X, \mathcal{E})$  is a mapping  $\mu : \mathcal{E} \rightarrow \mathbb{R}^m$  such that*

- $\mu(\emptyset) = 0$ ;
- For any sequence  $E_n$  of mutually disjoint subsets of  $\mathcal{E}$ , it holds

$$(2.A.1) \quad \mu\left(\bigcup_{n=0}^{\infty} E_n\right) = \sum_{n=0}^{\infty} \mu(E_n),$$

where it is understood that the series in the above right-hand side is absolutely convergent.

The total variation  $|\mu|$  of such an  $\mathbb{R}^m$ -valued measure  $\mu$  is the positive measure  $|\mu|$  defined by:

$$\forall E \in \mathcal{E}, \quad |\mu|(E) := \sup \left\{ \sum_{n=0}^{\infty} |\mu(E_n)|, \quad E_n \in \mathcal{E} \text{ mutually disjoint, } E = \bigcup_{n=0}^{\infty} E_n \right\}.$$

**Remark 2.A.4**

- It is natural to require that the sum in the right-hand side of (2.A.1) be absolutely convergent, since its value should not depend on the order of summation (as the left-hand side does not).
- Positive measures are not a particular case of the notion of  $\mathbb{R}^m$ -valued measure, since the definition of the latter requires finiteness, while positive measures may take infinite values.
- If  $\mu$  is an  $\mathbb{R}^m$ -valued measure on  $(X, \mathcal{E})$ , its total variation  $|\mu|$  is a finite positive measure.

The notion of measure can be explored further when  $X$  is a metric space, and  $\mathcal{E}$  is the associated Borel  $\sigma$ -algebra  $\mathcal{B}(X)$  (i.e. that generated by open subsets). More precisely, let us introduce the notion of locally compact and separable metric space:

**Definition 2.A.5** A metric space  $(X, d)$  is called locally compact and separable if

- For each point  $x \in X$ , there exists an open subset  $U$  such that  $x \in U$  and  $\overline{U}$  is compact;
- $X$  admits a dense subset.

It is easily proved that every open subset  $U$  of a locally compact and separable metric space  $X$  can be expressed as a countable reunion of compact subsets of  $X$ .

Throughout the rest of this section, unless stated otherwise, we assume that  $X$  is a locally compact and separable metric space.

In this setting, we proceed to define the notion of (positive) Radon measure, which loosely speaking corresponds to set functions inducing a (positive) measure on each compact subset of  $X$ .

**Definition 2.A.6** A positive measure  $\mu$  on  $(X, \mathcal{B}(X))$  is called a Borel measure. In addition, when  $\mu$  is finite on compact subsets of  $X$ , it is called a positive Radon measure.

**Definition 2.A.7** Let  $\mu$  be an  $\mathbb{R}^m$ -valued function on the Borel subsets of  $X$ ;

- $\mu$  is called a Radon measure if for every compact subset  $K \subset X$ , the induced mapping  $\mu : \mathcal{B}(K) \rightarrow \mathbb{R}^m$  is a measure on  $(K, \mathcal{B}(K))$  in the sense of [Definition 2.A.3](#). We denote by  $\mathcal{M}_{\text{loc}}(X)^m$  the set of  $\mathbb{R}^m$ -valued Radon measures on  $X$ .
- If  $\mu : \mathcal{B}(X) \rightarrow \mathbb{R}^m$  is in addition a measure on  $(X, \mathcal{B}(X))$ , it is called a finite Radon measure. We denote by  $\mathcal{M}(X)^m$  the set of such measures.

The notion of Radon measure is particularly interesting because of its duality with continuous functions. In order to state rigorously this property, let us introduce the following notation:

- $\mathcal{C}_c(X)$  is the locally convex topological vector space of real-valued continuous functions with compact support in  $X$ ; it is naturally endowed with the norm

$$\|u\|_{\infty} := \sup_{x \in X} |u(x)|.$$

- $\mathcal{C}_0(X)$  is the completion of  $\mathcal{C}_c(X)$  for this norm. This space is made of those continuous functions on  $X$  which “tend to 0 at infinity”, that is:

$$\forall \varepsilon > 0, \text{ there exists a compact subset } K \subset X \text{ s.t. } \forall x \in X \setminus K, \quad |u(x)| < \varepsilon.$$

**Remark 2.A.8** Obviously, when  $X$  is compact, the three spaces  $\mathcal{C}_c(X)$ ,  $\mathcal{C}_0(X)$  and  $\mathcal{C}(X)$  coincide.

We now arrive at the famous Riesz representation theorem, which guarantees the identification of bounded and linear functions on  $\mathcal{C}_0(X)^m$  and finite Radon measures.

**Theorem 2.A.9** (Riesz representation theorem) Let  $X$  be a locally compact and separable metric space, and let  $L : \mathcal{C}_0(X)^m \rightarrow \mathbb{R}$  be an additive and bounded functional, that is:

$$\forall u, v \in \mathcal{C}_0(X)^m, \quad L(u + v) = L(u) + L(v),$$

and

$$\|L\| := \sup \{L(u), u \in \mathcal{C}_0(X)^m, \|u\|_\infty \leq 1\} < \infty.$$

Then there exists a unique  $\mathbb{R}^m$ -valued finite Radon measure  $\mu$  on  $X$  such that

$$\forall u \in \mathcal{C}_0(X)^m, \quad L(u) = \sum_{i=1}^m \int_X u_i \, d\mu_i.$$

Moreover, it holds:

$$\|L\| = |\mu|(X).$$

In particular, the Riesz representation theorem asserts that the space  $\mathcal{M}(X)$  of finite-valued Radon measures is exactly the dual space of the space  $\mathcal{C}_0(X)$  of continuous functions on  $X$  tending to 0 at infinity, under the pairing

$$\forall \mu \in \mathcal{M}(X), u \in \mathcal{C}_0(X), \quad \langle \mu, u \rangle := \int_X u \, d\mu.$$

The total variation  $\mu \mapsto |\mu|(X)$  is exactly the dual norm on  $\mathcal{M}(X)$  to the norm  $u \mapsto \|u\|_\infty$  on  $\mathcal{C}_0(X)$  under this pairing.

This duality result finds a very useful application in the extraction of convergent subsequences from bounded sequences of measure, as a consequence of the Banach-Alaoglu theorem. In order to state the result precisely, let us introduce the following definition.

**Definition 2.A.10** Let  $\mu_n \in \mathcal{M}_{loc}(X)^m$  be a sequence of  $\mathbb{R}^m$ -valued Radon measures on  $X$ . The sequence  $\mu_n$  locally weakly \* converges to an element  $\mu \in \mathcal{M}_{loc}(X)$  if

$$\forall u \in \mathcal{C}_c(X), \quad \int_X u \, d\mu_n \rightarrow \int_X u \, d\mu.$$

If in addition the measures  $\mu_n$  and  $\mu$  are finite, the sequence  $\mu_n$  is said to converge weakly \* to  $\mu$  if

$$\forall u \in \mathcal{C}_0(X), \quad \int_X u \, d\mu_n \rightarrow \int_X u \, d\mu.$$

**Theorem 2.A.11** (Compactness criterion) Let  $\mu_n$  be a sequence of finite Radon measures such that

$$\sup_{n \geq 0} |\mu_n|(X) < \infty.$$

Then there exists a subsequence  $n_k$  of  $n$  such that  $\mu_{n_k}$  weakly \* converges to some  $\mu \in \mathcal{M}(X)$ . In addition, the mapping

$$\mathcal{M}(X) \ni \mu \mapsto |\mu|(X) \in \mathbb{R}$$

is lower semi-continuous for the weak \* convergence.

## 2.B THE KARHUNEN-LOÈVE DECOMPOSITION

On several occurrences in this chapter, as often in the literature, the data  $f$  arise as the sum of a known nominal value  $f_0$ , and an uncertain perturbations  $\hat{f}(\omega)$ ; one key assumption to reduce the complexity of the latter part is their finite-dimensional structure: they show up as a sum

$$\hat{f}(\omega) = \sum_{i=1}^N \xi_i(\omega) f_i,$$

where the  $\xi_i(\omega)$  are uncorrelated random variables and the  $f_i$  are deterministic data functions. In practice, such a structure often stems from a Karhunen-Loëve decomposition of  $\hat{f}$ , which roughly speaking allows to express it as an infinite sum of this form, which can be truncated.

In this appendix, we present this decomposition in a quite general setting. Although these results are not needed for the rest of this section, strictly speaking, we believe that it is instructive. In this presentation, we rely on the abstract and general point of view of e.g. [327] (see also Chap. XVII in [245]) which is based on the tensor product of Hilbert spaces.

After a brief reminder about the construction of tensor products of Hilbert spaces in [Section 2.B.1](#), we present a general decomposition theorem for elements in such spaces in [Section 2.B.2](#). We then specialize this abstract setting in [Section 2.B.3](#) to the case of random fields over a physical domain.

## 2.B.1. Preliminaries about tensor products of Hilbert spaces

In this section, we sketch an intuitive construction of the tensor product between Hilbert spaces, based on the notion of Hilbert-Schmidt operator, for which we refer to Chap. 12 of [50], see also §6.2 in [364] for a more abstract construction.

**Proposition-Definition 2.B.1** *Let  $(E, \langle \cdot, \cdot \rangle_E)$  and  $(F, \langle \cdot, \cdot \rangle_F)$  be two separable, real Hilbert spaces.*

- *A linear mapping  $T : E \rightarrow F$  is called a Hilbert-Schmidt operator if there exists an orthonormal basis  $\{e_n\}_{n \geq 1}$  of  $E$  such that:*

$$\|T\|_{\mathcal{L}^2(E,F)}^2 := \sum_{n=1}^{\infty} \|Te_n\|_F^2 < \infty.$$

*When this is the case, the value of the above sum does not depend on the choice of the basis  $\{e_n\}_{n \geq 1}$ .*

- *Let  $\{e_n\}_{n \geq 1}$  be an orthonormal basis of  $E$ , and let  $T_1, T_2$  be two Hilbert-Schmidt operators; then the quantity*

$$\langle T_1, T_2 \rangle_{\mathcal{L}^2(E,F)} := \sum_{n=1}^{\infty} \langle T_1 e_n, T_2 e_n \rangle_F$$

*is finite and does not depend on the choice of the basis  $\{e_n\}_{n \geq 1}$ .*

- *The pairing  $\langle \cdot, \cdot \rangle_{\mathcal{L}^2(E,F)}$  defines an inner product of the space  $\mathcal{L}^2(E,F)$  of Hilbert-Schmidt operators between  $E$  and  $F$ , for which the latter is a Hilbert space.*
- *The norm  $\|\cdot\|_{\mathcal{L}^2(E,F)}$  induces a topology on  $\mathcal{L}^2(E,F)$  which is stronger than that of the operator norm; more precisely:*

$$\forall T \in \mathcal{L}^2(E,F), \quad \|T\| \leq \|T\|_{\mathcal{L}^2(E,F)}.$$

- *If  $T : E \rightarrow F$  is a Hilbert-Schmidt operator, it is compact as the limit of a sequence of finite rank operators in the operator norm topology.*

This notion of Hilbert-Schmidt operator can be extended to bilinear mappings.

**Definition 2.B.2** *Let  $(E, \langle \cdot, \cdot \rangle_E)$ ,  $(F, \langle \cdot, \cdot \rangle_F)$  and  $(G, \langle \cdot, \cdot \rangle_G)$  be separable, real Hilbert spaces. A bilinear mapping  $a : E \times F \rightarrow G$  is called Hilbert-Schmidt if the series*

$$\|a\|_2^2 := \sum_{n=1}^{\infty} \sum_{m=1}^{\infty} \|a(e_n, f_m)\|_G^2$$

*is convergent for one (and then for all) choice of orthonormal bases  $\{e_n\}_{n \geq 1}$  and  $\{f_m\}_{m \geq 1}$  of  $E$  and  $F$  respectively.*

We now arrive to the main notion in this section.

**Proposition-Definition 2.B.3** *Let  $(E, \langle \cdot, \cdot \rangle_E)$  and  $(F, \langle \cdot, \cdot \rangle_F)$  be separable, real Hilbert spaces. The tensor product  $E \otimes F$  is the Hilbert space  $\mathcal{L}_2(E^*, F)$  of Hilbert-Schmidt operators from  $E^*$  into  $F$ .*

(i) For any orthonormal bases  $\{e_n\}_{n \geq 1}$  and  $\{f_m\}_{m \geq 1}$  of  $E$  and  $F$ , the collection  $\{e_n \otimes f_m\}_{n,m \geq 1}$ , made of the mappings

$$e_n \otimes f_m : E^* \ni x \mapsto \langle x, e_n \rangle f_m, ,$$

is an orthonormal basis of  $E \otimes F$ .

(ii) The bilinear mapping  $\pi : E \times F \rightarrow E \otimes F$  defined by

$$\forall e \in E, f \in F, \quad \pi(e, f) = e \otimes f$$

is a Hilbert-Schmidt operator in the sense of [Definition 2.B.2](#).

(iii) The tensor product  $E \otimes F$  is the unique Hilbert space (up to a Hilbert-Schmidt isomorphism) satisfying the following universal property: for any separable Hilbert space  $(G, \langle \cdot, \cdot \rangle_G)$ , and any Hilbert-Schmidt bilinear mapping  $a : E \times F \rightarrow G$ , there exists a unique Hilbert-Schmidt operator  $\ell : E \otimes F \rightarrow G$  such that  $\ell \circ \pi = a$ , i.e. the following diagram is commutative:

$$\begin{array}{ccc} E \times F & \xrightarrow{a} & G \\ \downarrow \pi & \nearrow \ell & \\ E \otimes F & & \end{array}$$

(iv) Let  $(\mathcal{O}, \mathcal{F}, \mathbb{P})$  be a measure space, and let  $E$  be a separable Hilbert space. The tensor product  $L^2(\mathcal{O}) \otimes E$  is isometric to the Bochner space  $L^2(\mathcal{O}, E)$  via the mapping  $I$  defined by:

$$\forall s \in L^2(\mathcal{O}), e \in E, \quad I(s, e) \in L^2(\mathcal{O}, E) \text{ is s.t. } \forall \omega \in \mathcal{O}, \quad I(s, e)(\omega) = s(\omega)e.$$

**Remark 2.B.4** It is tempting to identify the dual  $E^*$  with  $E$  and thus to define the tensor product  $E \otimes F$  by  $E \otimes F = \mathcal{L}_2(E, F)$  instead of  $\mathcal{L}_2(E^*, F)$ . Doing so results in versions of the mappings  $\pi$  and  $\ell$  which are no longer linear or bilinear when the Hilbert spaces  $E$  and  $F$  are complex. For this reason, even if we handle only real Hilbert spaces in this manuscript, we stick to this convention.

## 2.B.2. An abstract decomposition theorem for elements in tensor product spaces

Throughout this section,  $U$  and  $H$  are two separable Hilbert spaces. We first define the correlation between elements  $f$  and  $g$  in  $U \otimes H$ .

**Definition 2.B.5** Let  $f, g$  belong to the tensor product  $U \otimes H$ . Let  $\{\xi_n\}_{n \geq 0}$  be an orthonormal basis of  $U$ , and let  $\{f_n\}_{n \geq 1}$  and  $\{g_n\}_{n \geq 1}$  be the unique families of elements of  $H$  such that:

$$f = \sum_{n=1}^{\infty} \xi_n \otimes f_n, \text{ and } g = \sum_{n=1}^{\infty} \xi_n \otimes g_n,$$

see [Proposition-Definition 2.B.3](#) (i). Then,

- The correlation  $\text{Cor}(f, g) \in H \otimes H$  between  $f$  and  $g$  is defined by:

$$\text{Cor}(f, g) = \sum_{n=1}^{\infty} f_n \otimes g_n.$$

This quantity is easily proved to be independent of the choice of the basis  $\{\xi_n\}_{n \geq 1}$ .

- The covariance  $\text{Cov}(f) \in H \otimes H$  of  $f$  is:

$$\text{Cov}(f) = \sum_{n=1}^{\infty} f_n \otimes f_n.$$

The key decomposition result of this section is the following.

**Theorem 2.B.6** For any element  $f \in U \otimes H$ , there exist two orthonormal bases  $\{\xi_n\}_{n \geq 1}$  and  $\{\phi_n\}_{n \geq 1}$  of  $U$  and  $H$ , respectively, as well as a sequence  $\lambda_n$  of non negative real values decreasing to 0 such that the following decomposition holds:

$$f = \sum_{n=1}^{\infty} \sqrt{\lambda_n} \xi_n \otimes \phi_n.$$

The  $\lambda_n$  and  $\phi_n$  are the eigenelements of  $\text{Cov}(f)$  when the latter is seen as a Hilbert-Schmidt operator from  $H^*$  into  $H$ .

*Proof.* Introducing an orthonormal basis  $\{s_n\}_{n \geq 1}$  of  $U$ , there exists a unique family  $\{f_n\}_{n \geq 1}$  in  $H$  such that:

$$f = \sum_{n=1}^{\infty} s_n \otimes f_n, \text{ and then } \text{Cov}(f) = \sum_{n=1}^{\infty} f_n \otimes f_n.$$

According to [Proposition-Definition 2.B.3](#), we may identify  $\text{Cov}(f)$  with the operator  $H \rightarrow H$  defined by:

$$\forall h \in H, \quad \text{Cov}(f)(h) = \sum_{n=1}^{\infty} \langle f_n, h \rangle f_n.$$

The latter is obviously positive semi-definite and self-adjoint; it is also compact by virtue of [Proposition-Definition 2.B.1](#) (iii). The spectral theorem for compact, self-adjoint operators on a Hilbert space then yields a decomposition of the form:

$$\text{Cov}(f)(h) = \sum_{n=1}^{\infty} \lambda_n \langle \phi_n, h \rangle \phi_n,$$

where  $\lambda_n$  is a decreasing sequence of non negative numbers and  $\{\phi_n\}_{n \geq 1}$  is an orthonormal basis of  $H$ , see e.g. [\[320\]](#). Using tensor notations, this expression can be rewritten:

$$(2.B.1) \quad \text{Cov}(f) = \sum_{n=1}^{\infty} \lambda_n \phi_n \otimes \phi_n.$$

Let us now decompose  $f \in U \otimes H$  in the orthonormal basis  $\{s_m \otimes \phi_p\}_{m,p \geq 1}$ : there exist coefficients  $a_{mp} \in \mathbb{R}$  such that:

$$(2.B.2) \quad \sum_{m=1}^{\infty} \sum_{p=1}^{\infty} |a_{mp}|^2 < \infty, \text{ and } f = \sum_{m=1}^{\infty} \sum_{p=1}^{\infty} a_{mp} s_m \otimes \phi_p.$$

On the other hand,  $\text{Cov}(f)$  now equals:

$$\begin{aligned} \text{Cov}(f) &= \sum_{m=1}^{\infty} \left( \sum_{p=1}^{\infty} a_{mp} \phi_p \right) \left( \sum_{n=1}^{\infty} a_{mn} \phi_n \right) \\ &= \sum_{n=1}^{\infty} \sum_{p=1}^{\infty} \left( \sum_{m=1}^{\infty} a_{mp} a_{mn} \right) \phi_p \otimes \phi_n. \end{aligned}$$

Comparing with [\(2.B.1\)](#), it follows that

$$\sum_{m=1}^{\infty} a_{mp} a_{mn} = \begin{cases} \lambda_n & \text{if } n = p, \\ 0 & \text{otherwise.} \end{cases}$$

Hence, the collection

$$\xi_n = \frac{1}{\sqrt{\lambda_n}} \sum_{m=1}^{\infty} a_{mn} s_m$$

is an orthonormal basis of  $U$ , and it follows from [\(2.B.2\)](#) that

$$f = \sum_{n=1}^{\infty} \sqrt{\lambda_n} \xi_n \otimes \phi_n,$$

as desired. □

### 2.B.3. The Karhunen-Loève decomposition of square-integrable random fields

In this section, we specialize the previous material to the more practical situation of random fields.

Throughout this section,  $(\mathcal{O}, \mathcal{F}, \mathbb{P})$  denotes a probability space, and  $D \subset \mathbb{R}^d$  is a bounded “physical” domain, equipped with the Lebesgue measure  $\mathcal{L}$ . Intuitively, a random field associates a random variable  $f(x, \cdot)$  at each point  $x \in D$  in the physical domain  $D$ .

**Definition 2.B.7** *A real-valued random field  $f(x, \omega)$  on  $D$  is a measurable function on the set  $D \times \mathcal{O}$ , where the latter is endowed with the product measure  $\mathcal{L} \otimes \mathbb{P}$ .*

Specializing the theory of the previous [Section 2.B.2](#) to the case where  $U = L^2(\mathcal{O})$  and  $H = L^2(D)$ , and reading through the identifications presented before, we immediately obtain the following result.

**Theorem 2.B.8** *Let  $f(x, \omega)$  be a random field on  $D$  with 0 mean value, that is:*

$$\int_{\mathcal{O}} f(x, \omega) d\mathbb{P}(\omega) = 0 \text{ for a.e. } x \in D.$$

*Let the covariance kernel  $\text{Cov}(f) : L^2(D \times D)$  of  $f$  be defined by:*

$$\text{Cov}(f)(x, y) = \int_{\mathcal{O}} f(x, \omega) f(y, \omega) d\mathbb{P}(\omega).$$

*This kernel induces a Hilbert-Schmidt operator  $T(f) : L^2(D) \rightarrow L^2(D)$  via the formula:*

$$\forall \varphi \in L^2(D), \quad T(f)(\varphi)(x) = \int_D \text{Cov}(f)(x, y) \varphi(y) dy, \text{ a.e. } x \in D.$$

*Let  $\lambda_n$  be the decreasing sequence of the eigenvalues of this compact operator, and let  $\phi_n \in L^2(D)$  be the orthonormal basis of  $L^2(D)$  made of the associated eigenvectors. Then, the following decomposition holds:*

$$f(x, \omega) = \sum_{i=1}^{\infty} \sqrt{\lambda_i} \xi_i(\omega) \phi_i(x),$$

*where the  $\xi_i \in L^2(\mathcal{O})$  are the centered and uncorrelated random variables (i.e. satisfying [\(2.3.3\)](#)) defined by:*

$$\xi_i(\omega) = \frac{1}{\sqrt{\lambda_i}} \int_D f(x, \omega) \phi_i(x) dx.$$

**Remark 2.B.9** *The above result rests on minimum regularity on the covariance kernel  $\text{Cov}(f)$ , i.e. the latter is only supposed to belong to  $L^2(D \times D)$ . Upon stronger assumptions on this kernel, interesting properties hold about the decay rate of the eigenvalues  $\lambda_i$  as  $i \rightarrow \infty$ . Loosely speaking,*

- When  $\text{Cov}(f)$  is analytic on  $D \times D$  (actually, “piecewise analytic” is enough), there exist two positive constants  $\alpha_1, \alpha_2$  such that

$$\lambda_i \leq \alpha_1 e^{-\alpha_2 i^{1/d}}.$$

- When  $\text{Cov}(f)$  belongs to  $H^k(D) \otimes L^2(D)$  (actually, this property may hold only in a “piecewise” fashion), there exists a constant  $\alpha > 0$  such that

$$\lambda_i \leq \alpha i^{-k/d}.$$

We refer to [\[327\]](#) about these properties.

Let us conclude this presentation with a few words about the particular case of Gaussian random fields.

**Definition 2.B.10** *A real-valued random field  $f(x, \omega)$  is Gaussian if for any number  $N > 0$  and any points  $x_1, \dots, x_N$ , the multi-variate random vector  $(f(x_1, \omega), \dots, f(x_N, \omega))$  has a Gaussian probability distribution on  $\mathcal{O}$ , whose mean value and covariance matrix depend on  $x_1, \dots, x_N$ .*

The components of the Karhunen-Loève decomposition of [Theorem 2.B.8](#) enjoy interesting additional properties when the considered random field is Gaussian, as stated in the next results, which essentially

follows from the characterisation of the law a Gaussian random variable by its mean value and its covariance, see [246, 296].

**Proposition 2.B.11** *Let  $f(x, \omega)$  be a Gaussian random field on  $D$  with mean value 0. The random variables  $\xi_i \in L^2(\mathcal{O})$  featured in the Karhunen-Loève decomposition of  $f(x, \omega)$  are independent, Gaussian random variables.*



# Chapter 3

## Geometric and manufacturing constraints in shape and topology optimization

The design of realistic systems has to comply with multiple technical specifications, expressed as constraints in the mathematical formalization of the optimal design problems. These prescriptions may originate from mechanical concerns, such as the necessity to impose a maximum bound on the stress level inside the structure  $\Omega$ , or a minimum value on its fundamental vibration frequency. They may alternatively be about geometric features of  $\Omega$ , such as its volume, perimeter, or thickness. As a matter of fact, many constraints imposed by manufacturing processes are of the latter, geometric nature, as ad hoc models for requirements which are otherwise difficult to express. Despite their seemingly intuitive character, exacerbated by the fact that they a priori do not bring into play partial differential equations, geometric constraints are often difficult to formulate rigorously, and their numerical treatment raises quite specific issues.

The present chapter mainly deals with the modeling and treatment of several geometric or manufacturing constraints. The first [Section 3.1](#) is devoted to the signed distance function  $d_\Omega$  to a shape  $\Omega \subset \mathbb{R}^d$  – a ubiquitous mathematical tool in the modeling of geometric constraints. The main properties of this object are recalled, as well as its sensitivity with respect to the domain; we also provide examples of geometric constraints that can be conveniently modeled in terms of the signed distance function. The next [Section 3.2](#) introduces a general purpose constrained optimization algorithm, which is particularly well-suited for shape and topology optimization problems. In [Section 3.3](#), we present a new numerical method which conveniently simplifies the use of functionals depending on the domain via the function  $d_\Omega$ . We then turn to more concrete application contexts; we investigate in [Section 3.4](#) a few geometric constraints raised by optimal design problem in the field of architecture. The next [Sections 3.5 and 3.6](#) take place in the context where the optimized shape is assembled by an additive manufacturing methodology. The former [Section 3.5](#) aims to model constraint functions which would prevent it from developing so-called overhang features. Interestingly, the straightforward geometric formulation of such overhang constraints proves awkward from the numerical viewpoint, and we return to the mechanical justification of this requirement to build more efficient functionals. In [Section 3.6](#), we formulate a simplified model for the effective, anisotropic material properties of structures constructed by additive manufacturing, which depend on the path followed by the machine tool. Eventually, [Section 3.7](#) sketches an interesting direction for future research suggested by several of the aforementioned investigations: the device and implementation of constraints about the resemblance between the optimized design and a target object, based on the optimal transport theory.

### 3.1 PRELIMINARIES: THE SIGNED DISTANCE FUNCTION TO A DOMAIN AND ITS APPLICATIONS IN SHAPE OPTIMIZATION

The signed distance function is a recurring tool in most of the developments of this chapter, as a convenient means to express multiple geometric quantities related to a domain. In this first section, we collect some material from the literature about this rich concept and some of its usages in shape optimization.

### 3.1.1. About the signed distance function

Relying on the references [106], [28] (Chap. 1), [156] (Chap. 7) and [67] (Chap. 1), we first present a few generalities about the signed distance function, starting from the definition which we recall from [Section 1.4.7.1](#), see ([SDF](#)).

**Definition 3.1.1** *Let  $\Omega$  be an open subset of  $\mathbb{R}^d$ ; the signed distance function  $d_\Omega$  to  $\Omega$  is defined by*

$$\forall x \in \mathbb{R}^d, \quad d_\Omega(x) = \begin{cases} -d(x, \partial\Omega) & \text{if } x \in \Omega, \\ 0 & \text{if } x \in \partial\Omega, \\ d(x, \partial\Omega) & \text{if } x \in \mathbb{R}^d \setminus \overline{\Omega}, \end{cases}$$

where

$$(3.1.1) \quad d(x, \partial\Omega) = \min_{p \in \partial\Omega} |x - p|$$

is the usual Euclidean distance from  $x$  to  $\partial\Omega$ .

The signed distance function is related to several important objects, see [Fig. 3.1.1](#) for an illustration.

**Proposition-Definition 3.1.2** *Let  $\Omega$  be a bounded, Lipschitz domain in  $\mathbb{R}^d$ ;*

- For any point  $x \in \mathbb{R}^d$ , the projection set  $\Pi_{\partial\Omega}(x)$  of  $x$  onto  $\partial\Omega$  is the non empty and compact set of points  $p \in \partial\Omega$  minimizing the distance (3.1.1) from  $x$  to  $\partial\Omega$ .
- The skeleton  $\Sigma \subset \mathbb{R}^d$  of  $\Omega$  is the set of points  $x \in \mathbb{R}^d$  such that  $\Pi_{\partial\Omega}(x)$  is not a singleton.
- When  $x \notin \Sigma$  and thus  $\Pi_{\partial\Omega}(x)$  is a singleton, its unique element is denoted by  $p_{\partial\Omega}(x)$  and is called the projection of  $x$  onto  $\partial\Omega$ .
- The ray emerging from a point  $p \in \partial\Omega$  is the set  $\text{ray}_{\partial\Omega}(p)$  of elements  $x \in \mathbb{R}^d \setminus \Sigma$  having  $p$  as unique projection:

$$\text{ray}_{\partial\Omega}(p) = \{x \in \mathbb{R}^d \setminus \Sigma, p_{\partial\Omega}(x) = p\}.$$

The signed distance function  $d_\Omega$  to a domain  $\Omega$  and its derivatives encode a great deal of its geometric properties. To express these connections, we henceforth assume that the bounded domain  $\Omega$  is at least of class  $\mathcal{C}^2$ . Note that this assumption may not be minimal for some of the properties discussed below.

**Proposition 3.1.3** *The signed distance function  $d_\Omega$  is differentiable at a point  $x \in \mathbb{R}^d$  if and only if the latter does not belong to  $\Sigma$ ; its gradient is then given:*

$$(3.1.2) \quad \nabla d_\Omega(x) = n(p_{\partial\Omega}(x)) = \frac{x - p_{\partial\Omega}(x)}{d_\Omega(x)};$$

in particular,  $\nabla d_\Omega(x)$  is an extension of the normal vector field  $n : \partial\Omega \rightarrow \mathbb{R}^d$  to  $\mathbb{R}^d \setminus \Sigma$ .

Moreover, there exists an open neighborhood  $U$  of  $\partial\Omega$  in  $\mathbb{R}^d$  such that  $d_\Omega$  is differentiable on  $U$ .

Let us now turn to the second-order properties of the signed distance function. Their formulation involves the  $(d-1)$  principal curvatures  $\kappa_i(p)$  ( $i = 1, \dots, d-1$ ) of  $\partial\Omega$  at points  $p \in \partial\Omega$ , and an associated orthonormal basis  $(\tau_1(p), \dots, \tau_{d-1}(p))$  of the tangent plane  $T_p\partial\Omega$ , see [Section 1.A.1](#) about these notions.

**Proposition 3.1.4** *The following properties hold true:*

(i) *For any point  $x \in \mathbb{R}^d \setminus \overline{\Sigma}$ , one has:*

$$(3.1.3) \quad 1 + \kappa_i(p)d_\Omega(x) > 0, \quad i = 1, \dots, d-1, \text{ where } p \equiv p_{\partial\Omega}(x).$$

(ii) *The projection mapping  $p_{\partial\Omega} : \mathbb{R}^d \setminus \Sigma \rightarrow \partial\Omega$  is differentiable on  $\mathbb{R}^d \setminus \overline{\Sigma}$ , and its derivative reads:*

$$(3.1.4) \quad \forall x \in \mathbb{R}^d \setminus \overline{\Sigma}, \quad \nabla p_{\partial\Omega}(x) = \sum_{i=1}^{d-1} \frac{1}{1 + \kappa_i(p)d_\Omega(x)} \tau_i(p) \tau_i(p)^T, \quad p \equiv p_{\partial\Omega}(x).$$

**Remark 3.1.5**

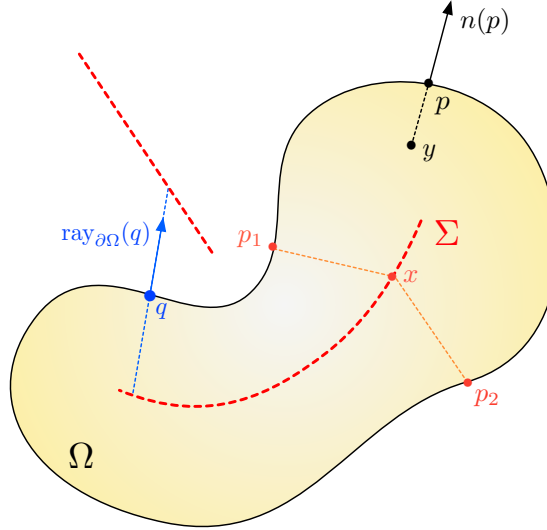


FIGURE 3.1.1. Illustration of the quantities related to the signed distance function introduced in [Section 3.1.1](#). The point  $x \in \Sigma$  has a projection set  $\Pi_{\partial\Omega}(x)$  composed of the two points  $p_1$  and  $p_2$ , while  $y \in \mathbb{R}^d \setminus \Sigma$  admits  $p$  as unique projection and  $\frac{y-p}{d_{\Omega}(y)} = n(p)$ .

- It easily follows from the formulas [\(3.1.2\)](#) and [\(3.1.4\)](#) that if  $\Omega$  is actually of class  $\mathcal{C}^k$  for some  $k \geq 2$ , then  $d_{\Omega}$  and  $p_{\Omega}$  are of class  $\mathcal{C}^k$  and  $\mathcal{C}^{k-1}$  on  $\mathbb{R}^d \setminus \bar{\Sigma}$ , respectively.
- The projection  $p_{\partial\Omega}$  is not differentiable on the boundary  $\partial\Sigma$  of the skeleton  $\Sigma$ . Actually, the following characterization of the closure  $\bar{\Sigma}$  is proved in [\[106\]](#):

$$\bar{\Sigma} = \Sigma \cup \mathcal{C},$$

where the set  $\mathcal{C}$  is made of the conjugate points of  $\Omega$ , which are, loosely speaking the centers of curvature of some region on  $\partial\Omega$ ; mathematically, these are defined as the points  $x \in \mathbb{R}^d$  where [\(3.1.3\)](#) is not satisfied for at least one index  $i$ . Note that  $\mathcal{C}$  is not necessarily disjoint from  $\Sigma$ .

The above material allows to define “natural”, smooth extensions to the whole open set  $\mathbb{R}^d \setminus \bar{\Sigma}$  of the unit normal vector field  $n : \partial\Omega \rightarrow \mathbb{R}^d$  and of any tangential vector field  $\tau : \partial\Omega \rightarrow \mathbb{R}^d$  via the formulas:

$$(3.1.5) \quad \forall x \in \mathbb{R}^d \setminus \bar{\Sigma}, \quad n(x) \equiv n(p_{\partial\Omega}(x)) = \nabla d_{\Omega}(x), \text{ and } \tau(x) \equiv \tau(p_{\partial\Omega}(x)).$$

For this reason at least, it is of great importance in practice to estimate the “size” of the skeleton  $\Sigma$  and of its closure  $\bar{\Sigma}$ , where such extensions are either not possible or not smooth.

### Proposition 3.1.6

- (i) The skeleton  $\Sigma$  has null Lebesgue measure.
- (ii) Provided  $\Omega$  is of class  $\mathcal{C}^3$ , the closure  $\bar{\Sigma}$  also has null Lebesgue measure.

The former statement actually holds true when  $\Omega$  is a general open subset of  $\mathbb{R}^d$ : it is actually a direct consequence of [Proposition 3.1.3](#), the Lipschitz character of  $d_{\Omega}$  and Rademacher’s theorem. The second, highly non trivial statement is proved in [\[106, 250\]](#); note that the additional assumption that  $\Omega$  be of class  $\mathcal{C}^3$  is not a mere technicality, see [\[250\]](#) for an example of a domain of class  $\mathcal{C}^2$  such that  $\bar{\Sigma}$  has positive Lebesgue measure.

**Remark 3.1.7** [Proposition 3.1.3](#) implies, in particular that the signed distance function satisfies the so-called Eikonal property, i.e.:

$$(3.1.6) \quad |\nabla d_{\Omega}(x)| = 1 \text{ for a.e. } x \in \mathbb{R}^d.$$

Unfortunately, many functions satisfy (3.1.6) beyond  $d_\Omega$ ; to turn this requirement into a characterization, one has to resort to the theory of viscosity solutions [137]. In this framework, it is proved in [28] that the unsigned distance function  $d(\cdot, \partial\Omega)$  is the unique viscosity solution to the Eikonal equation:

$$\begin{cases} |\nabla(d(x, \partial\Omega))| = 1 & \text{for } x \in \Omega, \\ d(x, \partial\Omega) = 0 & \text{for } x \in \partial\Omega. \end{cases}$$

The material in this section leads to the following result whereby an integral on the ambient space  $\mathbb{R}^d$  can be rewritten as nested integrals over the boundary  $\partial\Omega$  of a smooth bounded domain  $\Omega \subset \mathbb{R}^d$  and on the normal rays emerging from  $\partial\Omega$ . It follows from an application of the coarea formula in [Theorem 3.A.1](#) to the mapping  $p_{\partial\Omega} : \mathbb{R}^d \setminus \bar{\Sigma} \rightarrow \partial\Omega$ , and from the fact that when  $\Omega$  is of class  $\mathcal{C}^3$ ,  $\bar{\Sigma}$  has null Lebesgue measure.

**Proposition 3.1.8** *Let  $\Omega \subset \mathbb{R}^d$  be a bounded domain of class  $\mathcal{C}^3$ , and let  $\varphi \in L^1(\mathbb{R}^d)$ . Then the following equality holds true:*

$$\int_{\mathbb{R}^d} \varphi(x) \, dx = \int_{\partial\Omega} \int_{z \in \text{ray}_{\partial\Omega}(p)} \varphi(z) \left( \prod_{i=1}^{d-1} (1 + d_\Omega(z) \kappa_i(p)) \right) \, d\ell(z) \, ds(p),$$

where  $d\ell$  is the restriction of the one-dimensional Hausdorff measure to the lines  $\text{ray}_{\partial\Omega}(p)$ .

### 3.1.2. Differentiability of the signed distance function with respect to the domain

This section deals with the sensitivity of the signed distance function  $d_\Omega$  with respect to the domain  $\Omega$ , in the framework of the method of Hadamard presented in [Section 1.3.3](#). The properties recalled below are essentially proved in [155], see also Chap. 4 in [145] for a more detailed account. They have been used in our previous work [A34] to optimize smoothed approximations of multiphase elasticity systems, where the signed distance function to the sharp interface between two regions with different material properties is used to build a smooth transition layer between them. They have subsequently been involved in the modeling and treatment of geometric constraints, as reported in the next [Section 3.1.3](#).

Let us first consider the derivative of the mapping  $\Omega \mapsto d_\Omega(x)$  for a fixed point  $x \in \mathbb{R}^d$ ; an intuitive explanation of these formulas is provided in [Fig. 3.1.2](#).

**Proposition 3.1.9** *Let  $\Omega \subset \mathbb{R}^d$  be a bounded domain of class  $\mathcal{C}^2$ , let  $x \in \mathbb{R}^d \setminus \partial\Omega$  and let  $\theta \in W^{1,\infty}(\mathbb{R}^d, \mathbb{R}^d)$  be a given deformation field. Then, the function  $t \mapsto d_{\Omega_{t\theta}}(x)$  is differentiable at  $t = 0^+$ , and*

- If  $x \in \Omega$ , its derivative reads:

$$\frac{d}{dt} (d_{\Omega_{t\theta}}(x)) \Big|_{t=0^+} = - \inf_{p \in \Pi_{\partial\Omega}(x)} \theta(p) \cdot n(p).$$

- If  $x \in {}^c\bar{\Omega}$ , its derivative reads:

$$\frac{d}{dt} (d_{\Omega_{t\theta}}(x)) \Big|_{t=0^+} = - \sup_{p \in \Pi_{\partial\Omega}(x)} \theta(p) \cdot n(p).$$

If  $x \notin (\partial\Omega \cup \Sigma)$ , the mapping  $\theta \mapsto d_{\Omega_\theta}(x)$  is Gateaux differentiable at  $\theta = 0$ , and its derivative  $d'_\Omega(\theta)(x)$  reads:

$$\forall \theta \in W^{1,\infty}(\mathbb{R}^d, \mathbb{R}^d), \quad d'_\Omega(\theta)(x) = -(\theta \cdot n)(p_{\partial\Omega}(x)).$$

This result essentially follows from the application of a theorem about the differentiation of the minimum value of a parameter-dependent function, see Th. 2.1 in Chap. 10 of [156], and Chap. 4 in [145] for this particular application.

We next turn to the differentiability of integral functionals depending on the shape  $\Omega$  via the signed distance function  $d_\Omega$ , that we illustrate with the following template result.

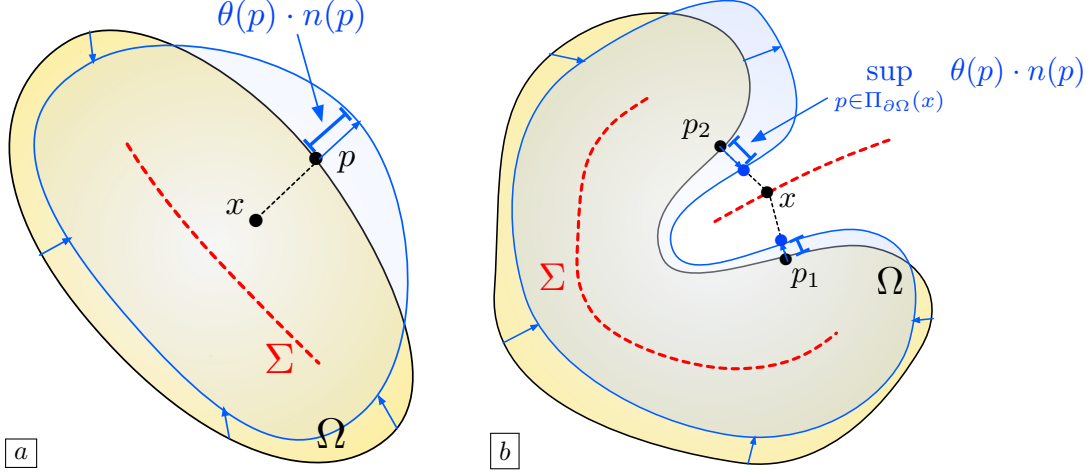


FIGURE 3.1.2. *Differentiation of the signed distance function  $d_\Omega$  with respect to the domain;* (a) *When  $x \in \Omega \setminus \Sigma$ , the (negative) value  $d_\Omega(x)$  decreases by ‘how much’ the closest region of  $\partial\Omega$  draws away;* (b) *When  $x \in \Sigma$  lies outside  $\Omega$ ,  $d_\Omega(x)$  decreases by the maximum distance by which one closest region of  $\partial\Omega$  draws nearer.*

**Proposition 3.1.10** *Let  $D \subset \mathbb{R}^d$  be a bounded domain, and let  $J(\Omega)$  be the function of the domain defined by:*

$$(3.1.7) \quad J(\Omega) = \int_D j(d_\Omega(x)) \, dx,$$

where  $j : \mathbb{R} \rightarrow \mathbb{R}$  is smooth. Let  $\Omega \Subset D$  be a bounded domain of class  $\mathcal{C}^3$ . Then the mapping  $\theta \mapsto J(\Omega_\theta)$  from  $W^{1,\infty}(\mathbb{R}^d, \mathbb{R}^d)$  into  $\mathbb{R}$  is Gateaux differentiable at  $\theta = 0$ , with derivative

$$J'(\Omega)(\theta) = \int_{\partial\Omega} v_\Omega(\theta \cdot n) \, ds, \text{ where } v_\Omega(x) = \int_{\text{ray}_{\partial\Omega}(x) \cap D} j'(d_\Omega(z)) \left( \prod_{i=1}^{d-1} (1 + \kappa_i(x) d_\Omega(z)) \right) \, d\ell(z).$$

*Hint of proof.:* Since  $\Omega$  is of class  $\mathcal{C}^3$ , [Proposition 3.1.6](#) ensure that the closure of the skeleton  $\Sigma$  of  $\Omega$  has 0 Lebesgue measure, and so the integration domain in (3.1.7) can be changed from  $D$  to  $D \setminus \overline{\Sigma}$ . Using the result of [Proposition 3.1.9](#) about the differentiability of the mapping  $\theta \mapsto d_{\Omega_\theta}(x)$  for a fixed point  $x \in D \setminus \overline{\Sigma}$ , together with the Lebesgue dominated convergence theorem (whose application is a little subtle, see Chap. 4 in [145]), we obtain that the mapping  $\theta \mapsto J(\Omega_\theta)$  is Gateaux differentiable, with derivative:

$$J'(\Omega)(\theta) = - \int_{D \setminus \overline{\Sigma}} j'(d_\Omega(x)) (\theta \cdot n)(p_{\partial\Omega}(x)) \, dx.$$

The desired result now follows from the version of the coarea formula in [Proposition 3.1.8](#). □

### 3.1.3. Modeling geometric constraints using the signed distance function

Among its multiple interests, the signed distance function plays a central role in modeling geometric quantities attached to a shape  $\Omega$ , in the perspective of their treatment as constraints in shape optimization problems. Let us mention a few examples among the most prominent such geometric constraints in the literature. We refer to [261] for a more detailed overview of this subject and to [17] for another, recent and interesting development around this theme, devoted to the modeling of accessibility constraints.

- Minimum thickness constraints impose that the optimized shape  $\Omega$  do not contain regions that are thinner than a prescribed threshold  $d_{\min}$ , as thin and frail members are more likely to break during machining or cooling. One possible expression of this property is that the motion of any point  $x \in \partial\Omega$  in the inward normal direction over a distance  $t < d_{\min}$  should result in a point which is

still inside  $\Omega$ , that is:

$$(3.1.8) \quad \forall x \in \partial\Omega, \forall t \in [0, d_{\min}], \quad d_{\Omega}(x - tn(x)) \leq 0,$$

see [Fig. 3.1.3 \(a\)](#). This requirement may be enforced thanks to an integral functional of the form:

$$P(\Omega) = \int_{\partial\Omega} \int_0^{d_{\min}} \left[ d_{\Omega}(x - tn(x)) \right]_+^2 dt dx.$$

In this manuscript, we shall rather use the following shape functional, which is perhaps more heuristic, but easier to handle:

$$(3.1.9) \quad P_{\min T}(\Omega) = - \int_{\Omega} d_{\Omega}^2(x) \left[ d_{\Omega}(x) + \frac{d_{\min}}{2} \right]_+^2 dx.$$

Intuitively,  $P_{\min T}(\Omega)$  favors “thick” regions, until they show the desired thickness value.

- Maximum thickness constraints impose that  $\Omega$  do not contain regions which are thicker than a certain threshold  $d_{\max}$ ; such thick regions are typically undesirable when  $\Omega$  is fabricated by casting as they require a long time to cool down. Mathematically, this boils down to demanding that the signed distance function  $d_{\Omega}$  take everywhere values larger than  $d_{\max}/2$ :

$$(3.1.10) \quad \forall x \in \Omega, \quad d_{\Omega}(x) \geq -\frac{d_{\max}}{2},$$

see [Fig. 3.1.3 \(b\)](#). In order to enforce such maximum thickness constraints, one naive possibility is to rely on an integral penalty functional of the form

$$P(\Omega) = \int_{\Omega} \left[ d_{\Omega}(x) + \frac{d_{\max}}{2} \right]_-^2 dx$$

which should be constrained to be equal to 0. This requirement turns out to be too strict in practice, and produces undesirable numerical artifacts, see [\[261\]](#). It is actually more efficient to impose the following constraint, which stems from the same line of thinking:

$$(3.1.11) \quad P_{\max T}(\Omega) \leq \frac{d_{\max}}{2}, \quad \text{where } P_{\max T}(\Omega) := \left( \frac{1}{\int_{\Omega} h(d_{\Omega}) dx} \int_{\Omega} h(d_{\Omega}) d_{\Omega}^2 dx \right)^{\frac{1}{2}}.$$

Intuitively,  $P_{\max T}(\Omega)$  is an average of (a power of)  $d_{\Omega}$  over the regions where the maximum thickness constraint is violated. It involves an approximate characteristic function  $h(d_{\Omega})$  for these regions, defined from the elementary functions

$$h(s) = H_{\varepsilon} \left( -\frac{2s}{d_{\max}} - 1 \right), \quad \text{where } H_{\varepsilon}(s) = \frac{1}{2} \left( 1 + \tanh \left( \frac{s}{\varepsilon} \right) \right), \quad \varepsilon \ll 1,$$

is a smoothed approximation of the Heaviside function.

- Molding constraints arise in the context where the shape  $\Omega$ , contained in a fixed hold-all domain  $D$ , is fabricated by casting: the mold occupies the region  $D \setminus \bar{\Omega}$ , and is made of several pieces  $D_i \setminus \bar{\Omega}$ , associated to a fixed subdivision  $D = \bigcup_{i=1}^N D_i$ . The shape is produced by pouring the molten material in the region  $\Omega$ , which then solidifies under cooling; each part of the mold is finally drawn for removal in a predefined parting direction  $\xi_i \in \mathbb{S}^{d-1}$ .

The achievement of this process implies that  $\Omega$  should not obstruct the removal of the mold, that is:

$$(3.1.12) \quad \forall i = 1, \dots, N, \quad \forall x \in \partial\Omega \cap D_i, \quad \xi_i \cdot n_{\Omega}(x) \geq 0,$$

see [Fig. 3.1.3 \(c\)](#). This can be imposed thanks to the following integral functional:

$$P_{\text{mold}}(\Omega) = \sum_{i=1}^N \int_{\partial\Omega \cap D_i} \left[ \xi_i \cdot n_{\Omega}(x) \right]_-^2 ds.$$

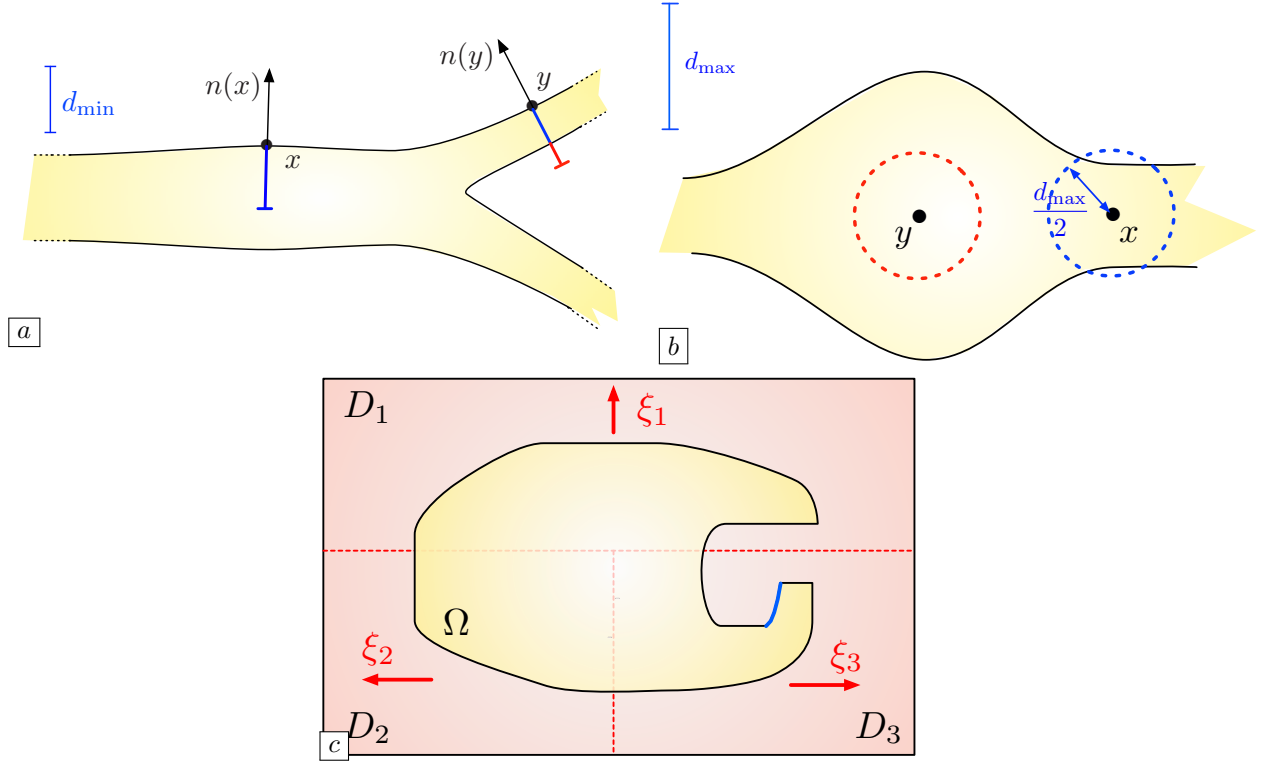


FIGURE 3.1.3. (a) The point  $x$  satisfies the minimum thickness requirement in (3.1.8); (b) Examples of a point  $x$  satisfying the maximum thickness constraint of (3.1.10), and of a point  $y$  violating it; (c) The blue region of  $\partial\Omega$  violates the molding criterion (3.1.12).

The shape derivatives of all the aforementioned functionals of the domain can be calculated with the help of the material of [Section 3.1.2](#); they can therefore be incorporated into standard shape optimization problems formulated in the classical framework outlined in [Section 1.2.3](#), either as objective or as constraint functionals.

**Remark 3.1.11** *In order to keep the previous exposition technically simple, we have focused on intuitive formulations of geometric constraints, sometimes at the expense of physical relevance or practical efficiency. Besides, the practical treatment of such geometric constraints may prove delicate, as it sometimes demands a careful formulation of the shape optimization problem. For instance, minimum thickness constraints may prevent the optimized shape from changing topology (notably, holes from merging), if they are imposed too strictly from the beginning of the optimization process; hence, they are often more efficient when used via a penalization of the objective with increasing strength; we refer to [261] for discussions about all these numerical issues.*

**Remark 3.1.12** *The material contained in this preliminary section about the signed distance function to a subdomain  $\Omega$  of  $\mathbb{R}^d$  can be extended, at least partially, to various contexts. In this manuscript, we shall encounter two instances of such:*

- In [Section 3.4.4](#), the signed distance function to a smooth subdomain  $\Omega$  of the ambient space  $\mathbb{R}^d$  is considered when the latter is equipped with the distance  $d^M(x, y)$  between points  $x, y \in \mathbb{R}^d$ , induced by a positive definite matrix  $M \in \mathbb{R}_{\text{sym}}^{d \times d}$ , as a means to define anisotropic notions of thickness.
- In [Section 4.3](#), the signed distance function to a region  $\Omega$  within an hypersurface  $S$  of  $\mathbb{R}^d$  is defined from the geodesic distance  $d^S(x, y)$  between points  $x, y \in S$  of [Definition 1.A.2](#), in order to describe thin tubular neighborhoods of  $\partial\Omega$ .

### 3.2 AN EFFICIENT, GENERAL PURPOSE OPTIMIZATION ALGORITHM

The present chapter being generally devoted to the understanding of various types of engineering design constraints, it is natural to inquire first about how such constraints can be efficiently incorporated into shape and topology optimization algorithms. Admittedly, several constrained optimization algorithms have been developed for infinite-dimensional settings: the augmented Lagrangian method [286], the Method of Moving Asymptotes [348], the Sequential Linear Programming algorithm [166], the Method of Feasible Directions [359], to name a few popular strategies. Surprisingly enough, relatively few of them are completely satisfactory in shape and topology optimization applications. In particular, they all involve non physical and rather unintuitive parameters (the penalty parameter in the augmented Lagrangian method, the size of the trust region in the Sequential Linear Programming algorithm, ...), whose tuning demands manual and costly trial-and-error steps that must be carried out before each application.

This section summarizes the work carried out in [A14] where a general purpose optimization algorithm is proposed and analyzed, which is capable of handling multiple equality and inequality constraints and is suitable for shape and topology optimization applications. Note that a quite similar optimization strategy was developed concurrently in the article [58].

#### 3.2.1. Abstract presentation of the algorithm

In this section, we describe our optimization algorithm in the general and abstract context of a Hilbert space  $(H, \langle \cdot, \cdot \rangle_H)$ . For simplicity of the presentation, we consider an equality-constrained optimization problem

$$(3.2.1) \quad \min_{h \in H} J(h) \text{ s.t. } G(h) = 0,$$

where  $J : H \rightarrow \mathbb{R}$  is a (smooth) objective function and  $G(h) := (G_i(h))_{i=1,\dots,p}$  is a collection of  $p$  (smooth) real-valued equality constraints. Let us emphasize that, up to a slight increase in technicality, our methodology can be adapted to problems which additionally feature multiple inequality constraints, as exemplified by the numerical examples presented in [Section 3.2.2](#) and the later [Chapter 5](#).

Let  $\theta_J$  and  $\theta_{G_i} \in H$  be the gradients associated to the derivatives  $J'(h)$  and  $G'_i(h)$  of  $J(h)$  and  $G_i(h)$  at a particular  $h \in H$ , that is:

$$\forall \hat{h} \in H, \quad J'(h)(\hat{h}) = \langle \theta_J, \hat{h} \rangle_H \text{ and } G'_i(h)(\hat{h}) = \langle \theta_{G_i}, \hat{h} \rangle_H,$$

and we assume that the following constraint qualification property is satisfied:

$$(3.2.2) \quad \text{The gradients } \theta_{G_i} \text{ are linearly independent.}$$

The null space  $\text{Ker } G'(h)$  of the derivative of the constraint function  $G(h)$  is given by:

$$\text{Ker } G'(h) = \left\{ \xi \in H, \langle \theta_{G_i}, \xi \rangle_H = 0, i = 1, \dots, p \right\} = \left( \text{span } \{ \theta_{G_i} \}_{i=1,\dots,p} \right)^\perp.$$

The iterative resolution of (3.2.1) relies on updates of the optimization variable  $h$  between two successive steps  $n$ ,  $(n+1)$  (the reference to which being omitted for simplicity) of the form

$$(3.2.3) \quad h + \Delta t \xi, \text{ with the descent direction } \xi = -(\alpha_J \xi_J + \alpha_G \xi_G).$$

Here,  $\Delta t$  is a pseudo-time step,  $\alpha_J, \alpha_G$  are fixed positive weights and the contributions  $\xi_J, \xi_G \in H$  are the two orthogonal vectors in  $H$  that we now define:

- The null-space step  $\xi_J$  is the orthogonal projection of  $\theta_J$  onto the null space of the constraints  $\text{Ker } G'(h)$ , that is:

$$\xi_J \in \text{Ker } G'(h) \text{ and } \theta_J - \xi_J \in \left( \text{Ker } G'(h) \right)^\perp.$$

Using the fact that  $(\text{Ker } G'(h))^\perp = \text{span } \{ \theta_{G_i} \}_{i=1,\dots,p}$ ,  $\xi_J$  turns out to be of the form:

$$\xi_J = \theta_J + \sum_{j=1}^p \lambda_j \theta_{G_j},$$

where the scalar coefficients  $\lambda_1, \dots, \lambda_p$  are characterized by the requirements

$$G'_i(h)(\xi_J) = \langle \theta_{G_i}, \xi_J \rangle_H = 0, \text{ for } i = 1, \dots, p,$$

that we may gather as a  $p \times p$  system for  $\lambda = (\lambda_1, \dots, \lambda_p) \in \mathbb{R}^p$ :

$$(3.2.4) \quad S\lambda = b, \text{ where } S_{ij} = \langle \theta_{G_i}, \theta_{G_j} \rangle_H \text{ and } b_i = -\langle \theta_J, \theta_{G_i} \rangle_H.$$

This system is invertible thanks to the constraint qualification condition (3.2.2).

The null space step  $\xi_J$  satisfies the intuitive property that the (negative) normalized vector  $-\xi_J/\|\xi_J\|_H$  is the best normalized descent direction for  $J$  that leaves the value of the constraint functional unaltered at first order, that is:

$$-\frac{\xi_J}{\|\xi_J\|_H} = \arg \min_{\xi \in H} J'(h)(\xi) \text{ s.t. } \begin{cases} G'(h)(\xi) = 0, \\ \langle \xi, \xi \rangle_H \leq 1, \end{cases}$$

a fact which is easily proved from the first-order optimality conditions of this convex program.

- The range step  $\xi_G$  is the contribution to the update (3.2.3) in charge of decreasing the violation of constraints. Its definition is based on the following observation: the set of solutions to the convex minimization problem

$$(3.2.5) \quad \min_{\xi \in H} \|G(h) + G'(h)(\xi)\|^2,$$

involving a Gauss-Newton measure of the violation of constraints, is exactly the affine subspace

$$\{-\xi_G + \zeta, \zeta \in \text{Ker } G'(h)\},$$

where  $-\xi_G \in H$  is the unique solution to (3.2.5) which is orthogonal to  $\text{Ker } G'(h)$ .

In fact,  $\xi$  is solution to (3.2.5) if and only if it satisfies the associated Euler-Lagrange equation:

$$(3.2.6) \quad \sum_{i=1, \dots, p} (G_i(h) - G'_i(h)(\xi)) \theta_{G_i} = 0.$$

Since the gradients  $\theta_{G_i}$  are linearly independent, this readily implies that the set of solutions to (3.2.5) is an affine subspace of  $H$  which is parallel to the null space  $\text{Ker } G'(h)$  of the constraints. Besides, any solution  $\xi_G$  to (3.2.5) (or (3.2.6)) which belongs to  $(\text{Ker } G'(h))^\perp = \text{span } \{\theta_{G_i}\}_{i=1, \dots, p}$  is of the form

$$-\xi_G = \sum_{i=1}^p \beta_i \theta_{G_i} \text{ for some } \beta_1, \dots, \beta_p \in \mathbb{R};$$

injecting this expression into (3.2.6) yields the following invertible  $p \times p$  system for the coefficient vector  $\beta = (\beta_1, \dots, \beta_p) \in \mathbb{R}^p$ :

$$S\beta = c \text{ where } S \text{ is defined in (3.2.4) and } c_i = G_i(h), i = 1, \dots, p,$$

which characterizes explicitly the range step  $\xi_G$ .

Intuitively, the weights  $\alpha_J$  and  $\alpha_G$  of the contributions  $\xi_J$  and  $\xi_G$  to the update  $\xi$  in (3.2.3) encode the relative rates of the decrease of the objective  $J(h)$  and of the violation of the constraints  $G(h) = 0$  entailed by the update vector  $\xi$ , respectively. This point is more clearly explained by the following calculation; the update of the variable  $h$  by the rule (3.2.3) ensures that:

$$\begin{aligned} G(h + \Delta t \xi) &\approx G(h) + \Delta t G'(h)(\xi) \\ &= G(h) - \alpha_G \Delta t G'(h)(\xi_G) \\ &= (1 - \alpha_G \Delta t) G(h), \end{aligned}$$

where the second line follows from the fact that  $\xi_J$  belongs to the null space  $\text{Ker } G'(h)$  of the constraints, and the last line follows from the property (3.2.6) of  $\xi_G$ . In other words, the violation of constraints decreases by a percentage of  $\alpha_G \Delta t$  in the course of the update (3.2.3).

Hence, as we have mentioned, one of the great assets of the above optimization strategy is that it features only a few parameters which have an intuitive interpretation and do not require any cumbersome fine tuning. In fact, beyond the time step  $\Delta t$ , only the values of  $\alpha_J$  and  $\alpha_G$  have to be specified by the user.

Let us eventually comment about the choice of the time step  $\Delta t$  in the update (3.2.3). In order to ensure that the latter be not “too large”, we utilize a so-called merit function  $M(h)$ , i.e. a function for which the

update vector  $\xi$  in (3.2.3) is a descent direction. One such function reads:

$$M(h) = \alpha_J \left( J(h) + \sum_{i=1}^p \lambda_i G_i(h) \right) + \frac{\alpha_G}{2} S^{-1} G(h) \cdot G(h).$$

During each iteration of the optimization process, we require that  $\Delta t$  be so small that:

$$M(h + \Delta t \xi) < M(h) \text{ (possibly up to a small tolerance).}$$

**Remark 3.2.1** *An open-source implementation of this algorithm, due to F. Feppon, is available at the following address:*

<https://gitlab.com/florian.feppon/null-space-optimizer>

### 3.2.2. Application in shape and topology optimization and a numerical example

This null space optimization algorithm naturally takes place in the context of a Hilbert space; its application in shape optimization in combination with Hadamard's boundary variation method (see Section 1.3.3.1) leverages the Hilbertian method introduced in Section 1.3.5. As we have seen, the latter restricts the considered deformations  $\theta$  of a reference shape  $\Omega \subset \mathbb{R}^d$  to a Hilbert space  $(H, \langle \cdot, \cdot \rangle_H)$  contained in  $W^{1,\infty}(\mathbb{R}^d, \mathbb{R}^d)$ . Thus, the search for a deformation  $\theta$  "improving" the performance of  $\Omega$  with respect to a constrained optimization problem of the form

$$\min_{\Omega} J(\Omega) \text{ s.t. } \begin{cases} G(\Omega) = 0, \\ H(\Omega) = 0, \end{cases} \text{ where } G(\Omega) \text{ and } H(\Omega) \text{ are equality and inequality constraint functions,}$$

boils down to the search of a an update vector  $\theta \in H$  from the initial value 0 for the problem

$$\min_{\theta \in H} J(\Omega_\theta) \text{ s.t. } \begin{cases} G(\Omega_\theta) = 0, \\ H(\Omega_\theta) = 0, \end{cases}$$

which fits in the abstract framework of the previous Section 3.2.1.

**Remark 3.2.2** *In this context where the optimized deformation  $\theta$  has a clear physical meaning, the weights  $\alpha_J, \alpha_G$  in the update (3.2.3) between two successive optimization steps  $n, (n+1)$  (whose related iteration-dependent quantities are labelled by  $^n$  and  $^{n+1}$ , respectively) can be directly tied to physical quantities. Indeed, choosing iteration dependent parameters  $\alpha_J \equiv \alpha_J^n, \alpha_G \equiv \alpha_G^n$  defined by*

$$\alpha_J^n = \frac{A_J \Delta x}{\|\xi_J^n\|_{L^\infty(D)^d}}, \text{ and } \alpha_G^n = \frac{A_G \Delta x}{\|\xi_G^n\|_{L^\infty(D)^d}},$$

where  $\Delta x$  stands for the average size of edges in the mesh of the computational domain  $D$  and  $A_J, A_G$  are fixed real values, ensures that the update  $\xi$  entails a motion with maximum spatial amplitude  $\Delta t(A_J + A_G)\Delta x$ ; the coefficients  $A_J, A_G$  are naturally interpretable as the relative contributions of the decrease of the objective function and of the violation of the constraints to this motion.

Let us apply this null space algorithm to deal with an example in structural optimization. The considered setting is that of a 2d bridge: the optimized shape  $\Omega$  is contained in a computational domain  $D$  with size  $10 \times 2$ , and it is clamped on two regions  $\Gamma_D$  near the lower-left and right corners of  $\partial D$ . Nine different situations are possible in terms of the applied loads; in each one of them, indexed by  $i = 0, \dots, 8$ , a unit vertical load  $g_i$  is applied on a region  $\Gamma_{N,i}$  of the upper side of  $\partial D$ , see Fig. 3.5.6. The performance of  $\Omega$  under the load case  $g_i$  is measured in terms of its compliance

$$C_i(\Omega) = \int_{\Omega} A e(u_{\Omega,i}) : e(u_{\Omega,i}) \, dx,$$

where  $u_{\Omega,i}$  is the elastic displacement of  $\Omega$  in this situation.

The shape optimization problem of interest consists in minimizing the volume  $\text{Vol}(\Omega)$  of the structure  $\Omega$  under the constraint that each individual compliance  $C_i(\Omega)$  do not exceed a given threshold  $C_T$ :

$$(3.2.7) \quad \min_{\Omega} \text{Vol}(\Omega) \text{ s.t. } C_i(\Omega) \leq C_T \text{ for all } i = 0, \dots, 8.$$

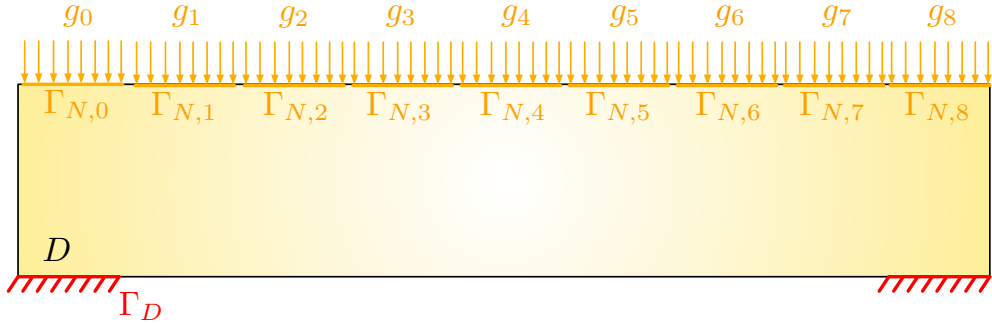


FIGURE 3.2.1. *Setting of the bridge optimization problem under multiple load cases considered in Section 3.2.*

The value of  $C_T$  is set to a fraction of the maximum of the compliances of the initial design  $\Omega^0$ , which is depicted on Fig. 3.2.3 (a):

$$(3.2.8) \quad C_T = 0.7 \max_{i=0,\dots,8} C_i(\Omega^0).$$

We solve (3.2.7) by the combination of the present null space optimization algorithm with the level set based mesh evolution strategy presented in Section 1.4.7. Several intermediate shapes are displayed on Fig. 3.2.3, and the meshes of the initial and final designs are represented on Fig. 3.2.2. The convergence histories are reported on Fig. 3.2.4; they allow to verify the decrease of the objective function even after the saturation of the constraints.

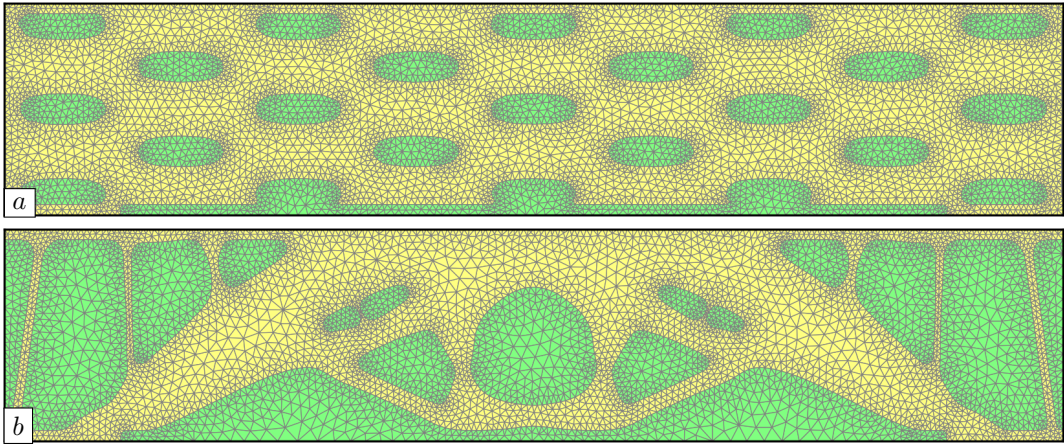


FIGURE 3.2.2. *Meshes of (a) The initial shape, (b) The optimized shape in the bridge optimization problem under multiple load cases of Section 3.2.*

### 3.3 A VARIATIONAL METHOD FOR THE EVALUATION OF THE SHAPE DERIVATIVES OF GEOMETRIC FUNCTIONS

As illustrated by the various geometric constraint models described in Section 3.1.3, functionals depending on the domain  $\Omega$  via the signed distance function  $d_\Omega$  to  $\Omega$ , say, of the form:

$$J(\Omega) = \int_D j(d_\Omega(x)) \, dx,$$

where  $D \subset \mathbb{R}^d$  is a fixed computational domain and  $j : \mathbb{R} \rightarrow \mathbb{R}$  is smooth enough, have manifold applications in shape optimization. The usage of such a functional in algorithms raises the need to compute its shape

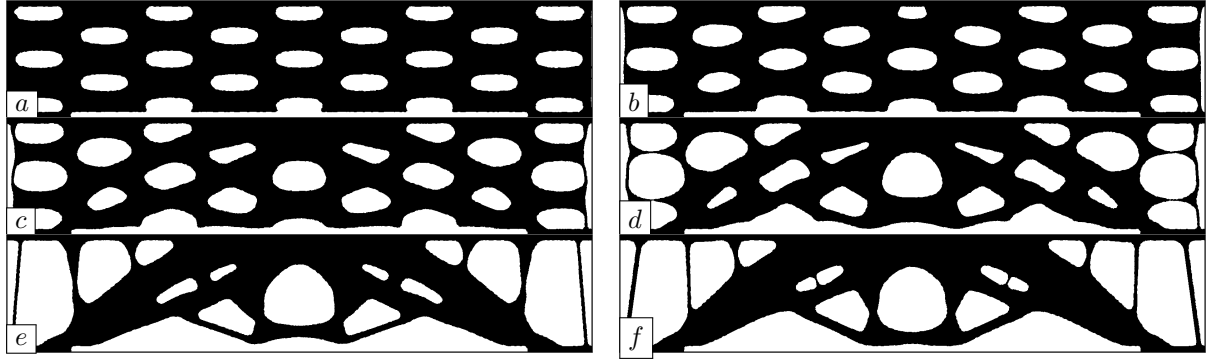


FIGURE 3.2.3. Iterations (a) 0, (b) 5, (c) 10, (d) 20, (e) 80, and (f) 300 in the bridge optimization problem under multiple load cases considered in [Section 3.2](#).

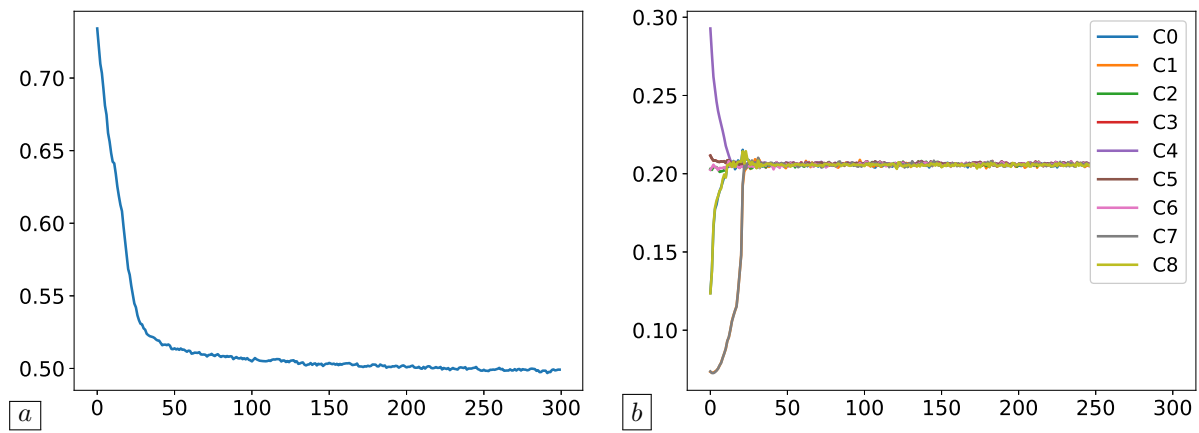


FIGURE 3.2.4. Convergence histories for the bridge optimization problem under multiple load cases of [Section 3.2](#); (a) Evolution of the volume  $\text{Vol}(\Omega)$ ; (b) Values of the constraints  $C_i(\Omega)$ .

derivative  $J'(\Omega)(\theta)$ , whose expression reads, under suitable regularity assumptions about  $\Omega$ :

$$(3.3.1) \quad J'(\Omega)(\theta) = \int_{\partial\Omega} v_\Omega(\theta \cdot n) \, ds, \text{ where } v_\Omega(x) = - \int_{\text{ray}_{\partial\Omega}(x) \cap D} j'(d_\Omega(z)) \left( \prod_{i=1}^{d-1} (1 + d_\Omega(z) \kappa_i(x)) \right) \, d\ell(z),$$

see [Section 3.1.2](#). However feasible, the numerical implementation of this formula is cumbersome for multiple reasons:

- At first, it requires the identification of the sets  $\text{ray}_{\partial\Omega}(x)$ ,  $x \in \partial\Omega$ . This task can be realized thanks to a variant of the method of characteristics, but it requires adequate data structures to travel efficiently the mesh of the computational domain  $D$ , especially when the latter is simplicial, see [Section 1.4.7.2](#) about this point.
- It then involves integrals along these normal rays. Notably, when  $J(\Omega)$  also depends on the solution  $u_\Omega$  to a boundary value problem posed on  $\Omega$ , the calculation of these implies to evaluate derivatives of  $u_\Omega$  (and of the adjoint state  $p_\Omega$ ) on these rays.
- It depends on the principal curvatures  $\kappa_i$ ,  $i = 1, \dots, d - 1$  of  $\partial\Omega$ . However ubiquitous in scientific computing, it is notoriously difficult to compute these functions with sufficient accuracy and robustness to numerical artifacts.

In this section, we summarize a novel numerical technique introduced in the work [\[A15\]](#) to evaluate derivative formulas of the form [\(3.3.1\)](#) via the solution to a “simple” variational problem, thus alleviating

the need to identify and handle the normal rays to the boundary of the shape. After a formal sketch of the main ideas in the next [Section 3.3.1](#), we present a validation example in [Section 3.3.2.1](#), and we treat a shape optimization example featuring geometric constraints with this method in [Section 3.3.2.2](#).

### 3.3.1. A formal insight about the main idea

Let  $D \subset \mathbb{R}^d$  be a fixed bounded, Lipschitz computational domain, and let  $\Omega \Subset D$  be a shape with skeleton  $\Sigma$ . We also introduce the open set  $U = D \setminus \overline{\Sigma}$  and we denote by  $\beta = \nabla d_\Omega : U \rightarrow \mathbb{R}^d$  the natural extension to  $U$  of the normal vector field  $n : \partial\Omega \rightarrow \mathbb{R}^d$ . For a given, smooth enough function  $f : U \rightarrow \mathbb{R}$ , we aim to calculate the quantity:

$$(3.3.2) \quad u_f(x) := \int_{\text{ray}_{\partial\Omega}(x)} f(z) \left( \prod_{i=1}^{d-1} (1 + d_\Omega(z) \kappa_i(x)) \right) d\ell(z), \quad \text{for } x \in \partial\Omega,$$

without having to identify the set  $\text{ray}_{\partial\Omega}(x)$  or to calculate integrals on the latter, compare with [\(3.3.1\)](#).

#### 3.3.1.1. From the calculation of a quantity along rays to the resolution of a variational problem

The key idea to achieve this is to express  $u_f$  in terms of the solution to a suitable variational problem. In this perspective, let us consider the following formulation:

$$(3.3.3) \quad \text{Search for } u \in V_\omega \text{ s.t. } \forall v \in V_\omega, \quad \int_{\partial\Omega} uv \, ds + \int_U \omega(\beta \cdot \nabla u)(\beta \cdot \nabla v) \, dx = \int_D fv \, dx,$$

where  $\omega : U \rightarrow \mathbb{R}$  is a continuous, positive weight function to be specified, and  $V_\omega$  is the Hilbert space

$$V_\omega = \left\{ v \in L^2_{\text{loc}}(U), \quad \int_U \omega v^2 \, dx + \int_U \omega(\beta \cdot \nabla v)^2 \, dx < \infty \right\}.$$

Let us assume for a moment that this problem has a unique solution  $u \in V_\omega$ , and that the space  $V_\omega$  has the following property:

$$\forall v_0 \in \mathcal{C}^\infty(\partial\Omega), \quad \exists v \in V_\omega \text{ s.t. } \begin{cases} v = v_0 \text{ on } \partial\Omega, \\ v \text{ is constant along the sets } \text{ray}_{\partial\Omega}(x) : \beta \cdot \nabla v = 0. \end{cases}$$

Then, for any  $v_0 \in \mathcal{C}^\infty(\partial\Omega)$ , introducing such a function  $v$ , we obtain:

$$\begin{aligned} \int_{\partial\Omega} uv_0 \, ds &= \int_{\partial\Omega} uv \, ds + \int_U \omega(\beta \cdot \nabla u)(\beta \cdot \nabla v) \, dx \\ &= \int_U fv \, dx \\ &= \int_{\partial\Omega} \left( \int_{\text{ray}_{\partial\Omega}(x)} f(z) \left( \prod_{i=1}^{d-1} (1 + d_\Omega(z) \kappa_i(x)) \right) d\ell(z) \right) v_0(x) \, ds(x), \end{aligned}$$

where the first line is a consequence of the fact that  $\beta \cdot \nabla v = 0$  and the last line follows from the coarea formula of [Proposition 3.1.8](#). Since this identity holds for any  $v_0 \in \mathcal{C}^\infty(\partial\Omega)$ , the solution  $u$  to [\(3.3.3\)](#) thus satisfies:

$$u(x) = \int_{\text{ray}_{\partial\Omega}(x)} f(z) \left( \prod_{i=1}^{d-1} (1 + d_\Omega(z) \kappa_i(x)) \right) d\ell(z), \quad \text{for } x \in \partial\Omega.$$

which is exactly the quantity  $u_f$  that we aim to calculate, see [\(3.3.2\)](#).

The rigorous realization of this idea demands that the weight  $\omega$  be chosen so that all the facts that we have admitted in the above argument hold true. This is guaranteed by the following result, whose quite technical assumptions are not rigorously stated to keep the presentation simple; let us solely mention that they are satisfied for a wide variety of practical choices for  $\omega$ .

**Theorem 3.3.1** *Let  $\omega : U \rightarrow \mathbb{R}$  be a continuous weight function taking positive values on  $U$ . Under “mild assumptions” about  $\omega$ , it holds:*

- (i) *(Existence and surjectivity of traces): There exists a bounded trace operator  $V_\omega \ni v \mapsto v|_{\partial\Omega} \in L^2(\partial\Omega)$ , which extends the usual restriction of smooth functions to  $\partial\Omega$ . Furthermore, for any  $v_0$  in  $L^2(\partial\Omega)$ , there exists one function  $v \in V_\omega$  such that  $\beta \cdot \nabla v = 0$  on  $U$  and  $v|_{\partial\Omega} = v_0$ .*

(ii) (Poincaré's inequality): There exists a constant  $C > 0$  such that

$$\forall v \in V_\omega, \quad \int_U \omega v^2 \, dx \leq C \left( \int_{\partial\Omega} v^2 \, ds + \int_U (\beta \cdot \nabla v)^2 \, dx \right).$$

(iii) The problem (3.3.3) is well-posed for any  $f \in L^\infty(U)$  and its unique solution  $u$  satisfies  $u|_{\partial\Omega} = u_f$ , where  $u_f$  is defined in (3.3.2).

**Remark 3.3.2** The above presentation only reports on a particular case of the general framework considered in [A15], where  $\beta : U \rightarrow \mathbb{R}^d$  is a more general vector field, and the sets  $\text{ray}_{\partial\Omega}(x)$  are replaced by the characteristic curves  $s \mapsto \eta(s, y)$  of  $\beta$  emerging from points  $y$  on the surface  $\partial\Omega$ , i.e. the solutions to the ordinary differential equation

$$\begin{cases} \frac{d\eta}{ds}(s, y) = \beta(\eta(s, y)) \\ \eta(0, y) = y. \end{cases}$$

### 3.3.1.2. About the choice of the weight function $\omega$

The previous section paves the way to a simple method for calculating the quantity  $u_f$  in (3.3.2): after selection of a weight  $\omega$  satisfying the “mild” assumptions of [Theorem 3.3.1](#), we calculate the solution  $u \in V_\omega$  to the variational problem (3.3.3) and  $u_f$  is obtained as the trace on  $\partial\Omega$  of  $u$ .

In principle, this process does not depend on the weight  $\omega$  as long as it fulfills the “mild hypotheses” of [Theorem 3.3.1](#), which leaves freedom about its definition. In practice, however, we would like to solve the variational problem (3.3.3) with a “simple” Lagrange  $\mathbb{P}_1$  finite element method, and some weight functions may be more adapted than others to this purpose.

In order to get a formal insight into this question, and not aiming at precise statements, let us assume that  $D$  is equipped with a simplicial mesh  $\mathcal{T}$ , and let  $V_\mathcal{T}$  denote the space of  $\mathbb{P}_1$  Lagrange finite element functions on  $\mathcal{T}$ , i.e.

$$V_\mathcal{T} = \{v_\mathcal{T} \in \mathcal{C}(\overline{D}), \forall T \in \mathcal{T}, v_\mathcal{T}|_T \text{ is affine}\}.$$

Let also  $u_\mathcal{T} \in V_\mathcal{T}$  be the solution to the finite element discretization of (3.3.3). A combination of the trace inequality with Céa's lemma yields:

$$\|u|_{\partial\Omega} - u_\mathcal{T}|_{\partial\Omega}\|_{L^2(\partial\Omega)} \leq C \|u - u_\mathcal{T}\|_{V_\omega} \leq C \inf_{v_\mathcal{T} \in V_\mathcal{T}} \|u - v_\mathcal{T}\|_{V_\omega},$$

for some constant  $C$  depending on  $\omega$ . In order to leave the possibility for the term in the above right-hand side to become “very small” upon refinement of  $\mathcal{T}$ , it seems appropriate to select a weight  $\omega$  vanishing near  $\overline{\Sigma}$ , so that a lesser weight be attributed to the region where  $u$  is discontinuous and  $u_\mathcal{T}$  is continuous.

A convenient class of weights built from this intuition is supplied by the next lemma.

**Lemma 3.3.3** For any  $p < 2$ , the weight function

$$\omega(x) = \frac{1}{1 + |\Delta d_\Omega(x)|^p}$$

satisfies the assumptions of [Theorem 3.3.1](#).

### Remark 3.3.4

- The weights in the above statement do not vanish on the whole set  $\overline{\Sigma}$  but only at the conjugate points  $x \in \mathcal{C}$ , see [Remark 3.1.5](#). Nevertheless, in practice, such functions  $\omega$  take very small values on  $\overline{\Sigma}$ , which is the crucial point in the selection of a suitable weight.
- The definition of the weight functions in [Lemma 3.3.3](#) depends on the principal curvatures  $\kappa_i$  of  $\partial\Omega$  via the second-order derivatives of the signed distance function  $d_\Omega$ , see [Proposition 3.1.4](#). This might seem to contradict the aforementioned desire to avoid the calculation of these quantities which are prone to numerical artifacts. Again, the evaluation of these curvatures does not need to be very precise when it comes to evaluating  $\omega$ , as the latter function should only be expected to take “small” values on  $\overline{\Sigma}$ .
- In practice, choosing  $p \geq 2$  also yields good results, although there is no rigorous justification of this fact.

### 3.3.2. Numerical illustrations

This section contains two types of numerical illustrations of our variational method for calculating integrals along rays. After a numerical validation of our method in [Section 3.3.2.1](#), we illustrate its use in the context of a shape and topology optimization problem containing geometric constraints in [Section 3.3.2.2](#).

#### 3.3.2.1. About the choice of the weight function

In this first example, we verify the accuracy of our variational method on a relatively simple problem, which already has its own interest. For given  $u_0 \in L^2(\partial\Omega)$ , we aim to construct a function  $u : U \rightarrow \mathbb{R}$  with trace  $u_0$  on  $\partial\Omega$ , and which is constant along the normal rays to  $\partial\Omega$ , viz.:

$$\begin{cases} \nabla d_\Omega \cdot \nabla u = 0 & \text{on } U, \\ u = u_0 & \text{on } \partial\Omega. \end{cases}$$

Let  $\omega : U \rightarrow \mathbb{R}$  be a weight function satisfying the assumptions of [Theorem 3.3.1](#). It is relatively simple to prove that this problem has a unique solution  $u \in V_\omega$ , a good approximation of which is obtained by solving the following (well-posed) variational problem

$$(3.3.4) \quad \text{Search for } u \in V_\omega \text{ s.t. } \forall v \in V_\omega, \quad \frac{1}{\varepsilon} \int_{\partial\Omega} uv \, ds + \int_U \omega(\beta \cdot \nabla u)(\beta \cdot \nabla v) \, dx = \frac{1}{\varepsilon} \int_{\partial\Omega} u_0 v \, ds,$$

where the boundary condition  $u = u_0$  on  $\partial\Omega$  is imposed by penalization, with a “small” parameter  $\varepsilon > 0$ .

Let  $D$  be the unit square  $(0, 1)^2$  in  $\mathbb{R}^2$ , and let  $\Omega \subset D$  be an ellipse, which is explicitly discretized in the mesh of  $D$ . We solve the variational problem (3.3.4) with the Lagrange  $\mathbb{P}_1$  finite element method in three situations, which are illustrated on [Fig. 3.3.1](#).

- (1) A simplicial mesh  $\mathcal{T}'$  of  $D$  is used where the skeleton  $\Sigma$  is truncated, with the weight  $\omega = 1$ ;
- (2) A simplicial mesh  $\mathcal{T}$  of  $D$  is used with the weight  $\omega = 1$ ;
- (3) A simplicial mesh  $\mathcal{T}$  of  $D$  is used with the weight  $\omega = \frac{2}{1+|\Delta d_\Omega|^2}$ .

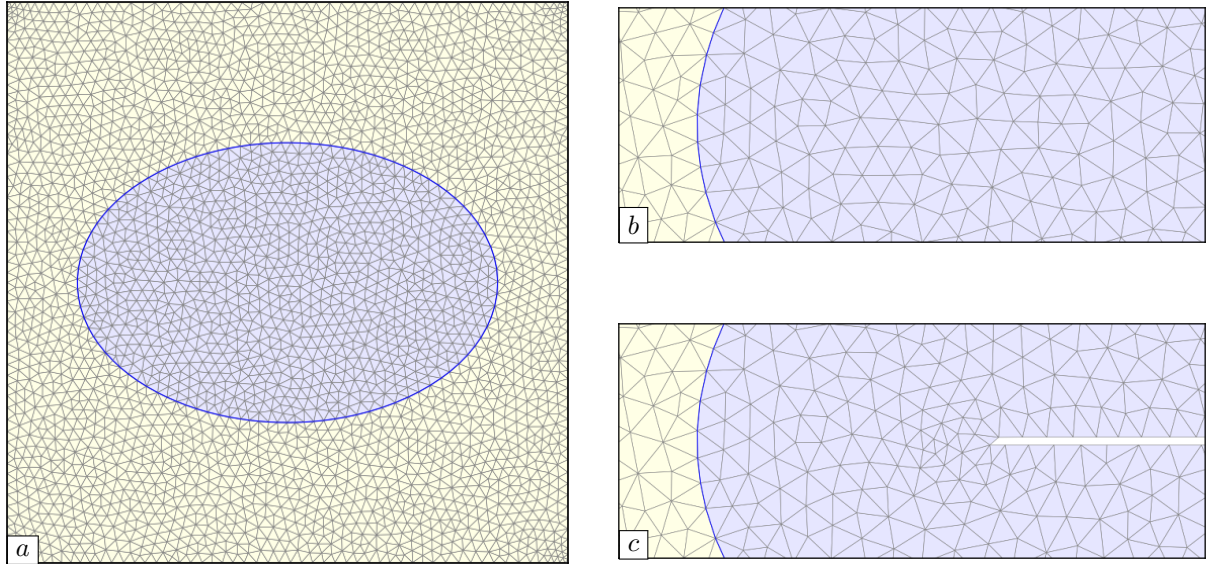


FIGURE 3.3.1. Meshes  $\mathcal{T}$  and  $\mathcal{T}'$  used for the test case of [Section 3.3.2.1](#); (a) Mesh  $\mathcal{T}$  of the hold-all domain  $D$  with  $\Omega \subset D$  discretized as a submesh (in blue); (b) Zoom on  $\mathcal{T}$ ; (c) Zoom on the mesh  $\mathcal{T}'$ .

The results are presented on [Fig. 3.3.2](#). As expected, the resolution of (3.3.4) on the mesh  $\mathcal{T}'$  where the skeleton  $\Sigma$  has been truncated flawlessly delivers a function  $u$  which is constant along the normal rays to  $\partial\Omega$ . In the second experiment, where no such truncation has been performed the mesh  $\mathcal{T}$  and where the weight  $\omega = 1$  is used, the numerical resolution of (3.3.4) is polluted by the very bad approximation of functions

$u : U \rightarrow \mathbb{R}$  which are constant along rays by Lagrange  $\mathbb{P}_1$  finite element functions. Finally, when the same mesh  $\mathcal{T}$  of  $D$  is used with the weight  $\omega = \frac{2}{1+|\Delta d_\Omega|^2}$ , the solution of (3.3.4) becomes much more accurate: the numerical solution  $u$  is “almost discontinuous” across  $\Sigma$ , up to what is allowed by the representation by  $\mathbb{P}_1$  finite element functions.

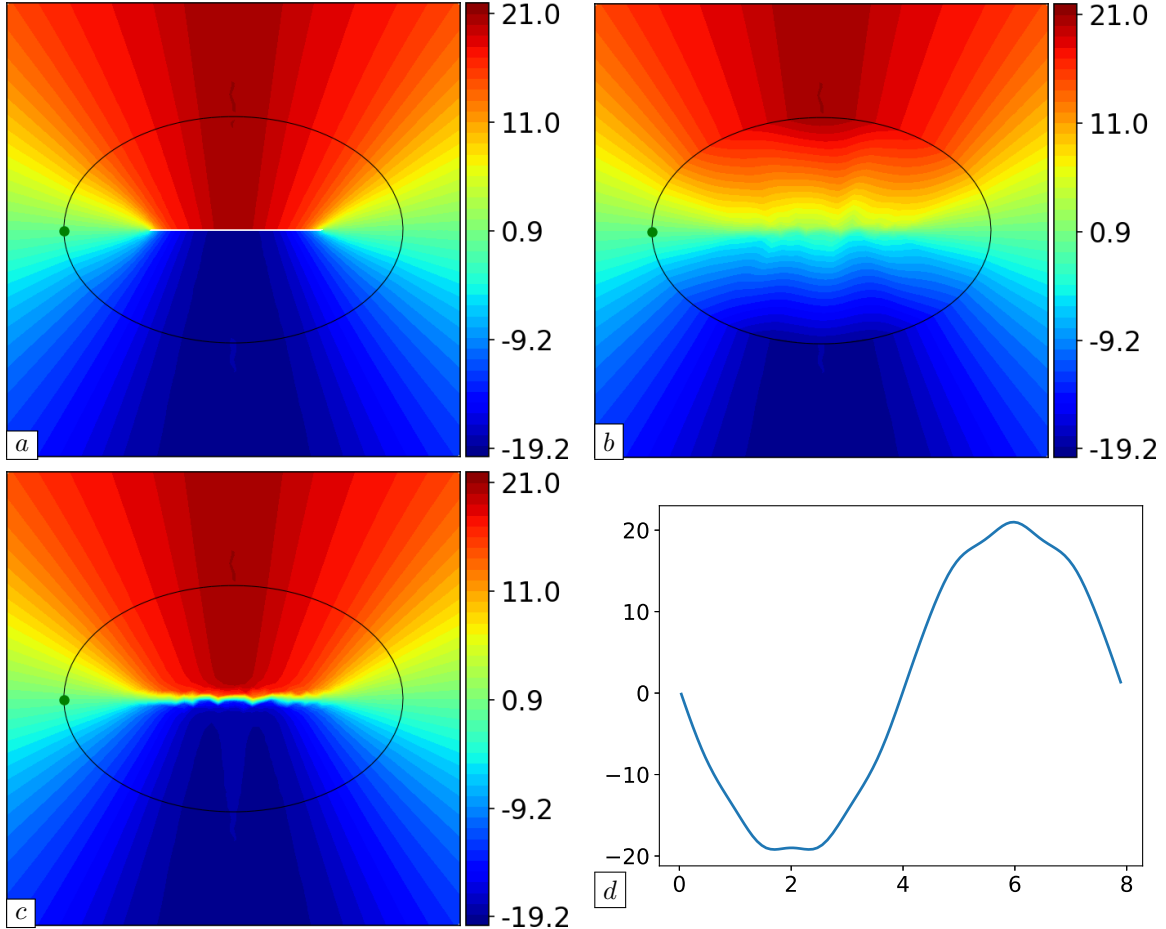


FIGURE 3.3.2. Calculation of the extension of a function  $u_0 \in L^2(\partial\Omega)$  which is constant along rays thanks to the variational problem (3.3.4) for (a) The mesh  $\mathcal{T}'$  and  $\omega = 1$ ; (b) The mesh  $\mathcal{T}$  and the weight  $\omega = 1$ ; (c) The mesh  $\mathcal{T}$  and the weight  $\omega = 2/(1+|\Delta d_\Omega|^2)$ ; (d) Input function  $u_0(y_1, y_2) = \cos(3y_1)^2 + 20y_2$ ; the horizontal coordinate is the arc length with the green point as reference point.

### 3.3.2.2. Application to the treatment of minimum thickness constraint

We now turn to the application of the variational method of Section 3.3.1 to the calculation of the shape derivative of a geometric constraint functional, in the context of the solution of a shape and topology optimization problem.

The physical situation is that of a 2d half MBB beam, as depicted on Fig. 3.3.3: the considered shapes  $\Omega$  are contained in a box  $D$  with size  $3 \times 1$ ; they are clamped on a small region near the lower-right corner of  $\partial D$ , a unit vertical load  $g = (0, -10)$  is applied near the upper-left corner of  $\partial D$ , and the horizontal displacement is prevented on the left-hand side of  $\partial D$ , as a means to represent the fact that the optimized shape is only the right half of a structure which is symmetric with respect to this axis.

We aim to optimize the compliance of this structure under constraints on its volume and on its minimum thickness, see Section 3.1.3 about this notion. As suggested in there, we consider the following shape

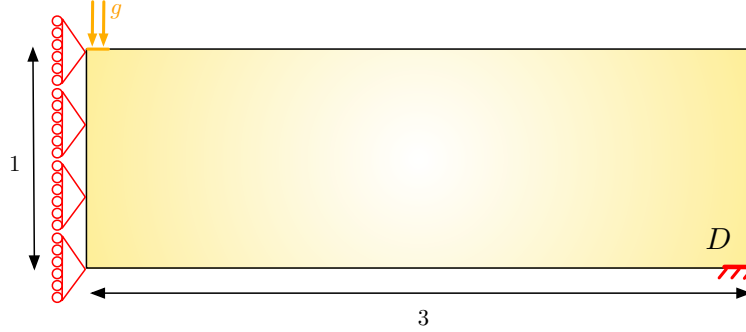


FIGURE 3.3.3. *Setting of the half MBB beam test case considered in Section 3.3.2.2.*

optimization problem

$$\min_{\Omega} P_{\min T}(\Omega), \text{ s.t. } \begin{cases} C(\Omega) \leq C_T, \\ \text{Vol}(\Omega) \leq V_T, \end{cases}$$

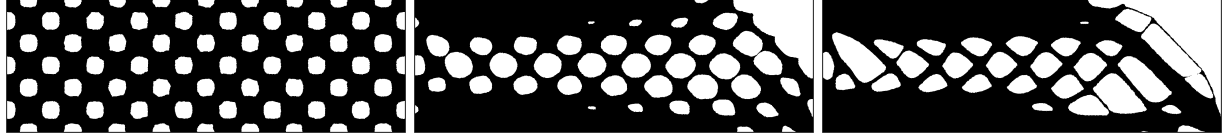
where the minimum thickness functional  $P_{\min T}(\Omega)$  defined in (3.1.9) is featured as an objective function. This problem is solved by combining the the level set based mesh evolution method of Section 1.4.7 with the null space optimization algorithm of Section 3.2, and the strategy of this section for the calculation of the shape derivative of  $P_{\min T}(\Omega)$ . The results are depicted on Fig. 3.3.4 for several values of the parameter  $d_{\min}$ . Note that this approach – and its treatment by our variational method – yield coherent results; even though the minimum thickness constraint is violated in the design obtained for  $d_{\min} = 0.2$ , the value of the functional  $P_{\min T}(\Omega)$  is significantly reduced in the process.

### 3.4 MODELING OF CONSTRAINTS ON SHAPES FOR ARCHITECTURAL DESIGN

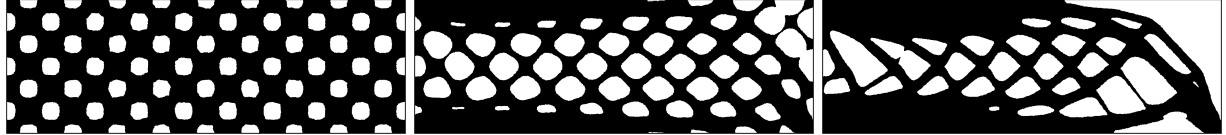
As we have hinted at in Section 1.1.2, architects have a long-standing interest in optimal design. However, modern optimal design techniques have only recently been considered in this field, for very specific applications at that. Beyond the relatively late acknowledgement of scientific computing techniques in architectural design, three main reasons may account for this fact:

- From the technical point of view, shape and topology optimization has essentially been developed in the realm of continuum mechanics, while most situations in architectural design deal with trusses (i.e. sets of bars), or flat structures, such as plates or shells.
- On a different note, architects usually follow construction rules guided by a long-established intuition. Only when the structure is exceptional, by nature or by size, or unique, and the aesthetics of the design is the utmost priority, is it worth deviating from these, see [8, 65] for examples.
- More fundamentally, even when designing a “unique” structure, architects do no wish to rely on sole mechanical considerations, whose results could be reproduced by anyone! See [371] for a related discussion. As a matter of fact, aesthetic criteria about the outline of the shape, which are then the main motivation of architects, do not lend themselves to an easy modeling.

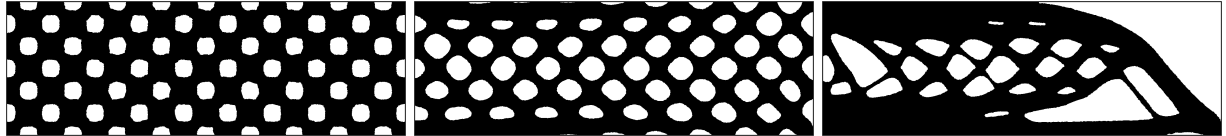
Based on the article [A27], and to a lesser extent on [A28], we presently investigate several applications of shape optimization methods in architectural design. In the first Section 3.4.1, we present the mechanical setting of our investigations together with a test-case that will serve as guide throughout the numerical experiments of this section. In Section 3.4.2, we report on a conceptually simple strategy to introduce diversity in the architectural designs suggested by shape and topology optimization techniques, which consists in playing on the boundary conditions of the mechanical problem. In the subsequent Section 3.4.3, we introduce and use a functional based on the signed distance function to a target shape  $\Omega_T$  to impose that the optimized shape resemble the latter. Finally, in Section 3.4.4, we show how the addition of an anisotropic flavor to the notion of signed distance function may help in producing designs made of branches or walls.



(A) No minimum thickness constraint is imposed (i.e.  $C(\Omega)$  is minimized under the volume constraint  $\text{Vol}(\Omega) \leq V_T$ ).



(B) A minimum thickness constraint is imposed with  $d_{\min} = 0.1$



(C) A minimum thickness constraint is imposed with  $d_{\min} = 0.2$

FIGURE 3.3.4. Intermediate shapes in the optimization of the MBB beam under minimum thickness constraints considered in [Section 3.3.2.2](#): (in each situation, from left to right, top to bottom) Iterations 0, 10, 40, 100, 150 and 200.

### 3.4.1. Presentation of the mechanical setting and of a guiding example

Throughout this section,  $\Omega \subset \mathbb{R}^d$  stands for an architectural design – an elastic structure filled by a material with Hooke's law  $A$ . The shape  $\Omega$  is clamped on a part  $\Gamma_D$  of its boundary  $\partial\Omega$ ; it is subjected to surface loads  $g \in L^2(\Gamma_N)^d$  applied on a disjoint subset  $\Gamma_N \subset \partial\Omega$ , and the remaining free boundary  $\Gamma := \partial\Omega \setminus (\overline{\Gamma_D} \cup \overline{\Gamma_N})$  is the only region subjected to optimization. In this setting, the displacement  $u_\Omega$  of  $\Omega$  is the unique solution in  $H_{\Gamma_D}^1(\Omega)^d$  to the linear elasticity system, whose expression is recalled for convenience:

$$(3.4.1) \quad \begin{cases} -\text{div}(Ae(u_\Omega)) = 0 & \text{in } \Omega, \\ u_\Omega = 0 & \text{on } \Gamma_D, \\ Ae(u_\Omega)n = g & \text{on } \Gamma_N, \\ Ae(u_\Omega)n = 0 & \text{on } \Gamma. \end{cases}$$

To illustrate the developments of this section, we shall consider throughout an example inspired by the Pylon Design Competition organized by the Royal Institute of British Architects (RIBA) in 2014 [319]. The setting is that depicted on [Fig. 3.4.1](#): the shape  $\Omega$  of interest represents an electric pylon; it is contained in a

box  $D \subset \mathbb{R}^3$  with size  $15 \times 15 \times 45$ , and six different loads cases  $g_i$ ,  $i = 1, \dots, 6$  are considered, associated to various sets of forces applied at the blue dots. Physically, these originate from wind and from the weight of the electric cables hanging at the arms of the structure. The central optimization problem in this situation, around which several variations will be considered, reads as follows:

$$(3.4.2) \quad \min_{\Omega} S(\Omega) \text{ s.t. } \text{Vol}(\Omega) = V_T,$$

where  $V_T$  is a volume target, and  $S(\Omega)$  is the sum of the compliances of  $\Omega$  in the six loads situations:

$$S(\Omega) = \sum_{i=1}^6 C_i(\Omega), \text{ where } C_i(\Omega) = \int_{\Omega} A e(u_{\Omega}^i) : e(u_{\Omega}^i) \, dx,$$

involving the elastic displacement  $u_{\Omega}^i$  of  $\Omega$  when it is submitted to the load case  $g_i$ .

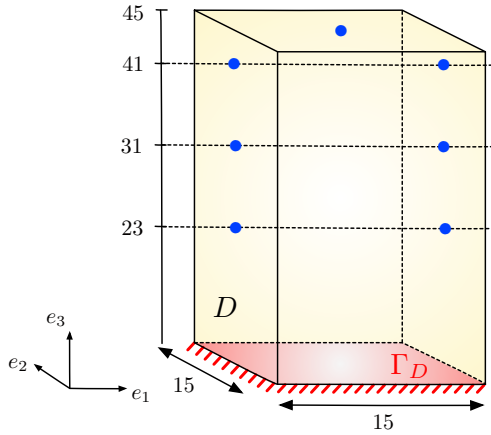


FIGURE 3.4.1. *Setting and boundary conditions of the pylon design example of Section 3.4.1.*

### 3.4.2. Instilling diversity in the optimized shape by changing the specifications of the test-case

In this section, we investigate a naive, albeit already quite efficient means to leave the room for diversity in the outcome of an optimal design problem, which consists in playing artificially on the mechanical specifications of the latter.

In the context of the model problem of Section 3.4.1, two simple instances of this idea are the following:

- The region  $\Gamma_D$  where shapes are clamped in the mechanical definition (3.4.1) of the problem could be reduced to a subset of the lower side of  $\partial D$ , so as to guide the ground fixation system of  $\Omega$  towards a particular geometry; a similar idea is used in [371].
- The volume target  $V_T$  in the statement (3.4.2) of the optimal design problem could be decreased in order to entice the structure to develop thin bars.

This practice is justified by the fact that not all the mechanical specifications of an optimal design problem such as (3.4.2) are determined so firmly that they cannot be slightly modified. On the other hand, as recalled in Section 1.3.2, shape and topology optimization problems are well-known to possess numerous local minimizers, and their convergence towards one or the other of them is very sensitive to even small variations of the parameters of the problem. Hence, “small” modifications of the clamping regions of  $\Omega$  or of the imposed volume target in the optimal design process may already help in producing significantly different designs.

A few results of such simple experiments are depicted on Fig. 3.4.2.



FIGURE 3.4.2. *Optimized designs of the pylon of Section 3.4.1 when (a) The volume constraint is  $V_T = 0.1\text{Vol}(D)$ , and the shape is clamped on the full lower side of  $\partial D$ , (b) The volume constraint is decreased to  $V_T = 0.05\text{Vol}(D)$ , and  $\Gamma_D$  is again the full lower side of  $\partial D$ , (c) The volume constraint  $V_T = 0.05\text{Vol}(D)$ , and where  $\Gamma_D$  is reduced.*

### 3.4.3. Constraints about the resemblance with a target design

Despite its diverse potential applications, the modeling and treatment of similarity constraints is scarce in shape and topology optimization. To the best of our knowledge, beyond our works [A28, A27], the only contributions in this direction are the articles [290, 377], taking place in the setting of density-based topology optimization and using a crude  $L^2$  discrepancy criterion between the optimized and target densities. This subject has been much more extensively tackled in the context of computer graphics applications, as we describe in Section 3.7 below with a little more details.

In our context, let  $\Omega_T \subset \mathbb{R}^d$  be a target shape; in order to impose that  $\Omega$  resemble  $\Omega_T$ , we consider the constraint functional  $P_m(\Omega)$  defined by:

$$(3.4.3) \quad P_m(\Omega) = \int_{\Omega} d_{\Omega_T} \, dx.$$

Intuitively, to minimize  $P_m(\Omega)$ , the optimized shape  $\Omega$  has to enclose all the interior of  $\Omega_T$ , where  $d_{\Omega_T}$  takes negative values, while avoiding the exterior of  $d_{\Omega_T}$ , where it takes positive values. In particular, the unique global minimizer of  $P_m(\Omega)$  is  $\Omega_T$  itself.

Let us illustrate the use of this functional  $P_m(\Omega)$  in the context of the optimal design of the pylon introduced in Section 3.4.1. Considering the target shape of Fig. 3.4.3 (a), we solve the optimization problem

$$(3.4.4) \quad \min_{\Omega} \mathcal{L}(\Omega), \text{ s.t. } \text{Vol}(\Omega) = V_T, \text{ and } \mathcal{L}(\Omega) = \alpha \frac{S(\Omega)}{S(\Omega_T)} + (1 - \alpha) \frac{P_m(\Omega)}{P_m(\Omega_T)},$$

for different values of the coefficient  $\alpha \in [0, 1]$ . Several results are presented in Fig. 3.4.3, as  $\alpha$  increases, they show a smooth transition between the target shape  $\Omega_T$  and the optimized shape of the pylon in view of its compliance and volume (without resemblance constraint) displayed on Fig. 3.4.2 (a).

Let us insist that this model of a similarity constraint is quite naive. We expect that, by leveraging more elaborated tools used in imaging (and notably using concepts from optimal transport theory), it is possible to devise resemblance functionals which are more “aware” of the global geometric characteristics of the compared shapes, see Section 3.7 for a few leads in this direction.

### 3.4.4. Promoting the emergence of bars and walls by using constraints based on the anisotropic signed distance function

In this section, we present a trick to encourage the optimized structure  $\Omega$  to be “thin” in one or two directions of space, as a means to promote patterns such as bars or shells, which are familiar in architectural design. To this end, we use an anisotropic version of the maximum thickness constraint presented in Section 3.1.3, which in turn involves an adaptation of the notion of signed distance function and the related material recalled in Section 3.1 to the case where the Euclidean norm on  $\mathbb{R}^d$  is replaced with an anisotropic norm.

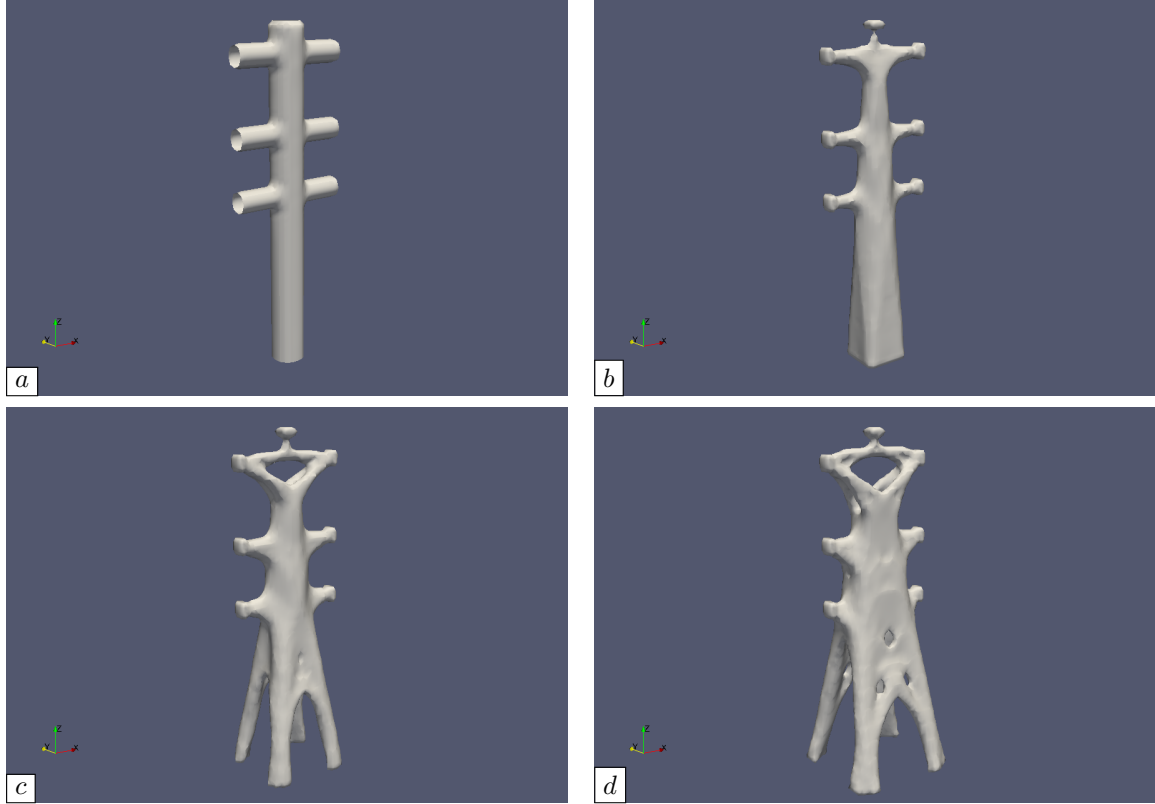


FIGURE 3.4.3. Optimization of the multi load compliance  $S(\Omega)$  of the pylon in [Section 3.4.3](#) while imposing its resemblance with the target shape  $\Omega_T$  in (a): optimized designs for the problem [\(3.4.4\)](#) with (b)  $\alpha = 0.2$ , (c)  $\alpha = 0.5$ , (d)  $\alpha = 0.8$ .

**Definition 3.4.1** Let  $M \in \mathbb{R}_{\text{sym}}^{d \times d}$  be a symmetric, positive definite  $d \times d$  matrix. For any bounded, Lipschitz domain  $\Omega \subset \mathbb{R}^d$ , the signed, anisotropic distance function  $d_\Omega^M$  to  $\Omega$  reads:

$$d_\Omega^M(x) = \begin{cases} -d^M(x, \partial\Omega) & \text{if } x \in \Omega, \\ 0 & \text{if } x \in \partial\Omega, \\ d^M(x, \partial\Omega) & \text{if } x \in \bar{\Omega}, \end{cases}$$

where

$$d^M(x, \partial\Omega) := \inf_{y \in \partial\Omega} |x - y|_M, \text{ and } \forall z \in \mathbb{R}^d, |z|_M := \sqrt{Mz \cdot z}.$$

Elementary verifications allow to adapt the material about the signed distance function recalled in [Section 3.1](#) to the present anisotropic context. As in the previous definition, we shall use an  $M$  superscript to denote the anisotropic counterpart of a quantity depending on the isotropic signed distance function.

To gain insight about this notion, let us consider the following example. Let  $\Omega$  be the 2d shape depicted in [Fig. 3.4.4](#) (a) and let  $M$  be the matrix

$$(3.4.5) \quad M = \begin{pmatrix} 0.1 & 0 \\ 0 & 1 \end{pmatrix}.$$

The use of a metric tensor  $M$  with a much lower coefficient in the horizontal direction than in the vertical one implies that traveling from a point  $x \in \mathbb{R}^2$  in the horizontal direction until hitting  $\partial\Omega$  “costs” almost nothing, whereas it does “cost” much when this travel has a vertical component. Hence, the quantity  $d_\Omega^M(x)$  evaluates almost exclusively the horizontal distance needed to reach  $\partial\Omega$  from  $x$ , which explains its very small values in the vertical bar of  $\Omega$ , and comparatively large values in the horizontal bar, see [Fig. 3.4.4](#) (b), (c).

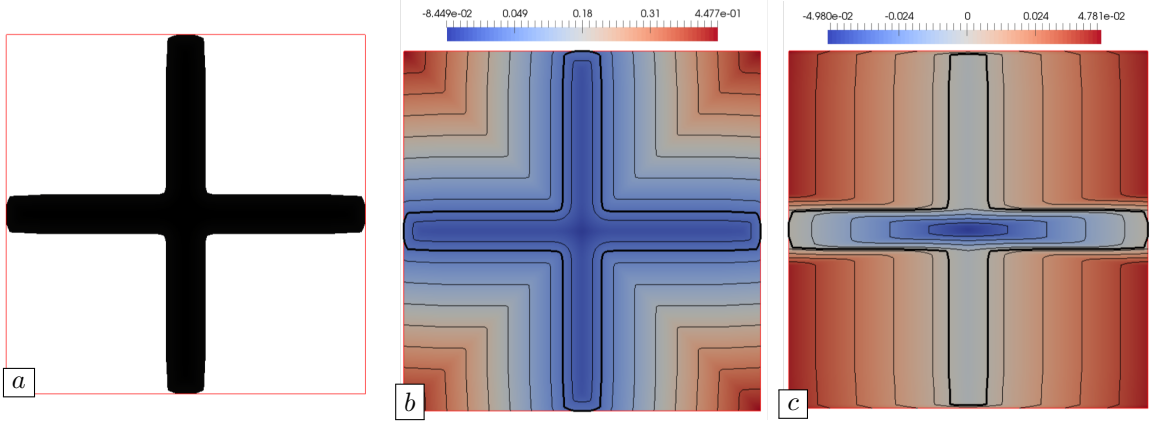


FIGURE 3.4.4. (a) One shape  $\Omega$  (in black); (b) Isolines of the isotropic distance function  $d_\Omega$ ; (c) Isolines of the anisotropic distance function  $d_\Omega^M$  associated to the tensor (3.4.5).

Let us now illustrate the use of quantities involving the anisotropic signed distance function in the context of the optimal design of the pylon of Section 3.4.1. In order to impose that the shape be “thin” in certain directions of space, we rely on several versions  $P_{\max T}^M(\Omega)$  of the maximum thickness function in (3.1.11) built from anisotropic metric tensors  $M$ . More precisely, in order to enforce that  $\Omega$  should be “thin” in both directions  $e_1, e_2$ , we solve the following version of the problem (3.4.2).

$$(3.4.6) \quad \min_{\Omega} S(\Omega) \text{ s.t. } \begin{cases} \text{Vol}(\Omega) = V_T, \\ P_{\max T}^{M_1} \leq \delta/2, \\ P_{\max T}^{M_2} \leq \delta/2, \end{cases}$$

where  $V_T = 0.1\text{Vol}(D)$  and  $\delta > 0$  is a fixed tolerance parameter. The tensors  $M_1$  and  $M_2$  are diagonal with entries

$$(M_1)_{11} = (M_1)_{33} = 0.01, \quad (M_1)_{22} = 1 \text{ (constraint on the thickness in the plane normal to } e_2\text{),} \\ (M_2)_{22} = (M_2)_{33} = 0.01, \quad (M_2)_{11} = 1 \text{ (constraint on the thickness in the plane normal to } e_1\text{).}$$

The optimized shapes resulting from the solution of (3.4.6) with different values of  $\delta$  are depicted on Fig. 3.4.5. As expected, these shapes tend to feature fewer extended surfaces in the directions  $e_1$  and  $e_2$ .

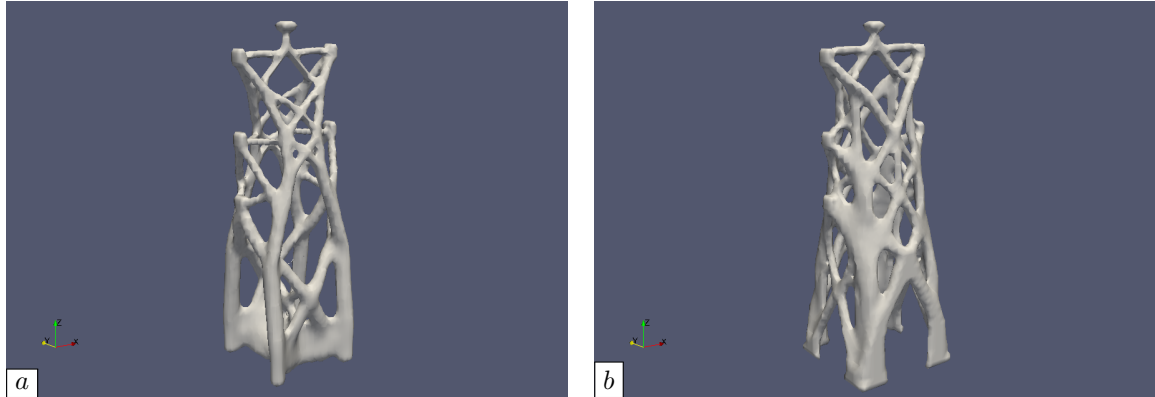


FIGURE 3.4.5. Optimized designs of the pylon for the minimization problem (3.4.6) of the multi load compliance under anisotropic maximum thickness constraints with (a)  $\delta = 4\sqrt{\min\{m_1, m_2, m_3\}}\Delta x$ ; (b)  $\delta = 3\sqrt{\min\{m_1, m_2, m_3\}}\Delta x$ .

### 3.5 IMPOSING CONSTRAINTS ON THE OVERHANG REGIONS OF SHAPES

This section – as well as the next one – aims at comprehending how the assembly of a shape by additive manufacturing imposes new requirements in terms of constructibility, affects its mechanical behavior, and thereby its optimality. We particularly focus on the concerns posed by overhangs – that is, large, nearly horizontal regions hanging over void: our goal in the present section is to devise constraint functionals which, when incorporated into a shape optimization problem, prevent the optimized shape from developing such patterns. Relying on [59, 191, 323], we first describe briefly additive manufacturing technologies in [Section 3.5.1](#); we then present in [Section 3.5.2](#) a naive idea to deal with overhangs, based on purely geometric constraint functionals. To overcome its limitations, we introduce in [Section 3.5.3](#) a mechanical constraint functional, which is based on a simplified model of the layer-by-layer construction process. Two numerical examples are eventually analyzed in [Section 3.5.4](#). The work reported in this section is based on the articles [A26, A22].

#### 3.5.1. A few facts about additive manufacturing

Additive manufacturing is a common label for different construction technologies, all of which starting by a slicing operation: the Computer Aided Design (CAD) model for the input shape (which is often supplied as a surface mesh under the popular **STL** format) is converted into a series of two-dimensional layers; see [Fig. 3.5.1](#). These layers are then assembled individually, one atop the other.

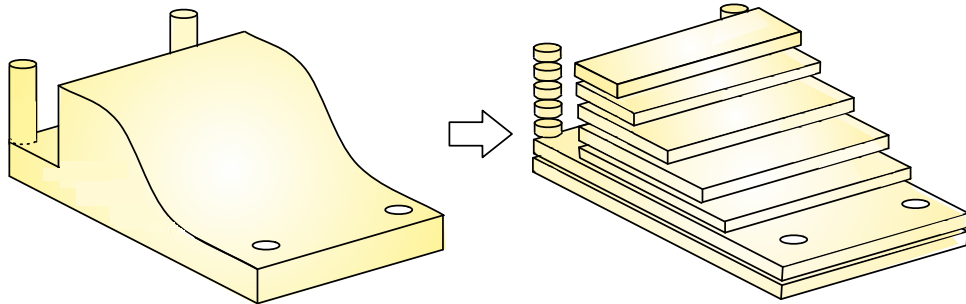


FIGURE 3.5.1. *Rough sketch of the slicing procedure initiating an additive manufacturing process.*

The different additive manufacturing processes correspond to as many different construction technologies for the successive 2d layers; these show competing features in terms of speed, cost, accuracy, and of the nature of the handled materials. Two important categories are the following (see [Fig. 3.5.2](#) for illustrations):

- Material extrusion methods, such as Fused Filament Fabrication (FFF), use a nozzle to extrude the molten material which is then deposited under the form of rasters; such methods are typically used to process plastic (ABS), although recent studies have considered applying the same principle with metal [265].
- Powder bed fusion strategies (such as Selective Laser Sintering, or Electron Beam Melting) are generally used to process metal; at the beginning of the construction of each layer, metallic powder is spread within the build chamber before a laser (or an electron beam) binds the grains together.

The recent breakthroughs in the development of additive manufacturing technologies have given a new impetus to the capabilities of construction techniques. Their unique potential in terms of the complexity of the assembled designs has been applied far beyond their original purpose of rapid prototyping, and they have already been integrated into various real-life, industrial environments. For instance, additive manufacturing technologies have penetrated the automotive industry [134], as well as the fields of civil engineering [186], biomedical engineering [259], etc., see [298] for an overview. They also give whole new perspectives to shape and topology optimization techniques, which are often reproached for predicting intricate designs, whose construction is difficult. In particular, additive manufacturing has aroused a renewed interest for

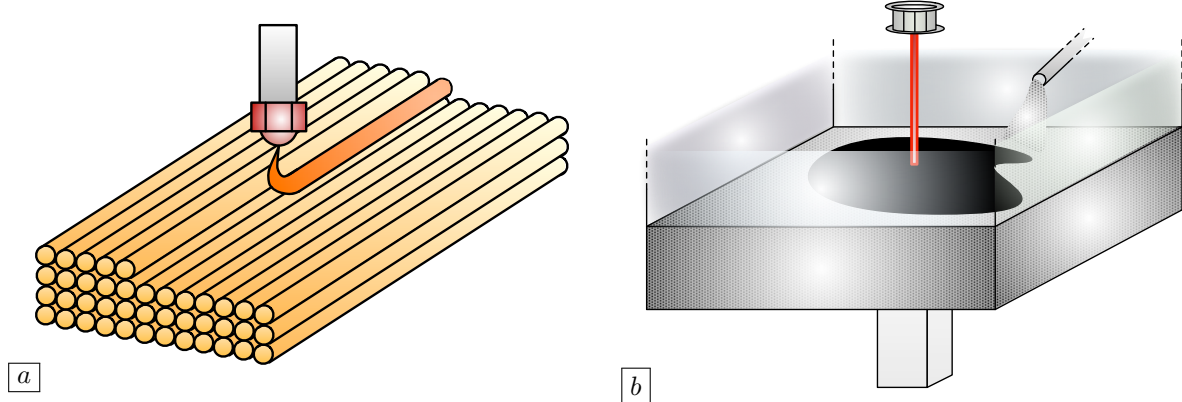


FIGURE 3.5.2. (a) *Fused Filament Fabrication (FFF)* methods proceed by deposition of a molten filament a nozzle along rasters; (b) with the *Electron Beam Melting (EBM)* technology, metallic powder is fused by an electron beam, giving birth to the desired shape.

the homogenization method (see [Section 1.3.2](#) for a short presentation), and more generally for multi-scale shape and topology optimization methods, working at the level of the microscopic structure of designs, see [\[189, 197\]](#) and [\[368\]](#) for an overview. We generally refer to [\[242\]](#) for an overview of the stakes of additive manufacturing in connection with the field of shape and topology optimization.

In spite of their unique assets, additive manufacturing technologies suffer from quite specific drawbacks: at first, they are not scalable, contrary to, for instance, casting techniques where the mold, once constructed, can serve to produce quickly and efficiently thousands of copies of the desired component. Besides, although designs with an unprecedented level of complexity can be assembled by additive manufacturing, these have to fulfill new, original constraints to be identified, and the mechanical quality of the resulting shapes has to be evaluated. In the present [Section 3.5](#) and the next [Section 3.6](#), we focus on two such aspects of additive manufacturing which have a direct impact on optimal design analyses.

- (i) Almost all additive manufacturing techniques experience difficulties in constructing parts showing large overhangs. These are defined as large regions hanging over void, without sufficient support from the lower structure; see [Fig. 3.5.3](#) for an illustration. Beyond the increased staircase effect entailed by such patterns, the reason for this difficulty varies from one additive manufacturing technology to the other:
  - In the case of material extrusion methods, structures with large overhangs cannot be produced as is, since this would demand that material be deposited over void.
  - In the case of powder bed fusion methods, the rapid melting and solidification of the material induces large thermal variations in the structure, incurring residual stresses, and eventually warpage. This phenomenon is all the more likely to occur in regions which are insufficiently anchored to the lower structure (such as overhangs); see [\[274\]](#). Another source of difficulties in the assembly of overhang regions lies in that the fused material may drip between the unfused powder of the lower structure, thus leaving the processed boundary with rough patches [\[103\]](#).
- (ii) The mechanical behavior of parts produced by additive manufacturing methods is not precisely controlled, as the specific path followed by the printing nozzle or the laser naturally induces an anisotropy in their material properties; see for instance [\[12, 385\]](#) and [Fig. 3.5.4](#) for an illustration.

The present [Section 3.5](#) deals with the issues raised by the presence of overhangs in the constructed shape. On the one hand, these concerns could be tackled by post-processing methods, that apply to the final shape and are not included in the prior design optimization stage. In this direction, much effort has been devoted to the construction of an efficient scaffold structure to support the shape, which has to be removed at the end of the process; see for instance [\[18, 165\]](#), although some works such as [\[102, 206, 227\]](#) propose to modify the constructed design so that it becomes self-supporting.

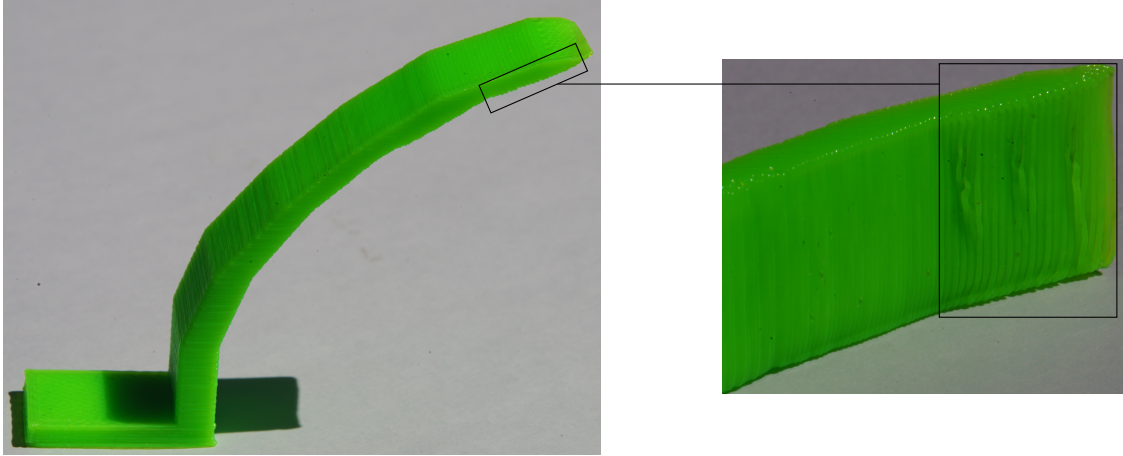


FIGURE 3.5.3. *The angle between the structural boundary and the build direction has a direct impact on the quality of the processed shape.*

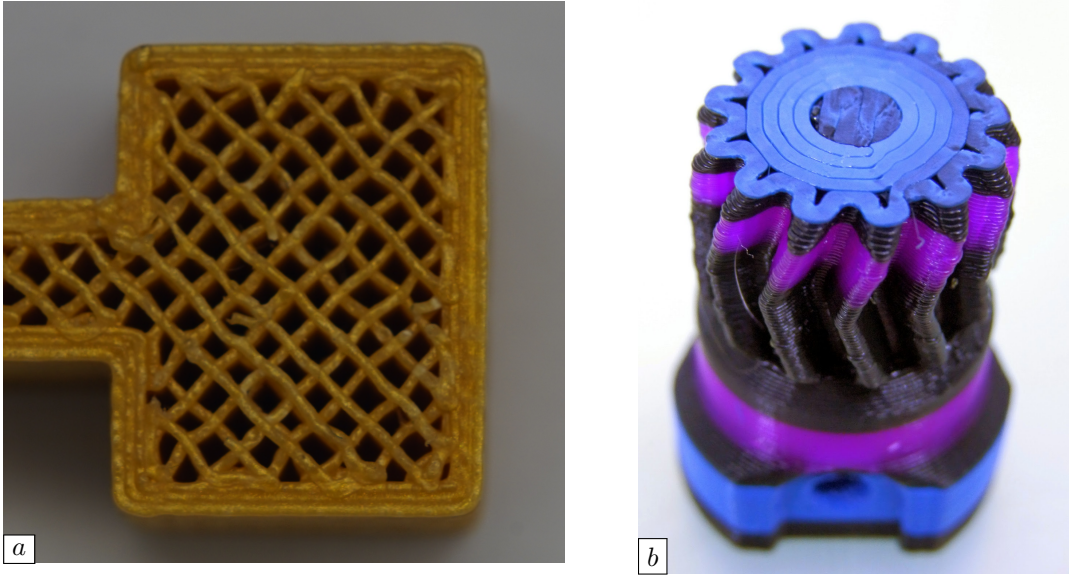


FIGURE 3.5.4. *Examples of two-dimensional layers constructed according to (a) the “crust-pattern” model, and (right) the “offset” model (Photo courtesy of Richard Horne).*

Here, we propose to tackle the penalization of overhangs at the level of the shape optimization problem. As far as this strategy is concerned, most investigations focus on criteria based on the angle between the structural boundary and the build direction, see for instance [93] for an early investigation, [188, 225, 226, 308] in the context of density-based topology optimization and [363, 365] in the context of parametric or level set shape optimization.

### 3.5.2. An intuitive, geometric description, and its limitations

In this section, we report on a naive, geometric attempt to penalize the emergence of overhangs, and we emphasize its limitations.

From the mathematical viewpoint, overhangs are identified as the regions of the boundary of a shape  $\Omega$  made of points  $x$  where the angle between the normal vector  $n_\Omega(x)$  and the negative vertical direction  $-e_d$  is below a certain threshold – the value  $\frac{\pi}{4}$  is frequently encountered in the literature. In order to penalize

the onset of such regions, it is therefore tempting to rely on a shape functional of the form

$$(3.5.1) \quad P_g(\Omega) = \int_{\partial\Omega} \varphi(n_\Omega) \, ds,$$

where  $\varphi : \mathbb{S}^{d-1} \rightarrow \mathbb{R}$  takes large values at elements  $n \in \mathbb{S}^{d-1}$  which are “close” to  $-e_d$ , and “small” values otherwise.

To emphasize the limitations of this simple approach, let us consider the optimization of a 2d MBB beam, as depicted on [Fig. 3.5.5](#) (a): the shape  $\Omega$  is contained in a box  $D$  with size  $6 \times 1$ ; it is clamped on its lower-left and lower-right corners, and a vertical load  $g = (0, -1)$  is applied at the middle of its upper side. We first consider the minimization of the compliance  $C(\Omega)$  of  $\Omega$  (see [\(1.2.10\)](#)) under a volume constraint:

$$(3.5.2) \quad \min_{\Omega} C(\Omega) \text{ s.t. } \text{Vol}(\Omega) = V_T,$$

where the volume target is  $V_T = 0.2\text{Vol}(D)$ . The optimized shape, depicted on [Fig. 3.5.5](#) (a), presents multiple large overhangs, especially in its upper part. These are essential to the mechanical performance of the shape, as they allow to withstand the bending effect induced by  $g$ , we therefore expect that they should be very difficult to circumvent. To try and drive the optimization path towards a design free of such patterns, we solve a modified version of [\(3.5.2\)](#) involving the geometric constraint functional  $P_g(\Omega)$ :

$$(3.5.3) \quad \min_{\Omega} \left( (1 - \alpha_g) \frac{C(\Omega)}{C(\Omega^*)} + \alpha_g \frac{P_g(\Omega)}{P_g(\Omega^*)} \right) \text{ s.t. } \text{Vol}(\Omega) = V_T,$$

with a weight  $\alpha_g = 0.5$ . The resulting design, depicted on [Fig. 3.5.5](#) (b), shows multiple sawtooth patterns. This “dripping effect” is not a numerical artifact. In fact, these features are relevant in the perspective of solving [\(3.5.3\)](#): to decrease the value of  $P_g(\Omega)$  without either adopting an altogether different system of bars for transferring the stress induced by  $g$  or jeopardizing dramatically the value of the compliance  $C(\Omega)$ , it is beneficial to create such patterns where the normal vector  $n_\Omega$  is almost everywhere “far” from the negative vertical direction, except at a few points which are barely seen by the numerical discretization.

One might think that the addition of yet another penalization to the problem [\(3.5.3\)](#) with the perimeter functional could neutralize this dripping effect. To appraise this strategy, we solve such a variant of [\(3.5.3\)](#) featuring an additional penalization with  $\text{Per}(\Omega)$ . The result in [Fig. 3.5.5](#) (c) reveals that this practice solely results in blurred sawtooth patterns.

Summarizing, the use of geometric functionals based on the angle between the normal vector  $n_\Omega$  and the direction  $-e_d$ , such as [\(3.5.1\)](#), to penalize the onset of overhangs is awkward for significant physical reasons. This pleads for the device of overhang constraint functionals based on an utterly different characterization.

### 3.5.3. A layer-by-layer mechanical functional for overhang constraints

In this section, based on the articles [\[A26, A22\]](#), we present an alternative, efficient construction to prevent the emergence of overhang features in the course of the shape optimization process, which appeals to the original mechanical reasons why these features are undesirable. Note that a very similar idea to that developed in this section was independently proposed in [\[254\]](#) in the context of density-based topology optimization.

More precisely, we rely on a simplified model of the mechanical behavior of the shape  $\Omega$  during its construction. In this situation,  $\Omega$  is comprised in a fixed domain  $D \subset \mathbb{R}^d$  of the form  $D = S \times (0, H)$ , where  $S \subset \mathbb{R}^2$  and  $H > 0$ , accounting for the build chamber.

For each value  $h \in [0, H]$  of the height, we introduce the intermediate shape

$$\Omega_h := \{x = (x_1, \dots, x_d) \in \Omega, x_d < h\},$$

corresponding to the stage of the construction process where the shape is erected up to the height  $h$ . We introduce the following decomposition of  $\partial\Omega_h$ , which is illustrated on [Fig. 3.5.6](#):

$$(3.5.4) \quad \partial\Omega_h = \overline{\Gamma_0} \cup \overline{\Gamma_h^u} \cup \overline{\Gamma_h^l},$$

where

- $\Gamma_0 = \{x \in \partial\Omega_h, x_d = 0\}$  is the contact region between the shape and the build plate;
- $\Gamma_h^u = \{x \in \partial\Omega_h, x_d = h\}$  is the upper side of  $\Omega_h$ ;
- $\Gamma_h^l = \partial\Omega_h \setminus (\overline{\Gamma_0} \cup \overline{\Gamma_h^u})$  is the lateral surface of  $\partial\Omega_h$ .

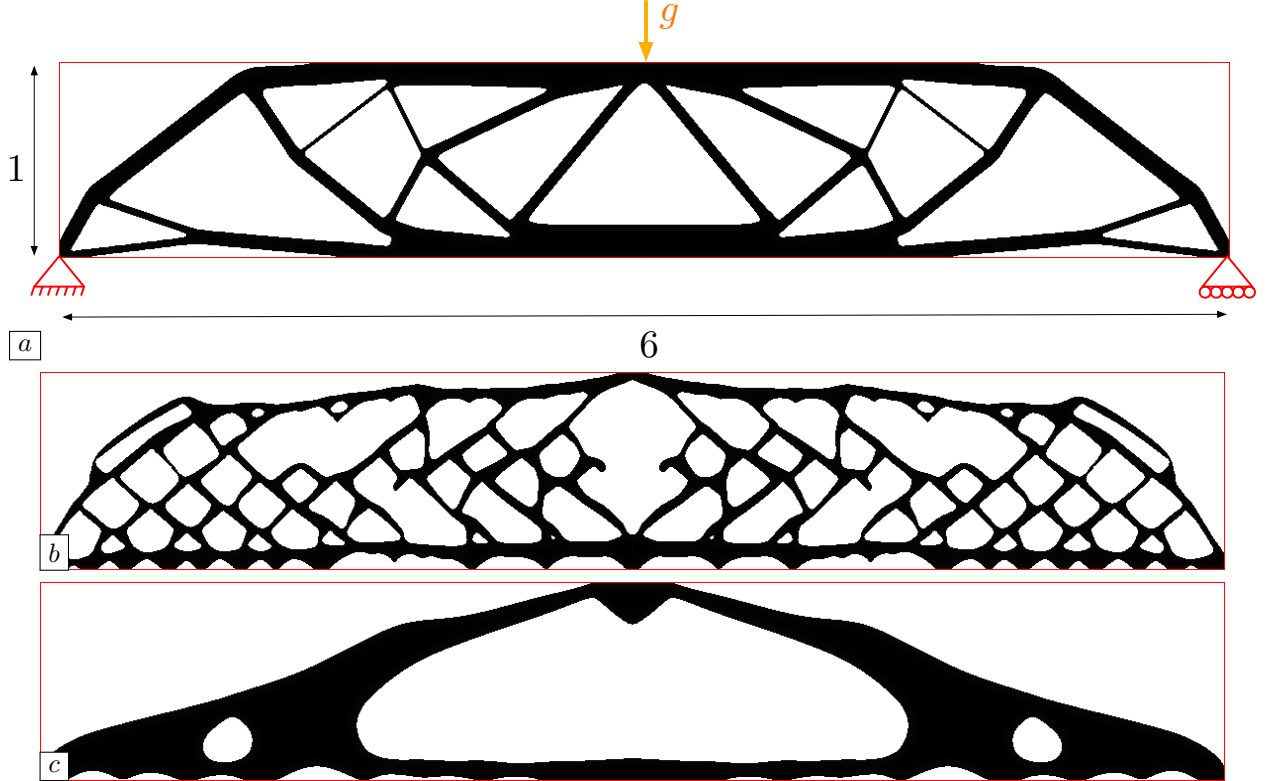


FIGURE 3.5.5. (a) Optimized shape in the MBB Beam example of [Section 3.5.2](#) for the problem (3.5.2) (where no geometric constraint is imposed), with details of the test-case; (b) Optimized shape for (3.5.3); (c) Optimized shape when a perimeter constraint is added.

At each stage  $h$  of the construction process,  $\Omega_h$  is clamped on  $\Gamma_0$ , and it is solely subjected to gravity effects, represented by a fixed volume force  $f : \mathbb{R}^d \rightarrow \mathbb{R}^d$ . Hence, the mechanical behavior of  $\Omega_h$  is characterized by the displacement  $u_{\Omega_h}^c \in H_{\Gamma_0}^1(\Omega_h)^d$ , which is the solution to the boundary value problem:

$$(3.5.5) \quad \begin{cases} -\operatorname{div}(Ae(u_{\Omega_h}^c)) = f & \text{in } \Omega_h, \\ u_{\Omega_h}^c = 0 & \text{on } \Gamma_0, \\ Ae(u_{\Omega_h}^c)n = 0 & \text{on } \partial\Omega_h \setminus \overline{\Gamma_0}. \end{cases}$$

The self-weight of  $\Omega_h$  in this situation, i.e. its compliance, then reads:

$$c_{\Omega_h} = \int_{\Omega_h} Ae(u_{\Omega_h}^c) : (u_{\Omega_h}^c) \, dx = \int_{\Omega_h} f \cdot u_{\Omega_h}^c \, dx.$$

Building on this model, we propose to evaluate the presence of overhangs on a shape  $\Omega$  thanks to the following “self-weight manufacturing compliance” functional, which aggregates the self-weights of all the intermediate structures  $\Omega_h$  of  $\Omega$  appearing in this course of its construction:

$$(3.5.6) \quad P_{\text{sw}}(\Omega) = \int_0^H j(c_{\Omega_h}) \, dh,$$

where  $j : \mathbb{R} \rightarrow \mathbb{R}$  is a smooth function (e.g.  $j(t) = t$ ). Intuitively, if  $\Omega$  features an overhang causing failure of the construction process for lack of support from the lower structure, the self-weights  $c_{\Omega_h}$  of the intermediate structures  $\Omega_h$  at levels  $h$  “close” to this overhang will be large, and so will  $P_{\text{sw}}(\Omega)$ .

**Remark 3.5.1** Let us insist that the functional  $P_{\text{sw}}(\Omega)$  is defined from the mechanical behavior of  $\Omega$  – more accurately that of the intermediate structures  $\Omega_h$  – during its construction, which is independent from that

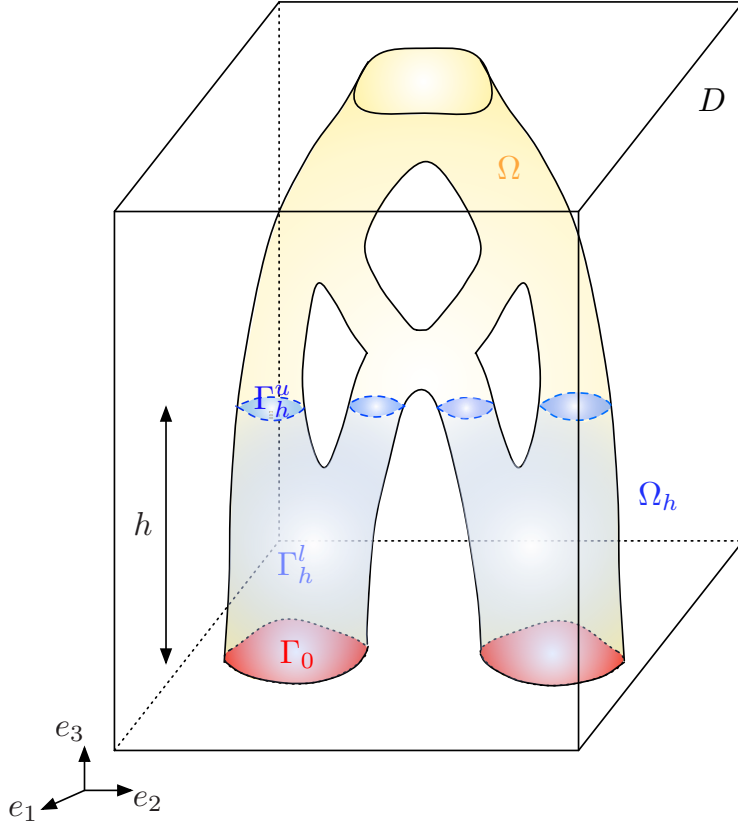


FIGURE 3.5.6. Situation of a shape  $\Omega$  during the layer-by-layer construction process presented in [Section 3.5.3](#).

observed during its final use, used to evaluate the mechanical performance of  $\Omega$  (in terms of the compliance, stress, etc.). In particular,  $u_{\Omega_h}^c$  differs from  $u_\Omega$ , and the decomposition (3.5.4) used to define the former is independent of that  $\partial\Omega = \overline{\Gamma_D} \cup \overline{\Gamma_N} \cup \overline{\Gamma}$  typically used to describe the final state of use of  $\Omega$ .

The functional  $P_{\text{sw}}(\Omega)$  features a quite complicated dependence on the domain  $\Omega$ , via the continuous sequence of intermediate structures  $\Omega_h$ , which makes the study of its differentiability non trivial. It turns out that, under “mild assumptions” on the actual shape  $\Omega$  which we omit for brevity,  $P_{\text{sw}}$  has a shape derivative at  $\Omega$ , which reads:

$$P'_{\text{sw}}(\Omega)(\theta) = \int_{\partial\Omega \setminus \overline{\Gamma_0}} v_\Omega \theta \cdot n \, ds,$$

where, for any point  $x = (x_1, \dots, x_d) \in \partial\Omega \setminus \overline{\Gamma_0}$ , the integrand  $v_\Omega(x)$  aggregates the shape derivatives of the self-weights  $c_{\Omega_h}$  of the structures  $\Omega_h$  lying above  $x$ :

$$v_\Omega(x) = \int_{x_d}^H j'(c_{\Omega_h}) \left( 2f \cdot u_{\Omega_h}^c - Ae(u_{\Omega_h}^c) : e(u_{\Omega_h}^c) \right) (x) \, dh.$$

This expression makes it possible to incorporate  $P_{\text{sw}}(\Omega)$  as a penalization or a constraint functional in general shape and topology optimization problems, such as those presented in [Section 1.2.3](#).

**Remark 3.5.2** The computational costs of evaluating  $P_{\text{sw}}(\Omega)$  and its shape derivative  $P'_{\text{sw}}(\Omega)(\theta)$  are a priori tremendous, as they require the solution of a very large number of linear elasticity systems on the intermediate structures of  $\Omega_h$  of  $\Omega$ . In practice, an acceleration procedure can be implemented, which takes advantage of the “derivative” of the mapping  $h \mapsto u_{\Omega_h}^c$  to reduce dramatically the number of needed finite element solutions.

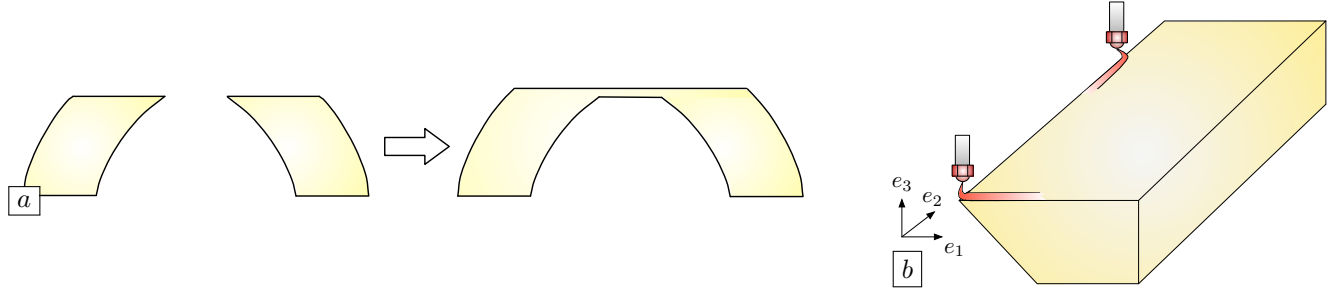


FIGURE 3.5.7. (a) The function  $P_{\text{sw}}(\Omega)$  in (3.5.6) only considers the stages of the construction process where the layers are completely assembled, as if their deposition were instantaneous; (b) One structure which is printable in the  $e_1$  direction, but not in the  $e_2$  direction.

A different physical effect could have been taken into account for the mechanical behavior of the intermediate shapes  $\Omega_h$ , in place of their elastic displacement  $u_{\Omega_h}^c$  under gravity effects. For instance, one may consider that the force applied near the upper part of  $\Omega_h$  by the nozzle of the 3d printing machine is the prevailing physical effect, in which case its displacement is the unique solution  $u_{\Omega_h}^a \in H_{\Gamma_0}^1(\Omega_h)^d$  to the system:

$$\begin{cases} -\text{div}(Ae(u_{\Omega_h}^a)) = f_h & \text{in } \Omega_h, \\ u_{\Omega_h}^a = 0 & \text{on } \Gamma_0, \\ Ae(u_{\Omega_h}^a)n = 0 & \text{on } \partial\Omega_h \setminus \overline{\Gamma_0}, \end{cases} \quad \text{where } f_h = f \mathbb{1}_{\{\in_h, \in [h-\varepsilon h, h]\}}.$$

This would give rise to the new “upper-weight manufacturing compliance” functional  $P_{\text{uw}}(\Omega)$ , defined by:

$$P_{\text{uw}}(\Omega) = \int_0^H j(c_{\Omega_h}^a) dh, \quad \text{where } c_{\Omega_h}^a = \int_{\Omega_h} Ae(u_{\Omega_h}^a) : (u_{\Omega_h}^a) dx$$

### Remark 3.5.3

- The second functional  $P_{\text{uw}}(\Omega)$  proves much more efficient than  $P_{\text{sw}}(\Omega)$  in penalizing overhangs. In a nutshell, the former one does not evaluate as bad completely horizontal structures, as our simplified model only considers intermediate stages of the construction process where each layer is completely assembled. Hence, in the case of a completely horizontal overhang, it only takes into account the stage where the layer is already fully connected to the lower structure, and not its whole construction, during which part of the layer is really hanging over void, see Fig. 3.5.7 (a).
- Several other models are possible for the behavior of the intermediate shapes  $\Omega_h$ , in the perspective of accounting for other possible sources of failure during the additive manufacturing construction process. For instance, in the work [23], each intermediate stage  $h$  is associated to a coupled thermal equation - elasticity system, and the thermal residual stress inside  $\Omega_h$ , or its vertical displacement (which could cause failure if it is so large that it hits the nozzle) is penalized.

### 3.5.4. Two numerical applications of layer-by-layer mechanical constraints for overhang features

#### 3.5.4.1. The 2d MBB Beam example

In order to appraise the efficiency of our mechanical approach to overhang constraints, we revisit the numerical example considered in Section 3.5.2. The physical situation is exactly that of the 2d MBB beam discussed in there, and we solve the following shape optimization problem involving the upper-weight manufacturing compliance functional:

$$(3.5.7) \quad \min_{\Omega} C(\Omega), \quad \text{s.t.} \quad \begin{cases} \text{Vol}(\Omega) \leq V_T, \\ P_{\text{uw}}(\Omega) \leq \alpha P_{\text{uw}}(\Omega^*), \end{cases}$$

where  $C(\Omega)$  is the compliance of  $\Omega$  in its final state of use, the target volume is set to  $V_T = 0.3\text{Vol}(D)$  and  $\Omega^*$  is the optimized design of the beam without overhang constraint, obtained in [Section 3.5.2](#) and reprinted on [Fig. 3.5.8](#) (a) for convenience.

Several optimized designs associated to different values of the threshold  $\alpha$  are represented on [Fig. 3.5.8](#). As  $\alpha$  decreases, the large overhangs in the upper regions of the shape are successfully replaced by self-supporting features oriented along the build direction, connected together by small arches with optimal rigidity for self-weight loadings.

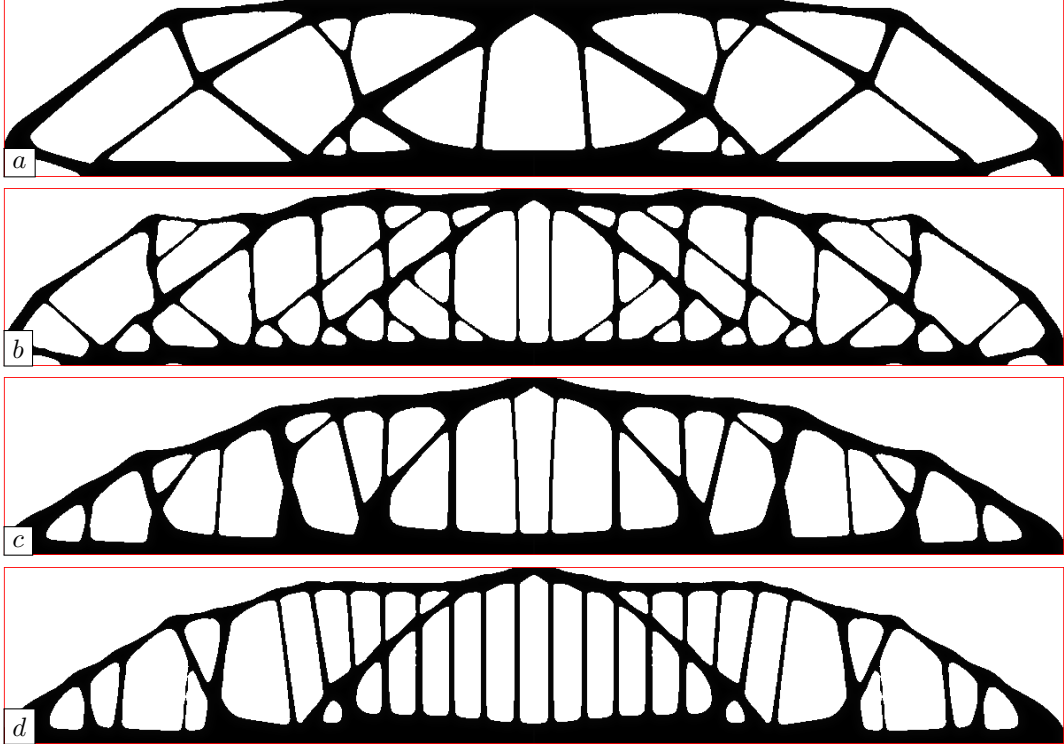


FIGURE 3.5.8. Optimized shapes for the two-dimensional MBB Beam example of [Section 3.5.4.1](#), solving (3.5.7) with values of the threshold  $\alpha$  (a) 0.30, (b) 0.10, (c) 0.05, and (d) 0.03.

#### 3.5.4.2. Optimization of a 3d bridge under overhang constraints

In this second example, we consider the three-dimensional configuration of a bridge depicted on [Fig. 3.5.9](#): in a computational domain  $D$  with size  $6 \times 1 \times 1$ , the structure  $\Omega$  is clamped at the lower-right corners, and its vertical displacement is prevented at the lower-left corners; a vertical load  $g = (0, 0, -1)$  is distributed over its upper side  $\Gamma_N$ .

The layer-by-layer construction of  $\Omega$  is realized from top to bottom, i.e. the region  $\Gamma_0$  in the description (3.5.5) of the behavior of the intermediate shapes during this stage coincides with the upper deck  $\Gamma_N$  where loads are applied in the context of final use of  $\Omega$ .

We first optimize the compliance of  $\Omega$  by imposing a volume constraint  $V_T = 0.3\text{Vol}(D)$ , i.e. we solve (3.5.2). The resulting optimal design  $\Omega^*$ , depicted on [Fig. 3.5.10](#) (a) (b), presents large overhangs, as revealed by the upside-down view in [Fig. 3.5.10](#) (b).

To try and remove these features, we next minimize the volume of  $\Omega$  while imposing that its final use compliance  $C(\Omega)$  be no greater than that of  $\Omega^*$ , with an additional constraint on its upper-weight

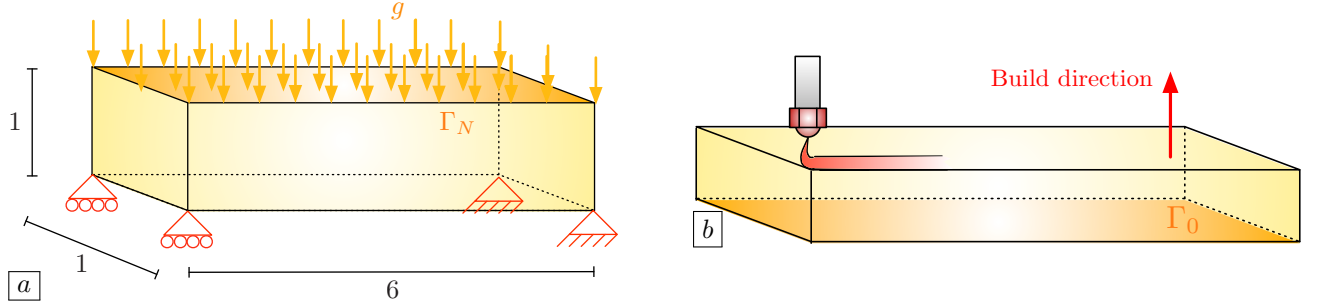


FIGURE 3.5.9. (a) Setting of the three-dimensional bridge example considered in Section 3.5.4.2; (b) Manufacturing context of the bridge.

manufacturing compliance, i.e. we solve:

$$(3.5.8) \quad \min \text{Vol}(\Omega) \text{ s.t. } \begin{cases} C(\Omega) \leq C(\Omega^*), \\ P_{uw}(\Omega) \leq \alpha P_{uw}(\Omega^*). \end{cases}$$

The resulting shapes for two different values of  $\alpha$  are represented on Fig. 3.5.10 (c) (d). Comparing with  $\Omega^*$ , most of the overhang regions have disappeared from the optimized design, but we observe a new, purely three-dimensional phenomenon which is sketched on Fig. 3.5.7 (b): when the value of  $\alpha_c$  is sufficiently small, the optimized shape shows, at each level, sufficient support from the lower structure to enable its manufacturability. However, there is no information about where this support comes from. More precisely, the shape could be self-supporting assuming that the printing direction of each layer is directed along the  $e_1$  axis, but not when it is printed along the  $e_2$  axis. This effect is another shortcoming of our simplified modeling of the construction process, which does not take into account the printing path of each individual layer, see Remark 3.5.3.

To remedy this last drawback, we couple this mechanical constraint with the purely geometric constraint  $P_g(\Omega)$  introduced in Section 3.5.2. Intuitively, the aforementioned patterns are undesirable for this functional, and we expect that the presence of the upper-weight manufacturing constraint in the problem will thwart the dripping effect it induces. We now solve the problem:

$$(3.5.9) \quad \min \left( \beta \frac{\text{Vol}(\Omega)}{\text{Vol}(\Omega^*)} + (1 - \beta) \frac{P_g(\Omega)}{P_g(\Omega^*)} \right) \text{ s.t. } \begin{cases} C(\Omega) \leq C(\Omega^*), \\ P_{uw}(\Omega) \leq \alpha P_{uw}(\Omega^*), \\ P_g(\Omega) \leq P_g(\Omega^*). \end{cases}$$

where  $\alpha, \beta$  are two parameters in  $[0, 1]$ . This results in the optimized designs displayed in Fig. 3.5.10 (e) (f), which are now completely free from overhangs, at the expense of a greater value of the volume.

### 3.6 TAKING INTO ACCOUNT THE ANISOTROPIC MATERIAL PROPERTIES INDUCED BY ADDITIVE MANUFACTURING INTO THE OPTIMAL DESIGN PROCESS

This section deals with another concern caused by additive manufacturing processes, and notably by Fused Filament Fabrication techniques: these inherently induce anisotropy in the effective material properties of the structure  $\Omega$ . Indeed, the bonds between regions of  $\Omega$  that melt and solidify jointly are stronger than those between regions which solidify apart from one another [12, 229, 387]; thus, the effective material properties within structures assembled by additive manufacturing are influenced by the build direction and by the construction pattern of each individual layer, which in turn depend on the shape  $\Omega$  itself. As the mechanical performance of  $\Omega$  is very sensitive to the properties of the constituent material, it is essential to appraise this anisotropic effect and to integrate it into the optimal design process.

This section summarizes the work conducted in [A21] in this direction. The next Section 3.6.1 describes two popular patterns used by additive manufacturing machine tools for constructing the 2d layers of a 3d structure, and it proposes a model for the resulting effective material properties. Two numerical examples are presented in the subsequent Section 3.6.2.

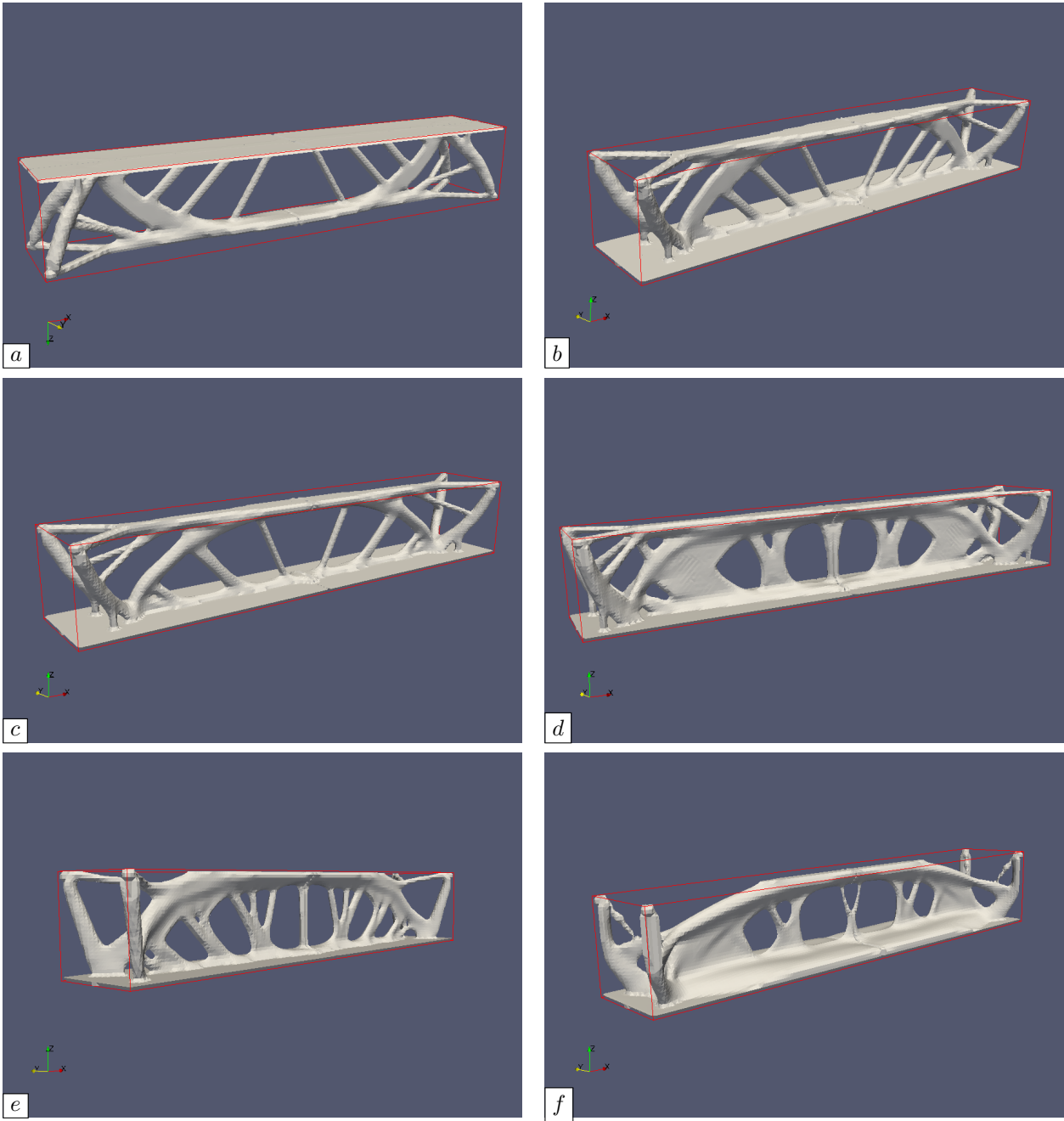


FIGURE 3.5.10. *Optimized designs for the three-dimensional bridge example of Section 3.5.4.2, (a) Optimized shape  $\Omega^*$  for (3.5.2) (without manufacturing constraints), (b) Upside-down view of  $\Omega^*$ ; (c) Optimized shape for (3.5.8) for  $\alpha = 0.7$  and (d)  $\alpha = 0.1$ ; (e) Optimized shape for (3.5.9) for  $\alpha = 0.1$  and  $\beta = 0.1$ ; (f)  $\alpha = 0.1$  and  $\beta = 0.9$ .*

### 3.6.1. Two different models for the construction of shapes

In order to simplify the exposition, we consider a 2d elastic structure  $\Omega$ , accounting for one of the individual layers of a real-life 3d structure. The developments of this section can be generalized to three-dimensional shapes in a conceptually simple way, at the expense of an increased level of technicality. The shape  $\Omega$  under scrutiny is therefore a 2d elastic structure, enclosed in a fixed computational domain  $D$ , whose mechanical

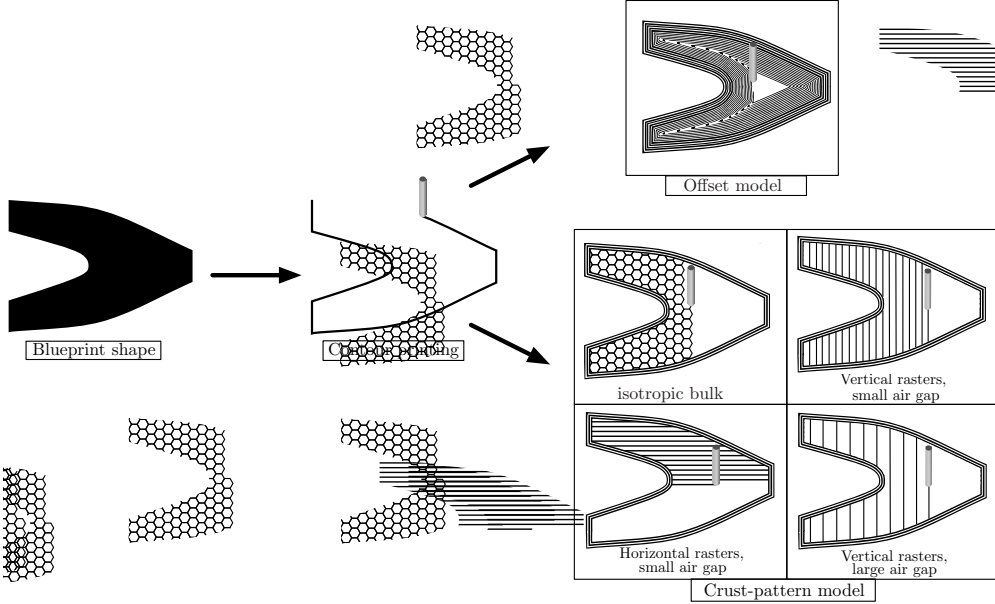


FIGURE 3.6.1. Illustration of the “crust-pattern” and “offset” models for printing the 2d layers of a structure within an additive manufacturing process, as presented in [Section 3.6.1](#).

behavior is appraised by the linearized elasticity system, in the setting of [Section 1.2.2.4](#). The Hooke’s tensor  $A \equiv A_\Omega$  encoding the properties of the constituent material depends on  $\Omega$  through the pattern used for its assembly.

Mainly two popular models are used to construct the layer  $\Omega$ , that we shall refer to as the “crust-pattern” and the “offset” models. Both start by printing carefully the boundary  $\partial\Omega$  in a rather slow and accurate way, which results in a thin crust of material, see [Fig. 3.6.1](#) for an illustration. They then differ from the way the bulk region of  $\Omega$  is assembled.

- In the “crust-pattern” model, it is printed according to a predefined pattern: rasters of material are deposited along a given direction, and separated by a user-specified air gap, see [Fig. 3.5.4](#) (a).
- In the “offset” model, the whole 2d layer  $\Omega$  is constructed by following the offsets of the contour  $\partial\Omega$ , as in [Fig. 3.5.4](#) (b). This is usually the way the upper and lower layers of a 3d structure are assembled so as to protect the infill part.

As we have mentioned, the constituent material of  $\Omega$  will be stiffer (in terms of Young’s modulus) in the direction of deposition of the material than in the transverse direction. The translation of this observation in terms of the Hooke’s tensor  $A_\Omega$  leverages the signed distance function  $d_\Omega$ , see [Section 3.1](#). Notably, we recall from there that the unit normal vector  $n_\Omega$  to  $\partial\Omega$  pointing outward  $\Omega$  has a natural extension  $n_\Omega(x) \equiv n_\Omega(p_{\partial\Omega}(x))$  to almost every point  $x \in D$ . Let us denote by  $A_{\text{ref}}$ ,  $A_{\text{cp}}$  and  $A_{\text{off}}$  the Hooke’s tensor of the elastic material in the reference situation where  $\Omega$  is built by casting, in the “crust-pattern” model and in the “offset” model, respectively. Likewise, we denote by  $\rho_{\text{cp}}$  and  $\rho_{\text{off}}$  the material density within  $\Omega$  depending on the model retained for its construction. We finally label with a <sup>crust</sup> (resp. <sup>bulk</sup>, <sup>void</sup>) superscript properties that hold within the crust (resp. bulk, void) regions of  $D$ .

In the “crust-pattern” model, a “small” parameter  $\varepsilon > 0$  is introduced, which stands for the half-thickness of the transition region between the bulk of  $\Omega$  and the void. The computational domain  $D$  is then decomposed into three regions, as exemplified on [Fig. 3.6.2](#) (a):

- The crust of  $\Omega$  is the band  $\{x \in D, -\varepsilon < d_\Omega(x) < \varepsilon\}$  with width  $2\varepsilon$  around  $\partial\Omega$ ; the elastic properties in this region are encoded in a tensor  $A^{\text{crust}}(n(x))$ , where  $A^{\text{crust}}(n)$  is “weak” in the direction  $n$  and enjoys the properties of the reference material in the orthogonal direction. The material density in this region equals  $\rho^{\text{crust}} = 1$ .

- The interior of  $\Omega$ , or “infill” region is the set  $\{x \in D, d_\Omega(x) < -\varepsilon\}$ ; the material properties in this region are encoded in a tensor  $A_{\text{cp}}^{\text{bulk}}$ , which shows “strong” properties in the direction of the rasters and weak properties in the orthogonal direction. depending on the air gap defined by the user, this region is more or less hollow; its density is denoted by  $\rho_{\text{cp}}^{\text{bulk}} \in (0, 1)$ .
- The void region is  $\{x \in D, d_\Omega(x) > \varepsilon\}$ ; its material properties equal  $A^{\text{void}} = \eta A_{\text{ref}}$ , for a “small” ersatz parameter  $\eta \ll 1$ .

According to this decomposition, the entries of the elasticity tensor  $A_\Omega^{\text{cp}}(x)$  encoding the material properties at a particular point  $x \in D$  of a 2d layer printed according to the “crust–pattern model” depend on the distance from  $x$  to the boundary  $\partial\Omega$ , and on the local orientation of  $\partial\Omega$ , say:

$$(3.6.1) \quad A_{\Omega, \text{cp}}(x) = A_{\text{cp}}(d_\Omega(x), n_\Omega(x)).$$

The tensor  $A_{\text{cp}}(d, n)$  is constructed by gluing the three Hooke’s tensors  $A_{\text{cp}}^{\text{bulk}}$ ,  $A^{\text{crust}}(n)$  and  $A^{\text{void}}$ :

$$A_{\text{cp}}(d, n) = h^{\text{m}}(d) A_{\text{cp}}^{\text{bulk}} + (1 - h^{\text{m}}(d) - h^{\text{p}}(d)) A^{\text{crust}}(n) + h^{\text{p}}(d) A^{\text{void}},$$

where  $h^{\text{m}}, h^{\text{p}} : \mathbb{R} \rightarrow \mathbb{R}$  are suitable approximate Heaviside functions, whose explicit expressions are omitted for brevity, see [Fig. 3.6.2 \(a\)](#).

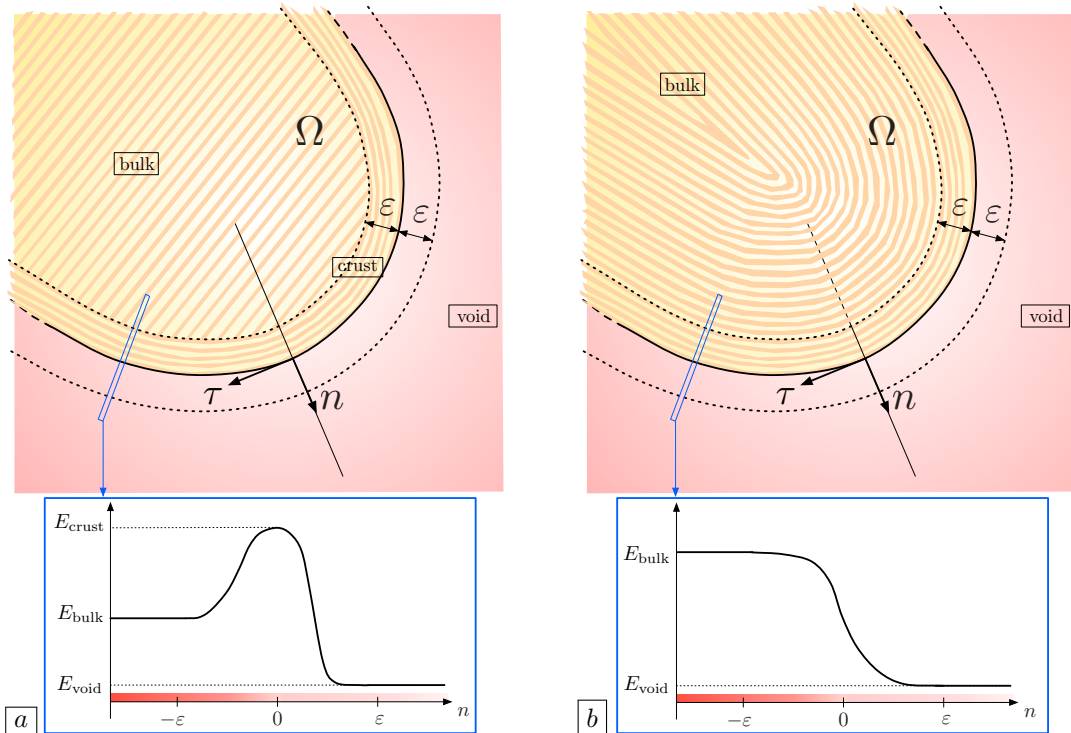


FIGURE 3.6.2. *Interpolation of the material properties between the bulk and the void regions according to (a) The “crust–pattern” model; (b) The “offset” model.*

The mass of the structure is defined in this case by

$$(3.6.2) \quad M_{\text{cp}}(\Omega) = 2\varepsilon\rho^{\text{crust}}\text{Per}(\Omega) + \rho_{\text{cp}}^{\text{bulk}}(\text{Vol}(\Omega) - \varepsilon\text{Per}(\Omega)),$$

A similar mathematical representation underlies the construction of the Hooke’s tensor  $A_{\text{off}}^\Omega$  encoding the material properties of a 2d layer  $\Omega$  printed along contour offsets.

- The interior of  $\Omega$  is the set  $\{x \in D, d_\Omega(x) < -\varepsilon\}$ ; the material properties in this region are described by a tensor  $A_{\text{off}}^{\text{bulk}}(n_\Omega(x))$ , where  $A_{\text{off}}^{\text{bulk}}(n)$  has “weak” properties in the direction  $n$  and enjoys the properties of the reference material in the orthogonal direction. The material density in this region is denoted by  $\rho_{\text{off}}^{\text{bulk}} \in (0, 1)$ ; it depends on the user-defined spacing between contour offsets.

- The void region is  $\{x \in D, d_\Omega(x) > 0\}$ ; its material properties read  $A^{\text{void}} = \eta A_{\text{ref}}$ .

We then glue the tensors  $A_{\text{off}}^{\text{bulk}}(n)$  and  $A^{\text{void}}$  for the bulk and void parts as:

$$(3.6.3) \quad A_{\Omega,\text{off}}(x) = A_{\text{off}}(d_\Omega(x), n(x)), \text{ where } A_{\text{off}}(d, n) = h^\circ(d) A_{\text{off}}^{\text{bulk}}(n) + (1 - h^\circ(d)) A^{\text{void}},$$

using a suitable approximate Heaviside function  $h^\circ : \mathbb{R} \rightarrow \mathbb{R}$ , see Fig. 3.6.2 (b).

In this situation, the mass of the structure is then simply:

$$(3.6.4) \quad M_{\text{off}}(\Omega) = \rho_{\text{off}}^{\text{bulk}} \text{Vol}(\Omega).$$

These models for the anisotropy in the material properties within a shape  $\Omega$  caused by additive manufacturing can readily be incorporated into the formulation of classical shape and topology optimization problems, such as those presented in Section 1.2.3. In the context presented in there, this task indeed simply requires to replace the Hooke's tensor  $A$  in the system (Elas) for the elastic displacement  $u_\Omega$  by one of the tensors  $A_{\Omega,\text{cp}}$  or  $A_{\Omega,\text{off}}$ . The various shape functionals presented in Section 1.2.3 can then be differentiated via elementary (albeit tedious) calculations based on the adjoint method, along the lines of Section 1.3.3.6, and on the material recalled in Section 3.1.2 devoted to the shape differentiation of the signed distance function.

### 3.6.2. Numerical examples

#### 3.6.2.1. Optimization of the shape of a cantilever taking into account 3d printing induced material properties

The situation considered in this section is that of a 2d cantilever, as depicted on Fig. 3.6.3 (a). The shape  $\Omega$  is contained in a computational domain  $D$  with size  $1 \times 0.5$ ; it is clamped on its left-hand side and a unit vertical load  $g = (0, -1)$  is applied at the middle of its right-hand side.

We aim to solve the following optimization problem:

$$(3.6.5) \quad \min_{\Omega} M(\Omega) \text{ s.t. } C(\Omega) \leq C_T.$$

Here, the mass  $M(\Omega)$  of the structure is defined by either (3.6.2) or (3.6.4), depending on the construction model for  $\Omega$ . Likewise, the compliance  $C(\Omega)$  involves the elastic displacement  $u_\Omega$ , solution to (Elas) where the Hooke's tensor  $A_\Omega$  encoding the material properties of shapes equals either  $A_{\Omega,\text{cp}}$  or  $A_{\Omega,\text{off}}$ .

Six different situations are considered as regards the construction model for  $\Omega$ :

- (1) The “molded case”, where shapes are filled with the isotropic reference material  $A_{\text{ref}}$ ;
- (2) The “offset” model;
- (3) The “crust-pattern” model, with isotropic crust and isotropic bulk;
- (4) The “crust-pattern” model, with isotropic crust and anisotropic infill made of horizontal rasters;
- (5) The “crust-pattern” model, with anisotropic crust and anisotropic infill made of horizontal rasters;
- (6) The “crust-pattern” model, with anisotropic crust and isotropic infill.

Several optimized shapes resulting from these investigations are depicted on Figs. 3.6.3 and 3.6.4.

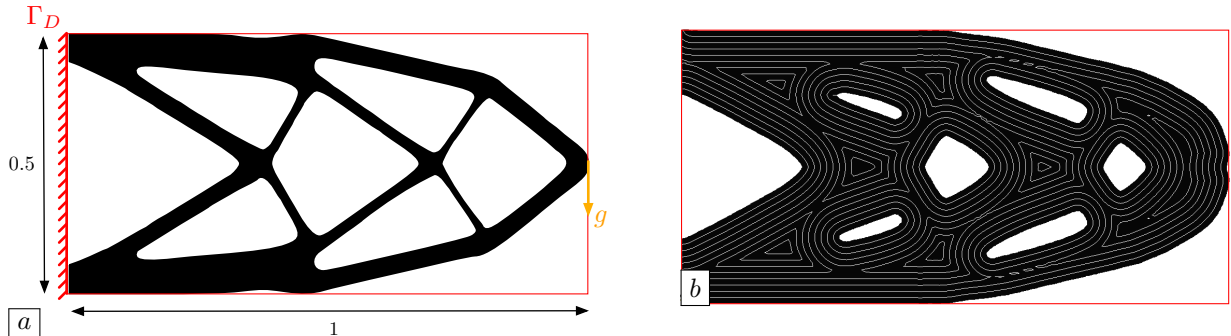


FIGURE 3.6.3. (a) Optimized shape of the 2d cantilever of Section 3.6.2.1, (a) In the “molded” case (with details of the test case); (b) With the material properties induced by the “offset” model.

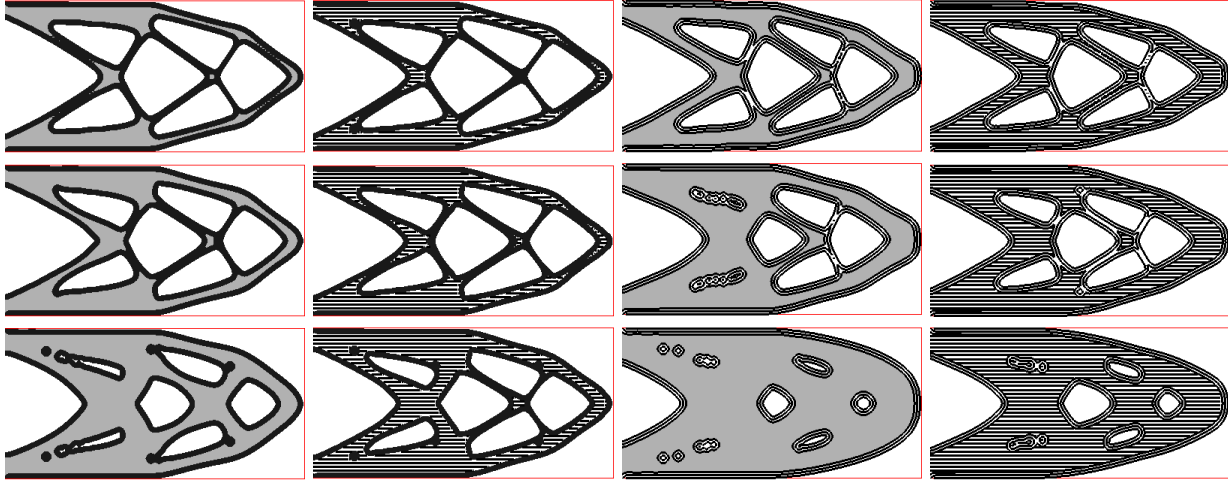


FIGURE 3.6.4. Optimized designs of the 2d cantilever of [Section 3.6.2.1](#) when the “crust-pattern” model is used for their construction with (from left to right) isotropic crust – isotropic bulk, isotropic crust – horizontal rasters in the bulk, anisotropic crust – isotropic bulk, anisotropic crust – anisotropic bulk; (Top row) With density  $\rho_{\text{cp}}^{\text{bulk}} = 0.9$  for the bulk region; (middle row)  $\rho_{\text{cp}}^{\text{bulk}} = 0.75$ ; (bottom row)  $\rho_{\text{cp}}^{\text{bulk}} = 0.6$ .

These results demonstrate that when the crust region of the shape has anisotropic properties, the optimization process takes advantage of the greater stiffness of the crust in the tangential direction: near the region where loads are applied, the structural boundary tends to align with the direction of the load; the portion of the boundary which is aligned with the load is wider as the bulk region is less dense (and so less efficient from the mechanical point of view). On a different note, as the density of the infill region decreases, shapes “inflate” so as to increase their moment of inertia.

More quantitative analyses reveal that the optimized design of [Fig. 3.6.3](#) (b) obtained using the “offset” model has a dramatically poor performance, even when compared with structures obeying the “crust-pattern” model with a much lower density for the infill region. For a given, common infill design (be it isotropic or anisotropic), shapes having an isotropic crust perform better than the ones with an anisotropic crust, which is to be expected, since the latter are almost as stiff in the tangential direction to the structural boundary, and weaker in the normal direction. Eventually, the shapes obtained with an anisotropic infill show good performance, as the horizontal direction of the rasters, in which the material is stiffer, approximately coincide with the main direction of efforts, which is more or less unique.

### 3.6.2.2. Optimization of the shape of an L-beam with 3d printing induced material properties

Our second example deals with the optimization of a 2d L-beam. The situation is that depicted in [Fig. 3.6.5](#) (a): the structure  $\Omega$  is contained in an L-shaped domain  $D$ ; it is clamped on its upper side, and a unit vertical load  $g = (0, -1)$  is applied at the middle of its right-hand side.

We solve the shape optimization problem [\(3.6.5\)](#) in the following six scenarii:

- (1) The “molded” case, where the shape is filled with the isotropic reference material  $A_{\text{ref}}$ ;
- (2) The “offset” model;
- (3) The “crust-pattern” model with isotropic crust and isotropic bulk;
- (4) The “crust-pattern” model with anisotropic crust and isotropic bulk;
- (5) The “crust-pattern” model with anisotropic crust and anisotropic bulk made of horizontal rasters;
- (6) The “crust-pattern” model with anisotropic crust and anisotropic bulk made of vertical rasters.

Several optimized designs resulting from these investigations are displayed on [Figs. 3.6.5](#) and [3.6.6](#); they partially confirm the trends of the previous section. Notably, the “offset” model is still that delivering the worst shape. On a different note, in this situation where the natural load path is more complex than in the

test case of the cantilever addressed in [Section 3.6.2.1](#), no orientation of rasters can provide a satisfactory performance of the shape when an anisotropic pattern is used for the bulk of the structure..

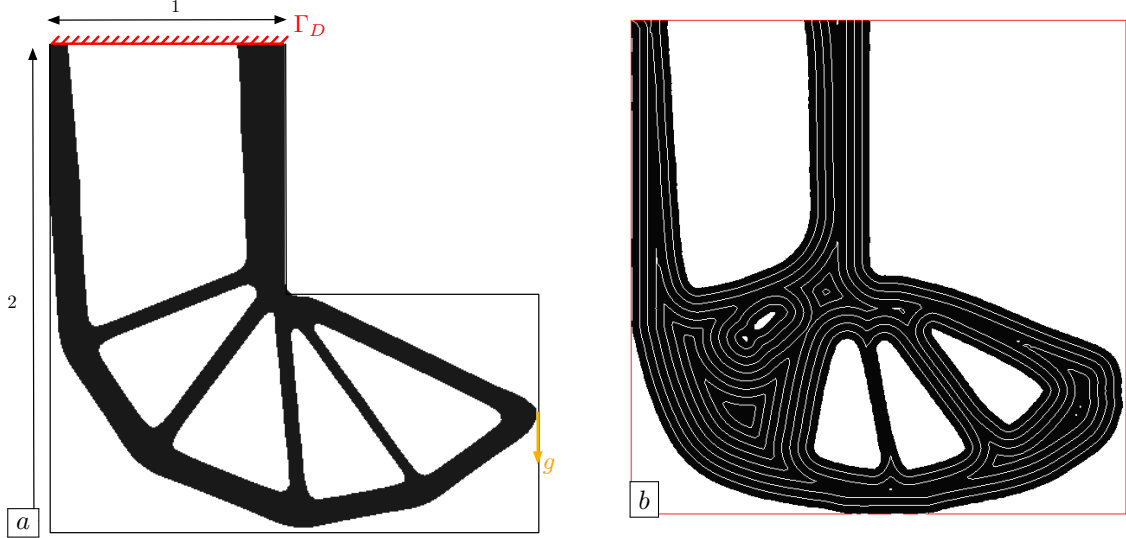


FIGURE 3.6.5. (a) Optimized shape of the 2d L-Beam of [Section 3.6.2.2](#) (a) With material properties granted by the casting process (with details of the test case); (b) With the material properties induced by the “offset” model.

Neither of the two anisotropic infill structures gives a convenient result, as the load path changes from the lower to the upper part of the structure.

### 3.7 PERSPECTIVE: SIMILARITY CONSTRAINTS USING OPTIMAL TRANSPORT

The previous [Section 3.4](#) has illustrated one motivation for functions of the domain  $\Omega$  appraising its “similarity” with a target object  $\Omega_T$ . The functional [\(3.4.3\)](#) introduced in there to achieve this goal is admittedly rough:

- It only compares  $\Omega$  and  $\Omega_T$  in a “pointwise”, or “least-square” fashion, evaluating whether points  $x \in \Omega$  also belong to  $\Omega_T$ . On the contrary, it is often more desirable to take into account higher level features of these shapes, e.g. to appraise whether some regions of  $\partial\Omega$  and  $\partial\Omega_T$  are “small” deformations of one another.
- The target object  $\Omega_T$  has to be a domain in  $\mathbb{R}^d$ , clearly delimiting interior and exterior regions, for the signed distance function  $d_{\Omega_T}$  to make sense, while it would be interesting to leave the room for objects  $\Omega_T$  of a more diverse nature, such as point clouds, density functions, etc.

The optimal transport theory, that we have encountered in a different context in [Section 2.4](#), is an appealing framework to overcome these limitations and construct more robust quantities appraising the resemblance between objects so general as measures, see e.g. [\[178\]](#). Efficient resemblance criterion have indeed been defined in the machine learning and imaging literatures thanks to the notion of Wasserstein distance  $W(\cdot, \cdot)$  defined in [\(2.4.1\)](#) or its entropic regularization  $W_\varepsilon(\cdot, \cdot)$  in [\(2.4.3\)](#), see e.g. [\[299, 354\]](#).

In the context of the optimization of a shape  $\Omega \subset \mathbb{R}^d$ , it is tempting to try and encode the resemblance of  $\Omega$  with a target “object” supplied as a probability measure  $\nu_T \in \mathcal{P}(\mathbb{R}^d)$  in a functional of the form:

$$(3.7.1) \quad J(\Omega) = W\left(\frac{1}{|\Omega|} \mathbb{1}_\Omega \, dx, \nu_T\right), \text{ or } J_\varepsilon(\Omega) = W_\varepsilon\left(\frac{1}{|\Omega|} \mathbb{1}_\Omega \, dx, \nu_T\right).$$

The impact of such functionals on the existence of optimal shapes has been investigated in the recent theoretical work [\[288\]](#). From the numerical vantage, a similar formalism was used in [\[344\]](#) to create a smooth interpolation between two shapes supplied via their characteristic functions.

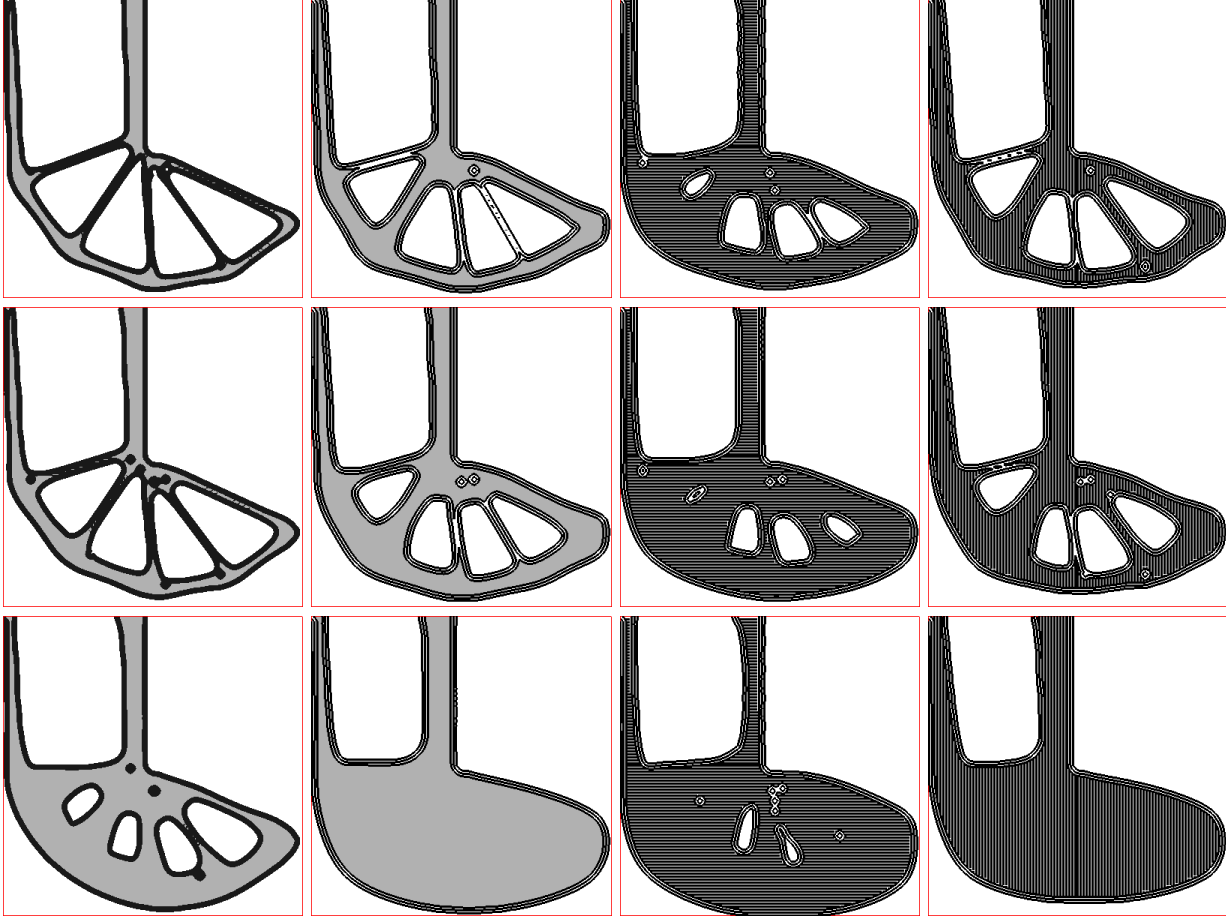


FIGURE 3.6.6. Optimized designs of the 2d L-shaped beam of [Section 3.6.2.2](#) when the “crust-pattern” model is used for their construction with (from left to right) isotropic crust – isotropic bulk, anisotropic crust – isotropic bulk, anisotropic crust – horizontal rasters in the bulk, anisotropic crust – vertical rasters in the bulk; (Top row) With density  $\rho_{\text{cp}}^{\text{bulk}} = 0.9$  for the bulk region; (middle row)  $\rho_{\text{cp}}^{\text{bulk}} = 0.75$ ; (bottom row)  $\rho_{\text{cp}}^{\text{bulk}} = 0.55$ .

This preliminary idea could be improved in several directions; notably:

- One could replace the functions  $W(\cdot, \cdot)$  and  $W_\varepsilon(\cdot, \cdot)$  in the above definitions of  $J(\Omega)$  and  $J_\varepsilon(\Omega)$  with unbalanced optimal transport distances (or even the Sinkhorn distance) [328, 329]; as these naturally compare measures with different masses, this substitution would alleviate the need for the biased normalization of the characteristic function  $\mathbb{1}_\Omega$  in (3.7.1).
- Yet another idea, which is popular in imaging, involves Wasserstein-like distances between histograms extracting relevant features from  $\Omega$  and  $\Omega_T$ , see e.g. [300].

This broader perspective on resemblance constraints in shape and topology optimization heralds multiple applications; let us outline a few of them:

- *A new method for retrieving shapes from densities.* As summarized in [Section 1.4.5](#), the popular density-based optimal design frameworks rely on a description of shapes by “grayscale” density functions  $D \rightarrow [0, 1]$ , accounting for the local fraction of solid and void within the computational domain  $D$ . A threshold of the resulting density  $h$  is usually applied as a post-processing stage, to interpret  $h$  as a true, “black-and-white” shape. This identification could be alternatively formulated as the search for the closest shape  $\Omega$  to  $h$  in terms of a resemblance criterion akin to those in (3.7.1).

- *Resemblance constraints in architectural design.* As we have seen in [Section 3.4](#), architects often expect from a design to be not only optimal from the mechanical viewpoint, but also aesthetically “pleasant”. In this perspective, we have formulated the design process as the solution of a shape and topology optimization problem involving indicators of the mechanical performance of  $\Omega$  (notably, its compliance) and an extra constraint about the similarity of the optimized shape with a target design supplied by the architect. The crude functional [\(3.4.3\)](#) used in this study could advantageously be replaced by one of the form [\(3.7.1\)](#).
- *Enforcing “black-box” constraints using resemblance constraints.* Engineering constraints on structures are sometimes unclear or too difficult to formulate or analyze mathematically; at best, an acceptable design can be inferred from a particular input after application of non explicit, “rule of thumbs” engineering rules. Requiring that the optimized shape  $\Omega$  should resemble a given “good” shape could be an original means to enforce such “black-box constraints”, which are usually dealt with by using derivative-free methods such as genetic algorithms, see e.g. [\[207\]](#).
- *Reconstructing a shape from an unorganized point cloud.* Beyond mechanical applications, the capability of Wasserstein distances to compare heterogeneous objects paves the way to an appealing way to deal with the well-known problem of reconstructing a shape from a noisy point cloud (obtained from 3d scanning, for instance), see [\[77\]](#) for an overview of this topic, [\[380\]](#) for an approach using a shape optimization formalism, or [\[151\]](#) for a use of the Wasserstein distance as an error measure between the sought reconstructed domain and the target point cloud. Solving a shape reconstruction problem from such a point cloud thanks to the level set based mesh evolution framework outlined in [Section 1.4.7](#) would supply a high-quality mesh of the reconstructed object; see Figure [3.7.1](#) (bottom row) for an example of this practice obtained by using the less sophisticated resemblance criterion [\(3.4.3\)](#).

A variation of this idea would allow to reconstruct a shape from digital data, a widely used format in Computer Graphics and visualization, consisting of unorganized cubes [\[133\]](#).

- *Calculating Wasserstein barycenters as shapes.* Following the notion introduced in [\[10\]](#), it is interesting to look for the Wasserstein barycenter of geometric objects of different natures under the form of a “true” shape. This could be a first step towards the very prospective idea of a model reduction procedure in shape optimization, where shapes would be parametrized as weighted means of a (small) set of “relevant” shapes, see for instance [\[202, 313\]](#) about the general idea of model reduction.

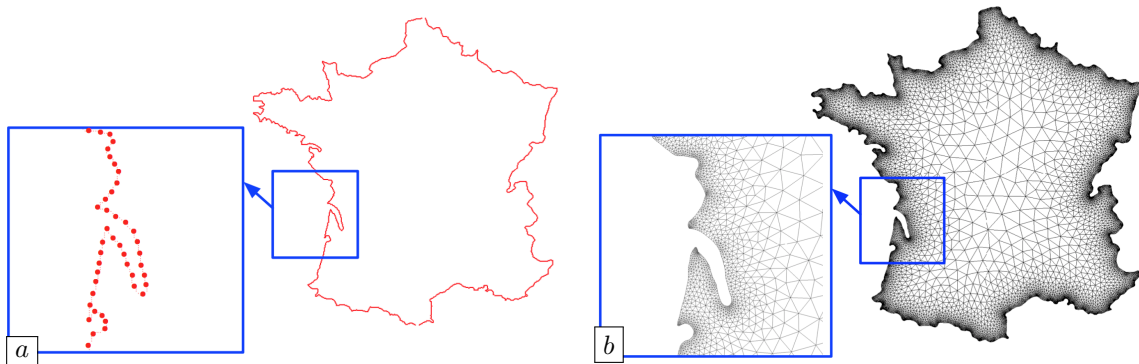


FIGURE 3.7.1. *An example of the use of similarity functionals in shape optimization: reconstruction of a meshed shape (b) from the input point cloud in (a).*

### 3.A THE COAREA FORMULA

In this appendix, we recall one version of the coarea formula, that we quote from [\[117\]](#). Loosely speaking, this result may be understood as a “curved” version of the Fubini theorem.

**Theorem 3.A.1** *Let  $X$  and  $Y$  be two smooth Riemannian manifolds with respective dimensions  $m \geq n$  and let  $f : X \rightarrow Y$  be a surjective mapping of class  $C^1$ , whose differential  $df_x : T_x X \rightarrow T_{f(x)} Y$  is surjective for any  $x \in X$ . Let  $\varphi$  be an integrable function on  $X$ ; then,*

$$(3.A.1) \quad \int_X \varphi(x) dx = \int_Y \left( \int_{z \in f^{-1}(y)} \varphi(z) \frac{1}{\text{Jac}(f)(z)} dz \right) dy.$$

*In the above formula, the Jacobian of  $f$  is defined by  $\text{Jac}(f)(z) = \sqrt{\det(\nabla f(z) \nabla f(z)^T)}$ , where the matrix  $\nabla f(z)$  of derivatives of  $f$  is expressed in any orthonormal bases of  $T_x X$  and  $T_{f(x)} Y$ .*

**Remark 3.A.2** *It follows from Sard's theorem that almost every point  $y \in Y$  is a regular value for  $f$ , so that  $f^{-1}(y)$  defines a submanifold of  $X$ , and the integral in the right-hand side of (3.A.1) is well-defined.*

# Chapter 4

## Asymptotic analysis of partial differential equations and applications in shape and topology optimization

The field of asymptotic analysis generally deals with the limiting properties of a perturbed version of a reference, “background” boundary value problem, as a “small” parameter  $\varepsilon$  involved in its expression vanishes. As a simple instance, one may wish to appraise the effect of perturbations of the order  $\varepsilon$  in the coefficients of an elliptic partial differential equation, but this framework encompasses multiple challenging questions beyond this one.

Aside from their theoretical interest, such investigations have crucial applications in inverse problems, sensitivity analysis, etc. Notably, there is a multifaceted interplay between asymptotic analysis and shape and topology optimization. Indeed, first and foremost, the sensitivity of a shape functional often brings into play “small” perturbations of the defining domain of a boundary value problem. Thus, the boundary variation method of Hadamard, presented in [Section 1.3.3](#), compares a smooth reference shape  $\Omega$  with perturbations by diffeomorphisms close to the identity mapping within an error of “small” norm  $\varepsilon$ . Topological sensitivity analysis, as broached in [Section 1.3.4](#) is based on more singular perturbations of  $\Omega$ , by the nucleation of holes with “small” radius  $\varepsilon$ . Another interaction of asymptotic analysis with shape and topology optimization, that we have touched on with the ersatz material method in [Section 1.2.1.3](#), concerns the construction of “smoothed”, approximate counterparts of singular boundary value problems, which are more convenient to handle, notably from the numerical point of view.

This chapter collects several theoretical investigations pertaining to the field of asymptotic analysis, and a few applications in shape and topology optimization. After some reminders about ubiquitous notions in asymptotic analysis such as the notion of Green’s function, fractional and exterior Sobolev spaces, and an introduction to the topic of “small inclusions” in [Section 4.1](#), we present in [Section 4.2](#) a unifying perspective on shape derivatives, topological derivatives, and density-based derivatives. The next [Sections 4.3](#) and [4.4](#) deal with perturbations of the regions supporting the boundary conditions of a boundary value problem, at first in a regular fashion, then in a singular one. We then analyze thin inhomogeneities in the two [Sections 4.5](#) and [4.6](#). In the former, which is of a rather theoretical nature, we identify the asymptotic behavior of the voltage potential when a thin inclusion vanishes, in a way which is uniform with respect to the conductivity inside the inclusion. In the latter [Section 4.6](#), we propose a general, intuitive method to derive asymptotic expansions of solutions to boundary value problems when the material properties are perturbed in thin and tubular inclusion subsets, and we present several applications of the results in shape and topology optimization. Finally, in [Section 4.7](#), we outline a few perspectives suggested by these works.

### 4.1 PRELIMINARIES: SMALL INCLUSIONS AS A REPRESENTATIVE STARTER

In this first section, we broach a few fundamental concepts from functional analysis and potential theory as well as some facts from the more specific subject of low-volume asymptotic expansions. In [Section 4.1.1](#), we briefly recall some material about Green’s functions for the conductivity equation and the linear elasticity

system. [Section 4.1.2](#) gathers some facts about two types of functional spaces, namely fractional Sobolev spaces on the boundaries of smooth domains and exterior Sobolev spaces. Then, we briefly overview layer potential operators in [Section 4.1.3](#). We next discuss the subject of low-volume fraction inclusions; after a general presentation in [Section 4.1.4](#), we present a model calculation in the particular case of diametrically small inclusions in [Section 4.1.5](#), which can be related to the notion of topological derivatives introduced in [Section 1.3.4](#). Although the results contained in these sections are not new, properly speaking, we believe that the presentation, which is inspired by the works reported in the next sections of this chapter, might offer new intuitions about these issues.

#### 4.1.1. Fundamental solutions and Green's functions

This section deals with the definition and the construction of Green's functions for (various avatars of) the conductivity equation presented in [Section 1.2.1.1](#); the generalization of this material to the context of linear elasticity is also evoked. We refer to [34, 180, 258] for further details about these issues.

In a nutshell, the Green's function of a class of boundary value problems is an impulse response function, which is the building block of explicit representation formulas for its solutions. Its construction relies on the notion of fundamental solution for the underlying operator in free space.

**Definition 4.1.1** *The fundamental solution  $G(x, y)$  of the negative Laplace operator  $-\Delta$  in the free space  $\mathbb{R}^d$  is:*

$$(4.1.1) \quad \forall x \neq y \in \mathbb{R}^d, \quad G(x, y) = \begin{cases} -\frac{1}{2\pi} \log|x - y| & \text{if } d = 2, \\ \frac{1}{(d-2)|\mathbb{S}^{d-1}|} \frac{1}{|x - y|^{d-2}} & \text{if } d \geq 3, \end{cases}$$

where  $|\mathbb{S}^{d-1}|$  is the measure of the  $(d-1)$ -dimensional unit sphere  $\mathbb{S}^{d-1}$ .

For any point  $x \in \mathbb{R}^d$ , the function  $y \mapsto G(x, y)$  satisfies:

$$-\Delta_y G(x, y) = \delta_{y=x} \text{ in the sense of distributions in } \mathcal{D}'(\mathbb{R}^d).$$

Equivalently, the above property means that for each point  $x \in \mathbb{R}^d$ , the function  $y \mapsto G(x, y)$  satisfies the following “variational problem”:

$$(4.1.2) \quad \forall \varphi \in \mathcal{C}_c^\infty(\mathbb{R}^d), \quad \varphi(x) = \int_{\mathbb{R}^d} \nabla_y G(x, y) \cdot \nabla \varphi(y) \, dy.$$

**Remark 4.1.2** *In view of the explicit expression (4.1.1) of  $G(x, y)$ , the above identity can be extended by density to functions  $\varphi$  which only belong to  $W^{1,1}(\mathbb{R}^d)$  and enjoy  $W^{1,\infty}$  regularity in a neighborhood of  $x$ .*

The function  $G(x, y)$  allows to give an integral representation of the solution to the Laplace equation

$$(4.1.3) \quad \text{Search for } u : \mathbb{R}^d \rightarrow \mathbb{R} \text{ s.t. } -\Delta u = f \text{ in } \mathbb{R}^d,$$

as made precise by the next proposition:

**Proposition 4.1.3** *For any distribution with compact support  $f \in \mathcal{E}'(\mathbb{R}^d)$ , the function*

$$\mathcal{N}f(x) := \int_{\mathbb{R}^d} G(x, y) f(y) \, dy,$$

where the integral accounts for a convolution, is one solution to (4.1.3) in the sense of distributions.

Moreover, for any smooth cutoff functions  $\chi_1, \chi_2 \in \mathcal{C}_c^\infty(\mathbb{R}^d)$ , the mapping

$$H^{s-1}(\mathbb{R}^d) \ni f \mapsto \chi_2 \mathcal{N}(\chi_1 f) \in H^{s+1}(\mathbb{R}^d)$$

is bounded for any  $s \in \mathbb{R}$ .

Let us now turn to the following problem involving the Laplace operator inside a smooth bounded domain  $\Omega \subset \mathbb{R}^d$ , and where homogeneous Dirichlet boundary conditions are imposed on  $\partial\Omega$ :

$$(4.1.4) \quad \text{Search for } u : \mathbb{R}^d \rightarrow \mathbb{R} \text{ s.t. } \begin{cases} -\Delta u = f & \text{in } \Omega, \\ u = 0 & \text{on } \partial\Omega. \end{cases}$$

A Green's function  $N(x, y)$  for (4.1.4) is defined by the fact that for each  $x \in \Omega$ ,  $y \mapsto N(x, y)$  is solution to:

$$(4.1.5) \quad \begin{cases} -\Delta_y N(x, y) = \delta_{y=x} & \text{in } \Omega, \\ N(x, y) = 0 & \text{for } y \in \partial\Omega. \end{cases}$$

This function is constructed from the fundamental solution  $G(x, y)$  of the Laplace operator in free space by setting:

$$N(x, y) = G(x, y) + R(x, y),$$

where the correction  $y \mapsto R(x, y)$  satisfies, for  $x \in \Omega$ :

$$\begin{cases} -\Delta_y R(x, y) = 0 & \text{in } \Omega, \\ R(x, y) = -G(x, y) & \text{for } y \in \partial\Omega. \end{cases}$$

Since  $G(x, \cdot)$  is smooth on  $\partial\Omega$ , the above problem has a unique solution in  $H^1(\Omega)$ . Besides, the elliptic regularity theory (sketched in Section 1.A.6) implies that for any  $x \in \Omega$ , the function  $R(x, \cdot)$  is smooth on  $\bar{\Omega}$ . For any  $x \in \Omega$ , the following “variational formulation” for  $N(x, \cdot)$  is easily obtained from (4.1.2):

$$(4.1.6) \quad \forall \varphi \in \mathcal{C}_c^\infty(\Omega), \quad \varphi(x) = \int_{\Omega} \nabla_y N(x, y) \cdot \nabla \varphi(y) \, dy.$$

Again, this identity is readily extended to functions  $\varphi \in W^{1,1}(\Omega)$  with vanishing trace on  $\partial\Omega$ , enjoying  $W^{1,\infty}$  regularity in a neighborhood of  $x$ .

Analogously to the result of Proposition 4.1.3,  $N(x, y)$  paves the way to an integral formula for the solution to the boundary value problem (4.1.4) in terms of its right-hand side:

#### Proposition 4.1.4

(i) *The Green's function  $N(x, y)$  is symmetric in its arguments:*

$$\text{For all } x \neq y \text{ in } \Omega, \quad N(x, y) = N(y, x).$$

(ii) *Let  $f \in L^\infty(\Omega)$ ; the unique solution  $u \in H_0^1(\Omega)$  to (4.1.4) then reads:*

$$(4.1.7) \quad u(x) = \int_{\Omega} N(x, y) f(y) \, dy.$$

*Proof.* (i): Let  $x \neq y$  be two given points in  $\Omega$ ; it holds:

$$N(x, y) - N(y, x) = \int_{\Omega} \nabla_y N(y, z) \cdot \nabla_y N(x, z) \, dz - \int_{\Omega} \nabla_y N(x, z) \cdot \nabla_y N(y, z) \, dz = 0.$$

Here, the notation  $\nabla_y N$  refers to the gradient of  $N$  with respect to the second variable; we have used twice the “variational problem” (4.1.6) to obtain the first equality, see Remark 4.1.2.

(ii): We already know by the standard Lax-Milgram theory that the equation (4.1.4) has a unique solution in  $H_0^1(\Omega)$ , so that we only need to verify that the function  $u$  in (4.1.7) is one such solution. At first, Proposition 4.1.3 implies that  $u$  belongs to  $H^1(\Omega)$ ; besides, it follows from the symmetry of  $N(x, y)$  with respect to its arguments that  $u(x) = 0$  on  $\partial\Omega$ . We then calculate, for an arbitrary test function  $\varphi \in \mathcal{C}_c^\infty(\Omega)$ ,

$$\begin{aligned} \langle -\Delta u, \varphi \rangle &= -\langle u, \Delta \varphi \rangle \\ &= - \int_{\Omega} \int_{\Omega} N(x, y) f(y) \Delta \varphi(x) \, dy \, dx \\ &= \int_{\Omega} f(y) \left( \int_{\Omega} N(x, y) (-\Delta \varphi)(x) \, dx \right) \, dy \\ &= \int_{\Omega} f(y) \varphi(y) \, dy, \end{aligned}$$

where we have used the property (4.1.5) and the symmetry of  $N(x, y)$  to obtain the last line.  $\square$

Arguing in a similar fashion, one can construct a Green's function for the counterpart of (4.1.4) featuring homogeneous Neumann boundary conditions on  $\partial\Omega$ , or for the following version of the conductivity equation,

involving an inhomogeneous (smooth) conductivity coefficient  $\gamma \in \mathcal{C}^\infty(\overline{\Omega})$  as well as mixed homogeneous Dirichlet and Neumann boundary conditions on two disjoint and complementary regions  $\Gamma_D, \Gamma_N$  of  $\partial\Omega$ :

$$\begin{cases} -\operatorname{div}(\gamma \nabla u) = f & \text{in } \Omega, \\ u = 0 & \text{on } \Gamma_D, \\ \gamma \frac{\partial u}{\partial n} = 0 & \text{on } \Gamma_N. \end{cases}$$

The functions  $R(x, y)$  and  $N(x, y)$  constructed in the latter case retain all the aforementioned properties, except for the smoothness of  $y \mapsto R(x, y)$  in the neighborhood of the region  $\overline{\Gamma_D} \cap \overline{\Gamma_N}$  of  $\partial\Omega$  where boundary conditions change types, see [Remark 1.A.14](#). In particular, the “variational equation” [\(4.1.6\)](#) and [Proposition 4.1.4](#) are still valid.

**Remark 4.1.5** *In a few particular situations, Green’s functions can be constructed analytically by leveraging the symmetries of the domain, thanks to the so-called method of images. For instance, let us consider the following boundary value problem posed in the lower half-space  $H = \{x = (x_1, \dots, x_d) \in \mathbb{R}^d, x_d < 0\}$ , featuring homogeneous Neumann boundary conditions:*

$$(4.1.8) \quad \begin{cases} -\Delta u = f & \text{in } H, \\ \frac{\partial u}{\partial n} = 0 & \text{on } \partial H. \end{cases}$$

One Green’s function for the latter is simply given by

$$N(x, y) = G(x, y) + G(x, \tilde{y}), \text{ where for } y = (y_1, \dots, y_d), \quad \tilde{y} := (y_1, \dots, y_{d-1}, -y_d).$$

Likewise, one Green’s function for the version of [\(4.1.8\)](#) where homogeneous Neumann boundary conditions are replaced by homogeneous Dirichlet conditions reads:

$$N(x, y) = G(x, y) - G(x, \tilde{y}).$$

To conclude this section, let us outline how the previous considerations can be adapted to the case of the linear elasticity operator. The latter acts on vector-valued functions  $u \in \mathcal{D}(\mathbb{R}^d)^d$  as:

$$-\operatorname{div}(Ae(u)) \text{ where } e(u) = \frac{1}{2}(\nabla u + \nabla u^T), \text{ for all } \xi \in \mathbb{R}_{\text{sym}}^{d \times d}, \quad A\xi = 2\mu\xi + \lambda \operatorname{tr}(\xi)I,$$

and the Lamé coefficients  $\lambda > 0, \mu > 0$  are given constants.

**Definition 4.1.6** *The fundamental solution of the (negative) linear elasticity operator  $-\operatorname{div}(Ae(\cdot))$  is the Kelvin matrix  $(\Gamma_{ij})_{i,j=1,\dots,d}$ , defined by*

$$\forall x \neq y \in \mathbb{R}^d, \quad \Gamma_{ij}(x, y) = \begin{cases} \frac{\alpha}{4\pi} \frac{\delta_{ij}}{|x-y|} + \frac{\beta}{4\pi} \frac{(x_i - y_i)(x_j - y_j)}{|x-y|^3} & \text{if } d = 3, \\ -\frac{\alpha}{2\pi} \delta_{ij} \log |x-y| + \frac{\beta}{2\pi} \frac{(x_i - y_i)(x_j - y_j)}{|x-y|^2} & \text{if } d = 2, \end{cases}$$

where the constants  $\alpha$  and  $\beta$  equal:

$$\alpha = \frac{1}{2} \left( \frac{1}{\mu} + \frac{1}{2\mu + \lambda} \right), \text{ and } \beta = \frac{1}{2} \left( \frac{1}{\mu} - \frac{1}{2\mu + \lambda} \right).$$

For a given point  $x \in \mathbb{R}^d$  and for all  $j = 1, \dots, d$ , the  $j^{\text{th}}$  column  $y \mapsto \Gamma_j(x, y)$  of  $\Gamma(x, y)$  satisfies

$$-\operatorname{div}_y(Ae_y(\Gamma_j)) = \delta_{y=x} e_j \text{ in } \mathcal{D}'(\mathbb{R}^d)^d,$$

where  $e_j$  is the  $j^{\text{th}}$  vector of the canonical basis of  $\mathbb{R}^d$

All the aforementioned properties of the fundamental solution and Green’s functions can be generalized to this setting, up to an increased level of technicality.

#### 4.1.2. Fractional and exterior Sobolev spaces

In this section, we recall a few theoretical ingredients about two types of perhaps not completely classical Sobolev spaces: we consider fractional Sobolev spaces defined on (a region of) the boundary of a domain in [Section 4.1.2.1](#), and [Section 4.1.2.2](#) deals with exterior Sobolev spaces, defined on the (unbounded) complements of bounded domains of  $\mathbb{R}^d$ .

#### 4.1.2.1. Fractional Sobolev spaces on the boundary of smooth domains

Let  $\Omega$  be a smooth bounded domain of  $\mathbb{R}^d$ . The definition of Sobolev spaces with fractional exponents on the closed hypersurface  $\partial\Omega$ , or on an open Lipschitz subset  $\Gamma \subset \partial\Omega$  gives rise to some subtleties, which we briefly describe in this section, referring to [258] and [196, 241] for more details.

Let us first consider Sobolev spaces of functions attached to the whole boundary  $\partial\Omega$ . Given a real number  $0 < s < 1$ , there are several equivalent ways of defining a norm on the fractional Sobolev Space  $H^s(\partial\Omega)$ , and we shall use the following definition

$$(4.1.9) \quad \|v\|_{H^s(\partial\Omega)}^2 = \|v\|_{L^2(\partial\Omega)}^2 + \int_{\partial\Omega} \int_{\partial\Omega} \frac{|v(x) - v(y)|^2}{|x - y|^{d-1+2s}} \, ds(x) \, ds(y) .$$

Note that, in the literature the geodesic distance between two points  $x, y \in \partial\Omega$  is often used in place of the Euclidean distance  $|x - y|$  in the above formula. However, since  $\partial\Omega$  is smooth and compact, the resulting norms are equivalent (with a constant depending on  $\Omega$ ). When  $-1 < s < 0$ ,  $H^s(\partial\Omega)$  is the topological dual of  $H^{-s}(\partial\Omega)$ .

We next turn to Sobolev spaces  $H^s(\Gamma)$ , defined on an open Lipschitz subset  $\Gamma$  of  $\partial\Omega$ . For any real number  $0 < s < 1$  we introduce the following two classes of Sobolev spaces on  $\Gamma$ :

- $\tilde{H}^s(\Gamma)$  denotes the space of (restrictions to  $\Gamma$  of) functions in  $H^s(\partial\Omega)$  with compact support inside  $\bar{\Gamma}$ . It is equipped with the norm  $\|\cdot\|_{H^s(\partial\Omega)}$ , and it is the closure in  $H^s(\partial\Omega)$  of the set of  $\mathcal{C}^\infty$  functions on  $\partial\Omega$  with compact support inside  $\Gamma$ . Equivalently,  $u$  belongs to  $\tilde{H}^s(\Gamma)$  if and only if its extension by 0 to all of  $\partial\Omega$  (which we still denote by  $u$ ), belongs to  $H^s(\partial\Omega)$ .
- $H^s(\Gamma)$  is the space of the restrictions to  $\Gamma$  of functions in  $H^s(\partial\Omega)$ , equipped with the norm:

$$(4.1.10) \quad \|v\|_{H^s(\Gamma)}^2 = \|v\|_{L^2(\Gamma)}^2 + |v|_{H^s(\Gamma)}^2, \text{ where } |v|_{H^s(\Gamma)}^2 := \int_{\Gamma} \int_{\Gamma} \frac{|v(x) - v(y)|^2}{|x - y|^{d-1+2s}} \, ds(x) \, ds(y) .$$

This quantity is equivalent to the quotient norm induced by that of  $H^s(\partial\Omega)$ , i.e.

$$v \mapsto \inf \left\{ \|w\|_{H^s(\partial\Omega)}, w \in H^s(\partial\Omega), w|_{\Gamma} = u \right\},$$

up to constants that may depend on  $\Gamma$ .

Let us point out a few facts about the relation between both types of spaces:

- When  $0 < s < 1/2$ , the spaces  $\tilde{H}^s(\Gamma)$  and  $H^s(\Gamma)$  are identical, with equivalent norms. On the other hand, when  $\frac{1}{2} \leq s < 1$ ,  $\tilde{H}^s(\Gamma)$  is a proper subspace of  $H^s(\Gamma)$ .
- When  $\frac{1}{2} < s < 1$ , the space  $\tilde{H}^s(\Gamma)$  coincides with  $H_0^s(\Gamma)$ , the closure in  $H^s(\Gamma)$  (for the natural norm (4.1.10)) of the set of  $\mathcal{C}^\infty$  functions with compact support  $K \Subset \Gamma$ .

For any real number  $-1 < s < 0$ ,  $H^s(\Gamma)$  is still defined as the space of restrictions to  $\Gamma$  of distributions in  $H^s(\partial\Omega)$  (equipped with the quotient norm). This space can be identified with the topological dual of  $\tilde{H}^{-s}(\Gamma)$ , using as pairing the natural extension of the  $L^2(\Gamma)$  inner product, that we denote by:

$$\langle u, v \rangle, \quad u \in H^s(\Gamma), \quad v \in \tilde{H}^{-s}(\Gamma).$$

Similarly,  $\tilde{H}^s(\Gamma)$  is the space of distributions in  $H^s(\partial\Omega)$  with compact support inside  $\bar{\Gamma}$ . It is identified with the dual space of  $H^{-s}(\Gamma)$ , using the same pairing (with the same notation).

Let us dwell a little longer on the particular case when  $s = 1/2$ :  $\tilde{H}^{1/2}(\Gamma)$  is a proper subspace of  $H^{1/2}(\Gamma)$ , with a strictly stronger norm, while the latter space, incidentally, coincides with  $H_0^{1/2}(\Gamma)$ . This distinction between  $\tilde{H}^{1/2}(\Gamma)$  and  $H^{1/2}(\Gamma)$  is better appraised by the calculation of the norm  $\|u\|_{\tilde{H}^{1/2}(\Gamma)} = \|u\|_{H^{1/2}(\partial\Omega)}$  of an arbitrary function  $u \in \tilde{H}^{1/2}(\Gamma)$ :

$$\begin{aligned} \|u\|_{\tilde{H}^{1/2}(\Gamma)}^2 &= \|u\|_{L^2(\Gamma)}^2 + \int_{\Gamma} \int_{\Gamma} \frac{|u(x) - u(y)|^2}{|x - y|^d} \, ds(x) \, ds(y) + 2 \int_{\Gamma} \rho_{\Gamma}(x) |u(x)|^2 \, ds(x) \\ &= \|u\|_{H^{1/2}(\Gamma)}^2 + 2 \int_{\Gamma} \rho_{\Gamma}(x) |u(x)|^2 \, ds(x) . \end{aligned}$$

The weight  $\rho_\Gamma$  is here defined by

$$\forall x \in \Gamma, \quad \rho_\Gamma(x) = \int_{\partial\Omega \setminus \Gamma} \frac{1}{|x - y|^d} \, ds(y) .$$

Hence, the norm  $\|\cdot\|_{\tilde{H}^{1/2}(\Gamma)}$  is stronger than  $\|\cdot\|_{H^{1/2}(\Gamma)}$ , and in particular

$$(4.1.11) \quad \left( \int_\Gamma \rho_\Gamma(x) |u(x)|^2 \, ds(x) \right)^{\frac{1}{2}} \leq \frac{1}{\sqrt{2}} \|u\|_{\tilde{H}^{1/2}(\Gamma)} .$$

The spaces with exponents  $\pm\frac{1}{2}$  are particularly relevant in the context of variational solutions to boundary value problems featuring mixed boundary conditions. To illustrate this point, let us consider the situation where the boundary  $\partial\Omega$  is made of two disjoint open regions  $\Gamma_D$  and  $\Gamma_N$  and let us consider the following boundary value problem:

$$\begin{cases} -\operatorname{div}(\gamma \nabla u) = f & \text{in } \Omega, \\ u = 0 & \text{on } \Gamma_D, \\ \gamma \frac{\partial u}{\partial n} = 0 & \text{on } \Gamma_N, \end{cases}$$

featuring smooth conductivity  $\gamma \in \mathcal{C}^\infty(\overline{\Omega})$  and source  $f \in \mathcal{C}^\infty(\overline{\Omega})$ . The variational solution to this problem is the unique function  $u$  in the functional space

$$H_{\Gamma_D}^1(\Omega) := \{u \in H^1(\Omega), \ u = 0 \text{ on } \Gamma_D\}$$

of  $H^1(\Omega)$  functions with vanishing trace on  $\Gamma_D$  (in other words  $u|_{\Gamma_N} \in \tilde{H}^{1/2}(\Gamma_N)$ ), and for which

$$\int_\Omega \gamma \nabla u \cdot \nabla v \, dx = \int_\Omega f v \, dx ,$$

for all  $v \in H_{\Gamma_D}^1(\Omega)$  (i.e.,  $v|_{\Gamma_N} \in \tilde{H}^{1/2}(\Gamma_N)$ ). Using integration by parts, this identity asserts that:

$$\gamma \frac{\partial u}{\partial n} = 0 \text{ as an element in } H^{-1/2}(\Gamma_N), \text{ and so } \gamma \frac{\partial u}{\partial n} \in \tilde{H}^{-1/2}(\Gamma_D) .$$

#### 4.1.2.2. Exterior Sobolev spaces

The boundary value problems that we have encountered so far take place in bounded domains of  $\mathbb{R}^d$ ; their well-posedness classically requires suitable boundary conditions, whose formulations leverage the theory of traces for Sobolev spaces. Occasionally in this manuscript, we shall need to consider exterior problems, posed in the complement of a bounded domain of  $\mathbb{R}^d$ . These usually require that decay conditions at infinity be imposed on the unknown function  $u$ , which can be conveniently encoded in exterior Sobolev spaces.

Let  $\Omega$  be a smooth (possibly empty) bounded domain in  $\mathbb{R}^d$  with  $d = 2$  or  $3$ . We denote by  $\Omega_e := \mathbb{R}^d \setminus \overline{\Omega}$  the unbounded complement of  $\overline{\Omega}$  in  $\mathbb{R}^d$ ; depending on the value of  $d$ , we introduce the following spaces of locally  $H^1$  functions: if  $d = 2$ ,

$$W^{1,-1}(\Omega_e) = \left\{ u \in L^2_{\text{loc}}(\Omega_e), \ \frac{1}{(1 + |x|^2)^{\frac{1}{2}} \log(2 + |x|^2)} u \in L^2(\Omega_e), \ \nabla u \in L^2(\Omega_e) \right\} ,$$

and if  $d = 3$ :

$$W^{1,-1}(\Omega_e) = \left\{ u \in L^2_{\text{loc}}(\Omega_e), \ \frac{1}{(1 + |x|^2)^{\frac{1}{2}}} u \in L^2(\Omega_e), \ \nabla u \in L^2(\Omega_e) \right\} .$$

The space  $W^{1,-1}(\Omega_e)$  possesses very different properties in the 2d and 3d cases. Notably, in 3d, functions  $u \in W^{1,-1}(\Omega_e)$  vanish at infinity, while in 2d,  $W^{1,-1}(\Omega_e)$  contains the constant functions.

**Remark 4.1.7** *The decay of functions  $u \in W^{1,-1}(\Omega_e)$  in the case when  $d = 3$  can be understood from the following interesting calculation, borrowed from the Appendix of [283]. In this situation, for any function  $u \in W^{1,-1}(\Omega_e)$ , we have, for any sequence  $R_n$  of radii tending to  $\infty$ :*

$$\int_{\{x \in \mathbb{R}^3, \ R_n < |x| < 2R_n\}} \frac{1}{1 + |x|^2} |u(x)|^2 \xrightarrow{n \rightarrow \infty} 0 .$$

Using a polar change of variables, this rewrites:

$$\int_{R_n}^{2R_n} \frac{r^2}{1+r^2} \left( \int_{\mathbb{S}^2} |u(r\omega)|^2 \, ds(\omega) \right) dr \xrightarrow{n \rightarrow \infty} 0.$$

Now, by the mean value theorem, there exists a number  $Q_n \in (R_n, 2R_n)$  such that

$$\frac{R_n Q_n}{1+Q_n^2} \int_{\mathbb{S}^2} |u(Q_n \omega)|^2 \, ds(\omega) = \int_{R_n}^{2R_n} \frac{r^2}{1+r^2} \left( \int_{\mathbb{S}^2} |u(r\omega)|^2 \, ds(\omega) \right) dr,$$

and so there exists a sequence  $Q_n \rightarrow \infty$  such that

$$Q_n \int_{\mathbb{S}^2} |u(Q_n \omega)|^2 \, ds(\omega) \xrightarrow{n \rightarrow \infty} 0,$$

which in loose terms accounts for the fact that  $u$  “vanishes at infinity”.

To harmonize notations, we introduce the space

$$W_0^{1,-1}(\Omega_e) := \begin{cases} W^{1,-1}(\Omega_e)/\mathbb{R} & \text{if } d = 2, \\ W^{1,-1}(\Omega_e) & \text{if } d = 3, \end{cases}$$

of functions in  $W^{1,-1}(\mathbb{R}^d)$  vanishing at infinity; see [282] §2.5 for further details about these issues.

We now state a version of the Poincaré inequality which is adapted to such exterior spaces:

**Proposition 4.1.8** *For  $d = 2$  or  $3$ , let  $\Omega$  be a smooth, non empty bounded domain in  $\mathbb{R}^d$ , with complement  $\Omega_e = \mathbb{R}^d \setminus \overline{\Omega}$ . There exists a constant  $C > 0$  such that:*

$$\forall u \in W^{1,-1}(\Omega_e) \text{ s.t. } u = 0 \text{ on } \partial\Omega, \quad \|u\|_{W^{1,-1}(\Omega_e)} \leq C \|\nabla u\|_{L^2(\Omega_e)^d}.$$

**Remark 4.1.9** *Another approach to exterior spaces which is frequently encountered in the literature consists in defining  $W^{1,-1}(\Omega_e)$  as the completion of the space  $\mathcal{C}_c^\infty(\mathbb{R}^d \setminus \Omega)$  for the norm  $u \mapsto \|\nabla u\|_{L^2(\Omega_e)^d}$ . This viewpoint is equivalent to that adopted in the present section, as proved in [223] and [15].*

#### 4.1.3. Layer potentials

In the present section, we briefly recall some background material about the layer potential operators associated with the Laplace equation, which are the building blocks of convenient representation formulas for the solutions to related boundary value problems, in close connection with the material introduced in Section 4.1.1. We refer to [34, 180, 258, 324] for more details about such operators.

Let  $D$  be a smooth bounded domain in  $\mathbb{R}^d$ . For a smooth function  $\phi \in \mathcal{C}^\infty(\partial D)$ , the single layer potential with density  $\phi$  is defined by

$$\mathcal{S}_D \phi(x) = \int_{\partial D} G(x, y) \phi(y) \, ds(y), \quad x \in \mathbb{R}^d \setminus \partial D,$$

where  $G(x, y)$  is the fundamental solution of the operator  $-\Delta$  in  $\mathbb{R}^d$ , see (4.1.1). The corresponding double layer potential is defined by

$$\mathcal{D}_D \phi(x) = \int_{\partial D} \frac{\partial G}{\partial n_y}(x, y) \phi(y) \, ds(y), \quad x \in \mathbb{R}^d \setminus \partial D.$$

These operators extend as bounded operators

$$\mathcal{S}_D : H^{-1/2}(\partial D) \rightarrow H^1_{\text{loc}}(\mathbb{R}^d), \quad \text{and} \quad \mathcal{D}_D : H^{1/2}(\partial D) \rightarrow H^1(D) \cup H^1_{\text{loc}}(\mathbb{R}^d \setminus \overline{D}).$$

For a given density  $\phi$ , both functions  $\mathcal{S}_D \phi$  and  $\mathcal{D}_D \phi$  are harmonic on  $D$  and  $\mathbb{R}^d \setminus \overline{D}$ , and their behavior at the interface  $\partial D$  is of particular interest. To express it, let us recall the notations

$$(4.1.12) \quad g^\pm(x) := \lim_{t \downarrow 0} g(x \pm tn(x)) \quad \text{and} \quad [g](x) := g^+(x) - g^-(x), \quad x \in \partial D$$

for the one-sided limits of a function  $g$  which is smooth enough from either side of  $\partial D$  and the corresponding jump across  $\partial D$ . For an arbitrary density  $\phi \in H^{-1/2}(\partial D)$ , the function  $\mathcal{S}_D \phi$  satisfies the well-known jump

relations:

$$[\mathcal{S}_D \phi] = 0 \text{ and } \left[ \frac{\partial}{\partial n} (\mathcal{S}_D \phi) \right] = -\phi.$$

Likewise, for  $\phi \in H^{1/2}(\partial D)$ , it holds:

$$[\mathcal{D}_D \phi] = \phi \text{ and } \left[ \frac{\partial}{\partial n} (\mathcal{D}_D \phi) \right] = 0.$$

The first and the last of these four jump relations allow to introduce the integral operators  $S_D$  and  $R_D$ , defined for a smooth density function  $\phi \in \mathcal{C}^\infty(\partial D)$  by:

$$S_D \phi = (\mathcal{S}_D \phi)|_{\partial D}, \quad S_D \phi(x) = \int_{\partial D} G(x, y) \phi(y) \, ds(y), \quad x \in \partial D,$$

and

$$R_D \phi = \frac{\partial}{\partial n} (\mathcal{D}_D \phi), \quad R_D \phi(x) = \text{f.p.} \int_{\eta \downarrow 0} \int_{\partial D \setminus B_\eta(x)} \frac{\partial^2 G}{\partial n_x \partial n_y}(x, y) \phi(y) \, ds(y), \quad x \in \partial D,$$

where f.p. refers to a finite part integral in the sense of Hadamard. These expressions extend as bounded mappings

$$S_D : H^{-1/2}(\partial D) \rightarrow H^{1/2}(\partial D), \text{ and } R_D : H^{1/2}(\partial D) \rightarrow H^{-1/2}(\partial D).$$

Finally, let us recall the decay properties of the above layer potential operators at infinity. For a given density  $\phi \in H^{-1/2}(\partial D)$ , it follows from the explicit expression (4.1.1) of the fundamental solution  $G(x, y)$  that, for  $d = 3$

$$\mathcal{S}_D \phi(x) = \mathcal{O}\left(\frac{1}{|x|}\right), \text{ and } |\nabla \mathcal{S}_D \phi(x)| = \mathcal{O}\left(\frac{1}{|x|^2}\right) \text{ as } |x| \rightarrow \infty,$$

where the notation  $\mathcal{O}\left(\frac{1}{|x|}\right)$  (resp.  $\mathcal{O}\left(\frac{1}{|x|^2}\right)$ ) stands for a function whose modulus is bounded by  $\frac{C}{|x|}$  (resp.  $\frac{C}{|x|^2}$ ) when  $|x|$  is large enough, for a suitable positive constant  $C$ .

The case  $d = 2$  is a little more subtle, and in general one only has

$$\mathcal{S}_D \phi(x) = \mathcal{O}(|\log|x||), \text{ and } |\nabla \mathcal{S}_D \phi(x)| = \mathcal{O}\left(\frac{1}{|x|}\right) \text{ as } |x| \rightarrow \infty.$$

However, if  $\int_{\partial D} \phi \, ds = 0$ , then it holds additionally

$$\mathcal{S}_D \phi(x) = \mathcal{O}\left(\frac{1}{|x|}\right), \text{ and } |\nabla \mathcal{S}_D \phi(x)| = \mathcal{O}\left(\frac{1}{|x|^2}\right).$$

As far as the double layer potential is concerned, one has for  $\phi \in H^{1/2}(\partial D)$  and  $d = 2, 3$

$$\mathcal{D}_D \phi(x) = \mathcal{O}\left(\frac{1}{|x|^{d-1}}\right), \text{ and } |\nabla \mathcal{D}_D \phi(x)| = \mathcal{O}\left(\frac{1}{|x|^d}\right).$$

**Remark 4.1.10** *The material of this section can be generalized to the context of the linear elasticity system, up to an increased level of technicality, see [34].*

#### 4.1.4. Asymptotic expansions in the presence of “small” inhomogeneities

This section enters the more specific field of asymptotic analysis, and it notably outlines some of the many investigations conducted in the literature to understand the effect of the presence of “small” inhomogeneities in the material properties of a reference, background medium. The reader may consult the books [35, 34] and the references therein for more extensive accounts of this rich topic.

To set ideas, we consider the following model situation, in the physical setting of the conductivity equation introduced in Section 1.2.1 (whose notations are adapted to the present context). Let  $\Omega$  be a smooth bounded domain in  $\mathbb{R}^d$ ; in a reference, “background” situation,  $\Omega$  is made of a material with conductivity  $\gamma_0 \in \mathcal{C}^\infty(\overline{\Omega})$  bounded away from 0 and  $\infty$  (see (Ell-Cond)), a source  $f \in \mathcal{C}^\infty(\overline{\Omega})$  is acting inside  $\Omega$  and

homogeneous Dirichlet boundary conditions are imposed on the boundary  $\partial\Omega$ . The resulting, “background” voltage potential  $u_0$  is the unique solution in  $H_0^1(\Omega)$  to the equation:

$$(4.1.13) \quad \begin{cases} -\operatorname{div}(\gamma_0 \nabla u_0) = f & \text{in } \Omega, \\ u_0 = 0 & \text{on } \partial\Omega. \end{cases}$$

The variational formulation of this problem reads:

$$(4.1.14) \quad \text{Search for } u_0 \in H_0^1(\Omega) \text{ s.t. } \forall v \in H_0^1(\Omega), \quad \int_{\Omega} \gamma_0 \nabla u_0 \cdot \nabla v \, dx = \int_{\Omega} f v \, dx.$$

Let us recall that, on account of the elliptic regularity theory, the function  $u_0$  is smooth on  $\overline{\Omega}$ , see [Section 1.A.6](#).

We now introduce a perturbed version of this problem, where the medium is polluted by the presence of inclusions of another material with conductivity  $\gamma_1 \in \mathcal{C}^\infty(\overline{\Omega})$  as in [\(Ell-Cond\)](#), occupying a “small” open subset  $\omega_\varepsilon \Subset \Omega$ . The voltage potential  $u_\varepsilon$  in this situation is the unique solution in  $H_0^1(\Omega)$  to:

$$(4.1.15) \quad \begin{cases} -\operatorname{div}(\gamma_\varepsilon \nabla u_\varepsilon) = f & \text{in } \Omega, \\ u_\varepsilon = 0 & \text{on } \partial\Omega, \end{cases} \quad \text{where } \gamma_\varepsilon(x) = \begin{cases} \gamma_1(x) & \text{if } x \in \omega_\varepsilon, \\ \gamma_0(x) & \text{otherwise.} \end{cases}$$

The variational formulation of this problem reads:

$$(4.1.16) \quad \text{Search for } u_\varepsilon \in H_0^1(\Omega) \text{ s.t. } \forall v \in H_0^1(\Omega), \quad \int_{\Omega} \gamma_\varepsilon \nabla u_\varepsilon \cdot \nabla v \, dx = \int_{\Omega} f v \, dx.$$

Our aim is to understand the behavior of the perturbed potential  $u_\varepsilon$  as  $\varepsilon \rightarrow 0$ , a limit in which the inclusion set  $\omega_\varepsilon$  vanishes, in the sense that the Lebesgue measure  $|\omega_\varepsilon|$  tends to 0. More precisely, it is a fairly simple matter to prove that  $u_\varepsilon \rightarrow u_0$  in  $H_0^1(\Omega)$  as  $\varepsilon \rightarrow 0$ , and we inquire about the structure of the first non trivial term of the asymptotic expansion of  $u_\varepsilon$ .

A few common instances of this general question are the following:

- Diametrically small inhomogeneities feature an inclusion set  $\omega_\varepsilon$  of the form

$$(4.1.17) \quad \omega_\varepsilon = \{x_0 + \varepsilon z, \quad z \in \omega\},$$

where  $x_0$  is a given point in  $\Omega$  and  $\omega$  is a Lipschitz, bounded open subset of  $\mathbb{R}^d$ , see [Fig. 4.1.1 \(a,b\)](#).

- Thin inhomogeneities are of the form

$$(4.1.18) \quad \omega_{S,\varepsilon} = \{x \in \mathbb{R}^d, \quad d(x, S) < \varepsilon\},$$

where  $S$  stands for a (closed or open) curve in 2d, or piece of surface in 3d, see [Fig. 4.1.1 \(c,d\)](#).

- Tubular inhomogeneities coincide with small inhomogeneities in 2d, but differ from the latter in 3d. They are of the form

$$(4.1.19) \quad \omega_{\sigma,\varepsilon} = \{x \in \mathbb{R}^d, \quad d(x, \sigma) < \varepsilon\},$$

where  $\sigma \Subset \Omega$  is a (closed or open) curve, see [Fig. 4.1.1 \(e\)](#).

A very general representation formula for the perturbed potential  $u_\varepsilon$  was derived in [\[110\]](#), expressing its first-order behavior in terms of quite abstract quantities, under minimal assumptions about the inclusion set  $\omega_\varepsilon$ . This work was extended in [\[73\]](#) to the case of the linear elasticity system, and in [\[195\]](#) to the context of the Maxwell’s equations. We provide a statement of this result in the setting of the conductivity equations [\(4.1.13\)](#) and [\(4.1.15\)](#), together with a formal hint of the proof, as the latter lends itself to multiple interesting adaptations.

**Theorem 4.1.11** *Let  $\omega_\varepsilon$  be a sequence of subsets in  $\Omega$ , contained in a fixed compact subset  $K \subset \Omega$ , such that  $|\omega_\varepsilon| \rightarrow 0$  as  $\varepsilon \rightarrow 0$ . Let  $N(x, y)$  be the Green’s function of the background operator [\(4.1.13\)](#). Then, up to a subsequence, still labelled by  $\varepsilon$ , there exists a probability measure  $\mu$  on  $\Omega$  with support in  $K$ , as well as a function  $\mathcal{M} \in L^2(\Omega, \mu)^{d \times d}$  taking values in the set of positive-definite matrices, such that the solution  $u_\varepsilon$  to [\(4.1.13\)](#) satisfies:*

$$(4.1.20) \quad \forall x \in \Omega \setminus K, \quad u_\varepsilon(x) = u_0(x) + |\omega_\varepsilon| \int_{\Omega} \mathcal{M}(y) \nabla u_0(y) \cdot \nabla_y N(x, y) \, d\mu(y) + o(|\omega_\varepsilon|).$$

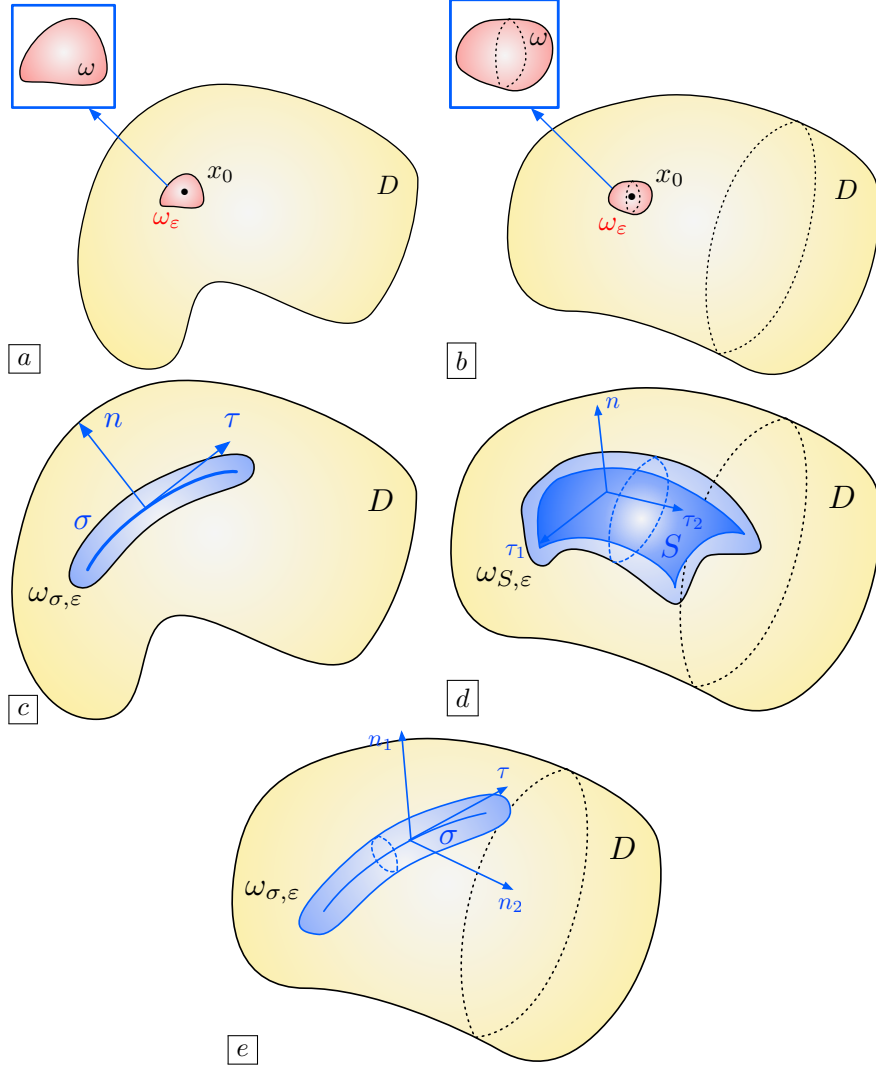


FIGURE 4.1.1. *Several particular instances of small inhomogeneities; (upper row) Diametrically small inhomogeneities (a) In 2d, (b) In (3d); (intermediate row) Thin inclusions (c) In 2d, (d) In 3d; (bottom) Small tubular inhomogeneities in 3d.*

*Sketch of the proof.* At first, subtracting the variational formulation (4.1.14) for  $u_0$  from that (4.1.16) for  $u_\varepsilon$ , we construct two variational problems for the difference  $r_\varepsilon := u_\varepsilon - u_0 \in H_0^1(\Omega)$ . On the one hand, this function satisfies:

$$(4.1.21) \quad \forall v \in H_0^1(\Omega), \quad \int_{\Omega} \gamma_0 \nabla r_\varepsilon \cdot \nabla v \, dx = - \int_{\omega_\varepsilon} (\gamma_1 - \gamma_0) \nabla u_\varepsilon \cdot \nabla v \, dx,$$

made from the “simple” background operator, but with an awkward right-hand side featuring the unknown function  $u_\varepsilon$ . On the other hand,  $r_\varepsilon$  also satisfies the variational problem:

$$(4.1.22) \quad \forall v \in H_0^1(\Omega), \quad \int_{\Omega} \gamma_\varepsilon \nabla r_\varepsilon \cdot \nabla v \, dx = - \int_{\omega_\varepsilon} (\gamma_1 - \gamma_0) \nabla u_0 \cdot \nabla v \, dx,$$

where the perturbed operator is used, but with a more convenient right-hand side.

Let us first estimate the error  $r_\varepsilon$  in terms of the “smallness” of the subset  $\omega_\varepsilon$  where the properties of the medium are perturbed. Taking  $v = r_\varepsilon$  in either (4.1.21) or (4.1.22) and using the Poincaré inequality,

we easily obtain the following a priori estimate:

$$(4.1.23) \quad \|r_\varepsilon\|_{H^1(\Omega)} \leq C|\omega_\varepsilon|^{\frac{1}{2}}, \text{ for some constant } C > 0 \text{ independent of } \varepsilon.$$

Actually, owing to the so-called ‘‘Aubin-Nitsche’’ trick, it is possible to prove that the  $L^2$  norm of the function  $r_\varepsilon$  decays to 0 faster than the above rate, namely:

$$(4.1.24) \quad \|r_\varepsilon\|_{L^2(\Omega)} \leq C|\omega_\varepsilon|^{\frac{1}{2}+\eta}, \text{ for some } \eta > 0,$$

see [Remark 4.1.12](#) below for further comments about this very general observation.

The starting point of the derivation of [\(4.1.20\)](#) is a representation formula for the value  $r_\varepsilon(x)$  of the error at a given point  $x \in \Omega \setminus K$  in terms of the Green’s function  $N(x, y)$  and the values of  $r_\varepsilon(y)$  at points  $y$  inside the inclusion  $\omega_\varepsilon$ . Let  $x \in \Omega \setminus K$  be given; we calculate:

$$(4.1.25) \quad \begin{aligned} r_\varepsilon(x) &= \int_{\Omega} \gamma_0(y) \nabla r_\varepsilon(y) \cdot \nabla_y N(x, y) dy, \\ &= - \int_{\omega_\varepsilon} (\gamma_1(y) - \gamma_0(y)) \nabla u_\varepsilon(y) \cdot \nabla_y N(x, y) dy, \\ &= -|\omega_\varepsilon| \int_{\Omega} \frac{1}{|\omega_\varepsilon|} (\gamma_1(y) - \gamma_0(y)) \mathbb{1}_{\omega_\varepsilon}(y) \nabla u_0(y) \cdot \nabla_y N(x, y) dy \\ &\quad - |\omega_\varepsilon| \int_{\Omega} \frac{1}{|\omega_\varepsilon|} (\gamma_1(y) - \gamma_0(y)) \mathbb{1}_{\omega_\varepsilon}(y) \nabla r_\varepsilon(y) \cdot \nabla_y N(x, y) dy. \end{aligned}$$

Here, the first equality follows from the ‘‘variational problem’’ of the Green’s function  $y \mapsto N(x, y)$ , see also [Remark 4.1.2](#). The second line is obtained by using  $y \mapsto N(x, y)$  as test function in [\(4.1.21\)](#), which is a priori formal since this function does not belong to the space  $H_0^1(\Omega)$ . This operation can however be justified by an approximation argument, based on the fact that  $N(x, \cdot)$  is smooth away from  $x$  and that  $r_\varepsilon$  is smooth near  $x$ , as follows from the standard elliptic regularity theory, see [Section 1.A.6](#).

Now, since the sequence  $\frac{1}{|\omega_\varepsilon|} \mathbb{1}_{\omega_\varepsilon}$  is bounded in  $L^1(\Omega)$ , we may extract a subsequence (still labelled by  $\varepsilon$ ) converging weakly \* to a probability measure  $\mu \in \mathcal{P}(\overline{\Omega})$ , that is:

$$(4.1.26) \quad \forall \phi \in \mathcal{C}(\overline{\Omega}), \quad \frac{1}{|\omega_\varepsilon|} \int_{\omega_\varepsilon} \phi(y) dy \xrightarrow{\varepsilon \rightarrow 0} \int_{\Omega} \phi d\mu,$$

see [Theorem 2.A.11](#). Physically,  $\mu$  is an indicator of the ‘‘limiting set’’ of the sequence  $\omega_\varepsilon$ . With this definition, the convergence of the first integral in the right-hand side of [\(4.1.25\)](#) is fairly straightforward, while that of the second one remains tedious.

The latter task boils down to taking limits in an integral expression of the form

$$I_\varepsilon := \int_{\Omega} \frac{1}{|\omega_\varepsilon|} (\gamma_1(y) - \gamma_0(y)) \mathbb{1}_{\omega_\varepsilon}(y) \nabla r_\varepsilon(y) \cdot e_i \phi(y) dy,$$

for a smooth function  $\phi(y)$  which stands for any of the  $y \mapsto \frac{\partial N}{\partial y_i}(x, y)$ ,  $i = 1, \dots, d$ . This integral can be rewritten:

$$I_\varepsilon = \int_{\Omega} \frac{1}{|\omega_\varepsilon|} (\gamma_1 - \gamma_0) \mathbb{1}_{\omega_\varepsilon} e_i \cdot \nabla(\phi r_\varepsilon) dy + R_{1,\varepsilon}, \text{ where } R_{1,\varepsilon} := - \int_{\Omega} \frac{1}{|\omega_\varepsilon|} (\gamma_1 - \gamma_0) \mathbb{1}_{\omega_\varepsilon} \nabla \phi \cdot e_i r_\varepsilon dy.$$

Here and in the following, the integral remainders  $R_{j,\varepsilon}$ ,  $j = 1, \dots$  appearing in the course of the calculation can be proved to vanish as  $\varepsilon \rightarrow 0$ , as a result of the  $H^1$  and improved  $L^2$  estimates [\(4.1.23\)](#) and [\(4.1.24\)](#).

Passing to the limit in the above expression is a priori difficult since both sequences  $\frac{1}{|\omega_\varepsilon|} \mathbb{1}_{\omega_\varepsilon}$  and  $\nabla r_\varepsilon$  converge only weakly, in the sense of measures and in  $L^2(\Omega)^d$ , respectively. The key idea to circumvent this difficulty borrows from the theory of compensated compactness [\[277\]](#): we use an adjoint state, solution to a problem featuring the same operator as that [\(4.1.22\)](#) for  $r_\varepsilon$ , and where the right-hand side is a copy of  $I_\varepsilon$  in which  $\phi r_\varepsilon$  is replaced by a test function. By duality, this allows to rewrite  $I_\varepsilon$  as an integral where this operator is applied to  $r_\varepsilon$ , and the adjoint state plays the role of test function – an expression which can be simplified thanks to [\(4.1.22\)](#).

More precisely, for  $i = 1, \dots, d$ , let us introduce the solution  $v_\varepsilon^i \in H_0^1(\Omega)$  to the following variational problem:

$$(4.1.27) \quad \forall w \in H_0^1(\Omega), \quad \int_{\Omega} \gamma_\varepsilon \nabla v_\varepsilon^i \cdot \nabla w \, dy = \int_{\Omega} (\gamma_1 - \gamma_0) \mathbb{1}_{\omega_\varepsilon} e_i \cdot \nabla w \, dy.$$

Note that this function does not depend on  $\phi$ . Besides, it satisfies similar estimates to those (4.1.23) and (4.1.24) about  $r_\varepsilon$ . Taking  $w = \phi r_\varepsilon$  as test function in (4.1.27), we obtain from a simple calculation:

$$\begin{aligned} I_\varepsilon &= \frac{1}{|\omega_\varepsilon|} \int_{\Omega} \gamma_\varepsilon \nabla v_\varepsilon^i \cdot \nabla (\phi r_\varepsilon) \, dy + R_{1,\varepsilon} \\ &= \frac{1}{|\omega_\varepsilon|} \int_{\Omega} \gamma_\varepsilon \nabla v_\varepsilon^i \cdot \nabla r_\varepsilon \phi \, dy + R_{1,\varepsilon} + R_{2,\varepsilon} \\ &= \frac{1}{|\omega_\varepsilon|} \int_{\Omega} \gamma_\varepsilon \nabla (\phi v_\varepsilon^i) \cdot \nabla r_\varepsilon \, dy + R_{1,\varepsilon} + R_{2,\varepsilon} + R_{3,\varepsilon}, \end{aligned}$$

where, in transferring the function  $\phi$  from one gradient to the other, we have introduced:

$$R_{2,\varepsilon} = \frac{1}{|\omega_\varepsilon|} \int_{\Omega} \gamma_\varepsilon \nabla v_\varepsilon^i \cdot \nabla \phi r_\varepsilon \, dy, \quad \text{and} \quad R_{3,\varepsilon} = -\frac{1}{|\omega_\varepsilon|} \int_{\Omega} \gamma_\varepsilon \nabla \phi \cdot \nabla r_\varepsilon v_\varepsilon^i \, dy.$$

We are now in position to use the variational problem (4.1.22) satisfied by  $r_\varepsilon$  with  $v = \phi v_\varepsilon^i$  as test function. This yields:

$$\begin{aligned} I_\varepsilon &= -\frac{1}{|\omega_\varepsilon|} \int_{\omega_\varepsilon} (\gamma_1 - \gamma_0) \nabla u_0 \cdot \nabla (\phi v_\varepsilon^i) \, dy + R_{1,\varepsilon} + R_{2,\varepsilon} + R_{3,\varepsilon} \\ &= -\frac{1}{|\omega_\varepsilon|} \int_{\omega_\varepsilon} (\gamma_1 - \gamma_0) \nabla u_0 \cdot \nabla v_\varepsilon^i \phi \, dy + R_{1,\varepsilon} + R_{2,\varepsilon} + R_{3,\varepsilon} + R_{4,\varepsilon}, \end{aligned}$$

where, eventually

$$R_{4,\varepsilon} := -\frac{1}{|\omega_\varepsilon|} \int_{\omega_\varepsilon} (\gamma_1 - \gamma_0) \nabla u_0 \cdot \nabla \phi v_\varepsilon^i \, dy.$$

Let us now return to the representation formula (4.1.25); using the above calculation for  $\phi = \frac{\partial N}{\partial y_i}(x, \cdot)$ ,  $i = 1, \dots, d$  and summing, we obtain:

$$\begin{aligned} (4.1.28) \quad r_\varepsilon(x) &= -|\omega_\varepsilon| \int_{\Omega} \frac{1}{|\omega_\varepsilon|} (\gamma_1(y) - \gamma_0(y)) \mathbb{1}_{\omega_\varepsilon}(y) \left( \nabla u_0(y) + \nabla r_\varepsilon(y) \right) \cdot \nabla_y N(x, y) \, dy \\ &= -|\omega_\varepsilon| \int_{\Omega} \frac{1}{|\omega_\varepsilon|} (\gamma_1(y) - \gamma_0(y)) \mathbb{1}_{\omega_\varepsilon}(y) \nabla u_0(y) \cdot \left( \sum_{i=1}^d \frac{\partial N}{\partial y_i}(x, y) (e_i - \nabla v_\varepsilon^i(y)) \right) \, dy \\ &\quad - |\omega_\varepsilon| R_\varepsilon, \quad \text{where } R_\varepsilon := \sum_{j=1}^4 R_{j,\varepsilon}. \end{aligned}$$

Now, from the counterpart of the a priori estimate (4.1.23) for the adjoint equations (4.1.27), there exists a constant  $C$  such that, for each  $i = 1, \dots, d$ :

$$\left\| \frac{1}{|\omega_\varepsilon|} \mathbb{1}_{\omega_\varepsilon} (e_i - \nabla v_\varepsilon^i) \right\|_{L^1(\Omega)^d} \leq C,$$

and so up to further extraction of subsequences from  $\varepsilon$ , there exist vector-valued Radon measures  $\mathcal{M}_i \in \mathcal{M}(\overline{\Omega})^d$  on  $\overline{\Omega}$  such that

$$(4.1.29) \quad -\frac{1}{|\omega_\varepsilon|} \mathbb{1}_{\omega_\varepsilon} (e_i - \nabla v_\varepsilon^i) \xrightarrow{\varepsilon \rightarrow 0} \mathcal{M}_i \text{ weakly } * \text{ in } \mathcal{M}(\overline{\Omega})^d, \quad i = 1, \dots, d,$$

see again Theorem 2.A.11.

Simple manipulations of these quantities reveal that the measures  $\mathcal{M}_i$  have square integrable density (still denoted by  $\mathcal{M}_i$ ) with respect to the measure  $\mu$ , and that the matrix  $\mathcal{M}(y)$  with columns  $\mathcal{M}_i(y)$  takes values in the set of positive definite matrices for  $\mu$  a.e  $y \in \Omega$ .

Finally, gathering (4.1.26) and (4.1.29) and taking limits in (4.1.25), we obtain the desired formula:

$$r_\varepsilon(x) = |\omega_\varepsilon| \int_\Omega (\gamma_1(y) - \gamma_0(y)) \mathcal{M}(y) \nabla u_0(y) \cdot \nabla_y N(x, y) d\mu(y) + o(|\omega_\varepsilon|).$$

□

**Remark 4.1.12** The “improved”  $L^2$  estimate (4.1.24) about  $r_\varepsilon$  calls for comments. This conclusion follows from the so-called “Aubin-Nitsche” trick, a general duality argument arising in a situation where “simple” a priori estimates are known about the solution  $r_\varepsilon$  to an elliptic equation satisfying a “regularizing principle”, and “better” estimates are desired about a quantity depending on  $r_\varepsilon$  and not on its derivatives.

In the context of the previous proof, where we aim to estimate  $\|r_\varepsilon\|_{L^2(\Omega)}$ , let us write:

$$(4.1.30) \quad \begin{aligned} \int_\Omega r_\varepsilon^2 dx &= - \int_\Omega \gamma_\varepsilon \nabla p_\varepsilon \cdot \nabla r_\varepsilon dx \\ &= \int_{\omega_\varepsilon} (\gamma_1 - \gamma_0) \nabla u_0 \cdot \nabla p_\varepsilon dx, \end{aligned}$$

where  $p_\varepsilon$  is an adjoint state, defined as the unique solution in  $H_0^1(\Omega)$  to the variational problem:

$$(4.1.31) \quad \forall w \in H_0^1(\Omega), \quad \int_\Omega \gamma_\varepsilon \nabla p_\varepsilon \cdot \nabla w dx = - \int_\Omega r_\varepsilon w dx.$$

Note that  $p_\varepsilon$  is defined exactly so that the quantity of interest at the left-hand side of (4.1.30) can be expressed in a way which allows to exploit our knowledge about  $r_\varepsilon$ , via the variational problem (4.1.22); see again Section 1.3.3.6 for generalities about adjoint-based strategies.

Owing to standard Sobolev inclusions, the function  $r_\varepsilon$  can be bounded in  $L^q(\Omega)$ , for some real number  $q > 2$ :

$$\|r_\varepsilon\|_{L^q(\Omega)} \leq C \|r_\varepsilon\|_{H^1(\Omega)} \text{ for some constant } C > 0.$$

We now invoke Meyer’s theorem – which is a by-product of elliptic regularity, see [71] – to express that, up to decreasing the value of  $q > 2$ , the solution  $p_\varepsilon$  to (4.1.31), whose right-hand side is bounded in  $L^q(\Omega)$ , is actually bounded in  $W^{1,q}(\Omega)$ :

$$\|p_\varepsilon\|_{W^{1,q}(\Omega)} \leq C \|r_\varepsilon\|_{L^q(\Omega)} \leq C \|r_\varepsilon\|_{H^1(\Omega)}.$$

Hence, we obtain from (4.1.30) and Hölder’s inequality that

$$\begin{aligned} \|r_\varepsilon\|_{L^2(\Omega)}^2 &\leq C |\omega_\varepsilon|^{\frac{1}{p}} \|\nabla p_\varepsilon\|_{L^q(\Omega)^d} \\ &\leq C |\omega_\varepsilon|^{\frac{1}{p}} \|r_\varepsilon\|_{H^1(\Omega)} \\ &\leq C |\omega_\varepsilon|^{\frac{1}{2} + \frac{1}{p}}; \end{aligned}$$

since  $\frac{1}{p} + \frac{1}{q} = 1$ , one has  $p < 2$ , which proves (4.1.24). This method was introduced in [49, 284], see also [130]. Note that the general fact that the adjoint state is usually more regular than the direct state in optimal control problems was also used in [241, 240]. In the context of this section, the fact that the improved  $L^2$  estimate (4.1.24) hold, which in turn relies on the regularizing effect of the perturbed conductivity operator, can be somehow considered as an evidence of the fact that the perturbation  $\gamma_\varepsilon$  of  $\gamma_0$  is “small”.

The general asymptotic expansion of Theorem 4.1.11 can be made explicit when the nature of the inclusion set  $\omega_\varepsilon$  is known more explicitly. Notably,

- When  $\omega_\varepsilon$  is a diametrically small inhomogeneity of the form (4.1.17), the limiting measure  $\mu$  is a Dirac mass  $\delta_{x_0}$  at the point  $x_0$ ; the polarization tensor  $\mathcal{M}$  is constructed from the solution to an exterior problem, posed on the rescaled inclusion  $\omega$  and its complement  $\mathbb{R}^d \setminus \bar{\omega}$ . We refer to the next Section 4.1.5 for more precise expressions, and to [39, 113] for rigorous proofs; see also [38] in the context of the linear elasticity system and [40] in the context of the Maxwell’s equations.
- When  $\omega_\varepsilon$  is a thin inhomogeneity of the form (4.1.18), the limiting measure  $\mu$  is the integration measure on the limiting surface  $S$ ; for  $y \in S$ , the polarization tensor  $\mathcal{M}(y)$  is diagonal in a local orthonormal frame of  $\mathbb{R}^d$  made of a basis  $(\tau_1(y), \dots, \tau_{d-1}(y))$  of the tangent plane  $T_y S$  and the normal vector  $n(y)$ , see Sections 4.5 and 4.6 for more details, as well as the references [76, 214] and [75] in the context of linear elasticity.

- When  $\omega_\varepsilon$  is a three-dimensional tubular inhomogeneity of the form (4.1.19), the limiting measure  $\mu$  is the integration measure on the curve  $\sigma$ , and for  $y \in \sigma$ , the polarization tensor  $\mathcal{M}(y)$  is diagonal in an orthonormal frame made from a tangent vector  $\tau(y)$  to  $\sigma$  and a basis of the normal plane to the latter, see [Section 4.6](#) and the reference [74].

Such results are typically proved by either variational methods or by layer potential techniques, based on the integral representation formulas presented in [Sections 4.1.1](#) and [4.1.3](#).

**Remark 4.1.13** *Throughout this section, we have taken for granted that the “correct” notion of “smallness” for the sets  $\omega_\varepsilon$  is their Lebesgue measure – and this is indeed confirmed by the rigorous analysis. However, this fact is by no means a generality, as revealed by the conclusions of the article [85]. The latter deals with a 2d situation where the domain  $\Omega$  is made of two materials with different conductivities, occupying complementary regions separated by an interface  $\Gamma$  (so that the background coefficient  $\gamma_0$  is discontinuous across  $\Gamma$ ). The perturbed version (4.1.15) of the conductivity equation (4.1.13) is considered in the situation where  $\omega_\varepsilon$  is a diametrically small inclusion centered at a point  $x_0$  on  $\Gamma$  where the latter has an angle with aperture  $\alpha \in (0, \pi)$ . It is then shown that the first non-trivial term in the asymptotic expansion of  $u_\varepsilon$  is no longer of the order  $|\omega_\varepsilon|$ , but that its “smallness” also depends on the value of the angle  $\alpha$ .*

*In this next sections of this chapter, we shall see other versions of the problems (4.1.13) and (4.1.15) where different notions of “capacity” of the  $\omega_\varepsilon$  control the “smallness” of this set.*

#### 4.1.5. A model calculation of a low-volume asymptotic expansion, and return to topological derivatives

As we have mentioned in the previous section, the general structure of [Theorem 4.1.11](#) for the perturbed potential  $u_\varepsilon$  in the presence of inhomogeneities occurring in a “small” inclusion set  $\omega_\varepsilon$  can be made explicit under more specific assumptions about the nature of  $\omega_\varepsilon$ . In this section, we present a formal derivation of such formula in the context of diametrically small inhomogeneities. We also exemplify how the result can be used to calculate topological derivatives in an optimal design context, see [Section 1.3.4](#).

The results of this section were proved rigorously in [39, 113]. Here, we provide a simple argument adapted from [A9] which, although heuristic, allows to obtain the correct formula with a minimum amount of effort.

The physical situation is that sketched at the beginning of the previous [Section 4.1.4](#), where the considered inclusion set  $\omega_\varepsilon$  is diametrically small, of the form (4.1.17), and we set  $x_0 = 0$  for simplicity. The main result of interest reads as follows.

**Theorem 4.1.14** *The following expansion holds at any point  $x \in \Omega \setminus \{0\}$ :*

$$(4.1.32) \quad u_\varepsilon(x) = u_0(x) + \varepsilon^d u_1(x) + o(\varepsilon^d), \text{ where } u_1(x) := -\mathcal{M} \nabla u_0(0) \cdot \nabla_y N(x, 0).$$

In here, the polarization tensor  $\mathcal{M} = (\mathcal{M}_{ij})_{i,j=1,\dots,d}$  is defined by:

$$(4.1.33) \quad \forall \xi \in \mathbb{R}^d, \quad \mathcal{M}\xi = (\gamma_1(0) - \gamma_0(0)) \int_\omega (\xi + \nabla \phi_\xi(y)) \, dy,$$

where for any  $\xi \in \mathbb{R}^d$ ,  $\phi_\xi$  is the unique solution in  $W_0^{1,-1}(\mathbb{R}^d)$  to the exterior problem:

$$\begin{cases} -\Delta \phi_\xi = 0 & \text{in } \omega \cup (\mathbb{R}^d \setminus \bar{\omega}), \\ \gamma_0(0) \frac{\partial \phi_\xi^+}{\partial n} - \gamma_1(0) \frac{\partial \phi_\xi^-}{\partial n} = -(\gamma_0(0) - \gamma_1(0)) \xi \cdot n & \text{on } \partial\omega, \\ |\phi_\xi(y)| \rightarrow 0 & \text{when } y \rightarrow \infty. \end{cases}$$

*Hint of proof.* Let us define the error  $r_\varepsilon := \frac{1}{\varepsilon^d} (u_\varepsilon - u_0) \in H_0^1(\Omega)$ ; as in the proof of [Theorem 4.1.11](#), the latter can be characterized as the solution to two different variational problems:

$$(4.1.34) \quad \forall w \in H_0^1(\Omega), \quad \int_\Omega \gamma_0 \nabla r_\varepsilon \cdot \nabla w \, dx = -\frac{1}{\varepsilon^d} \int_{\omega_\varepsilon} (\gamma_1 - \gamma_0) \nabla u_\varepsilon \cdot \nabla w \, dx,$$

and also:

$$(4.1.35) \quad \forall w \in H_0^1(\Omega), \quad \int_\Omega \gamma_\varepsilon \nabla r_\varepsilon \cdot \nabla w \, dx = -\frac{1}{\varepsilon^d} \int_{\omega_\varepsilon} (\gamma_1 - \gamma_0) \nabla u_0 \cdot \nabla w \, dx.$$

Let us now consider a fixed point  $x \in \Omega \setminus \{0\}$ ; the derivation of the expansion (4.1.32) proceeds in three steps.

*Step 1: We represent  $r_\varepsilon(x)$  in terms of the values of  $r_\varepsilon$  inside  $\omega_\varepsilon$ .*

This task follows the beginning of the proof of [Theorem 4.1.11](#): introducing the Green's function  $y \mapsto N(x, y)$  for the background operator  $-\operatorname{div}(\gamma_0 \nabla \cdot)$  and using (4.1.34), we calculate:

$$\begin{aligned} r_\varepsilon(x) &= \int_{\Omega} \gamma_0(y) \nabla r_\varepsilon(y) \cdot \nabla_y N(x, y) \, dy \\ &= -\frac{1}{\varepsilon^d} \int_{\omega_\varepsilon} (\gamma_1 - \gamma_0)(y) \nabla u_\varepsilon(y) \cdot \nabla_y N(x, y) \, dy \\ &= -\frac{1}{\varepsilon^d} \int_{\omega_\varepsilon} (\gamma_1 - \gamma_0)(y) (\nabla u_0(y) + \varepsilon^d \nabla r_\varepsilon(y)) \cdot \nabla_y N(x, y) \, dy, \end{aligned}$$

where we have again “inserted”  $y \mapsto N(x, y)$  as test function in the variational problem (4.1.34) to pass from the first line to the second one. A change of variables now yields:

$$(4.1.36) \quad r_\varepsilon(x) = - \int_{\omega} (\gamma_1(\varepsilon z) - \gamma_0(\varepsilon z)) (\nabla u_0(\varepsilon z) + \nabla s_\varepsilon(z)) \cdot \nabla_y N(x, \varepsilon z) \, dz.$$

where we have set  $s_\varepsilon(z) := \varepsilon^{d-1} r_\varepsilon(\varepsilon z) \in H_0^1(\frac{1}{\varepsilon}\Omega)$ .

*Step 2: We glean information about the behavior of  $s_\varepsilon$  inside the rescaled inclusion  $\omega$ .*

To this end, we now rely on the characterization (4.1.35) of  $r_\varepsilon$  in terms of the perturbed operator: equivalently,  $r_\varepsilon$  is the unique solution to the minimization problem:

$$\min_{v \in H_0^1(\Omega)} \left( \frac{1}{2} \int_{\Omega} \gamma_\varepsilon |\nabla v|^2 \, dx + \frac{1}{\varepsilon^d} \int_{\omega_\varepsilon} (\gamma_1 - \gamma_0) \nabla u_0 \cdot \nabla v \, dx \right).$$

By a change of variables, it follows that  $s_\varepsilon$  is the unique solution to the rescaled problem (4.1.37)

$$\min_{w \in H_0^1(\frac{1}{\varepsilon}\Omega)} \frac{1}{\varepsilon^d} \left( \frac{1}{2} \int_{\frac{1}{\varepsilon}\Omega \setminus \bar{\omega}} \gamma_0(\varepsilon z) |\nabla w|^2 \, dz + \frac{1}{2} \int_{\omega} \gamma_1(\varepsilon z) |\nabla w|^2 \, dz + \int_{\omega} (\gamma_1(\varepsilon z) - \gamma_0(\varepsilon z)) \nabla u_0(\varepsilon z) \cdot \nabla w \, dz \right).$$

We now intuitively expect that  $s_\varepsilon$  will behave like

$$(4.1.38) \quad s_\varepsilon(z) \approx \hat{s}(z) \text{ as } \varepsilon \rightarrow 0,$$

where  $\hat{s}(z)$  is the minimizer of the following approximate minimization problem, obtained from (4.1.37) by dropping the common multiplicative factor  $\frac{1}{\varepsilon^d}$ , replacing the space  $H_0^1(\frac{1}{\varepsilon}\Omega)$  with  $W_0^{1,-1}(\mathbb{R}^d)$  and retaining only leading-order terms:

$$\min_{w \in W_0^{1,-1}(\mathbb{R}^d)} \left( \frac{1}{2} \int_{\mathbb{R}^d \setminus \omega} \gamma_0(0) |\nabla w|^2 \, dz + \frac{1}{2} \int_{\omega} \gamma_1(0) |\nabla w|^2 \, dz + \int_{\omega} (\gamma_1(0) - \gamma_0(0)) \nabla u_0(0) \cdot \nabla w \, dz \right).$$

Writing down the associated Euler-Lagrange equations, a simple calculations reveals that:

$$\hat{s}(z) = \sum_{i=1}^d \frac{\partial u_0}{\partial x_i}(0) \phi_{e_i}(z),$$

where the  $\phi_{e_i} \in W_0^{1,-1}(\mathbb{R}^d)$  are the functions defined in (4.1.35).

*Step 3: We pass to the limit in the representation formula (4.1.36).*

A straightforward use of the Lebesgue dominated convergence theorem together with (4.1.38) yields:

$$r_\varepsilon(x) \approx - \int_{\omega} (\gamma_1(0) - \gamma_0(0)) (\nabla u_0(0) + \nabla \hat{s}(z)) \cdot \nabla_y N(x, 0) \, dz,$$

which leads to the desired formula (4.1.32) after a simple calculation.  $\square$

Let us eventually appraise the connections between this result and the calculation of the topological derivative of a function of the domain (see [Section 1.3.4](#) about this notion). To this end, we cast the latter

question in the language of the present section: the domain  $\Omega$  now stands for the design variable of a shape and topology optimization problem, which we aim to optimize with respect to a shape functional of the form

$$\Omega \mapsto \int_{\Omega} j(u_0) \, dx, \text{ where } u_0 \text{ is the solution to (4.1.13),}$$

and  $j : \mathbb{R} \rightarrow \mathbb{R}$  is a smooth function, satisfying suitable growth conditions, see (Growth- $j$ ). To evaluate whether it is beneficial to nucleate a tiny hole  $\omega_\varepsilon$  of the form (4.1.17) inside  $\Omega$ , we consider the quantity:

$$J(\varepsilon) = \int_{\Omega} j(u_\varepsilon) \, dx.$$

The result of interest is the following.

**Proposition 4.1.15** *The following asymptotic expansion holds:*

$$(4.1.39) \quad J(\varepsilon) = J(0) + \varepsilon^d J'(0) + o(\varepsilon^d), \text{ where } J'(0) := \mathcal{M} \nabla u_0(x_0) \cdot \nabla p_0(x_0),$$

$\mathcal{M}$  is the polarization tensor defined in (4.1.33) and the adjoint state  $p_0$  is the unique solution in  $H_0^1(\Omega)$  to the following equation

$$\begin{cases} -\operatorname{div}(\gamma_0 \nabla p_0) = -j'(u_0) & \text{in } \Omega, \\ p_0 = 0 & \text{on } \partial\Omega. \end{cases}$$

*Sketch of proof.* For notational simplicity, we assume that  $x_0 = 0$ . At first, a simple use of Taylor's formula yields:

$$\frac{J(\varepsilon) - J(0)}{\varepsilon^d} = \frac{1}{\varepsilon^d} \int_{\Omega} (j(u_\varepsilon) - j(u_0)) \, dx = \frac{1}{\varepsilon^d} \int_{\Omega} \int_0^1 j'(u_0 + t(u_\varepsilon - u_0))(u_\varepsilon - u_0) \, dt \, dx.$$

Now using the result of the previous [Theorem 4.1.14](#) and passing to the limit under the integral sign, we obtain:

$$J'(0) = \lim_{\varepsilon \rightarrow 0} \frac{J(\varepsilon) - J(0)}{\varepsilon^d} = \int_{\Omega} j'(u_0(x)) u_1(x) \, dx, \text{ where } u_1(x) = -\mathcal{M} \nabla u_0(0) \cdot \nabla_y N(x, 0).$$

Note that the application of the dominated convergence theorem to rigorously justify this limit is not completely straightforward: the uniform integrability of the quotient  $\frac{u_\varepsilon - u_0}{\varepsilon^d}$  with respect to  $\varepsilon$  is required, which follows from another use of the “Aubin-Nitsche trick”, see [Remark 4.1.12](#) and the appendix in [A9] for a complete argument.

Thence, a simple calculation yields:

$$J'(0) = \mathcal{M} \nabla u_0(0) \cdot \nabla_y \left( - \int_{\Omega} j'(u_0(x)) N(x, y) \, dx \right) \Big|_{y=0}.$$

Using finally the symmetry of  $N(x, y)$  in its arguments and the integral representation formula of  $p_0$  in terms of this function (see [Proposition 4.1.4](#)), the last parenthesis in the above right-hand side equals  $p_0(y)$ , and so:

$$J'(0) = \mathcal{M} \nabla u_0(0) \cdot \nabla p_0(0),$$

as desired. □

The first non trivial term  $J'(0)$  in the expansion (4.1.39) can be understood as a topological derivative of the functional  $J$ , when the latter is seen as a function of the domain  $\Omega$ . However, contrary to the setting in [Section 1.3.4](#), the present version of topological derivative does not account for the nucleation of a hole inside  $\Omega$ , but for the replacement of the material conductivity  $\gamma_0$  by  $\gamma_1$  inside  $\omega_\varepsilon$ . As we have seen in [Section 1.2.1.3](#), when  $\gamma_1$  takes “very small” values,  $u_\varepsilon$  is a good approximation of the version of (4.1.15) where a “true” hole, bearing homogeneous Neumann boundary conditions is nucleated in place of  $\omega_\varepsilon$ ; however, the fact that the quantity  $J'(0)$  be close to the “true” topological derivative of  $J$ , as defined in [Section 1.3.4](#), is formal.

## 4.2 A PARADIGM TO UNDERSTAND SHAPE, TOPOLOGICAL AND DENSITY DERIVATIVES IN A UNIFIED FASHION

As reflected by the various numerical strategies described in [Section 1.4](#), shape and topology optimization algorithms featuring a clear, “black-and-white” representation of the shape usually rely on the information contained in shape or topological derivatives. However very different in essence, these indicators of sensitivity usually enjoy quite similar mathematical expressions, see for instance [\(4.2.4\)](#) and [\(4.2.6\)](#) below in the context of the two-phase conductivity equation. This puzzling observation suggests that both notions might actually be tightly connected.

One possible explanation was put forward in the article [\[112\]](#), where the topological derivative of a function of the domain is calculated as the limiting expression of the values of its shape derivative on the boundary of a vanishing hole around the considered point; we refer to the book [\[289\]](#) for a more systematic implementation of this idea.

The work reported in this section, which is based on the articles [\[A25, A6\]](#), offers another interpretation of this similarity between the shape and topological derivatives of a function of the domain, by relating them with the derivative of a density-based counterpart of the latter.

The main idea is presented in [Section 4.2.1](#) in the simple setting of the two-phase conductivity equation. These developments pave the way to a shape and topology optimization algorithm taking into account both types of sensitivity of the shape functionals at play, which is presented and illustrated in [Section 4.2.2](#). The last [Section 4.2.3](#) is devoted to the treatment of a particular function of the domain which does not fall into the general framework, namely, the total perimeter functional.

### 4.2.1. A consistent, density-based relaxation of a shape optimization problem

For simplicity, the exposition takes place in the setting of the two-phase conductivity equation introduced in [Section 1.2.1.2](#), but our developments hold in various other situations, and notably in that of the two-phase elasticity system.

Within a fixed, smooth and bounded hold-all domain  $D \subset \mathbb{R}^d$  ( $d = 2, 3$  in practice), a shape  $\Omega \Subset D$  accounts for two complementary phases  $\Omega_1 := \Omega$  and  $\Omega_0 := D \setminus \overline{\Omega}$  made of materials with constant conductivities  $\gamma_1, \gamma_0 > 0$ , respectively. The potential  $u_\Omega : D \rightarrow \mathbb{R}$  is set to 0 on a region  $\Gamma_D$  of  $\partial D$  and an electric current  $g \in L^2(\Gamma_N)$  is imposed on the complement  $\Gamma_N := \partial D \setminus \overline{\Gamma_D}$ . Introducing a volume source  $f \in L^2(D)$ ,  $u_\Omega$  is the unique solution in the space

$$H_{\Gamma_D}^1(D) := \{u \in H^1(D), u = 0 \text{ on } \Gamma_D\}$$

to the two-phase conductivity equation

$$(4.2.1) \quad \begin{cases} -\operatorname{div}(\gamma_\Omega \nabla u_\Omega) = f & \text{in } D, \\ u_\Omega = 0 & \text{on } \Gamma_D, \\ \gamma_\Omega \frac{\partial u_\Omega}{\partial n} = g & \text{on } \Gamma_N, \end{cases} \quad \text{where } \gamma_\Omega(x) = \begin{cases} \gamma_1 & \text{if } x \in \Omega_1, \\ \gamma_0 & \text{if } x \in \Omega_0. \end{cases}$$

Once again to keep the exposition simple, we consider the unconstrained minimization problem of a weighted sum of the compliance  $C(\Omega)$  and the volume  $\operatorname{Vol}(\Omega)$  of  $\Omega$ :

$$(4.2.2) \quad \min_{\Omega} \mathcal{L}(\Omega), \text{ where } \mathcal{L}(\Omega) = C(\Omega) + \ell \operatorname{Vol}(\Omega), \text{ and } C(\Omega) = \int_D \gamma_\Omega |\nabla u_\Omega|^2 \, dx.$$

As we have mentioned, the theoretical and numerical treatments of this problem usually elaborate on one or both of the following notions:

- The shape derivative  $\mathcal{L}'(\Omega)(\theta)$  appraises the sensitivity of  $\mathcal{L}(\Omega)$  to perturbations of  $\Omega$  of the form

$$(4.2.3) \quad \Omega_\theta := (\operatorname{Id} + \theta)(\Omega), \text{ where } \theta \in W^{1,\infty}(\mathbb{R}^d, \mathbb{R}^d) \text{ is a “small” vector field,}$$

i.e. the following expansion holds:

$$\mathcal{L}(\Omega_\theta) = \mathcal{L}(\Omega) + \mathcal{L}'(\Omega)(\theta) + o(\theta), \text{ where } \frac{o(\theta)}{\|\theta\|_{W^{1,\infty}(\mathbb{R}^d, \mathbb{R}^d)}} \xrightarrow{\theta \rightarrow 0} 0,$$

see [Section 1.3.3.1](#). In the present context,  $\mathcal{L}'(\Omega)(\theta)$  equals:

$$(4.2.4) \quad \mathcal{L}'(\Omega)(\theta) = \int_{\partial\Omega} g_\Omega^S \theta \cdot n \, ds, \text{ where for all } x \in \partial\Omega,$$

$$g_\Omega^S(x) := (\gamma_0 - \gamma_1) |\nabla_{\partial\Omega} u_\Omega|^2(x) - \left( \frac{1}{\gamma_0} - \frac{1}{\gamma_1} \right) \left| \gamma_\Omega \frac{\partial u_\Omega}{\partial n} \right|^2(x) + \ell,$$

and we recall from [Section 1.2.1.2](#) that the quantities  $u_\Omega$  and  $(\gamma_\Omega \frac{\partial u_\Omega}{\partial n})$  are continuous across  $\partial\Omega$ .

- The topological derivative  $g_\Omega^T : \Omega_0 \cup \Omega_1 \rightarrow \mathbb{R}$  evaluates the sensitivity of  $\mathcal{L}(\Omega)$  with respect to the nucleation or the addition of an infinitesimally small hole. This quantity is based on variations of  $\Omega$  of the form

$$(4.2.5) \quad \text{For } x \in \Omega_0 \cup \Omega_1 \text{ and } r > 0 \text{ “small enough”, } \Omega_{x,r} := \begin{cases} \Omega \setminus \overline{B(x,r)} & \text{if } x \in \Omega, \\ \Omega \cup B(x,r) & \text{if } x \in D \setminus \overline{\Omega}. \end{cases}$$

It is defined as the first non trivial term in the expansion of the mapping  $r \mapsto \mathcal{L}(\Omega_{x,r})$  around  $r = 0$ . In the present context, it is convenient to write the latter under the form:

$$\mathcal{L}(\Omega_{x,r}) = \mathcal{L}(\Omega) + |B(x,r)| s_\Omega(x) g_\Omega^T(x) + o(|B(x,r)|), \text{ where } s_\Omega(x) = \begin{cases} -1 & \text{if } x \in \Omega, \\ 1 & \text{otherwise.} \end{cases}$$

In the present situation,  $g_\Omega^T$  has the following expression:

$$(4.2.6) \quad g_\Omega^T(x) = \begin{cases} -(\gamma_1 - \gamma_0) k^0 |\nabla u_\Omega|^2(x) + \ell, & \text{if } x \in \Omega^0, \\ -(\gamma_1 - \gamma_0) k^1 |\nabla u_\Omega|^2(x) + \ell, & \text{if } x \in \Omega^1, \end{cases} \text{ and } \begin{cases} k^0 = \frac{2\gamma_0}{\gamma_0 + \gamma_1}, & k^1 = \frac{2\gamma_1}{\gamma_0 + \gamma_1} & \text{if } d = 2, \\ k^0 = \frac{3\gamma_0}{2\gamma_0 + \gamma_1}, & k^1 = \frac{3\gamma_1}{\gamma_0 + 2\gamma_1} & \text{if } d = 3. \end{cases}$$

The shape and topological derivatives  $g_\Omega^S : \partial\Omega \rightarrow \mathbb{R}$  and  $g_\Omega^T : D \setminus \partial\Omega \rightarrow \mathbb{R}$  are the building blocks of the necessary conditions for one shape  $\Omega \Subset D$  to be a local minimizer of [\(4.2.2\)](#) with respect to both types of variations [\(4.2.3\)](#) and [\(4.2.5\)](#). For this to happen, it must hold that:

$$\forall x \in D, \quad \begin{cases} g_\Omega^T(x) \geq 0 & \text{if } x \in \Omega_0, \\ g_\Omega^T(x) \leq 0 & \text{if } x \in \Omega_1, \\ g_\Omega^S(x) = 0 & \text{if } x \in \partial\Omega. \end{cases}$$

Let us now consider a density-based relaxation of the above setting, in the spirit of [Section 1.4.5](#). The shape  $\Omega \Subset D$  is replaced by a density function  $h \in L^\infty(D, [0, 1])$ , accounting for the characteristic function of the phase  $\Omega^1 = \Omega$  in the sense that

- $h(x) = 1$  when  $x \in D$  is in a “black” region, occupied only by the material with conductivity  $\gamma_1$ ;
- $h(x) = 0$  when  $x \in D$  is in a “white” region, occupied only by the material with conductivity  $\gamma_0$ ;
- $h(x) \in (0, 1)$  when  $x \in D$  is surrounded by a “grayscale” mixture of materials  $\gamma_1$  and  $\gamma_0$  in respective proportions  $h(x)$ ,  $(1 - h(x))$ .

The intermediate regions where  $h(x)$  lies in  $(0, 1)$  are endowed with physical properties by a material law, of the form:

$$\gamma_{h,\varepsilon} = \gamma_0 + (\gamma_1 - \gamma_0) \zeta(L_\varepsilon h).$$

Here,  $\zeta : \mathbb{R} \rightarrow \mathbb{R}$  is an interpolation profile, satisfying the natural assumptions

$$(4.2.7) \quad \zeta \in \mathcal{C}^\infty(\mathbb{R}), \quad -\delta \leq \zeta \leq 1 + \delta, \text{ and } \zeta(0) = 0, \quad \zeta(1) = 1, \text{ for some parameter } 0 < \delta < \min(\gamma_0, \gamma_1).$$

Following a common practice in engineering, whose mathematical fundations are explained in [\[90, 96\]](#), the conductivity  $\gamma_{h,\varepsilon}$  depends on  $h$  via a density filter  $L_\varepsilon : L^2(D) \rightarrow L^\infty(D)$ , see [Section 1.4.5](#). Intuitively,  $L_\varepsilon$  is a linear and continuous regularizing operator which is “closer and closer” to the identity mapping as  $\varepsilon \rightarrow 0$ . In our applications, this operator may be:

- A convolution operator  $L_\varepsilon^{\text{conv}}$ , defined for any  $h \in L^2(D)$  by:

$$\forall x \in D, \quad L_\varepsilon^{\text{conv}}(h)(x) = (\eta_\varepsilon * h)(x) = \int_{\mathbb{R}^d} \eta_\varepsilon(x - y) h(y) \, dy, \quad (h \text{ being extended by 0 outside } D),$$

constructed from a smooth convolution kernel

$$\eta_\varepsilon(y) = \frac{1}{\varepsilon^d} \eta\left(\frac{y}{\varepsilon}\right), \text{ where } \eta \in \mathcal{C}_c^\infty(\mathbb{R}^d) \text{ is radial, } 0 \leq \eta \leq 1 \text{ and } \int_{\mathbb{R}^d} \eta(y) \, dy = 1.$$

- An elliptic regularization operator  $L_\varepsilon^{\text{ell}}$ :

For all  $h \in L^2(D)$ ,  $L_\varepsilon^{\text{ell}}(h) = q_\varepsilon$ , where  $q_\varepsilon$  is the solution to  $\begin{cases} -\Delta q_\varepsilon + q_\varepsilon = h & \text{in } D, \\ \frac{\partial q_\varepsilon}{\partial n} = 0 & \text{on } \partial D, \end{cases}$

and belongs to  $H^2(D)$  on account of the elliptic regularity theory, see [Section 1.A.6](#).

With these definitions, the potential  $u_{h,\varepsilon}$  associated to a density  $h \in L^\infty(D, [0, 1])$  is the unique solution in  $H_{\Gamma_D}^1(D)$  to the following counterpart of [\(4.2.1\)](#):

$$\begin{cases} -\operatorname{div}(\gamma_{h,\varepsilon} \nabla u_{h,\varepsilon}) = f & \text{in } \Omega, \\ u_{h,\varepsilon} = 0 & \text{on } \Gamma_D, \\ \gamma_{h,\varepsilon} \frac{\partial u_{h,\varepsilon}}{\partial n} = g & \text{on } \Gamma_N. \end{cases}$$

Accordingly, the density-based relaxation of the optimal design problem [\(4.2.2\)](#) reads:

$$(4.2.8) \quad \min_{h \in L^\infty(D, [0, 1])} \mathcal{L}_\varepsilon(h), \text{ where } \mathcal{L}_\varepsilon(h) = C_\varepsilon(h) + \ell \operatorname{Vol}_\varepsilon(h), \text{ and } \begin{cases} C_\varepsilon(h) := \int_D \gamma_{h,\varepsilon} |\nabla u_{h,\varepsilon}|^2 \, dx, \\ \operatorname{Vol}_\varepsilon(h) := \int_D L_\varepsilon h \, dx. \end{cases}$$

The derivative  $\mathcal{L}'_\varepsilon(h)(\hat{h})$  of the functional  $\mathcal{L}_\varepsilon(h)$ , characterized by the expansion

$$\forall \hat{h} \in L^\infty(D), \quad \mathcal{L}_\varepsilon(h + \hat{h}) = \mathcal{L}_\varepsilon(h) + \mathcal{L}'_\varepsilon(h)(\hat{h}) + o(\hat{h}),$$

can be calculated thanks to the adjoint method presented in [Section 1.3.3.6](#); it reads:

$$(4.2.9) \quad \forall \hat{h} \in L^\infty(D), \quad \mathcal{L}'_\varepsilon(h)(\hat{h}) = \int_D g_{h,\varepsilon} \hat{h} \, dx, \text{ where } g_{h,\varepsilon} = -(\gamma_1 - \gamma_0) L_\varepsilon \left( \zeta'(L_\varepsilon h) |\nabla u_{h,\varepsilon}|^2 \right) + L_\varepsilon 1.$$

With the help of this derivative, the necessary conditions for a density function  $h \in L^\infty(D, [0, 1])$  to be optimal in view of [\(4.2.8\)](#) read as follows:

- $\{g_{h,\varepsilon} > 0\} \subset \{h = 0\} \subset \{g_{h,\varepsilon} \geq 0\}$ ,
- $\{g_{h,\varepsilon} < 0\} \subset \{h = 1\} \subset \{g_{h,\varepsilon} \leq 0\}$ ,
- $\{0 < h < 1\} \subset \{g_{h,\varepsilon} = 0\}$ ,

where the above inclusions hold up to subsets of  $D$  of null Lebesgue measure.

The main result of this study is the following theorem, whose rather technical and unintuitive proof is omitted.

**Theorem 4.2.1** *Let  $h = \mathbf{1}_\Omega$  be the characteristic function of a smooth domain  $\Omega \Subset D$ . Then the function  $g_{h,\varepsilon}$  in [\(4.2.9\)](#) satisfies:*

$$g_{h,\varepsilon} \xrightarrow{\varepsilon \rightarrow 0} g_\Omega^S \text{ in } L^1(\partial\Omega).$$

Furthermore, if the interpolation profile  $\zeta$  in [\(4.2.7\)](#) satisfies the additional conditions

$$\zeta'(0) = k_0, \quad \zeta'(1) = k_1, \text{ where } k_0 \text{ and } k_1 \text{ are defined in } (4.2.6),$$

then it holds

$$g_{h,\varepsilon} \xrightarrow{\varepsilon \rightarrow 0} g_\Omega^T \text{ in } L^p(\Omega_0 \cup \Omega_1), \text{ for } 1 \leq p < \infty.$$

This theorem makes the connection between [\(4.2.2\)](#) and [\(4.2.8\)](#) by expressing the latter density-based topology optimization problem as a consistent relaxation of the former, shape and topology optimization problem: the shape and topological derivatives attached to the function  $\mathcal{L}(\Omega)$  are limits of the density-based derivative  $g_{h,\varepsilon}$  of  $\mathcal{L}_\varepsilon(h)$  at  $h = \mathbf{1}_\Omega$ , when the smoothing parameter  $\varepsilon$  of the density filter  $L_\varepsilon$  tends to 0.

### 4.2.2. A shape and topology optimization algorithm and numerical example

The material of the previous Section 4.2.1 paves the way to an elegant numerical strategy for optimizing a function of the domain with respect to both shape and topological sensitivities at the same time.

The proposed algorithm is based on a similar rationale as the fixed-point topology optimization algorithm of Section 1.4.8.2: we have seen in Section 4.2.1 that if the characteristic function  $h = \mathbf{1}_\Omega$  of a shape  $\Omega \Subset D$  is a local minimizer of the density-based counterpart (4.2.8) – a notion which leaves the room for a very large gammut of variations –, it must hold:

$$\forall x \in D, \quad \begin{cases} g_{\Omega, \varepsilon} \leq 0 & \text{if } x \in \Omega, \\ g_{\Omega, \varepsilon} \geq 0 & \text{if } x \in D \setminus \overline{\Omega}, \end{cases} \quad \text{with the shorthand } g_{\Omega, \varepsilon} := g_{\mathbf{1}_\Omega, \varepsilon}.$$

A slightly stronger version of these requirements reads:

$$g_{\Omega, \varepsilon} = \phi, \quad \text{where } \phi \text{ is a level set function for } \Omega, \text{ i.e. } \begin{cases} \phi(x) < 0 & \text{if } x \in \Omega, \\ \phi(x) = 0 & \text{if } x \in \partial\Omega, \\ \phi(x) > 0 & \text{if } x \in D \setminus \overline{\Omega}. \end{cases}$$

In turn, for this to hold, it is enough that

$$\frac{1}{\|g_{\Omega, \varepsilon}\|_{L^2(D)}} g_{\Omega, \varepsilon} = \phi, \quad \text{where } \phi \text{ is a level set function for } \Omega \text{ s.t. } \|\phi\|_{L^2(D)} = 1.$$

We impose this condition by a fixed point algorithm with relaxation, thanks to the spherical linear interpolation procedure described in Section 1.A.5. The values of the various iteration-dependent quantities at any stage  $n = 0, \dots$  are denoted with a superscript  $n$ : the evolving shape is  $\Omega^n$ , an associated level set function is  $\phi^n$ , the derivative of the objective is  $g^n := g_{\Omega^n, \varepsilon}$ , and we let  $\tilde{g}^n := \frac{1}{\|g^n\|_{L^2(D)}} g^n$ . This leads to the following formula for the update of  $\phi$ :

$$\phi^{n+1} = \frac{1}{\sin a^n} \left( \sin((1 - \tau^n)a^n) \phi^n + \sin(\tau^n a^n) \tilde{g}^n \right),$$

where  $a^n \in [0, \pi]$  is the angle  $a^n = \arccos((\phi^n, \tilde{g}^n)_{L^2(D)})$  and  $\tau^n \in (0, 1)$  is a time step.

Let us illustrate this strategy with a 2d numerical example in the physical setting of mechanical structures presented in Section 1.2.3. We consider the optimal design of a gripping mechanism, whose specifications are displayed on Fig. 4.2.1 (a). The shape is contained in a domain  $D$  with size  $1 \times 1$  and it is fixed at the middle of its left- and right-hand sides. A vertical load  $g_1 = (0, \pm 10)$  is applied on a region  $\Gamma_{N,1}$  near its upper and lower right corners, and another load  $g_2 = (0, \pm 1)$  concentrated on another region  $\Gamma_{N,2}$  near the jaws mimicks the reaction of an object pressed by the mechanism. We consider the optimization problem

$$\min_{\Omega} \mathcal{L}(\Omega), \quad \text{where } \mathcal{L}(\Omega) = \int_{\Gamma_N} k(x) \cdot u_{\Omega} \, ds + \ell \text{Vol}(\Omega),$$

$\Gamma_N := \Gamma_{N,1} \cup \Gamma_{N,2}$  and  $u_{\Omega}$  is the elastic displacement of  $\Omega$ , solution to (Elas). The weight  $k(x) \in \mathbb{R}^2$  is chosen so that the minimization of this functional encourage the shape to maximize its vertical displacement on  $\Gamma_{N,2}$ , while minimizing it near  $\Gamma_{N,1}$ .

### 4.2.3. A density-based counterpart to the perimeter functional

The relaxation framework of Section 4.2.1 can handle various physical situations and multiple functionals of the domain. However, despite its seemingly simple formulation, the perimeter functional is one unfortunate exception to this flexibility. The ubiquity of the notion of perimeter in shape optimization, be it in theory (where it helps to ensure existence of optimal shapes, see Section 1.3.2 and [27]) or in numerical practice (where it imposes a desirable “smoothing” of shapes, blurring their sharp features) has motivated the device of suitable generalizations of this functional in the realm of density functions.

Before proceeding, we should be a little more precise about the terminology “perimeter”. All our discussions take place within a fixed, bounded hold-all domain  $D \subset \mathbb{R}^d$ , and two distinct versions of this

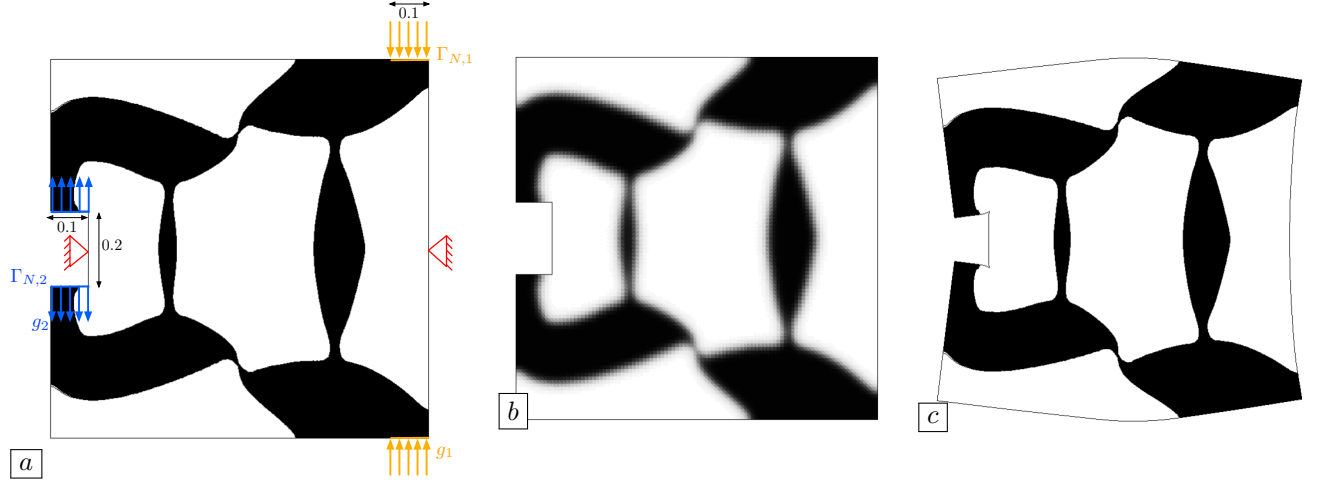


FIGURE 4.2.1. Optimization of the design of a gripping mechanism by using the level set topology optimization algorithm of [Section 4.2.2](#); (a) Optimized shape  $\Omega$  (with details of the test case); (b) Corresponding smoothed characteristic function  $L_\varepsilon 1_\Omega$ ; (c) Deformed configuration.

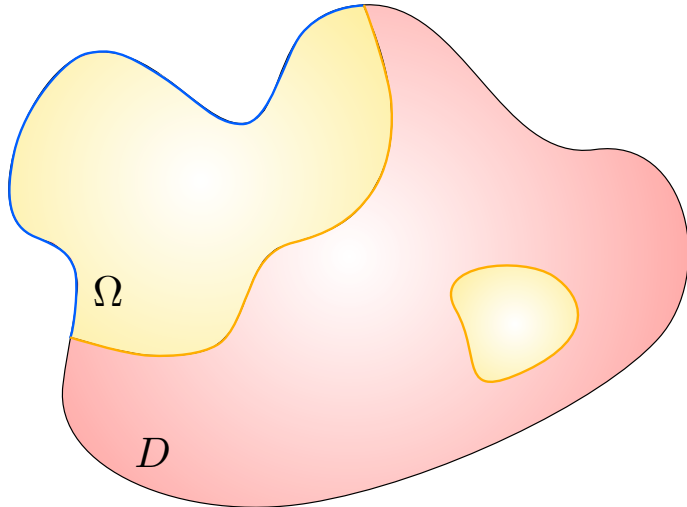


FIGURE 4.2.2. Difference between the relative and total perimeters of a shape  $\Omega$  with respect to a bounding box  $D$ ; the relative perimeter corresponds to the orange regions of  $\partial\Omega$ , while the total perimeter additionally takes into account the blue region of  $\partial\Omega$  lying on  $\partial D$ .

functional are available: the relative perimeter  $\text{Per}^R(\Omega)$  and the total perimeter  $\text{Per}^T(\Omega)$  of a Lipschitz domain  $\Omega \subset D$  are respectively defined by:

$$\text{Per}^R(\Omega) = \int_{\partial\Omega \cap D} ds, \text{ and } \text{Per}^T(\Omega) = \int_{\partial(\Omega \cap D)} ds,$$

that is,  $\text{Per}^R(\Omega)$  only measures the portion of  $\partial\Omega$  which is strictly inside  $D$ , while  $\text{Per}^T(\Omega)$  additionally takes into account the region  $\partial\Omega \cap \partial D$ , see [Fig. 4.2.2](#).

A great deal of the existing literature about density-based versions of the perimeter functional is concerned with its relative version. One natural way to define the relative perimeter of more general objects than (characteristic functions of) Lipschitz domains  $\Omega \subset D$  hinges on the framework of functions with bounded

variations,  $h \in BV(D, [0, 1])$ , which is briefly recalled in [Section 4.A](#). Indeed, one sets:

$$\forall h \in BV(D, [0, 1]), \quad \text{Per}^R(h) := \int_D |Dh|,$$

where  $|Dh|$  is the total variation of  $h$ , a positive measure on  $D$ , capturing its smooth variations and abrupt jumps. This functional is unfortunately difficult to calculate numerically; moreover, since its dependence on the density function  $h$  is not smooth, its management by numerical optimization algorithms is non trivial.

One idea to cope with these difficulties consists in regularizing this quantity; the perhaps most famous result in this direction features the so-called Cahn-Hilliard energy functional  $F_\varepsilon(h) : L^1(D) \rightarrow \mathbb{R}$ , defined by:

$$F_\varepsilon(h) = \begin{cases} \int_D \left( \varepsilon |\nabla h|^2 + \frac{1}{\varepsilon} W(h) \right) dx & \text{if } h \in H^1(D), \\ +\infty & \text{otherwise,} \end{cases}$$

where  $W : \mathbb{R} \rightarrow \mathbb{R}$  is a double well potential, achieving two global minima at 0 and 1. Grossly speaking, to minimize  $F_\varepsilon(h)$ , a function  $h$  has to find a compromise between showing “not too sharp variations” (so that the first term do not take too large values), while taking mostly values 0 or 1 (in an effort to minimize the second term). The emphasis on the latter requirement is more and more stringent as  $\varepsilon \rightarrow 0$ , while the “smoothness” requirement is loosened.

The quality of the approximation of  $\text{Per}^R(h)$  by  $F_\varepsilon(h)$  as  $\varepsilon \rightarrow 0$  is usually appraised in terms of the notion of  $\Gamma$ -convergence. The latter is briefly recalled in [Section 4.B](#); intuitively, it evaluates the convergence of the minimum points of a sequence of functionals. It was proved in [\[267, 268\]](#) that  $F_\varepsilon(h)$   $\Gamma$ -converges to the function  $F : L^1(D) \rightarrow \mathbb{R}$  defined by:

$$F(h) = \begin{cases} c_W \text{Per}^R(h) & \text{if } h \in BV(D, \{0, 1\}), \\ +\infty & \text{otherwise,} \end{cases}$$

where  $c_W$  is a constant depending only on the potential  $W$ . This celebrated result has been used in a wide variety of settings, for instance to construct approximations of the popular Mumford-Shah functional in image segmentation and mechanics, see [\[57\]](#) for an overview. It leads notably to the Ambrosio-Tortorelli approximation [\[30\]](#), which is the basic ingredient of variational models for fracture [\[91\]](#), and it is also a popular tool in the simulation of the mean curvature flow.

The functional  $F_\varepsilon(h)$  is still not that easy to handle from the numerical viewpoint. It indeed depends on the gradient of the function  $h$ , which is quite undesirable as it prohibits the use of characteristic functions as for  $h$ . For this reason also, the gradient flow of this functional – the so-called Allen-Cahn equation – involves the second-order derivatives of  $h$ , which calls for sophisticated computational algorithms.

To alleviate these issues, among others, it was proposed in [\[46\]](#) (see also [\[13, 264\]](#)) to consider the functional  $P_\varepsilon^R$  defined on  $L^1(D)$  by:

$$P_\varepsilon^R(h) = \begin{cases} \frac{1}{\varepsilon} \int_D \left( 1 - L_\varepsilon^{\text{Neu}} h \right) h dx & \text{if } h \in L^\infty(D, [0, 1]), \\ +\infty & \text{otherwise,} \end{cases}$$

where  $L_\varepsilon^{\text{Neu}} h$  is the solution  $q_\varepsilon$  to  $\begin{cases} -\varepsilon^2 \Delta q_\varepsilon + q_\varepsilon = h & \text{in } D, \\ \frac{\partial q_\varepsilon}{\partial n} = 0 & \text{on } \partial D. \end{cases}$

Loosely speaking,  $L_\varepsilon^{\text{Neu}} h$  is a smeared version of  $h$  and  $\varepsilon$  plays the role of a regularizing length-scale: when  $h$  is the characteristic function of a smooth shape  $\Omega \subset D$ , the function  $L_\varepsilon^{\text{Neu}} h$  presents a smooth transition between the values 1 and 0 over a band with thickness  $2\varepsilon$  around  $\partial\Omega$ ; the integrand in the above definition of  $P_\varepsilon^R(h)$  is then a measure of the “size” of this band, see [Fig. 4.2.3](#).

This intuition is confirmed by the analysis: it is proved in [\[46\]](#) that  $P_\varepsilon^R(h)$   $\Gamma$ -converges to the function defined by:

$$\forall h \in L^\infty(D, [0, 1]), \quad \begin{cases} \frac{1}{2} \text{Per}^R(h) & \text{if } h \in BV(D, \{0, 1\}), \\ +\infty & \text{otherwise.} \end{cases}$$

The aforementioned results concern the density-based relaxation of the relative perimeter functional  $\text{Per}^R(\Omega)$ . In the article [\[46\]](#), we have worked towards deriving a similar approximation for the total perimeter

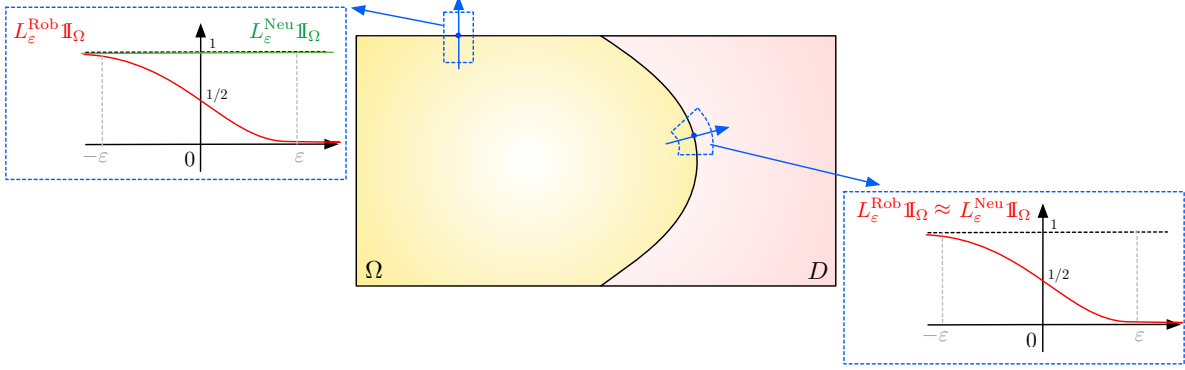


FIGURE 4.2.3. The regularized characteristic functions  $L_\varepsilon^{\text{Neu}} \mathbb{1}_\Omega$  and  $L_\varepsilon^{\text{Rob}} \mathbb{1}_\Omega$  have a similar behavior near the part  $D \cap \partial\Omega$  of  $\partial\Omega$  which is “well-inside”  $D$ , but they differ significantly near  $\partial D$ .

functional  $\text{Per}^T(\Omega)$ . It turns out that this version of the perimeter is rarely used in numerical practice; often, its relative counterpart is tacitly used, as in the practice of the level set method for shape optimization. This is actually quite surprising, since in a fair number of applications, the total perimeter appears more natural than its relative counterpart: the boundary of the “hold-all” domain  $D$  has to be taken into account in the evaluation of the perimeter of the shape  $\Omega$  when it has a “physical meaning”. This is the case, for instance, in situations involving contact mechanics, where at least one part of  $\partial D$  is in contact with an external device; see [168] about this physical setting and [256] for examples of related shape optimization problems.

The total perimeter functional can be defined for an arbitrary density function by the formula:

$$\forall h \in BV(D, [0, 1]), \quad \text{Per}^T(h) = \int_{\mathbb{R}^d} |D\tilde{h}|, \text{ where } \tilde{h} \text{ is the extension of } h \text{ to } \mathbb{R}^d \text{ by } 0.$$

Like in the case of the relative perimeter functional mentioned above, it is desirable to construct a “smooth”, approximate version of this functional which does not bring into play the gradient of  $h$ .

A careful analysis reveals that a suitable counterpart of  $P_\varepsilon^R$  in the perspective of approximating the total perimeter is the functional  $P_\varepsilon^T : L^1(D) \rightarrow \mathbb{R}$  defined by:

$$(4.2.10) \quad P_\varepsilon^T(h) = \begin{cases} \frac{1}{\varepsilon} \int_D (1 - L_\varepsilon^{\text{Rob}} h) h \, dx & \text{if } h \in L^\infty(D, [0, 1]), \\ +\infty & \text{otherwise,} \end{cases}$$

where  $L_\varepsilon^{\text{Rob}} h$  is the solution  $q_\varepsilon$  to  $\begin{cases} -\varepsilon^2 \Delta q_\varepsilon + q_\varepsilon = h & \text{in } D, \\ \varepsilon \frac{\partial q_\varepsilon}{\partial n} + q_\varepsilon = 0 & \text{on } \partial D. \end{cases}$

Intuitively, the function  $L_\varepsilon^{\text{Rob}} h$  behaves in the same way as that  $L_\varepsilon^{\text{Neu}} h$  used in the construction of the functional  $P_\varepsilon^R(h)$ , except near the boundary  $\partial D$ , where the Robin boundary condition imposes a behavior that allows to “see” this portion of the boundary, see Fig. 4.2.3.

More precisely, the main result of this study is the following, whose quite technical proof, relying on notions of geometric measure theory, is omitted for simplicity.

**Theorem 4.2.2** *The following assertions hold true:*

(i) *The functional sequence  $P_\varepsilon^T : L^1(D) \rightarrow \mathbb{R}$   $\Gamma$ -converges to the functional defined by:*

$$\forall h \in L^\infty(D, [0, 1]), \quad \begin{cases} \frac{1}{2} \text{Per}^T(h) & \text{if } h \in BV(D, \{0, 1\}), \\ +\infty & \text{otherwise.} \end{cases}$$

(ii) *The functional sequence  $P_\varepsilon^T : L^1(D) \rightarrow \mathbb{R}$  is equi-coercive, see [Definition 4.B.3](#) about this notion.*

**Remark 4.2.3** As in the previous Section 4.2.1, it is possible to propose a similar formula to (4.2.10) for the total perimeter function  $P_\varepsilon^T(h)$  using a convolution-based regularization operator in place of  $L_\varepsilon^{Rob}$ , but the latter does not have so neat mathematical properties, in terms of  $\Gamma$  convergence notably.

From the numerical viewpoint, the functional  $P_\varepsilon^T(h)$  is easily incorporated into a density-based topology optimization algorithm, such as that presented in the previous Section 4.2.1. As an illustration, we consider a numerical example in the physical configuration of the benchmark 2d cantilever test case, see Fig. 4.2.4. The computational domain  $D$  is a rectangle with size  $2 \times 1$  and the clamping region of shapes  $\Gamma_D$  is the left-hand side of  $\partial D$ . A unit vertical load  $g = (0, -1)$  is applied on a region  $\Gamma_N$  around the middle of the right-hand side of  $\partial D$ . In this setting, we solve the problem

$$(4.2.11) \quad \min_{h \in L^\infty(D, [0,1])} \mathcal{L}(h) \text{ s.t. } \text{Vol}(h) = V_T, \text{ where } \mathcal{L}(h) = C(h) + \ell P_\varepsilon(h),$$

$C(h)$  is the relaxed version of the compliance functional introduced in Section 4.2.1, and  $P_\varepsilon(h)$  stands for the relaxed relative perimeter or the relaxed total perimeter  $P_\varepsilon^R(h)$  or  $P_\varepsilon^T(h)$ , depending on the situation.

The volume target is set to  $V_T = 0.4\text{Vol}(D)$  and the initial design  $\Omega^0$  is the solution to a standard compliance minimization problem under the volume constraint  $\text{Vol}(\Omega) = V_T$  (corresponding to the version of (4.2.11) without perimeter penalization). We solve both instances of (4.2.11) featuring the approximate relative and total perimeter functionals.

The results are displayed in Fig. 4.2.4. In both cases, the small features of the initial design are removed in the course of the process. Both optimized designs admittedly look similar, except for the fact that the shape  $\Omega$  obtained by using the total perimeter functional presents more natural, “straight” members near the junction with the boundary of the computational domain  $D$ . This expected effect shows that it is actually more natural to rely on the total version of the perimeter functional in such a context, so as to ensure that the boundary  $\partial D$  is “counted” as a part of the boundary of shapes, and that the region  $\partial\Omega \cap \partial D$  is optimized as such.

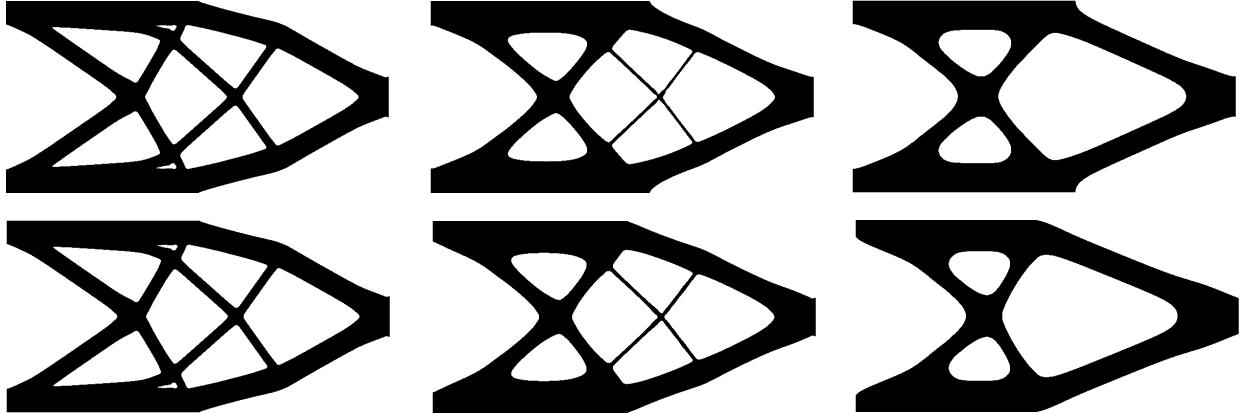


FIGURE 4.2.4. (From left to right) Several iterations in the solution of the minimization problem (4.2.11) when (Upper row) The relative perimeter functional is used; (lower row) The total perimeter functional is used.

### 4.3 OPTIMIZATION OF THE SHAPE OF REGIONS SUPPORTING BOUNDARY CONDITIONS

In most concrete shape and topology optimization problems, the physical environment of the shape  $\Omega$  is described by the solution to a boundary value problem featuring various types of boundary conditions, borne by different regions of  $\partial\Omega$ . Often, only one of these regions is subject to optimization, the others being imposed by the context. However, there are situations where, besides the shape  $\Omega$ , it is interesting to optimize the repartition of these regions within  $\partial\Omega$ . Here are a few examples:

- In thermal mechanics,  $u_\Omega$  is the temperature inside a cavity  $\Omega$ , and it is the solution to the stationary heat equation – an avatar of the conductivity equation (Cond) of [Section 1.2.1.1](#). A measured temperature profile is observed on the regions of  $\partial\Omega$  equipped with Dirichlet boundary conditions, while Neumann boundary conditions account for heat fluxes. In this context, it may then be desirable to optimize the regions of  $\partial\Omega$  kept at fixed temperature, or those where heat is injected into  $\Omega$ , in view of minimizing the mean temperature inside  $\Omega$ .
- In the setting of [Section 1.2.2.4](#) where  $\Omega$  is a mechanical structure, homogeneous Dirichlet boundary conditions account for the regions of  $\partial\Omega$  where the shape is fixed, while inhomogeneous (resp. homogeneous) Neumann boundary conditions model the regions of  $\partial\Omega$  where external loads are applied (resp. traction-free regions). Some problems posed in this physical context raise the need to optimize the design of fixations or the region where loads are applied, see [310] and [Section 4.3.6](#) below about such investigations.
- In acoustics, the sound pressure  $u_\Omega$  within a room  $\Omega$  is the solution to the time-harmonic Helmholtz equation. In this situation, one may wish to optimize the repartition of an absorbing material (whose effect is modeled by Robin-like boundary conditions) on the walls of  $\partial\Omega$  in order to minimize the sound intensity [158].

The calculation of the sensitivity of a performance criterion with respect to variations of these regions bearing boundary conditions is unfortunately far from trivial. The main reason for this fact is the typical lack of regularity of the state function  $u_\Omega$  in the optimized transition zones where boundary conditions change types, see [Remark 1.A.14](#).

The work reported in this section is described in full detail in the journal article [A13]. For the sake of simplicity, the presentation is based on the simple setting of the conductivity equation, where the analysis of a model optimization problem of the regions supporting boundary conditions can be conducted without too much technicality. Most of the conclusions of this study and of the numerical method derived from them can be adapted to various more challenging contexts, including the setting of elastic shapes. After introducing this simple model setting in [Section 4.3.1](#), we catch a glimpse of the regularity theory for solutions to elliptic boundary value problems featuring mixed boundary conditions in [Section 4.3.2](#), as it has a strong impact on the mathematical properties of the considered shape and topology optimization problems. In [Sections 4.3.3](#) to [4.3.5](#), we discuss the calculation of derivatives with respect to the shape of the interfaces between inhomogeneous Neumann - homogeneous Neumann and homogeneous Dirichlet - homogeneous Neumann boundary conditions, respectively. Two numerical examples are eventually proposed in [Section 4.3.6](#).

### 4.3.1. A model problem in the conductivity setting

As in [Section 1.2.1](#), the shape  $\Omega$  is a smooth bounded domain in  $\mathbb{R}^d$  ( $d = 2, 3$ ), filled with a material whose smooth conductivity  $\gamma \in \mathcal{C}^\infty(\overline{\Omega})$  is bounded away from 0 and  $\infty$ , see (Ell-Cond). Its boundary  $\partial\Omega$  is divided into three smooth, disjoint regions

$$\partial\Omega = \overline{\Gamma_D} \cup \overline{\Gamma} \cup \overline{\Gamma_N} \text{ such that } \overline{\Gamma_D} \cap \overline{\Gamma_N} = \emptyset,$$

where homogeneous Dirichlet, homogeneous Neumann and inhomogeneous Neumann boundary conditions  $g \in \mathcal{C}^\infty(\overline{\Gamma_N})$  are imposed, respectively. We denote by  $\Sigma_D := \partial\Gamma_D$  (resp.  $\Sigma_N := \partial\Gamma_N$ ) the contour marking the transition between homogeneous Dirichlet and homogeneous Neumann (resp. between homogeneous Neumann and inhomogeneous Neumann) boundary conditions, and by  $n_{\Sigma_D} : \Sigma_D \rightarrow \mathbb{R}^d$  (resp.  $n_{\Sigma_N} : \Sigma_N \rightarrow \mathbb{R}^d$ ) the corresponding unit normal vector which is parallel to  $\partial\Omega$ , and points outward  $\Gamma_D$  (resp.  $\Gamma_N$ ), see [Fig. 4.3.1](#) (a). Introducing a source  $f \in \mathcal{C}^\infty(\overline{\Omega})$ , the potential  $u_\Omega \in H_{\Gamma_D}^1(\Omega)$  inside  $\Omega$  is the unique solution to the boundary value problem:

$$(4.3.1) \quad \left\{ \begin{array}{ll} -\operatorname{div}(\gamma \nabla u_\Omega) = f & \text{in } \Omega, \\ u_\Omega = 0 & \text{on } \Gamma_D, \\ \gamma \frac{\partial u_\Omega}{\partial n} = g & \text{on } \Gamma_N, \\ \gamma \frac{\partial u_\Omega}{\partial n} = 0 & \text{on } \Gamma. \end{array} \right.$$

Here and throughout this study, the slightly abusive notation  $u_\Omega$  mentions only the dependence of this function on the domain  $\Omega$ , but one should bear in mind that it also depends on the repartition of the regions  $\Gamma_N$ ,  $\Gamma_D$ ,  $\Gamma$  within  $\partial\Omega$ .

In this setting, we aim to calculate the derivative of a model function of the domain  $\Omega$  (and of the repartition of  $\Gamma_D$ ,  $\Gamma_N$  and  $\Gamma$  within  $\partial\Omega$ ) of the form

$$(4.3.2) \quad J(\Omega) = \int_{\Omega} j(u_{\Omega}) \, dx,$$

where  $j : \mathbb{R} \rightarrow \mathbb{R}$  is a smooth function satisfying adequate growth conditions, see (Growth- $j$ ). To this end, we rely on the boundary variation method of Hadamard, featuring variations of  $\Omega$  of the form

$\Omega_\theta = (\text{Id} + \theta)(\Omega)$ , where  $\theta$  is a “small” vector field in a subset  $\Theta_{\text{ad}}$  of  $\mathcal{C}^{2,\infty}(\mathbb{R}^d, \mathbb{R}^d)$ ,

see [Section 1.3.3](#). As opposed to “classical” shape and topology optimization settings, such as that introduced in [Section 1.2.3](#), the regions  $\Gamma_D$  and  $\Gamma_N$  are not necessarily fixed, which leaves the room for deformations  $\theta$  that may not vanish on  $\overline{\Gamma_D}$  or  $\overline{\Gamma_N}$ . In the next sections, we shall consider two different situations, corresponding to the following choices as for the set  $\Theta_{\text{ad}}$  of admissible deformations:

- When it comes to optimizing the region  $\Gamma_D$  within  $\partial\Omega$  (and  $\Gamma_N$  is kept fixed), we leave the room for  $\theta$  to alter the “homogeneous Dirichlet–homogeneous Neumann” boundary  $\Sigma_D$  between  $\Gamma_D$  and  $\Gamma_N$ :

$\Theta_{\text{ad}} = \Theta_{\text{DN}}$ , where  $\Theta_{\text{DN}} := \left\{ \theta \in \mathcal{C}^{2,\infty}(\mathbb{R}^d, \mathbb{R}^d), \theta = 0 \text{ on } \overline{\Gamma_N} \right\}$ .

- When optimizing  $\Gamma_N$  (and  $\Gamma_D$  is kept fixed), the deformations  $\theta$  may alter the “homogeneous Neumann – inhomogeneous Neumann” boundary  $\Sigma_N$  between  $\Gamma_N$  and  $\Gamma$ :

$\Theta_{\text{ad}} = \Theta_{\text{NN}}$ , where  $\Theta_{\text{NN}} := \left\{ \theta \in \mathcal{C}^{2,\infty}(\mathbb{R}^d, \mathbb{R}^d), \theta = 0 \text{ on } \overline{\Gamma_D} \right\}$ .

As we shall see, the analysis of the former situation involves a few technicalities, and sometimes, our exposition will be simplified by relying on the following assumption, which is illustrated on Fig. 4.3.1 (b). (4.3.3)

The dimension  $d$  equals 2, the conductivity  $\gamma$  is constant,

and

the boundary  $\partial\Omega$  is flat around  $s_0$  and  $s_1$ .

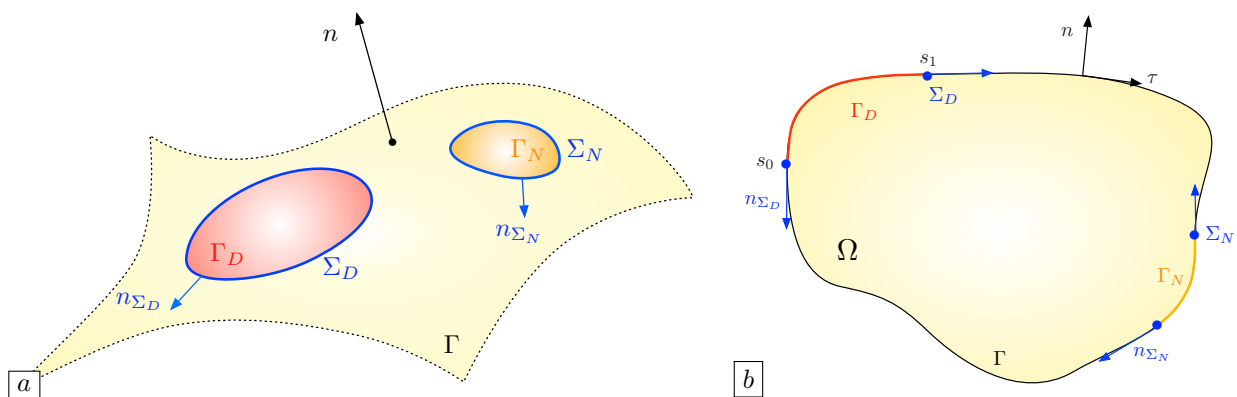


FIGURE 4.3.1. (a) Sketch of the considered setting in Section 4.3.1; (b) The simplified situation where Assumption (4.3.3) is fulfilled.

### 4.3.2. A brief account of the regularity of $u_\Omega$

As we have hinted at, one of the main difficulties posed by the differentiability of the functional  $J(\Omega)$  in (4.3.2) and by shape optimization problems involving this sensitivity, is the lack of regularity of the state function  $u_\Omega$  near the regions  $\Sigma_D$  and  $\Sigma_N$ .

The classical Lax-Milgram theory for (4.3.1) naturally yields a solution  $u_\Omega$  in the space  $H^1(\Omega)$ . Moreover, since the boundary  $\partial\Omega$  is smooth and  $\gamma, f \in \mathcal{C}^\infty(\overline{\Omega})$  and  $g \in \mathcal{C}^\infty(\overline{\Gamma_N})$  are smooth functions, the “classical” elliptic regularity theory ensures that  $u_\Omega$  has at least  $H^2$  regularity except near the transitions zones  $\Sigma_D$  and  $\Sigma_N$ , see Section 1.A.6.

The description of the “weakly singular” behavior of  $u_\Omega$  in the latter regions is a difficult mathematical subject, about which we refer for instance to the books [150, 196, 218]. To set ideas, let us quote the following result from [196] (see Chap. 4 and notably Th. 4.4.3.7) about the behavior of  $u_\Omega$  near  $\Sigma_D$ , which takes place under Assumption (4.3.3).

**Proposition 4.3.1** *Let (4.3.3) be satisfied; for any point  $x_0 \in \overline{\Omega} \setminus (\Sigma_D \cup \Sigma_N)$ , there exists an open neighborhood  $W$  of  $x_0$  in  $\mathbb{R}^2$  such that  $u_\Omega$  belongs to  $H^2(\Omega \cap W)$ .*

*On the other hand, for  $i = 0$  or  $i = 1$ , there exists an open neighborhood  $V$  of  $s_i$  with the following property. Denoting by  $(r, \nu)$  the polar coordinates at  $s_i$  and assuming without loss of generality that*

$$s_i = 0, \quad \Omega \cap V = \{x \in V, \text{ s.t. } x_2 > 0\}, \quad \text{and} \quad \Gamma_D \cap V = \{x \in V, \text{ s.t. } x_2 = 0, x_1 < 0\},$$

*there exist a function  $u_r^i \in H^2(V)$ , and a constant  $c^i \in \mathbb{R}$  such that:*

$$(4.3.4) \quad u_\Omega = u_r^i + c^i S^i \text{ on } V, \quad \text{where } S^i(r, \nu) = r^{\frac{1}{2}} \cos\left(\frac{\nu}{2}\right).$$

The function  $S^i$  in (4.3.4) belongs to  $H^1(V)$ , but not to  $H^2(V)$ , and it is sometimes called “weakly singular”. More precisely, invoking Theorem 1.4.5.3 in [196] to estimate the Sobolev regularity of functions of the form  $r^\alpha \varphi(\nu)$ , one proves that  $u_\Omega$  belongs to all the spaces  $H^s(V)$  with  $0 \leq s < \frac{3}{2}$  and that:

$$\|u_\Omega\|_{H^s(V)} \leq C_s \|f\|_{L^2(\Omega)},$$

for a constant  $C_s$  depending on  $s$ .

**Remark 4.3.2** *Higher-order versions of the expansion (4.3.4) are available. Actually, for any integer  $m \geq 2$ , if  $f \in H^{m-2}(\mathbb{R}^d)$ , the following decomposition holds in a neighborhood  $V$  of  $s_i$  (see [196], Th. 5.1.3.5):*

$$u_\Omega = u_{r,m}^i + \sum_{k=1}^{m-1} c_k^i S_k^i, \quad \text{where } u_{r,m}^i \in H^m(V) \text{ and } S_k^i(r, \nu) = r^{k-\frac{1}{2}} \cos\left(\left(k - \frac{1}{2}\right)\nu\right).$$

**Remark 4.3.3** *When  $d = 2$ , an expansion of  $u_\Omega$  of the form (4.3.4) is generally available at those points  $s_i \in \Sigma_D$  marking the transition between homogeneous Dirichlet and homogeneous Neumann boundary conditions, even when the boundary  $\partial\Omega$  is not flat in the vicinity of  $\Sigma_D$ . The weakly singular function  $S^i$  shows the same dependence  $r^{\frac{1}{2}}$  with respect to  $r$ , but its dependence with respect to  $\nu$  is no longer explicit. The function  $u_\Omega$  stills belongs to  $H^s(V)$  with an estimate of the form Section 4.3.2, where  $V$  is an open neighborhood of  $\Sigma_D$  in  $\Omega$  and  $0 \leq s < \frac{3}{2}$  is arbitrary; see Chap. 5 in [196] or [136].*

### 4.3.3. Calculation of the shape derivative of $J(\Omega)$ when $\Sigma_N$ is optimized

In this section, we calculate the derivative of the model shape functional  $J(\Omega)$  in (4.3.2) in the framework of the method of Hadamard by using vector fields  $\theta \in \Theta_{\text{NN}}$  which leave the room for deformations of the interface  $\Sigma_N$  between the inhomogeneous Neumann - homogeneous Neumann regions.

The main result in this context is the following.

**Proposition 4.3.4** Let  $\Omega$  be a shape as in [Section 4.3.1](#); the function  $J(\Omega)$  defined by [\(4.3.2\)](#) is shape differentiable at  $\Omega$  when deformations are considered in  $\Theta_{\text{NN}}$ . Its shape derivative reads (volume form):

$$(4.3.5) \quad \forall \theta \in \Theta_{\text{NN}}, \quad J'(\Omega)(\theta) = \int_{\partial\Omega} (j(u_\Omega) - fp_\Omega) \theta \cdot n \, ds - \int_{\Omega} j'(u_\Omega) \nabla u_\Omega \cdot \theta \, dx \\ + \int_{\Omega} (\nabla \gamma \cdot \theta) \nabla u_\Omega \cdot \nabla p_\Omega \, dx + \int_{\Omega} \gamma (\operatorname{div} \theta \mathbf{I} - \nabla \theta - \nabla \theta^T) \nabla u_\Omega \cdot \nabla p_\Omega \, dx \\ + \int_{\Omega} f \nabla p_\Omega \cdot \theta \, dx - \int_{\Gamma_N} ((\operatorname{div}_{\partial\Omega} \theta) g + \nabla g \cdot \theta) p_\Omega \, ds,$$

where  $\operatorname{div}_{\partial\Omega}$  stands for the tangential divergence on  $\partial\Omega$  (see [Section 1.A.1](#)), and the adjoint state  $p_\Omega$  is the unique solution in  $H_{\Gamma_D}^1(\Omega)$  to the equation:

$$(4.3.6) \quad \begin{cases} -\operatorname{div}(\gamma \nabla p_\Omega) = -j'(u_\Omega) & \text{in } \Omega, \\ p_\Omega = 0 & \text{on } \Gamma_D, \\ \gamma \frac{\partial p_\Omega}{\partial n} = 0 & \text{on } \Gamma_N \cup \Gamma. \end{cases}$$

The shape derivative  $J'(\Omega)(\theta)$  has the equivalent, surface expression:

$$(4.3.7) \quad \forall \theta \in \Theta_{\text{NN}}, \quad J'(\Omega)(\theta) = \int_{\Gamma \cup \Gamma_N} j(u_\Omega) \theta \cdot n \, ds + \int_{\Gamma \cup \Gamma_N} \gamma \nabla u_\Omega \cdot \nabla p_\Omega \theta \cdot n \, ds - \int_{\Gamma \cup \Gamma_N} f p_\Omega \theta \cdot n \, ds \\ - \int_{\Gamma_N} \left( \frac{\partial g}{\partial n} + \kappa g \right) p_\Omega \theta \cdot n \, ds - \int_{\Sigma_N} g p_\Omega \theta \cdot n_{\Sigma_N} \, d\ell,$$

where the mean curvature  $\kappa$  of  $\partial\Omega$  is defined in [Section 1.A.1](#) and  $d\ell$  is the restriction to  $\Sigma_N$  of the  $(d-2)$ -dimensional Hausdorff measure.

*Hint of proof.:* The calculation of the volume form [\(4.3.5\)](#) of  $J'(\Omega)(\theta)$  follows exactly the general trail exemplified in [Section 1.3.3.5](#), which does not require the solution  $u_\Omega$  to [\(4.3.1\)](#) to have better regularity than that  $H^1$  predicted by the Lax-Milgram theory.

The derivation of the surface form [\(4.3.7\)](#) follows from integration by parts as in [Section 1.3.3.5](#); these operations can be conducted as in there, but they demand slightly more careful justifications, due to the limited regularity of  $u_\Omega$  near  $\Sigma_N$ , see the next [Remark 4.3.5](#).  $\square$

**Remark 4.3.5** The precise mathematical meaning of [\(4.3.7\)](#), and notably that of the term

$$(4.3.8) \quad \int_{\Gamma \cup \Gamma_N} \gamma \nabla u_\Omega \cdot \nabla p_\Omega \theta \cdot n \, ds$$

featured in there is not completely straightforward. The function  $u_\Omega$  belongs to the space

$$(4.3.9) \quad E(\operatorname{div}(\gamma \nabla \cdot), L^2(\Omega)) := \{u \in H^1(\Omega), \operatorname{div}(\gamma \nabla u) \in L^2(\Omega)\},$$

and as such, it has a normal trace  $\gamma \frac{\partial u_\Omega}{\partial n} \in H^{-1/2}(\partial\Omega)$ , which is defined via the Green's formula:

$$(4.3.10) \quad \forall w \in H^1(\Omega), \quad \int_{\partial\Omega} \gamma \frac{\partial u_\Omega}{\partial n} w \, ds := \int_{\Omega} \operatorname{div}(\gamma \nabla u_\Omega) w \, dx + \int_{\Omega} \gamma \nabla u_\Omega \cdot \nabla w \, dx;$$

see [\[196\]](#), Th. 1.5.3.10 for more details about this point. Also, since  $u_\Omega \in H^{1/2}(\partial\Omega)$ , the tangential gradient  $\nabla_{\partial\Omega} u_\Omega$  naturally belongs to the dual space  $H^{-1/2}(\partial\Omega)^{d-1}$ . On the other hand, the function  $p_\Omega$  in [\(4.3.6\)](#) enjoys  $H^2$  regularity except in the neighborhood of  $\Sigma_D$  where it has a weak singularity of the form [\(4.3.4\)](#). Since deformations  $\theta \in \Theta_{\text{NN}}$  are smooth and vanish identically on  $\Gamma_D$ , the product  $(\nabla p_\Omega) \theta \cdot n$  has a trace in  $H^{1/2}(\partial\Omega)$ , and so the integral [\(4.3.8\)](#) is well-defined as a duality product between functions in  $H^{-1/2}(\partial\Omega)$  and  $H^{1/2}(\partial\Omega)$ .

#### 4.3.4. Calculation of the shape derivative of $J(\Omega)$ when $\Sigma_D$ is optimized

In this section, we investigate the shape differentiability of the functional  $J(\Omega)$  defined in (4.3.2) when the boundary  $\Sigma_D$  between the regions  $\Gamma_D$  and  $\Gamma$  bearing homogeneous Dirichlet and homogeneous Neumann boundary conditions is also subject to optimization, i.e. we suppose that  $\Theta_{\text{ad}} = \Theta_{\text{DN}}$ .

The difficulty of the present situation lies in the weakly singular behavior of the solution  $u_\Omega$  to (4.3.1) near  $\Sigma_D$ . In particular, this behavior has a major influence on the structure of the shape derivative of  $J(\Omega)$ , as stated by the next proposition, whose conclusion was already observed in [52, 181].

**Proposition 4.3.6** *Let  $\Omega$  be a shape as in Section 4.3.1; the functional  $J(\Omega)$  is shape differentiable at  $\Omega$  and its shape derivative reads (volume form):*

$$(4.3.11) \quad \forall \theta \in \Theta_{\text{DN}}, \quad J'(\Omega)(\theta) = \int_{\partial\Omega} (j(u_\Omega) - fp_\Omega) \theta \cdot n \, ds - \int_{\Omega} j'(u_\Omega) \nabla u_\Omega \cdot \theta \, dx \\ + \int_{\Omega} (\nabla \gamma \cdot \theta) \nabla u_\Omega \cdot \nabla p_\Omega \, dx + \int_{\Omega} \gamma((\text{div} \theta) \mathbf{I} - \nabla \theta - \nabla \theta^T) \nabla u_\Omega \cdot \nabla p_\Omega \, dx + \int_{\Omega} f \nabla p_\Omega \cdot \theta \, dx,$$

where the adjoint state  $p_\Omega$  is the unique solution in  $H_{\Gamma_D}^1(\Omega)$  to the boundary value problem:

$$(4.3.12) \quad \begin{cases} -\text{div}(\gamma \nabla p_\Omega) = -j'(u_\Omega) & \text{in } \Omega, \\ p_\Omega = 0 & \text{on } \Gamma_D, \\ \frac{\partial p_\Omega}{\partial n} = 0 & \text{on } \Gamma_N \cup \Gamma. \end{cases}$$

Moreover, under Assumption (4.3.3), let us write the local structure of  $u_\Omega$  and  $p_\Omega$  in an open neighborhood  $V^i$  of  $s_i$ ,  $i = 0, 1$  as follows:

$$(4.3.13) \quad u_\Omega = u_s^i + u_r^i \text{ and } p_\Omega = p_s^i + p_r^i;$$

in the above formula,  $u_r^i, p_r^i$  belong to  $H^2(V^i)$  and the weakly singular functions  $u_s^i$  and  $p_s^i \in H^1(V^i)$  have the following expressions in local polar coordinates centered at  $s_i$ :

$$(4.3.14) \quad u_s^i(r, \nu) = c_u^i r^{\frac{1}{2}} \cos\left(\frac{\nu}{2}\right), \text{ and } p_s^i(r, \nu) = c_p^i r^{\frac{1}{2}} \cos\left(\frac{\nu}{2}\right), \text{ if } n_{\Sigma_D}(s_i) = e_1,$$

or

$$(4.3.15) \quad u_s^i(r, \nu) = c_u^i r^{\frac{1}{2}} \sin\left(\frac{\nu}{2}\right), \text{ and } p_s^i(r, \nu) = c_p^i r^{\frac{1}{2}} \sin\left(\frac{\nu}{2}\right), \text{ if } n_{\Sigma_D}(s_i) = -e_1.$$

Then (4.3.11) rewrites (surface form):

$$(4.3.16) \quad J'(\Omega)(\theta) = \int_{\Gamma_D \cup \Gamma} (j(u_\Omega) - fp_\Omega) \theta \cdot n \, ds - \int_{\Gamma_D} \gamma \frac{\partial p_\Omega}{\partial n} \frac{\partial u_\Omega}{\partial n} \theta \cdot n \, ds + \int_{\Gamma} \gamma \frac{\partial u_\Omega}{\partial \tau} \frac{\partial p_\Omega}{\partial \tau} \theta \cdot n \, ds \\ + \frac{\pi}{4} \sum_{i=0,1} c_u^i c_p^i (\theta \cdot n_{\Sigma_D})(s_i).$$

*Hint of proof.* Again, the volume form (4.3.11) of  $J'(\Omega)(\theta)$  follows from the general strategy for calculating shape derivatives, see Section 1.3.3.5. As in there, we expect the surface formula (4.3.16) to result from integration by parts in the integrals of (4.3.11) containing derivatives of  $\theta$ , which is not straightforward because of the limited regularity of  $u_\Omega$  and  $p_\Omega$ , see Section 4.3.2. To overcome this obstruction, we use an approximation argument: for a fixed deformation  $\theta \in \Theta_{\text{ad}}$ , the Lebesgue dominated convergence theorem implies that:

$$J'(\Omega)(\theta) = \lim_{\varepsilon \rightarrow 0} I_\varepsilon, \text{ where } I_\varepsilon := \int_{\partial\Omega} (j(u_\Omega) - fp_\Omega) \theta \cdot n \, ds - \int_{\Omega} j'(u_\Omega) \nabla u_\Omega \cdot \theta \, dx \\ + \int_{\Omega} (\nabla \gamma \cdot \theta) \nabla u_\Omega \cdot \nabla p_\Omega \, dx + \int_{\Omega \setminus (\overline{B(s_0, \varepsilon)} \cup \overline{B(s_1, \varepsilon)})} \gamma((\text{div} \theta) \mathbf{I} - \nabla \theta - \nabla \theta^T) \nabla u_\Omega \cdot \nabla p_\Omega \, dx + \int_{\Omega} f \nabla p_\Omega \cdot \theta \, dx$$

is obtained from the formula (4.3.11) for  $J'(\Omega)(\theta)$  by cutting a small half-ball  $\Omega \cap B(s_i, \varepsilon)$  around each point  $s_i$ ,  $i = 0, 1$  in the domain of the integral

$$\int_{\Omega} \gamma((\operatorname{div} \theta) \mathbf{I} - \nabla \theta - \nabla \theta^T) \nabla u_{\Omega} \cdot \nabla p_{\Omega} \, dx$$

where we intend to integrate by parts.

Since  $u_{\Omega}$  and  $p_{\Omega}$  enjoy at least  $H^2$  regularity on  $\Omega \setminus (\overline{B(s_0, \varepsilon)} \cup \overline{B(s_1, \varepsilon)})$ , integration by parts can be conducted as needed in the expression of  $I_{\varepsilon}$ . The surface integrals on the half-circles  $\Omega \cap \partial B(s_i, \varepsilon)$  resulting from this operation can be calculated explicitly, as well as their limit as  $\varepsilon \rightarrow 0$ , from the local behavior (4.3.13) to (4.3.15) of  $u_{\Omega}$  and  $p_{\Omega}$  near the points  $s_i$ .  $\square$

**Remark 4.3.7** *In the surface formula (4.3.16), the integrals*

$$-\int_{\Gamma_D} \gamma \frac{\partial p_{\Omega}}{\partial n} \frac{\partial u_{\Omega}}{\partial n} \theta \cdot n \, ds + \int_{\Gamma} \gamma \frac{\partial u_{\Omega}}{\partial \tau} \frac{\partial p_{\Omega}}{\partial \tau} \theta \cdot n \, ds$$

*are not well-defined individually, since they may blow up around the points  $s_i$ , judging from the structure (4.3.14) and (4.3.15) of the singular parts of  $u_{\Omega}$  and  $p_{\Omega}$ . However, these integrals have compensating singularities at  $s_i$ , so that their sum is well-defined as a Cauchy principal value.*

#### 4.3.5. An approximate shape derivative in the Dirichlet-Neumann case

The surface formula (4.3.16) for the shape derivative  $J'(\Omega)(\theta)$  in the setting where  $\Sigma_D$  is optimized is unfortunately delicate to handle. From the theoretical viewpoint, it involves the precise knowledge of the weakly singular behaviors (4.3.14) and (4.3.15) of  $u_{\Omega}$  and  $p_{\Omega}$  near  $\Sigma_D$ , which is only available in few situations beyond the present one of the 2d conductivity equation. From the numerical viewpoint, the calculation of these weakly singular behaviors requires advanced numerical strategies, based e.g. on an enrichment of the finite element basis with the singular functions featured in (4.3.14) and (4.3.15), or adapted p/hp mesh refinement methods, see [55, 170, 234] and the references therein.

To cope with these difficulties, we rely on an approximation method inspired from [20, 158], which does not require the expression of these singular behaviors and can be generalized to a wide variety of physical situations. The latter is based on the following approximate counterpart to  $J(\Omega)$ :

$$(4.3.17) \quad J_{\varepsilon}(\Omega) = \int_{\Omega} j(u_{\Omega, \varepsilon}) \, dx,$$

where the solution  $u_{\Omega}$  to the problem (4.3.1) showing a sharp transition between Dirichlet and Neumann boundary conditions is replaced with that  $u_{\Omega, \varepsilon}$  to a boundary value problem involving a Robin boundary condition on  $\Gamma_D \cup \Gamma$ :

$$(4.3.18) \quad \begin{cases} -\operatorname{div}(\gamma \nabla u_{\Omega, \varepsilon}) = f & \text{in } \Omega, \\ \gamma \frac{\partial u_{\Omega, \varepsilon}}{\partial n} + h_{\varepsilon} u_{\Omega, \varepsilon} = 0 & \text{on } \Gamma_D \cup \Gamma, \\ \gamma \frac{\partial u_{\Omega, \varepsilon}}{\partial n} = g & \text{on } \Gamma_N. \end{cases}$$

Here, the coefficient  $h_{\varepsilon}$  is defined by:

$$(4.3.19) \quad \forall x \in \partial \Omega, \quad h_{\varepsilon}(x) = \frac{1}{\varepsilon} h \left( \frac{d_{\Gamma_D}^{\partial \Omega}(x)}{\varepsilon} \right),$$

where  $h : \mathbb{R} \rightarrow \mathbb{R}$  is a smooth function with the properties:

$$0 \leq h \leq 1, \quad h \equiv 1 \text{ on } (-\infty, -1], \quad h(0) > 0, \quad h \equiv 0 \text{ on } [1, \infty).$$

The function  $d_{\Gamma_D}^{\partial \Omega}(x)$  in (4.3.19) is the (geodesic) signed distance to  $\Gamma_D$  on the surface  $\partial \Omega$ :

$$d_{\Gamma_D}^{\partial \Omega}(x) = \begin{cases} -d^{\partial \Omega}(x, \Sigma_D) & \text{if } x \in \Gamma_D, \\ 0 & \text{if } x \in \Sigma_D, \\ d^{\partial \Omega}(x, \Sigma_D) & \text{if } x \in \partial \Omega \setminus \overline{\Gamma_D}, \end{cases}$$

where  $d^{\partial \Omega}(x, \Sigma_D) = \inf_{p \in \Sigma_D} d^{\partial \Omega}(x, p)$  is the shortest geodesic distance between  $x$  and a point on  $\Sigma_D$ , see Remark 3.1.12.

With this definition,  $h_\varepsilon$  takes the “large” value  $\frac{1}{\varepsilon}$  inside  $\Gamma_D$ , “far” from  $\Sigma_D$  (and so the Robin boundary condition in (4.3.18) emulates a homogeneous Dirichlet boundary condition) and 0 on  $\Gamma$  “far” from  $\Sigma_D$  (i.e. homogeneous Neumann boundary conditions are satisfied), and it shows a smooth transition between these two values in a tubular neighborhood of  $\Sigma_D$  with (geodesic) width  $2\varepsilon$ . As a result,  $u_{\Omega,\varepsilon}$  satisfies approximately the boundary conditions in (4.3.1), see Fig. 4.3.2.

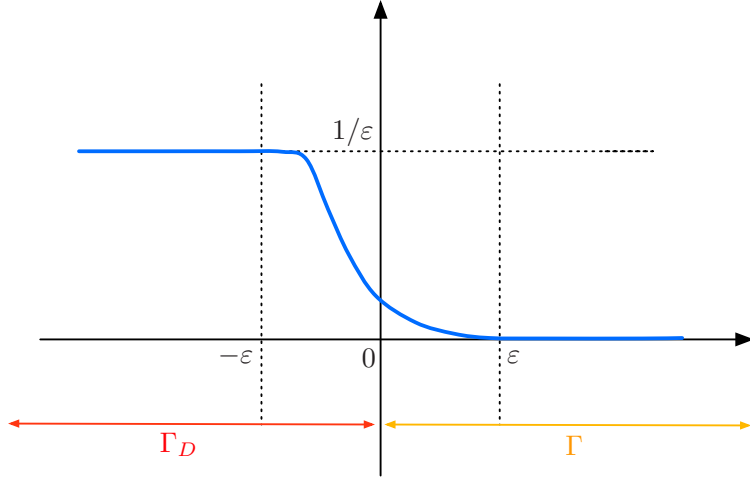


FIGURE 4.3.2. Graph of the function  $h_\varepsilon$  defined by (4.3.19).

It follows from the standard Lax-Milgram theory that the boundary value problem (4.3.18) is well-posed. In addition, elementary verifications allow to adapt the material about the signed distance function recalled in Section 3.1 to the present surface context: in particular,  $d_{\Gamma_D}^{\partial\Omega}$  is smooth on a sufficiently small open neighborhood of  $\Gamma_D$  in  $\partial\Omega$ . Since  $\Omega$  and  $h$  are smooth, for a fixed value of  $\varepsilon > 0$ ,  $u_{\Omega,\varepsilon}$  actually enjoys  $H^2$  regularity on a neighborhood of  $\Sigma_D$ , as a consequence of the “classical” elliptic regularity theory, see again Section 1.A.6.

The shape functional  $J_\varepsilon(\Omega)$  in (4.3.17) resulting from this approximation can be proved to be shape differentiable, and its shape derivative can be calculated following the classical method exposed in Section 1.3.3.5, after a simple, albeit lengthy calculation, which is omitted for brevity.

This approximation process is justified by the following result, whose quite technical proof is also omitted.

**Theorem 4.3.8** *Let  $\Omega \subset \mathbb{R}^2$  be a shape satisfying Assumption (4.3.3); then*

- *The function  $u_{\Omega,\varepsilon}$  converges to  $u_\Omega$  strongly in  $H^1(\Omega)$ , and the following estimate holds:*

$$\|u_{\Omega,\varepsilon} - u_\Omega\|_{H^1(\Omega)} \leq C_s \varepsilon^s \|f\|_{L^2(\Omega)},$$

*for any  $0 < s < \frac{1}{4}$ , where the constant  $C_s$  depends on  $s$ .*

- *The approximate shape derivative  $J'_\varepsilon(\Omega)$  converges to its exact counterpart  $J'(\Omega)$  in the sense that:*

$$\sup_{\substack{\theta \in \Theta_{\text{DN}}, \\ \|\theta\|_{\Theta_{\text{DN}}} \leq 1}} |J'_\varepsilon(\Omega)(\theta) - J'(\Omega)(\theta)| = 0.$$

#### 4.3.6. Two numerical examples

In this section, we present two numerical illustrations of the previous developments. These examples leverage the level set method when it comes to optimizing the regions  $\Gamma_D$  and  $\Gamma_N$  bearing the homogeneous Dirichlet or inhomogeneous Neumann boundary conditions of a boundary value problem within the meshed boundary of the total domain  $\Omega$ , along the lines of Section 1.4.6.2. In both examples,  $\Gamma_D$  and  $\Gamma_N$  are optimized within a flat portion of  $\partial\Omega$ ; this technical limitation is due to the fact that, at the time this study was conducted, the

numerical ingredients involved in the practice of the level set method (see [Section 1.4.6.1](#)) were not available in the situation where the ambient medium is a curved surface, see [Section 4.7.2](#) for the presentation of a perspective for future research related to the tracking of the evolution of a region within a surface by an avatar of the level set based mesh evolution method of [Section 1.4.7](#).

#### 4.3.6.1. Optimization of the clamping – locator system of a mechanical part

In this first example, we apply the ideas of [Sections 4.3.3](#) and [4.3.5](#) to the optimization of the clamping – locator fixture system of a mechanical structure  $\Omega$ . This type of device is widely used during the fabrication of a part in order to guarantee its precise positioning when large efforts are applied by the machine tool. In a nutshell, the fixed shape  $\Omega$  is attached on one region of its boundary thanks to a “locator”, so that its displacement is forbidden in there; a load is applied on a disjoint, “clamped” region of  $\partial\Omega$  so as to hold  $\Omega$  against the locator. Clamps and locators are both expensive devices: it is desirable to minimize the measure of the regions of  $\partial\Omega$  where they operate, while still guaranteeing an efficient fixture of the part during its construction. The optimal design of such systems was investigated for instance in [\[213, 249, 330, 369, 370, 378\]](#) by different mathematical and numerical techniques.

Let us consider the 3d situation depicted on [Fig. 4.3.3](#). The mechanical part of interest is a box  $\Omega$  in  $\mathbb{R}^3$  with size  $4 \times 1 \times 1$ . During its fabrication, a vertical load  $g_{\text{tool}} = (0, 0, -1)$  is exerted on  $\Omega$  by the machine tool on its upper side  $\Gamma_T$ . To withstand the latter,  $\Omega$  is attached on a region  $\Gamma_D$  of its left-hand side, and a load  $g = (0, -1, 0)$  is applied on a region  $\Gamma_N$  of its right-hand side. The displacement  $u_\Omega$  of  $\Omega$  in this situation is the solution to the linear elasticity system, see [\(Elas\)](#).

Adapting the theoretical findings of [Sections 4.3.3](#) and [4.3.5](#) to the present context, we optimize both regions  $\Gamma_D$ ,  $\Gamma_N$  within the fixed boundary  $\partial\Omega$ , so as to minimize the displacement of  $\Omega$  during this construction setting, under constraints on the measures of  $\Gamma_D$  and  $\Gamma_N$ :

$$(4.3.20) \quad \min_{\Omega} J(\Omega), \text{ where } J(\Omega) = \int_{\Omega} |u_\Omega|^2 \, dx + \ell_D \int_{\Gamma_D} \, ds + \ell_N \int_{\Gamma_N} \, ds + \ell_L \int_{\Sigma_D} \, d\ell,$$

and  $\ell_D$ ,  $\ell_N$  and  $\ell_L$  are suitable penalization parameters. Let us recall the abuse of notation whereby only the dependences of the shape functional  $J(\Omega)$  and the elastic displacement  $u_\Omega$  with respect to the shape  $\Omega$  are mentioned in formulations such as [\(4.3.20\)](#), but these quantities also depend on the repartition of the regions  $\Gamma_D$  and  $\Gamma_N$  within  $\partial\Omega$ .

The results of this experiment are depicted on [Fig. 4.3.4](#).

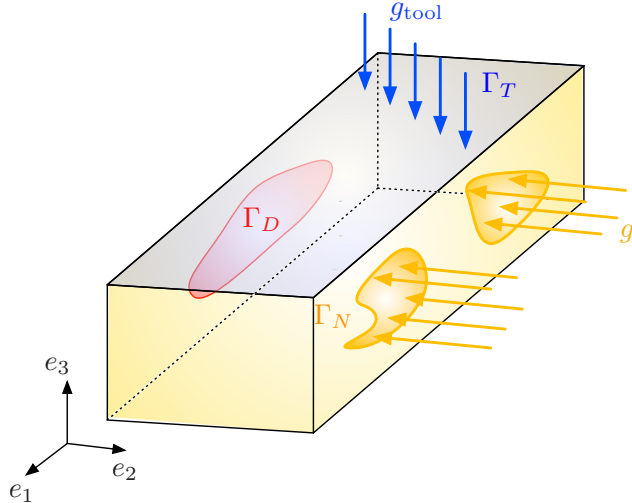


FIGURE 4.3.3. Setting of the example of [Section 4.3.6.1](#) dealing with the optimal repartition of clamps and locators on the boundary of an elastic structure.

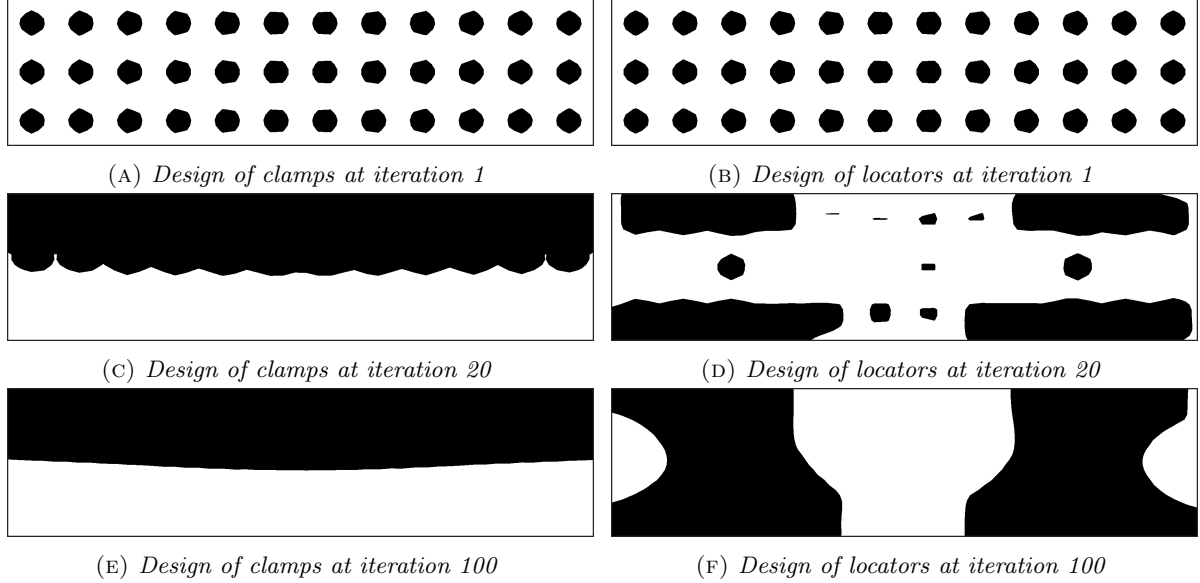


FIGURE 4.3.4. *Initial, intermediate and optimized designs of clamps and locators in the test-case of Section 4.3.6.1.*

#### 4.3.6.2. Optimization of the Dirichlet regions of a force inverter

Our second example also arises in a physical situation which is described by the linear elasticity system. It deals with the concurrent optimization of the shape and the fixation regions of a force inverter mechanism, that is, a device which converts a pulling force into a pushing one. The details of the considered 2d test case are presented on Fig. 4.3.5: the shapes  $\Omega$  are contained in a box  $D$  with size  $1 \times 1$ ; they are subjected to a given load  $g = (-1, 0)$  applied on a non optimizable subset  $\Gamma_N$  of their left-hand side, and they are attached on another subset  $\Gamma_D$  of  $\partial\Omega$ , contained in the upper and lower sides of  $\partial D$ . In this context, the aim is to optimize the overall shape  $\Omega$  and the location of the fixations  $\Gamma_D$  so as to maximize the elastic displacement of  $\Omega$  on a non optimizable subset  $\Gamma_T$  at the right-hand side of  $\partial D$ . More precisely, we solve:

$$\min_{\Omega} J(\Omega), \text{ where } J(\Omega) := \alpha_T \int_{\Gamma_T} |u_{\Omega} - u_T|^2 \, ds - \alpha_N \int_{\Gamma_N} u_{\Omega} \cdot e_1 \, ds + \ell_V \text{Vol}(\Omega) + \ell_D \int_{\Gamma_D} \, ds,$$

and  $\alpha_T$  and  $\alpha_N$  are weights for balancing the wishes to maximize the pushing force near  $\Gamma_T$  and the need to pull the region  $\Gamma_N$ ;  $\ell_V$  and  $\ell_D$  account for penalizations of the volume of the structure and the surface area of the fixations  $\Gamma_D$ .

The optimized shape resulting from the solution of this problem is depicted on Fig. 4.3.5. The corresponding deformed configuration allows to appraise the efficiency of the mechanism.

#### 4.4 SENSITIVITY WITH RESPECT TO SINGULAR CHANGES IN THE SUPPORT OF BOUNDARY CONDITIONS

The previous Section 4.3 was concerned with the analysis of the sensitivity of the solution to a boundary value problem (and of a related quantity of interest) with respect to “regular” perturbations of the regions bearing its boundary conditions, via smooth diffeomorphisms. The present section aims to complement this study with the asymptotic analysis of such a solution when these regions undergo “singular” perturbations, and notably alterations of their nature inside a “small” subset  $\omega_{\varepsilon}$  of  $\partial\Omega$ .

More precisely, let us consider the following situation:  $\Omega$  is a smooth bounded domain in  $\mathbb{R}^d$ ,  $d = 2, 3$ , whose boundary  $\partial\Omega$  is divided into two disjoint regions  $\Gamma_D, \Gamma_N$ :

$$\partial\Omega = \overline{\Gamma_D} \cup \overline{\Gamma_N};$$

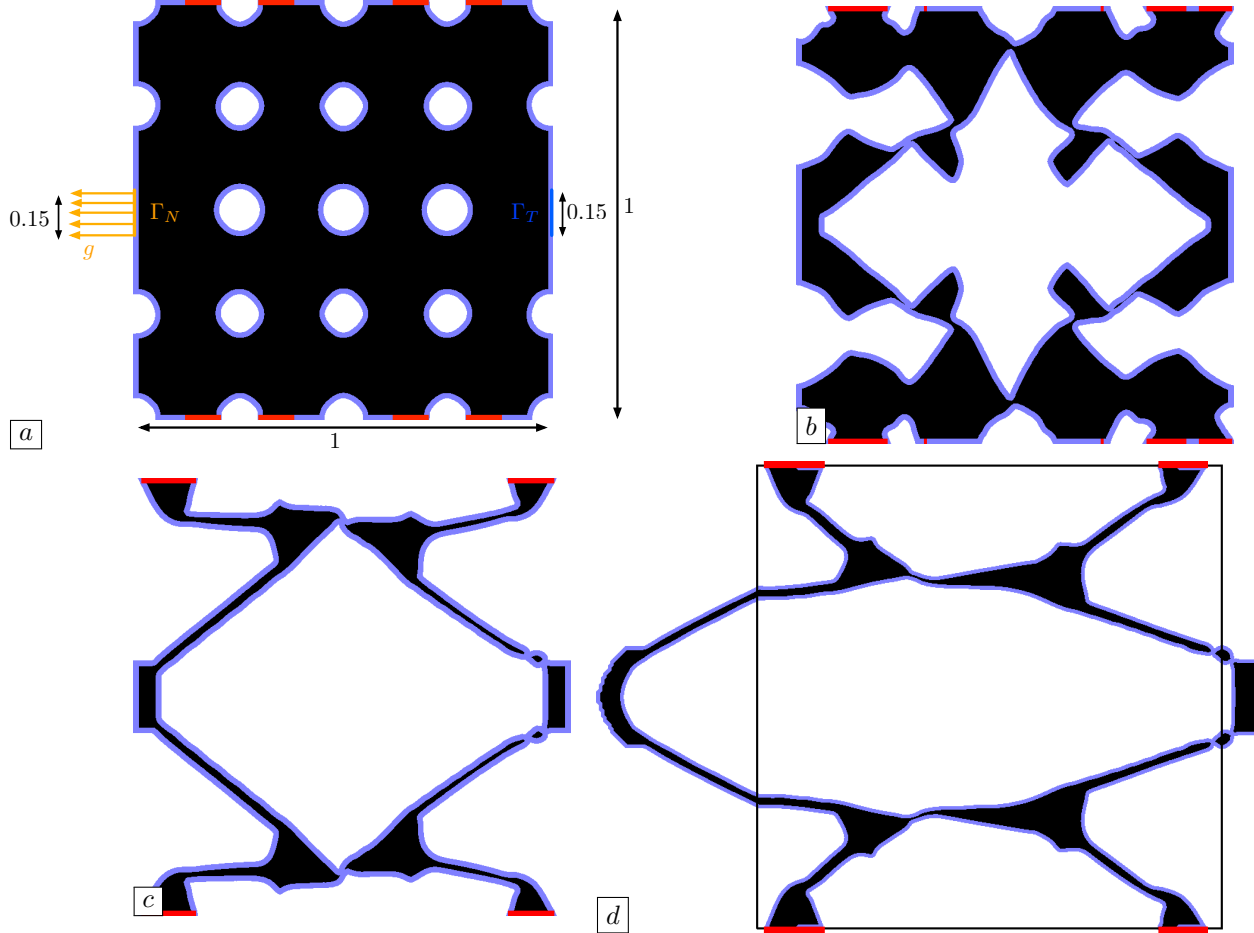


FIGURE 4.3.5. Concurrent optimization of the shape and the fixation regions of the force inverter of [Section 4.3.6.2](#); iterations (a) 0 (with details of the test-case), (b) 50, (c) 100, and (d) Deformed configuration of the optimized design.

homogeneous Dirichlet boundary conditions are imposed on  $\Gamma_D$ , while  $\Gamma_N$  bears homogeneous Neumann boundary conditions. The conductivity  $\gamma \in \mathcal{C}^\infty(\bar{\Omega})$  inside the medium is assumed to be elliptic in the sense that (Ell-Cond) holds; the potential  $u_\Omega$  induced by a smooth source  $f \in \mathcal{C}^\infty(\bar{\Omega})$  in this ‘‘background’’ situation is the solution to the boundary value problem:

$$(4.4.1) \quad \begin{cases} -\operatorname{div}(\gamma \nabla u_0) = f & \text{in } \Omega, \\ u_0 = 0 & \text{on } \Gamma_D, \\ \gamma \frac{\partial u_0}{\partial n} = 0 & \text{on } \Gamma_N. \end{cases}$$

Let us recall that, on account of the elliptic regularity theory,  $u_0$  is smooth except on a neighborhood of the set  $\Sigma = \partial\Gamma_D = \partial\Gamma_N$  where the boundary conditions change types, see [Section 1.A.6](#). We also recall for further reference that the Green’s function  $N(x, y)$  attached to this boundary value problem is defined for any point  $x \in \Omega$  by:

$$(4.4.2) \quad \begin{cases} -\operatorname{div}_y(\gamma(y) \nabla_y N(x, y)) = \delta_{y=x} & \text{in } \Omega, \\ N(x, y) = 0 & \text{for } y \in \Gamma_D, \\ \gamma(y) \frac{\partial N}{\partial n_y}(x, y) = 0 & \text{for } y \in \Gamma_N, \end{cases}$$

see [Section 4.1.1](#).

Let us then consider the perturbed situation where the homogeneous Neumann boundary condition on  $\Gamma_N$  is replaced by a homogeneous Dirichlet boundary condition inside a “small” subset  $\omega_\varepsilon \subset \Gamma_N$ . The perturbed potential  $u_\varepsilon$  is then the unique solution in  $H^1(\Omega)$  to the problem:

$$(4.4.3) \quad \begin{cases} -\operatorname{div}(\gamma \nabla u_\varepsilon) = f & \text{in } \Omega, \\ u_\varepsilon = 0 & \text{on } \Gamma_D \cup \omega_\varepsilon, \\ \gamma \frac{\partial u_\varepsilon}{\partial n} = 0 & \text{on } \Gamma_N \setminus \overline{\omega_\varepsilon}. \end{cases}$$

In this setting, we aim to understand the behavior of the perturbed potential  $u_\varepsilon$  when the set  $\omega_\varepsilon$  where boundary conditions are altered becomes “very small”. This problem is sometimes referred to as the “narrow escape problem” in the literature. Originating from acoustics, it has recently attracted much attention due to its significance in biology. We refer to [204] and the references therein for an overview of the physical relevance of this problem and for an account of recent developments, and [33, 119, 125, 301] about mathematical analyses around this question.

Limiting ourselves to stating results for brevity, we shall also report on the mirror situation, where the “small” subset  $\omega_\varepsilon$  lies inside the Dirichlet region  $\Gamma_D$ , and the Dirichlet boundary condition on  $\omega_\varepsilon$  is replaced by a homogeneous Neumann boundary condition: the potential  $u_\varepsilon$  is then the solution to:

$$(4.4.4) \quad \begin{cases} -\operatorname{div}(\gamma \nabla u_\varepsilon) = f & \text{in } \Omega, \\ u_\varepsilon = 0 & \text{on } \Gamma_D \setminus \overline{\omega_\varepsilon}, \\ \gamma \frac{\partial u_\varepsilon}{\partial n} = 0 & \text{on } \Gamma_N \cup \omega_\varepsilon. \end{cases}$$

We refer to [32] for results about this second setting and to [31] for applications to the theory of metasurfaces.

In both situations, we proceed under the assumption that  $\omega_\varepsilon$  is “well-separated” from the boundary  $\Sigma$  between  $\Gamma_D$  and  $\Gamma_N$ , see [Fig. 4.4.1](#):

$$(4.4.5) \quad \text{There exists a constant } d_{\min} > 0 \text{ such that, for all } \varepsilon > 0, \quad d^H(\overline{\omega_\varepsilon}, \Sigma) \geq d_{\min}.$$

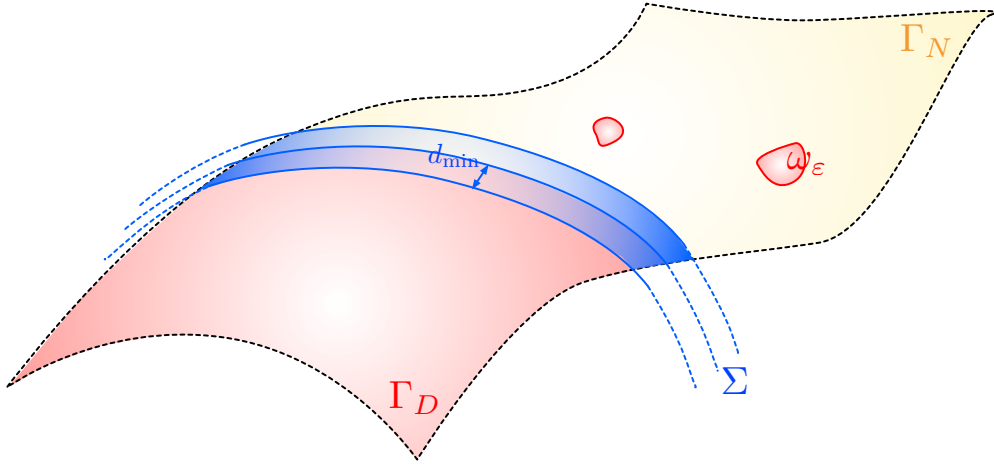


FIGURE 4.4.1. *Replacement of homogeneous Neumann boundary conditions by homogeneous Dirichlet boundary conditions on a “small” subset  $\omega_\varepsilon \subset \Gamma_N$  as in [Section 4.4](#).*

This section, based on the journal article [A5], investigates several questions about the asymptotic behavior of the perturbed potential  $u_\varepsilon$  when the set  $\omega_\varepsilon$  where boundary conditions are altered becomes “small”.

In the first [Section 4.4.1](#), an abstract representation formula is derived for the behavior of  $u_\varepsilon$  as  $\omega_\varepsilon$  vanishes, with minimal assumptions on the structure of this set. In [Section 4.4.2](#), we additionally assume that  $\omega_\varepsilon$  is a vanishing surface ball on  $\partial\Omega$  to obtain a completely explicit asymptotic formula for  $u_\varepsilon$ .

Before proceeding, let us mention that the non trivial extensions of these results to situations involving the linear elasticity operator is the subject of an ongoing work, see [Section 4.7.2](#).

#### 4.4.1. A general representation formula for the perturbed potential by the alteration of boundary conditions on a “small” subset of $\partial\Omega$

This section aims to understand the general behavior of the perturbed potential  $u_\varepsilon$  in (4.4.3) when no particular assumption is made about the set  $\omega_\varepsilon$ , except that it be “small”. We identify the adequate notion of “smallness” for  $\omega_\varepsilon$  and derive an abstract representation formula in the spirit of that presented in Section 4.1.4.

##### 4.4.1.1. Replacement of a homogeneous Neumann boundary condition with a homogeneous Dirichlet condition

In this first situation where the set  $\omega_\varepsilon \subset \Gamma_N$  is the support of the replacement of a homogeneous Neumann boundary condition with a homogeneous Dirichlet boundary condition, the key quantity measuring the “smallness” of  $\omega_\varepsilon$  turns out to be the capacity of this set.

**Definition 4.4.1** *The capacity  $\text{cap}(E)$  of an arbitrary subset  $E \subset \mathbb{R}^d$  is defined by:*

$$(4.4.6) \quad \text{cap}(E) = \inf \left\{ \|v\|_{H^1(\mathbb{R}^d)}^2, v \in H^1(\mathbb{R}^d), v(x) \geq 1 \text{ a.e. on an open neighborhood of } E \right\}.$$

Our main result about the general asymptotic behavior of the perturbed potential  $u_\varepsilon$  is then the following.

**Theorem 4.4.2** *Let  $\omega_\varepsilon$  be a sequence of non-empty, open Lipschitz subsets of  $\partial\Omega$ , which are all contained in  $\Gamma_N$  and are well-separated from  $\Gamma_D$  in the sense that (4.4.5) holds. Assume furthermore that the capacity  $\text{cap}(\omega_\varepsilon)$  of  $\omega_\varepsilon$  goes to 0 as  $\varepsilon \rightarrow 0$ . Then there exists a subsequence, still denoted by  $\varepsilon$ , and a non-trivial, non negative Radon measure  $\mu$  on  $\partial\Omega$ , such that the solution  $u_\varepsilon$  to (4.4.3) satisfies, for each  $x \in \Omega$ :*

$$(4.4.7) \quad u_\varepsilon(x) = u_0(x) - \text{cap}(\omega_\varepsilon) \int_{\partial\Omega} u_0(y) \gamma(y) N(x, y) \, d\mu(y) + o(\text{cap}(\omega_\varepsilon)).$$

*The measure  $\mu$  depends only on the subsequence  $\omega_\varepsilon$ ,  $\Omega$ , and  $\Gamma_N$ . The support of  $\mu$  lies inside any compact subset  $K \subset \partial\Omega$  containing the  $\omega_\varepsilon$  for  $\varepsilon > 0$  small enough, and the term  $o(\text{cap}(\omega_\varepsilon))$  goes to zero faster than  $\text{cap}(\omega_\varepsilon)$  uniformly (in  $x$ ) on compact subsets of  $\Omega$ .*

The proof of this result is quite close in spirit to that of the representation formula of Theorem 4.1.11 in the context of “small” inhomogeneities in the material properties of a background medium; we provide a sketch of the proof, mainly insisting on the differences.

*Hint of proof.* Let the error  $r_\varepsilon := u_\varepsilon - u_0$  be the unique solution in  $H_{\Gamma_D}^1(\Omega)$  to

$$(4.4.8) \quad \begin{cases} -\text{div}(\gamma \nabla r_\varepsilon) = 0 & \text{in } \Omega, \\ r_\varepsilon = 0 & \text{on } \Gamma_D, \\ r_\varepsilon = -u_0 & \text{on } \omega_\varepsilon, \\ \gamma \frac{\partial r_\varepsilon}{\partial n} = 0 & \text{on } \Gamma_N \setminus \overline{\omega_\varepsilon}. \end{cases}$$

As a preliminary observation, relying on a fairly standard analysis of the boundary value problem (4.4.8) and the use of the Aubin-Nitsche method (see Remark 4.1.12), we obtain the following a priori  $H^1$  and improved  $L^2$  estimates about  $r_\varepsilon$ :

$$(4.4.9) \quad \|r_\varepsilon\|_{H^1(\Omega)} \leq C \text{cap}(\omega_\varepsilon)^{\frac{1}{2}} \|u_0\|_{C^1(\partial\Omega)}, \text{ and } \|r_\varepsilon\|_{L^2(\Omega)} \leq C \text{cap}(\omega_\varepsilon)^{\frac{3}{4}} \|u_0\|_{C^1(\partial\Omega)},$$

where the constant  $C$  only depends on  $\Omega$  and the bounds on the ellipticity constants of  $\gamma$  in (Ell-Cond).

We then represent the value  $r_\varepsilon(x)$  of  $r_\varepsilon$  at a point  $x \in \Omega$  in terms of its values inside  $\omega_\varepsilon$ . To this end, we use the Green’s function  $N(x, y)$  for the background problem, see (4.4.2), and we integrate by parts twice to obtain:

$$(4.4.10) \quad \begin{aligned} r_\varepsilon(x) &= - \int_{\Omega} \text{div}_y(\gamma(y) \nabla_y N(x, y)) r_\varepsilon(y) \, dy, \\ &= \int_{\Omega} \gamma(y) \nabla_y N(x, y) \cdot \nabla r_\varepsilon(y) \, dy, \\ &= \int_{\omega_\varepsilon} N(x, y) \gamma(y) \frac{\partial r_\varepsilon}{\partial n}(y) \, ds(y), \end{aligned}$$

where we have used the fact that  $\gamma \frac{\partial N}{\partial n_y}(x, \cdot) = 0$  on  $\Gamma_N$  and  $r_\varepsilon = 0$  on  $\Gamma_D$  to obtain the second line, and the fact that  $N(x, \cdot) = 0$  on  $\Gamma_D$  and  $\gamma \frac{\partial r_\varepsilon}{\partial n} = 0$  on  $\Gamma_N \setminus \overline{\omega_\varepsilon}$  to obtain the last line.

This formula raises the need to pass to the limit in an integral expression of the form

$$I_\varepsilon := \int_{\omega_\varepsilon} \phi(y) \gamma(y) \frac{\partial r_\varepsilon}{\partial n}(y) \, ds(y),$$

for a smooth function  $\phi$  which stands for  $N(x, \cdot)$ , after a proper rescaling with the correct measure of “smallness” for  $\omega_\varepsilon$ . To achieve this, let us introduce the following corrector function (or adjoint state)  $\chi_\varepsilon$ , solution in  $H_{\Gamma_D}^1(\Omega)$  to the boundary value problem:

$$\begin{cases} -\operatorname{div}(\gamma \nabla \chi_\varepsilon) = 0 & \text{in } \Omega, \\ \chi_\varepsilon = 0 & \text{on } \Gamma_D, \\ \chi_\varepsilon = 1 & \text{on } \omega_\varepsilon, \\ \gamma \frac{\partial \chi_\varepsilon}{\partial n} = 0 & \text{on } \Gamma_N \setminus \overline{\omega_\varepsilon}. \end{cases}$$

The function  $\chi_\varepsilon$  satisfies similar estimates to (4.4.9); intuitively, we shall transform the expression of  $I_\varepsilon$  by “transferring” the normal trace  $\gamma \frac{\partial}{\partial n}$  from  $r_\varepsilon$  to the function  $\chi_\varepsilon$ , which only depends on  $\Omega$  and the “small” subset  $\omega_\varepsilon$ , and not on  $u_0$ . To achieve this, we calculate:

$$\begin{aligned} I_\varepsilon &= \int_{\omega_\varepsilon} \phi(y) \chi_\varepsilon(y) \gamma(y) \frac{\partial r_\varepsilon}{\partial n}(y) \, ds(y) \\ &= \int_{\partial\Omega} \phi(y) \chi_\varepsilon(y) \gamma(y) \frac{\partial r_\varepsilon}{\partial n}(y) \, ds(y) \\ &= \int_{\Omega} \gamma(y) \nabla r_\varepsilon(y) \cdot \nabla(\phi \chi_\varepsilon)(y) \, dy, \end{aligned}$$

where we have used Green’s formula and the boundary conditions for  $r_\varepsilon$  and  $\chi_\varepsilon$ . Now,

$$I_\varepsilon = \int_{\Omega} \gamma(y) \nabla(\phi r_\varepsilon)(y) \cdot \nabla \chi_\varepsilon(y) \, dy + R_{1,\varepsilon} + R_{2,\varepsilon},$$

where the integral remainders  $R_{1,\varepsilon}$  and  $R_{2,\varepsilon}$  are defined by:

$$R_{1,\varepsilon} = \int_{\Omega} \gamma(y) \nabla r_\varepsilon(y) \cdot \nabla \phi(y) \chi_\varepsilon(y) \, dy, \text{ and } R_{2,\varepsilon} = - \int_{\Omega} \gamma(y) \nabla \chi_\varepsilon(y) \cdot \nabla \phi(y) r_\varepsilon(y) \, dy.$$

It follows from (4.4.9) that:

$$(4.4.11) \quad |R_{1,\varepsilon}| + |R_{2,\varepsilon}| = o(\operatorname{cap}(\omega_\varepsilon)).$$

Another integration by parts and the boundary conditions satisfied by  $r_\varepsilon$  and  $\chi_\varepsilon$  now allow to see that:

$$\begin{aligned} I_\varepsilon &= \int_{\partial\Omega} \phi(y) r_\varepsilon(y) \gamma(y) \frac{\partial \chi_\varepsilon}{\partial n}(y) \, ds(y) + R_{1,\varepsilon} + R_{2,\varepsilon} \\ &= - \int_{\partial\Omega} \phi(y) u_0(y) \chi_\varepsilon(y) \gamma(y) \frac{\partial \chi_\varepsilon}{\partial n}(y) \, ds(y) + R_{1,\varepsilon} + R_{2,\varepsilon}, \end{aligned}$$

where we have used the fact that  $\gamma \frac{\partial \chi_\varepsilon}{\partial n} = 0$  on  $\Gamma_N \setminus \overline{\omega_\varepsilon}$  and  $r_\varepsilon + u_0 \chi_\varepsilon = 0$  on  $\Gamma_D \cup \omega_\varepsilon$  to pass from the first line to the second one. Now using the estimates (4.4.11), we see that the sequence  $\frac{1}{\operatorname{cap}(\omega_\varepsilon)} \chi_\varepsilon \gamma \frac{\partial \chi_\varepsilon}{\partial n}$  is bounded in  $L^1(\partial\Omega)$ . Hence, up to a subsequence (still indexed by  $\varepsilon$ ), there exists a Radon measure  $\mu$  on  $\partial\Omega$  such that

$$\frac{1}{\operatorname{cap}(\omega_\varepsilon)} \chi_\varepsilon \gamma \frac{\partial \chi_\varepsilon}{\partial n} \xrightarrow{\varepsilon \rightarrow 0} \mu \text{ weakly } * \text{ in } \mathcal{M}(\partial\Omega),$$

see Theorem 2.A.11. This measure is easily seen to enjoy the properties in the statement of the theorem.

Combining these results, we are eventually in position to pass to the limit in the representation formula (4.4.10) for the value  $r_\varepsilon(x)$  at some given point  $x \in \Omega$ , which yields the desired result.  $\square$

**Remark 4.4.3** The first non trivial term in (4.4.7) is the superposition of the potentials  $u_0(y)\gamma(y)N(x, y)$  created at  $x$  by point sources (monopoles) which are distributed on the “limiting location” of the vanishing subsets  $\omega_\varepsilon$ . The negative sign in front of this term indicates that these point sources have been replaced by a “ground” (homogeneous Dirichlet boundary condition) when passing from the background situation to the perturbed one.

#### 4.4.1.2. Replacement of a homogeneous Dirichlet boundary condition with a homogeneous Neumann condition

Let us now consider the situation where  $\omega_\varepsilon$  is a subset of the region  $\Gamma_D$  and the homogeneous Dirichlet boundary condition featured in (4.4.1) is replaced by a homogeneous Neumann condition on  $\omega_\varepsilon$ ; the perturbed potential  $u_\varepsilon$  is now the solution to (4.4.4). The relevant quantity measuring the “smallness” of  $\omega_\varepsilon$  in this situation is new to the best of our knowledge, and it deserves the name of “Neumann capacity”:

**Definition 4.4.4** The Neumann capacity  $e(\omega)$  of an arbitrary finite collection of disjoint Lipschitz hypersurfaces  $\omega \subset \mathbb{R}^d$  is defined by:

$$(4.4.12) \quad e(\omega) = \max_{\substack{\kappa \in C_c^\infty(\mathbb{R}^d \setminus \overline{\omega}), \\ \kappa(x) = \pm 1 \text{ for } x \in \omega}} \left\{ \int_{\mathbb{R}^d} (z^2 + |\nabla z|^2) \, dx, \quad z \in H^1(\mathbb{R}^d \setminus \overline{\omega}) \text{ s.t. } \begin{cases} -\Delta z + z = 0 & \text{in } \mathbb{R}^d \setminus \overline{\omega}, \\ \frac{\partial z}{\partial n} = \kappa & \text{on } \omega \end{cases} \right\}.$$

The general structure of  $u_\varepsilon$  as  $e(\omega_\varepsilon) \rightarrow 0$  is given by the following result, whose proof is fairly similar to that of [Theorem 4.4.2](#).

**Theorem 4.4.5** Let  $\omega_\varepsilon$  be a sequence of non-empty, open Lipschitz subsets of  $\partial\Omega$ , which are all contained in  $\Gamma_D$  and are well-separated from  $\Gamma_N$ , in the sense that (4.4.5) holds; let  $u_\varepsilon$  denote the solution to (4.4.4). Assume that the quantity  $e(\omega_\varepsilon)$ , defined by (4.4.12), tends to 0 as  $\varepsilon \rightarrow 0$ . Then there exists a subsequence, still indexed by  $\varepsilon$ , and a non-trivial, non negative Radon measure  $\mu$  on  $\partial\Omega$ , whose support is included in any compact subset  $K \subset \partial\Omega$  containing the  $\omega_\varepsilon$  for  $\varepsilon > 0$  small enough, such that the following asymptotic expansion holds at any fixed point  $x \in \Omega$ :

$$u_\varepsilon(x) = u_0(x) + e(\omega_\varepsilon) \int_{\partial\Omega} \gamma(y) \frac{\partial u_0}{\partial n}(y) \frac{\partial N}{\partial n_y}(x, y) \, d\mu(y) + o(e(\omega_\varepsilon)).$$

The term  $o(e(\omega_\varepsilon))$  goes to zero faster than  $e(\omega_\varepsilon)$  uniformly (in  $x$ ) on compact subsets of  $\Omega$ .

#### 4.4.2. Replacement of boundary conditions on a vanishing surface ball

This section focuses on a particular case regarding the geometry of the set  $\omega_\varepsilon$ : the latter is supposed to be a surfacic ball on  $\partial\Omega$  with radius  $\varepsilon$  centered at some point  $x_0$  in the Neumann region  $\Gamma_N$ :

$$\omega_\varepsilon = \{x \in \partial\Omega, |x - x_0| < \varepsilon\}.$$

The representation formula of [Theorem 4.4.2](#) for the perturbed potential  $u_\varepsilon$  by the replacement of the Neumann condition on  $\omega_\varepsilon$  by a homogeneous Dirichlet condition can then be made explicit in this case, as asserted by the following result, where we set  $x_0 = 0$  for simplicity.

**Theorem 4.4.6** Assume that  $x_0 = 0$  belongs to the region  $\Gamma_N \subset \partial\Omega$ ; then the following asymptotic expansion for the solution  $u_\varepsilon$  to (4.4.3) holds at any point  $x \in \overline{\Omega}$ ,  $x \notin \Sigma \cup \{0\}$ :

$$\begin{aligned} \text{If } d = 2, \quad u_\varepsilon(x) &= u_0(x) - \frac{\pi}{|\log \varepsilon|} \gamma(0) u_0(0) N(x, 0) + o\left(\frac{1}{|\log \varepsilon|}\right), \\ \text{If } d = 3, \quad u_\varepsilon(x) &= u_0(x) - 4\varepsilon \gamma(0) u_0(0) N(x, 0) + o(\varepsilon). \end{aligned}$$

*Sketch of proof.* We provide a formal outline of the proof in the case  $d = 3$ , under the simplifying assumption that  $\partial\Omega$  is completely flat around  $x = 0$  and that the conductivity  $\gamma$  inside  $\Omega$  is constant. In this situation,  $\omega_\varepsilon$  is the flat disk  $\mathbb{D}_\varepsilon = \{x = (x_1, x_2, 0) \in \mathbb{R}^3, |x| < \varepsilon\}$ .

Let  $r_\varepsilon := u_\varepsilon - u_0$  be the error between the perturbed and background potentials; the proof follows the three-step trail of that of [Theorem 4.1.14](#).

*Step 1:* We express  $r_\varepsilon(x)$  at some point  $x \in \overline{\Omega} \setminus (\Sigma \cup \{0\})$  in terms of the values of  $r_\varepsilon$  inside  $\omega_\varepsilon$ .

For any point  $x \in \overline{\Omega} \setminus (\Sigma \cup \{0\})$ , the definition (4.4.2) of the Green's function  $N(x, y)$  and the Green's formula yield:

$$\begin{aligned} r_\varepsilon(x) &= - \int_{\Omega} \operatorname{div}_y (\gamma(y) \nabla_y N(x, y)) r_\varepsilon(y) \, dy \\ &= - \int_{\partial\Omega} \gamma(y) \frac{\partial N}{\partial n_y}(x, y) r_\varepsilon(y) \, ds(y) + \int_{\Omega} \gamma(y) \nabla_y N(x, y) \cdot \nabla r_\varepsilon(y) \, dy \\ &= - \int_{\partial\Omega} \gamma(y) \frac{\partial N}{\partial n_y}(x, y) r_\varepsilon(y) \, ds(y) + \int_{\partial\Omega} N(x, y) \gamma(y) \frac{\partial r_\varepsilon}{\partial n}(y) \, ds(y), \end{aligned}$$

where we have used the equation (4.4.8) satisfied by  $r_\varepsilon$  to obtain the last line. Using now the boundary conditions satisfied by both functions  $r_\varepsilon$  and  $y \mapsto N(x, y)$ , the integrals in the above right-hand side reduce to:

$$r_\varepsilon(x) = \int_{\omega_\varepsilon} N(x, y) \gamma(y) \frac{\partial r_\varepsilon}{\partial n}(y) \, ds(y).$$

Changing variables, we transport the above integral to the unit flat disk  $\mathbb{D}_1 := \{x = (x_1, x_2, 0) \in \mathbb{R}^3, |x| < 1\}$ :

$$(4.4.13) \quad r_\varepsilon(x) = \int_{\mathbb{D}_1} N(x, \varepsilon z) \varphi_\varepsilon(z) \, ds(z), \text{ where } \varphi_\varepsilon(z) := \varepsilon^{d-1} \left( \gamma \frac{\partial r_\varepsilon}{\partial n} \right) (\varepsilon z) \in \tilde{H}^{-1/2}(\mathbb{D}_1).$$

Obviously, passing to the limit in the above formula requires some knowledge about the behavior of  $\varphi_\varepsilon$  as  $\varepsilon \rightarrow 0$ .

*Step 2: We glean information about  $\varphi_\varepsilon$ .*

An intuitive way to achieve this is to let  $x$  approach  $\omega_\varepsilon$  in (4.4.13): in the left-hand side of this formula,  $r_\varepsilon(x)$  then tends to  $-u_0(x)$  (see (4.4.8)), while the right-hand side is continuous with respect to  $x$ , see Section 4.1.3 about the jump relations of layer potential operators. Replacing the variable  $x \in \omega_\varepsilon$  with  $\varepsilon x$ ,  $x \in \mathbb{D}_1$ , (4.4.13) thus yields an integral equation for  $\varphi_\varepsilon$ , which unfortunately features the non explicit kernel  $N(\varepsilon x, \varepsilon z)$ .

To circumvent this difficulty, we repeat the procedure of the first step by replacing  $N(x, y)$  with the Green's function  $L(x, y)$  for the lower half-space  $H = \{x = (x_1, x_2, x_3) \in \mathbb{R}^3, x_3 < 0\}$ , with homogeneous Neumann boundary conditions on  $\partial H$ , see Remark 4.1.5. This function has an explicit expression in terms of  $x$  and  $y$ , see Remark 4.1.5, and it “has the same effect” as  $N(x, y)$  when  $x$  and  $y$  are “close points” on  $\omega_\varepsilon$ .

More precisely, a calculation similar to that conducted in the previous step yields, for  $x \in \Omega$ :

$$r_\varepsilon(x) = \int_{\omega_\varepsilon} L(x, y) \gamma(y) \frac{\partial r_\varepsilon}{\partial n}(y) \, ds(y) + \mathcal{K}r_\varepsilon(x),$$

where  $\mathcal{K}r_\varepsilon$  involves integrals of  $r_\varepsilon$  and its derivatives supported outside a fixed neighborhood of the point 0. Now letting  $x$  tend to  $\omega_\varepsilon$ , which is possible because of the jump relations of single layer potentials (again, see Section 4.1.3), we obtain

$$\forall x \in \omega_\varepsilon, \quad r_\varepsilon(x) = -u_0(x) = \int_{\omega_\varepsilon} L(x, y) \gamma(y) \frac{\partial r_\varepsilon}{\partial n}(y) \, ds(y) + \mathcal{K}r_\varepsilon(x),$$

and so, after rescaling

$$\forall x \in \mathbb{D}_1, \quad -u_0(0) \approx \int_{\mathbb{D}_1} L(\varepsilon x, \varepsilon z) \varphi_\varepsilon(z) \, ds(z),$$

where  $\varphi_\varepsilon \in \tilde{H}^{-1/2}(\mathbb{D}_1)$  is defined by (4.4.13) and the remainder  $\mathcal{K}r_\varepsilon(\varepsilon x)$  tends to 0 faster than the integral in the above right-hand side, as it only involves values of  $r_\varepsilon$  which are “far” from  $\omega_\varepsilon$ .

Using the explicit form of the kernel  $L(\varepsilon x, \varepsilon z)$ , this rewrites as an integral equation

$$\frac{2}{\varepsilon \gamma} \mathcal{S}_1 \varphi_\varepsilon(x) = -u_0(0),$$

where the operator  $\mathcal{S}_1 : \tilde{H}^{-1/2}(\mathbb{D}_1) \rightarrow H^{1/2}(\mathbb{D}_1)$  is defined by

$$\mathcal{S}_1 \varphi(x) = \frac{1}{4\pi} \int_{\mathbb{D}_1} \frac{1}{|x - y|} \varphi(y) \, ds(y).$$

Using known results about this operator, and notably the explicit expression of a solution to this equation, see [135, 311], we eventually obtain that:

$$(4.4.14) \quad \int_{\mathbb{D}_1} \varphi_\varepsilon(z) \, ds(z) \approx -4\varepsilon\gamma u_0(0),$$

which is the desired information in the perspective of the next step.

*Step 3: We pass to the limit in the representation formula (4.4.13).*

Using the Lebesgue dominated convergence theorem and the relation (4.4.14) obtained during the second step, we obtain:

$$r_\varepsilon(x) \approx N(x, 0) \int_{\mathbb{D}_1} \varphi_\varepsilon(z) \, ds(z) \approx -4\varepsilon\gamma u_0(0)N(x, 0),$$

which is the expected result.  $\square$

**Theorem 4.4.6** and its proof can be adapted to the mirror situation where 0 (and the subsets  $\omega_\varepsilon$ ) belongs to the region  $\Gamma_D$  where a homogeneous Dirichlet boundary condition is imposed in the background situation (4.4.1), which is replaced by a homogeneous Neumann condition in the perturbed situation.

**Theorem 4.4.7** *Assume that  $x_0 = 0 \in \Gamma_N$ ; then the following asymptotic expansion for the solution  $u_\varepsilon$  to (4.4.4) holds at any point  $x \in \overline{\Omega}$ ,  $x \notin \Sigma \cup \{0\}$ :*

$$u_\varepsilon(x) = u_0(x) + a_d \varepsilon^d \gamma(0) \frac{\partial u_0}{\partial n}(0) \frac{\partial N}{\partial n_y}(x, 0) + o(\varepsilon^d),$$

where the constant  $a_d$  is given by

$$a_d = \begin{cases} \frac{\pi}{2} & \text{if } d = 2, \\ \frac{4}{3} & \text{if } d = 3. \end{cases}$$

**Remark 4.4.8** *The asymptotic formulas of Theorems 4.4.6 and 4.4.7 make it possible to calculate the expansion of a quantity of interest  $J(\varepsilon)$  involving the perturbed potential  $u_\varepsilon$ , of the form:*

$$J(\varepsilon) = \int_{\Omega} j(u_\varepsilon) \, dx,$$

where  $j : \mathbb{R} \rightarrow \mathbb{R}$  is a “smooth enough” function, see Proposition 4.1.15 about this point.

## 4.5 UNIFORM ESTIMATES IN THE PRESENCE OF THIN INHOMOGENEITIES

The advent of metamaterials, i.e. artificial materials exhibiting properties which are not common in nature (such as a negative index refraction in optics, a negative thermal expansion in thermo-mechanics, etc.), has spurred the analysis of partial differential equations with degenerate material properties, see [221] for a brief introduction, and [171, 347] for more in-depth presentations of this topic. For instance, the celebrated work [205] proposes a construction of a dielectric material with negative permittivity by homogenization of a set of parallel fibers filled with a material whose conductivity tends to  $\infty$ . In a similar spirit, the theory of passive cloaking predicts how to make an object (nearly) invisible to boundary measurements by surrounding it with an anisotropic, nearly degenerate material [132, 263, 297].

Inspired by these results, and returning to the model setting of the conductivity equation of Section 1.2.1, one may wonder about the behavior of the voltage potential when the conductivity of the medium is altered within a “small” subset, made of a nearly degenerate material. In this line of thinking, the article [283] has studied the perturbation of a smooth “background” medium by a diametrically small inhomogeneity  $\omega_\varepsilon$  (of the form (4.1.17)) filled with a material whose positive and bounded conductivity  $a_\varepsilon$  is allowed to degenerate to 0 or  $\infty$  as  $\varepsilon \rightarrow 0$ . It is shown that the perturbed potential  $u_\varepsilon$  tends to its background counterpart  $u_0$  regardless of the behavior of  $a_\varepsilon$ . Moreover, the first-order expansion derived in Section 4.1.5, under the assumption that  $a_\varepsilon$  stays bounded away from 0 and  $\infty$ , essentially remains valid in this more general context, in a way which is uniform with respect to  $a_\varepsilon$ .

The present section is based on the article [A29], where we address this question in the case of a thin inhomogeneity  $\omega_{S,\varepsilon}$ , with width  $\varepsilon$  around a closed surface  $S$ , see (4.1.18). The same conclusion as in the case of diametrically small inclusions cannot possibly hold in this context: intuitively, for a fixed value of the

width parameter  $\varepsilon$ , the inclusion  $\omega_{S,\varepsilon}$  becomes insulating (resp. superconducting) upon taking the formal limit  $a_\varepsilon \rightarrow 0$  (resp.  $a_\varepsilon \rightarrow \infty$ ); then, as  $\varepsilon \rightarrow 0$ , we expect that the potential  $u_\varepsilon$  should feel a “crack” equipped with insulating (or superconducting) boundary conditions. In particular,  $u_\varepsilon$  cannot converge to  $u_0$  uniformly with respect to  $a_\varepsilon$ , and it is natural to wonder whether there is a “simple”, explicit replacement of  $u_\varepsilon$ , which is a “good” approximation of  $u_\varepsilon$ , in a uniform way with respect to  $a_\varepsilon$ .

Let us formulate this question more rigorously. The background situation is described by the following conductivity equation for the voltage potential  $u_0 \in H_0^1(\Omega)$ :

$$(4.5.1) \quad \begin{cases} -\operatorname{div}(\gamma_0 \nabla u_0) = f & \text{in } \Omega, \\ u_0 = 0 & \text{on } \partial\Omega, \end{cases}$$

where the background conductivity  $\gamma_0$  and the source  $f$  are smooth functions on  $\overline{\Omega}$ .

Let  $\mathcal{O} \Subset \Omega$  be a smooth subdomain, with boundary  $S = \partial\mathcal{O}$ . We denote by  $\mathcal{O}^- := \mathcal{O}$  and  $\mathcal{O}^+ := \Omega \setminus \overline{\mathcal{O}}$  the two regions of  $\Omega$  delimited by the closed surface  $S$  and we define the thin inclusion set

$$\omega_{S,\varepsilon} := \{x \in \mathbb{R}^d, d(x, S) < \varepsilon\}.$$

Let us emphasize that in this study, the limiting surface  $S$  of  $\omega_{S,\varepsilon}$  is closed, which significantly simplifies the analysis, see [Remark 4.5.3](#) about the recent treatment of a particular instance of this problem where  $S$  is an open surface.

Introducing a sequence  $a_\varepsilon$  of positive real numbers, the perturbed potential  $u_\varepsilon$  when the conductivity inside  $\omega_{S,\varepsilon}$  is replaced by the constant  $a_\varepsilon$  is the unique solution in  $H_0^1(\Omega)$  to the equation:

$$(4.5.2) \quad \begin{cases} -\operatorname{div}(\gamma_\varepsilon \nabla u_\varepsilon) = f & \text{in } \Omega, \\ u_\varepsilon = 0 & \text{on } \partial\Omega, \end{cases} \quad \text{where } \gamma_\varepsilon(x) := \begin{cases} a_\varepsilon & \text{if } x \in \omega_{S,\varepsilon}, \\ \gamma_0(x) & \text{otherwise.} \end{cases}$$

In this context, we look for a simple replacement of  $u_\varepsilon$  in the limit  $\varepsilon \rightarrow 0$  where the inclusion  $\omega_{S,\varepsilon}$  vanishes, which is valid uniformly, that is, regardless of the values of  $a_\varepsilon$ . The main result is the following.

**Theorem 4.5.1** *Let  $K$  be a fixed compact subset of  $\Omega \setminus \overline{\mathcal{O}}$ , and let the source  $f$  have compact support inside  $K$ . Then it holds:*

$$(4.5.3) \quad \|u_\varepsilon - u_\varepsilon^0\|_{L^2(K)} \leq C\varepsilon\|f\|_{L^2(K)},$$

where the constant  $C$  depends on  $K$ ; the function  $u_\varepsilon^0$  belongs to the space

$$V_S := \{u \in H^1(\Omega \setminus S), u^+, u^- \in H^1(S)\}$$

and it is the unique solution in the latter to the minimization problem:

$$(4.5.4) \quad \min_{\substack{u \in V_S \\ u=0 \text{ on } \partial\Omega}} \widetilde{E}_\varepsilon(u), \quad \text{where } \widetilde{E}_\varepsilon(u) := \frac{1}{2} \int_{\Omega \setminus S} \gamma_0 |\nabla u|^2 \, dx + \frac{a_\varepsilon}{4\varepsilon} \int_S (u^+(p) - u^-(p))^2 \, ds(p) + \frac{\varepsilon a_\varepsilon}{3} \int_S \left( |\nabla_S u^+|^2 + |\nabla_S u^-|^2 + \nabla_S u^+ \cdot \nabla_S u^- \right) \, ds(p) - \int_\Omega f u \, dx,$$

where we recall that  $\nabla_S u$  is the tangential gradient of  $u$  (see [Section 1.A.1](#)), and that  $u^\pm$  denote the one-sided traces of a function which is smooth enough on either side of  $S$ , see [\(4.1.12\)](#).

Equivalently,  $u_\varepsilon^0$  is the unique solution in  $V_S$  to the boundary value problem:

$$\begin{cases} -\operatorname{div}(\gamma_0 \nabla u_\varepsilon^0) = f & \text{in } \Omega \setminus S \\ u_\varepsilon^0 = 0 & \text{on } \partial\Omega \\ \gamma_0 \frac{\partial u_\varepsilon^0}{\partial n} = \frac{a_\varepsilon}{2\varepsilon} (u_\varepsilon^0 - u_\varepsilon^{0-}) - \frac{\varepsilon a_\varepsilon}{3} (2\Delta_S u_\varepsilon^{0+} + \Delta_S u_\varepsilon^{0-}) & \text{on } S \\ \gamma_0 \frac{\partial u_\varepsilon^0}{\partial n} = \frac{a_\varepsilon}{2\varepsilon} (u_\varepsilon^{0+} - u_\varepsilon^{0-}) + \frac{\varepsilon a_\varepsilon}{3} (2\Delta_S u_\varepsilon^{0-} + \Delta_S u_\varepsilon^{0+}) & \text{on } S, \end{cases}$$

where  $\Delta_S$  is the Laplace-Beltrami operator attached to the smooth hypersurface  $S$ , see [Section 1.A.1](#).

*Sketch of proof.* We provide here an intuitive energy argument, which resembles that of the proof of [Theorem 4.1.14](#), considering the two-dimensional case for simplicity. This formal justification can be made rigorous, up to a slightly more delicate analysis.

The starting point of our analysis is the following variational problem for  $u_\varepsilon$ :

$$\text{Search for } u_\varepsilon \in H_0^1(\Omega) \text{ s.t. } \forall v \in H_0^1(\Omega), \quad \int_{\Omega} \gamma_\varepsilon \nabla u_\varepsilon \cdot \nabla v \, dx = \int_{\Omega} f v \, dx,$$

which is equivalent to the following energy minimization problem:

$$\min_{v \in H_0^1(\Omega)} E_\varepsilon(v), \text{ where } E_\varepsilon(v) := \frac{1}{2} \int_{\Omega} \gamma_\varepsilon |\nabla v|^2 \, dx - \int_{\Omega} f v \, dx.$$

We reformulate this problem in terms of the restriction of the sought function inside and outside the vanishing inclusion set  $\omega_{S,\varepsilon}$ : the couple  $(u_\varepsilon|_{\Omega \setminus \overline{\omega_{S,\varepsilon}}}, u_\varepsilon|_{\omega_{S,\varepsilon}})$  is the unique solution to:

$$(4.5.5) \quad \min \left( \frac{1}{2} \int_{\Omega \setminus \overline{\omega_{S,\varepsilon}}} \gamma_0 |\nabla u|^2 \, dx + \frac{1}{2} a_\varepsilon \int_{\omega_{S,\varepsilon}} |\nabla v|^2 \, dx - \int_{\Omega} f u \, dx \right).$$

This minimization takes place on the subspace of  $H^1(\Omega \setminus \overline{\omega_{S,\varepsilon}}) \times H^1(\omega_{S,\varepsilon})$  defined by:

$$\left\{ (u, v) \in H^1(\Omega \setminus \overline{\omega_{S,\varepsilon}}) \times H^1(\omega_{S,\varepsilon}), \quad u = 0 \text{ on } \partial\Omega, \text{ and } \forall p \in S \quad \begin{cases} u(p + \varepsilon n(p)) = v(p + \varepsilon n(p)) \\ u(p - \varepsilon n(p)) = v(p - \varepsilon n(p)) \end{cases} \right\}.$$

In this formula,  $n : S \rightarrow \mathbb{R}^2$  is the unit normal vector to  $S$ , pointing outward  $\mathcal{O}$ . We now use a change of variables in the integral posed on  $\omega_{S,\varepsilon}$  in the two-scale energy featured in (4.5.5). To achieve this, we leverage the material contained in [Section 3.1](#) about the signed distance function  $d_{\mathcal{O}}$  to the domain  $\mathcal{O}$ , and the related projection  $p_S$  onto  $S$ ; we assume for simplicity that the skeleton  $\Sigma$  of  $\mathcal{O}$  lies outside the rescaled inclusion set  $\omega_{S,1}$  and we define the smooth mapping:

$$\begin{aligned} m_\varepsilon : \omega_{S,1} &\longrightarrow \omega_{S,\varepsilon} \\ x &\longmapsto p_S(x) + \varepsilon n(p_S(x)). \end{aligned}$$

A change of variables reveals that the couple  $(u_\varepsilon|_{\Omega \setminus \overline{\omega_{S,\varepsilon}}}, u_\varepsilon|_{\omega_{S,\varepsilon}} \circ m_\varepsilon)$  is the unique solution to the minimization problem

$$(4.5.6) \quad \min_{\substack{(u,v) \in V_\varepsilon \\ u=0 \text{ on } \partial\Omega}} F_\varepsilon(u, v), \text{ where } F_\varepsilon(u, v) = \frac{1}{2} \int_{\Omega \setminus \overline{\omega_{S,\varepsilon}}} \gamma_0 |\nabla u|^2 \, dx + \frac{\varepsilon}{2} a_\varepsilon \int_{\omega_{S,1}} \frac{1 + \kappa d_{\mathcal{O}}}{1 + \varepsilon \kappa d_{\mathcal{O}}} \left( \frac{\partial v}{\partial \tau} \right)^2 \, dx \\ + \frac{1}{2\varepsilon} a_\varepsilon \int_{\omega_{S,1}} \frac{1 + \varepsilon \kappa d_{\mathcal{O}}}{1 + \kappa d_{\mathcal{O}}} \left( \frac{\partial v}{\partial n} \right)^2 \, dx - \int_{\Omega} f u \, dx,$$

where  $\tau : S \rightarrow \mathbb{R}^d$  is the tangent vector to  $S$  (the  $90^\circ$  clockwise rotate of  $n$ ). The space  $V_\varepsilon$  is defined by:

$$V_\varepsilon = \left\{ (u, v) \in H^1(\Omega \setminus \overline{\omega_{S,\varepsilon}}) \times H^1(\omega_{S,1}), \quad \forall p \in S \quad \begin{cases} u(p + \varepsilon n(p)) = v(p + n(p)) \\ u(p - \varepsilon n(p)) = v(p - n(p)) \end{cases} \right\}.$$

and we recall from [Section 3.1](#) that the normal vector  $n : S \rightarrow \mathbb{R}^d$  can be extended from the surface  $S$  to the whole open set  $\omega_{S,1}$  via the formula  $n(x) \equiv n(p_S(x))$ ; similar extensions hold for the mean curvature  $\kappa$ , the tangent vector  $\tau$ , etc.

We approximate the function  $F_\varepsilon(u, v)$  by the following two-scale energy obtained by retaining only leading order terms in (4.5.6):

$$\widetilde{F}_\varepsilon(u, v) = \frac{1}{2} \int_{\Omega \setminus S} \gamma_0 |\nabla u|^2 \, dx + \frac{\varepsilon}{2} a_\varepsilon \int_{\omega_{S,1}} (1 + \kappa d_{\mathcal{O}}) \left( \frac{\partial v}{\partial \tau} \right)^2 \, dx + \frac{1}{2\varepsilon} a_\varepsilon \int_{\omega_{S,1}} \frac{1}{1 + \kappa d_{\mathcal{O}}} \left( \frac{\partial v}{\partial n} \right)^2 \, dx - \int_{\Omega} f u \, dx.$$

We also approximate the space  $V_\varepsilon$  by that  $\widetilde{V}$  defined by:

$$(4.5.7) \quad \widetilde{V} = \left\{ (u, v) \in H^1(\Omega \setminus S) \times H^1(\omega_{S,1}), \quad \forall p \in S \quad \begin{cases} u^+(p) = v(p + n(p)) \\ u^-(p) = v(p - n(p)) \end{cases} \right\}.$$

Now, the approximate problem for the couple  $(u_\varepsilon|_{\Omega \setminus \overline{\omega_{S,\varepsilon}}}, u_\varepsilon|_{\omega_{S,\varepsilon}} \circ m_\varepsilon)$  obtained by retaining only leading order terms from (4.5.6) rewrites:

$$\min_{\substack{(u,v) \in \widetilde{V} \\ u=0 \text{ on } \partial\Omega}} \widetilde{F}_\varepsilon(u, v).$$

In turn, we obtain the problem:

$$(4.5.8) \quad \min_{\substack{u \in V_S \\ u=0 \text{ on } \partial\Omega}} \left( \frac{1}{2} \int_{\Omega \setminus \sigma} \gamma_0 |\nabla u|^2 \, dx - \int_{\Omega} f u \, dx + \min_{\substack{v(p+n(p))=u^+(p) \\ v(p-n(p))=u^-(p)}} G(v) \right),$$

where  $G(v) = \frac{\varepsilon}{2} a_\varepsilon \int_{\omega_{S,1}} (1 + \kappa d_{\mathcal{O}}) \left( \frac{\partial v}{\partial \tau} \right)^2 \, dx + \frac{a_\varepsilon}{2\varepsilon} \int_{\omega_{S,1}} \frac{1}{1 + \kappa d_{\mathcal{O}}} \left( \frac{\partial v}{\partial n} \right)^2 \, dx.$

On the other hand, let us recall the following consequence of the coarea formula of [Proposition 3.1.8](#), which allows to rewrite the integral of a function  $\varphi \in L^1(\omega_{S,1})$  as nested integrals over  $S$  and the interval  $(-1, 1)$ :

$$(4.5.9) \quad \int_{\omega_{S,1}} \varphi(x) \, dx = \int_{\sigma} \int_{-1}^1 (1 + t\kappa(p)) \varphi(p + tn(p)) \, dt \, ds(p).$$

The inner minimization problem in [\(4.5.8\)](#) can be solved approximately, by following the intuition that the second integral in the definition of  $G(v)$  should be minimized in priority, as its bears the stronger weight. Writing down the Euler-Lagrange equation, an approximate minimizer  $\hat{v}$  for this problem should be such that:

$$t \mapsto \hat{v}(p + tn(p)) \text{ is affine.}$$

Using the transmission conditions encoded in the definition [\(4.5.7\)](#) of the space  $\tilde{V}$ , we obtain that:

$$\hat{v}(p + tn(p)) \approx \frac{t}{2}(u^+(p) - u^-(p)) + \frac{1}{2}(u^+(p) + u^-(p)).$$

Now injecting this expression in the definition of  $G(v)$  and using [\(4.5.9\)](#), we obtain, after some calculation:

$$\begin{aligned} \min_{\substack{v(p+n(p))=u^+(p) \\ v(p-n(p))=u^-(p)}} G(v) &\approx G(\hat{v}) \\ &= \frac{\varepsilon a_\varepsilon}{3} \int_{\sigma} \left( \left( \frac{\partial u^+}{\partial \tau} \right)^2 + \left( \frac{\partial u^-}{\partial \tau} \right)^2 + \frac{\partial u^+}{\partial \tau} \frac{\partial u^-}{\partial \tau} \right) \, ds(p) + \frac{a_\varepsilon}{4\varepsilon} \int_{\sigma} (u^+(p) - u^-(p))^2 \, ds(p). \end{aligned}$$

Injecting this expression into [\(4.5.8\)](#), we obtain that the limiting behavior for  $u$  is given by the minimization problem [\(4.5.4\)](#), as desired.  $\square$

This theorem is complemented with the following result which identifies the limit of the approximate function  $u_\varepsilon^0$  in [\(4.5.4\)](#) – and thus that of the perturbed potential  $u_\varepsilon$  – when the behavior of the conductivity  $a_\varepsilon$  is known.

**Lemma 4.5.2** *Let  $a_\varepsilon$  be any sequence of positive real numbers, and let  $u_\varepsilon^0 \in V_S$  be the unique solution to the minimization problem [\(4.5.4\)](#). Let the source  $f$  have compact support inside some compact subset  $K$  of  $\Omega \setminus \overline{\mathcal{O}}$ , and suppose that both sequences  $\varepsilon a_\varepsilon$  and  $\frac{a_\varepsilon}{\varepsilon}$  have a (possibly null or infinite) limit as  $\varepsilon \rightarrow 0$ . The following five cases describe the associated limiting behaviour of  $u_\varepsilon^0$ :*

*Case 1:  $\varepsilon a_\varepsilon \rightarrow \infty$  (thus  $\frac{a_\varepsilon}{\varepsilon} \rightarrow \infty$ ). The limit of  $u_\varepsilon^0$  is  $u_\infty^\infty \in H_{c,S}^1(\Omega) := \{u \in H^1(\Omega), u = \text{cst on } S\}$ , the unique solution to the minimization problem*

$$\min_{\substack{u \in H_{c,S}^1(\Omega) \\ u=0 \text{ on } \partial\Omega}} E_\infty^\infty(u), \quad E_\infty^\infty(u) := \frac{1}{2} \int_{\Omega} \gamma_0 |\nabla u|^2 \, dx - \int_{\Omega} f u \, dx,$$

*and there exists a constant  $C$  independent of  $\varepsilon$  and  $a_\varepsilon$  such that*

$$\|u_\varepsilon^0 - u_\infty^\infty\|_{L^2(\Omega)} \leq \frac{C}{\varepsilon a_\varepsilon} \|f\|_{L^2(\Omega)}.$$

*Case 2:  $\varepsilon a_\varepsilon \rightarrow a_0$  for a certain real value  $0 < a_0 < \infty$  (thus  $\frac{a_\varepsilon}{\varepsilon} \rightarrow \infty$ ). The limit of  $u_\varepsilon^0$  is  $u_{a_0}^\infty \in H^1(\Omega) \cap V_S = \{u \in H^1(\Omega), u|_S \in H^1(S)\}$ , the unique solution to the minimization problem*

$$\min_{\substack{u \in H^1(\Omega) \cap V_S \\ u=0 \text{ on } \partial\Omega}} E_{a_0}^\infty(u), \quad E_{a_0}^\infty(u) := \frac{1}{2} \int_{\Omega} \gamma_0 |\nabla u|^2 \, dx + a_0 \int_S |\nabla_S u|^2 \, ds - \int_{\Omega} f u \, dx,$$

and there exists a constant  $C$  independent of  $\varepsilon$  and  $a_\varepsilon$  such that

$$\|u_\varepsilon^0 - u_{a_0}^\infty\|_{L^2(\Omega)} \leq C \left( \left| \frac{\varepsilon a_\varepsilon}{a_0} - 1 \right| + \left| \frac{a_0}{\varepsilon a_\varepsilon} - 1 \right| + \frac{\varepsilon}{a_\varepsilon} \right) \|f\|_{L^2(\Omega)}.$$

Case 3:  $\varepsilon a_\varepsilon \rightarrow 0$  and  $\frac{a_\varepsilon}{\varepsilon} \rightarrow \infty$ . The limit of  $u_\varepsilon^0$  is the background potential  $u_0^\infty = u_0 \in H^1(\Omega)$ , the unique solution to the minimization problem

$$\min_{\substack{u \in H^1(\Omega) \\ u=0 \text{ on } \partial\Omega}} E_0^\infty(u), \quad E_0^\infty(u) := \frac{1}{2} \int_\Omega \gamma_0 |\nabla u|^2 \, dx - \int_\Omega f u \, dx,$$

and there exists a constant  $C$  independent of  $\varepsilon$  and  $a_\varepsilon$  such that

$$\|u_\varepsilon^0 - u_0^\infty\|_{L^2(\Omega)} \leq C \left( \varepsilon a_\varepsilon + \frac{\varepsilon}{a_\varepsilon} \right) \|f\|_{L^2(\Omega)}.$$

Case 4:  $\frac{a_\varepsilon}{\varepsilon} \rightarrow b_0$  for a certain real value  $0 < b_0 < \infty$  (thus  $\varepsilon a_\varepsilon \rightarrow 0$ ). The limit of  $u_\varepsilon^0$  is  $u_0^{b_0} \in H^1(\Omega \setminus S)$ , the unique solution to the minimization problem

$$\min_{\substack{u \in H^1(\Omega \setminus S) \\ u=0 \text{ on } \partial\Omega}} E_0^{b_0}(u), \quad E_0^{b_0}(u) := \frac{1}{2} \int_{\Omega \setminus S} \gamma_0 |\nabla u|^2 \, dx + \frac{b_0}{4} \int_\sigma (u^+ - u^-)^2 \, ds - \int_\Omega f u \, dx,$$

and there exists a constant  $C$  independent of  $\varepsilon$  and  $a_\varepsilon$  such that

$$\|u_\varepsilon^0 - u_0^{b_0}\|_{L^2(\mathcal{O}^+)} + \|u_\varepsilon^0 - u_0^{b_0}\|_{L_0^2(\mathcal{O}^-)} \leq C \left( \varepsilon a_\varepsilon + \left| \frac{a_\varepsilon}{\varepsilon b_0} - 1 \right| + \left| \frac{\varepsilon b_0}{a_\varepsilon} - 1 \right| \right) \|f\|_{L^2(\Omega)},$$

where we have introduced the notation

$$\|u\|_{L_0^2(\mathcal{O}^-)} = \left\| u - \frac{1}{|\mathcal{O}^-|} \int_{\mathcal{O}^-} u \, dx \right\|_{L^2(\mathcal{O}^-)}.$$

Case 5:  $\frac{a_\varepsilon}{\varepsilon} \rightarrow 0$  (thus  $\varepsilon a_\varepsilon \rightarrow 0$ ). The limit of  $u_\varepsilon^0$  is  $u_0^0 \in H^1(\Omega \setminus S)$ , a solution to the minimization problem

$$\min_{\substack{u \in H^1(\Omega \setminus S) \\ u=0 \text{ on } \partial\Omega}} E_0^0(u), \quad E_0^0(u) := \frac{1}{2} \int_{\Omega \setminus S} \gamma_0 |\nabla u|^2 \, dx - \int_\Omega f u \, dx.$$

This solution is unique up to an additive constant on  $\mathcal{O}^-$ . There exists a constant  $C$  independent of  $\varepsilon$  and  $a_\varepsilon$  such that

$$\|u_\varepsilon^0 - u_0^0\|_{L^2(\mathcal{O}^+)} + \|u_\varepsilon^0 - u_0^0\|_{L_0^2(\mathcal{O}^-)} \leq C \left( \varepsilon a_\varepsilon + \frac{a_\varepsilon}{\varepsilon} \right) \|f\|_{L^2(\Omega)}.$$

### Remark 4.5.3

- By the elliptic regularity theory, the estimate (4.5.3) holds in higher-order Sobolev norms if  $f$  is more regular, see [Section 1.A.6](#).
- The procedure used in the proof of [Theorem 4.5.1](#) can be iterated to provide a higher-order uniform expansion of  $u_\varepsilon$ , at the expense of much more tedious calculations.
- The work presented in this section was extended in the later articles [115, 116], where the asymptotic expansion of the voltage potential is conducted in the case of an open curve  $S$  in 2d. The analysis is significantly more technical than that reported in this section.

## 4.6 THE TOPOLOGICAL LIGAMENT

As we have seen repeatedly in the course of this manuscript, two different types of sensitivity of a function  $J(\Omega)$  with respect to the domain  $\Omega$  are commonly used, and sometimes combined, in the implementation of shape and topology optimization algorithms:

- The shape derivative  $J'(\Omega)(\theta)$  of  $J(\Omega)$  is based on variations of  $\Omega$  of the form

$$\Omega_\theta := (\text{Id} + \theta)(\Omega), \text{ where } \theta \text{ is a ‘small’ vector field in } W^{1,\infty}(\mathbb{R}^d, \mathbb{R}^d).$$

It appraises the sensitivity of  $J(\Omega)$  when  $\Omega$  is perturbed by a diffeomorphism close to the identity, see [Section 1.3.3](#) and [Fig. 4.6.1](#) (b) for an illustration.

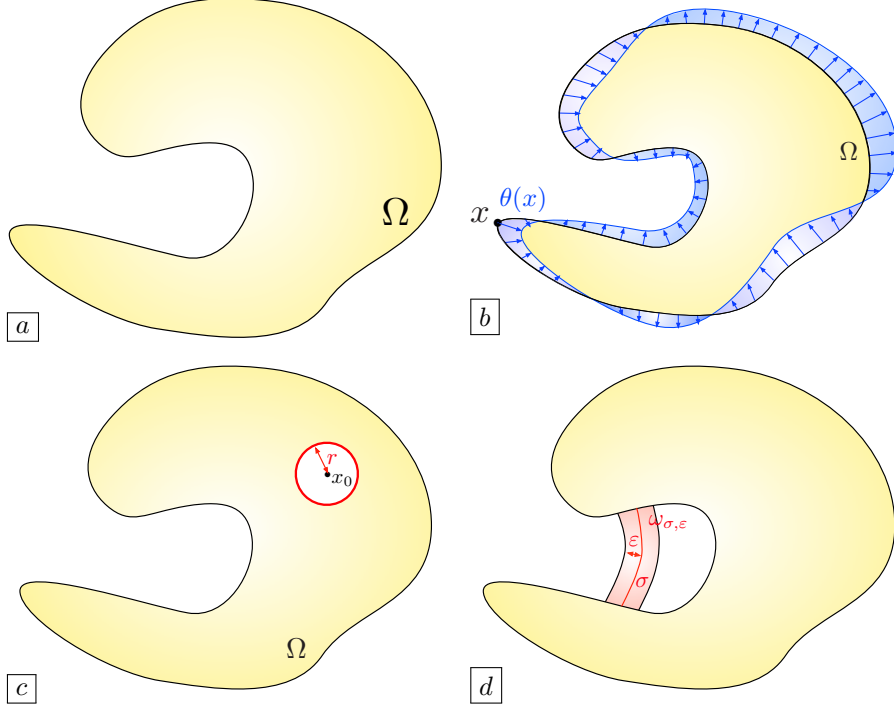


FIGURE 4.6.1. *Different types of “small” perturbations for the shape depicted on (a): (b) Boundary perturbation in the framework of Hadamard’s method; (c) Nucleation of a tiny hole near  $x_0 \in \Omega$ ; (d) Graft of a thin ligament around a base curve  $\sigma$ .*

- The topological derivative  $dJ_T(\Omega)(x)$  of  $J(\Omega)$  is based on variations of  $\Omega$  of the form

$$\Omega_{x,r} := \Omega \setminus \overline{B(x,r)}, \text{ where } x \in \Omega, \text{ and } r \ll 1.$$

It evaluates the change in the value of  $J(\Omega)$  entailed by the nucleation of an infinitesimally small hole centered at  $x \in \Omega$ , see [Section 1.3.4](#) and [Fig. 4.6.1 \(c\)](#).

Besides these prevalent notions, one third and perhaps more exotic type of sensitivity for  $J(\Omega)$  was introduced in the theory-oriented articles [\[279, 280, 281\]](#). The latter features perturbed versions  $\Omega_{\sigma,\varepsilon}$  of a shape  $\Omega$  by the graft of a thin ligament with base curve  $\sigma$  and thickness  $\varepsilon \ll 1$ , that is:

$$(4.6.1) \quad \Omega_{\sigma,\varepsilon} := \Omega \cup \omega_{\sigma,\varepsilon}, \text{ where } \omega_{\sigma,\varepsilon} := \{x \in \mathbb{R}^d, d(x, \sigma) < \varepsilon\},$$

see [Fig. 4.6.1 \(d\)](#).

This practice results in expansions of the shape functional  $J(\Omega)$  of the form

$$(4.6.2) \quad J(\Omega_{\sigma,\varepsilon}) = J(\Omega) + \varepsilon^{d-1} dJ_L(\Omega)(\sigma) + o(\varepsilon^{d-1}),$$

where the decay rate  $\varepsilon^{d-1}$  is proportional to the measure of the vanishing set  $\omega_{\sigma,\varepsilon}$  and the sign of the “topological ligament derivative”  $dJ_L(\Omega)(\sigma)$  indicates whether it is beneficial to add a thin tube  $\omega_{\sigma,\varepsilon}$  to  $\Omega$  with respect to  $J(\Omega)$ .

Unfortunately, the rigorous calculations of asymptotic expansions of the form (4.6.2) conducted in [\[280, 279, 281\]](#) are very technical and difficult to extend beyond the physical context of the conductivity equation. Furthermore, by the authors’ own admission, the practical use of the resulting formulas seems awkward.

This section is based on the work [\[A9\]](#), announced in the short note [\[A10\]](#), where an alternative strategy is proposed to add a ligament to a shape in an optimized way. The proposed method is formal, but it requires relatively few technical subtleties, and it can be used in a wide variety of physical situations, including that of mechanical structures, as described by the linear elasticity system. It leverages a formal connection with the topic of “small” inhomogeneities in asymptotic analysis, that we have broached in [Section 4.1.4](#).

We present the theoretical fundations of this method in the first [Section 4.6.1](#), before providing in [Section 4.6.2](#) three application examples and numerical illustrations of this idea in the context of mechanical structures. Interestingly, this problem of adding bars to a shape in an optimized fashion has since then fostered several contributions, based on different strategies, see [\[216, 287\]](#).

#### 4.6.1. Approximate ligament derivatives based on thin tubular inhomogeneities

In order to present our formal strategy for approximating topological ligament expansions of the form [\(4.6.2\)](#), we slip into the model context of the conductivity equation, where arguments can be exposed with a minimum amount of technicality. Let us emphasize, however, that these developments could be conducted in the context of the linear elasticity system, up to an increased level of technicality.

##### 4.6.1.1. From the graft of a thin ligament to a problem of thin tubular inhomogeneities

Let  $\Omega$  be a shape in  $\mathbb{R}^d$  ( $d = 2, 3$  in practice) accounting for a medium filled with a material whose smooth conductivity  $\gamma \in \mathcal{C}^\infty(\bar{\Omega})$  is bounded away from 0 and  $\infty$ , see [\(Ell-Cond\)](#). The potential  $u_\Omega$  inside  $\Omega$  is set to 0 on a region  $\Gamma_D \subset \partial\Omega$ , and a heat flux  $g$  is imposed on a disjoint subset  $\Gamma_N$  of  $\partial\Omega$ ; the remaining region  $\Gamma := \partial\Omega \setminus (\overline{\Gamma_D} \cup \overline{\Gamma_N})$  is free of flux, and a source  $f \in \mathcal{C}^\infty(\bar{\Omega})$  is acting inside the medium. The potential  $u_\Omega$  in this situation is the unique solution to the equation

$$(4.6.3) \quad \begin{cases} -\operatorname{div}(\gamma \nabla u_\Omega) = f & \text{in } \Omega, \\ u_\Omega = 0 & \text{on } \Gamma_D, \\ \gamma \frac{\partial u_\Omega}{\partial n} = g & \text{on } \Gamma_N, \\ \gamma \frac{\partial u_\Omega}{\partial n} = 0 & \text{on } \Gamma. \end{cases}$$

Let us also introduce a quantity of interest depending on  $\Omega$  via  $u_\Omega$ , say

$$(4.6.4) \quad J(\Omega) = \int_{\Omega} j(u_\Omega) \, dx,$$

where  $j : \mathbb{R} \rightarrow \mathbb{R}$  is a smooth function, satisfying adequate growth conditions, see [\(Growth- \$j\$ \)](#).

Our first step is to approximate this state equation by a counterpart posed inside a larger, fixed computational domain  $D$ , made of a material with conductivity  $\gamma_0$ , whose boundary is assumed to contain  $\Gamma_D$  and  $\Gamma_N$  for simplicity:

$$(4.6.5) \quad \begin{cases} -\operatorname{div}(\gamma_0 \nabla u_0) = f & \text{in } D, \\ u_0 = 0 & \text{on } \Gamma_D, \\ \gamma_0 \frac{\partial u_0}{\partial n} = g & \text{on } \Gamma_N, \\ \gamma_0 \frac{\partial u_0}{\partial n} = 0 & \text{on } \partial D \setminus (\overline{\Gamma_D} \cup \overline{\Gamma_N}). \end{cases}$$

We have denoted the solution to this problem  $u_0 \in H_{\Gamma_D}^1(D)$  as a reference to the asymptotic analysis framework discussed in [Section 4.1.4](#). Roughly speaking, the problem [\(4.6.5\)](#) is a generalization of [\(4.6.3\)](#) in the sense that when  $\gamma_0$  is defined as (a smoothed version of) the function

$$\forall x \in D, \quad \gamma_0(x) = \begin{cases} \gamma & \text{if } x \in \Omega, \\ \eta\gamma & \text{otherwise,} \end{cases} \quad \text{for a small ‘ersatz’ parameter } \eta \ll 1,$$

the ersatz material method described in [Section 1.2.1.3](#) ensures that  $u_0$  is a close approximation of  $u_\Omega$ .

We next consider the following perturbed version of [\(4.6.5\)](#):

$$(4.6.6) \quad \begin{cases} -\operatorname{div}(\gamma_\varepsilon \nabla u_\varepsilon) = f & \text{in } D, \\ u_\varepsilon = 0 & \text{on } \Gamma_D, \\ \gamma_\varepsilon \frac{\partial u_\varepsilon}{\partial n} = g & \text{on } \Gamma_N, \\ \gamma_\varepsilon \frac{\partial u_\varepsilon}{\partial n} = 0 & \text{on } \Gamma, \end{cases} \quad \text{where } \gamma_\varepsilon(x) = \begin{cases} \gamma_1(x) & \text{if } x \in \omega_{\sigma, \varepsilon}, \\ \gamma_0(x) & \text{otherwise.} \end{cases}$$

Intuitively, if [\(4.6.5\)](#) is an ersatz material approximation of [\(4.6.3\)](#), then [\(4.6.5\)](#) is an approximation of the version of [\(4.6.3\)](#) where a thin tube around  $\sigma$  is grafted to  $\Omega$ , see [Fig. 4.6.2](#) for an illustration of this approximation.

Let us finally consider the following approximation of  $J(\Omega_{\sigma, \varepsilon})$ :

$$(4.6.7) \quad J_\sigma(\varepsilon) := \int_D j(u_\varepsilon) \, dx,$$

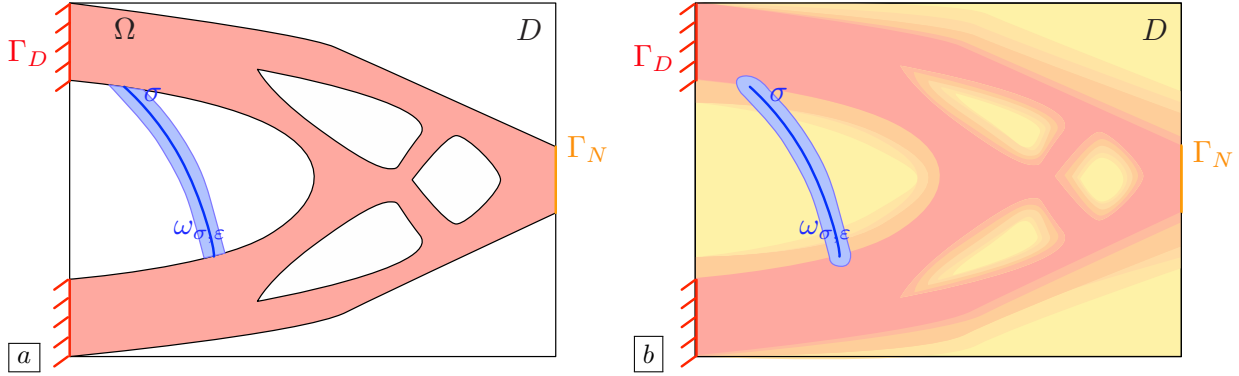


FIGURE 4.6.2. (a) Graft of a ligament with base curve  $\sigma$  to a shape  $\Omega$ ; (b) Corresponding thin tubular inclusion inside an approximating background medium occupying the hold-all domain  $D$ .

up to trading the function  $j$  in (4.6.4) for another smooth function which depends also on the spatial variable  $x$  – a technicality which is omitted for notational simplicity. We then formally replace the sought asymptotic expansion (4.6.2) of  $J(\Omega_{\sigma, \varepsilon})$  as the thickness  $\varepsilon$  of the grafted ligament vanishes by that of the approximate function  $J_\sigma(\varepsilon)$ .

From the mathematical viewpoint, the study of this last problem falls into the framework of thin tubular inhomogeneities presented in Section 4.1.4, and we expect to obtain an expansion of the form

$$(4.6.8) \quad J_\sigma(\varepsilon) = J_\sigma(0) + \varepsilon^{d-1} J'_\sigma(0) + o(\varepsilon^{d-1}),$$

where the sign and amplitude of the first non trivial term  $J'_\sigma(0)$  indicate how beneficial it is to add a thin ligament  $\omega_{\sigma, \varepsilon}$  to the shape.

**Remark 4.6.1** The approximate framework (4.6.5) to (4.6.8) for the “true” topological ligament problem (4.6.1) and (4.6.2) can easily approximate the situation where the grafted ligament  $\omega_{\sigma, \varepsilon}$  in (4.6.1) contains a material with different properties than those of  $\Omega$ , see Section 4.6.2.2 for an application.

#### 4.6.1.2. From the graft of a thin ligament to a problem of thin tubular inhomogeneities

The perturbed version (4.6.6) of the approximate background equation (4.6.5) can be analyzed by techniques pertaining to the field of asymptotic analysis, in the spirit of those recalled in Sections 4.1.4 and 4.1.5.

In the two-dimensional instance of the physical situation described in Section 4.6.1.1, the result of interest is the following.

**Theorem 4.6.2** The following expansion holds at any point  $x \in D \setminus \sigma$ :

$$(4.6.9) \quad u_\varepsilon(x) = u_0(x) + \varepsilon u_1(x) + o(\varepsilon), \text{ where } u_1(x) := \int_\sigma \mathcal{M}(y) \nabla u_0(y) \cdot \nabla_y N(x, y) d\ell(y),$$

and the remainder  $o(\varepsilon)$  is uniform when  $x$  belongs to a fixed compact subset of  $D \setminus \sigma$ . Here,  $N(x, y)$  is the Green’s function of the background operator (4.6.3) (see Section 4.1.1 about this notion), and for any point  $y \in \sigma$ , the polarization tensor  $\mathcal{M}(y)$  is a symmetric  $2 \times 2$  matrix. Its expression reads, in the local orthonormal frame  $(\tau(y), n(y))$  of  $\mathbb{R}^2$  made of a unit tangent vector  $\tau(y)$  to  $\sigma$  at  $y$  and its  $90^\circ$  counterclockwise rotate  $n(y)$ :

$$(4.6.10) \quad \mathcal{M}(y) = \begin{pmatrix} 2(\gamma_1(y) - \gamma_0(y)) & 0 \\ 0 & 2\gamma_0(y) \left(1 - \frac{\gamma_0(y)}{\gamma_1(y)}\right) \end{pmatrix}.$$

The rigorous proof of this result was achieved in [76] by using variational methods, and in [214] thanks to layer potential techniques. The asymptotic formula (4.6.9) can alternatively be obtained by a formal energy

argument, which resembles much that introduced in [Section 4.1.5](#), and exemplified in [Sections 4.3 to 4.5](#). As the implementation of the latter is fairly similar to that presented in there, we omit the details for brevity.

Asymptotic expansions of the solution to a boundary value problem when the material properties are altered within a thin inhomogeneity (in 2d) or a thin tubular inhomogeneity (in 3d)  $\omega_{\sigma,\varepsilon}$  of the form [\(4.6.1\)](#) have been considered in multiple physical situations beyond the model one reported in this section:

- In 2d linear elasticity, the (tedious) counterpart to [Theorem 4.6.2](#) was proved in [\[75\]](#).
- In the case of the 3d conductivity equation, such an asymptotic expansion was proved in [\[74\]](#) in the case where the base curve  $\sigma$  is straight, and recently, in the general case in [\[108\]](#).
- A similar analysis has been conducted in this context of the 3d Maxwell's equations in [\[108\]](#).

Interestingly, the above mentioned formal energy argument can be worked to treat all these situations, as well as some other situations where rigorous derivations are, to the best of our knowledge, unknown from the literature, and notably the crucial case of 3d elasticity.

Results like [Theorem 4.6.2](#) make it possible to calculate an approximate topological ligament expansion, thanks to a calculation similar to that presented in [Proposition 4.1.15](#).

**Corollary 4.6.3** *The approximate ligament derivative reads:*

$$J'_\sigma(0) = \int_\sigma \mathcal{M}(y) \nabla u_0(y) \cdot \nabla p_0(y) \, ds(y),$$

where the adjoint state  $p_0$  is defined as the unique solution in  $H_{\Gamma_D}^1(D)$  to the boundary value problem:

$$\begin{cases} -\operatorname{div}(\gamma_0 \nabla p_0) = -j'(u_0) & \text{in } D, \\ p_0 = 0 & \text{on } \Gamma_D, \\ \gamma_0 \frac{\partial p_0}{\partial n} = 0 & \text{on } \Gamma_N \cup \Gamma. \end{cases}$$

#### 4.6.2. Three applications of topological ligaments in structural mechanics

This section exemplifies three practical usages of the proposed approach for topological ligament derivatives.

The physical context of interest is that of mechanical structures, described by the linear elasticity system [\(Elas\)](#), see the presentation in [Section 1.2.3](#) whose notations are reused in this section. Let  $\Omega$  be a shape, contained in a fixed computational domain  $D \subset \mathbb{R}^d$ ,  $d = 2, 3$ . The optimized graft of a straight bar with base curve  $\sigma$  to  $\Omega$  with respect to a performance criterion  $J(\Omega)$  of the form [\(4.6.4\)](#) proceeds along the following trail:

- (1) Convert the physical boundary value problem [\(Elas\)](#) posed in  $\Omega$  into a two-phase elasticity problem posed in  $D$  thanks to the ersatz material method, see [\(4.6.3\)](#) and [\(4.6.5\)](#).
- (2) Calculate the ersatz material approximations  $u_0, p_0$  of the elastic displacement  $u_\Omega$  and adjoint state  $p_\Omega$ , see [\(4.6.5\)](#).
- (3) For “many” line segments  $\sigma \subset D$ , calculate the “derivative”

$$J'_\sigma(0) = \int_\sigma \mathcal{M}(y) e(u_0)(y) : e(p_0)(y) \, d\ell(y),$$

supplied by [Corollary 4.6.3](#) as an approximate measure of the sensitivity of  $J(\Omega)$  to the addition of a thin bar with direction  $\sigma$  to  $\Omega$ . Note that these computations are inexpensive, as the quantity  $J'_\sigma(0)$  features the integration over  $\sigma$  of a pre-computed integrand, so that it is reasonable to perform this task for many configurations of  $\sigma$ .

- (4) The curve  $\sigma$  with the largest negative value of  $J'_\sigma(0)$  yields the “optimal” bar to be added to  $\Omega$ .

This strategy is applied in section [Section 4.6.2.1](#) to enrich the topology of an elastic shape in the course of the shape optimization process. In [Section 4.6.2.2](#), we apply it to the design of an optimized scaffold structure for a shape to be produced by additive manufacturing. Finally, in [Section 4.6.2.3](#), we leverage this idea to provide a “clever” initial design for the optimization of a truss-like shape.

#### 4.6.2.1. Optimal graft of a ligament to a shape with poor topology

This first application of the above procedure is the original motivation for this investigation: in the course of a “classical” shape and topology optimization process based on the shape derivatives of the functionals at play, such as those presented in [Sections 1.4.6.2](#) and [1.4.7](#), it may accidentally happen that the topology of the shape becomes prematurely poor, for instance because the algorithm tries to satisfy the volume constraint “too fast”. It is then desirable to reintroduce bars into the structure in an optimized way.

To illustrate this idea, let us consider the example of the shape and topology optimization of a 3d bridge. As presented on [Fig. 4.6.4](#), the shapes are contained inside a domain  $D$  with dimensions  $4 \times 1 \times 1$ . They are clamped on the reunion  $\Gamma_D$  of four disjoint regions located on the side and bottom parts of  $\partial D$ , while a unit vertical load  $g = (0, 0, -1)$  is distributed on their upper side  $\Gamma_N$ . Starting from the initial design of [Fig. 4.6.3](#) (top, left), we solve the compliance minimization problem

$$(4.6.11) \quad \min_{\Omega} C(\Omega) \text{ s.t. } \text{Vol}(\Omega) = V_T, \text{ where } C(\Omega) := \int_{\Omega} Ae(u_{\Omega}) : e(u_{\Omega}) \, dx,$$

and the value  $V_T = 0.12$  is used for the volume constraint; the results are depicted on [Fig. 4.6.3](#).

To this end, we first rely on the combination of the level set based mesh evolution method of [Section 1.4.7](#) with the null space optimization algorithm described in [Section 3.2](#). An awkward choice of the optimization parameters provokes a rapid satisfaction of the volume constraint, so that the shape accidentally gets disconnected from two of the four clamping regions composing  $\Gamma_D$ . The resulting optimized shape in this case has a poor structural performance, see [Fig. 4.6.3](#) for several snapshots of the process.

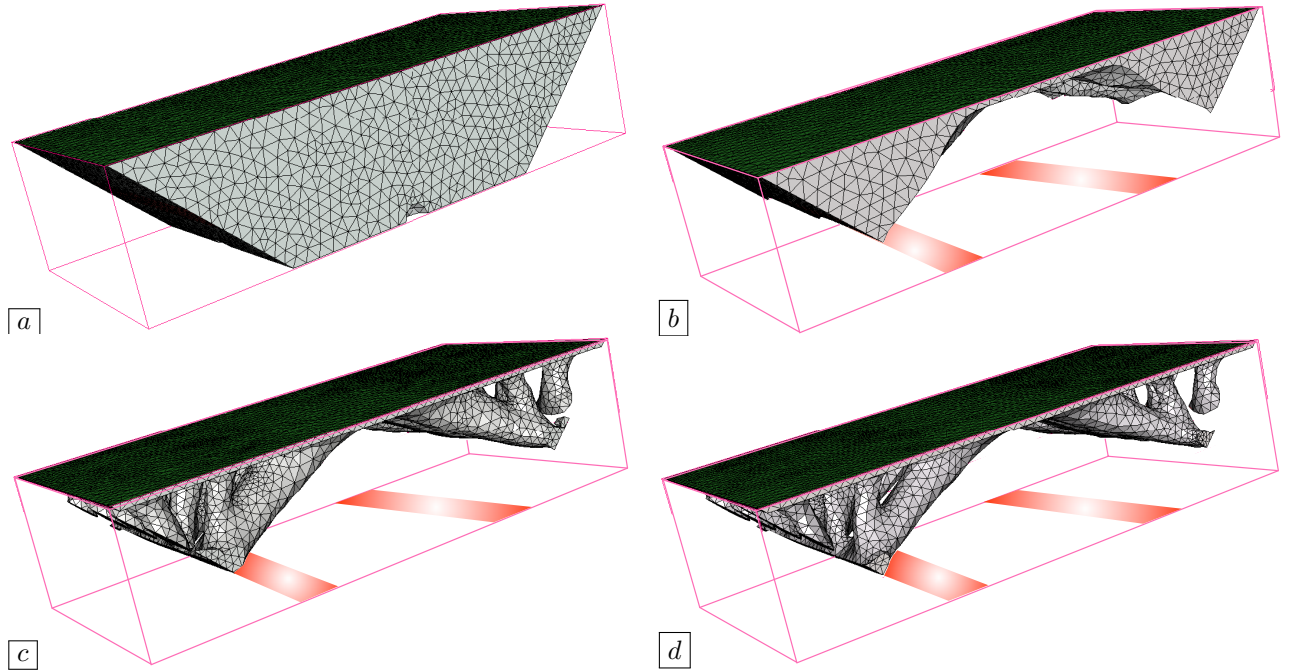


FIGURE 4.6.3. Iterations (a) 0, (b) 40, (c) 100 and (d) 200 in the 3d bridge test case of [Section 4.6.2.1](#) solved by using the level set based mesh evolution method of [Section 1.4.7](#). Due to an unfortunate choice of the parameters of the optimization algorithm, the shape gets disconnected from the clamping regions on the lower side of  $\partial D$ .

In a second time, we repeat this experiment, up to the use of our topological ligament approach: we occasionally interrupt the main procedure in [Algorithm 1](#) to try and add a bar to  $\Omega$  which connects either two points of  $\partial\Omega$ , or one point of  $\partial\Omega$  and one point on  $\Gamma_D$ . As evidenced by [Fig. 4.6.4](#), this strategy manages to detect that it is beneficial to insert bars between the shape and the isolated components of the clamping region  $\Gamma_D$ ; the optimized shape in this case has a much lower compliance value than in the previous situation.

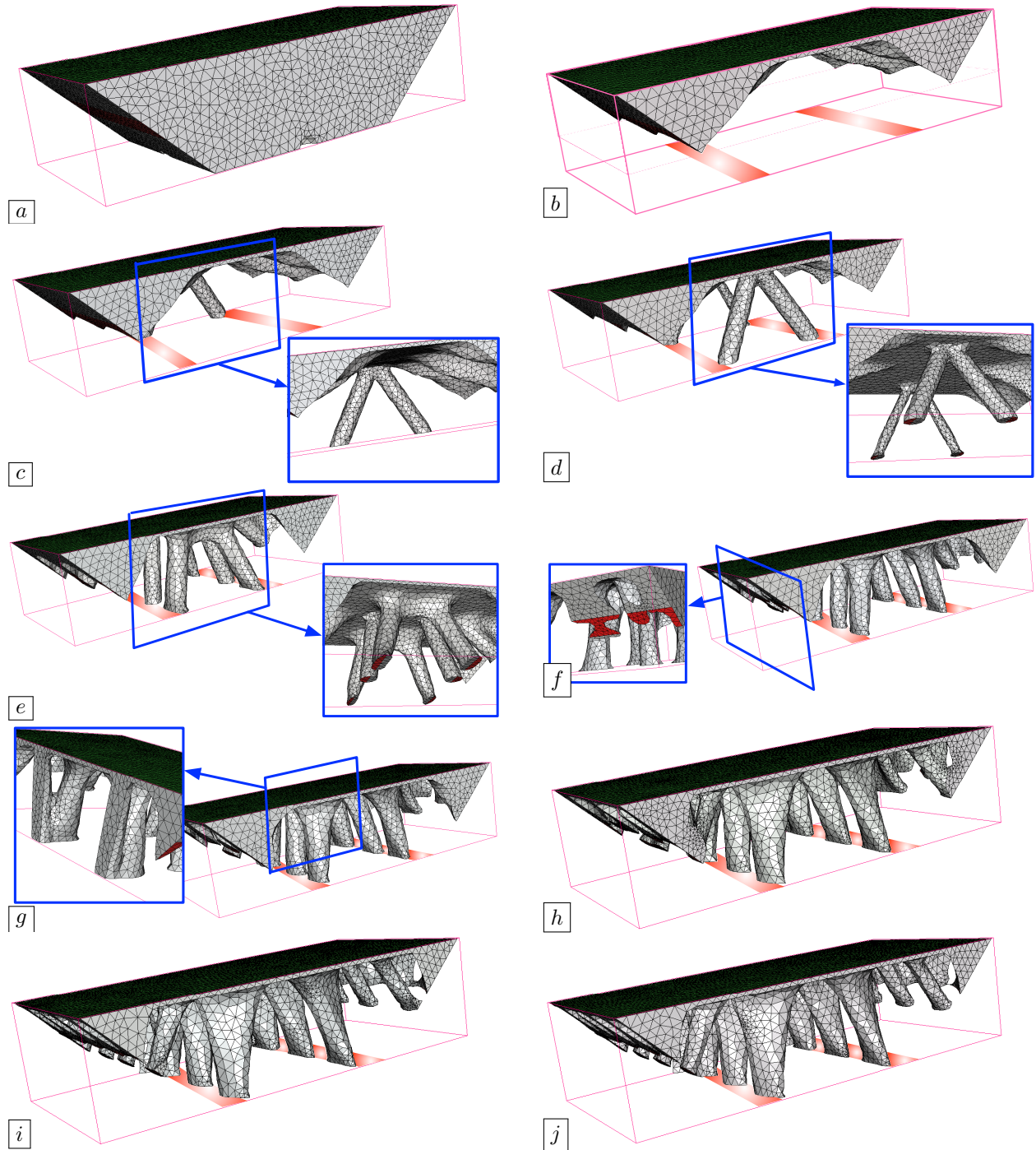


FIGURE 4.6.4. Iterations (a) 0, (b) 40, (c) 41, (d) 51, (e) 61, (f) 71, (g) 81, (h) 100, (i) 150 and (j) 200 in the 3d bridge test case of [Section 4.6.2.1](#) with occasional insertion of a bar in an optimized way.

#### 4.6.2.2. Optimization of the supporting pillar structure for additive manufacturing

We now apply our methodology to devise an optimized scaffold structure for a shape in the perspective of its construction by additive manufacturing.

As we have seen indeed in [Section 3.5.1](#), one means to cope with the presence of overhangs in a shape  $\Omega$  during its construction by an additive process consists in the simultaneous erection of a sacrificial scaffold structure  $S$  anchoring its overhang regions to the ground. Understandably enough, the relevance of this strategy requires that the scaffold structure  $S$  be itself free of overhangs.

In order to design a suitable scaffold structure  $S$  for a given shape  $\Omega$  contained in a fixed computational domain  $D \subset \mathbb{R}^d$ , let us use the simplified physical model introduced in [\[18\]](#) for the total structure  $\Omega \cup S$  during the fabrication process – note that a more involved variation of the layer-by-layer model of [Section 3.5.3](#) could alternatively be considered. The structure  $\Omega \cup S$  is clamped on the bottom part  $\Gamma_0$  of  $D$  and is submitted to gravity loads, represented by a body force  $f : \mathbb{R}^d \rightarrow \mathbb{R}^d$ . The displacement  $u_S$  of  $\Omega \cup S$  in this situation is the solution to the boundary value problem:

$$\begin{cases} -\operatorname{div} A_S e(u_S) = \rho f & \text{in } \Omega \cup S, \\ u_S = 0 & \text{on } \Gamma_0, \\ A e(u_S) n = 0 & \text{on } \partial(\Omega \cup S) \setminus \overline{\Gamma_0}, \end{cases} \quad \text{where } A_S(x) := \begin{cases} A & \text{if } x \in \Omega, \\ \eta_S A & \text{if } x \in S. \end{cases}$$

Here  $\rho$  is the density of material, which equals 1 inside the structure  $\Omega$ , and 0 inside the supports for simplicity. The parameter  $\eta_S$  characterizing the elastic behavior of the material in  $S$  is  $\eta_S = 0.4$ .

A suitable scaffold structure  $S$  for  $\Omega$  is obtained by solving the following shape optimization problem:

$$(4.6.12) \quad \min_{S \subset D} \operatorname{Vol}(S) \text{ s.t. } C(S) \leq C_T,$$

where the compliance of the total structure  $\Omega \cup S$  during its manufacturing, defined by

$$C(S) := \int_{\Omega \cup S} A_S e(u_S) : e(u_S) \, dx = \int_{\Omega \cup S} f \cdot u_S \, dx$$

is required not to exceed the user-defined threshold  $C_T$ .

To address this problem, we leverage our topological ligament approach and proceed in two steps:

- (1) In a first stage, we start from a void scaffold structure and repeatedly use our topological ligament methodology to insert vertical bars in an optimized fashion in view of [\(4.6.12\)](#); this yields a temporary scaffold structure  $S_{\text{temp}}$  made of a collection of straight vertical pillars.
- (2) In a second stage, we solve [\(4.6.12\)](#) with the level set based mesh evolution method of [Section 1.4.7](#) to optimize further the design of  $S$ , starting from  $S_{\text{temp}}$ , expecting that the vertical features of  $S_{\text{temp}}$  lead to a “close enough” optimized design which is free of overhangs.

To illustrate this idea, we consider a 2d example where the fixed shape  $\Omega$  is the MBB Beam of [Fig. 4.6.5](#) (a). Obviously,  $\Omega$  presents large overhangs, and we solve Problem [\(4.6.12\)](#) so as to calculate a suitable support structure  $S$ , which eases its construction by additive manufacturing.

The optimized scaffold structures resulting from both stages are represented on [Fig. 4.6.5](#). Interestingly, the final design resembles much the intermediate design  $S_{\text{temp}}$  resulting from the first, bar insertion stage.

#### 4.6.2.3. An efficient initial guess in the design of truss structures

One third, natural application of our approach to topological ligaments is a “clever” initialization methodology for the optimal design of truss-like shapes, that are collections of bars. In the literature, the optimization of this type of structures is usually based on the so-called “ground structure” method [\[163\]](#). In a nutshell, the initial structure is made of a very large amount of bars, connecting all the nodes of a user-defined set. The thickness of each bar is optimized with respect to a given mechanical performance criterion, a vanishing thickness indicating that it should be removed from the structure. One obvious drawback of this optimal control formulation is that it typically features a very large number of variables, of the order of the squared number of points within the given node set.

Taking advantage of our topological ligament methodology, we propose on the contrary to initialize the design of a truss with an empty structure, and to incrementally add bars to the latter in an optimized fashion. Depending on whether the optimized structure is expected to be exactly a set of bars, or rather a continuous structure “resembling” a truss, the resulting design from this first stage may then be optimized further by using a more “classical” boundary variation algorithm, such as the level set based mesh evolution method of [Section 1.4.7](#).

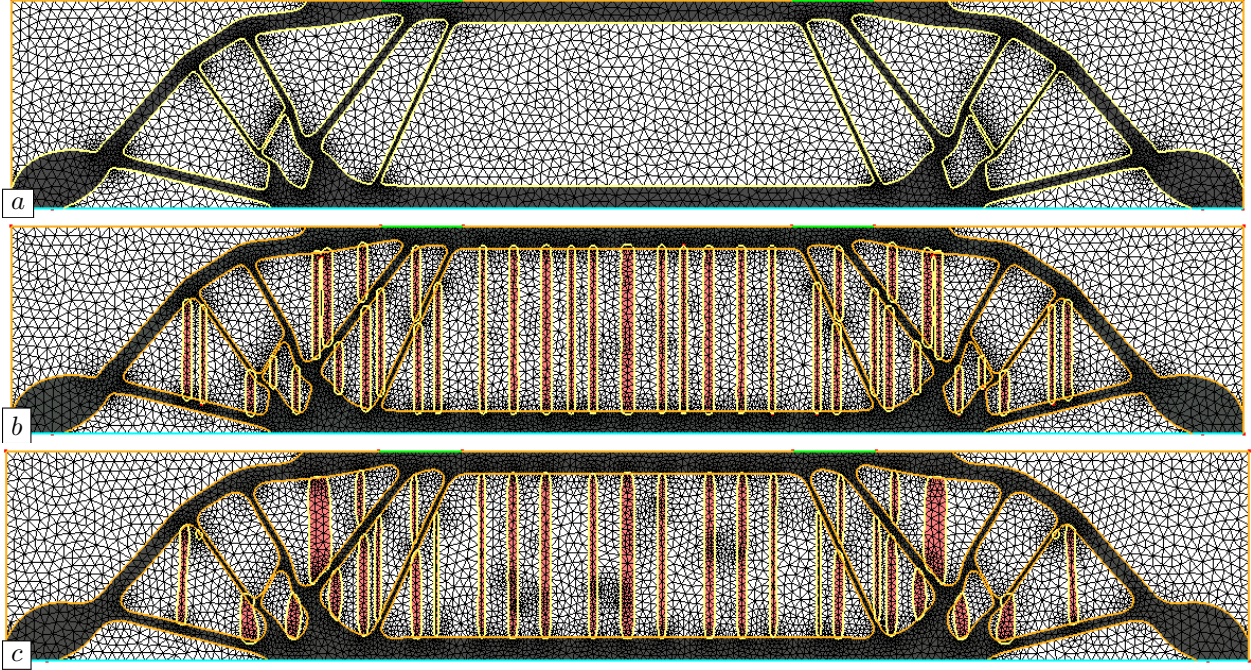


FIGURE 4.6.5. (a) Shape  $\Omega$  of an MBB Beam to be produced by additive manufacturing; (b) optimized collection of pillars  $S_{\text{temp}}$  resulting from the first stage of the scaffold optimization procedure of [Section 4.6.2.2](#) (in red); (c) optimized support structure  $S$  resulting from the second stage of this methodology.

Let us illustrate this idea with the example of a two-dimensional crane, as depicted on [Fig. 4.6.6](#) (a). The considered shapes  $\Omega$  are enclosed in a box with size  $5 \times 4$ ; two vertical loads  $g = (0, -1)$  are applied on the front and rear parts  $\Gamma_N$  of the crane, mimicking the weight of the lifted object and the counterweight, respectively. We consider the optimization problem

$$\min_{\Omega} \text{Vol}(\Omega) \text{ s.t. } C(\Omega) \leq C_T,$$

where, again,  $C(\Omega)$  is the compliance of  $\Omega$  (see [\(4.6.11\)](#)) and the value  $C_T = 120$  is used for the imposed threshold on the compliance of shapes.

We apply the proposed methodology to the resolution of this problem; several iterates of the optimization process are depicted on [Fig. 4.6.6](#). Interestingly, the optimized shape resembles very much a truss and its outline is very reminiscent of the intermediate collection of bars resulting from the first, bar insertion stage.

**Remark 4.6.4** *Multiple applications of the proposed approach to topological ligaments can be thought of beyond those discussed in the previous [Sections 4.6.2.1](#) to [4.6.2.3](#); for instance,*

- *In connection with powder-based additive manufacturing (see [Section 3.5.1](#) for a brief presentation), this approach could be used to optimize the path of the laser in charge of fusing the processed metallic powder, in order to e.g. evacuate heat as fast as possible; we refer to [\[81, 82\]](#) for further details about this question, where a totally different method is used.*
- *Adapting the present work to the mathematical setting of the Stokes equations from fluid mechanics would allow to design the outline of the channels conveying the refrigerating liquid within molds, in an optimized way with respect to the cooling of the molten material. These intrinsically take the form of tubes, whose base curves may not be straight segments; see for instance [\[382\]](#) and the references therein for more details about this so-called conformal cooling problem.*

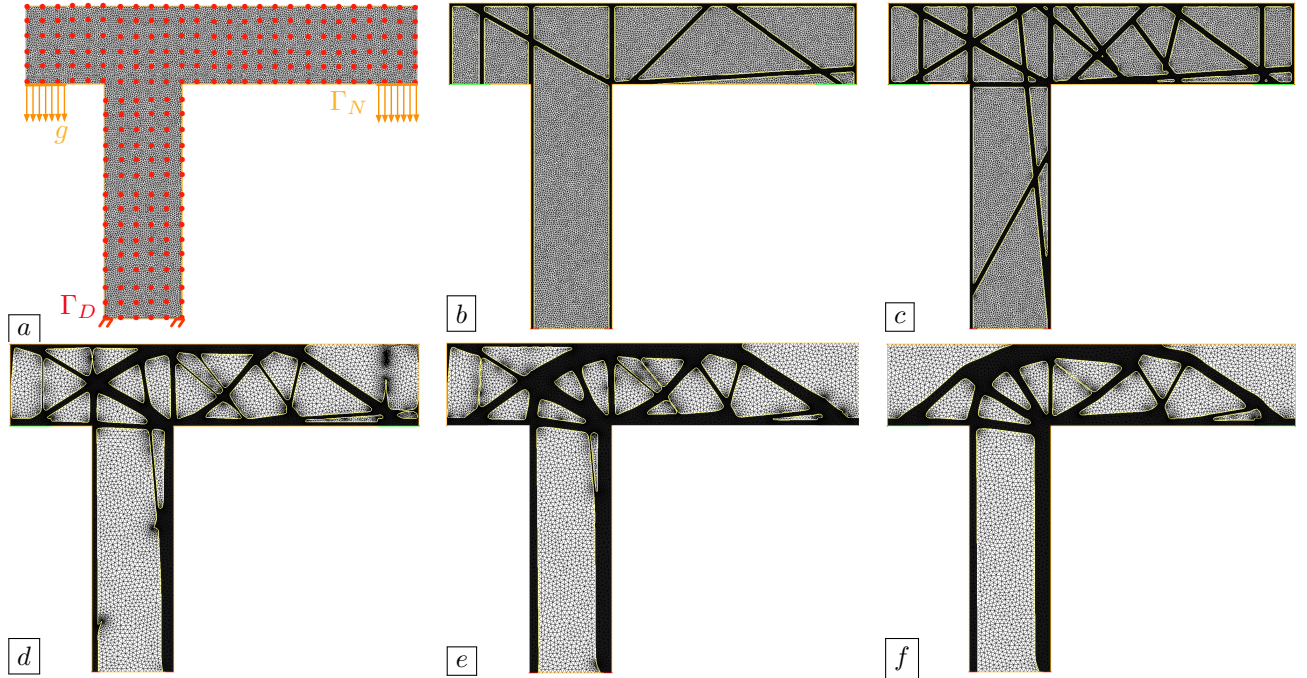


FIGURE 4.6.6. (Top row) Iterations (a) 0 (with details of the test-case), (b) 4 and (c) 9 of the first phase; (bottom row) Iterations (d) 11, (e) 91 and (f) 200 of the second phase in the crane optimization example with design of a truss-like initial guess, as considered in Section 4.6.2.3.

## 4.7 A FEW PERSPECTIVES ABOUT ASYMPTOTIC ANALYSIS

The work reported in this chapter suggests diverse, enthralling leads for future investigations. We sketch in Section 4.7.1 two rather theoretical questions inspired by Section 4.5, devoted to the search for asymptotic expansions of solutions to perturbations of boundary value problems in a way which is uniform with respect to a parameter entering its definition. Perhaps closer to concrete applications and motivated by the strong interplay between asymptotic analysis and shape and topology optimization, we outline in Section 4.7.2 how the results of Sections 4.3 and 4.4 can serve to construct a very general optimization strategy of the shape and topology of the regions bearing the boundary conditions of a physical problem, applicable to realistic situations in terms of the geometry of the domain, and challenging physical contexts such as those of mechanical structures or acoustics. We eventually describe in Section 4.7.3 a problem motivated by fracture mechanics, dealing with the asymptotic analysis of the solution to the conductivity equation with respect to the onset of a “small” crack near the boundary of the defining domain.

### 4.7.1. Uniform replacements of solutions to parameter dependent boundary value problems

Most investigations related to asymptotic analysis take place in physical situations where the boundary value problem depends on a parameter  $a$  in addition to the vanishing parameter  $\varepsilon$  labeling the asymptotic regime under scrutiny; symbolically, let us write such as problem by:

$$\text{Search for } u_{\varepsilon,a} \text{ s.t. } \mathcal{F}(\varepsilon, a, u_{\varepsilon,a}) = 0.$$

For instance, in the model situation of Section 4.5,  $\mathcal{F}(\varepsilon, a, u) = -\operatorname{div}(\gamma_\varepsilon \nabla u)$ , where the conductivity  $\gamma_\varepsilon$  equals  $a$  inside  $\omega_\varepsilon$  and coincides with the background conductivity  $\gamma_0$  outside  $\omega_\varepsilon$ .

The asymptotic behavior of  $u_{\varepsilon,a}$  as  $\varepsilon$  vanishes depends, sometimes dramatically, on the parameter  $a$ . For instance, we have seen in Lemma 4.5.2 that if  $\omega_\varepsilon$  is a thin inclusion, of the form (4.1.18), the very limit of  $u_{\varepsilon,a}$  as  $\varepsilon \rightarrow 0$  depends on  $a$ . In such cases, it is interesting to look for a uniform replacement (not necessarily

a limit) for the mapping  $\varepsilon \mapsto u_{\varepsilon,a}$  as  $\varepsilon \rightarrow 0$ , i.e. a function  $\widetilde{u_{\varepsilon,a}}$  with a “simple expression” satisfying

$$u_{\varepsilon,a} - \widetilde{u_{\varepsilon,a}} \xrightarrow{\varepsilon \rightarrow 0} 0 \text{ uniformly with respect to } a.$$

The knowledge of such a “simple replacement”  $\widetilde{u_{\varepsilon,a}}$  usually sheds light on the different regimes for  $u_{\varepsilon,a}$  at the limit  $\varepsilon \rightarrow 0$  and on the transitions between them.

We describe below two situations where such investigations could be relevant.

#### 4.7.1.1. Vanishing inclusions with arbitrary conductivity

Let us get back to the model physical situation considered in [Section 4.5](#). Inside a smooth bounded domain  $\Omega \subset \mathbb{R}^d$  ( $d = 2$  or  $3$ ), made of a material with conductivity  $\gamma_0 \in \mathcal{C}^\infty(\overline{\Omega})$ , the “background” potential  $u_0$  induced by a source  $f \in \mathcal{C}^\infty(\overline{\Omega})$  is the unique solution in  $H_0^1(\Omega)$  to the conductivity equation

$$\begin{cases} -\operatorname{div}(\gamma_0 \nabla u_0) = f & \text{in } \Omega, \\ u_0 = 0 & \text{on } \partial\Omega. \end{cases}$$

In a perturbed situation, the constituent material of  $\Omega$  is replaced by another material with conductivity  $a_\varepsilon$  within a “small” subset  $\omega_\varepsilon \Subset \Omega$ , and the potential  $u_\varepsilon$  is the unique solution in  $H_0^1(\Omega)$  to the equation:

$$\begin{cases} -\operatorname{div}(\gamma_\varepsilon \nabla u_\varepsilon) = f & \text{in } \Omega, \\ u_\varepsilon = 0 & \text{on } \partial\Omega, \end{cases} \quad \text{where } \gamma_\varepsilon(x) = \begin{cases} a_\varepsilon & \text{if } x \in \omega_\varepsilon, \\ \gamma_0(x) & \text{if } x \in \Omega \setminus \overline{\omega_\varepsilon}. \end{cases}$$

At a fixed index  $\varepsilon$ , the conductivity  $a_\varepsilon$  inside  $\omega_\varepsilon$  is homogeneous (i.e. it is constant with respect to the space variable); it is bounded away from  $0$  and  $\infty$ , i.e.  $0 < a_\varepsilon < \infty$ , but contrary to the situation considered in [Section 4.1.4](#) (and like in [Section 4.5](#)), its value depends on  $\varepsilon$ , and it may degenerate to  $0$  or  $\infty$  as  $\varepsilon \rightarrow 0$ .

A minor modification of the analysis conducted in [Section 4.1.4](#) reveals that when  $a_\varepsilon$  remains bounded away from  $0$  and  $\infty$  as  $\varepsilon$  tends to  $0$ , the perturbed potential  $u_\varepsilon$  still converges to  $u_0$  and the representation formula of [Theorem 4.1.11](#) stays valid (with the conductivity  $\gamma_1$  inside  $\omega_\varepsilon$  being replaced by  $a_\varepsilon$ ). However, when  $a_\varepsilon$  degenerates to  $0$  and  $\infty$ , the situation is far from being so clear. Indeed, it is shown in [283] that when the inclusion  $\omega_\varepsilon$  is diametrically small, i.e. of the form [\(4.1.17\)](#), the properties that we have just mentioned hold regardless of the behavior of  $a_\varepsilon$ . However, when the inclusion  $\omega_\varepsilon$  is thin, see [\(4.1.18\)](#), such is not the case, and we have seen in [Section 4.5](#) that  $u_\varepsilon$  converges to  $u_0$  as  $\varepsilon \rightarrow 0$  if and only if:

$$\varepsilon a_\varepsilon \xrightarrow{\varepsilon \rightarrow 0} \text{and } \frac{\varepsilon}{a_\varepsilon} \xrightarrow{\varepsilon \rightarrow 0} 0.$$

Recently, in the article [109], a sufficient condition is given in terms of the conductivity  $a_\varepsilon$  and the arbitrarily shaped inclusion  $\omega_\varepsilon$  so that the convergence  $u_\varepsilon \rightarrow u_0$  and the asymptotic expansion in [Theorem 4.1.11](#) stay valid: essentially,

$$\left( a_\varepsilon + \frac{1}{a_\varepsilon} \right) |\omega_\varepsilon| \xrightarrow{\varepsilon \rightarrow 0} 0.$$

This condition is however not sharp: as we have just seen, it is too restrictive in the case of a diametrically small inclusion.

The previous studies suggest that the convergence of  $u_\varepsilon$  to  $u_0$  might be conditioned by a more intricate measure of “capacity” of the inclusion  $\omega_\varepsilon$ , which would depend on its aspect, size, possibly in strong connection with the conductivity  $a_\varepsilon$  inside  $\omega_\varepsilon$ . Together with Y. Capdebocq and M. Vogelius, we conjecture that a careful extension of the proof of [Theorem 4.1.11](#) might allow to deal with the more general situation considered in this section. More precisely, analyzing the exact formula [\(4.1.28\)](#) for the error  $r_\varepsilon(x) = u_\varepsilon(x) - u_0(x)$  resulting from the compensated compactness argument, we expect to identify sharp sufficient conditions for the convergence to  $0$  of the main term and the relatively faster decay of the remainder terms  $R_{j,\varepsilon}$  featured in this formula. In order to better identify these, it might be interesting to investigate first a representation formula for  $u_\varepsilon$  as in [Theorem 4.1.11](#) in the two “limiting cases” where the conductivity  $a_\varepsilon$  inside  $\omega_\varepsilon$  equals exactly  $0$  or  $\infty$ .

#### 4.7.1.2. Uniform asymptotic expansion in the case of replacement of boundary conditions with respect to the Robin parameter

Roughly speaking, the work broached in [Section 4.3](#) illustrates the ability of Robin boundary conditions to create a “smooth transition” between a homogeneous Dirichlet and a homogeneous Neumann boundary conditions. For instance, let us consider the situation of [Section 4.4](#): the potential  $u_0$  is the unique solution in  $H_{\Gamma_D}^1(\Omega)$  to the mixed boundary value problem

$$(4.7.1) \quad \begin{cases} -\operatorname{div}(\gamma \nabla u_0) = f & \text{in } \Omega, \\ u_0 = 0 & \text{on } \Gamma_D, \\ \gamma \frac{\partial u_0}{\partial n} = 0 & \text{on } \Gamma_N, \end{cases}$$

where  $\gamma \in \mathcal{C}^\infty(\overline{\Omega})$  and  $f \in \mathcal{C}^\infty(\overline{\Omega})$ .

We consider a perturbed problem where the Neumann boundary condition is replaced by a Robin boundary conditions with parameter  $k_\varepsilon$  on a “small” Lipschitz subset  $\omega_\varepsilon \Subset \Gamma_N$ :

$$(4.7.2) \quad \begin{cases} -\operatorname{div}(\gamma \nabla u_\varepsilon) = f & \text{in } \Omega, \\ u_\varepsilon = 0 & \text{on } \Gamma_D, \\ \gamma \frac{\partial u_\varepsilon}{\partial n} + k_\varepsilon u_\varepsilon = 0 & \text{on } \omega_\varepsilon, \\ \gamma \frac{\partial u_\varepsilon}{\partial n} = 0 & \text{on } \Gamma_N \setminus \overline{\omega_\varepsilon}. \end{cases}$$

For a given level of perturbation  $\varepsilon$ ,  $k_\varepsilon$  takes a given, positive real value: formally, taking  $k_\varepsilon = 0$  yields  $u_\varepsilon = u_0$ , while, on the other hand,  $k_\varepsilon = \infty$  formally transforms (4.7.2) into the perturbed version of (4.7.1) where the homogeneous Neumann condition is replaced with a homogeneous Dirichlet condition on  $\omega_\varepsilon$ , as we have addressed in [Section 4.4](#).

It was proved in [\[237, 238\]](#) that when  $k_\varepsilon = k$  is independent of  $k_\varepsilon$ , the value of the perturbed potential  $u_\varepsilon(x)$  in (4.7.2) at some point  $x$  “far” from the set  $\omega_\varepsilon$  converges to  $u_0(x)$  with a rate equal to the surface measure of  $\omega_\varepsilon$ . On the other hand, we have seen that such is not the case in the formal limit  $k_\varepsilon = \infty$ , that is, when Robin boundary condition are replaced with Dirichlet conditions in (4.7.2), where the convergence rate equals  $\operatorname{cap}(\omega_\varepsilon)$ , see [Theorems 4.4.2](#) and [4.4.6](#).

It would be interesting to have an asymptotic replacement of  $u_\varepsilon$  with respect to the Robin parameter  $k_\varepsilon$ , which would allow to understand this change in the convergence rate of the perturbed to the background potential.

#### 4.7.2. Shape and topology optimization of the regions bearing boundary conditions

The investigations conducted in [Sections 4.3](#) and [4.4](#) deal with the asymptotic analysis of the solution to a boundary value problem under regular and singular perturbations of the regions bearing boundary conditions, respectively.

The range of the numerical applications of this line of work has been pretty limited so far: we have hiterto considered the optimization of such regions with respect to regular perturbations, that is, in the framework of Hadamard’s method, see [Section 4.3](#). Moreover, the simulations performed in there are limited to the case where the optimized regions lie in a flat portion of  $\partial\Omega$ , for lack of availability of numerical methods for the main operations involved in the practice of the level set method in the context where the ambient medium is a surface.

These considerations suggest an interesting line of research about the extension of the level set based mesh evolution method presented in [Section 1.4.7](#) to deal with the optimization of the shape and topology of regions bearing boundary conditions by coupling shape and topological sensitivity information as in [Section 1.4.8.1](#) in the case of 2d and 3d domains. This issue is currently under scrutiny in the context of the Ph.D. thesis of C. Brito-Pacheco (co-advised with E. Bonnetier and R. Estevez), and the main bottlenecks are the following:

- One needs to extend the algorithms dedicated to the main stages in the practice of the level set method to the case where the ambient medium is a triangulation of a 3d surface, and notably, the calculation of the signed distance function (see [Section 1.4.7.1](#)), the solution of the level set evolution equation (see [Section 1.4.7.2](#)) and the remeshing operations discussed in [Section 1.4.7.3](#).

This extension was recently achieved, paving the way to the application of the numerical methods of [Section 4.3](#) on a curved surface, see [Fig. 4.7.1](#) for a preliminary example.

- From the theoretical point of view, an approximate calculation of the sensitivity of a function with respect to regular perturbations of regions supporting boundary conditions, as in [Section 4.3](#), is already available in multiple physical situations of interest, and notably in the case of the linear elasticity system, see [Section 4.3.6.1](#). On the contrary, the singular expansions of the solutions to perturbed boundary value problems by the replacement of boundary conditions on small subsets developed in [Section 4.4](#) are unknown beyond the case of the conductivity equation. We wish to extend these studies to the cases of the Helmholtz equation and the linear elasticity system.

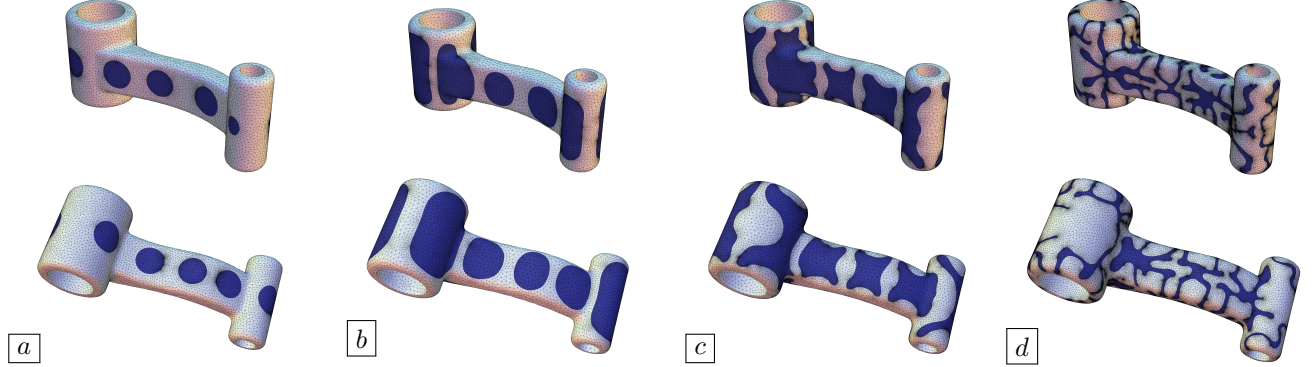


FIGURE 4.7.1. Optimization of the shape of the regions  $\Gamma_D$  (in blue) and  $\Gamma_N := \partial\Omega \setminus \overline{\Gamma_D}$  (in pink) bearing homogeneous Dirichlet and Neumann boundary conditions, respectively, with respect to the mean value of the potential inside  $\Omega$ ; iterations (a) 0, (b) 10, (c) 20 and (d) 40 of the process.

#### 4.7.3. Sensitivity of the voltage potential within a domain with respect to the onset of a crack on its boundary

Another setting of interest in the field of asymptotic analysis arises when a boundary value problem undergoes a singular perturbation shaped as a small crack near the boundary of the defining domain. More precisely, let us consider the following “background” problem:

$$(4.7.3) \quad \begin{cases} -\operatorname{div}(\gamma \nabla u_0) = f & \text{in } \Omega, \\ u_0 = 0 & \text{on } \Gamma_D, \\ \gamma \frac{\partial u_0}{\partial n} = 0 & \text{on } \Gamma_N, \end{cases}$$

posed inside a smooth bounded domain  $\Omega \in \mathbb{R}^d$ , where the conductivity  $\gamma$  and the source  $f$  are smooth functions. Let  $x_0 \in \partial\Omega$  be given, and let  $\sigma$  be a “short” curve with length  $\varepsilon$  and endpoints  $x_0$  and  $x^* \in \Omega$ , accounting for a crack inside  $\Omega$ . We consider the solution  $u_\varepsilon \in H_{\Gamma_D}^1(\Omega \setminus \sigma)$  to the perturbed version of (4.7.3):

$$\begin{cases} -\operatorname{div}(\gamma \nabla u_\varepsilon) = f & \text{in } \Omega, \\ u_\varepsilon = 0 & \text{on } \Gamma_D, \\ \gamma \frac{\partial u_\varepsilon}{\partial n} = 0 & \text{on } \Gamma_N, \\ \gamma \frac{\partial u_\varepsilon}{\partial n} = 0 & \text{on } \sigma. \end{cases}$$

This model was extensively investigated in the case where the crack  $\sigma$  lies completely inside the bulk domain  $\Omega$ , see e.g. [37] in the context of the Helmholtz equation or [45] in the context of the linear elasticity system. In the present setting where the crack emerges from a point  $x_0$  on the boundary of the domain  $\Omega$ , an asymptotic analysis is conducted in [358] in the case of the 2d linear elasticity equation: a crack with homogeneous Neumann boundary conditions and with length  $\varepsilon$  is present either inside the bulk of a domain  $\Omega$ , or it is attached to one point  $x \in \partial\Omega$ . It is proposed that the resulting derivative could be used as an

indicator of the region in  $\Omega$  where the release of energy due to the onset of a crack is largest, thus indicating where this phenomenon is most likely to occur. The derivative of the elastic energy with respect to the length of the crack at  $\varepsilon = 0$  is calculated in both cases, by taking the limit of the “shape” derivative of this functional with respect to an elongation of the crack, see [289] about this method. The rigorous calculation is addressed only in the case where  $\sigma \Subset \Omega$ . The same results are derived in [36] (still in the case of a bulk crack) by an integral equation method.

Together with E. Bonnetier and M. Vogelius, we would like to revisit this problem with an integral equation method close to that introduced in [Section 4.4](#), at first in 2d to retrieve the aforementioned existing results, then in 3d where such an analysis would be new, to the best of our knowledge.

#### 4.A FUNCTIONS WITH BOUNDED VARIATIONS

In this appendix, we recall a few definitions about functions with bounded variations, which is a very convenient framework to describe “regular functions with jumps”. Our main references about this topic are [29, 48].

Let  $D$  be a bounded Lipschitz domain in  $\mathbb{R}^d$ .

**Definition 4.A.1** *A function  $u : D \rightarrow \mathbb{R}$  with bounded variations on  $D$  is a function  $u \in L^1(D)$  whose distributional gradient  $\nabla u$ , defined by:*

$$\forall \varphi \in \mathcal{C}_c^1(D, \mathbb{R}^d), \quad \langle \nabla u, \varphi \rangle := - \int_D u \operatorname{div} \varphi \, dx,$$

*is an  $\mathbb{R}^d$ -valued Borel measure on  $D$ .*

*We denote by  $BV(D)$  the space of functions with bounded variations in  $D$ .*

Note that, as in [Section 2.A](#), this definition implicitly assumes that the total variation of the measure  $\nabla u$  is bounded when  $u \in BV(D)$ , that is:

$$(4.A.1) \quad |\nabla u|(D) = \int_D |\nabla u| = \sup_{\substack{\varphi \in \mathcal{C}_c^1(D, \mathbb{R}^d) \\ \|\varphi\|_{L^\infty(D)^d} \leq 1}} \int_D u \operatorname{div} \varphi \, dx < +\infty.$$

As a result of the last fact, the integral

$$\int_D f \cdot \nabla u$$

can be defined for all continuous and bounded functions  $f \in \mathcal{C}(\overline{D})^d$ .

**Definition 4.A.2** *Let  $u \in L^1(D)$ ; the quantity  $|\nabla u|(D)$  in (4.A.1) (be it finite or infinite) is called the total variation of  $u$ ; since it is the supremum of a family of linear functionals, the mapping  $L^1(D) \ni u \mapsto |\nabla u|(D) \in \mathbb{R} \cup \{\infty\}$  is lower semi-continuous.*

The following proposition asserts that smooth functions are dense in the space  $BV(D)$ , when an adapted notion of convergence is considered on the latter space, see Th. 10.1.2 in [48].

**Proposition 4.A.3** *For any function  $u \in BV(D)$ , there exists a sequence  $u_n \in \mathcal{C}^\infty(\overline{D})$  converging to  $u$  for the intermediate convergence, that is:*

$$u_n \xrightarrow{n \rightarrow \infty} u \text{ strongly in } L^1(D), \quad \text{and} \quad \int_D |\nabla u_n| \, dx \xrightarrow{n \rightarrow \infty} \int_D |\nabla u|.$$

Like functions in the Sobolev space  $H^1(D)$ , functions with bounded variations in  $D$  possess a trace on the boundary  $\partial D$ , as asserted by the following result.

**Proposition-Definition 4.A.4** *The usual restriction operator*

$$\mathcal{C}^\infty(\overline{D}) \ni u \mapsto u|_{\partial D} \in L^1(\partial D)$$

*has a bounded extension to the space  $BV(D)$ , which we refer to as the trace operator on  $BV(D)$ .*

Moreover, the mapping  $\gamma_0 : BV(D) \rightarrow L^1(\partial D)$  is continuous when  $BV(D)$  is equipped with the topology of the intermediate convergence.

In this context, an adapted version of the Green's formula holds for functions  $u \in BV(D)$ , see [48], Th. 10.2.1:

**Proposition 4.A.5** *Let  $u \in BV(D)$ ; then for any function  $\varphi \in \mathcal{C}^1(\overline{D})^d$ , one has:*

$$(4.A.2) \quad \int_D \varphi \cdot \nabla u = - \int_D u \operatorname{div} \varphi \, dx + \int_{\partial D} \gamma_0(u) \varphi \cdot n_D \, d\mathcal{H}^{d-1}.$$

Let us denote by  $\mathcal{H}^t$  the  $t$ -dimensional Hausdorff measure on  $\mathbb{R}^d$  for any non negative real number  $t \geq 0$ . We recall that  $\mathcal{H}^{d-1}$  is simply the surface measure  $ds$  when it is restricted to the boundary  $\partial D$ , while  $\mathcal{H}^d$  coincides with the Lebesgue measure of Borel subsets of  $\mathbb{R}^d$ . The vector field  $n_D$  in (4.A.2) (or simply  $n$  when the context is clear) is the unit normal vector to  $\partial D$ , pointing outward  $D$ .

Denoting by  $\tilde{v}$  the extension by 0 to  $\mathbb{R}^d$  of a function  $v \in L^1(D)$ , the previous identity rewrites:

$$\forall \varphi \in \mathcal{C}^1(\overline{D})^d, \quad - \int_{\mathbb{R}^d} \tilde{u} \operatorname{div} \varphi \, dx = - \int_D u \operatorname{div} \varphi \, dx = \int_D \varphi \cdot \nabla u - \int_{\partial D} \gamma_0(u) \varphi \cdot n \, d\mathcal{H}^{d-1},$$

and so we have the following identity between  $\mathbb{R}^d$ -valued measures on  $\mathbb{R}^d$ :

$$(4.A.3) \quad \nabla \tilde{u} = \nabla u|_D - \gamma_0(u) n \mathcal{H}^{d-1}|_{\partial D}.$$

Close to the notion of function with bounded variations is that of set with finite perimeter, which corresponds to those sets whose characteristic functions have bounded variations. These enjoy multiple desirable properties.

**Definition 4.A.6** *A Borel subset  $E \subset D$  has (relative) finite perimeter if its characteristic function  $\mathbf{1}_E$  belongs to the set  $BV(D, \{0, 1\})$  of functions with bounded variations taking values 0 or 1.*

## 4.B A BRIEF REMINDER OF $\Gamma$ -CONVERGENCE

In this appendix, we summarize a few basic ingredients about the notion of  $\Gamma$ -convergence, which gives flexible conditions for the convergence of (quasi-)minimizers of a sequence of abstract functionals. We refer to [48], Chap. 12 and [94] for further details.

Let us first present the main notion under scrutiny:

**Definition 4.B.1** *Let  $(X, d)$  be a metric space,  $F_\varepsilon : X \rightarrow \mathbb{R} \cup \{\infty\}$  be a sequence of functions on  $X$ , and let  $F : X \rightarrow \mathbb{R} \cup \{\infty\}$  be another such function. The sequence  $F_\varepsilon$  is said to  $\Gamma$ -converge to  $F$  if the following two conditions hold at every point  $x \in X$ :*

- ( $\Gamma$ -lim inf inequality) For every sequence  $x_\varepsilon \in X$  such that  $d(x_\varepsilon, x) \rightarrow 0$ ,

$$F(x) \leq \liminf_{\varepsilon \rightarrow 0} F_\varepsilon(x_\varepsilon).$$

- ( $\Gamma$ -lim sup inequality) There exists a sequence  $x_\varepsilon \in X$  with  $d(x_\varepsilon, x) \rightarrow 0$  such that:

$$\limsup_{\varepsilon \rightarrow 0} F_\varepsilon(x_\varepsilon) \leq F(x).$$

The relevance of the notion of  $\Gamma$ -convergence comes from the next theorem, according to which any cluster point  $x^*$  of any sequence  $x_\varepsilon$  of quasi-minimizers of a  $\Gamma$ -convergent sequence of functions  $F_\varepsilon$  is a minimizer of the  $\Gamma$ -limit  $F$ .

**Theorem 4.B.2** *Let  $(X, d)$  be a metric space, and let  $F_\varepsilon : X \rightarrow \mathbb{R} \cup \{\infty\}$  be a sequence of functions which  $\Gamma$ -converges to  $F : X \rightarrow \mathbb{R} \cup \{\infty\}$ . Then,*

- (i) *Let  $x_\varepsilon \in X$  be a sequence of quasi-minimizers of  $F_\varepsilon$ , i.e. there exists a sequence of positive real numbers  $\lambda_\varepsilon$  converging to 0 such that:*

$$F_\varepsilon(x_\varepsilon) \leq \inf_{x \in X} F_\varepsilon(x) + \lambda_\varepsilon;$$

then every cluster point  $x^*$  of  $x_\varepsilon$  is a minimizer of  $F$  over  $X$ , and:

$$F(x^*) = \inf_{x \in X} F(x) = \lim_{\varepsilon \rightarrow 0} \inf_{x \in X} F_\varepsilon(x).$$

(ii) If  $G : X \rightarrow \mathbb{R} \cup \{\infty\}$  is a continuous function, then  $(G + F_\varepsilon)$   $\Gamma$ -converges to  $(G + F)$ .

The second statement is essential in applications, as many objective functions featured by optimization problems show up as the sum of a continuous function and a regularized constraint functional which  $\Gamma$ -converges to a non smooth  $\Gamma$ -limit.

Note that [Definition 4.B.1](#) of a  $\Gamma$ -convergent sequence  $F_\varepsilon$  says nothing about the existence of cluster points for sequences of quasi-minimizers. This notion is often complemented with that of equi-coercivity, which is precisely about the compactness of sequences of (quasi-)minimizers of  $F_\varepsilon$ .

**Definition 4.B.3** Let  $(X, d)$  be a metric space; a sequence of functions  $F_\varepsilon : X \rightarrow \mathbb{R} \cup \{\infty\}$  is said to be equi-coercive if from every sequence  $x_\varepsilon \in X$  such that  $\sup_\varepsilon F_\varepsilon(x_\varepsilon) < \infty$ , one can extract a subsequence  $x_{\varepsilon_j}$  which converges to an element  $x^* \in X$ .



# Chapter 5

## Shape and topology optimization in challenging physical contexts

The impressive achievements of shape and topology optimization in the historical application fields of structural mechanics and external aerodynamics have aroused the desire to deploy these techniques to larger scales and to address ever more challenging physical models, closer and closer to realistic industrial concerns.

In this chapter, we summarize several contributions dealing with the application of shape and topology optimization methods in challenging physical contexts, which are perhaps a bit more unusual in the optimal design literature, but no less important in practice. At first, in [Section 5.1](#), we consider the optimization of coupled thermal-fluid-structure systems. The next [Section 5.2](#) deals with a rather unexpected foray of shape optimization in the field of quantum chemistry, where this framework is used to model and simulate the identification of the electronic structure of a molecule. Eventually, [Section 5.3](#) is about the device of nanophotonic components, whose intricate physical behavior is governed by the Maxwell's equations.

### 5.1 SHAPE AND TOPOLOGY OPTIMIZATION OF THERMAL-FLUID-STRUCTURE INTERACTING SYSTEMS

Complex, realistic situations are often the site of several inter-dependent physical phenomena. Notably, systems governed by coupled fluid, structural and thermal effects are ubiquitous in nature: pipes, turbines, pumps and heat exchangers are only a few instances of such. As the industrial challenges are crucial, there is a wide literature devoted to the optimization of the shape and topology of such multi-physics systems. For instance, the density-based topology optimization of fluid-structure interaction systems is considered in [\[248, 376, 375\]](#); similar problems are addressed in [\[210, 209\]](#) by combining the level set method on a fixed mesh to represent the design with X-FEM or immersed boundary methods to calculate the interfacial effects at play in the physical boundary value problem. We also refer to [\[340\]](#) and the references therein for another category of numerical strategies using a binary variable representation of the design and a CAD software for generating a corresponding smooth geometric representation amenable to finite element computations. It transpires from these works that the discretization of the fluid-solid interface is the pivotal ingredient guaranteeing an accurate understanding of the behavior of the interface, and thus of the sensitivity of the optimized criterion with respect to variations of the design.

This section gathers the investigations conducted in the journal articles [\[A20, A11, A8\]](#), which are devoted to the optimization of the shape and topology of fluid-structure-thermal systems. This general framework covers several applications: convective heat transfer, featuring coupled fluid and thermal equations, where the physical response of the solid is omitted, fluid-structure interaction problems, where thermal effects are neglected, and thermoelasticity, where a single solid phase is at play, with properties depending on the temperature. We leverage the level set based mesh evolution strategy outlined in [Section 1.4.7](#) to guarantee an accurate numerical simulation of the physical equations at play.

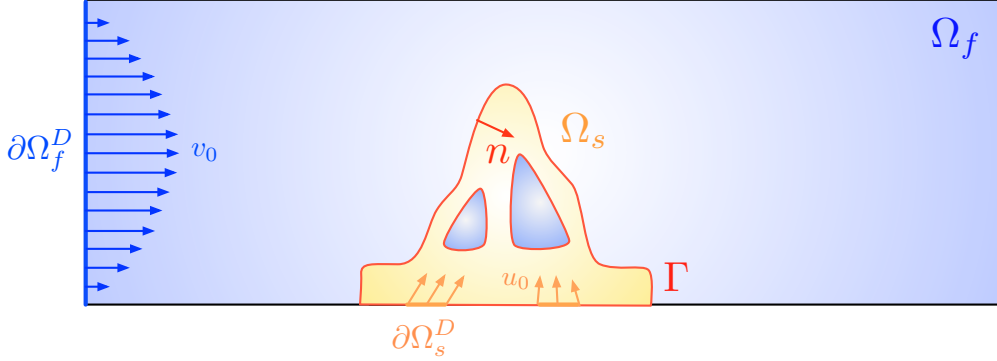


FIGURE 5.1.1. *Physical setting of the generic three-physics problem introduced in Section 5.1.1; the various regions of  $\partial D$  bearing the boundary conditions of the three physical boundary value problems are not all represented.*

The first Section 5.1.1 sets the scene of our investigations; a few details of our implementation are provided before the discussion of numerical examples in Section 5.1.2.

### 5.1.1. Presentation of the general framework

In this section, we introduce the generic setting of our investigations, variations of which will be considered in the examples of Section 5.1.2. Given a fixed “hold-all” domain  $D \subset \mathbb{R}^d$  ( $d = 2, 3$  in practice), a shape  $\Omega \subset D$  delimits a solid phase  $\Omega_s := \Omega$  and a complementary fluid phase  $\Omega_f := D \setminus \overline{\Omega_s}$ . These are separated by an interface  $\Gamma = \partial\Omega \cap D$ , whose unit normal vector field, oriented from  $\Omega_f$  to  $\Omega_s$ , is denoted by  $n : \Gamma \rightarrow \mathbb{R}^d$ , see Fig. 5.1.1 for an illustration.

Three physical phenomena are concurrently at play within  $D$ :

- (i) The motion of the fluid occupying the phase  $\Omega_f$ ;
- (ii) The diffusion of heat through the total domain  $D$ , and its convection by the fluid in the phase  $\Omega_f$ ;
- (iii) The deformation of the solid phase  $\Omega_s$  under the stress applied by the fluid, and its dilation or contraction due to thermoelastic effects.

We next describe briefly each of these problems, omitting the precise functional setting to keep the exposition at an elementary level.

The phase  $\Omega_f$  is filled with a fluid having density  $\rho$  and viscosity  $\nu$ . Its behavior is characterized by the velocity  $v_\Omega : \Omega_f \rightarrow \mathbb{R}^d$  and pressure  $p_\Omega : \Omega_f \rightarrow \mathbb{R}$ , which are the solutions to the incompressible, steady-state Navier–Stokes equations:

$$(5.1.1) \quad \left\{ \begin{array}{ll} -\operatorname{div}(\sigma_f(v_\Omega, p_\Omega)) + \rho \nabla v_\Omega \cdot v_\Omega = f_f & \text{in } \Omega_f, \\ \operatorname{div}(v_\Omega) = 0 & \text{in } \Omega_f, \\ v_\Omega = v_{\text{in}} & \text{on } \partial\Omega_f^D, \\ \sigma_f(v_\Omega, p_\Omega)n = 0 & \text{on } \partial\Omega_f^N, \\ v_\Omega = 0 & \text{on } \Gamma. \end{array} \right.$$

In the above system, the internal efforts within the fluid are described by the fluid stress tensor  $\sigma_f(v, p)$  which is related to the rate of strain tensor  $e(v) := \frac{1}{2}(\nabla v + \nabla v^T)$  via the Newton’s law:

$$\sigma_f(v, p) := 2\nu e(v) - pI,$$

where  $I$  is the  $d \times d$  identity matrix. This relation reflects the fact that the stress felt by a small volume of fluid is caused by friction effects and pressure forces from its environment. The external stresses, such as gravity, are accounted for by the body force  $f_f$ .

The system (5.1.1) features a decomposition of the boundary of the fluid phase into three disjoint regions:

$$\partial\Omega_f = \overline{\partial\Omega_f^D} \cup \overline{\partial\Omega_f^N} \cup \overline{\Gamma},$$

where

- $\partial\Omega_f^D$  is the Dirichlet, or inlet region, where the flow enters with given velocity  $v_\Omega = v_{\text{in}}$ ;
- $\partial\Omega_f^N$  is the Neumann, or outlet region, where zero normal stress is observed;
- $\Gamma$  is the interface between  $\Omega_f$  and the solid domain  $\Omega_s$ , where no-slip boundary conditions are imposed.

The velocity  $v_\Omega$  of the fluid determines the temperature  $T_\Omega$  in the total domain  $D$ , as a result of convection and diffusion effects inside the fluid domain  $\Omega_f$  and of pure diffusion inside the solid domain  $\Omega_s$ . More precisely, denoting by  $k_f$  and  $k_s$  the thermal conductivity coefficients of the fluid and solid, respectively, and by  $c_p$  the thermal capacity of the fluid,  $T_\Omega : D \rightarrow \mathbb{R}$  is the solution to the steady-state convection-diffusion equation:

$$(5.1.2) \quad \left\{ \begin{array}{ll} -\operatorname{div}(k_f \nabla T_{\Omega,f}) + \rho c_p v_\Omega \cdot \nabla T_{\Omega,f} = Q_f & \text{in } \Omega_f, \\ -\operatorname{div}(k_s \nabla T_{\Omega,s}) = Q_s & \text{in } \Omega_s, \\ T_\Omega = T_0 & \text{on } \partial\Omega_T^D, \\ -k_f \frac{\partial T_{\Omega,f}}{\partial n} = h & \text{on } \partial\Omega_T^N \cap \partial\Omega_f, \\ -k_s \frac{\partial T_{\Omega,s}}{\partial n} = h & \text{on } \partial\Omega_T^N \cap \partial\Omega_s, \\ T_{\Omega,f} = T_{\Omega,s} & \text{on } \Gamma, \\ -k_f \frac{\partial T_{\Omega,f}}{\partial n} = -k_s \frac{\partial T_{\Omega,s}}{\partial n} & \text{on } \Gamma, \end{array} \right.$$

where  $T_{\Omega,f}$  and  $T_{\Omega,s}$  are the restrictions of  $T_\Omega$  to  $\Omega_f$  and  $\Omega_s$  respectively. The temperature  $T_\Omega$  as well as the normal heat flux are continuous across the interface  $\Gamma$  between  $\Omega_f$  and  $\Omega_s$ , and volumic heat sources  $Q_f$  and  $Q_s$  are at work inside  $\Omega_f$  and  $\Omega_s$ .

This system features another decomposition of the boundary  $\partial D$ :

$$\partial D = \overline{\partial\Omega_T^N} \cup \overline{\partial\Omega_T^D}$$

into

- A Dirichlet region  $\partial\Omega_T^D$  where a temperature  $T_0$  is imposed,
- A Neumann boundary  $\partial\Omega_T^N$  where a given incoming heat flux  $h$  is applied.

The regions  $\partial\Omega_T^N$  and  $\partial\Omega_T^D$  are independent of those  $\partial\Omega_f^D$ ,  $\partial\Omega_f^N$  and  $\Gamma$  featured in (5.1.1). For instance,  $\partial\Omega_T^N$  may partially or totally overlap  $\partial\Omega_f^N$  or  $\partial\Omega_f^D$ .

Eventually, the velocity  $v_\Omega$  and pressure  $p_\Omega$  inside the fluid phase  $\Omega_f$ , together with the temperature  $T_\Omega$  within the total domain  $D$ , allow to characterize the displacement  $u_\Omega : \Omega_s \rightarrow \mathbb{R}^d$  of the solid domain  $\Omega_s$ . The latter is filled with an isotropic thermoelastic material with Lamé coefficients  $\lambda$  and  $\mu$ , thermal expansion parameter  $\alpha$ , and temperature at rest  $T_{\text{ref}}$ . Then,  $u_\Omega$  is the solution to the linear thermoelasticity system:

$$(5.1.3) \quad \left\{ \begin{array}{ll} -\operatorname{div}(\sigma_s(u_\Omega, T_{\Omega,s})) = f_s & \text{in } \Omega_s, \\ u_\Omega = u_0 & \text{on } \partial\Omega_s^D, \\ \sigma_s(u_\Omega, T_{\Omega,s})n = g & \text{on } \partial\Omega_s^N, \\ \sigma_s(u_\Omega, T_{\Omega,s})n = \sigma_f(v_\Omega, p_\Omega)n & \text{on } \Gamma, \end{array} \right.$$

where the solid stress tensor is given by

$$(5.1.4) \quad \sigma_s(u, T_s) := Ae(u) - \alpha(T_s - T_{\text{ref}})\mathbf{I} \text{ with } Ae(u) := 2\mu e(u) + \lambda \operatorname{tr}(e(u))\mathbf{I},$$

meaning that the stress applied to an elementary volume inside the structure  $\Omega_s$  is caused on the one hand by the internal mechanical forces exerted by its immediate surroundings, and on the other hand by thermal dilation (resp. contraction) effects when the temperature  $T_{\Omega,s}$  inside the material is larger (resp. lower) than  $T_{\text{ref}}$ . The term  $f_s : \Omega_s \rightarrow \mathbb{R}^d$  is an applied body force. In (5.1.3), the boundary  $\partial\Omega_s$  is decomposed as

$$\partial\Omega_s = \overline{\partial\Omega_s^D} \cup \overline{\partial\Omega_s^N} \cup \overline{\Gamma},$$

where:

- $\partial\Omega_s^D$  is equipped with a Dirichlet boundary condition, indicating that the displacement  $u_\Omega$  of the structure is imposed;
- $\partial\Omega_s^N$  is a Neumann region, where a known stress  $g$  is applied;

- $\Gamma$  is the interface with  $\Omega_f$ , where  $\Omega_s$  is subject to the pressure imposed by the fluid, the latter being given by the normal component of the fluid stress tensors:  $\sigma_f(v_\Omega, p_\Omega)n$ .

Again, this decomposition of  $\partial\Omega_s$  is independent of the decompositions of  $\partial\Omega_f$  and  $\partial D$  featured in the boundary value problems (5.1.1) and (5.1.2).

**Remark 5.1.1** *The coupling between the above three physical systems is weak, insofar as the deformation of the fluid domain is neglected: as a result there is no influence of the solid deformation  $u_\Omega$  onto the fluid variables  $(v_\Omega, p_\Omega)$ .*

In this three-physics setting, we consider a shape and topology optimization problem of the generic form

$$(5.1.5) \quad \min_{\Omega \subset D} J(\Omega) \text{ s.t. } \begin{cases} G(\Omega) = 0, \\ H(\Omega) \leq 0, \end{cases}$$

where the (real-valued) objective function  $J(\Omega)$ , the ( $\mathbb{R}^p$ -valued) equality constraint function  $G(\Omega)$  and the ( $\mathbb{R}^q$ -valued) inequality constraint function  $H(\Omega)$  depend on  $\Omega$  via the physical quantities  $v_\Omega$ ,  $p_\Omega$ ,  $T_\Omega$  and  $u_\Omega$ . The calculation of the shape derivatives of these functionals is technically tedious, but conceptually no more difficult than those considered hitherto in this manuscript, see again Section 1.3.3.5 about this issue.

## 5.1.2. Numerical examples of optimal design of three-physics systems

This section illustrates the general setting of the previous section with several concrete application instances. After the discussion of a few implementation details in Section 5.1.2.1, we present a simple 2d example in the context of linear thermoelasticity (where no fluid part is involved) in Section 5.1.2.2; a large-scale 3d optimization example of a fluid-structure system (which does not feature thermal effects) is then considered in Section 5.1.2.3. Finally, another large-scale shape and topology optimization problem is tackled in Section 5.1.2.4 – that of a heat exchanger, in which the elastic deformation of the solid part is neglected.

### 5.1.2.1. A foreword about the numerical implementation

The various instances of the shape and topology optimization problem (5.1.5) presented below are addressed by leveraging the level set based mesh evolution method of Section 1.4.7. The latter indeed makes it possible to account for arbitrarily large deformations of the phases at stake, while featuring an exact, adequately refined and high-quality mesh of them, which is the key to the accurate simulation of the fine phenomena predicted by the state equations (5.1.1) to (5.1.3), especially in the vicinity of the fluid–structure boundary  $\Gamma$ .

The calculation of a descent direction for the optimization program (5.1.5) is realized thanks to the null space algorithm of Section 3.2. In some of the considered situations, one or several constraint functionals are of a geometric nature, depending on the optimized shape  $\Omega$  via the signed distance function  $d_\Omega$ , see Section 3.1.3; then, the variational method introduced in Section 3.3 is used to calculate their shape derivatives.

The fine physical effects characterizing these three-physics systems require a large spatial resolution, so that one of the major difficulties of the considered applications lies in the size of the involved finite element systems. These large linear systems are typically solved by iterative methods, such as the conjugate gradient algorithm or GMRES, whose convergence speed critically depends on the condition number of the finite element matrices at stake. In order to improve this number, we rely on efficient preconditioning techniques based on domain decomposition strategies, which are specific to each of the physical systems at play:

- As far as the resolution of the linear thermoelasticity system (5.1.3) is concerned, we use the smooth-aggregation Geometric Algebraic Multigrid preconditioner from PETSc [6].
- When it comes to the resolution of the thermal equation (5.1.2), we use the additive Schwarz method [164] with one level of algebraic overlap and exact subdomain solvers.
- The Navier-Stokes system (5.1.1) is solved by the Newton method, with the addition of a penalization of the pressure constraint. The PETSc FieldSplit type of preconditioner is used.

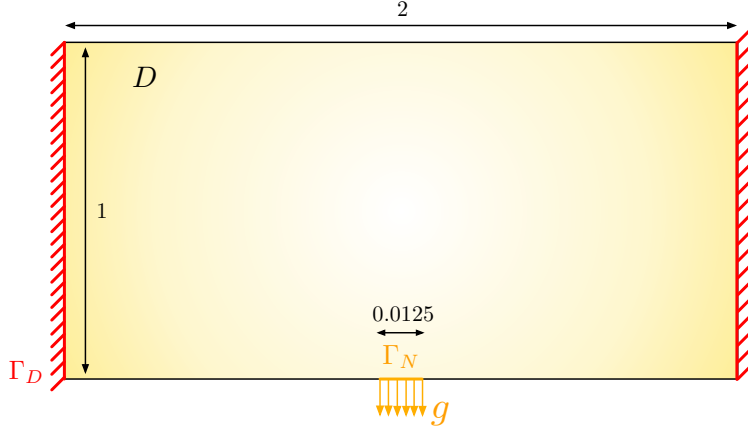


FIGURE 5.1.2. *Physical setting of the compliance minimization problem of a thermoelastic structure considered in Section 5.1.2.2.*

### 5.1.2.2. Minimum compliance problem in thermoelasticity

This first numerical example deals with the minimization of the compliance of a thermoelastic structure. The shape  $\Omega$  is contained in a fixed computational domain  $D = (0, 2) \times (0, 1)$ ; it is clamped on the left and right sides of  $\partial D$ , whose reunion is denoted by  $\Gamma_D$ , and a traction load  $g = (0, -80)$  is applied on a small region  $\Gamma_N$  with size 0.0125 centered at the middle of the bottom boundary, see Fig. 5.1.2.

The shape  $\Omega$  is filled with a thermoelastic material, characterized by the Lamé parameters  $\lambda = 11510$ ,  $\mu = 7673$ , the thermal expansion coefficient  $\alpha = 0.77$ , and the reference temperature  $T_{\text{ref}} = 0$ . In this example, the constant temperature field  $T = 5$  is imposed to the structure, causing it to expand.

The displacement  $u_\Omega$  of the shape in this setting is the solution to the linear thermoelasticity system:

$$\begin{cases} -\text{div}(\sigma_s(u_\Omega, T)) = 0 & \text{in } \Omega, \\ u_\Omega = 0 & \text{on } \Gamma_D, \\ \sigma_s(u_\Omega, T)n = g & \text{on } \Gamma_N, \\ \sigma_s(u_\Omega, T)n = 0 & \text{on } \Gamma, \end{cases}$$

where the stress tensor  $\sigma_s(u, T)$  is defined in (5.1.4).

In this setting, we solve the following compliance minimization problem:

$$\min_{\Omega \subset D} J(\Omega) \text{ s.t. } \text{Vol}(\Omega) \leq V_T, \text{ where } J(\Omega) = \int_{\Omega} A e(u_\Omega) : e(u_\Omega) \, dx,$$

and the target volume is  $V_T = 0.7$ .

The optimization results are shown on Figs. 5.1.3 and 5.1.4, which include respectively plots of a few intermediate shapes, and the mesh of the optimized design obtained at convergence.

### 5.1.2.3. A three-dimensional fluid–structure interaction test case

Our second example is concerned with a 3d fluid–structure interaction problem. The situation is depicted on Fig. 5.1.5: the computational domain is the box  $D = (0, 4) \times (0, 1) \times (0, 1)$  and the shape  $\Omega \subset D$  defines a mechanical structure  $\Omega_s = \Omega$  and a fluid region  $\Omega_f = D \setminus \overline{\Omega}$ . The behavior of the fluid is characterized by its velocity  $v_\Omega : \Omega_f \rightarrow \mathbb{R}^d$  and pressure  $p_\Omega : \Omega_f \rightarrow \mathbb{R}$ . The fluid is entering  $D$  from its left boundary  $\partial\Omega_f^D$  with known velocity  $v_{\text{in}}(x_1, x_2, x_3) = x_2 e_1$ ; a no-slip boundary condition  $v_\Omega = 0$  is prescribed on the bottom face of the domain, while the top and side faces bear a free-slip boundary condition  $v_\Omega \cdot n = 0$ . The flow exits the domain with zero normal stress, i.e.  $\sigma_f(v_\Omega, p_\Omega)n = 0$ . The mechanical structure  $\Omega_s \subset D$  represents an obstacle to the flow; it is described by its elastic displacement  $u_\Omega : \Omega_s \rightarrow \mathbb{R}^d$ , solution to the system (5.1.3) in which thermal effects are omitted and the boundary conditions are set as follows:  $\Omega_s$  is fixed on a square patch  $\partial\Omega_s^D$  of the bottom face of  $D$  (i.e. the Dirichlet boundary condition  $u_\Omega = 0$  is imposed on this region)

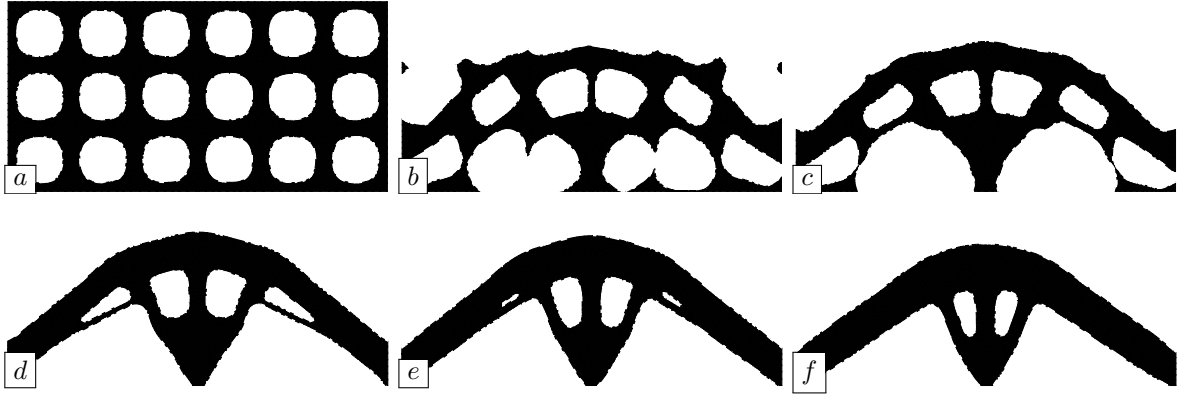


FIGURE 5.1.3. (From (a) to (f)) Intermediate shapes obtained at iterations 0, 5, 10, 30, 50 and 100 of the thermoelastic test case of [Section 5.1.2.2](#)

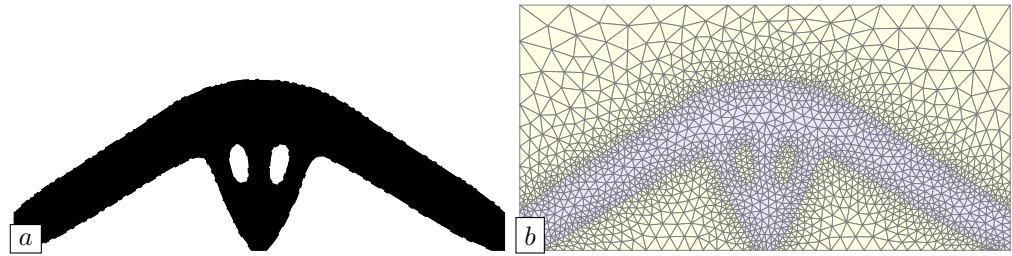


FIGURE 5.1.4. (a) Optimized design (iteration 200) in the thermoelastic test case of [Section 5.1.2.2](#); (b) Associated mesh of the computational domain  $D$ .

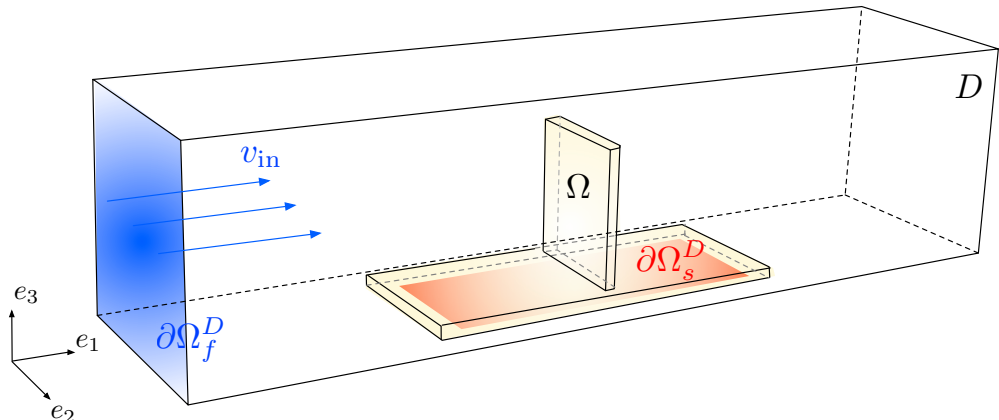


FIGURE 5.1.5. Setting of the fluid-structure interaction test case of [Section 5.1.2.3](#).

and it is subjected to the stress induced by the fluid on the complementary region  $\Gamma$  of its boundary. A vertical plate is set as a non-optimizable part of the mechanical structure, as well as a small layer above the bottom Dirichlet boundary  $\partial\Omega_s^D$ .

In this context, our goal is to optimize the shape  $\Omega_s = \Omega$  of the structure so that it be as rigid as possible, under a constraint on its volume:

$$(5.1.6) \quad \min_{\Omega} J(\Omega) \text{ s.t. } \text{Vol}(\Omega_s) = V_T, \text{ where } J(\Omega) = \int_{\Omega_s} A e(u_{\Omega}) : e(u_{\Omega}) \, dx.$$

The Reynolds number, fluid density, and viscosity are respectively set to  $\text{Re} = 60$ ,  $\rho = 1$ , and  $\nu = \rho H \|\mathbf{v}_{\text{in}}\|_{\infty} / \text{Re} = 0.012$ . The characteristic length corresponding to the height of the non-optimizable plate is  $H = 0.7$  and  $\|\mathbf{v}_{\text{in}}\|_{\infty} = 1$ . The Lamé coefficients of the mechanical structure are  $\lambda = 0.00529$  and  $\mu = 0.0476$  and the volume target equals  $V_T = 0.03\text{Vol}(D)$ .

The optimized shape resulting from the solution of (5.1.6) is depicted on Fig. 5.1.6; it features an aerodynamic profile in order to reduce the stress applied by the fluid flow.

As expected, the most computationally demanding task of the optimization process is the solution of the state equations. The finite element computations are realized in parallel on 24 processes. At the first iteration, the mesh of the computational domain  $D$  (containing an explicit discretization of the initial shape) has about 220,283 vertices, 132,775 of which lie in the fluid domain, corresponding to approximately 1.7 million degrees of freedom for each linearized fluid system. The mesh associated to the last iteration contains 82,454 vertices, 66,021 of which belong to the fluid domain.

#### 5.1.2.4. Design of a 3d heat exchanger

This last example is concerned with the design of a three-dimensional two-tube heat exchanger – a type of device which is ubiquitous in industry, see [177] for a more in-depth presentation. Here, the hold-all domain is the cube  $D = (0, 1)^3$ , and the shape optimization problem is more naturally formulated in terms of the fluid phase  $\Omega_f = \Omega$  (and so  $\Omega_s = D \setminus \overline{\Omega}$ ), see Fig. 5.1.9. The latter is composed of two disjoint channels  $\Omega_{f,\text{hot}}$  and  $\Omega_{f,\text{cold}}$ , but with a small abuse of notation, we figure the dependence of the various quantities at stake (velocity, pressure, etc) with the subscript  $\Omega$ . The cold channel is entering  $D$  with a known velocity oriented in the  $e_1$ -direction, via a disk-shaped inlet  $\partial\Omega_{f,\text{cold}}^D$  of radius  $a = 0.1$  located on the left face of  $\partial D$ ; it exits through a disk  $\partial\Omega_{f,\text{cold}}^N$  with the same radius  $a$  located on the opposite face. The hot channel  $\Omega_{f,\text{hot}}$  is flowing in the  $e_3$ -direction between similar disk-shaped input and output  $\partial\Omega_{f,\text{hot}}^D$  and  $\partial\Omega_{f,\text{hot}}^N$  located on the bottom and top faces of  $\partial D$ . The input temperatures for the hot and cold channels are  $T_{\text{hot}} = 100$  and  $T_{\text{cold}} = 0$ , and the lateral boundaries of the channels bear no-slip boundary conditions.

The physical behavior of the device is described by a weak coupling between the Navier–Stokes system (5.1.1) and the convection–diffusion equation (5.1.2) for the velocity, pressure, and temperature fields  $v_{\Omega} : \Omega_f \rightarrow \mathbb{R}^d$ ,  $p_{\Omega} : \Omega_f \rightarrow \mathbb{R}$  and  $T_{\Omega} : D \rightarrow \mathbb{R}$ .

In this setting, we aim to maximize the heat transferred from  $\Omega_{f,\text{hot}}$  to  $\Omega_{f,\text{cold}}$ . To this end, the following shape functional is minimized:

$$J(\Omega) := - \left( \int_{\Omega_{f,\text{cold}}} \rho c_p v_{\Omega} \cdot \nabla T_{\Omega} dx - \int_{\Omega_{f,\text{hot}}} \rho c_p v_{\Omega} \cdot \nabla T_{\Omega} dx \right).$$

The rationale behind this definition is the following: after integrating by parts and taking into account the boundary conditions of the problem,  $J(\Omega)$  rewrites, up to design-independent quantities:

$$\int_{\partial\Omega_{f,\text{hot}}^N} \rho c_p T_{\Omega} v_{\Omega} \cdot n ds - \int_{\partial\Omega_{f,\text{hot}}^D} \rho c_p T_{\Omega} v_{\Omega} \cdot n ds;$$

hence, minimizing  $J(\Omega)$  amounts to minimize the amount of heat leaving the computational domain  $D$  via  $\Omega_{f,\text{hot}}$  and to maximize that leaving through  $\Omega_{f,\text{cold}}$ .

This difficult example raises a few specific issues. At first, the thermal conductivity  $k_s$  of the solid phase  $\Omega_s$  is larger than that  $k_f$  of the fluid phase, and so the algorithm may accidentally find it beneficial to reduce dramatically the cross-sections of the pipes to favor the transport of heat through diffusion in the solid phase. In order to prevent this effect, it is crucial to impose two static pressure loss constraints, one for each of the channels  $\Omega_{f,\text{hot}}$  and  $\Omega_{f,\text{cold}}$ ; these write:

$$\int_{\partial\Omega_{f,\text{hot}}^D} p_{\Omega} ds - \int_{\partial\Omega_{f,\text{hot}}^N} p_{\Omega} ds \leq \text{DP}_T, \quad \text{and} \quad \int_{\partial\Omega_{f,\text{cold}}^D} p_{\Omega} ds - \int_{\partial\Omega_{f,\text{cold}}^N} p_{\Omega} ds \leq \text{DP}_T,$$

where  $\text{DP}_T$  is a prescribed threshold.

Another central issue in this example, which is typical of the design of heat exchangers, is the necessity to impose a non mixing constraint between the hot and cold channels. One possible modeling of such is based

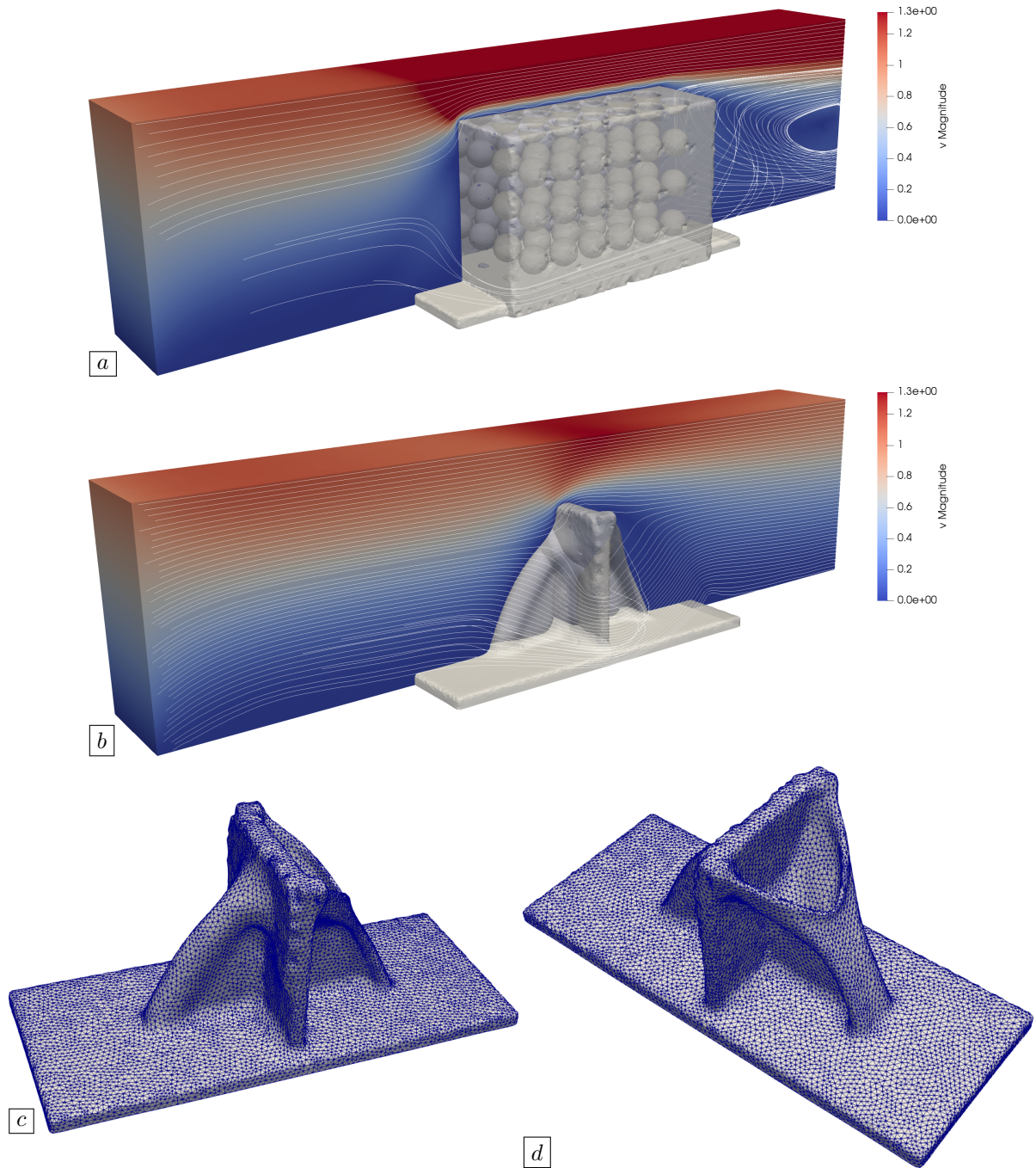


FIGURE 5.1.6. *Optimized design in the three-dimensional fluid-structure interaction example of Section 5.1.2.3; (a) Initial design; (b) Final design; (c) Front view of the optimized solid obstacle; (d) Back view of this obstacle.*

on the notion of signed distance function, recalled in Section 3.1. Mathematically, imposing that  $\Omega_{f,\text{cold}}$  stay at a distance  $d_{\min}$  from  $\Omega_{f,\text{hot}}$  writes:

$$\forall x \in \partial\Omega_{f,\text{cold}}, \quad d_{\Omega_{f,\text{hot}}}(x) \geq d_{\min}.$$

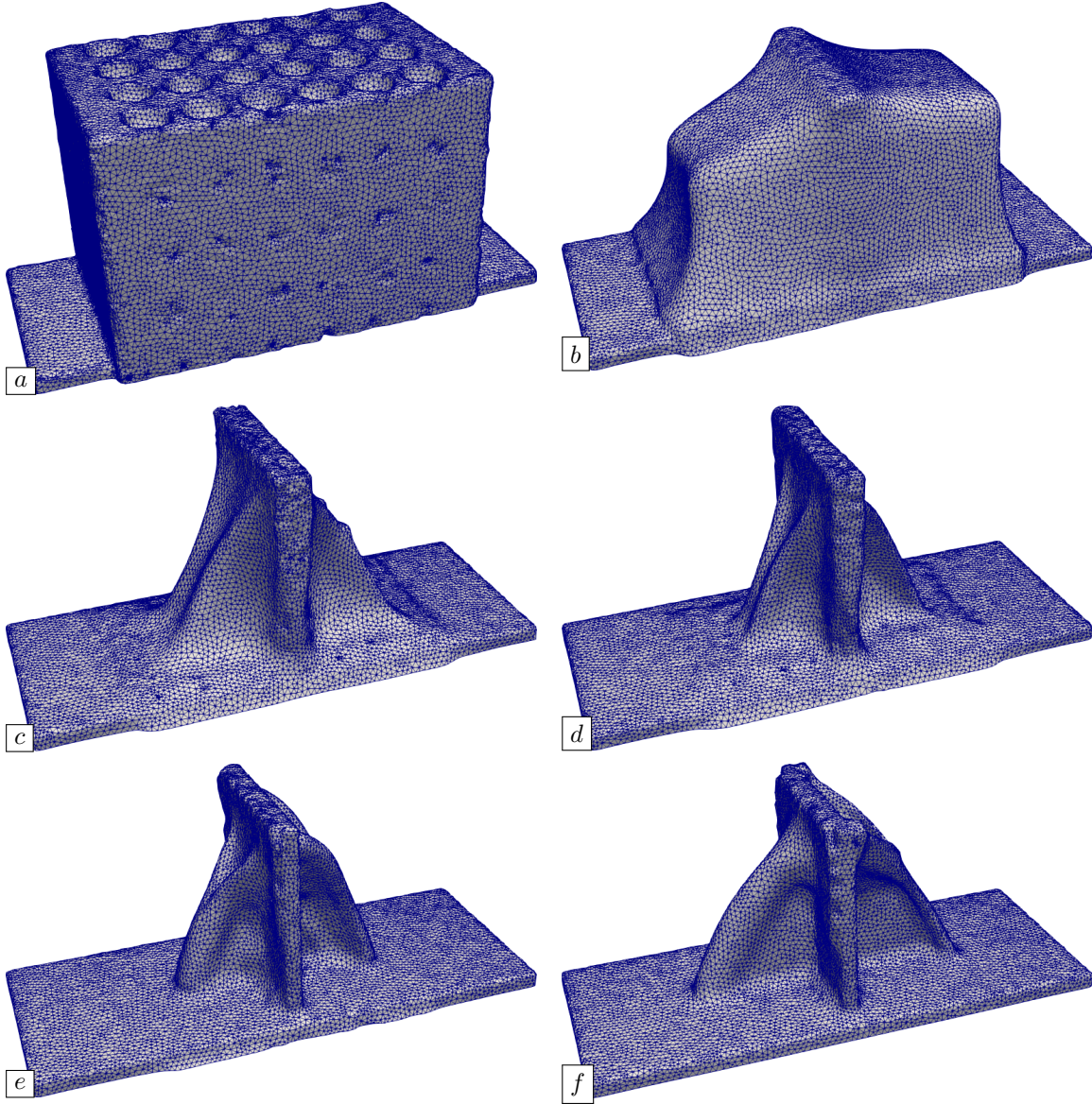


FIGURE 5.1.7. Intermediate structures at iterations (a) 0, (b) 40, (c) 100, (d) 125, (e) 175 and (f) 300 for the fluid-structure interaction test case of [Section 5.1.2.3](#).

This requirement is equivalent to the following condition:

$$\left\| \frac{1}{d_{\Omega_{f,\text{hot}}}} \right\|_{L^\infty(\partial\Omega_{f,\text{cold}})}^{-1} \geq d_{\min}.$$

In turn, this can be conveniently incorporated into the formulation of the shape and topology optimization problem via a suitable approximation of the supremum norm with a  $p$ -norm:

$$P_{\text{cold} \rightarrow \text{hot}}(\Omega) \geq d_{\min}, \text{ where } P_{\text{cold} \rightarrow \text{hot}}(\Omega) = \left( \int_{\partial\Omega_{f,\text{cold}}} \frac{1}{|d_{\Omega_{f,\text{hot}}}|^p} \, ds \right)^{-\frac{1}{p}}.$$

We choose  $p = 4$  in practice. A similar constraint functional  $P_{\text{cold} \rightarrow \text{hot}}(\Omega)$  is constructed to impose that the hot channel stay at minimum distance  $d_{\min}$  from the cold one.

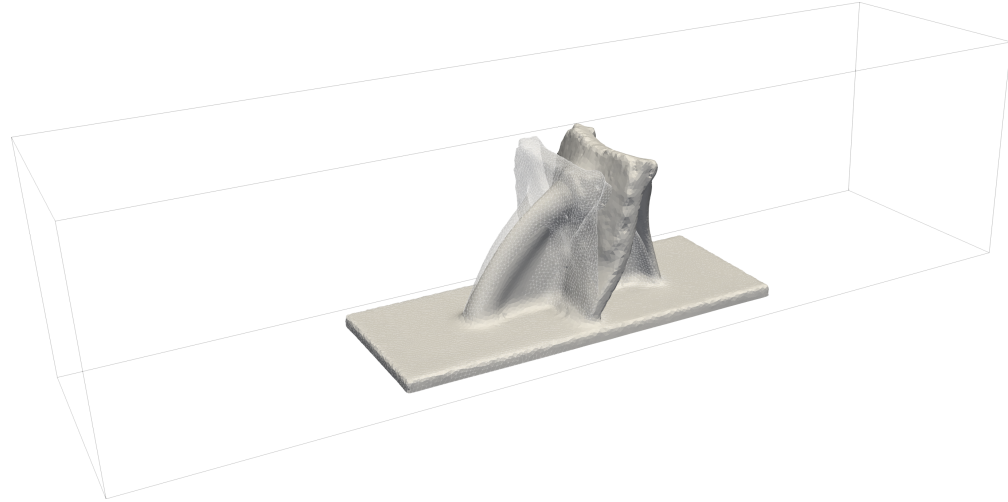


FIGURE 5.1.8. Deformed configuration of the optimized solid obstacle under the force exerted by the fluid for the test case of [Section 5.1.2.3](#).

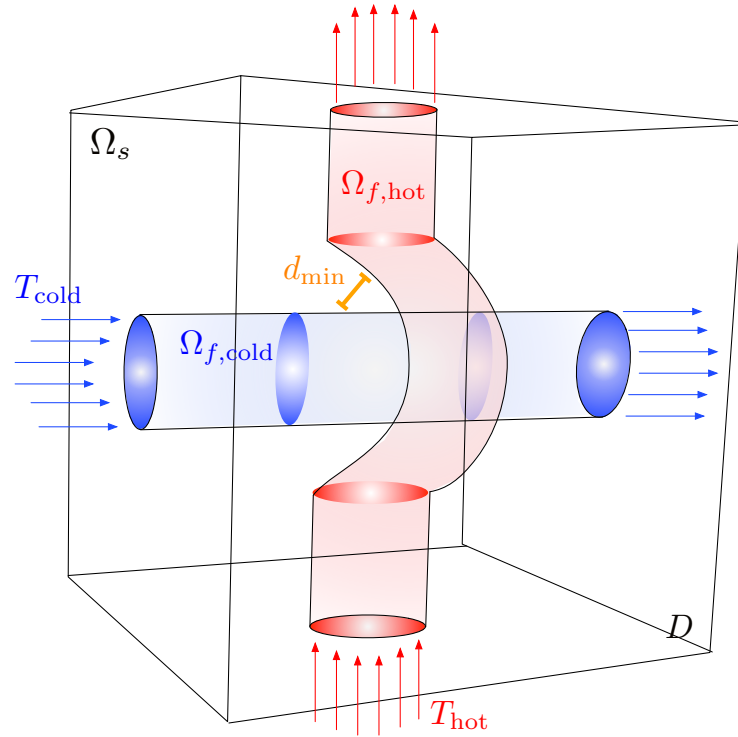


FIGURE 5.1.9. Setting of the optimal design test case of a fluid-fluid heat exchanger considered in [Section 5.1.2.4](#).

Finally, we impose that the volume of each of the two channels be lower than an imposed bound  $V_T$  in order to ensure that they be approximately balanced in mass.

All things considered, the optimal design problem of interest reads:

$$\min_{\Omega \subset D} J(\Omega) \quad \text{s.t.} \quad \left\{ \begin{array}{l} \text{Vol}(\Omega_{f,\text{hot}}) \leq V_T, \\ \text{Vol}(\Omega_{f,\text{cold}}) \leq V_T, \\ \int_{\partial\Omega_{f,\text{hot}}^D} p_\Omega \, ds - \int_{\partial\Omega_{f,\text{hot}}^N} p_\Omega \, ds \leq \text{DP}_T, \\ \int_{\partial\Omega_{f,\text{cold}}^D} p_\Omega \, ds - \int_{\partial\Omega_{f,\text{cold}}^N} p_\Omega \, ds \leq \text{DP}_T, \\ P_{\text{hot} \rightarrow \text{cold}}(\Omega_f) \geq d_{\min}, \\ P_{\text{cold} \rightarrow \text{hot}}(\Omega_f) \geq d_{\min}. \end{array} \right.$$

The optimized distribution of the channels  $\Omega_{f,\text{hot}}$  and  $\Omega_{f,\text{cold}}$ , as well as several views of the fluid and solid components  $\Omega_f$  and  $\Omega_s$  are represented on [Fig. 5.1.10](#). This design is rather unconventional, since it does not feature a network of pipes as one would have intuitively expected, but rather an arrangement of fluid surfaces. A few iterations of the optimization process are shown on [Fig. 5.1.11](#). These plots emphasize the fact that valid designs with a well-defined solid–fluid interface are available throughout the optimization process. We note that the optimization algorithm favors the appearance of transverse tubes in the hot phase during the first 200 iterations, before making them disappear in the last ones so that the pressure drop constraint be enforced more stringently.

For information purpose, the computational time required for running 359 iterations of the optimization algorithm is about 8 days on 30 processing units of an Intel(R) Xeon(R) CPU E5-2407 @ 2.4 Gh. The initial mesh features about 3.8 million tetrahedra, 2.3 million of which lie inside the fluid domain.

## 5.2 OPTIMIZATION OF MAXIMUM PROBABILITY DOMAINS IN QUANTUM CHEMISTRY

This section is devoted to an original application of shape and topology optimization techniques in the field of quantum chemistry. It is based on a line of research initiated by A. Savin in the seminal article [325], which proposes to identify “classical” molecular structures, such as the electron pairs featured by the Lewis theory, as the solutions to a shape optimization problem. This novel point of view raises elegant and fascinating questions at the fundamental level, as well as computational challenges.

The present section summarizes the work contained in the article [A7]. We first provide a little background about the general stakes of quantum chemistry and the more specific subject of maximum probability domains in [Section 5.2.1](#), borrowing from the reference books [64, 233, 350] and the articles [5, 325]. We then expose our theoretical investigations and the numerical techniques inspired from them in the next [Section 5.2.2](#). Two numerical examples are eventually discussed in [Section 5.2.3](#).

### 5.2.1. Presentation of the physical context

#### 5.2.1.1. A few basic notions from quantum mechanics

The traditional vision of the electron cloud of a molecule rests on the assumption that these electrons are “localized” in well-defined regions of space, arranged as pairs or shells around the nuclei; this is for instance the basic postulate of the celebrated Lewis model, see [Fig. 5.2.1](#) (a)(b). Despite its major achievements, this vision is incompatible with a number of important phenomena, and notably with the interference patterns evidenced by the historical Davisson and Germer experiment, see [Fig. 5.2.1](#) (c).

Contrary to this classical perspective, the modern quantum mechanics theory features a “delocalized”, probabilistic viewpoint: any quantity of interest attached to the electrons, such as their position or momentum, can only be known via its expectation over all possible states of the system. More precisely, each electron  $i = 1, \dots, n$  in the cloud is described by its spatial position  $x_i \in \mathbb{R}^3$  and its spin  $\sigma_i \in \{-\frac{1}{2}, \frac{1}{2}\}$  – a purely quantic quantity whose direct physical interpretation is awkward, but which roughly corresponds to an intrinsic angular momentum. The configuration of the electron cloud is then characterized by a complex-valued wave function  $\Psi$ . The latter belongs to the Hilbert space  $L^2((\mathbb{R}^3 \times \{-\frac{1}{2}, \frac{1}{2}\})^n, \mathbb{C})$ , whose natural

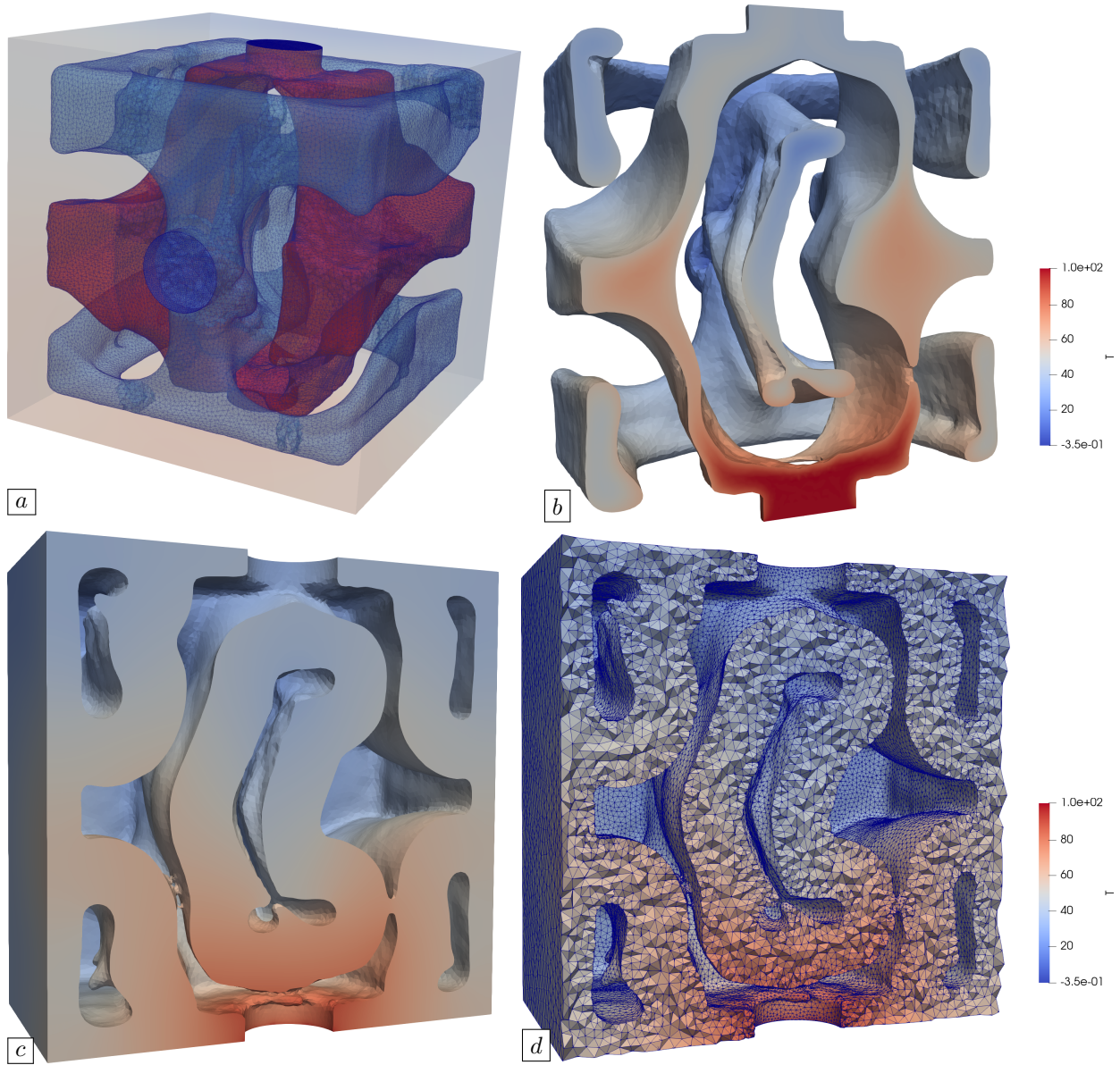


FIGURE 5.1.10. *Optimized design for the three-dimensional heat exchanger test case of Section 5.1.2.4; (a) Optimized distribution of the cold and hot fluid components (in blue and red, respectively); (b,c,d) Views of the optimized fluid domain, where the color scale corresponds to the temperature profile.*

inner product  $\langle \cdot, \cdot \rangle$  is defined by:

$$\forall \Psi, \Phi \in L^2 \left( \left( \mathbb{R}^3 \times \left\{ -\frac{1}{2}, \frac{1}{2} \right\} \right)^n, \mathbb{C} \right),$$

$$\langle \Psi, \Phi \rangle := \sum_{\sigma \in \left\{ -\frac{1}{2}, \frac{1}{2} \right\}^n} \int_{\mathbb{R}^{3n}} \Psi \left[ \begin{pmatrix} x_1 \\ \sigma_1 \end{pmatrix}, \dots, \begin{pmatrix} x_n \\ \sigma_n \end{pmatrix} \right] \overline{\Phi \left[ \begin{pmatrix} x_1 \\ \sigma_1 \end{pmatrix}, \dots, \begin{pmatrix} x_n \\ \sigma_n \end{pmatrix} \right]} \, dx_1 \dots dx_n,$$

and whose associated norm reads  $\|\Psi\| := \langle \Psi, \Psi \rangle^{1/2}$ . The wave function  $\Psi$  encodes all the accessible information about the system, in the following sense: the probability that the spatial position of each electron  $x_i$

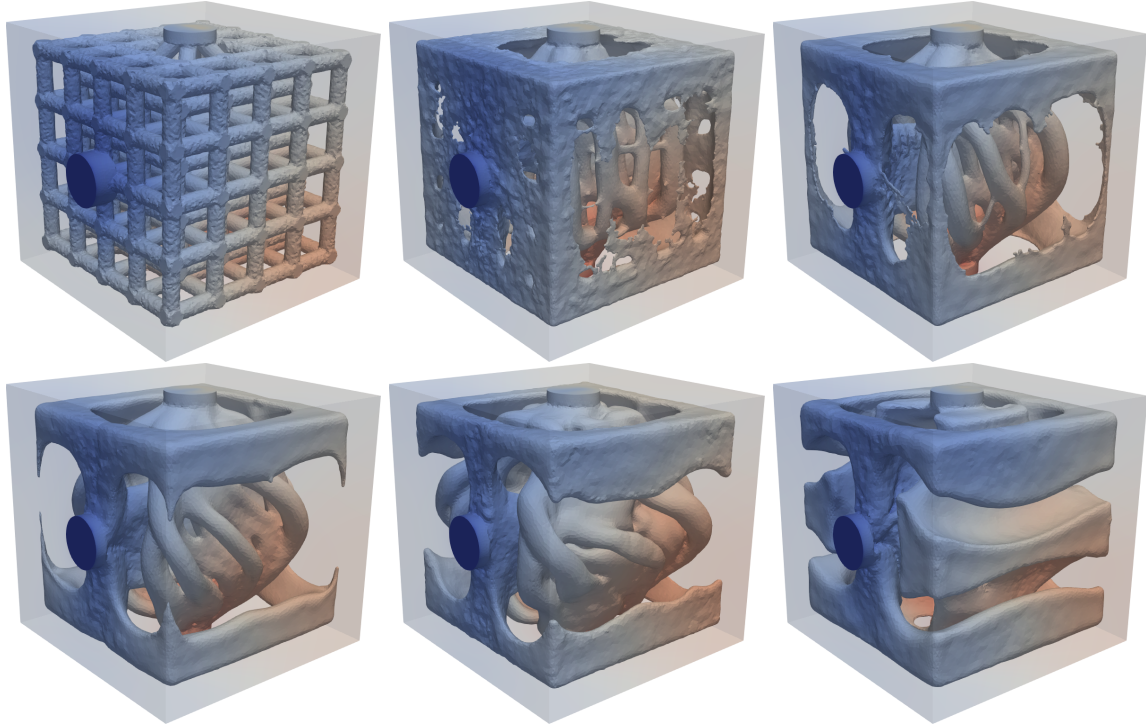


FIGURE 5.1.11. (From left to right, top to bottom) Iterations 0, 25, 50, 110, 180, and 360 of the shape optimization of the solid–fluid interface in the three-dimensional heat exchanger test case of [Section 5.1.2.4](#).

lie within a region  $\Omega_i \subset \mathbb{R}^3$  and that its spin have a value  $\sigma_i \in \{-\frac{1}{2}, \frac{1}{2}\}$  equals:

$$(5.2.1) \quad \int_{\Omega_1 \times \dots \times \Omega_n} \left| \Psi \left[ \begin{pmatrix} x_1 \\ \sigma_1 \end{pmatrix}, \dots, \begin{pmatrix} x_n \\ \sigma_n \end{pmatrix} \right] \right|^2 dx_1 \dots dx_n;$$

in particular,  $\Psi$  is normalized, i.e.  $\|\Psi\| = 1$ . One last key property of the wave function  $\Psi$  of a many-electron system is the antisymmetry principle, also referred to as the Pauli exclusion principle, whereby  $\Psi$  must be antisymmetric in its arguments. This requirement has two important consequences:

- The different electrons are indistinguishable since the probability (5.2.1) that each electron  $i = 1, \dots, n$  belong to a region  $\Omega_i \subset \mathbb{R}^3$  and have spin  $\sigma_i$  is symmetric in its arguments.
- No two electrons in the system can share the same spatial and spin coordinates, as  $\Psi$  vanishes when any two of its arguments  $\begin{pmatrix} x_i \\ \sigma_i \end{pmatrix}$  and  $\begin{pmatrix} x_j \\ \sigma_j \end{pmatrix}$  are equal, and then so does the probability (5.2.1) for this to occur.

As we have mentioned, one of the fundamental principles of quantum mechanics is that the various quantities of interest attached to the system cannot be known exactly: the only available information is their expectation over all its possible configurations. This expectation is evaluated through the action of an associated observable  $\mathcal{A}$  on the wave function  $\Psi$  of the system. From the mathematical viewpoint,  $\mathcal{A}$  is a (possibly unbounded) self-adjoint operator

$$\mathcal{A} : L^2 \left( \left( \mathbb{R}^3 \times \left\{ -\frac{1}{2}, \frac{1}{2} \right\} \right)^n, \mathbb{C} \right) \rightarrow L^2 \left( \left( \mathbb{R}^3 \times \left\{ -\frac{1}{2}, \frac{1}{2} \right\} \right)^n, \mathbb{C} \right),$$

and the expectation of the quantity at stake equals:

$$\langle \mathcal{A}\Psi, \Psi \rangle.$$

Here are two examples of physical observables:

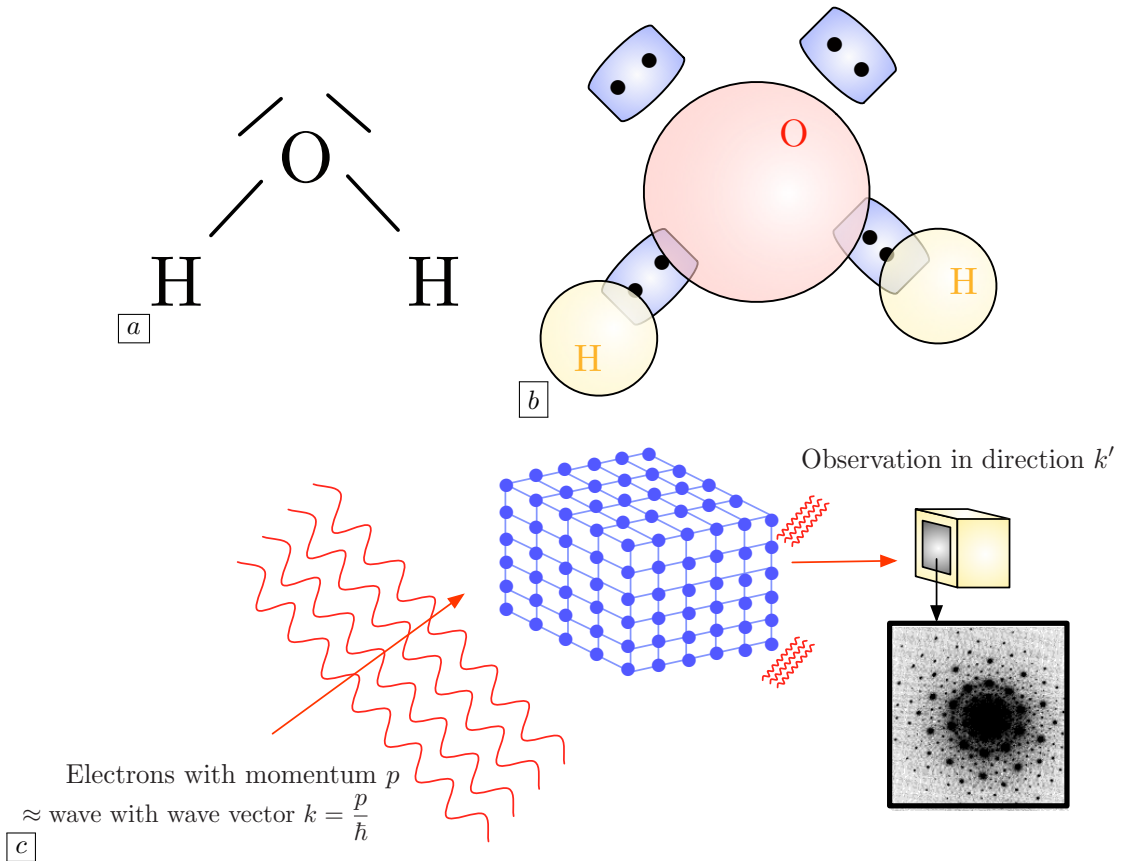


FIGURE 5.2.1. (a) The Lewis representation of the  $H_2O$  molecule; (b) Arrangement of the electrons in its valence shell as pairs; (c) The Davisson and Germer experiment is a historical evidence that electrons can behave like a wave: a nickel crystal is irradiated by an electron beam with momentum  $p$ ; the density of outgoing electrons in a direction  $k'$  shows a similar diffraction pattern as if the incoming flux were a wave with wave vector  $k = p/\hbar$ .

- The position of the  $i^{\text{th}}$  electron is associated to the operator

$$\mathcal{X}_i \Psi = x_i \Psi,$$

reflecting that the expected value of this position equals

$$\langle \mathcal{X}_i \Psi, \Psi \rangle = \sum_{\sigma \in \{-\frac{1}{2}, \frac{1}{2}\}^n} \int_{\mathbb{R}^{3n}} x_i \left| \Psi \left[ \begin{pmatrix} x_1 \\ \sigma_1 \end{pmatrix}, \dots, \begin{pmatrix} x_n \\ \sigma_n \end{pmatrix} \right] \right|^2 dx_1 \dots dx_n.$$

- Advanced physical considerations reveal that the observable  $\mathcal{P}$  for the momentum of the  $i^{\text{th}}$  electron is given by the following formula:

$$(5.2.2) \quad \mathcal{P}_i \Psi = \frac{\hbar}{i} \nabla_{x_i} \Psi.$$

The quantum mechanics theory reconciles this statistical perspective about the physical quantities of the system with the necessarily deterministic outcome of their concrete measurement thanks to a fundamental postulate called “reduction of the wave packet” or “wave function collapse”. The mathematical formulation of the latter rests on spectral theory: let  $\mathcal{A}$  be the observable of a quantity of interest and let  $a_k$  and  $\Psi_k \in L^2((\mathbb{R}^3 \times \{-\frac{1}{2}, \frac{1}{2}\})^n, \mathbb{C})$  ( $k = 0, \dots$ ) denote its eigenvalues (whose multiplicities may be larger than

one) and a corresponding orthonormal basis made of associated eigenstates, respectively, i.e.

$$(5.2.3) \quad \mathcal{A}\Psi_k = a_k \Psi_k, \text{ and } \|\Psi_k\| = 1.$$

According to the spectral decomposition theorem, any wave function  $\Psi \in L^2((\mathbb{R}^3 \times \{-\frac{1}{2}, \frac{1}{2}\})^n, \mathbb{C})$  of the system can be written as a Hilbertian sum:

$$\Psi = \sum_{k=0}^{\infty} c_k \Psi_k, \text{ for some coefficients } c_k \in \mathbb{C} \text{ such that } \sum_{k=0}^{\infty} |c_k|^2 = 1,$$

see e.g. [314]. The principle of reduction of the wave packet interprets this structure as the fact that any wave function  $\Psi$  is the superposition of “pure” eigenstates  $\Psi_k$  for the observable  $\mathcal{A}$ . Any measurement of the corresponding physical quantity can only produce one of the eigenvalues  $a = a_0, a_1, \dots$  of  $\mathcal{A}$  and the probability of this scenario is

$$\sum_{\substack{k=0, \dots, \\ a_k=a}} |c_k|^2.$$

Besides, immediately after the measurement, the wave function  $\Psi$  “collapses” to one eigenstate  $\Psi_k$  associated to  $a$  via (5.2.3).

#### 5.2.1.2. More details about the wave function: the Hartree-Fock model

The expression of the wave function  $\Psi$  of the  $n$ -electron system of a molecule containing  $R$  nuclei with positions  $y_r \in \mathbb{R}^3$  and electric charges  $Z_r$  ( $r = 1, \dots, R$ ) is very complicated as soon as the size of the molecule is moderately large. Several models are available to provide approximate, tractable expressions for  $\Psi$ . The most famous of these is perhaps the Hartree-Fock model, based on energy minimization considerations, that we briefly describe in the present section.

The energy of the  $n$ -electron system is evaluated with the help of the Hamiltonian observable  $\mathcal{H}$ :

$$\mathcal{H}\Psi = -\frac{1}{2} \sum_{i=1}^n \Delta_{x_i} \Psi - \sum_{i=1}^n \sum_{r=1}^R \frac{Z_r}{|x_i - y_r|} + \sum_{i=1}^n \sum_{j>i} \frac{1}{|x_i - x_j|}.$$

The first term of this expression is the sum of the kinetic energies of the individual electrons, involving their squared momenta (5.2.2), the second term comes from the electron-nuclei attraction forces, and the last one corresponds to the electron-electron repulsion forces.

The eigenvalues  $E_k$  of  $\mathcal{H}$  ( $k = 0, \dots$ ) encode the energy levels of the system, and its eigenfunctions are the corresponding electronic configurations. Of particular interest is the lowest energy level  $E_0$ , whose associated eigenfunction  $\Psi_0$  is called ground state. These objects are given by the classical Rayleigh formulas:

$$\Psi_0 = \arg \min_{\substack{\Psi \in L^2((\mathbb{R}^3 \times \{-\frac{1}{2}, \frac{1}{2}\})^n, \mathbb{C}) \\ \Psi \text{ antisymmetric} \\ (\Psi, \Psi) = 1}} \langle \mathcal{H}\Psi, \Psi \rangle, \text{ and } E_0 = \langle \mathcal{H}\Psi_0, \Psi_0 \rangle.$$

Intuitively,  $\Psi_0$  is the most stable configuration of the electron system, and it should then describe its most likely configuration. The Hartree-Fock method is based on an approximation of this ground state, obtained by minimizing the energy  $\langle \mathcal{H}\Psi, \Psi \rangle$  among wave functions taking the form of Slater determinants:

$$(5.2.4) \quad \Psi \left[ \begin{pmatrix} x_1 \\ \sigma_1 \end{pmatrix}, \dots, \begin{pmatrix} x_n \\ \sigma_n \end{pmatrix} \right] = \frac{1}{\sqrt{n!}} \det \begin{bmatrix} \phi_1(x_1)_{\sigma_1} & \dots & \phi_1(x_n)_{\sigma_n} \\ \vdots & & \vdots \\ \phi_n(x_1)_{\sigma_1} & \dots & \phi_n(x_n)_{\sigma_n} \end{bmatrix}.$$

This structure is indeed the most simple expression of the variables  $(x_1)_{\sigma_1}, \dots, (x_n)_{\sigma_n}$  which satisfies the anti-symmetry principle. The one-electron functions  $\phi_1(x)_{\sigma}, \dots, \phi_n(x)_{\sigma}$ , called spin orbitals, represent uncorrelated approximate wave functions for each individual electron. They are required to form an orthonormal family in  $L^2(\mathbb{R}^3 \times \{-\frac{1}{2}, \frac{1}{2}\}, \mathbb{C})$ , that is

$$\forall i, j = 1, \dots, n, \quad \sum_{\sigma \in \{-\frac{1}{2}, \frac{1}{2}\}} \int_{\mathbb{R}^3} \phi_i(x)_{\sigma} \overline{\phi_j(x)_{\sigma}} \, dx = \begin{cases} 1 & \text{if } i = j, \\ 0 & \text{otherwise,} \end{cases}$$

and they are defined as pure spin orbitals:

$$(5.2.5) \quad \text{either} \quad \begin{cases} \phi_i\left(\begin{smallmatrix} x \\ 1/2 \end{smallmatrix}\right) = \psi_i(x), \\ \phi_i\left(\begin{smallmatrix} x \\ -1/2 \end{smallmatrix}\right) = 0, \end{cases} \quad \text{or} \quad \begin{cases} \phi_i\left(\begin{smallmatrix} x \\ 1/2 \end{smallmatrix}\right) = 0, \\ \phi_i\left(\begin{smallmatrix} x \\ -1/2 \end{smallmatrix}\right) = \psi_i(x), \end{cases}$$

where the functions  $\psi_i : \mathbb{R}^3 \rightarrow \mathbb{C}$ , called spatial orbitals, depend on the variable  $x \in \mathbb{R}^3$  only.

In turn, these spatial orbitals  $\psi_i$  are defined as linear combinations of Gaussian basis functions, namely:

$$(5.2.6) \quad \forall x \in \mathbb{R}^3, \quad \psi_i(x) = \sum_{r=1}^R c_r (x - y_r)^{\alpha_r} e^{-a_r|x-y_r|^2},$$

where:

- $y_r \in \mathbb{R}^3$  is the center of the  $r^{\text{th}}$  nucleus of the molecule;
- $\alpha_r \in \mathbb{N}^3$  is a multi-index, accounting for the type of the spatial orbital;
- The coefficients  $c_r \in \mathbb{C}$  and  $a_r > 0$ ,  $r = 1, \dots, R$  are characterized by the requirement that  $\Psi$  should minimize the energy  $\langle \mathcal{H}\Psi, \Psi \rangle$  among all wave functions  $\Psi$  of the form (5.2.4) to (5.2.6).

In practice, the description of the optimized spatial orbitals  $\psi_i$  is supplied by the computational chemistry package **Gaussian** [183].

### 5.2.1.3. Maximum probability domains

The theory of maximum probability domains is one of the multiple interpretative methods that have been devised to try and reconcile the classical and quantum viewpoints about the structure of the electron cloud and thereby explain the success and limitations of the former.

From the mathematical viewpoint, maximum probability domains are defined as the solutions to the following shape optimization problem:

$$(\text{MPD}_\nu) \quad \max_{\Omega \subset \mathbb{R}^3} \mathbb{P}_\nu(\Omega),$$

where  $\nu \in \{0, \dots, n\}$  and  $\mathbb{P}_\nu(\Omega)$  is the probability that exactly  $\nu$  electrons lie in  $\Omega$ , see Fig. 5.2.2. Taking advantage of the antisymmetry of the wave function  $\Psi$ , this quantity reads:

$$(5.2.7) \quad \mathbb{P}_\nu(\Omega) = \int_{\Omega^\nu \times (\mathbb{R}^3 \setminus \Omega)^{n-\nu}} \mathcal{S}_\nu(x_1, \dots, x_n) dx_1 \dots dx_n,$$

where  $\mathcal{S}_\nu(x_1, \dots, x_n) := \binom{n}{\nu} \sum_{\sigma \in \{-\frac{1}{2}, \frac{1}{2}\}^n} \left| \Psi \left[ \begin{pmatrix} x_1 \\ \sigma_1 \end{pmatrix}, \dots, \begin{pmatrix} x_n \\ \sigma_n \end{pmatrix} \right] \right|^2.$

## 5.2.2. Shape optimization for maximum probability domains

Our investigations about the shape optimization problem  $(\text{MPD}_\nu)$  go in two directions: on the one hand, in Section 5.2.2.1 we prove the existence of maximum probability domains under “mild” assumptions; in spite of the seemingly simple formulation  $(\text{MPD}_\nu)$ , this task is not trivial. The proof is interesting, as it provides a convenient expression of the optimality conditions, which lends itself to the device of an efficient numerical algorithm, that we present in Section 5.2.2.2.

### 5.2.2.1. Existence of maximum probability domains

Our study of the existence of maximum probability domains hinges on a relaxed version of  $(\text{MPD}_\nu)$  formulated in the framework of density-based topology optimization, see Section 1.4.5. Let us indeed introduce the following density optimization problem:

$$(\text{MPD}_\nu^{\text{relax}}) \quad \max_{m \in L^\infty(\mathbb{R}^3, [0,1])} J_\nu(m), \quad \text{where} \quad J_\nu(m) := \int_{\mathbb{R}^{3n}} P_\nu(m)(x_1, \dots, x_n) \mathcal{S}_\nu(x_1, \dots, x_n) dx_1 \dots dx_n$$

and  $P_\nu(m)(x_1, \dots, x_n) = \prod_{i=1}^{\nu} m(x_i) \prod_{j=\nu+1}^n (1 - m(x_j)).$

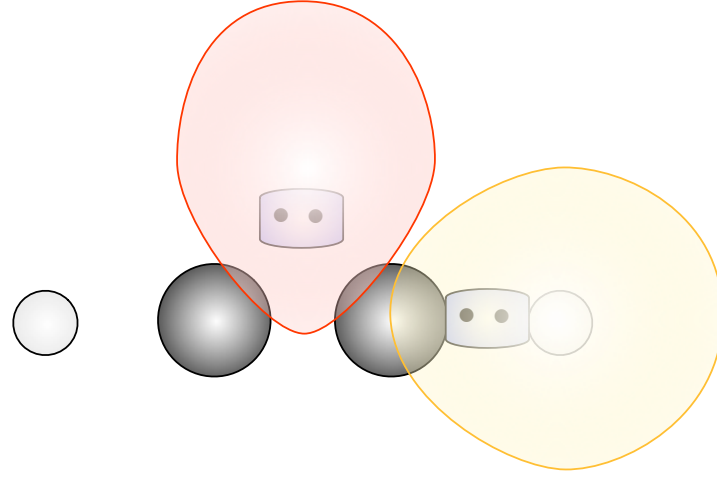


FIGURE 5.2.2. *An intuitive interpretation of maximum probability domains: regions  $\Omega \subset \mathbb{R}^3$  with maximum probability  $\mathbb{P}_2(\Omega)$  of finding exactly two electrons can be interpreted as the electron pairs of the Lewis model.*

The latter is obtained from  $(\text{MPD}_\nu)$  by replacing the characteristic function  $\mathbb{1}_\Omega$  of the optimized “black-and-white” shape  $\Omega$  with a “grayscale” density function  $m \in L^\infty(\mathbb{R}^3, [0, 1])$ . For such design  $m$ , we also define the function  $F_\nu^m : \mathbb{R}^3 \rightarrow \mathbb{R}$  by:

$$F_\nu^m(x) = \int_{\mathbb{R}^{3(n-1)}} (\nu - nm(x_{\nu+1})) \prod_{i=2}^{\nu} m(x_i) \prod_{j=\nu+2}^n (1 - m(x_j)) \mathcal{S}_\nu(x, x_2, \dots, x_n) dx_2 \dots dx_n,$$

and for any Lebesgue measurable subset  $\Omega \subset \mathbb{R}^3$ , we set  $F_\nu^\Omega \equiv F_\nu^{\mathbb{1}_\Omega}$ .

Our main theoretical result regarding the analysis of  $(\text{MPD}_\nu)$  reads as follows:

**Theorem 5.2.1** *Let  $\Psi \in L^2((\mathbb{R}^3 \times \{-\frac{1}{2}, \frac{1}{2}\})^n, \mathbb{C})$  be an antisymmetric function of the variables  $(\frac{x_1}{\sigma_1}, \dots, \frac{x_n}{\sigma_n})$  such that*  
 $(5.2.8)$  *For  $\sigma_1, \dots, \sigma_n \in \left\{-\frac{1}{2}, \frac{1}{2}\right\}$ , the mapping  $\mathbb{R}^{3n} \ni (x_1, \dots, x_n) \mapsto \Psi\left[\left(\frac{x_1}{\sigma_1}, \dots, \frac{x_n}{\sigma_n}\right)\right] \in \mathbb{C}$  is real analytic.*

*Assume in addition that:*

$$(5.2.9) \quad \exists m_0 \in L^\infty(\mathbb{R}^3, [0, 1]), \text{ such that } J_\nu(m_0) \geq \left(1 + \frac{n-\nu}{\nu} + \frac{\nu}{n-\nu}\right)^{-1}.$$

*Then,*

- (i) *The problem  $(\text{MPD}_\nu^{\text{relax}})$  has a (possibly non unique) global solution  $m^*$  in  $L^\infty(\mathbb{R}^3, [0, 1])$ .*
- (ii) *This solution  $m^*$  is of the form  $m^* = \mathbb{1}_{\Omega^*}$  where  $\Omega^*$  is a Lebesgue measurable subset of  $\mathbb{R}^3$  which is a (possibly non unique) global solution to  $(\text{MPD}_\nu)$ .*
- (iii) *Any global solution  $\Omega^*$  to  $(\text{MPD}_\nu)$  is an open subset of  $\mathbb{R}^3$  which satisfies*

$$\Omega^* = \left\{ F_\nu^{\Omega^*} > 0 \right\} := \left\{ x \in \mathbb{R}^3, F_\nu^{\Omega^*}(x) > 0 \right\},$$

*up to a subset of  $\mathbb{R}^3$  with null Lebesgue measure.*

*Hint of proof.* We proceed in three steps.

*Step 1:* *We prove that there exists a global solution  $m^*$  to the relaxed problem  $(\text{MPD}_\nu^{\text{relax}})$ .*

This fact is a relatively classical application of the direct method of calculus of variations: it follows from the weak-\* compactness of  $L^\infty(\mathbb{R}^3, [0, 1])$  and the sequential continuity of  $J_\nu$  for the weak-\* topology of  $L^\infty(\mathbb{R}^3, [0, 1])$ .

*Step 2: We express the optimality conditions for  $(\text{MPD}_\nu^{\text{relax}})$ .*

These are based on the Fréchet derivative of  $J_\nu(m)$ , which is obtained after a fairly standard calculation:

$$\forall h \in L^\infty(\mathbb{R}^3), \quad J'_\nu(m^*)(h) = \int_{\mathbb{R}^3} F_\nu^{m^*}(x)h(x) \, dx.$$

An elementary analysis of this expression reveals that if  $m \in L^\infty(\mathbb{R}^3, [0, 1])$  is a local maximizer for  $(\text{MPD}_\nu^{\text{relax}})$ , the following inclusions hold, up to subsets of  $\mathbb{R}^3$  with null Lebesgue measure:

- (i)  $\{F_\nu^m < 0\} \subset \{m = 0\} \subset \{F_\nu^m \leq 0\}$ ,
- (ii)  $\{F_\nu^m > 0\} \subset \{m = 1\} \subset \{F_\nu^m \geq 0\}$ ,
- (iii)  $\{0 < m < 1\} \subset \{F_\nu^m = 0\}$ .

*Step 3: We prove that any global solution  $m^*$  to  $(\text{MPD}_\nu^{\text{relax}})$  is the characteristic function of a Lebesgue measurable subset  $\Omega^* \subset \mathbb{R}^3$ .*

To achieve thus, we argue by contradiction, and we assume that there exists one global solution  $m^*$  to  $(\text{MPD}_\nu^{\text{relax}})$  which is not the characteristic function of a Lebesgue measurable subset of  $\mathbb{R}^3$ , i.e. the set  $\{0 < m^* < 1\}$  has positive Lebesgue measure. The necessary optimality conditions derived in Step 2 show that the function  $F_\nu^{m^*}(x)$  must vanish on a set with positive Lebesgue measure, and since it is analytic, because of (5.2.8), it must vanish identically on  $\mathbb{R}^3$ . Simple calculations then reveal that:

$$F_\nu^{m^*} \equiv 0 \text{ on } \mathbb{R}^3 \Rightarrow J_\nu(m^*) < \left(1 + \frac{n-\nu}{\nu} + \frac{\nu}{n-\nu}\right)^{-1} \text{ and so } J_\nu(m^*) < J_\nu(m_0),$$

where  $m_0 \in L^\infty(\mathbb{R}^3, [0, 1])$  is the density function in (5.2.9); this is the expected contradiction with the global optimality of  $m^*$ . Hence, any global solution  $m^*$  to  $(\text{MPD}_\nu^{\text{relax}})$  is the characteristic function of a Lebesgue measurable subset  $\Omega^*$  of  $\mathbb{R}^3$ , which is necessarily a global maximizer of the problem  $(\text{MPD}_\nu)$ .  $\square$

**Remark 5.2.2** *The assumption (5.2.9) of the theorem is admittedly not very eloquent; however, the calculation of  $J_\nu(m_0)$  for a few explicit functions  $m_0 \in L^\infty(\mathbb{R}^3, [0, 1])$  and elementary algebraic manipulations show that it is automatically satisfied in a number of important situations, and notably when  $\nu = 0, 1$ , or  $2$ , regardless of the total number  $n$  of electrons in the considered system.*

#### 5.2.2.2. A numerical algorithm for the identification of maximum probability domains

Our practical treatment of the shape and topology optimization problem  $(\text{MPD}_\nu)$  combines two numerical ingredients.

On the one hand, we use the level set based mesh evolution method presented in Section 1.4.7, which is well-adapted to the sensitive numerical evaluation of  $\mathbb{P}_\nu(\Omega)$ . The calculation of the shape derivative of this objective function is similar to that of the Fréchet derivative of the functional  $J_\nu(m)$ , conducted in the proof of Theorem 5.2.1; hence, Algorithm 3 can be applied as described in Section 1.4.7. Let us however outline two specificities of the problem  $(\text{MPD}_\nu)$  that demand particular attention.

- Algorithm 3 operates in a bounded computational domain  $D$ , while the problem  $(\text{MPD}_\nu)$  features shapes that are a priori unbounded, and its local and global maximizers may very well be so. This raises the need to define a “suitably large” computational domain  $D$ , containing a significant portion of the sought maximum probability domains, but which is also not vainly large, so as to keep the computational effort reasonable. To achieve this, we first consider a very large computational domain  $\tilde{D}$ , equipped with a very coarse mesh, and we search for a domain  $D \subset \tilde{D}$  which makes the probability  $\mathbb{P}_n(D)$  of finding all the  $n$  electrons of the system “very close” to 1. This domain  $D$  is the desired computational box for the solution of  $(\text{MPD}_\nu)$  with Algorithm 3.
- Although  $\mathbb{P}_\nu(\Omega)$  has a closed form expression, its calculation via (5.2.7) (and that of its shape derivative) is computationally intense, even for moderately large values of the number of electrons  $n$ . Indeed, the evaluation of the integrand in (5.2.7) at each quadrature point of the  $3n$ -dimensional

domain  $\Omega^\nu \times (\mathbb{R}^3 \setminus \overline{\Omega})^{n-\nu}$  involves the calculation of  $2^n$  determinants of size  $n$ . To achieve this calculation efficiently, we rely on “clever” reformulations of  $\mathbb{P}_\nu(\Omega)$  and  $\mathbb{P}'_\nu(\Omega)(\theta)$  derived in [105].

On the other hand, we leverage the optimality conditions for the relaxed problem  $(\text{MPD}_\nu^{\text{relax}})$  to develop a fixed-point topology optimization algorithm in the spirit of that presented in Section 1.4.8.2. The latter allows to change topology in the course of the shape optimization process – notably via dramatic operations which are not permitted by the framework of Hadamard’s method, such as the addition of small connected components or the nucleation of tiny holes in the optimized shape. The basic observation underlying this algorithm is that if a Lebesgue measurable domain  $\Omega \subset \mathbb{R}^3$  is such that  $\mathbf{1}_\Omega$  is a local maximizer for the relaxed problem  $(\text{MPD}_\nu^{\text{relax}})$  (which is a stronger condition than  $\Omega$  being a local maximizer for  $(\text{MPD}_\nu)$ ), then  $-F_\nu^\Omega$  is one level set function for  $\Omega$ , see again Step 2 in the proof of Theorem 5.2.1.

One step of the fixed point strategy of Section 1.4.8.2 to impose this condition reads:

$$(5.2.10) \quad \phi^{k+1} = \frac{1}{\sin a^k} \left( \sin((1 - \tau^k)a^k) \phi^k + \sin(\tau^k a^k) \tilde{g}^k \right),$$

where  $\tilde{g}^k := -\frac{1}{\|F_\nu^{\Omega^k}\|_{L^2(D)}} F_\nu^{\Omega^k}$ ,  $a^k = \arccos((\phi^k, \tilde{g}^k)_{L^2(D)})$ ,  $\tau^k \in [0, 1]$  is a time step,

and  $\phi^k$  (resp.  $\phi^{k+1}$ ) is one level set function for the shape  $\Omega^k$  (resp. for  $\Omega^{k+1}$ ), see (LS). Numerical experiments not reported in this manuscript show that the use of this fixed point strategy in a standalone fashion is very unstable in the present context, leading to multiple numerical artifacts.

Our numerical strategy thus alternates between “classical” iterations of the boundary variation Algorithm 3 with occasional steps of the form (5.2.10) which allow to dramatically alter the topology of the optimized shape.

### 5.2.3. Two numerical examples

We now turn to two numerical illustrations of the strategy introduced in Section 5.2.2.2: in either case, we calculate the maximum probability domains of a molecule to try and retrieve its classical Lewis structure. Before proceeding, let us recall that the classical Lewis theory distinguishes three types of electron pairs within a molecule:

- The core electron pairs are attached to one specific nucleus; they are chemically inert.
- The valence lone pairs are also attached to a particular nucleus, but they may be chemically reactive and responsible for specific properties of the molecule.
- The chemical bonds are electron pairs shared by two atoms.

We search for MPDs associated to  $\nu = 2$  electrons, which should intuitively account for such Lewis electron pairs. We expect to identify as many electron pairs as local optimizers of the MPD problem, attached to different initializations, which account for as many stable configurations of the system.

#### 5.2.3.1. The water molecule $H_2O$

In this section, we consider the water molecule  $H_2O$ . According to the Lewis theory, the  $n = 10$  electrons of this molecule are arranged in five electron pairs: one core pair and two valence lone pairs are attached to the oxygen nucleus, and each hydrogen atom is connected to the oxygen via a chemical bond.

The search for the maximum probability domains of the  $H_2O$  molecule accounting for these five pairs goes through the solution of  $(\text{MPD}_\nu)$  with  $\nu = 2$  by using different initial shapes  $\Omega^0$ . The wave function  $\Psi$  describing the present electron cloud is a single Slater determinant of the form (5.2.4), involving  $n = 10$  spin orbitals  $\phi_i$ , each of them being of the form (5.2.6) with  $R = 67$  Gaussian primitives.

We first look for the maximum probability domain associated to the core electron pair of the molecule; to this end, we solve  $(\text{MPD}_\nu)$  by using a ball with radius 0.55 times the distance O–H, centered at the oxygen atom as for initial shape  $\Omega^0$ , see Fig. 5.2.3 (a). The optimized shape obtained in this situation is displayed on Fig. 5.2.3 (b). Similar numerical experiments (not reported in this manuscript) associated to initial shapes which are slightly shifted away from the oxygen atom result in the same local maximizer of  $(\text{MPD}_\nu)$ .

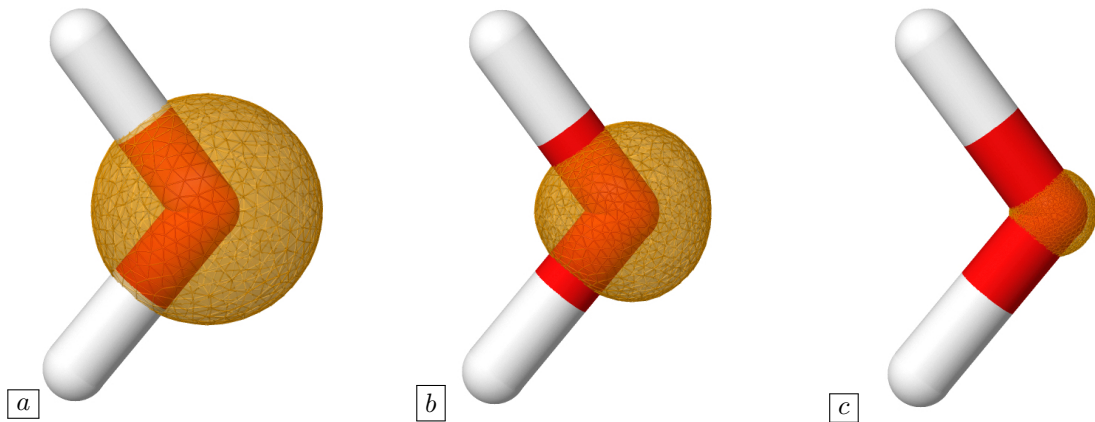


FIGURE 5.2.3. *Maximum probability domains attached to the core electron pair of the oxygen atom in the  $\text{H}_2\text{O}$  molecule. The oxygen atom is represented in red, and the two hydrogen atoms are in white, at the ends of the bicolor stick representing the two  $\text{O}-\text{H}$  bonds; iterations (a) 0, (b) 2 and (c) 8.*

We next turn to the identification of the four valence electron pairs of the water molecule. The four initial shapes used in this context are depicted on Fig. 5.2.4 (upper row), and the corresponding local optimizers of  $(\text{MPD}_\nu)$  are displayed in Fig. 5.2.4 (bottom row). These may be grouped into two sets of symmetrically related solutions: the optimized shapes on the two leftmost columns in Fig. 5.2.4 correspond to the oxygen lone pairs, and the optimized shapes on the two rightmost columns are the  $\text{O}-\text{H}$  bonds of the molecule. Interestingly, the numerical strategy of Section 5.2.2.2 manages to capture unbounded shapes with several connected components, even when a bounded and connected initial guess is used. Note that the smaller connected components featured by these MPDs are not artifacts from the calculation.

These calculations suggest a possible answer about an old, but still lively debate between two rival visions for the structure of the two valence lone pairs of the  $\text{H}_2\text{O}$  molecule. On the one hand, the prevailing representation within the organic chemistry community, provided by the so-called “hybridization theory”, features two “rabbit-ear” lone pairs with identical shapes, see Fig. 5.2.5 (a). On the other hand, the Molecular Orbital reading of the  $\text{H}_2\text{O}$  molecule predicts two different lone pairs, one of so-called  $\sigma$  type, and the other of so-called  $\pi$  type, see Fig. 5.2.5 (b). The numerical results of Fig. 5.2.4 feature two distinct lone pairs with very similar shapes, and thus tend to speak in favor of the former, “rabbit-ear” shaped lone pairs hypothesis.

### 5.2.3.2. The ethylene molecule $\text{C}_2\text{H}_4$

We now study the ethylene molecule  $\text{C}_2\text{H}_4$ , which features  $n = 16$  electrons, and we more particularly focus on the double  $\text{C}=\text{C}$  bond between the two carbon atoms. Similarly to what happens for multiply bonded hydrocarbons in general, it was originally suggested that this double bond should correspond to two *bent bonds* with similar shapes, also called *banana bonds*. Yet, another description featuring two different bonds of  $\sigma$  and  $\pi$  types has become increasingly popular within the chemical community; see Fig. 5.2.6 for a schematic representation of both orbital sets. In order to put both hypotheses to the test, we search for the maximum probability domains of the ethylene molecule in the  $\text{C}-\text{C}$  interatomic region (thus leaving aside the core pairs).

Our first experiment consists in searching for a local maximizer of  $(\text{MPD}_\nu)$  starting from a sphere  $\Omega^0$  located in the  $\text{C}-\text{C}$  interatomic axis or slightly above, with radius 0.79 times the distance between carbon atoms, see Fig. 5.2.7 (a). The optimized domain  $\Omega$  is displayed on Fig. 5.2.7 (b). Judging from its symmetry with respect to the plane of the molecule, it is tempting to associate  $\Omega$  to a  $\text{C}-\text{C}$  bond of  $\sigma$  type. However, despite many attempts, we did not find any corresponding complementary maximum probability domain that would correspond to a  $\pi$ -bond between those two carbon atoms.

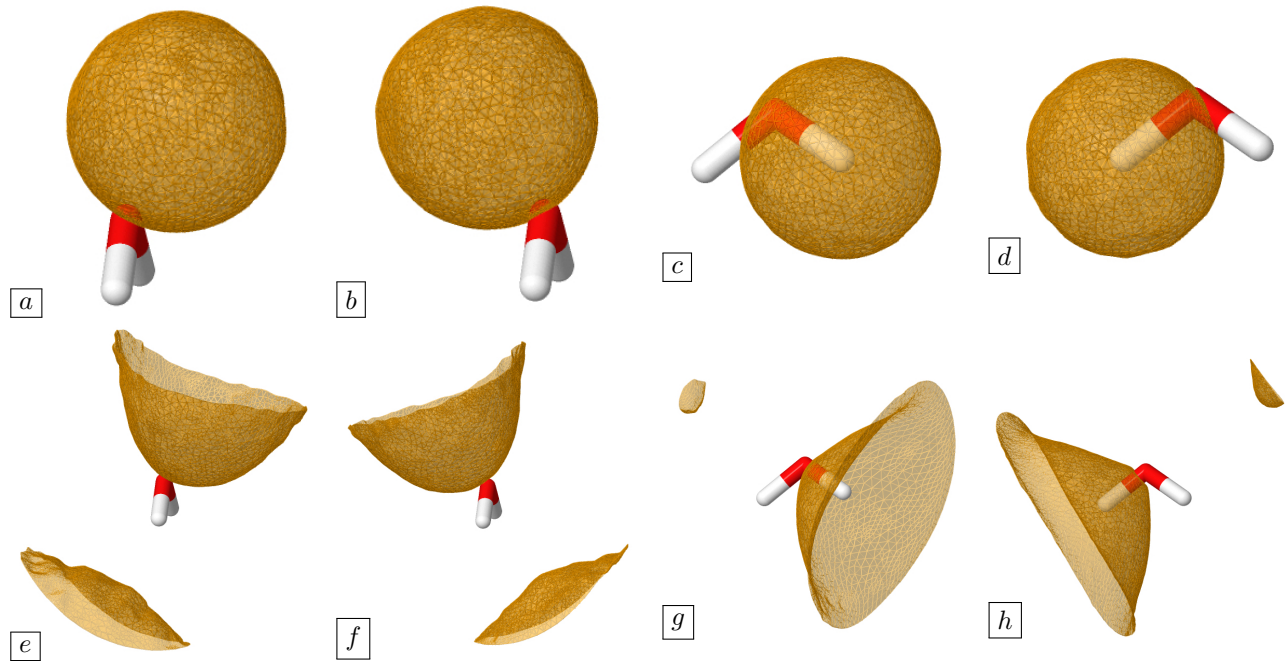


FIGURE 5.2.4. Maximum probability domains associated with the valence electron pairs in the  $H_2O$  molecule; the initial domains are displayed on the upper row, and the optimized ones are on the bottom row. The two domains in (e) (f) correspond to the oxygen lone pairs, while the other two in (g) (h) are associated with the O–H chemical bonds.



FIGURE 5.2.5. (a) In the  $H_2O$  molecule, the “rabbit-ear” description of the water lone pairs predicts that the oxygen atom has two lone pairs with equivalent shapes, which are symmetric with respect to the plane of the molecule; (b) The  $\sigma - \pi$  vision features two different electron pairs, one of  $\sigma$ -type (comprised in the plane of the molecule), the other of  $\pi$ -type (which is orthogonal to it).

In a second set of experiments, using initial domains  $\Omega_0$  situated from either side of the plane of symmetry of the molecule (see Fig. 5.2.8, left column) we obtain two maximum probability domains in the C–C interatomic region, which are represented on Fig. 5.2.8 (right column). These could correspond to two equivalent “banana bonds”, which are symmetric with respect to the plane of the molecule. Besides, the final value 0.404 of the probability  $\mathbb{P}_2(\Omega)$  for either of these two domains  $\Omega$  is slightly larger than that 0.401 obtained in the first experiment, in the case of the potential  $\sigma$ -bond maximum probability domain of Fig. 5.2.7.

All things considered, both arguments suggest that the “banana bond” model may be the most plausible structure for the two bonds between the carbon atoms of the ethylene.

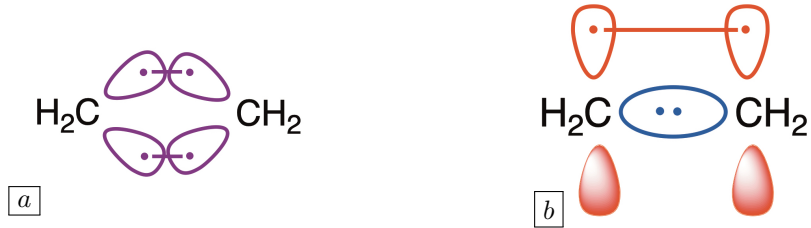


FIGURE 5.2.6. (a) The “bent-bond” model for the double  $C=C$  bond of the ethylene molecule features two electron pairs which are symmetric with respect to the plane of the molecule; (b) The  $\sigma - \pi$  description of this bond involves one  $\sigma$  electron pair within the molecule plane, and a  $\pi$  electron pair, orthogonal to it.

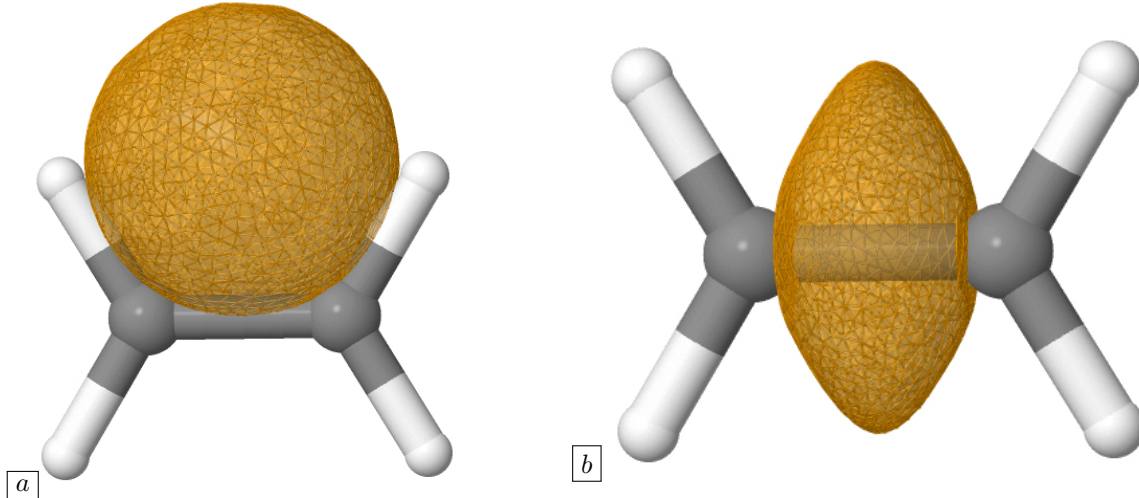


FIGURE 5.2.7. Maximum Probability Domain associated to the potential  $\sigma$  bond pair between the two carbon atoms of the ethylene molecule, as discussed in [Section 5.2.3.2](#) (no corresponding  $\pi$  MPD has been found). The carbon atoms are in grey, and the hydrogen ones are in white: (a) Initial guess; (b) Optimized shape

### 5.3 OPTIMIZATION OF THE SHAPE OF NANOPHOTONIC DEVICES

Nanophotonic devices are components used to manipulate light, considered as an electromagnetic field, at the nanometric scale. They are tailored to specific tasks such as guiding an incident wave with negligible loss, splitting it into several output ports depending on the wavelength, converting a mode from an incoming waveguide into another mode of an outgoing waveguide, etc. These components are the building blocks of the photonic integrated circuits (PICs) used, for instance, in fiber optic communications, microscopy, biosensing, to name a few applications, see [Fig. 5.3.1](#) and [\[176\]](#) for an overview.

The non trivial properties of nanophotonic devices are generally obtained by a clever repartition of “core” and “cladding” materials. As the difficult underlying physics leaves very little room for intuition, shape and topology optimization techniques have naturally become an essential tool in their design, see [\[211\]](#) for an overview of such applications.

This section summarizes the investigations conducted in the articles [\[A17, A16\]](#) around the optimal design of nanophotonic devices. It is composed of a short description of these (in [Section 5.3.1](#)), an exposition of the stakes of optimal design in this context, including the crucial issue of robustness (see [Section 5.3.2](#)), and a few numerical examples (in [Section 5.3.3](#)).

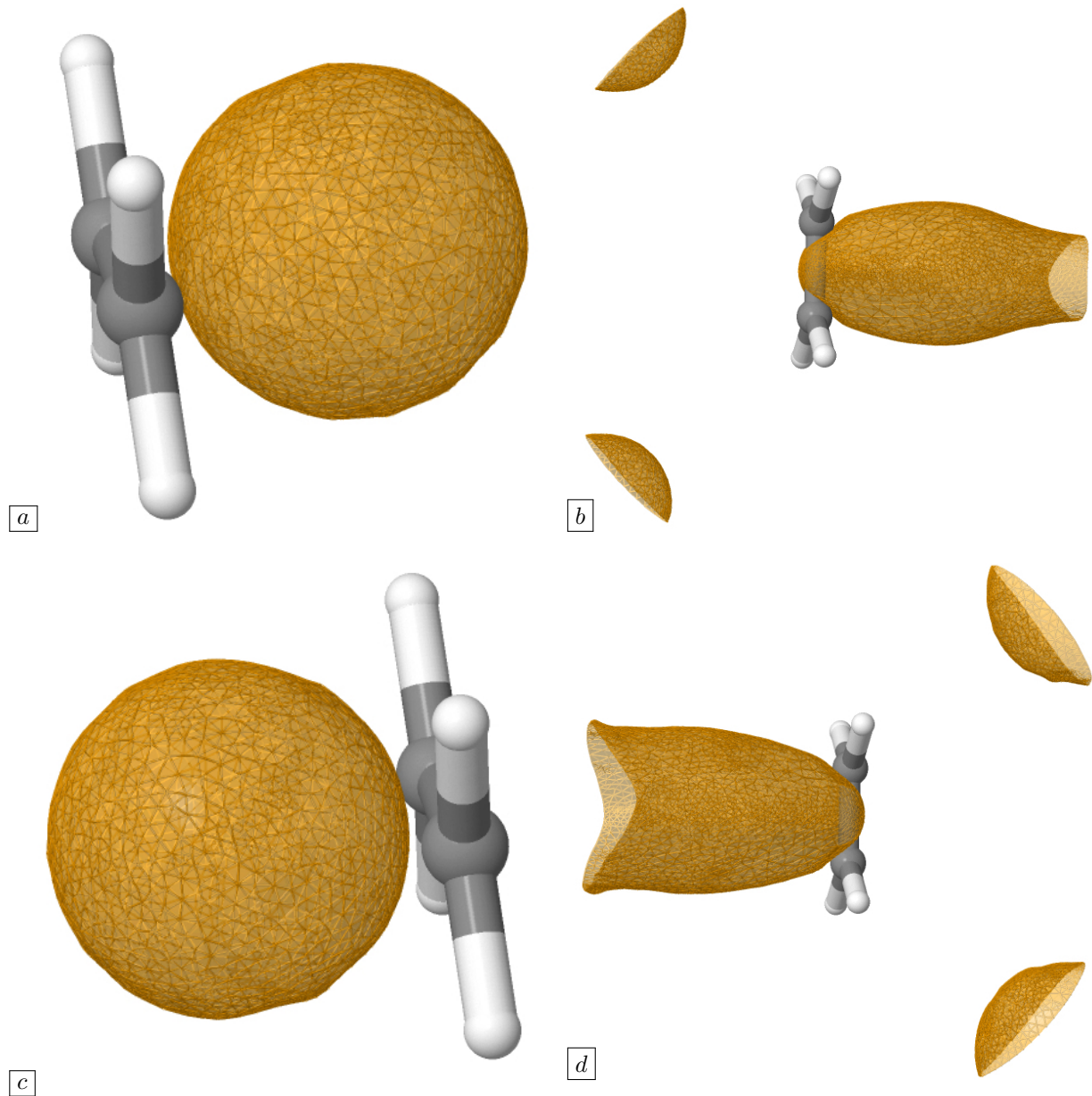


FIGURE 5.2.8. Maximum probability domains associated with the C–C bond pairs in the ethylene molecule  $C_2H_4$ , investigated in [Section 5.2.3.2](#). The carbon atoms are represented in grey, and the hydrogens are in white: (a)(c) Initial guesses; (b)(d) Corresponding maximum probability domain interpreted as banana bonds.

### 5.3.1. Nanophotonic devices and the transport of light

#### 5.3.1.1. Physical description of nanophotonic devices

This section aims to provide a minimal physical background around the subject of nanophotonic components, a more exhaustive account of which can be found in Chap. 13 in [\[217\]](#) and [\[228\]](#).

In a nutshell, the typical configuration of interest features a substrate, usually made of silica  $SiO_2$ , mounted by a core region made of silicon Si, as well as several waveguides entering or exiting the latter. More precisely, the situation is that illustrated on [Fig. 5.3.2](#) (a):

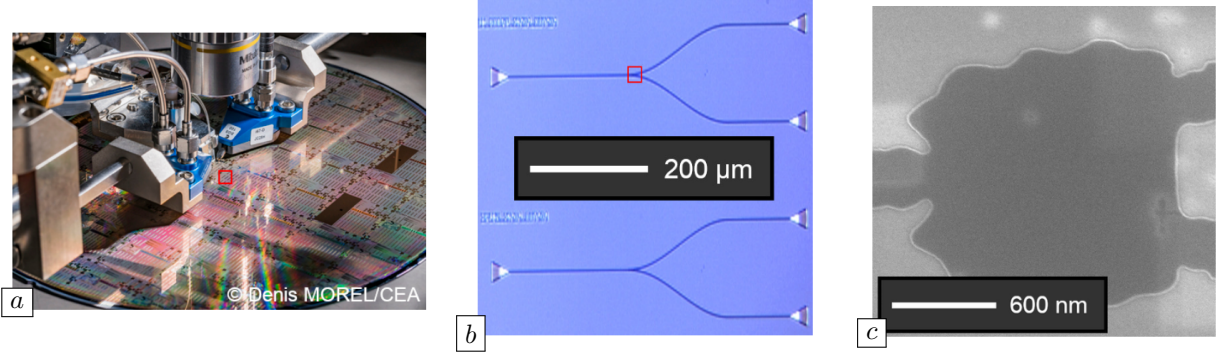


FIGURE 5.3.1. *Three different levels of detail for an engraved wafer, supporting numerous nanophotonic components; (a) Full wafer (200 mm diameter); (b) Two particular photonic circuits; (c) One individual component.*

- The total “hold-all” domain  $D \subset \mathbb{R}^3$  where investigations take place is a box.
- The lower part  $D_{\text{subs}}$  of  $D$  is occupied by the substrate; this region is made of insulating material, typically silica  $\text{SiO}_2$ .
- The core region, or design domain,  $D_{\text{opt}}$  is a box with thickness  $h$  mounted on the substrate. This active region of the device is composed of two phases, occupied by core material (typically silicon Si) and cladding material (such as air), respectively. Due to its fabrication by lithography and etching, this region is invariant in the vertical,  $e_2$  direction.
- Several waveguides, collectively denoted by  $D_{\text{wg}}$ , are connected to the core region, conveying light in and out of the latter; they are also made of core material.
- Light is injected into the computational domain via the region  $\Gamma_{\text{in}}$  of  $\partial D$ .
- The quantities of interest appraising the performance of the design are measured on an internal hypersurface  $\Gamma_{\text{obj}} \subset D$ ; in practice,  $\Gamma_{\text{obj}}$  is often chosen to be a section of an outgoing waveguide.
- The “Perfectly Matched Layer” region  $D_{\text{PML}}$  is an open neighborhood of  $\partial D$  made of a fictitious absorbing material. It is introduced for purely numerical purpose, as a means of mimicking the radiation conditions at infinity featured in the Maxwell’s equation, in the present context where the numerical simulation takes place in the bounded domain  $D$ .

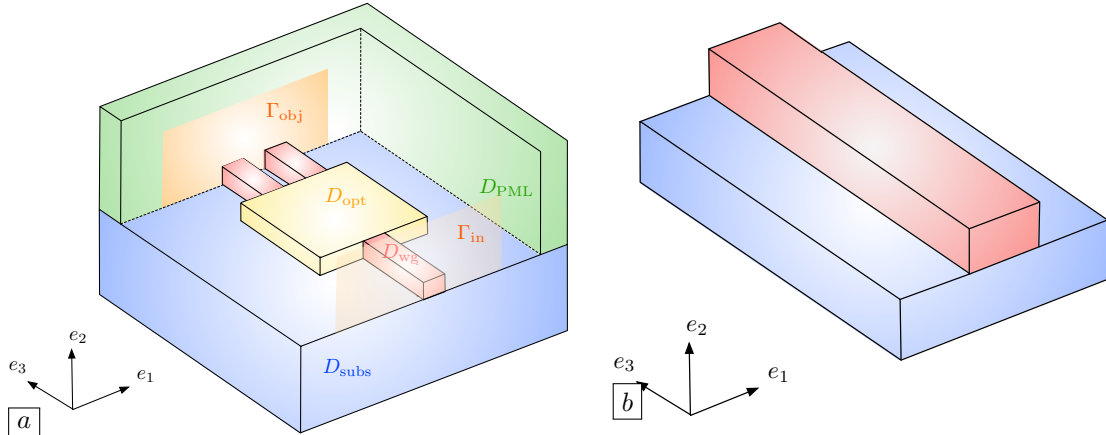


FIGURE 5.3.2. (a) *Physical setting of the nanophotonic devices considered in Section 5.3;* (b) *Schematics of a waveguide.*

The constituent materials of these regions are homogeneous and isotropic; they are characterized by their (real-valued) electric permittivity  $\varepsilon$  and magnetic permeability  $\mu$ , which appraise their ability to polarize

in response of an applied electric field and to develop magnetization under the effect of a magnetic field, respectively. Another useful quantity is the refractive index  $\nu^2 = \varepsilon/\varepsilon_0$ , involving the vacuum permittivity  $\varepsilon_0$ , which expresses the ratio between the speed of light in the vacuum and that in the considered medium. The refractive index  $\nu_{\text{core}}$  of the core material is typically much larger than those  $\nu_{\text{clad}}$  and  $\nu_{\text{subs}}$  of the cladding and substrate, which ensures a better confinement of light in this region.

### 5.3.1.2. Nanophotonic devices and the Maxwell's equations

The physical behavior of nanophotonic devices is governed by the time-harmonic Maxwell's equations, about which we refer to [208, 212], or Chap. 1 in [272].

Let  $\omega$  denote the considered optical frequency and let  $k = \omega/c$  and  $\lambda = 2\pi/k$  be the associated wavenumber and wavelength (where  $c$  is the velocity of light in the vacuum), respectively: a time dependence of the form  $e^{-i\omega t}$  is assumed for the electric and magnetic fields. Their spatial components  $E : D \rightarrow \mathbb{R}^3$  and  $H : D \rightarrow \mathbb{R}^3$  satisfy the four Maxwell's equations, which write:

$$\begin{aligned}
 \text{curl}(E) &= i\omega\mu H && \text{(Maxwell-Faraday),} \\
 \text{div}(\varepsilon E) &= 0 && \text{(Maxwell-Gauss),} \\
 \text{curl}(H) &= -i\omega\varepsilon E && \text{(Maxwell-Ampère),} \\
 \text{div}(\mu H) &= 0 && \text{(Maxwell-Thomson),}
 \end{aligned}
 \tag{Maxwell}$$

where, as we have mentioned, the permittivity  $\varepsilon$  and permeability  $\mu$  inside  $D$  are piecewise constant real-valued functions. Here, we recall the definition of the curl of a vector field  $v : \mathbb{R}^3 \rightarrow \mathbb{R}^3$  of class  $\mathcal{C}^1$ :

$$\text{curl}(v)(x) = \left( \frac{\partial v_3}{\partial x_2} - \frac{\partial v_2}{\partial x_3}, \frac{\partial v_1}{\partial x_3} - \frac{\partial v_3}{\partial x_1}, \frac{\partial v_2}{\partial x_1} - \frac{\partial v_1}{\partial x_2} \right), \quad x \in \mathbb{R}^3.$$

Elementary manipulations allow to reduce this coupled system to two independent equations, one for the electric field  $E$ ,

$$(5.3.1) \quad \text{curl}(\text{curl}(E)) - k^2\nu^2 E = 0,$$

and the other for the magnetic field  $H$ :

$$\text{curl} \left( \frac{1}{\nu^2} \text{curl}(H) \right) - k^2 H = 0;$$

where, in turn, the refractive index  $\nu$  is a piecewise real-valued function on  $D$ . Since the knowledge of one of the two fields  $E$  and  $H$  easily allows to retrieve the other via (Maxwell), only the first equation (5.3.1) (for instance) needs to be solved in practice.

This equation is endowed with boundary conditions whose modeling and precise mathematical definition are a little involved, and which can be informally described as follows:

- A boundary condition accounting for the injection of a desired mode for the electric field is imposed on the entrance port  $\Gamma_{\text{in}}$  of the device, see the next Section 5.3.1.3 about modes in waveguides, and §11.1.2 in [212] or §6.3 in [386] for more details about such boundary conditions.
- The natural mechanism to express the decay of the electric field  $E$  “far” from the device is the Silver-Müller radiation condition at infinity:

$$(5.3.2) \quad \lim_{|x| \rightarrow \infty} |x| \left( \text{curl}(E) \times \frac{x}{|x|} - i\omega E \right) = 0,$$

where we recall the notation  $\times$  for the vector product between vectors in  $\mathbb{R}^3$ . Since the numerical simulation takes place in the bounded domain  $D$ , this condition is approximated by the so-called perfectly matched layer method: the region  $\partial D \setminus \overline{\Gamma_{\text{in}}}$  is surrounded by a thin layer  $D_{\text{PML}}$  of artificial absorbing material, so that any boundary condition for  $E$  on  $\partial D$  will emulate (5.3.2), starting from the simple one  $n \times E = 0$ , see [72].

### 5.3.1.3. The behavior of electromagnetic fields inside waveguides: a closer look to modes

Waveguides are the elementary structures used to transport light in one particular direction with minimum loss; in the physical setting of [Section 5.3.1.1](#), they convey the light in and out the considered nanophotonic device where it is processed. A few elements about the behavior of electromagnetic fields inside waveguides are in order, which are pivotal in the expression of the light injection boundary conditions complementing [\(5.3.1\)](#) and in the expression of the physical performance of nanophotonic devices; we refer to [\[341\]](#) for further details about these issues.

As depicted in [Fig. 5.3.2](#) (b), the considered waveguides have the form of a tube oriented in the propagation direction (hereafter set to  $e_3$ , without loss of generality) with a “simple” cross section, made of core material Si. The electric and magnetic fields  $E$  and  $H$  inside such a waveguide can be expanded as follows:

$$(5.3.3) \quad E(x) = \sum_{j=1}^N a_j E_j(x) + \sum_{j=1}^N a_{-j} E_{-j}(x) + E_{\text{rad}}(x), \quad \text{and} \quad H(x) = \sum_{j=1}^N a_j H_j(x) + \sum_{j=1}^N a_{-j} H_{-j}(x) + H_{\text{rad}}(x).$$

The basis functions  $(E_j, H_j)$  and  $(E_{\text{rad}}, H_{\text{rad}})$  featured in this decomposition are the modes of the waveguide; they account for the fundamental structure of an electromagnetic wave propagating through the latter:

- The guided modes  $(E_j, H_j)$  are those for which the energy is concentrated near the core region of the waveguide; they propagate in the forward direction of the guide when  $j > 0$  and in the backward direction if  $j < 0$ .
- The radiating fields  $(E_{\text{rad}}, H_{\text{rad}})$  are contributions whose energy is not confined near the core region, and which are therefore undesirable for our purpose.

From the mathematical viewpoint, these functions are obtained from the solution of a 2d eigenvalue problem posed in the unbounded transverse section  $\Gamma_{\text{obj}}$  of the waveguide – which is therefore referred to as “open” in the literature. They satisfy orthonormality relations, which we omit for brevity.

The coefficients  $a_j$  featured in both decompositions in [\(5.3.3\)](#) are equal and given by the following formulas:

$$\forall j = 1, \dots, N, \quad a_j = \frac{1}{4} \int_{\Gamma_{\text{obj}}} (E \times \overline{H_m} + \overline{E_m} \times H) \cdot n \, ds, \quad \text{and} \quad a_{-j} = \frac{1}{4} \int_{\Gamma_{\text{obj}}} (E \times \overline{H_j} - \overline{E_j} \times H) \cdot n \, ds.$$

Let us conclude this brief sketch with a word about the classical terminology in the literature. The guided modes of a waveguide usually carry a label of the form  $\text{TE}_j$  or  $\text{TM}_j$ , where the polarization of the mode is transverse electric (TE) (resp. transverse magnetic (TM)) if the triplet  $(E_1, H_2, E_3)$  contains more energy than  $(H_1, E_2, H_3)$  (resp. if it is the other way around), and they are ordered with respect to this distinction thanks to the index  $j = 0, \dots$ . For instance,  $\text{TE}_0$  (resp.  $\text{TM}_0$ ) is the first forward-propagating guided mode which is transverse electric (resp. transverse magnetic).

## 5.3.2. Optimization of nanophotonic devices

In this section, we enter into the realm of shape and topology optimization problems, that we formulate in the context of the design of nanophotonic devices in [Section 5.3.2.1](#), before evoking the crucial issue of robustness in [Section 5.3.2.2](#).

### 5.3.2.1. Shape optimization setting

The optimized shape  $\Omega$  accounts for the region of the design domain  $D_{\text{opt}}$  which is occupied by core material. We denote the electric and magnetic fields by  $E_\Omega$  and  $H_\Omega$  in this situation; these are the solutions to the Maxwell's equations [\(Maxwell\)](#) or [\(5.3.1\)](#) in the situation where the refractive index  $\nu \equiv \nu_\Omega$  reads:

$$\forall x \in D, \quad \nu_\Omega(x) = \begin{cases} \nu_{\text{core}} & \text{if } x \in \Omega \cup D_{\text{wg}}, \\ \nu_{\text{subs}} & \text{if } x \in D_{\text{subs}}, \\ \nu_{\text{clad}} & \text{if } x \in D \setminus (\overline{\Omega} \cup \overline{D_{\text{wg}}} \cup \overline{D_{\text{subs}}}). \end{cases}$$

Most of the considered shape optimization problems in this context involve the energy  $J_p(\Omega)$  crossing the objective surface  $\Gamma_{\text{obj}}$ . The expression of the latter is:

$$J_p(\Omega) = \int_{\Gamma_{\text{obj}}} \Pi_\Omega \cdot n \, ds, \quad \text{where the Poynting vector } \Pi_\Omega \text{ is defined by } \Pi_\Omega = \frac{1}{2} \text{Re} \left( E_\Omega \times \overline{H_\Omega} \right).$$

Often,  $\Gamma_{\text{obj}}$  is the transverse section of a waveguide connected to the device; introducing the guided modes  $(E_j, H_j)$ ,  $j = -N, \dots, -1, 1, \dots, N$  and exploiting the orthonormality relations between them, the energy  $J_p(\Omega)$  can be decomposed as:

$$J_p(\Omega) = \sum_{j=1}^N J_{o,j}(\Omega) - \sum_{j=1}^N J_{o,-j}(\Omega),$$

where the energy  $J_{o,j}(\Omega)$  conveyed by the  $j^{\text{th}}$  mode which crosses the surface  $\Gamma_{\text{obj}}$  is:

$$(5.3.4) \quad J_{o,j}(\Omega) = \left| \frac{1}{4} \int_{\Gamma_{\text{obj}}} (E_\Omega \times \overline{H_j} + \overline{E_j} \times H_\Omega) \cdot n \, ds \right|^2.$$

The generic shape and topology optimization problem considered in our investigations is then of the form:

$$(5.3.5) \quad \max_{\Omega \subset D_{\text{opt}}} J(\Omega),$$

where  $J(\Omega)$  stands for one of the functionals  $J_{o,j}(\Omega)$ ,  $j = 1, \dots, N$ .

The numerical resolution of this problem by the methods introduced in [Section 1.4.6.2](#) relies on the shape derivative of the functionals  $J_{o,j}(\Omega)$ . These expressions can be obtained thanks to elementary, albeit tedious calculations based on the methods recalled in [Section 1.3.3](#).

**Remark 5.3.1** *Although the above expression of the physical problem of interest and of the related optimal design problem feature an arbitrary region  $\Omega \subset D_{\text{opt}}$ , we have seen that the active part  $D_{\text{opt}}$  of nanophotonic devices is typically required to be invariant in the  $e_2$  direction. This constraint can be incorporated into the above framework in a straightforward manner.*

### 5.3.2.2. Robustness with respect to uncertainties in the optimal design of nanophotonic components

The physical performance of nanophotonic devices is tremendously sensitive to even very small perturbations of the parameters entering the model of [Section 5.3.1](#). Such perturbations are unfortunately inevitable in practice:

- The index of refraction  $\nu_{\text{core}}$  of the core material undergoes significant variations due to fluctuations of the ambient temperature;
- Imperfections of the laser used to inject light into the device may cause uncertainties in the frequency  $\omega$  and in the related wavelength;
- The geometry of the considered nanophotonic component itself may be subject to uncontrolled dilations or erosions with respect to the intended blueprint design, incurred by the lithography-etching manufacturing process.

The means to address uncertainties in this context differs from the general strategies proposed in [Chapter 2](#). On the one hand, the intense computational effort entailed by one single solution of the Maxwell's equation limits drastically the affordable number of applications of the numerical solver. On the other hand, the aforementioned sources of uncertainties concern parameters in very low-dimensional spaces (typically, one). These specific features call for the use of "exhaustive" methods for introducing robustness into the optimal design problem, based on a sampling of the parameter space.

Schematically, let  $\xi$  denote the considered parameter, lying inside a subset  $\Xi$  of a "low-dimensional" vector space. Let also  $\mathcal{C}(\Omega, \xi)$  stand for the objective function of interest in the situation where the actual value of the parameter equals  $\xi$ . In our applications,

- $\xi$  may stand for the operating frequency, so that  $\mathcal{C}(\Omega, \xi)$  is one of the functions  $J_{o,j}(\Omega)$  defined in [\(5.3.4\)](#) with  $\omega = \xi$ ;
- $\xi$  may represent the length scale over which the lithography stage of the fabrication process causes a smearing of  $\Omega$ , in which case:

$$(5.3.6) \quad \mathcal{C}(\Omega, \xi) = J_{o,j}(\widetilde{\Omega}_\xi),$$

where  $\widetilde{\Omega}_\xi$  is the "smeared version of  $\Omega$ " over a thickness  $\xi$ .

- $\xi$  may represent a uniform erosion or dilation parameter to account for uncertainties caused by the etching stage of the fabrication process:

$$\mathcal{C}(\Omega, \xi) = J_{o,j}((\text{Id} + \xi n_\Omega)(\Omega)).$$

The nominal optimal design problem, when  $\xi$  is assumed to be known exactly, reads:

$$\max_{\Omega \subset D_{\text{opt}}} \mathcal{C}(\Omega, \xi).$$

Sampling the set  $\Xi$  with the values  $\xi_1, \dots, \xi_p$ , we then simply consider the following robust optimal design problem:

$$\max_{\Omega \subset D_{\text{opt}}} \min_{i=1, \dots, p} \mathcal{C}(\Omega, \xi_i).$$

The latter can be turned into a standard constrained optimization program after introduction of a dummy variable  $s$ :

$$\max_{\substack{\Omega \subset D_{\text{opt}} \\ s \geq 0}} s \quad \text{s.t.} \quad s \leq \mathcal{C}(\Omega, \xi_i), \quad i = 1, \dots, p.$$

This program can be solved thanks to a classical constrained optimization algorithm, such as that introduced in [Section 3.2](#).

### 5.3.3. Numerical examples

In this section, we illustrate the above framework with the optimal design of two nanophotonic components: a duplexer and a mode converter. Our numerical implementation is based on the solver **COMSOL Multiphysics** for the three-dimensional Maxwell's equation [\(5.3.1\)](#). The optimized shape  $\Omega \subset D_{\text{opt}}$  is represented and updated via the “classical” level set method on a fixed mesh of  $D_{\text{opt}}$ , as described in [Section 1.4.6.2](#). Note that, since  $\Omega$  is required to be invariant in the  $e_2$  direction, only the 2d cross-section of  $\Omega$  in the  $(e_1, e_3)$  plane is optimized; however, the physical calculations involved in the solution of [\(5.3.5\)](#) are conducted in 3d, see [Remark 5.3.1](#) about this point.

#### 5.3.3.1. Robust shape optimization of a duplexer under uncertainties on the incoming wavelength

In this section, we consider the optimal design of a duplexer. The physical situation is depicted on [Fig. 5.3.3 \(a\)](#): the central region  $D_{\text{opt}}$  is connected to one input waveguide, whose cross-section is denoted by  $\Gamma_{\text{in}}$  and two output waveguides with cross-sections  $\Gamma_{\text{out},1}$ ,  $\Gamma_{\text{out},2}$ . We aim to optimize the shape  $\Omega \subset D_{\text{opt}}$  of the core phase so that the incoming light exit through either  $\Gamma_{\text{out},1}$  or  $\Gamma_{\text{out},2}$  depending on whether the incident wavelength equals  $\lambda_1 = 1.55 \mu\text{m}$  or  $\lambda_2 = 1.31 \mu\text{m}$ , respectively. We additionally require this behavior to be robust with respect to “small” variations of  $\lambda_1$ ,  $\lambda_2$ , with maximum amplitude  $m = 25 \text{ nm}$ .

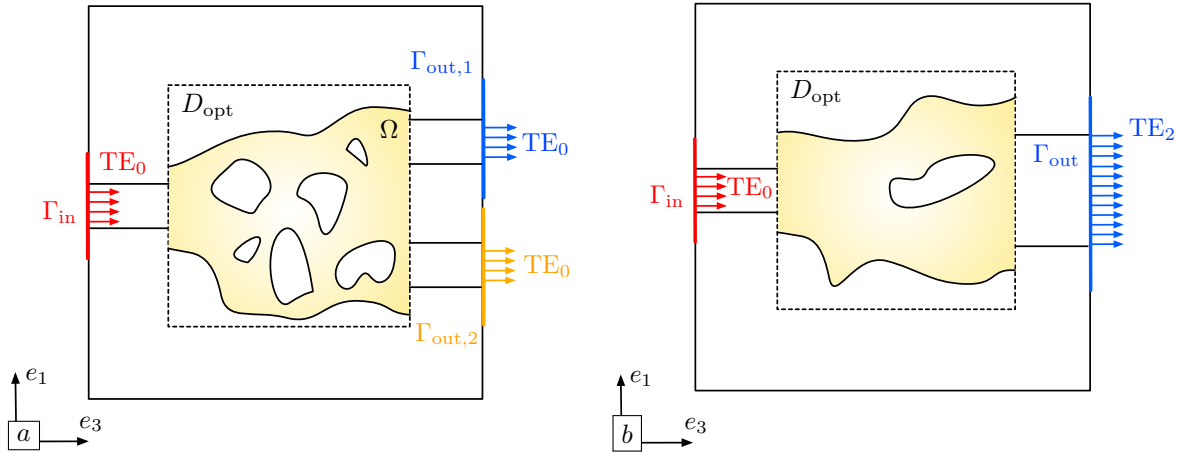


FIGURE 5.3.3. (a) Physical setting of the duplexer test case considered in [Sections 5.3.3.1](#) and [5.3.3.2](#); (b) Schematics of the mode converter test case considered in [Section 5.3.3.3](#).

To achieve this, we consider the following robust shape optimization problem:

$$\max_{\Omega \subset D_{\text{opt}}} \min_{i=1,2} \min \{ J_i^-(\Omega), J_i^+(\Omega) \},$$

where  $J_i^\pm(\Omega)$  is the function  $J_{0,1}(\Omega)$  in (5.3.4), involving the objective surface  $\Gamma_{\text{obj}} = \Gamma_{\text{out},i}$ , in the situation where the operating wavelength equals  $(\lambda_i \pm m)$ .

The initial design in this example is shaped as an array of  $8 \times 8$  regularly spaced holes. After about 100 iterations and roughly 40 hours of computation, our numerical algorithm yields the shape represented on Fig. 5.3.4. The plots of the electric field in the four situations where the injected light has wavelength  $\lambda_i \pm m$ ,  $i = 1, 2$  confirm that the optimized design manages to efficiently redirect the light to the desired channels in a robust fashion with respect to the incoming wavelength.

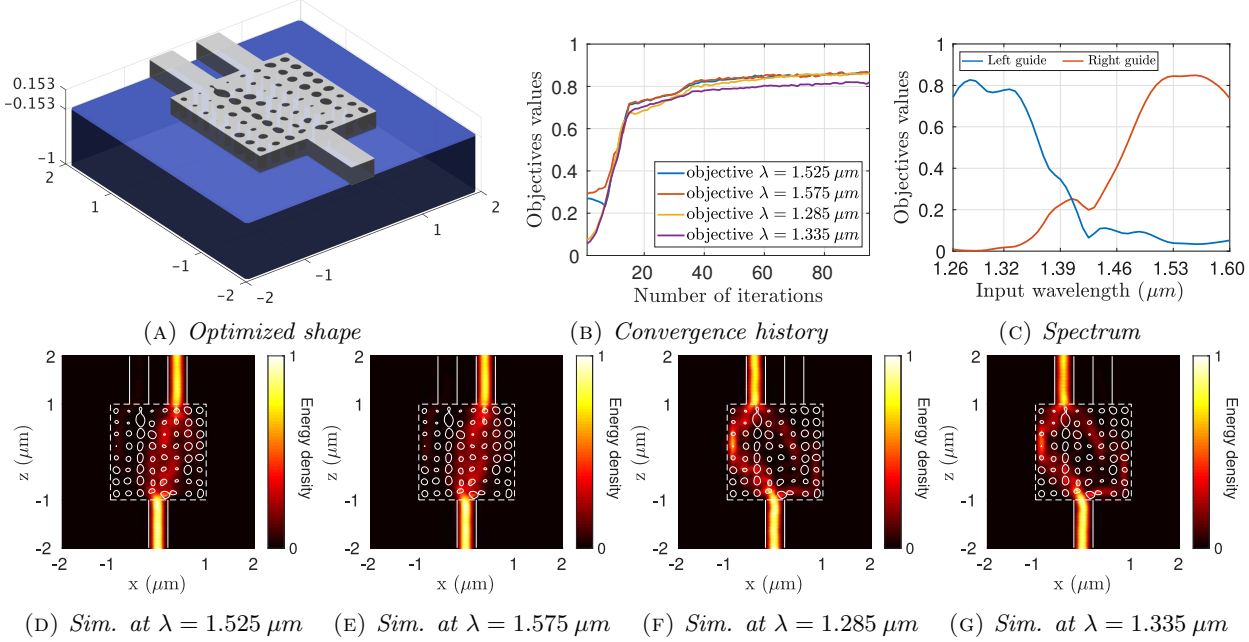


FIGURE 5.3.4. Optimized shape and details of the optimization process in the duplexer test-case considering wavelength robustness of Section 5.3.3.1.

### 5.3.3.2. Robust optimization of a duplexer with respect to uncertainties caused by etching

The present section revisits the duplexer test case considered in the previous Section 5.3.3.1; in this setting, we aim to impose that the design be robust with respect to geometric imperfections caused by the etching fabrication process, which may indeed incur an uncontrolled, uniform dilation or erosion of the design of the order of 10 nm.

So as to remedy this concern, we solve the following robust problem with respect to uncertainties over a uniform dilation or erosion of shapes by a value  $m = 10 \text{ nm}$ :

$$\max_{\Omega} \min_{i=1,2} \min \{ J_i((\text{Id} - mn_{\Omega})(\Omega)), J_i(\Omega), J_i((\text{Id} + mn_{\Omega})(\Omega)) \},$$

where, again, we have denoted by  $J_i(\Omega)$  the amount of power  $J_{0,1}(\Omega)$  carried by the first guided mode of the output waveguide  $\Gamma_{\text{out},i}$  when the operating wavelength is  $\lambda_i$ .

After 150 iterations, our shape optimization algorithm produces the shape represented on Fig. 5.3.5, whose performance is robust with respect to dilation and erosion effects.

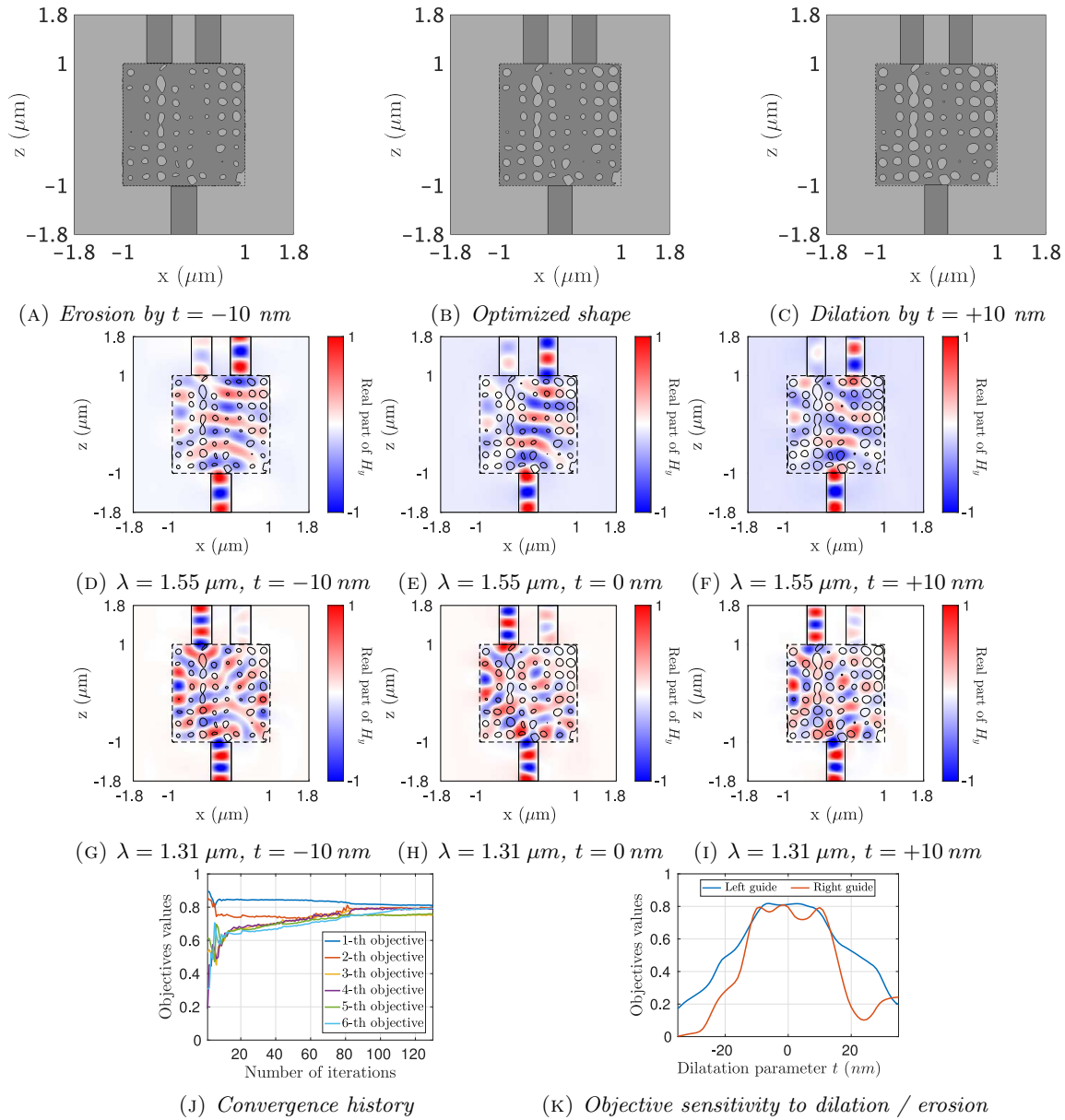


FIGURE 5.3.5. *Results of the robust shape optimization of a duplexer with respect to uncertainties linked to etching in Section 5.3.3.2.*

### 5.3.3.3. Robust optimization of a mode converter with respect to uncertainties caused by lithography

In this section, we consider the optimization of the shape of a mode converter, as depicted in Fig. 5.3.3 (b). The design domain  $D_{\text{opt}}$  is connected to one input waveguide with cross-section  $\Gamma_{\text{in}}$  and one output waveguide whose cross-section  $\Gamma_{\text{out}}$  is wide enough to allow for the existence of multiple guided modes. Light is injected into the device via the fundamental mode  $\text{TE}_0$  of the input waveguide, and we aim to transfer this power to the third mode  $\text{TE}_2$  of the output waveguide.

In addition to these requirements, we wish to enforce the robustness of the design with respect to uncertainties caused by the lithography fabrication process. To this end, we solve the problem

$$(5.3.7) \quad \max_{\Omega} \min \left\{ J_{\text{o},3}(\Omega), J_{\text{o},3}(\widetilde{\Omega}_{\xi}) \right\},$$

where we recall that the perturbation  $\widetilde{\Omega}_\xi$  is a smeared version of  $\Omega$  over the length-scale  $\xi$ , the value of which is taken as  $\xi = 30$  nm, see (5.3.6).

Starting with an array of  $8 \times 8$  holes as for initial design, we obtain the optimized shape in Fig. 5.3.6, where we have also reported the optimized shape resulting from the non robust counterpart of (5.3.7).

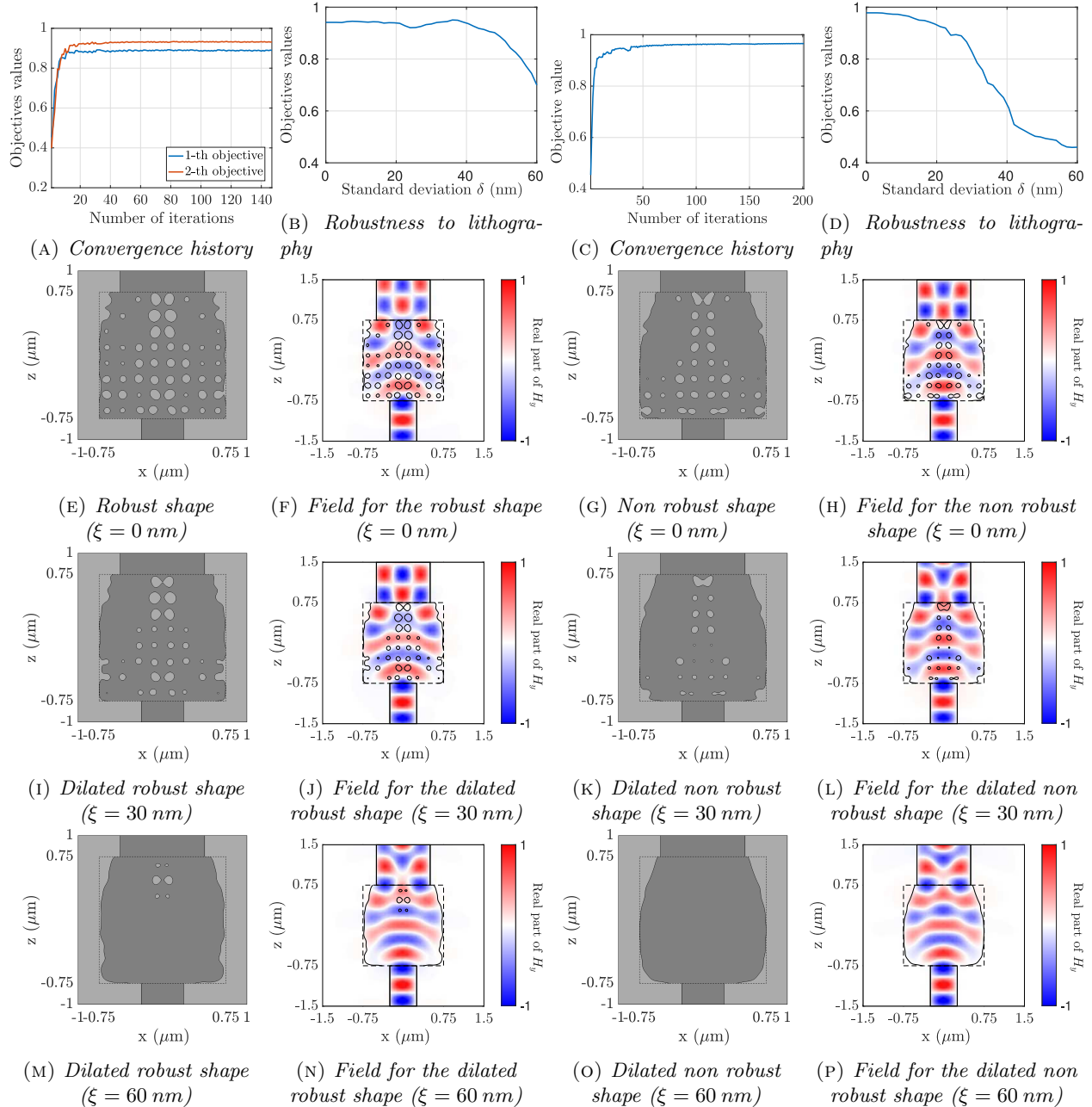


FIGURE 5.3.6. Optimization of the mode converter of Section 5.3.3.3 with an initial shape of  $8 \times 8$  holes, with and without lithography robustness.

## 5.4 PERSPECTIVES: OPTIMAL DESIGN OF AN ELECTRIC MOTOR

Electric motors are devices meant to convert electric energy into mechanical energy. They have recently aroused a tremendous enthusiasm in the academic and industrial communities with the rapidly growing emergency of realizing energy savings – electric engines can achieve much superior yield to their classical thermal counterparts – and the need for realistic alternatives to fossile fuels. They are also deemed to be a promising solution against the environmental crisis, as their carbon footprint can be inferior to that of thermal motors by up to 80%.

In a nutshell, an electric motor is composed of two parts: the fixed, outermost part is called stator, and the rotating inner part is called rotor; at least one of these components is equipped with electric coils. The current flowing through them induces an electromagnetic field giving the impetus to the rotation of the rotor. The resulting torque steers a shaft, whose mechanical work can be exploited or stored for further use, see [Fig. 5.4.1 \(a\)](#).

The inner structure of the stator–rotor assembly is complex. It is made of the coils, air, of a ferromagnetic material, and it optionally contains (costly) permanent magnets meant to boost its performance, see [Fig. 5.4.1 \(b\)](#) for an illustration and [\[219\]](#) for a more detailed presentation. A crucial challenge is to optimize the repartition of these regions in order to maximize the torque of the rotor.

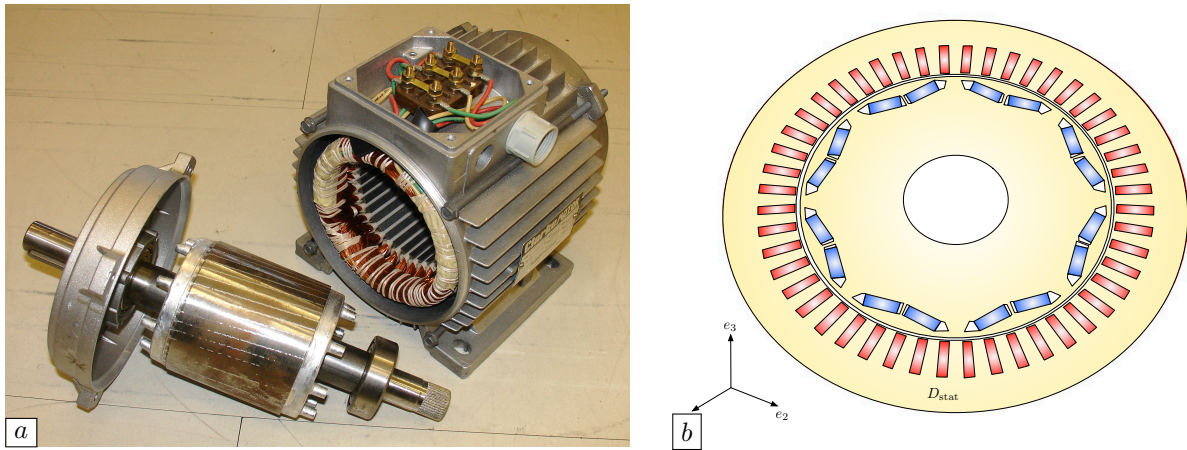


FIGURE 5.4.1. (a) Stator and rotor components of an electric motor; (b) Schematic of the 2d cross-section of an electric motor; air is depicted in white; the ferromagnetic material is in yellow, the coils are in red, and the permanent magnets are in blue.

Let us consider the following simplified, albeit realistic model based on [\[184\]](#) for this problem. In the permanent regime, the rotor rotates at constant angular velocity  $\alpha = 2\pi/T$  over a time period  $[0, T]$ , around the axis passing through the origin and oriented along  $e_3$ . Owing to the invariance of the structure of the motor in the  $e_3$  direction, the physical effects at stake can be described by a two-dimensional problem posed on its cross-section  $D$ . In the rest configuration (i.e. at time  $t = 0$ , before the rotation is initiated), the latter is decomposed into three disjoint phases

$$D = \overline{D_{\text{stat}}} \cup \overline{D_{\text{rot}}} \cup \overline{D_{\text{gap}}},$$

accounting for the stator, the rotor, and the thin air gap between them, respectively. In turn, the rotor part can be decomposed as:

$$\overline{D_{\text{rot}}} = \overline{D_{\text{mag}}} \cup \overline{\Omega} \cup \overline{\Omega_{\text{air}}}$$

where  $D_{\text{mag}}$  represents the position of the permanent magnets, and the remaining phases  $\Omega$  and  $\Omega_{\text{air}}$  are filled with ferromagnetic material and air, respectively. As  $D_{\text{mag}}$  is assumed to be non optimizable, we shall describe the optimized structure of the rotor part in terms of the phase  $\Omega$ .

As a consequence of the rotation of the rotor, the position  $\varphi_t(x)$  at time  $t$  of an arbitrary point located at  $x \in D_{\text{rot}}$  at time 0 is given by

$$\forall x = (x_1, x_2) \in D_{\text{rot}}, \quad \varphi_t(x) = \begin{pmatrix} \cos(\alpha t) & -\sin(\alpha t) \\ \sin(\alpha t) & \cos(\alpha t) \end{pmatrix} \begin{pmatrix} x_1 \\ x_2 \end{pmatrix},$$

and the velocity field driving the motion of this point is:

$$v(t, \varphi_t(x)) := \frac{\partial}{\partial t}(\varphi_t(x)).$$

At an arbitrary time  $t$ , the rotor part, and all its constituent subdomains are displaced according to this motion: the regions  $D_{\text{mag}}(t)$ ,  $\Omega(t)$  and  $\Omega_{\text{air}}(t)$  which are occupied by permanent magnets, ferromagnetic material and air in the rotated configuration are respectively  $D_{\text{mag}}(t) = \varphi_t(D_{\text{mag}})$ ,  $\Omega(t) := \varphi_t(\Omega)$  and  $\Omega_{\text{air}}(t) := \varphi_t(\Omega_{\text{air}})$ .

The three-dimensional magnetic field  $B$  within the motor is expressed in terms of the three-dimensional vector potential  $A$ ,

$$B = \text{curl}(A), \text{ where } A(t, x) = (0, 0, u(t, x_1, x_2))$$

is directed along the  $e_3$  axis and depends only on time and on the reduced variable  $x = (x_1, x_2) \in D$ . In the present low-frequency regime, one proves that the full Maxwell's equations within the motor give rise to the following 2d partial differential equation for the only non trivial component  $u$  of  $A$ :

$$(5.4.1) \quad \sigma_{\Omega(t)}(x) \left( \frac{\partial u}{\partial t} + v \cdot \nabla u \right) - \text{div}(\nu_{\Omega(t)}(x, |\nabla u|) \nabla u) = f \text{ in } (0, T) \times D,$$

which is complemented with suitable boundary conditions and time periodicity conditions. In this problem, the physical properties of the motor are characterized by the conductivity  $\sigma_{\Omega(t)}$  and the reluctivity  $\nu_{\Omega(t)}$  inside  $D$ , which take different values in the various phases at play. All these values are constant, except for the reluctivity inside the ferromagnetic material  $\Omega$ , which is a non linear function of  $\nabla u$ .

In this setting, the shape optimization problem under scrutiny consists in maximizing the average torque produced over one period:

$$(5.4.2) \quad \max_{\Omega \subset D_{\text{rot}}} J(\Omega), \text{ where } J(\Omega) := \frac{1}{T} \frac{L \nu_{\text{air}}}{r_{\text{max}} - r_{\text{min}}} T \int_0^T \int_{\Sigma} Q(x) \nabla u_{\Omega} \cdot \nabla u_{\Omega} \, dx \, dt,$$

$$\text{and } Q(x) := \frac{1}{|x|} \begin{pmatrix} x_1 x_2 & \frac{1}{2}(x_2^2 - x_1^2) \\ \frac{1}{2}(x_2^2 - x_1^2) & -x_1 x_2 \end{pmatrix}.$$

Here,  $u_{\Omega}$  is the third component of the vector potential when the phase occupied by ferromagnetic material is  $\Omega$ , solution to (5.4.1); the constant  $L$  is the length of the machine in the  $e_3$  direction,  $\Sigma$  is an annulus in the air gap  $D_{\text{gap}}$  with inner and outer radii  $r_{\text{min}}$  and  $r_{\text{max}}$ , respectively, and  $\nu_{\text{air}}$  is the reluctivity of air.

The shape optimization problem (5.4.2) has several specificities, making its study non standard:

- The boundary value problem (5.4.1) for  $u_{\Omega}$  is non linear, as the reluctivity of the ferromagnetic material depends on the gradient of  $u$ ; this makes the numerical resolution difficult. In particular, this problem has to be studied in the time domain, or by a sophisticated method of reduction to a finite number of Fourier modes.
- This boundary value problem is also expressed on a moving geometry, undergoing a known rotation. One possible method to conduct numerical simulations in this context is to take advantage of the 2d character of the problem and to rely on a (2+1)d space-time finite element method, see [345] about these.
- Likewise, the objective functional  $J(\Omega)$  depends on the shape  $\Omega$  via all its rotated versions  $\Omega(t)$  in time, which makes the calculation of the shape derivative of  $J(\Omega)$  quite technical.

A. Cesarano, P. Gangl (Radon Institute, Linz) and I have started a collaboration about such problems related to the optimization of the structure of an electric motor; a preliminary example of an optimized cross-section of a rotor is depicted on Fig. 5.4.2.

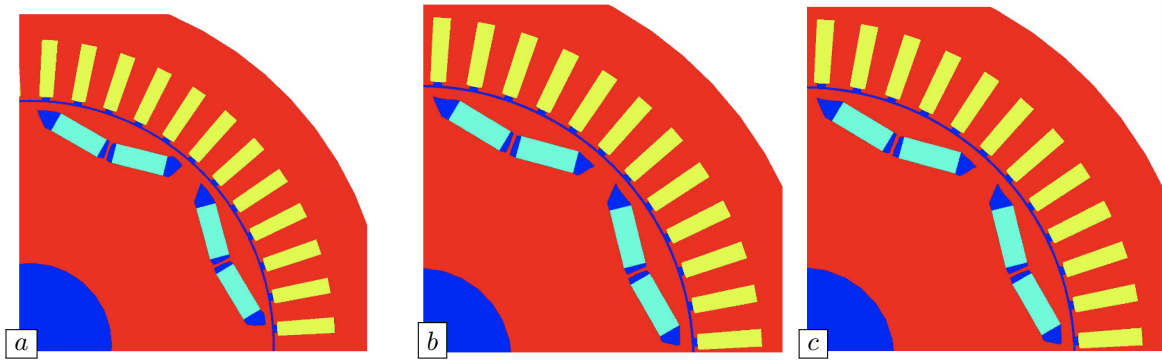


FIGURE 5.4.2. (a) Optimized design of the air pockets (in dark blue) near the permanent magnets of an electric motor as considered in [Section 5.4](#) at time  $T = 0$ ; (b) Rotated version of the optimized design at time  $t = T/2$ ; (c) Rotated version at time  $t = T$ ; only the upper-right quadrant is displayed out of symmetry.

# Chapter 6

## A few more general and long-term perspectives

This chapter outlines a few directions for future research which are more general and yet more prospective than those described in the previous chapters. In [Section 6.1](#), we present three natural developments related to remeshing algorithms, heralding promising physical applications. Then, in [Section 6.2](#), we investigate the construction of a novel optimal design framework, based on a representation of the optimized shape by the cells of a Laguerre diagram associated to a set of seed points and suitably chosen weights.

Most importantly, these few possible leads for future work are by no means an exhaustive account of the multiple mathematical theories and numerical tools that I long to discover in the future.

### 6.1 FURTHER DEVELOPMENTS ABOUT REMESHING

Mesh processing is at the heart of a great deal of the numerical experiments reported in the present manuscript; the computational tools at play are gathered in the open-source library `mmg` [[S2](#)], which is regularly updated and maintained<sup>1</sup>. In this section, we present three long-term projects, implying non trivial developments of new meshing operations.

#### 6.1.1. Insertion of lines into a simplicial mesh

The first of these operations is conceptually close to the isovalue discretization procedure described in [Section 1.4.7.3](#): it consists in the explicit insertion of a curve network into a computational mesh. More precisely, let  $D \subset \mathbb{R}^d$  ( $d = 2$  or  $3$ ) be a fixed computational domain, equipped with a simplicial mesh  $\mathcal{T}$ , and let  $\mathcal{L}$  be a collection of line segments  $\{a_i\}_{i=1,\dots,N_{\mathcal{L}}}$ , whose endpoints belong to the set  $\{p_k\}_{k=1,\dots,K_{\mathcal{L}}}$ . We wish to construct a new mesh  $\tilde{\mathcal{T}}$  of  $D$  where each element  $a_i$  of  $\mathcal{L}$  appears explicitly, possibly up to a covering – that is,  $a_i$  itself is an edge of  $\tilde{\mathcal{T}}$  or it is the reunion of several edges of  $\tilde{\mathcal{T}}$ .

Here are two potential applications of this procedure:

- In geophysics, fault lines represent features of interest inside the underground medium  $D$ , such as the limits of cracks. The number, location and geometry of these fault lines are unknown, and one simple and popular approach to identify them consists in testing multiple scenarii: the likelihood of each one is appraised by inserting the alleged lines into a mesh  $\mathcal{T}$  of  $D$  and confronting mechanical simulations performed on the resulting mesh  $\tilde{\mathcal{T}}$  with the observed behavior of the underground. A similar strategy allows to optimize the placement of drill holes with respect to geothermal heat recovery; we refer to [[231](#)] for 2d numerical implementations of such techniques and to [Fig. 6.1.1](#) for an illustration. The application of this procedure to more realistic, three-dimensional models would benefit from the development of this meshing feature in the more involved, 3d context.
- One interesting and rather original application of the procedure of [Section 1.4.7.3](#) realizing the explicit discretization of the negative subdomain of a level set function  $\phi : D \rightarrow \mathbb{R}$  into a mesh  $\mathcal{T}$  of the considered computational domain  $D$  is the creation of a mesh of a domain  $\Omega \subset D$  from

<sup>1</sup>mainly thanks to the efforts of A. Froehly!

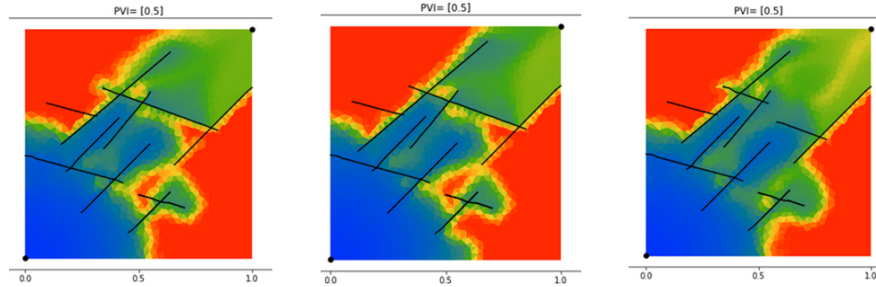


FIGURE 6.1.1. *Perturbation of a fracture network in a porous medium; result from [231].*

a possibly ill-shaped (sometimes invalid) triangulation  $\mathcal{S}$  of its boundary  $\partial\Omega$ . This application is described in [A35, A4] and it is illustrated on Fig. 6.1.2: briefly, the signed distance function  $d_\Omega$  to  $\Omega$  is calculated at the vertices of  $\mathcal{T}$  from the datum of  $\mathcal{S}$ , see Section 1.4.7.1 about this operation. The negative subdomain of  $d_\Omega$  is then explicitly discretized into  $\mathcal{T}$  thanks to the methodology of Section 1.4.7.3. This strategy is robust to “small imperfections” of  $\mathcal{S}$ , such as overlaps or “small” holes, which are ubiquitous features in data resulting from CAD models or scanning processes. Indeed, as long as the distance  $d_\Omega$  can be computed at the vertices of  $\mathcal{T}$  and that, crucially, its sign can be identified in a consistent way, the above methodology automatically produces a valid, conforming mesh of  $\Omega$ .

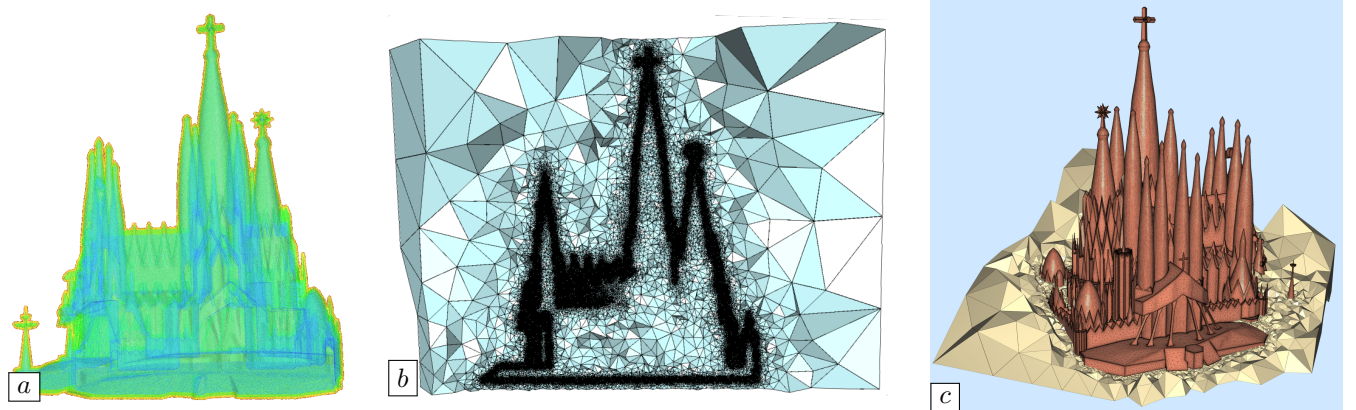


FIGURE 6.1.2. *Creation of a mesh of the Sagrada Familia  $\Omega \subset D$  from a possibly invalid triangulation  $\mathcal{S}$  of  $\partial\Omega$ ; (a) Isolines of the signed distance function  $d_\Omega$ ; (b) Refined computational mesh  $\mathcal{T}$  of  $D$  near the 0 isosurface of  $d_\Omega$ ; (c) Resulting high-quality mesh of  $\Omega$ .*

Unfortunately, this methodology does not allow to capture the sharp features of the input surface mesh  $\mathcal{S}$ , such as its corners and ridges: these entities will inevitably appear via a smoothed counterpart in the resulting mesh of  $\Omega$ , unless they are explicitly discretized in the mesh  $\mathcal{T}$  of  $D$  before the calculation of  $d_\Omega$  is conducted.

One possible idea to realize the explicit discretization of a line mesh  $\mathcal{L}$  into the computational mesh  $\mathcal{T}$  of  $D$  proceeds in the following way, which is sketched in Fig. 6.1.3.

- Insert each vertex  $p_k$  of  $\mathcal{L}$ ,  $k = 1, \dots, K_{\mathcal{L}}$  into the mesh  $\mathcal{T}$ . This stage relies on patterns, depending on whether  $p_k$  belongs to an edge, a face, or to the interior of a simplex  $T$  of  $\mathcal{T}$ .
- For each edge  $a_i$  of  $\mathcal{L}$  with endpoints  $p_k, p_l$ , identify all the simplices  $T \in \mathcal{T}$  crossed by  $a_i$ . For each such simplex  $T$ , enforce the portion  $a_i \cap \mathcal{T}$  of  $a_i$  inside  $T$  by using a suitable pattern, depending on the geometry of this intersection.

(iii) At this point, the computational mesh is a valid, conforming mesh containing all the segments  $a_i$  of  $\mathcal{L}$ , up to a covering, but it has poor finite element quality. A final quality-oriented remeshing stage yields a high-quality mesh  $\tilde{\mathcal{T}}$  of  $D$  where  $\mathcal{L}$  is explicitly discretized, see [Section 1.4.3](#).

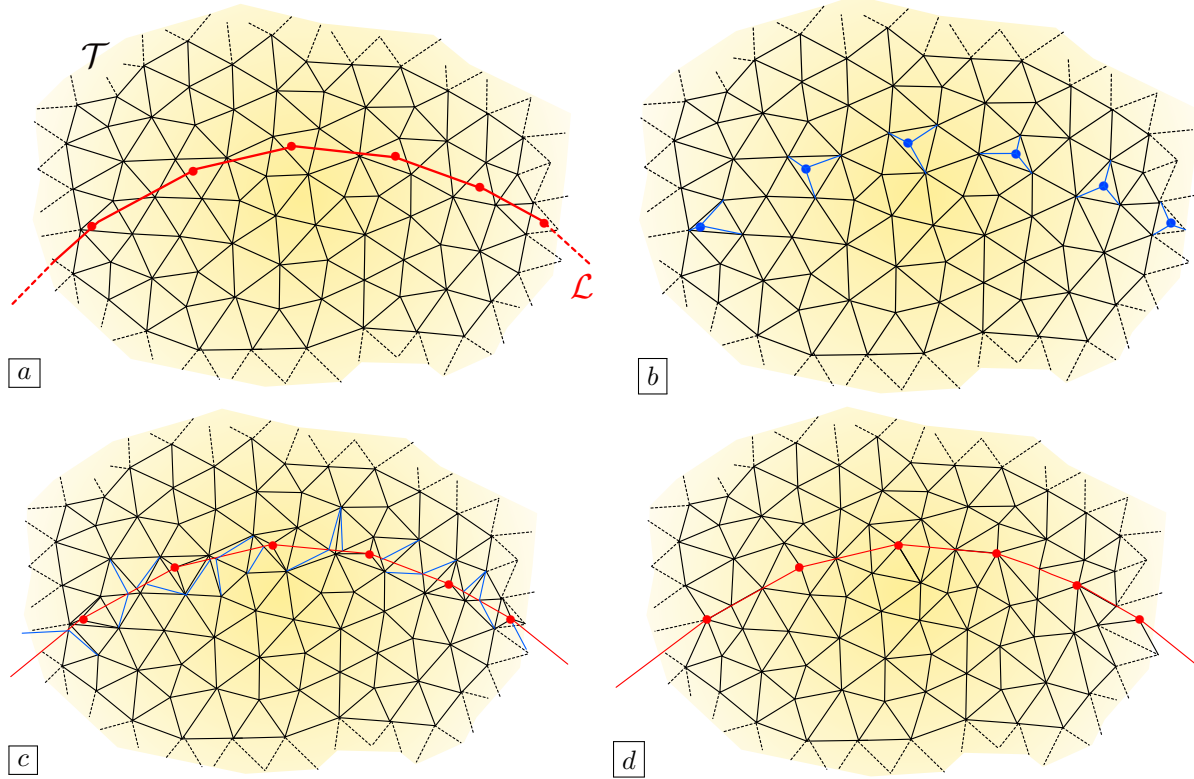


FIGURE 6.1.3. (a) Simplicial mesh  $\mathcal{T}$  of the computational domain  $D$  together with the line mesh  $\mathcal{L}$  to be inserted; (b) First step of the proposed approach in [Section 6.1.1](#): insertion of the vertices of the line mesh  $\mathcal{L}$ ; (c) Second stage: enforcement of the segments of  $\mathcal{L}$  (up to covering) by relying on patterns; (d) Final stage: quality-oriented remeshing.

### 6.1.2. Evolution of open curves and surfaces

The numerical investigations reported in this manuscript essentially concern the evolution of a domain  $\Omega(t)$  in  $\mathbb{R}^d$  over a time period  $[0, T]$ , or that of the closed surface  $\partial\Omega(t)$ . There are, however, multiple contexts where it is desirable to track the large evolution of an open surface  $S(t) \subset \mathbb{R}^d$ , while maintaining a precise, high-quality mesh of the latter throughout the process. For instance,

- In fracture mechanics, one category of numerical simulation approaches for the dynamics of crack propagation relies on an explicit discretization of the crack surfaces at every iteration of the process. Precise mechanical computations conducted on a mesh of the surrounding domain where the crack appears explicitly, or on the meshed crack surface directly, are required to evaluate the velocity field driving this motion, see e.g. [\[78, 262\]](#).
- In acoustics or in electromagnetism, open surfaces may represent screens, that is, scattering panels whose thickness is much smaller than the wavelength, see [\[3, 98\]](#). These screens are the support of specific boundary conditions in the mathematical formulation of the physical boundary value problem. Reconstruction algorithms aimed at identifying their shapes and locations from far field measurements naturally raise the need to account for their evolution.

- In structural mechanics, open surfaces may stand for shells, i.e. very thin structures which are for instance key components of aircraft fuselages or building roofs. As such, the optimization of the design of such structures has become a major issue over the recent years, see e.g. [179]. To the best of our knowledge, this issue has only been treated by delicate mesh deformation techniques, similar to those described in [Section 1.4.4](#) [104], or as a reinforcement problem, where the local thickness or the distribution of void is optimized within a fixed base surface [355, 374].

Interestingly, so-called “fractured meshes”, featuring an explicit discretization of an open surface, have recently inspired theoretical studies, see [51].

From the numerical viewpoint, the simulation of an evolving open surface has been tackled in e.g. [122, 89]. In these works, an open surface  $S$  contained in a computational domain  $D$  is represented by two level set functions  $\phi, \psi : D \rightarrow \mathbb{R}$ , as:

$$(6.1.1) \quad S = \{x \in D, \phi(x) = 0 \text{ and } \psi(x) < 0\}.$$

Here, the 0 level set of  $\phi$  is a closed extension  $\tilde{S}$  of  $S$ , and the negative subdomain of  $\psi$  within the latter coincides with  $S$ , see [Fig. 6.1.4](#).

The evolution of a surface  $S(t)$  thus described by two functions  $\phi(t, \cdot)$  and  $\psi(t, \cdot)$  with respect to a velocity field  $V(t, x)$  is achieved by solving the level set advection equation (LS-adv) for  $\phi$  and  $\psi$  in an independent fashion. Like in the “classical” practice of the level set method, the numerical stability of this strategy demands that  $\phi$  and  $\psi$  have neither “too steep”, nor “too flat” variations, see [Remark 1.4.3](#). An additional requirement, which is more specific of this setting, is that the 0 level sets of  $\phi(t, \cdot)$  and  $\psi(t, \cdot)$  should not become tangent to one another, namely:

$$(6.1.2) \quad \forall x \in D \text{ s.t. } \phi(x) = \psi(x) = 0, \text{ it holds } \nabla \phi(x) \cdot \nabla \psi(x) = 0.$$

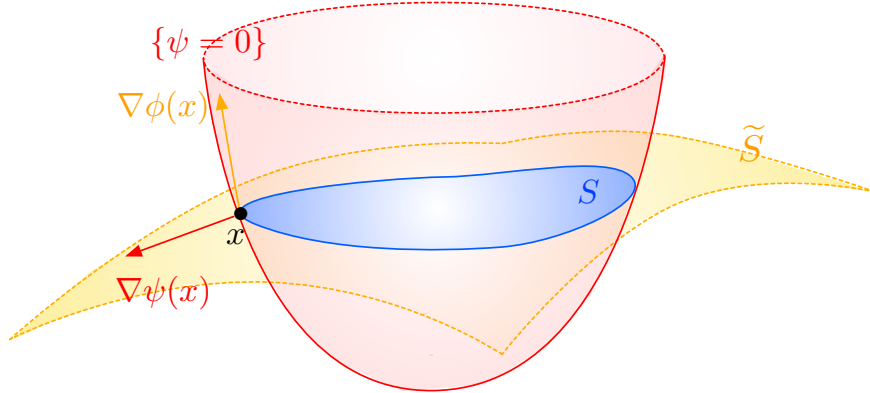


FIGURE 6.1.4. An open surface  $S \subset \mathbb{R}^d$  can be represented as the intersection of a closed surface  $\tilde{S} = \{x \in \mathbb{R}^d, \phi(x) = 0\}$  defined by a level set function  $\phi : \mathbb{R}^d \rightarrow \mathbb{R}$  with the negative subdomain of another level set function  $\psi : \mathbb{R}^d \rightarrow \mathbb{R}$ .

The combination of this evolution strategy with the remeshing techniques presented in [Section 1.4.3](#) would result in an interesting extension of the level set based mesh evolution method of [Section 1.4.7](#) for tracking the arbitrarily large evolution of an open surface  $S(t)$  while allowing an exact, high-quality meshed description of the latter throughout the process.

Let us sketch an attempted workflow to realize this operation. At each iteration  $n = 0, \dots$ , corresponding to the time  $t^n$ , the domain  $D$  is equipped with a simplicial mesh  $\mathcal{T}^n$  where the surface  $S^n := S(t^n)$  is explicitly discretized. The update between two consecutive steps  $t^n, t^{n+1}$  would then proceed as follows.

- Generate two level set functions  $\phi^n, \psi^n : D \rightarrow \mathbb{R}$  at the vertices of the mesh  $\mathcal{T}^n$  of  $D$ , representing the surface  $S^n$  in the sense that (6.1.1) holds.
- Solve the level set advection equation (LS-adv) for both functions  $\phi$  and  $\psi$  between times  $t^n$  and  $t^{n+1}$ .

- (iii) Discretize explicitly the 0 level set  $\tilde{S}^{n+1}$  of  $\phi^{n+1}$  into the mesh  $\mathcal{T}^n$ , by using the numerical algorithm of [Section 1.4.7](#).
- (iv) Discretize explicitly the negative subdomain of  $\psi^{n+1}$  into the resulting mesh of  $D$  by the same token.
- (v) Use the remeshing operations of [Section 1.4.3](#) to obtain a new, high-quality mesh  $\mathcal{T}^{n+1}$  of  $D$  where  $S^{n+1}$  is explicitly discretized.

The only ingredient of this workflow which is not yet available is an algorithm realizing its first stage. The device of such a method is a non trivial adaptation of “classical” methods for calculating the signed distance function to a domain, as presented in [Section 1.4.7.1](#), and we wish to address this issue in the near future.

### 6.1.3. Parallel remeshing

The wish to conduct numerical simulations at increasingly large scales calls for the parallel implementation of all the stages of the workflow. While the parallelization of numerical solvers, and notably the device of efficient preconditioning techniques, is by now a fairly mature subject, see e.g. [162], parallel mesh adaptation techniques, able to process very large meshes in a reasonable amount of time, have received far less attention.

Judging from the fact that the processed mesh  $\mathcal{T}$  is sometimes so large that it can barely be held in memory, it seems more efficient to prefer a shared memory implementation of parallel remeshing to one based on a distributed memory philosophy. An iterative remeshing – repartitioning strategy was proposed in this perspective in [68], which is exemplified in [Fig. 6.1.5](#). In a nutshell, at each iteration  $n = 0, \dots$ , the mesh  $\mathcal{T}^n$  is subdivided into several disjoint submeshes  $\mathcal{T}_k^n$ ,  $k = 1, \dots, K$ , the interface  $\mathcal{O}^n$  between them being a surface mesh, i.e. a collection of edges in 2d, triangles in 3d. Each submesh  $\mathcal{T}_k^n$  is remeshed in parallel by applying the sequential remeshing algorithm while leaving intact the entities of  $\mathcal{O}^n$ . The total mesh  $\mathcal{T}^{n+1}$  is then reassembled and the next iteration  $n + 1$  starts with a new partition  $\mathcal{T}_k^{n+1}$ ,  $k = 1, \dots, K$ , featuring a different interface mesh  $\mathcal{O}^{n+1}$ , so that, hopefully, after a few iterations, all the entities of the mesh have been processed.

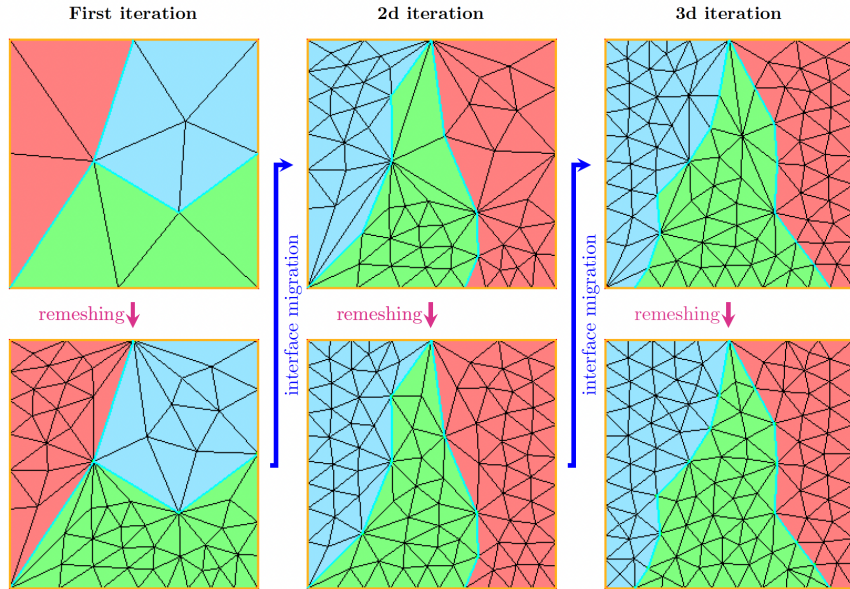


FIGURE 6.1.5. *Illustration of an iterative remeshing-repartitioning parallel mesh adaptation strategy conducted over 3 processors: at each iteration  $n$ , the mesh is divided into 3 submeshes  $\mathcal{T}_k^n$ ,  $k = 1, 2, 3$ , which are distributed over as many processors; each  $\mathcal{T}_k^n$  is remeshed, independently of the other two, while the entities of the interface mesh  $\mathcal{O}^n$  (cyan edges) are preserved.*

This strategy is admittedly simple from the conceptual point of view, but its implementation is very tedious, especially in terms of the specific data structures needed. Besides it is essential to guarantee a correct balance between the work load affected to each submesh, so as to fully exploit the potential of the parallel application of the sequential remeshing algorithm, and the redefinition procedure of the interface mesh  $\mathcal{O}^n$  between each iteration must guarantee that no region of  $\mathcal{T}$  stays untouched after a few iterations.

These considerations have already given rise to considerable developments<sup>2</sup>, see [131]. Several challenges remain to be addressed, though; notably, the parallel implementation of the explicit discretization of the negative subdomain of a level set function presented in [Section 1.4.7.3](#) still poses many technical difficulties.

## 6.2 A SHAPE AND TOPOLOGY OPTIMIZATION FRAMEWORK FEATURING A REPRESENTATION OF SHAPES WITH LAGUERRE DIAGRAMS

As we have discussed repeatedly in this manuscript (see e.g. [Section 1.4](#)), one of the major challenges faced by shape and topology optimization algorithms is the difficulty to find a representation of the shape  $\Omega \subset \mathbb{R}^d$  which is suitable for all the stages of the workflow: while a meshed representation allows for the convenient solution of boundary value problems posed on  $\Omega$ , e.g. via the finite element method, its update under this form is very intricate, and it easily produces ill-shaped, not to say downright overlapping elements. On the contrary, implicit representations of the shape (e.g. by the level set method, or via a density-based paradigm) circumvent the use of a mesh and thereby allow for a robust description of its evolution. This comes at the expense of a precise solution of the boundary value problem characterizing the physical behavior of  $\Omega$ , which has to be given an approximate counterpart posed on a larger, fixed computational domain.

This dilemma is not specific to shape and topology optimization: any application featuring the evolution of a region under the effect of a physical phenomenon described by a boundary value problem encounters the same issue (e.g. the dynamical simulation of bifluid flows, inverse problems, etc.).

An original idea to track an arbitrarily large motion of a shape  $\Omega$  embedded into a fixed computational domain  $D \subset \mathbb{R}^d$  was recently introduced by B. Levy in the article [232], taking place in the context of fluid mechanics. The latter hinges on the notion of Laguerre diagram from computational geometry, a weighted version of the more conventional one of Voronoi diagram [86]:

**Definition 6.2.1** *Let  $D \subset \mathbb{R}^d$  be a bounded open domain, and let  $s = \{s_i\}_{i=1,\dots,N}$  and  $\psi = \{\psi_i\}_{i=1,\dots,N}$  be sets of seed points  $s_i \in D$  and corresponding weights  $\psi_i \in \mathbb{R}$ . The Laguerre diagram associated to  $s$  and  $\psi$  is the following subdivision of  $\overline{D}$ :*

$$\overline{D} = \bigcup_{i=1}^N \text{Lag}_i(s, \psi), \text{ where } \text{Lag}_i(s, \psi) := \{x \in \overline{D}, |x - s_i|^2 - \psi_i \leq |x - s_j|^2 - \psi_j \ \forall j \neq i\}.$$

The fluid region  $\Omega$  considered in [232] is represented by such sets of seed points  $s = \{s_i\}_{i=1,\dots,N}$ , representing fluid particles, and weights  $\psi = \{\psi_i\}_{i=1,\dots,N}$ . These data induce the following modified Laguerre diagram:

$$(6.2.1) \quad \overline{\Omega} = \bigcup_{i=1}^N V_i(s, \psi), \text{ where } V_i(s, \psi) := \left\{ x \in \overline{D}, \begin{array}{l} |x - s_i|^2 - \psi_i \leq |x - s_j|^2 - \psi_j, \forall j \neq i \\ |x - s_i|^2 - \psi_i^2 \leq 0 \end{array} \right\},$$

is obtained after intersection of  $\text{Lag}_i(s, \psi)$  by the ball with center  $s_i$  and radius  $\psi_i^{1/2}$ . Note that, after the choice of a discretization of the spherical portions of the cell boundaries, this decomposition induces a representation of  $\Omega$  by convex polygons whose vertices are denoted by  $q_j$ ,  $j = 1, \dots, J$ , see [Fig. 6.2.1](#).

The shape  $\Omega \subset D$  in (6.2.1) is thus completely characterized by the positions of the particles  $s_i$  and the weights  $\psi_i$ . This representation can be conveniently replaced by the equivalent datum of the seed points  $s_i$  and of a volume prescription  $\nu_i$  for each cell, physically representing a region of influence for  $s_i$ : a deep result from the optimal transport theory indeed states that for each set  $s$  of seeds, there exists a unique weight vector  $\psi$  such that the volume of each cell  $V_i(s, \psi)$  equals  $\nu_i$ . Besides, these weights can be calculated by an efficient Newton algorithm, as proposed [260]. Thus setting the volume of each cell once and for all ensures

<sup>2</sup>thanks to the efforts of A. Froehly, L. Cirrotola, and a number of external contributors

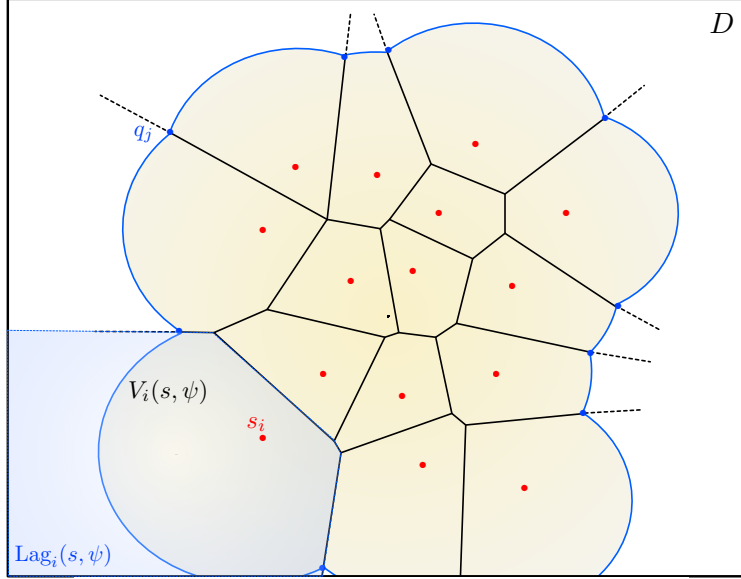


FIGURE 6.2.1. Representation (6.2.1) of a shape  $\Omega \subset D$  via the modified Laguerre diagram (6.2.1) associated to a set of seed points  $s = \{s_i\}_{i=1,\dots,N}$  and weights  $\psi = \{\psi_i\}_{i=1,\dots,N}$ .

the strict conservation of the mass of the fluid throughout the evolution; besides, it presents the technical advantage to avoid the degeneration of the cells  $V_i(s, \psi)$  in the course of the numerical evolution.

The advocated strategy in [232] to account for the evolution of a fluid region  $\Omega(t)$  over a time period  $[0, T]$  is summarized in [Algorithm 4](#). In the latter, we label with an  $n$  superscript all the values of time-dependent quantities at the discrete times  $t^n = n\Delta t$ , where  $\Delta t$  is the time step and  $n = 0, \dots$

---

**Algorithm 4** Laguerre diagram based shape evolution algorithm proposed in [232].

---

**Initialization:** Initial shape  $\Omega^0$ , described as the modified Laguerre diagram (6.2.1) associated to

- Seed points  $s^0 := \{s_i^0\}_{i=1,\dots,N}$ ,
- Weights  $\psi^0 := \{\psi_i^0\}_{i=1,\dots,N}$ , associated to prescribed measures  $\nu = \{\nu_i\}_{i=1,\dots,N}$ .

**for**  $n = 0, \dots$ , until convergence **do**

- (1) Compute the velocity of the fluid as a vector  $v_i^n \in \mathbb{R}^d$  for each seed  $s_i^n$  by a heuristic method based solely on the geometry of the cell  $V_i(s^n, \psi^n)$ .
- (2) Update the positions of the seeds as:

$$s_i^{n+1} = s_i^n + \Delta t v_i^n.$$

- (3) Calculate the new weight vector  $\psi^{n+1}$  so that each cell  $V_i(s^{n+1}, \psi^{n+1})$  have volume  $\nu_i$ .

**end for**

**return** Shape  $\Omega^n$  defined as the diagram (6.2.1) associated to seeds  $s^n$  and weights  $\psi^n$ .

---

Together with B. Levy and É. Oudet, we wish to adapt this evolution strategy, allowing for dramatic evolutions of the shape  $\Omega$  (including changes in its topology), to the solution of shape and topology optimization problems, of the form  $(\mathcal{P})$  presented in [Section 1.2.3](#). This task raises several major challenges:

- The method of [Algorithm 4](#) conveniently alleviates the solution of the flow equations (e.g. the Stokes, or the Navier-Stokes equations) on the shape  $\Omega$  by resorting to a heuristic method for calculating the velocity  $v_i$  of each seed  $s_i$ . In the context of the solution of a shape optimization problem such as  $(\mathcal{P})$ , the velocity field driving the motion stems from the shape derivatives of the objective and constraint functionals  $J(\Omega)$ ,  $G(\Omega)$ ,  $H(\Omega)$  involved in the problem. As we have

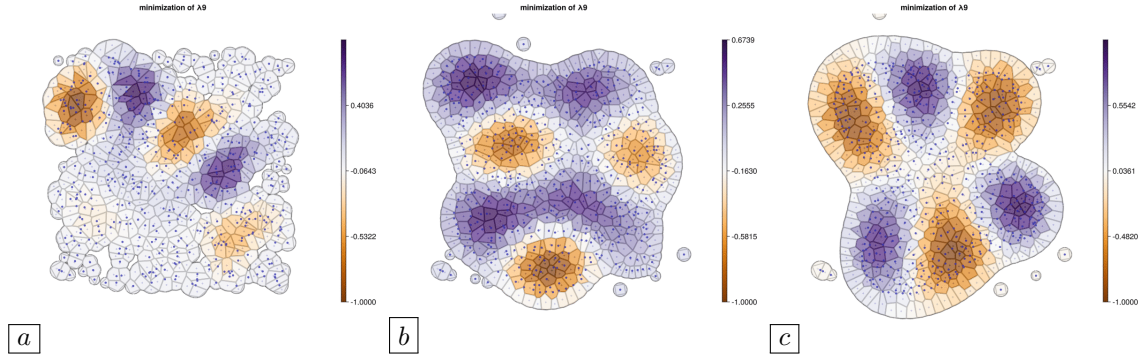


FIGURE 6.2.2. (a) Initial shape, (b) Intermediate shape, (c) Final shape resulting from the optimization of the 9<sup>th</sup> eigenvalue of the Laplace operator with homogeneous Dirichlet boundary conditions with the numerical strategy of [Section 6.2](#).

seen repeatedly throughout the manuscript, their expressions often involve the solutions to one or several boundary value problems posed on  $\Omega$ . To achieve this operation while exploiting directly the representation (6.2.1) of  $\Omega$  as a collection of convex polygons, we wish to rely on the recent “Virtual Element Method” (VEM), a finite element method tailored to polygonal tessellations of the domain [66].

- In line with this need to solve finite element problems on the polygonal mesh supplied by the modified Laguerre diagram (6.2.1), it is essential to guarantee that the elements of the latter be “well-shaped” (i.e. not too flat, etc.) – a difficulty which is absent from the original work [232], where no boundary value problem is solved. To achieve this, we could rely on a Laguerre diagram version of the well-known Lloyd relaxation algorithm, introduced in [243] to compute centroidal Voronoi tessellations, see [372].
- Another difficulty lies in the fact that the computed sensitivity of the functions  $J(\Omega)$ ,  $G(\Omega)$ ,  $H(\Omega)$  will be naturally obtained at the vertices  $q_j$  of the polygonal representation of  $\Omega$  supplied by (6.2.1). This raises the need to convert this information into sensitivities with respect to modifications of the seeds  $s$  and weights  $\psi$ , which are the “true” design variables of the problem: mathematically, this boils down to differentiate the vertices  $q_j$  with respect to the seeds  $s$  and weights  $\psi$  in (6.2.1).

An example of the use of this numerical strategy in shape and topology optimization is depicted on [Fig. 6.2.2](#); we wish to extend this preliminary study to more complex physical problems, and to three-dimensional situations.

Last but not least, this shape evolution strategy suggests interesting investigations from the theoretical point of view: loosely speaking, the choice of the seeds  $s$  and weights  $\psi$  as design variables seems to be capable of “seeing” both sensitivities of the functionals of the domain at play with respect to variations of its boundary and to its perforation by “small” holes. One possible means to shed light on these observations would be to give a continuous counterpart to the above formulation, for instance in connection with the optimal transport theory; this would perhaps suggest a connection between the derivatives of a shape functional in terms of the seeds and weights and continuous quantities such as shape and topological derivatives.

# Bibliography

- [1] N. AAGE, E. ANDREASSEN, B. S. LAZAROV, and O. SIGMUND, *Giga-voxel computational morphogenesis for structural design*, Nature 550.7674 (2017), pp. 84–86.
- [2] N. AAGE, N. MORTENSEN, and O. SIGMUND, *Topology optimization of metallic devices for microwave applications*, International Journal for numerical methods in engineering 83.2 (2010), pp. 228–248.
- [3] T. ABOUD and F. STARLING, *Scattering of an electromagnetic wave by a screen*, in Boundary value problems and integral equations in nonsmooth domains (1995), pp. 1–18.
- [4] R. ABGRALL, *Numerical discretization of the first-order Hamilton-Jacobi equation on triangular meshes*, Communications on pure and applied mathematics 49.12 (1996), pp. 1339–1373.
- [5] G. ACKE, S. DE BAERDEMACKER, P. W. CLAEYS, M. VAN RAEMDONCK, W. POELMANS, D. VAN NECK, and P. BULTINCK, *Maximum probability domains for Hubbard models*, Molecular Physics 114.7-8 (2016), pp. 1392–1405.
- [6] M. F. ADAMS, H. H. BAYRAKTAR, T. M. KEAVENY, and P. PAPADOPoulos, *Ultrascalable implicit finite element analyses in solid mechanics with over a half a billion degrees of freedom. SC'04: Proceedings of the 2004 ACM/IEEE Conference on Supercomputing*. IEEE. 2004, pp. 34–34.
- [7] R. A. ADAMS and J. J. FOURNIER, *Sobolev spaces*. Vol. 140. Academic press, 2003.
- [8] S. ADRIAENSENS, P. BLOCK, D. VEENENDAAL, and C. WILLIAMS, *Shell structures for architecture: form finding and optimization*. Routledge, 2014.
- [9] S. AGMON, A. DOUGLIS, and L. NIRENBERG, *Estimates near the boundary for solutions of elliptic partial differential equations satisfying general boundary conditions. I*, Communications on pure and applied mathematics 12.4 (1959), pp. 623–727.
- [10] M. AGUEH and G. CARLIER, *Barycenters in the Wasserstein space*, SIAM Journal on Mathematical Analysis 43.2 (2011), pp. 904–924.
- [11] A. AHMADI-JAVID, *Entropic value-at-risk: A new coherent risk measure*, Journal of Optimization Theory and Applications 155 (2012), pp. 1105–1123.
- [12] S.-H. AHN, M. MONTERO, D. ODELL, S. ROUNDY, and P. K. WRIGHT, *Anisotropic material properties of fused deposition modeling ABS*, Rapid prototyping journal (2002).
- [13] G. ALBERTI and G. BELLETTINI, *A nonlocal anisotropic model for phase transitions*, Mathematische Annalen 310.3 (1998), pp. 527–560.
- [14] G. ALLAIRE, *Analyse numérique et optimisation: Une introduction à la modélisation mathématique et à la simulation numérique*. Editions Ecole Polytechnique, 2005.

- [15] G. ALLAIRE, *Continuity of the Darcy's law in the low-volume fraction limit*, Annali della Scuola Normale Superiore di Pisa-Classe di Scienze 18.4 (1991), pp. 475–499.
- [16] G. ALLAIRE, *Shape optimization by the homogenization method*. Vol. 146. Springer Science & Business Media, 2002.
- [17] G. ALLAIRE, M. BIHR, B. BOGOSEL, and M. GODOY, *Accessibility constraints in structural optimization via distance functions*, Hal preprint: <https://hal.science/hal-03864841/> (2022).
- [18] G. ALLAIRE and B. BOGOSEL, *Optimizing supports for additive manufacturing*, Structural and Multidisciplinary Optimization 58.6 (2018), pp. 2493–2515.
- [19] G. ALLAIRE, E. BONNETIER, G. FRANCFORT, and F. JOUVE, *Shape optimization by the homogenization method*, Numerische Mathematik 76.1 (1997), pp. 27–68.
- [20] G. ALLAIRE, C. DAPOGNY, G. DELGADO, and G. MICHAILIDIS, *Multi-phase structural optimization via a level set method*, ESAIM: Control, Optimisation and Calculus of Variations 20.2 (2014), pp. 576–611.
- [21] G. ALLAIRE, F. DE GOURNAY, F. JOUVE, and A.-M. TOADER, *Structural optimization using topological and shape sensitivity via a level set method*, Control and cybernetics 34.1 (2005), p. 59.
- [22] G. ALLAIRE, P. GEOFFROY-DONDERS, and O. PANTZ, *Topology optimization of modulated and oriented periodic microstructures by the homogenization method*, to appear in Computers and Mathematics with Applications (2018).
- [23] G. ALLAIRE and L. JAKABČIN, *Taking into account thermal residual stresses in topology optimization of structures built by additive manufacturing*, Mathematical Models and Methods in Applied Sciences 28.12 (2018), pp. 2313–2366.
- [24] G. ALLAIRE, F. JOUVE, and A.-M. TOADER, *A level-set method for shape optimization*, Comptes Rendus Mathematique 334.12 (2002), pp. 1125–1130.
- [25] G. ALLAIRE, F. JOUVE, and A.-M. TOADER, *Structural optimization using sensitivity analysis and a level-set method*, Journal of computational physics 194.1 (2004), pp. 363–393.
- [26] G. ALLAIRE and M. SCHOENAUER, *Conception optimale de structures*. Vol. 58. Springer, 2007.
- [27] L. AMBROSIO and G. BUTTAZZO, *An optimal design problem with perimeter penalization*, Calculus of Variations and Partial Differential Equations 1.1 (1993), pp. 55–69.
- [28] L. AMBROSIO and N. DANCER, *Geometric evolution problems, distance function and viscosity solutions*. Springer, 2000.
- [29] L. AMBROSIO, N. FUSCO, and D. PALLARA, *Functions of bounded variation and free discontinuity problems*. Vol. 254. Clarendon Press, 2000.
- [30] L. AMBROSIO and V. TORTORELLI, *On the approximation of free discontinuity problems*, Boll. Un. Mat. Ita.1 B 6 (1992), pp. 105–123.
- [31] H. AMMARI, O. BRUNO, K. IMERI, and N. NIGAM, *Wave enhancement through optimization of boundary conditions*, SIAM Journal on Scientific Computing 42.1 (2020), B207–B224.
- [32] H. AMMARI, K. IMERI, and W. WU, *A mathematical framework for tunable metasurfaces. Part II*, Asymptotic Analysis 114.3-4 (2019), pp. 181–209.
- [33] H. AMMARI, K. KALIMERIS, H. KANG, and H. LEE, *Layer potential techniques for the narrow escape problem*, Journal de mathématiques pures et appliquées 97.1 (2012), pp. 66–84.
- [34] H. AMMARI and H. KANG, *Polarization and moment tensors: with applications to inverse problems and effective medium theory*. Vol. 162. Springer Science & Business Media, 2007.

[35] H. AMMARI and H. KANG, *Reconstruction of small inhomogeneities from boundary measurements*. Springer, 2004.

[36] H. AMMARI, H. KANG, H. LEE, and J. LIM, *Boundary perturbations due to the presence of small linear cracks in an elastic body*, Journal of Elasticity 113.1 (2013), pp. 75–91.

[37] H. AMMARI, H. KANG, H. LEE, and W.-K. PARK, *Asymptotic imaging of perfectly conducting cracks*, SIAM Journal on Scientific Computing 32.2 (2010), pp. 894–922.

[38] H. AMMARI, H. KANG, G. NAKAMURA, and K. TANUMA, *Complete asymptotic expansions of solutions of the system of elastostatics in the presence of an inclusion of small diameter and detection of an inclusion*, Journal of elasticity and the physical science of solids 67.2 (2002), pp. 97–129.

[39] H. AMMARI and J. K. SEO, *An accurate formula for the reconstruction of conductivity inhomogeneities*, Advances in Applied Mathematics 30.4 (2003), pp. 679–705.

[40] H. AMMARI, M. S. VOGELIUS, and D. VOLKOV, *Asymptotic formulas for perturbations in the electromagnetic fields due to the presence of inhomogeneities of small diameter II. The full Maxwell equations*, Journal de mathématiques pures et appliquées 80.8 (2001), pp. 769–814.

[41] S. AMSTUTZ, *Analysis of a level set method for topology optimization*, Optimization Methods and Software 26.4-5 (2011), pp. 555–573.

[42] S. AMSTUTZ, *Topological sensitivity analysis and applications in shape optimization*, Habilitation thesis, Université d’Avignon (2011).

[43] S. AMSTUTZ and H. ANDRÄ, *A new algorithm for topology optimization using a level-set method*, Journal of Computational Physics 216.2 (2006), pp. 573–588.

[44] S. AMSTUTZ and M. CILIGOT-TRAVAIN, *A notion of compliance robustness in topology optimization*, ESAIM: Control, Optimisation and Calculus of Variations 22.1 (2016), pp. 64–87.

[45] S. AMSTUTZ, I. HORCHANI, and M. MASMOUDI, *Crack detection by the topological gradient method*, Control and Cybernetics 34.1 (2005), p. 81.

[46] S. AMSTUTZ and N. VAN GOETHEM, *Topology optimization methods with gradient-free perimeter approximation*, Interfaces and Free Boundaries 14 (2012), pp. 401–430.

[47] E. ANDREASSEN, A. CLAUSEN, M. SCHEVENELS, B. S. LAZAROV, and O. SIGMUND, *Efficient topology optimization in MATLAB using 88 lines of code*, Structural and Multidisciplinary Optimization 43.1 (2011), pp. 1–16.

[48] H. ATTOUTCH, G. BUTTAZZO, and G. MICHAILLE, *Variational analysis in Sobolev and BV spaces: applications to PDEs and optimization*. Vol. 17. Siam, 2014.

[49] J. P. AUBIN, *Behavior of the error of the approximate solutions of boundary value problems for linear elliptic operators by Galerkin’s and finite difference methods*, Annali della Scuola Normale Superiore di Pisa-Classe di Scienze 21.4 (1967), pp. 599–637.

[50] J.-P. AUBIN, *Applied functional analysis*. John Wiley & Sons, 2011.

[51] M. AVERSENG, X. CLAEYS, and R. HIPTMAIR, *Fractured meshes*, Finite Elements in Analysis and Design 220 (2023), p. 103907.

[52] H. AZEGAMI, K. OHTSUKA, and M. KIMURA, *Shape derivative of cost function for singular point: Evaluation by the generalized J integral*, JSIAM Letters 6 (2014), pp. 29–32.

[53] H. AZEGAMI and Z. C. WU, *Domain optimization analysis in linear elastic problems: approach using traction method*, JSME international journal. Ser. A, Mechanics and material engineering 39.2 (1996), pp. 272–278.

[54] W. AZIZIAN, F. IUTZELER, and J. MALICK, *Regularization for Wasserstein Distributionally Robust Optimization*, arXiv preprint arXiv:2205.08826 (2022).

[55] I. BABUŠKA and M. SURI, *The  $p$ -and  $hp$  versions of the finite element method, an overview*, Computer methods in applied mechanics and engineering 80.1-3 (1990), pp. 5–26.

[56] T. BAKER and P. CAVALLO, *Dynamic adaptation for deforming tetrahedral meshes. 14th Computational Fluid Dynamics Conference*. 1999, p. 3253.

[57] L. BAR, T. F. CHAN, G. CHUNG, M. JUNG, N. KIRYATI, N. SOCHEN, and L. A. VESE, *Mumford and Shah model and its applications to image segmentation and image restoration*, Handbook of mathematical methods in imaging (2014), pp. 1–52.

[58] C. BARBAROSIE, S. LOPES, and A.-M. TOADER, *An algorithm for constrained optimization with applications to the design of mechanical structures. International Conference on Engineering Optimization*. Springer. 2018, pp. 272–284.

[59] C. BARLIER and A. BERNARD, *Fabrication additive-2e éd.: Du prototypage rapide à l'impression 3D*. Dunod, 2020.

[60] N. BARRAL and F. ALAUZET, *Three-dimensional CFD simulations with large displacement of the geometries using a connectivity-change moving mesh approach*, Engineering with Computers 35.2 (2019), pp. 397–422.

[61] T. J. BARTH and J. A. SETHIAN, *Numerical schemes for the Hamilton–Jacobi and level set equations on triangulated domains*, Journal of Computational Physics 145.1 (1998), pp. 1–40.

[62] D. BARTL, S. DRAPEAU, J. OBŁÓJ, and J. WIESEL, *Sensitivity analysis of Wasserstein distributionally robust optimization problems*, Proceedings of the Royal Society A 477.2256 (2021), p. 20210176.

[63] C. BARTLETT, *The design of the Great Pyramid of Khufu*, Nexus Network Journal 16.2 (2014), pp. 299–311.

[64] J.-L. BASDEVANT and J. DALIBARD, *Quantum mechanics*. Springer Science & Business Media, 2005.

[65] L. L. BEGHINI, A. BEGHINI, N. KATZ, W. F. BAKER, and G. H. PAULINO, *Connecting architecture and engineering through structural topology optimization*, Engineering Structures 59 (2014), pp. 716–726.

[66] L. BEIRÃO DA VEIGA, F. BREZZI, L. D. MARINI, and A. RUSSO, *The hitchhiker's guide to the virtual element method*, Mathematical models and methods in applied sciences 24.08 (2014), pp. 1541–1573.

[67] G. BELLETTINI, *Lecture notes on mean curvature flow: barriers and singular perturbations*. Vol. 12. Springer, 2014.

[68] P. BENARD, G. BALARAC, V. MOUREAU, C. DOBRZYNSKI, G. LARTIGUE, and Y. d'ANGELO, *Mesh adaptation for large-eddy simulations in complex geometries*, International journal for numerical methods in fluids 81.12 (2016), pp. 719–740.

[69] M. P. BENDSOE and N. KIKUCHI, *Generating optimal topologies in structural design using a homogenization method*, Computer methods in applied mechanics and engineering 71.2 (1988), pp. 197–224.

[70] M. P. BENDSOE and O. SIGMUND, *Topology optimization: theory, methods, and applications*. Springer Science & Business Media, 2013.

[71] A. BENOUSSAN, J.-L. LIONS, and G. PAPANICOLAOU, *Asymptotic analysis for periodic structures*. Vol. 374. American Mathematical Soc., 2011.

[72] J.-P. BERENGER, *A perfectly matched layer for the absorption of electromagnetic waves*, Journal of computational physics 114.2 (1994), pp. 185–200.

[73] E. BERETTA, E. BONNETIER, E. FRANCINI, and A. L. MAZZUCATO, *Small volume asymptotics for anisotropic elastic inclusions*, Inverse Problems and Imaging 6.1 (2012), pp. 1–23.

[74] E. BERETTA, Y. CAPDEBOSQ, F. DE GOURNAY, and E. FRANCINI, *Thin cylindrical conductivity inclusions in a three-dimensional domain: a polarization tensor and unique determination from boundary data*, Inverse Problems 25.6 (2009), p. 065004.

[75] E. BERETTA and E. FRANCINI, *An asymptotic formula for the displacement field in the presence of thin elastic inhomogeneities*, SIAM journal on mathematical analysis 38.4 (2006), pp. 1249–1261.

[76] E. BERETTA, E. FRANCINI, and M. S. VOGELIUS, *Asymptotic formulas for steady state voltage potentials in the presence of thin inhomogeneities. A rigorous error analysis*, Journal de mathématiques pures et appliquées 82.10 (2003), pp. 1277–1301.

[77] M. BERGER, A. TAGLIASACCHI, L. M. SEVERSKY, P. ALLIEZ, G. GUENNEBAUD, J. A. LEVINE, A. SHARF, and C. T. SILVA, *A survey of surface reconstruction from point clouds*. Computer Graphics Forum. Vol. 36. 1. Wiley Online Library. 2017, pp. 301–329.

[78] I. BERRE, F. DOSTER, and E. KEILEGAVLEN, *Flow in fractured porous media: A review of conceptual models and discretization approaches*, Transport in Porous Media 130.1 (2019), pp. 215–236.

[79] D. BERTSIMAS, G. J. LAUPRETE, and A. SAMAROV, *Shortfall as a risk measure: properties, optimization and applications*, Journal of Economic Dynamics and control 28.7 (2004), pp. 1353–1381.

[80] D. BERTSIMAS and I. POPESCU, *Optimal inequalities in probability theory: A convex optimization approach*, SIAM Journal on Optimization 15.3 (2005), pp. 780–804.

[81] M. BOISSIER, G. ALLAIRE, and C. TOURNIER, *Additive manufacturing scanning paths optimization using shape optimization tools*, Structural and Multidisciplinary Optimization 61.6 (2020), pp. 2437–2466.

[82] M. BOISSIER, G. ALLAIRE, and C. TOURNIER, *Concurrent shape optimization of the part and scanning path for additive manufacturing*, Hal preprint: <https://hal.science/hal-03124075/document> (2021).

[83] M. BONNET and G. DELGADO, *The topological derivative in anisotropic elasticity*, Quarterly Journal of Mechanics and Applied Mathematics 66.4 (2013), pp. 557–586.

[84] E. BONNETIER and C. DAPOGNY, *An introduction to shape and topology optimization*. Online course (slides, codes) available at: <https://membres-ljk.imag.fr/Charles.Dapogny/coursoptim.html>. 2020.

[85] E. BONNETIER and F. TRIKI, *Asymptotics in the presence of inclusions of small volume for a conduction equation: a case with a non-smooth reference potential*, Contemporary Mathematics 494 (2009), p. 95.

[86] B. BOOTS, K. SUGIHARA, S. N. CHIU, and A. OKABE, *Spatial tessellations: concepts and applications of Voronoi diagrams*. John Wiley & Sons, 2009.

[87] H. BOROUCHAKI and P. L. GEORGE, *Meshing, Geometric Modeling and Numerical Simulation 1: Form Functions, Triangulations and Geometric Modeling*. John Wiley & Sons, 2017.

[88] T. BORRVALL and J. PETERSSON, *Topology optimization of fluids in Stokes flow*, International journal for numerical methods in fluids 41.1 (2003), pp. 77–107.

[89] B. BOSE, *Detecting open surfaces in three dimensions*. PhD thesis. Massachusetts Institute of Technology, Department of Electrical Engineering ..., 2009.

[90] B. BOURDIN, *Filters in topology optimization*, International journal for numerical methods in engineering 50.9 (2001), pp. 2143–2158.

[91] B. BOURDIN, G. A. FRANCFOR, and J.-J. MARIGO, *The variational approach to fracture*, Journal of elasticity 91 (2008), pp. 5–148.

[92] F. BOYER and P. FABRIE, *Mathematical Tools for the Study of the Incompressible Navier-Stokes Equations and Related Models*. Vol. 183. Springer Science & Business Media, 2012.

[93] D. BRACKETT, I. ASHCROFT, and R. HAGUE, *Topology optimization for additive manufacturing. Proceedings of the Solid Freeform Fabrication Symposium, Austin, TX*. 2011, pp. 348–362.

[94] A. BRAIDES, *Gamma-convergence for Beginners*. Vol. 22. Clarendon Press, 2002.

[95] H. BREZIS, *Functional analysis, Sobolev spaces and partial differential equations*. Springer Science & Business Media, 2010.

[96] T. E. BRUNS and D. A. TORTORELLI, *Topology optimization of non-linear elastic structures and compliant mechanisms*, Computer methods in applied mechanics and engineering 190.26-27 (2001), pp. 3443–3459.

[97] D. BUCUR and G. BUTTAZZO, *Variational methods in some shape optimization problems*. Springer, 2002.

[98] A. BUFFA and S. H. CHRISTIANSEN, *The electric field integral equation on Lipschitz screens: definitions and numerical approximation*, Numerische Mathematik 94 (2003), pp. 229–267.

[99] C. BUI, C. DAPOGNY, and P. FREY, *advection, a solver for linear advection equation on a simplicial computational mesh*. 2023. URL: <https://github.com/ISCDtoolbox/Advection> (visited on 01/01/2023).

[100] M. BURGER, *A framework for the construction of level set methods for shape optimization and reconstruction*, Interfaces and Free boundaries 5.3 (2003), pp. 301–329.

[101] M. BURGER, B. HACKL, and W. RING, *Incorporating topological derivatives into level set methods*, Journal of Computational Physics 194.1 (2004), pp. 344–362.

[102] S. CACACE, E. CRISTIANI, and L. ROCCHI, *A level set based method for fixing overhangs in 3D printing*, Applied Mathematical Modelling 44 (2017), pp. 446–455.

[103] F. CALIGNANO, *Design optimization of supports for overhanging structures in aluminum and titanium alloys by selective laser melting*, Materials & Design 64 (2014), pp. 203–213.

[104] N. CAMPRUBI, M. BISCHOFF, and K.-U. BLETZINGER, *Shape optimization of shells and locking*, Computers & structures 82.29-30 (2004), pp. 2551–2561.

[105] E. CANCÈS, R. KERIVEN, F. LODIER, and A. SAVIN, *How electrons guard the space: shape optimization with probability distribution criteria*, Theoretical Chemistry Accounts 111.2-6 (2004), pp. 373–380.

[106] P. CANNARSA and P. CARDALIAGUET, *Representation of equilibrium solutions to the table problem of growing sandpiles*, Journal of the European Mathematical Society 6.4 (2004), pp. 435–464.

[107] S. CAO, H. WANG, X. LU, J. TONG, and Z. SHENG, *Topology Optimization Considering Porosity Defects in Metal Additive Manufacturing*, Applied Sciences 11.12 (2021), p. 5578.

[108] Y. CAPDEBOSCH, R. GRIESMAIER, and M. KNÖLLER, *An asymptotic representation formula for scattering by thin tubular structures and an application in inverse scattering*, Multiscale Modeling & Simulation 19.2 (2021), pp. 846–885.

[109] Y. CAPDEBOSCH and S. C. Y. ONG, *Extending representation formulas for boundary voltage perturbations of low volume fraction to very contrasted conductivity inhomogeneities*, Comptes Rendus. Mathématique 360.G2 (2022), pp. 127–150.

[110] Y. CAPDEBOSQ and M. S. VOGELIUS, *A general representation formula for boundary voltage perturbations caused by internal conductivity inhomogeneities of low volume fraction*, ESAIM: Mathematical Modelling and Numerical Analysis 37.1 (2003), pp. 159–173.

[111] J. CÉA, *Conception optimale ou identification de formes, calcul rapide de la dérivée directionnelle de la fonction coût*, ESAIM: Mathematical Modelling and Numerical Analysis 20.3 (1986), pp. 371–402.

[112] J. CÉA, S. GARREAU, P. GUILLAUME, and M. MASMOUDI, *The shape and topological optimizations connection*, Computer methods in applied mechanics and engineering 188.4 (2000), pp. 713–726.

[113] D. CEDIO-FENGYA, S. MOSKOW, and M. VOGELIUS, *Identification of conductivity imperfections of small diameter by boundary measurements. Continuous dependence and computational reconstruction*, Inverse problems 14.3 (1998), p. 553.

[114] M. CHAMBERLAND, *Single Digits. Single Digits*. Princeton University Press, 2015.

[115] M. CHARNLEY and M. S. VOGELIUS, *A uniformly valid model for the limiting behaviour of voltage potentials in the presence of thin inhomogeneities I. The case of an open mid-curve*, to appear in Asymptotic Analysis (2019).

[116] M. CHARNLEY and M. S. VOGELIUS, *A uniformly valid model for the limiting behaviour of voltage potentials in the presence of thin inhomogeneities II. A local energy approximation result*, to appear in Asymptotic Analysis (2019).

[117] I. CHAVEL, *Riemannian geometry: a modern introduction*. Vol. 98. Cambridge university press, 2006.

[118] S. CHEN and W. CHEN, *A new level-set based approach to shape and topology optimization under geometric uncertainty*, Structural and Multidisciplinary Optimization 44 (2011), pp. 1–18.

[119] X. CHEN and A. FRIEDMAN, *Asymptotic analysis for the narrow escape problem*, SIAM journal on mathematical analysis 43.6 (2011), pp. 2542–2563.

[120] D. CHENAIS, *On the existence of a solution in a domain identification problem*, Journal of Mathematical Analysis and Applications 52.2 (1975), pp. 189–219.

[121] S.-W. CHENG, T. K. DEY, J. SHEWCHUK, and S. SAHNI, *Delaunay mesh generation*. CRC Press Boca Raton, FL, 2013.

[122] L.-T. CHENG, P. BURCHARD, B. MERRIMAN, and S. OSHER, *Motion of curves constrained on surfaces using a level-set approach*, Journal of Computational Physics 175.2 (2002), pp. 604–644.

[123] A. CHERKAEV, *Variational methods for structural optimization*. Vol. 140. Springer Science & Business Media, 2012.

[124] A. CHERKAEV and E. CHERKAEVA, *Optimal design for uncertain loading condition. Homogenization: In Memory of Serguei Kozlov*. World Scientific, 1999, pp. 193–213.

[125] A. F. CHEVIAKOV, M. J. WARD, and R. STRAUBE, *An asymptotic analysis of the mean first passage time for narrow escape problems: Part II: The sphere*, Multiscale Modeling & Simulation 8.3 (2010), pp. 836–870.

[126] S.-K. CHOI, R. GRANDHI, and R. A. CANFIELD, *Reliability-based structural design*. Springer Science & Business Media, 2006.

[127] D. L. CHOPP, *Computing Minimal Surfaces via Level Set Curvature Flow*, Journal of Computational Physics 106.1 (1993), pp. 77–91.

[128] A. N. CHRISTIANSEN, M. NOBEL-JORGENSEN, N. AAGE, O. SIGMUND, and J. A. BÆRENTZEN, *Topology optimization using an explicit interface representation*, Structural and Multidisciplinary Optimization 49.3 (2014), pp. 387–399.

[129] P. G. CIARLET, *Mathematical elasticity: Three-dimensional elasticity*. SIAM, 2021.

[130] P. G. CIARLET, *The finite element method for elliptic problems*. Vol. 40. Siam, 2002.

[131] L. CIRROTTOLA and A. FROEHLY, *Parallel unstructured mesh adaptation using iterative remeshing and repartitioning*. 2019.

[132] *Cloaking via change of variables in electric impedance tomography*, Inverse Problems 24.1 (2008), p. 015016.

[133] D. COEURJOLLY, J.-O. LACHAUD, and P. GUETH, *Digital surface regularization with guarantees*, IEEE Transactions on Visualization and Computer Graphics 27.6 (2021), pp. 2896–2907.

[134] D. E. COOPER, M. STANFORD, K. A. KIBBLE, and G. J. GIBBONS, *Additive manufacturing for product improvement at Red Bull Technology*, Materials & Design 41 (2012), pp. 226–230.

[135] E. COPSON, *On the problem of the electrified disc*, Proceedings of the Edinburgh Mathematical Society 8.1 (1947), pp. 14–19.

[136] M. COSTABEL and E. STEPHAN, *Curvature terms in the asymptotic expansions for solutions of boundary integral equations on curved polygons*, The Journal of Integral Equations (1983), pp. 353–371.

[137] M. G. CRANDALL, H. ISHII, and P.-L. LIONS, *User’s guide to viscosity solutions of second order partial differential equations*, Bulletin of the American mathematical society 27.1 (1992), pp. 1–67.

[138] M. CUTURI, *Sinkhorn distances: Lightspeed computation of optimal transport*, Advances in neural information processing systems 26 (2013).

[139] M. DAMBRINE, H. HARBRECHT, and B. PUIG, *Computing quantities of interest for random domains with second order shape sensitivity analysis*, ESAIM: Mathematical Modelling and Numerical Analysis 49.5 (2015), pp. 1285–1302.

[140] M. DAMBRINE and D. KATEB, *On the ersatz material approximation in level-set methods*, ESAIM: Control, Optimisation and Calculus of Variations 16.3 (2010), pp. 618–634.

[141] C. DAPOGNY, *An introduction to the level set method*. Online course (slides, lecture notes) available at: <https://membres-ljk.imag.fr/Charles.Dapogny/teaching.html>. 2015.

[142] C. DAPOGNY, *An introduction to the level set method and its applications to meshing*. Mini-course (slides) available at: <https://membres-ljk.imag.fr/Charles.Dapogny/teaching.html>. 2023.

[143] C. DAPOGNY, *Localized plasmonic resonances and the Neumann-Poincaré operator: homogenization and bowties*. Mini-course (slides) available at: <https://membres-ljk.imag.fr/Charles.Dapogny/teaching.html>. 2019.

[144] C. DAPOGNY, *Refresher: differential calculus and applications*. Online course (lecture notes) available at: <https://membres-ljk.imag.fr/Charles.Dapogny/teaching.html>. 2022.

[145] C. DAPOGNY, *Shape optimization, level set methods on unstructured meshes and mesh evolution*. PhD thesis. Paris 6, 2013.

[146] C. DAPOGNY, C. DOBRZYNSKI, P. FREY, and A. FROELHY, *mmg, a platform for 2d, 3d and surface remeshing*. 2023. URL: <https://www.mmgtools.org> (visited on 01/01/2023).

[147] C. DAPOGNY and F. FEPPON, *S0tuto, a pedagogic and open-source implementation of the level set based mesh evolution method*. 2023. URL: <https://github.com/dapogny/s0tuto> (visited on 01/01/2023).

[148] C. DAPOGNY and P. FREY, *Computation of the signed distance function to a discrete contour on adapted triangulation*, Calcolo 49.3 (2012), pp. 193–219.

[149] C. DAPOGNY and P. FREY, *mshdist, an algorithm for calculating the signed distance function on a simplicial computational mesh*. 2023. URL: <https://github.com/ISCDtoolbox/Mshdist> (visited on 01/01/2023).

[150] M. DAUGE, *Elliptic boundary value problems on corner domains: smoothness and asymptotics of solutions*. Vol. 1341. Springer, 2006.

[151] F. DE GOES, D. COHEN-STEINER, P. ALLIEZ, and M. DESBRUN, *An optimal transport approach to robust reconstruction and simplification of 2d shapes*. Computer Graphics Forum. Vol. 30. 5. Wiley Online Library. 2011, pp. 1593–1602.

[152] F. DE GOURNAY, *Velocity extension for the level-set method and multiple eigenvalues in shape optimization*, SIAM journal on control and optimization 45.1 (2006), pp. 343–367.

[153] F. DE GOURNAY, G. ALLAIRE, and F. JOUVE, *Shape and topology optimization of the robust compliance via the level set method*, ESAIM: Control, Optimisation and Calculus of Variations 14.1 (2008), pp. 43–70.

[154] E. DELAGE and Y. YE, *Distributionally robust optimization under moment uncertainty with application to data-driven problems*, Operations research 58.3 (2010), pp. 595–612.

[155] M. DELFOUR and J.-P. ZOLÉSIO, *Shape identification via metrics constructed from the oriented distance function*, Control and Cybernetics 34.1 (2005), pp. 137–164.

[156] M. C. DELFOUR and J.-P. ZOLÉSIO, *Shapes and geometries: metrics, analysis, differential calculus, and optimization*. SIAM, 2011.

[157] A. DELYON, *Shape optimisation problems around the geometry of Branchiopod eggs*. PhD thesis. Université de Lorraine, 2020.

[158] J. DESAI, A. FAURE, G. MICHAILIDIS, G. PARRY, and R. ESTEVEZ, *Topology optimization in acoustics and elasto-acoustics via a level-set method*, Journal of Sound and Vibration 420 (2018), pp. 73–103.

[159] J. DESAI, G. ALLAIRE, and F. JOUVE, *Topology optimization of structures undergoing brittle fracture*, Journal of Computational Physics 458 (2022), p. 111048.

[160] C. DOBRZYNSKI and P. FREY, *Anisotropic Delaunay mesh adaptation for unsteady simulations*. Proceedings of the 17th international Meshing Roundtable. Springer, 2008, pp. 177–194.

[161] A. DOI and A. KOIDE, *An efficient method of triangulating equi-valued surfaces by using tetrahedral cells*, IEICE TRANSACTIONS on Information and Systems 74.1 (1991), pp. 214–224.

[162] V. DOLEAN, P. JOLIVET, and F. NATAF, *An introduction to domain decomposition methods: algorithms, theory, and parallel implementation*. Vol. 144. SIAM, 2015.

[163] W. DORN, *Automatic design of optimal structures*, J. de Mecanique 3 (1964), pp. 25–52.

[164] M. DRYJA and O. WIDLUND, *An additive variant of the Schwarz alternating method for the case of many subregions*. Ultracomputer Research Laboratory, Univ., Courant Inst. of Mathematical ..., 1987.

[165] J. DUMAS, J. HERGEL, and S. LEFEBVRE, *Bridging the gap: automated steady scaffoldings for 3D printing*, ACM Transactions on Graphics (TOG) 33.4 (2014), pp. 1–10.

[166] P. D. DUNNING and H. A. KIM, *Introducing the sequential linear programming level-set method for topology optimization*, Structural and Multidisciplinary Optimization 51.3 (2015), pp. 631–643.

[167] P. D. DUNNING, H. A. KIM, and G. MULLINEUX, *Introducing loading uncertainty in topology optimization*, AIAA journal 49.4 (2011), pp. 760–768.

[168] G. DUVAUT and J. L. LIONS, *Inequalities in mechanics and physics*. Vol. 219. Springer Science & Business Media, 2012.

[169] M. EIGEL, J. NEUMANN, R. SCHNEIDER, and S. WOLF, *Risk averse stochastic structural topology optimization*, Computer Methods in Applied Mechanics and Engineering 334 (2018), pp. 470–482.

[170] M. ELLIOTIS, G. GEORGIOU, and C. XENOPHONTOS, *Solving Laplacian problems with boundary singularities: a comparison of a singular function boundary integral method with the p/hp version of the finite element method*, Applied Mathematics and Computation 169.1 (2005), pp. 485–499.

[171] N. ENGHETA and R. W. ZIOLKOWSKI, *Metamaterials: physics and engineering explorations*. John Wiley & Sons, 2006.

[172] A. ERN and J.-L. GUERMOND, *Discontinuous Galerkin methods for Friedrichs' systems. I. General theory*, SIAM journal on numerical analysis 44.2 (2006), pp. 753–778.

[173] A. ERN and J.-L. GUERMOND, *Theory and practice of finite elements*. Vol. 159. Springer Science & Business Media, 2013.

[174] L. C. EVANS and R. F. GARIEPY, *Measure theory and fine properties of functions*. CRC press, 2015.

[175] G. FARIN, J. HOSCHEK, and M.-S. KIM, *Handbook of computer aided geometric design*. Elsevier, 2002.

[176] S. FATHPOUR and B. JALALI, *Silicon photonics for telecommunications and biomedicine*. CRC Press, 2011.

[177] F. FEPPON, *Shape and topology optimization applied to Compact Heat Exchangers*, Lectures notes from a course given at the Von Karman institute (2021).

[178] J. FEYDY, *Analyse de données géométriques, au delà des convolutions*. PhD thesis. Université Paris-Saclay, 2020.

[179] M. FIRL, *Optimal shape design of shell structures*. 2010.

[180] G. B. FOLLAND, *Introduction to partial differential equations*. Princeton university press, 1995.

[181] G. FREMIOT and J. SOKOLOWSKI, *Shape sensitivity analysis of problems with singularities*, Lecture notes in pure and applied mathematics (2001), pp. 255–276.

[182] P. J. FREY and P.-L. GEORGE, *Mesh generation: application to finite elements*. ISTE, 2007.

[183] M. e. FRISCH, G. TRUCKS, H. B. SCHLEGEL, G. SCUSERIA, M. ROBB, J. CHEESEMAN, G. SCALMANI, V. BARONE, G. PETERSSON, H. NAKATSUJI, et al., *Gaussian 16*. 2016.

[184] P. GANGL, *Sensitivity-based topology and shape optimization with application to electrical machines*. PhD thesis. Ph. D. thesis, Johannes Kepler University Linz, 2016.

[185] R. GAO and A. J. KLEYWEGT, *Distributionally robust stochastic optimization with Wasserstein distance*, arXiv preprint arXiv:1604.02199 (2016).

[186] L. GARDNER, P. KYVELOU, G. HERBERT, and C. BUCHANAN, *Testing and initial verification of the world's first metal 3D printed bridge*, Journal of constructional steel research 172 (2020), p. 106233.

[187] S. GARREAU, P. GUILLAUME, and M. MASMOUDI, *The topological asymptotic for PDE systems: the elasticity case*, SIAM journal on control and optimization 39.6 (2001), pp. 1756–1778.

[188] A. GAYNOR and J. GUEST, *Topology optimization considering overhang constraints: Eliminating sacrificial support material in additive manufacturing through design*, Structural and Multidisciplinary Optimization (2016), pp. 1–16.

[189] P. GEOFFROY-DONDERS, G. ALLAIRE, and O. PANTZ, *3-d topology optimization of modulated and oriented periodic microstructures by the homogenization method*, Journal of Computational Physics 401 (2020), p. 108994.

[190] M. GIACOMINI, O. PANTZ, and K. TRABELSI, *Volumetric expressions of the shape gradient of the compliance in structural shape optimization*, arXiv preprint arXiv:1701.05762 (2017).

[191] I. GIBSON, D. ROSEN, B. STUCKER, M. KHORASANI, D. ROSEN, B. STUCKER, and M. KHORASANI, *Additive manufacturing technologies*. Vol. 17. Springer, 2021.

[192] Y. GIGA, *Surface evolution equations*. Springer, 2006.

[193] S. M. GIUSTI, A. FERRER, and J. OLIVER, *Topological sensitivity analysis in heterogeneous anisotropic elasticity problem. Theoretical and computational aspects*, Computer Methods in Applied Mechanics and Engineering 311 (2016), pp. 134–150.

[194] P. L. GOULD and Y. FENG, *Introduction to linear elasticity*. Springer, 1994.

[195] R. GRIESMAIER, *A general perturbation formula for electromagnetic fields in presence of low volume scatterers*, ESAIM: Mathematical Modelling and Numerical Analysis 45.6 (2011), pp. 1193–1218.

[196] P. GRISVARD, *Elliptic problems in nonsmooth domains*. SIAM, 2011.

[197] J. P. GROEN and O. SIGMUND, *Homogenization-based topology optimization for high-resolution manufacturable microstructures*, International Journal for Numerical Methods in Engineering 113.8 (2018), pp. 1148–1163.

[198] X. GUO, W. ZHANG, and L. ZHANG, *Robust structural topology optimization considering boundary uncertainties*, Computer Methods in Applied Mechanics and Engineering 253 (2013), pp. 356–368.

[199] A. HABOUDOU, P. PEYRE, A. VANNES, and G. PEIX, *Reduction of porosity content generated during Nd: YAG laser welding of A356 and AA5083 aluminium alloys*, Materials Science and Engineering: A 363.1-2 (2003), pp. 40–52.

[200] J. HADAMARD, *Mémoire sur le problème d'analyse relatif à l'équilibre des plaques élastiques encastrées*. Vol. 33. Imprimerie nationale, 1908.

[201] A. HENROT and M. PIERRE, *Shape Variation and Optimization*. EMS Tracts in Mathematics Vol. 28, 2018.

[202] J. S. HESTHAVEN, G. ROZZA, B. STAMM, et al., *Certified reduced basis methods for parametrized partial differential equations*. Vol. 590. Springer.

[203] R. HIPTMAIR, A. PAGANINI, and S. SARGHEINI, *Comparison of approximate shape gradients*, BIT Numerical Mathematics 55.2 (2015), pp. 459–485.

[204] D. HOLCMAN and Z. SCHUSS, *The narrow escape problem*, siam REVIEW 56.2 (2014), pp. 213–257.

[205] *Homogenization of a set of parallel fibres*, Waves in random media 7.2 (1997), p. 245.

[206] K. HU, S. JIN, and C. C. WANG, *Support slimming for single material based additive manufacturing*, Computer-Aided Design 65 (2015), pp. 1–10.

[207] X. HUANG and Y.-M. XIE, *A further review of ESO type methods for topology optimization*, Structural and Multidisciplinary Optimization 41 (2010), pp. 671–683.

[208] J. D. JACKSON, *Classical electrodynamics*. John Wiley & Sons, 2007.

[209] N. JENKINS and K. MAUTE, *An immersed boundary approach for shape and topology optimization of stationary fluid-structure interaction problems*, Structural and Multidisciplinary Optimization 54 (2016), pp. 1191–1208.

[210] N. JENKINS and K. MAUTE, *Level set topology optimization of stationary fluid-structure interaction problems*, Structural and Multidisciplinary Optimization 52 (2015), pp. 179–195.

[211] J. S. JENSEN and O. SIGMUND, *Topology optimization for nano-photonics*, Laser & Photonics Reviews 5.2 (2011), pp. 308–321.

[212] J.-M. JIN, *The finite element method in electromagnetics*. John Wiley & Sons, 2015.

[213] N. KAYA, *Machining fixture locating and clamping position optimization using genetic algorithms*, Computers in industry 57.2 (2006), pp. 112–120.

[214] A. KHELIFI and H. ZRIBI, *Asymptotic expansions for the voltage potentials with two-dimensional and three-dimensional thin interfaces*, Mathematical Methods in the Applied Sciences 34.18 (2011), pp. 2274–2290.

[215] R. KIMMEL and J. A. SETHIAN, *Computing geodesic paths on manifolds*, Proceedings of the national academy of Sciences 95.15 (1998), pp. 8431–8435.

[216] M. H. KOBAYASHI, R. A. CANFIELD, and R. M. KOLONAY, *On a cellular developmental method for layout optimization via the two-point topological derivative*, Structural and Multidisciplinary Optimization 64.4 (2021), pp. 2343–2360.

[217] O. KONONCHUK and B.-Y. NGUYEN, *Silicon-on-insulator (soi) technology: Manufacture and applications*. Elsevier, 2014.

[218] V. A. KOZLOV, V. MAZIA, and J. ROSSMANN, *Elliptic boundary value problems in domains with point singularities*. Vol. 52. American Mathematical Soc., 1997.

[219] P. C. KRAUSE, O. WASYNCZUK, S. D. SUDHOFF, and S. D. PEKAREK, *Analysis of electric machinery and drive systems*. Vol. 75. John Wiley & Sons, 2013.

[220] L. KROG, A. TUCKER, M. KEMP, and R. BOYD, *Topology optimisation of aircraft wing box ribs. 10th AIAA/ISSMO multidisciplinary analysis and optimization conference*. 2004, p. 4481.

[221] R. S. KSHETRIMAYUM, *A brief intro to metamaterials*, IEEE potentials 23.5 (2004), pp. 44–46.

[222] D. KUHN, P. M. ESFAHANI, V. A. NGUYEN, and S. SHAFIEEZADEH-ABADEH, *Wasserstein distributionally robust optimization: Theory and applications in machine learning. Operations research & management science in the age of analytics*. Informs, 2019, pp. 130–166.

[223] O. A. LADYZHENSKAYA, *The mathematical theory of viscous incompressible flow*, Gordon & Breach (1969).

[224] S. LANG, *Fundamentals of differential geometry*. Vol. 191. Springer Science & Business Media, 2012.

[225] M. LANGELAAR, *An additive manufacturing filter for topology optimization of print-ready designs*, Structural and Multidisciplinary Optimization 55 (2016), pp. 1–13.

[226] M. LANGELAAR, *Topology optimization of 3D self-supporting structures for additive manufacturing*, Additive Manufacturing 12 (2016), pp. 60–70.

[227] M. LEARY, L. MERLI, F. TORTI, M. MAZUR, and M. BRANDT, *Optimal topology for additive manufacture: a method for enabling additive manufacture of support-free optimal structures*, Materials & Design 63 (2014), pp. 678–690.

[228] N. LEBBE, *Contribution in topological optimization and application to nanophotonics*. PhD thesis. Université Grenoble Alpes, 2019.

[229] C. LEE, S. KIM, H. KIM, and S.-H. AHN, *Measurement of anisotropic compressive strength of rapid prototyping parts*, Journal of materials processing technology 187 (2007), pp. 627–630.

[230] S. H. LEE and W. CHEN, *A comparative study of uncertainty propagation methods for black-box-type problems*, Structural and multidisciplinary optimization 37 (2009), pp. 239–253.

[231] C. LEGENTIL, J. PELLERIN, P. CUPILLARD, A. FROEHLY, and G. CAUMON, *Testing scenarios on geological models: Local interface insertion in a 2D mesh and its impact on seismic wave simulation*, Computers & Geosciences 159 (2022), p. 105013.

[232] B. LÉVY, *Partial optimal transport for a constant-volume Lagrangian mesh with free boundaries*, Journal of Computational Physics 451 (2022), p. 110838.

[233] M. LEWIN, *Théorie spectrale et mécanique quantique*. Ecole Polytechnique, 2019.

[234] Z.-C. LI and T.-T. LU, *Singularities and treatments of elliptic boundary value problems*, Mathematical and Computer Modelling 31.8-9 (2000), pp. 97–145.

[235] H. LI, T. KONDOH, P. JOLIVET, K. FURUTA, T. YAMADA, B. ZHU, K. IZUI, and S. NISHIWAKI, *Three-dimensional topology optimization of a fluid–structure system using body-fitted mesh adaption based on the level-set method*, Applied Mathematical Modelling 101 (2022), pp. 276–308.

[236] H. LI, M. YU, P. JOLIVET, J. ALEXANDERSEN, T. KONDOH, T. HU, K. FURUTA, K. IZUI, and S. NISHIWAKI, *Reaction–diffusion equation driven topology optimization of high-resolution and feature-rich structures using unstructured meshes*, Advances in Engineering Software 180 (2023), p. 103457.

[237] X. LI, *Matched asymptotic analysis to solve the narrow escape problem in a domain with a long neck*, Journal of Physics A: Mathematical and Theoretical 47.50 (2014), p. 505202.

[238] X. LI, H. LEE, and Y. WANG, *Asymptotic analysis of the narrow escape problem in dendritic spine shaped domain: three dimensions*, Journal of Physics A: Mathematical and Theoretical 50.32 (2017), p. 325203.

[239] F. LIN, X. FANG, and Z. GAO, *Distributionally Robust Optimization: A review on theory and applications*, Numerical Algebra, Control & Optimization 12.1 (2022), p. 159.

[240] J. LIONS, *Optimal control of systems governed by partial differential equations*. Grundlehren der mathematischen Wissenschaften. Springer-Verlag, 1971.

[241] J.-L. LIONS and E. MAGENES, *Problèmes aux limites non homogènes et applications. Volume I* (1968).

[242] J. LIU, A. T. GAYNOR, S. CHEN, Z. KANG, K. SURESH, A. TAKEZAWA, L. LI, J. KATO, J. TANG, C. C. WANG, et al., *Current and future trends in topology optimization for additive manufacturing*, Structural and Multidisciplinary Optimization (), pp. 1–27.

[243] S. LLOYD, *Least squares quantization in PCM*, IEEE transactions on information theory 28.2 (1982), pp. 129–137.

[244] D. S. LO, *Finite element mesh generation*. CRC Press, 2014.

[245] M. LOÈVE, *Probability theory*. Courier Dover Publications, 2017.

[246] G. J. LORD, C. E. POWELL, and T. SHARDLOW, *An introduction to computational stochastic PDEs*. Vol. 50. Cambridge University Press, 2014.

[247] W. E. LORENSEN and H. E. CLINE, *Marching cubes: A high resolution 3D surface construction algorithm*, ACM siggraph computer graphics 21.4 (1987), pp. 163–169.

[248] C. LUNDGAARD, J. ALEXANDERSEN, M. ZHOU, C. S. ANDREASEN, and O. SIGMUND, *Revisiting density-based topology optimization for fluid-structure-interaction problems*, Structural and Multidisciplinary Optimization 58 (2018), pp. 969–995.

[249] J. MA, M. Y. WANG, and X. ZHU, *Compliant fixture layout design using topology optimization method*. 2011 IEEE International Conference on Robotics and Automation. IEEE. 2011, pp. 3757–3763.

[250] C. MANTEGAZZA and A. C. MENNUCCI, *Hamilton-Jacobi Equations and Distance Functions on Riemannian Manifolds*, Applied Mathematics & Optimization 47.1 (2003).

[251] J. MARTÍNEZ-FRUTOS and D. HERRERO-PÉREZ, *GPU acceleration for evolutionary topology optimization of continuum structures using isosurfaces*, Computers & Structures 182 (2017), pp. 119–136.

[252] J. MARTÍNEZ-FRUTOS and D. HERRERO-PÉREZ, *Large-scale robust topology optimization using multi-GPU systems*, Computer Methods in Applied Mechanics and Engineering 311 (2016), pp. 393–414.

[253] J. MARTÍNEZ-FRUTOS, D. HERRERO-PÉREZ, M. KESSLER, and F. PERIAGO, *Robust shape optimization of continuous structures via the level set method*, Computer Methods in Applied Mechanics and Engineering 305 (2016), pp. 271–291.

[254] Y. MASS and O. AMIR, *Topology optimization for additive manufacturing: Accounting for overhang limitations using a virtual skeleton*, Additive Manufacturing 18 (2017), pp. 58–73.

[255] S. MAUCH, *A fast algorithm for computing the closest point and distance transform* (2000).

[256] A. MAURY, G. ALLAIRE, and F. JOUVE, *Shape optimisation with the level set method for contact problems in linearised elasticity*, The SMAI journal of computational mathematics 3 (2017), pp. 249–292.

[257] K. MAUTE, *Topology optimization under uncertainty*, in Topology optimization in structural and continuum mechanics (2014), pp. 457–471.

[258] W. C. H. MCLEAN, *Strongly elliptic systems and boundary integral equations*. Cambridge university press, 2000.

[259] F. P. MELCHELS, M. A. DOMINGOS, T. J. KLEIN, J. MALDA, P. J. BARTOLO, and D. W. HUTMACHER, *Additive manufacturing of tissues and organs*, Progress in Polymer Science 37.8 (2012), pp. 1079–1104.

[260] Q. MERIGOT and B. THIBERT, *Optimal transport: discretization and algorithms. Handbook of Numerical Analysis*. Vol. 22. Elsevier, 2021, pp. 133–212.

[261] G. MICHAILIDIS, *Manufacturing constraints and multi-phase shape and topology optimization via a level-set method*. PhD thesis. 2014.

[262] C. MIEHE and E. GÜRSSES, *A robust algorithm for configurational-force-driven brittle crack propagation with r-adaptive mesh alignment*, International Journal for Numerical Methods in Engineering 72.2 (2007), pp. 127–155.

[263] G. W. MILTON, M. BRIANE, and J. R. WILLIS, *On cloaking for elasticity and physical equations with a transformation invariant form*, New Journal of Physics 8.10 (2006), p. 248.

[264] M. MIRANDA JR, D. PALLARA, F. PARONETTO, and M. PREUNKERT, *Short-time heat flow and functions of bounded variation in  $\mathbb{R}^N$* . Annales de la Faculté des sciences de Toulouse: Mathématiques. Vol. 16. 1. 2007, pp. 125–145.

[265] J. MIRELES, D. ESPALIN, D. ROBERSON, B. ZINNIEL, F. MEDINA, and R. WICKER, *Fused deposition modeling of metals. 2012 International Solid Freeform Fabrication Symposium*. University of Texas at Austin. 2012.

[266] M. K. MISZTAL and J. A. BÆRENTZEN, *Topology-adaptive interface tracking using the deformable simplicial complex*, ACM Transactions on Graphics (TOG) 31.3 (2012), pp. 1–12.

[267] L. MODICA and S. MORTOLA, *Un esempio di  $\Gamma$ -convergenza*, Unione Mat. Ital. Sez. B 14 (1977), pp. 285–299.

[268] L. MODICA, *The gradient theory of phase transitions and the minimal interface criterion*, Archive for Rational Mechanics and Analysis 98.2 (1987), pp. 123–142.

[269] N. MOES, J.-F. REMACLE, J. LAMBRECHTS, B. LE, and N. CHEVAUGEON, *The eXtreme Mesh deformation approach (X-MESH) for the Stefan phase change model*, Journal of Computational Physics (2023), p. 111878.

[270] P. MOHAJERIN ESFAHANI and D. KUHN, *Data-driven distributionally robust optimization using the Wasserstein metric: Performance guarantees and tractable reformulations*, Mathematical Programming 171.1 (2018), pp. 115–166.

[271] B. MOHAMMADI and O. PIRONNEAU, *Applied shape optimization for fluids*. Oxford university press, 2010.

[272] P. MONK, *Finite element methods for Maxwell's equations*. Oxford University Press, 2003.

[273] R. MONROE, *Porosity in castings*, AFS Transactions 113 (2005), pp. 519–546.

[274] K. MUMTAZ, P. VORA, and N. HOPKINSON, *A method to eliminate anchors/supports from directly laser melted metal powder bed processes*. Proc. Solid Freeform Fabrication Symposium. Sheffield. 2011, pp. 55–64.

[275] F. MURAT and J. SIMON, *Sur le contrôle par un domaine géométrique*, Pré-publication du Laboratoire d'Analyse Numérique,(76015) (1976).

[276] F. MURAT, *Contre-exemples pour divers problèmes ou le contrôle intervient dans les coefficients*, Annali di Matematica Pura ed Applicata 112.1 (1977), pp. 49–68.

[277] F. MURAT and L. TARTAR, *H-convergence. Topics in the mathematical modelling of composite materials*. Springer, 2018, pp. 21–43.

[278] C. NARDONI, D. DANAN, C. MANG, F. BORDEU, and J. CORTIAL, *A R&D software platform for shape and topology optimization using body-fitted meshes. Mesh Generation and Adaptation: Cutting-Edge Techniques*. Springer, 2022, pp. 23–39.

[279] S. NAZAROV, A. SLUTSKIJ, and J. SOKOŁOWSKI, *Topological derivative of the energy functional due to formation of a thin ligament on a spatial body*, Folia Mathematicae, Acta Universitatis Lodzienis 12 (2005), pp. 39–72.

[280] S. NAZAROV and J. SOKOŁOWSKI, *The topological derivative of the Dirichlet integral due to formation of a thin ligament*, Siberian Mathematical Journal 45.2 (2004), pp. 341–355.

[281] S. A. NAZAROV and J. SOKOŁOWSKI, *Self-adjoint extensions of differential operators and exterior topological derivatives in shape optimization*, Control and Cybernetics 34 (2005), pp. 903–925.

[282] J.-C. NÉDÉLEC, *Acoustic and electromagnetic equations: integral representations for harmonic problems*. Vol. 144. Springer Science & Business Media, 2001.

[283] H.-M. NGUYEN and M. S. VOGELIUS, *A representation formula for the voltage perturbations caused by diametrically small conductivity inhomogeneities. Proof of uniform validity*, Annales de l'Institut Henri Poincaré (C) Non Linear Analysis 26.6 (2009), pp. 2283–2315.

[284] J. NITSCHE, *Ein kriterium für die quasi-optimalität des ritzschen verfahrens*, Numerische Mathematik 11.4 (1968), pp. 346–348.

[285] F. NOBILE, R. TEMPONE, and C. G. WEBSTER, *A sparse grid stochastic collocation method for partial differential equations with random input data*, SIAM Journal on Numerical Analysis 46.5 (2008), pp. 2309–2345.

[286] J. NOCEDAL and S. J. WRIGHT, *Numerical optimization* 2nd. Springer, 2006.

[287] M. NODA, K. MATSUSHIMA, and T. YAMADA, *TOPOLOGY OPTIMIZATION ALGORITHM USING TWO-POINT TOPOLOGICAL DERIVATIVE ()*.

[288] M. NOVACK, I. TOPALOGLU, and R. VENKATRAMAN, *Least Wasserstein distance between disjoint shapes with perimeter regularization*, Journal of Functional Analysis 284.1 (2023), p. 109732.

[289] A. A. NOVOTNY and J. SOKOŁOWSKI, *Topological derivatives in shape optimization*. Springer Science & Business Media, 2012.

[290] S. OH, Y. JUNG, S. KIM, I. LEE, and N. KANG, *Deep generative design: Integration of topology optimization and generative models*, Journal of Mechanical Design 141.11 (2019).

[291] S. OSHER and R. FEDKIW, *Level set methods and dynamic implicit surfaces*. Vol. 153. Springer Science & Business Media, 2006.

[292] S. OSHER and J. A. SETHIAN, *Fronts propagating with curvature-dependent speed: algorithms based on Hamilton-Jacobi formulations*, Journal of computational physics 79.1 (1988), pp. 12–49.

[293] S. J. OSHER and F. SANTOSA, *Level set methods for optimization problems involving geometry and constraints: I. Frequencies of a two-density inhomogeneous drum*, Journal of Computational Physics 171.1 (2001), pp. 272–288.

[294] O. PANTZ, *Sensibilité de l'équation de la chaleur aux sauts de conductivité*, Comptes Rendus Mathématique 341.5 (2005), pp. 333–337.

[295] O. PANTZ and K. TRABELSI, *A post-treatment of the homogenization method for shape optimization*, SIAM Journal on Control and Optimization 47.3 (2008), pp. 1380–1398.

[296] G. A. PAVLIOTIS, *Stochastic processes and applications: diffusion processes, the Fokker-Planck and Langevin equations*. Vol. 60. Springer, 2014.

[297] J. B. PENDRY, D. SCHURIG, and D. R. SMITH, *Controlling electromagnetic fields*, science 312.5781 (2006), pp. 1780–1782.

[298] V. PETROVIC, J. VICENTE HARO GONZALEZ, O. JORDA FERRANDO, J. DELGADO GORDILLO, J. RAMON BLASCO PUCHADES, and L. PORTOLES GRINAN, *Additive layered manufacturing: sectors of industrial application shown through case studies*, International Journal of Production Research 49.4 (2011), pp. 1061–1079.

[299] G. PEYRÉ, M. CUTURI, et al., *Computational Optimal Transport: With Applications to Data Science*, Foundations and Trends in Machine Learning 11.5-6 (2019), pp. 355–607.

[300] G. PEYRÉ, J. FADILI, and J. RABIN, *Wasserstein active contours. 2012 19th IEEE International Conference on Image Processing*. IEEE. 2012, pp. 2541–2544.

[301] S. PILLAY, M. J. WARD, A. PEIRCE, and T. KOLOKOLNIKOV, *An asymptotic analysis of the mean first passage time for narrow escape problems: Part I: Two-dimensional domains*, Multiscale Modeling & Simulation 8.3 (2010), pp. 803–835.

[302] O. PIRONNEAU, *Finite element methods for fluids*. Wiley Chichester, 1989.

[303] O. PIRONNEAU, *Optimal shape design for elliptic systems*. Springer, 1982.

[304] R.-E. PLESSIX, *A review of the adjoint-state method for computing the gradient of a functional with geophysical applications*, Geophysical Journal International 167.2 (2006), pp. 495–503.

[305] G. PÓLYA and G. SZEGÖ, *Isoperimetric inequalities in mathematical physics*. 27. Princeton University Press, 1951.

[306] A. N. PRESSLEY, *Elementary differential geometry*. Springer Science & Business Media, 2010.

[307] B. PROTAS, T. R. BEWLEY, and G. HAGEN, *A computational framework for the regularization of adjoint analysis in multiscale PDE systems*, Journal of Computational Physics 195.1 (2004), pp. 49–89.

[308] X. QIAN, *Undercut and overhang angle control in topology optimization: a density gradient based integral approach*, International Journal for Numerical Methods in Engineering 111 (2017), pp. 247–272.

[309] H. RAHIMIAN and S. MEHROTRA, *Distributionally robust optimization: A review*, arXiv preprint arXiv:1908.05659 (2019).

[310] L. RAKOTONDRAINIBE, *Modélisation mécanique d'une "Face Accessoire Assemblée" et optimisation d'un modèle simplifié*. PhD thesis. Ecole Polytechnique X, 2017.

[311] P. RAMACIOTTI MORALES, *Theoretical and numerical aspects of wave propagation phenomena in complex domains and applications to remote sensing*. PhD thesis. Université Paris-Saclay (ComUE), 2016.

[312] J. W. S. B. RAYLEIGH, *The theory of sound*. Vol. 2. Macmillan, 1896.

[313] *Reduced basis approximation and a posteriori error estimation for affinely parametrized elliptic coercive partial differential equations: application to transport and continuum mechanics*, Archives of Computational Methods in Engineering 15.3 (2008), p. 229.

[314] M. REED and B. SIMON, *Methods of modern mathematical physics. vol. 1. Functional analysis*. Academic New York, 1980.

[315] R. T. ROCKAFELLAR, *Coherent approaches to risk in optimization under uncertainty. OR Tools and Applications: Glimpses of Future Technologies*. Informs, 2007, pp. 38–61.

[316] R. T. ROCKAFELLAR and J. O. ROYSET, *On buffered failure probability in design and optimization of structures*, Reliability engineering & system safety 95.5 (2010), pp. 499–510.

[317] R. T. ROCKAFELLAR and S. URYASEV, *Conditional value-at-risk for general loss distributions*, Journal of banking & finance 26.7 (2002), pp. 1443–1471.

[318] R. T. ROCKAFELLAR, S. URYASEV, et al., *Optimization of conditional value-at-risk*, Journal of risk 2 (2000), pp. 21–42.

[319] P. OF THE ROYAL INSTITUTE OF BRITISH ARCHITECTS, <http://www.ribapylondesign.com/home>.

[320] W. RUDIN, *Functional Analysis*. McGraw-Hill, 2006.

[321] J. SALENÇON, *Handbook of continuum mechanics: General concepts thermoelasticity*. Springer Science & Business Media, 2012.

[322] F. SANTAMBROGIO, *Optimal transport for applied mathematicians*. Birkhäuser, 2015.

[323] D. SARKER, E. TOYSERKANI, O. O. IBHADODE, F. LIRAVI, P. RUSSO, and K. TAHERKHANI, *Metal additive manufacturing* (2021).

[324] S. A. SAUTER and C. SCHWAB, *Boundary element methods*, Boundary Element Methods (2011), pp. 183–287.

[325] A. SAVIN, *Probability distributions and valence shells in atoms. Reviews of Modern Quantum Chemistry: A Celebration of the Contributions of Robert G Parr (In 2 Volumes)*. World Scientific, 2002, pp. 43–62.

[326] R. I. SAYE and J. A. SETHIAN, *A review of level set methods to model interfaces moving under complex physics: Recent challenges and advances*, Handbook of Numerical Analysis 21 (2020), pp. 509–554.

[327] C. SCHWAB and R. A. TODOR, *Karhunen–Loève approximation of random fields by generalized fast multipole methods*, Journal of Computational Physics 217.1 (2006), pp. 100–122.

[328] T. SÉJOURNÉ, J. FEYDY, F.-X. VIALARD, A. TROUVÉ, and G. PEYRÉ, *Sinkhorn divergences for unbalanced optimal transport*, arXiv preprint arXiv:1910.12958 (2019).

[329] T. SÉJOURNÉ, G. PEYRÉ, and F.-X. VIALARD, *Unbalanced Optimal Transport, from theory to numerics*, arXiv preprint arXiv:2211.08775 (2022).

[330] S. SELVAKUMAR, K. ARULSHRI, K. PADMANABAN, and K. SASIKUMAR, *Design and optimization of machining fixture layout using ANN and DOE*, The International Journal of Advanced Manufacturing Technology 65 (2013), pp. 1573–1586.

[331] J. A. SETHIAN, *Fast marching methods*, SIAM review 41.2 (1999), pp. 199–235.

[332] J. A. SETHIAN and A. WIEGMANN, *Structural boundary design via level set and immersed interface methods*, Journal of computational physics 163.2 (2000), pp. 489–528.

[333] J. A. SETHIAN, *Level set methods and fast marching methods: evolving interfaces in computational geometry, fluid mechanics, computer vision, and materials science*. Vol. 3. Cambridge university press, 1999.

[334] A. SHAPIRO, D. DENTCHEVA, and A. RUSZCZYNSKI, *Lectures on stochastic programming: modeling and theory*. SIAM, 2021.

[335] K. SHOEMAKE, *Animating rotation with quaternion curves*. ACM SIGGRAPH computer graphics. Vol. 19. 3. ACM, 1985, pp. 245–254.

[336] O. SIGMUND, *A 99 line topology optimization code written in Matlab*, Structural and multidisciplinary optimization 21.2 (2001), pp. 120–127.

[337] O. SIGMUND, *On the design of compliant mechanisms using topology optimization*, Journal of Structural Mechanics 25.4 (1997), pp. 493–524.

[338] O. SIGMUND and K. MAUTE, *Topology optimization approaches*, Structural and Multidisciplinary Optimization 48.6 (2013), pp. 1031–1055.

[339] G. A. DA SILVA, E. L. CARDOSO, and A. T. BECK, *Comparison of robust, reliability-based and non-probabilistic topology optimization under uncertain loads and stress constraints*, Probabilistic Engineering Mechanics 59 (2020), p. 103039.

[340] K. SILVA, R. SIVAPURAM, S. RANJBARZADEH, R. GIORIA, E. SILVA, and R. PICELLI, *Topology optimization of stationary fluid–structure interaction problems including large displacements via the TOBS-GT method*, Structural and Multidisciplinary Optimization 65.11 (2022), p. 337.

[341] A. W. SNYDER, J. D. LOVE, et al., *Optical waveguide theory*. Vol. 175. Chapman and hall London, 1983.

[342] J. SOKOŁOWSKI and A. ZOCHOWSKI, *On the Topological Derivative in Shape Optimization*, SIAM Journal on Control and Optimization 37.4 (1999), pp. 1251–1272.

[343] J. SOKOŁOWSKI and J.-P. ZOLÉSIO, *Introduction to shape optimization*. Springer, 1992.

[344] J. SOLOMON, F. DE GOES, G. PEYRÉ, M. CUTURI, A. BUTSCHER, A. NGUYEN, T. DU, and L. GUIBAS, *Convolutional wasserstein distances: Efficient optimal transportation on geometric domains*, ACM Transactions on Graphics (TOG) 34.4 (2015), pp. 1–11.

[345] O. STEINBACH, *Space-time finite element methods for parabolic problems*, Computational methods in applied mathematics 15.4 (2015), pp. 551–566.

[346] J. STRAIN, *Semi-Lagrangian methods for level set equations*, Journal of Computational Physics 151.2 (1999), pp. 498–533.

[347] J. U. SURJADI, L. GAO, H. DU, X. LI, X. XIONG, N. X. FANG, and Y. LU, *Mechanical metamaterials and their engineering applications*, Advanced Engineering Materials 21.3 (2019), p. 1800864.

[348] K. SVANBERG, *The method of moving asymptotes—A new method for structural optimization*, International journal for numerical methods in engineering 24.2 (1987), pp. 359–373.

[349] V. SVERÁK, *On optimal shape design*, Journal de mathématiques pures et appliquées 72.6 (1993), pp. 537–551.

[350] A. SZABO and N. S. OSTLUND, *Modern quantum chemistry: introduction to advanced electronic structure theory*. Courier Corporation, 2012.

[351] G. TAPIA, A. H. ELWANY, and H. SANG, *Prediction of porosity in metal-based additive manufacturing using spatial Gaussian process models*, Additive Manufacturing 12 (2016), pp. 282–290.

[352] R. TEMAM and A. MIRANVILLE, *Mathematical modeling in continuum mechanics*. Cambridge University Press, 2005.

[353] J. F. THOMPSON, B. K. SONI, and N. P. WEATHERILL, *Handbook of grid generation*. CRC press, 1998.

[354] L. C. TORRES, L. M. PEREIRA, and M. H. AMINI, *A survey on optimal transport for machine learning: Theory and applications*, arXiv preprint arXiv:2106.01963 (2021).

[355] E. A. TRÄFF, O. SIGMUND, and N. AAGE, *Topology optimization of ultra high resolution shell structures*, Thin-Walled Structures 160 (2021), p. 107349.

[356] F. TRÖLTZSCH, *Optimal control of partial differential equations: theory, methods, and applications*. Vol. 112. American Mathematical Soc., 2010.

[357] Y.-H. R. TSAI, *Rapid and accurate computation of the distance function using grids*, Journal of Computational Physics 178.1 (2002), pp. 175–195.

[358] N. VAN GOETHEM and A. NOVOTNY, *Crack nucleation sensitivity analysis*, Mathematical Methods in the Applied Sciences 33.16 (2010), pp. 1978–1994.

[359] G. N. VANDERPLAATS and F. MOSES, *Structural optimization by methods of feasible directions*, Computers & Structures 3.4 (1973), pp. 739–755.

[360] F. WANG, B. S. LAZAROV, and O. SIGMUND, *On projection methods, convergence and robust formulations in topology optimization*, Structural and Multidisciplinary Optimization 43.6 (2011), pp. 767–784.

[361] J. WANG, R. GAO, and Y. XIE, *Sinkhorn distributionally robust optimization*, arXiv preprint arXiv:2109.11926 (2021).

[362] M. Y. WANG, X. WANG, and D. GUO, *A level set method for structural topology optimization*, Computer methods in applied mechanics and engineering 192.1-2 (2003), pp. 227–246.

[363] Y. WANG, J. GAO, and Z. KANG, *Level set-based topology optimization with overhang constraint: Towards support-free additive manufacturing*, Computer Methods in Applied Mechanics and Engineering 339 (2018), pp. 591–614.

[364] J. WEIDMANN, *Linear operators in Hilbert spaces*. Vol. 68. Springer Science & Business Media, 2012.

[365] F. WEIN and M. STINGL, *A combined parametric shape optimization and ersatz material approach*, Structural and Multidisciplinary Optimization 57 (2018), pp. 1297–1315.

[366] C. WEINGARTEN, D. BUCHBINDER, N. PIRCH, W. MEINERS, K. WISSENBACH, and R. POPRAWE, *Formation and reduction of hydrogen porosity during selective laser melting of AlSi10Mg*, Journal of Materials Processing Technology 221 (2015), pp. 112–120.

[367] W. WIESEMANN, D. KUHN, and M. SIM, *Distributionally robust convex optimization*, Operations Research 62.6 (2014), pp. 1358–1376.

[368] J. WU, O. SIGMUND, and J. P. GROEN, *Topology optimization of multi-scale structures: a review*, Structural and Multidisciplinary Optimization (2021), pp. 1–26.

[369] Q. XIA and T. SHI, *Topology optimization of compliant mechanism and its support through a level set method*, Computer Methods in Applied Mechanics and Engineering 305 (2016), pp. 359–375.

[370] Q. XIA, M. Y. WANG, and T. SHI, *A level set method for shape and topology optimization of both structure and support of continuum structures*, Computer Methods in Applied Mechanics and Engineering 272 (2014), pp. 340–353.

[371] Y. M. XIE, *Generalized topology optimization for architectural design*, Architectural Intelligence 1.1 (2022), p. 2.

[372] S.-Q. XIN, B. LÉVY, Z. CHEN, L. CHU, Y. YU, C. TU, and W. WANG, *Centroidal power diagrams with capacity constraints: Computation, applications, and extension*, ACM Transactions on Graphics (TOG) 35.6 (2016), pp. 1–12.

[373] T. YAMADA, K. IZUI, S. NISHIWAKI, and A. TAKEZAWA, *A topology optimization method based on the level set method incorporating a fictitious interface energy*, Computer Methods in Applied Mechanics and Engineering 199.45-48 (2010), pp. 2876–2891.

[374] Q. YE, Y. GUO, S. CHEN, N. LEI, and X. D. GU, *Topology optimization of conformal structures on manifolds using extended level set methods (X-LSM) and conformal geometry theory*, Computer Methods in Applied Mechanics and Engineering 344 (2019), pp. 164–185.

[375] G. H. YOON, *Stress-based topology optimization method for steady-state fluid–structure interaction problems*, Computer Methods in Applied Mechanics and Engineering 278 (2014), pp. 499–523.

[376] G. H. YOON, *Topology optimization for stationary fluid–structure interaction problems using a new monolithic formulation*, International journal for numerical methods in engineering 82.5 (2010), pp. 591–616.

[377] M. S. YOUSAF, M. BUJNY, N. ZURBRUGG, D. DETWILER, and F. DUDDECK, *Similarity control in topology optimization under static and crash loading scenarios*, Engineering Optimization (2020), pp. 1–16.

[378] W. ZHANG, L. ZHAO, and S. CAI, *Shape optimization of Dirichlet boundaries based on weighted B-spline finite cell method and level-set function*, Computer Methods in Applied Mechanics and Engineering 294 (2015), pp. 359–383.

[379] W. ZHANG and Z. KANG, *Robust shape and topology optimization considering geometric uncertainties with stochastic level set perturbation*, International Journal for Numerical Methods in Engineering 110.1 (2017), pp. 31–56.

[380] H.-K. ZHAO, S. OSHER, and R. FEDKIW, *Fast surface reconstruction using the level set method. Variational and Level Set Methods in Computer Vision, 2001. Proceedings. IEEE Workshop on*. IEEE. 2001, pp. 194–201.

[381] H. ZHAO, *A fast sweeping method for eikonal equations*, Mathematics of computation 74.250 (2005), pp. 603–627.

[382] X. ZHAO, M. ZHOU, O. SIGMUND, and C. S. ANDREASEN, *A “poor man’s approach” to topology optimization of cooling channels based on a Darcy flow model*, International Journal of Heat and Mass Transfer 116 (2018), pp. 1108–1123.

[383] J. ZHEN, D. KUHN, and W. WIESEMANN, *Mathematical foundations of robust and distributionally robust optimization*, arXiv preprint arXiv:2105.00760 (2021).

[384] J. ZHOU and H.-L. TSAI, *Porosity formation and prevention in pulsed laser welding* (2007).

[385] Y. ZHU, X. TIAN, J. LI, and H. WANG, *The anisotropy of laser melting deposition additive manufacturing Ti-6.5 Al-3.5 Mo-1.5 Zr-0.3 Si titanium alloy*, Materials & Design 67 (2015), pp. 538–542.

[386] Y. ZHU and A. C. CANGELLARIS, *Multigrid finite element methods for electromagnetic field modeling*. Vol. 28. John Wiley & Sons, 2006.

[387] C. ZIEMIAN, M. SHARMA, and S. ZIEMIAN, *Anisotropic mechanical properties of ABS parts fabricated by fused deposition modelling*, Mechanical engineering 23 (2012), pp. 159–180.

# Index

$\Gamma$ -convergence, 216  
additive manufacturing, 141  
adjoint state, 47  
ambiguity set, 105  
Céa's method, 47  
Cahn-Hilliard energy, 180  
capacity, 194  
    Neumann, 196  
coarea formula, 157  
compliance, 37  
conductivity equation, 26  
conjugate point, 120  
constitutive law, 33  
correlation, 114  
covariance, 114  
curvature  
    mean, 77  
    principal, 77  
density function, 61  
density-based topology optimization, 60  
distance  
    geodesic, 76  
dripping effect, 144  
Eikonal equation, 121  
elastic energy, 36  
elastic material, 33  
    isotropic, 33  
    orthotropic, 33  
    transversely isotropic, 34  
electric motor, 250  
Electron Beam Melting (EBM), 141  
elliptic regularity, 79  
equi-coercivity, 217  
Eulerian derivative, 45  
filter, 62  
Frobenius inner product, 11  
fundamental solution  
    Laplace operator, 160  
    linear elasticity operator, 162  
Fused Filament Fabrication (FFF), 141  
Green's formula, 78  
Green's function, 160  
growth condition, 46  
Hadamard's boundary variation method, 41  
Hartree-Fock model, 233  
Hausdorff distance, 11  
heat exchanger, 225  
Hilbert-Schmidt operator, 113  
Hilbertian method, 54  
homogenization, 39  
Hooke's tensor, 33  
implicit function theorem, 79  
inhomogeneity  
    diametrically small, 167  
    thin, 167  
    tubular, 167  
interpolation law, 61  
Karhunen-Loëve decomposition, 112  
Lagrangian derivative, 45  
Laguerre diagram, 258  
Laplace-Beltrami operator, 76  
level set based mesh evolution method, 67  
level set method, 64  
linear elasticity, 29  
locally compact and separable metric space, 111  
maximum probability domain, 234  
Maxwell's equations, 243  
measure  
     $\mathbb{R}^m$ -valued, 110

positive, 110  
 probability, 110  
 mesh, 57  
 mode  
     guided, 244  
     radiating, 244  
     transverse electric, 244  
     transverse magnetic, 244  
 nanophotonic device, 241  
 normal vector, 76  
 observable, 231  
 overhang, 142  
 perimeter, 37  
     relative, 178  
     total, 178  
 plane strain, 30  
 plane stress, 30  
 Poisson's ratio, 33  
 porosity, 91  
 probability law, 97  
 projection  
     point, 120  
     set, 120  
 Radon measure  
      $\mathbb{R}^m$ -valued, 111  
     positive, 111  
 random field, 116  
     Gaussian, 116  
 ray, 120  
 remeshing, 58  
 Riesz representation theorem, 112  
 scaffold structure, 142  
 second fundamental form, 77  
 shape derivative  
     calculation, 43  
     definition, 41  
     structure, 42  
     surface form, 47  
     volume form, 47  
 shear modulus, 33  
 signed distance function, 119  
     geodesic, 188  
 SIMP law, 61  
 SIMP method, 60  
 skeleton, 120  
 Sobolev spaces, 12  
     exterior, 164  
     fractional, 163  
 spherical linear interpolation, 79  
 strain tensor, 30  
 stress tensor, 32  
 tangent  
     plane, 76  
     vector, 76  
 tangential  
     divergence, 76  
     gradient, 76  
 tensor product of Hilbert spaces, 113  
 thickness  
     anisotropic maximum, 138  
     maximum, 124  
     minimum, 123  
 topological derivative, 53  
     calculation, 172  
     definition, 53  
     numerical use, 72  
 transmission boundary conditions, 28  
 velocity method, 42  
 volume, 37  
 Wasserstein distance, 104  
 wave function, 229  
 waveguide, 244  
 weak \* convergence of measures, 112  
 Young's modulus, 33